Investigation and Control of Gigahertz Frequency Spin Wave Dynamics in Magnonic Crystals

Thesis submitted for the degree of

Doctor of Philosophy (Science)

in

Physics (Experimental)

by

Samiran Choudhury

Department of Physics

Jadavpur University

2019

CERTIFICATE FROM THE SUPERVISOR

This is to certify that the thesis entitled "Investigation and Control of Gigahertz Frequency Spin Wave Dynamics in Magnonic Crystals" submitted by Sri Samiran Choudhury who got his name registered on 26th April, 2016 for the award of Ph. D. (Science) degree of Jadavpur University, is absolutely based upon his own work under the supervision of Prof. Anjan Barman and that neither this thesis nor any part of it has been submitted for either any degree / diploma or any other academic award anywhere before.

Anjan Barman 28/7/19

(Signature of the Supervisor date with official seal)

Dr. Anjan Barman, Ph.D.
Senior Professor & Associate Dean (Faculty)
Dept. of Condensed Matter Physics and Material Sciences
S. N. Bose National Centre for Basic Sciences
Block-JD, Sector-III, Salt Lake, Kolkata-700106, India

মা, বাবা, দাদা, বৌমা, তিতলি, মামনি-কে.....

Abstract

Magnetically coupled and periodically modulated magnetic materials form a new class of artificial crystals known as magnonic crystals (MCs) where collective excitations of spin waves (magnons) can be used to carry and process information. Due to the low speed of propagation, spin waves (SWs) with frequencies in the range of high GHz have wavelengths in the nanometer regime, make MCs ideal candidates for cellular nonlinear networks and nanoscale on-chip data communications, including magnonic waveguides, SW filters, splitters, phase shifters and emitters. As a result, a new research field named magnonics has emerged which has the capability to replace current semiconductor technology. The aim of this thesis is to investigate and control the spin wave dynamics in ferromagnetic nanostructures by changing various physical and geometrical parameters such as material, shape, size, lattice spacing, lattice symmetry, and also strength and orientation of the external bias field. The static and dynamics magnetic properties of ferromagnet/nonmagnet heterostructures have been tailored by modulating external parameters such as magnetic field and electric field to develop low power consuming magnonic devices for on-chip microwave communication. The ultrafast spin dynamics have been investigated in different magnetic networks including patterned ferromagnetic structures as well as multilayered magnetic heterostructures. We have employed (1) broadband ferromagnetic resonance (FMR), (2) time-resolved magneto-optical Kerr effect (TRMOKE) magnetometer and (3) Brillouin light scattering (BLS) spectroscopy to probe the frequency-, time- and wavevector-resolved magnetization dynamics, respectively. The modulation of magnetic properties has been explored in three distinct genres of magnetic systems during this doctoral work:

I. 2D Magnetic Antidot Systems: We have investigated the effects of geometrical parameters and the applied magnetic field orientation on the spin wave properties in a two-dimensional array of $Ni_{80}Fe_{20}$ antidots in the form of 2D magnonic crystals.

II. 2D Bicomponent Magnetic Nanostructures: We have probed the modification of the spin dynamics in 2D bicomponent magnonic crystals (BMCs) where one ferromagnetic element is embedded periodically in another magnetic matrix with contrasting magnetic parameters (e.g. saturation magnetization). As a result, the coupling is enhanced between these two materials through their lateral interfaces. The

effects of geometrical parameters and the applied magnetic field orientation on the magnetization properties have been investigated.

III. Magnetic Heterostructures with Ultrathin Ferromagnetic Layers: We have further studied the dynamic magnetic properties in CoFeB/MgO heterostructures using magneto-electric effect by controlling perpendicular magnetic anisotropy present at CoFeB/MgO interfaces under the application of electric field (voltage). We have further investigated the reconfigurable magnonic band structure and band gap in a dynamic 1D magnonic crystal composed of CoFeB/MgO heterostructure under the influence of electric field. This can unlock a gateway to develop a new genre of MCs invoked by an energy-efficient stimulus, i.e. electric field which may play a key role in devicing spin-based magnonic circuits with ultralow power consuption.

List of Publications

I. Published/Submitted in Journals

A. Included in the Thesis

1. "Shape and Interface Induced Control of Spin Dynamics of Two-dimensional Bi-component Magnonic Crystals"
S. Choudhury, S. Saha, R. Mandal, S. Barman, Y. Otani and A. Barman, *ACS Appl. Mater. Interfaces* **8**,18339 (2016).

2. "Efficient Modulation of Spin Waves in Two-Dimensional Octagonal Magnonic Crystal"
S. Choudhury, S. Barman, Y. Otani and A. Barman, *ACS Nano* **11**, 8814 (2017).

3. "Active Control of Mode Crossover and Mode Hopping of Spin Waves in a Ferromagnetic Antidot Lattice"
S. Choudhury, S. Majumder, S. Barman, Y. Otani, and A. Barman, *Phys. Rev. Appl.* **10**, 064044 (2018).

4. "Controlled Evolution of Spin Waves in Unconventional Defective Honeycomb Antidot Lattices"
S. Choudhury, S. Barman, Y. Otani and A. Barman *J. Magn. Magn. Mater.* **489**, 165408 (2019).

5. "Anisotropic Spin Waves in Two-Dimensional Triangular Shaped Bi-Component Magnonic Crystal"
S. Choudhury, S. Pan, S. Barman, Y. Otani and A. Barman, *J. Magn. Magn. Mater.* **490**, 165484 (2019).

6. "Electric Field Control of Spin Waves in Ultrathin CoFeB Films"
B. Rana, **S. Choudhury**, K. Miura, H. Takahashi, A. Barman and Y. Otani (Communicated)

7. "Electric Field Controlled Dynamic Spin Wave Band Structure in Reconfigurable Magnonic Crystal"
S. Choudhury et al. (Manuscript to be submitted)

B. Not Included in the Thesis

8. "All Optical Study of Angle Dependent Mode Conversion and Mode Hopping in 2D Annular Antidot Lattice"
N. Porwal, A. De, S. Mondal, K. Dutta, **S. Choudhury**, J. Sinha, A. Barman and P. K. Datta (Communicated)

9. "Contrasting Hydration Behavior of Amphiphilic Solutes Heterogeneous Heterogeneity of Binary Mixtures"
D. Das Mahanta, S. I. Islam, **S. Choudhury**, D. Das, R. K. Mitra, and A. Barman, *J. Mol. Liq.* **290**, 111194 (2019)

10. "Shape Dependent High Frequency Spin-Wave Dynamics in Nanoscale Magnonic Crystals"
A. De, S. Mondal, **S. Choudhury**, S. Sahoo, S. Majumder, S. Barman, Y. Otani and A. Barman, *J. Magn. Magn. Mater.* **487**, 165263 (2019).

11. "All-Optical Detection of Interfacial Spin Transparency from Spin Pumping in β-Ta/CoFeB Thin Films"
S. N. Panda, S. Mondal, J. Sinha, **S. Choudhury** and A. Barman, *Sci. Adv.* **5**, eaav7200 (2019)

12. "Influence of Anisotropic Dipolar Interaction on the Spin Dynamics of $Ni_{80}Fe_{20}$ Nanodot Arrays Arranged in Honeycomb and Octagonal Lattices"
S. Mondal, S. Barman, **S. Choudhury**, Y. Otani and A. Barman, *J. Magn. Magn. Mater.* **458**, 95 (2018)

13. "Tunable Magnonic Spectra of Two-dimensional $Ni_{80}Fe_{20}$ Annular Antidot Lattices"
N. Porwal, S. Mondal, **S. Choudhury**, A. De, J. Sinha, A. Barman and P. K. Datta, *J. Phys. D: Appl. Phys.* **51**, 055004 (2018).

14. "Dependence of Interfacial Dzyaloshinskii-Moriya Interaction on Layer Thicknesses in Ta/Co-Fe-B/TaO_x Heterostructures from Brillouin Light Scattering"
A. K. Chaurasiya, **S. Choudhury**, J. Sinha and A. Barman, *Phys. Rev. Appl.* **9**, 014008 (2018).

15. "Extrinsic Spin Orbit Coupling Induced Large Modulation of Gilbert Damping Coefficient in CoFeB Thin Film on Graphene Stack with Different Defect Density"
S. Sinha, S. Pan, **S. Choudhury**, J. Sinha and A. Barman, *J. Phys. Chem C* **121**, 17442 (2017)

16. "All-optical Detection of the Spin Hall Angle in W/CoFeB/SiO_2 Heterostructures by Varying Tungsten Layer Thickness"
S. Mondal, **S. Choudhury**, N. Jha, A. Ganguly, J. Sinha and A. Barman, *Phys. Rev. B* **96**, 054414 (2017)

17. "Pseudo One-Dimensional Magnonic Crystals for High Frequency Nanoscale Devices"
C. Banerjee, **S. Choudhury**, J. Sinha and A. Barman, *Phys. Rev. Appl.* **8**, 014036 (2017)

18. “Efficient Terahertz Anti-Reflection Properties of Metallic Anti-Dot Structures”
K. Neeraj, **S. Choudhury**, D. Polley, R. Acharya, J. Sinha, A. Barman, and R. K. Mitra, *Opt. Lett.* **42**, 1764 (2017)

19. “Collective Hydration Dynamics in Some Amino Acid Solutions: A Combined GHz-THz Spectroscopic Study”
N. Samanta, D. Das Mahanta, **S. Choudhury**, A. Barman and R. K. Mitra, *J. Chem. Phys.* **146**, 125101 (2017)

20. “Bias Field Tunable Magnetic Configuration and Magnetization Dynamics in $Ni_{80}Fe_{20}$ Nano-cross Structures with Varying Arm Length”
K. Adhikari, **S. Choudhury**, R. Mandal, S. Barman, Y. Otani and A. Barman, *J. Appl. Phys.* **121**, 043909 (2017)

21. “Transition from Strongly Collective to Completely Isolated Ultrafast Magnetization Dynamics in Two-Dimensional Hexagonal Arrays of Nanodots with Varying Inter-Dot Separation”
S. Mondal, **S. Choudhury**, S. Barman, Y. Otani and A. Barman, *RSC Adv.* **6**, 110393 (2016)

22. “Direct Observation of Interfacial Dzyaloshinskii-Moriya Interaction in $W/CoFeB/SiO_2$ Heterostructures Using Brillouin Light Scattering”
A. K. Chaurasiya, C. Banerjee, S. Pan, S. Sahoo, **S. Choudhury**, J. Sinha and A. Barman, *Sci. Rep.* **6**, 32592 (2016)

23. “Dielectric Relaxations of (Acetamide + Electrolyte) Deep Eutectic Solvents in the Frequency Window, $0.2 \leq \nu/\mathrm{GHz} \leq 50$: Anion and Cation Dependence”
K. Mukherjee, A. Das, **S. Choudhury**, A. Barman, and R. Biswas, *J. Phys. Chem. B* **119**, 8063 (2015).

24. “Tunable Configurational Anisotropy in Collective Magnetization Dynamics in $Ni_{80}Fe_{20}$ Nanodot Arrays with Varying Dot Shapes”
B. K. Mahato, **S. Choudhury**, R. Mandal, S. Barman, Y. Otani and A. Barman, *J. Appl. Phys.* **117**, 213909 (2015).

25. “Non-reciprocal Spin Pumping in a Dual Spin Sink Magnetic Trilayer”
S. Pan, **S. Choudhury**, J. Sinha, and A. Barman (Communicated)

26. “Observation of Band Narrowing and Mode Conversion in Two-Dimensional Binary Magnonic Crystal”
N. Porwal, K. Dutta, S. Mondal, **S. Choudhury**, J. Sinha, A. Barman and P. K. Datta (Communicated)

II. Published/Submitted in Books

1. “Tunable picosecond magnetization dynamics in ferromagnetic nanostructures” **S. Choudhury**, S. Mondal, A. De and A. Barman, 21st century Nanoscience: A Handbook, Taylor & Francis Books, Inc. (Accepted).

Acknowledgements

When I joined S. N. Bose National Centre for Basic Sciences (SNBNCBS) in 2012 as a part of an integrated PhD (IPhD) programme, I knew nothing about the jargon “Research”! So, the journey from being a small city (Berhampore) student to a growing research scholar on the verge of accomplishing PhD is indeed a long but memorable one as the first quarter of my life gets completed. And, I absolutely cherish all the moments (irrespective of good or bad) that I have shared with others on the course of my life.

Firstly, I express my profound gratitude to my supervisor Prof. Anjan Barman for his excellent guidance throughout my PhD journey and also before that when I was a project intern. I clearly remember those early days when he was very meticulous (even now) about all the works that I presented no matter how insignificant it was. But back then, I was too young (I am still a Lilliput as compared to his stature) to understand the reason behind his agitation when I made any mistake (which I used to do very often). Now on the verge of completing my PhD, I can realize how much effort he has put into any work and he expects the same from each and every individual from the group. He is a perfect mixture of positivity and intelligence blended with deep insight, patience and a tinge of emotion. Overall, he gave me countless pep talks to cultivate proper research ethics with professionalism which will be always a great lesson for my future life.

I shall be always grateful to Dr. Jaivardhan Sinha for sharing in-depth knowledge of fabrication and deposition tools. He taught me each and every minute details regarding lithography with his immense patience and this lesson has built the backbone of my PhD life at SNBNCBS. I have never encountered such a polite and humble person in my life who used to say “sorry” even when I made any mistake! Afterwards, I also received great training from one of my seniors, Bivas da during my visit to RIKEN, Japan. He has always amazed me by his honest opinions and straight-forward reasoning while dealing with any research work. I thank Atin da for his sharing his experience and knowledge about fabrication with me. I sincerely thank Prof. Rajib Kumar Mitra and Dr. Manoranjan Kumar for giving me prudent advices during the seminars throughout my PhD.

I am extremely thankful to my teachers starting from my schooling where I got deeply influenced by Amrita didibhai, Dhruba dadabhai, Nimai dadabhai, Tapan Sir, Kalyan Sir, Jayanta Sir and Abhijit Sir. I was spellbound by Basudeb Sir, Debojyoti Sir and Nurul Sir as they taught me the simple way of learning any sophisticated topic by elucidating every layer of it with proper reasoning. During my graduation, Manab Sir, Basir Sir and

Krishnakali Madam and Samiran Sir (my doppelgänger in terms of the name!) and Sourav da have invoked the thrust to pursue my PhD. However, my best teachers have been my grandparents (দাদু ও দিদা) who always adored me with pure love and affection and taught me everything since my childhood. I will be always grateful to Uttam Sir as my teacher with enormous patience.

I am very lucky that I have got great friends since my very early age which requires a chronological order for acknowledgement. Starting with my first schooling, I met Soumendu and Ritam after which I built a strong bonding with Anindya (ভেকত্বক) who was very possessive about me and protected me from all sorts of trouble along with my other school friends Amartya and Saswata. Next, I became good friends with Sankarshan (পিকাই), Mustak in higher schooling. My life took a massive turn during my graduation when I met Subir (and উজ্জ্বলদা ও লক্ষণদা), Soumik (and উদয়দা), Newton (চুসকি), Tarun, Kalyan, Abhishek, Toton (ফোতন). We have created so much memorable moments throughout my graduation which gets further amplified by Tuli (ডাকাত). Subir, Tuli and Soumik never lost hope on me as they are the ones who always talked to me first keeping aside all their ego or anger as I was too lazy to call them and I can tell anything to them without having a second thought, even now. Later on, I came to a completely new environment at SNBNCBS leaving my hometown after 21 years, as an IPhD student, where I clearly remembered the very first day when the whole city went out of electricity, which bestowed me at the same time with new friends: Monalisa (মুন), Ayan (genius), Kausik (কচি/লাল্টু), Arka (ধড়িবাজ) and Subodha (সাহুজি মহারাজ). I have enjoyed many indelible memories with them during this time period. I express my gratitude to my SNBNCBS seniors: Debashish da (my badminton partner), Subhashis da, Biplab da, Sreeraj da, Shinde da (মরাঠী মাণুস), Supriya da, Asutosh da, Sagar da, Shaili, Sankar da (বিশেষজ্ঞ), Subhadip da (লালু), Aslam da, Rakesh da, Rajkumar da (সাধুদা), Arghya da; batchmates: Mahebub, Dhrimadri (খাটা), Suchetana, Debasmita, Damayanti, Priya, Suraka; and juniors: Balwant, Subhadip, Biswajit, Samir, Riju, Manjari (মন-চুরি), Imadul, Jayita, Sumanti, Didhiti, Anupam, Ananda (জমিদার), Anirban, Rituparna, Neeraj and Vishal. A very special thanks to the ladies: Chaoba di, Sayani di, Poonam di and especially Shauri di for tolerating all my nuisance and supporting me during any difficult time.

I sincerely thank Prof. YoshiChika Otani for providing us with various samples in collaboration. I have also been very lucky to interact and discuss with him during my

visit to RIKEN, Japan. I also thank Kondou-san, Kim-san, Jorge-san, Mingran, Florent and Heeman for sharing their knowledge with me. I thank Akash, Takian, Thomas and Obed for being a part of successful project that won the award for best Students'-led project proposal during the IEEE summer school in 2016. I also experienced my best tour during that summer school in Spain after which I took a memorable tour to Barcelona (Camp Nou) and Real Madrid (Santiago Bernabéu) football stadiums! I sincerely acknowledge Prof. Caroline A. Ross for insightful discussion during my visit to MIT, USA. I express my heartiest thanks to all my lab seniors: Arabinda da, Semanti di (and Nitish da), Susmita di, Ruma di, Bipul da, Kallol da (কেল্টো), Dheeraj da, Arnab da, Debanjan da (and Ishita di). I have to mention Chandrima di separately not only because of her affection and extreme tolerance towards my constant leg-pulling, but also due to her in-depth knowledge with a clear vision and relentless effort for any small or big work. Sometimes, she had applied her "kung fu" (জাপানি) on me being motivated by my pranks and chased me with her lethal weapon (ছাতা) which she used to carry 24×7! I would like to thank my lab colleagues: Sucheta, Santanu and Anulekha for sharing their knowledge with me. My lab juniors: Shubham, Pratap (বোল্ড), Amrit, Sourav (কাঁঠাল), Koustuv, Arundhati (ফাঁকিবাজ), Anuj, Amit (পার্থ), Neha, Neeraj, Avinash, Kartik and some of the project interns: Bikas, Biswajit, Daisy have created a great ambience in the lab. I cherish every moment that I have lived with my lab juniors-cum-friends: Sourav (খাজা), Sudip (চিডি) and Surya (পান্ডা) and I have argued and discussed with them over almost every issue that exists in this world while, constantly making fun of each other. In this context, I must thank the food apps "Zomato" and "Swiggy" for delivering delicious food at midnight. I express my heartiest gratitude to Sanjay da and his team in our students' canteen for preparing delicious meal every day reminding me of my home! I thank the students' mess committee (of which, I was also a member for two years) for running the canteen smoothly and efficiently. I also thank the institute canteen (Bhagirathi) and Dulal da and ভাই-দা for making/providing evening snacks.

I sincerely acknowledge all the staff of the technical cell at SNBNCBS: Dipankar da, Surajit da, Amit da and especially "Iron Lady" Urmi di for their assistance while using the characterization tools. Also, I am grateful to Shihoyama-san and Nakatomi-san for their help in the cleanroom despite the language barrier during my visit to RIKEN, Japan.

I express my heartiest gratitude to my parents for their unconditional love, support and trust. They have never lost hope on me and let me pursue whatever profession I opt in the future. My elder brother, Soumitra (দাদা) is been the sensible always since my childhood and he has constantly supported me with his unconditional love while, his wife (বৌমা/দিদিমনি) has understood me very well and always tried to convince other family members when I demand anything unwarranted! My niece Somdipa (তিতলি/বাঁদর) will always remain the "mitochondria" (powerhouse) of my life for her non-stop energy and love towards me. I will remain always indebted to "The Woman" Monalisa Singh Roy (পুঁটি/ম্যাডাম/মামনি) for tolerating me for all my nonsense and childish activities and she has taught me a very important lesson for my life as well as in profession: "agree to disagree"! She has always been there for me throughout my IPhD life and encouraged me to be myself with all her love while, arching her eyebrows during the fights between us (I always lost those verbal altercations because of her inevitable logic while, carrying the legacy of being a রাজপুত!). I cannot thank enough her family (কাকিমা, কাকু and especially দিদা) for their love, especially the food and that "Tea". Also, the two of us have tried to explore as many food joints/restaurants as possible to endeavour different cuisine available in Kolkata. To me, the wide range of food options with their rich flavours has made this cosmopolitan city one of the best in the country with a unique cocktail of modern and traditional cultures emulsified with diverse ethnicities. I will always remain grateful to my cousins Santu (and Priyanka বৌদি) and Tubai for being very good friends since my childhood. I also thank Anushka (বুড়ি) and her parents for their unconditional love and support.

Finally, I thank S. N. Bose National Centre for Basic Sciences for giving me the opportunity to work using the common research facilities in such a wonderful environment and providing me junior and senior research fellowships. Lastly, I also acknowledge various funding agencies including Council of Scientific and Industrial Research (CSIR), Department of Science and Technology (DST), Government of India and IEEE Magnetics Society for other funding during my PhD study.

Samiran Choudhury

S. N. Bose National Centre for Basic Sciences

Salt Lake, Kolkata, India

List of Abbreviations

AFM	Atomic force microscopy
ADL	: Antidot lattice
(A)FM	: (Anti) Ferromagnet
ASI	: Artificial spin ice
AGM	: Alternating gradient magnetometry
AHE	: Anomalous Hall effect
AR	: Antireflection
BLS	: Brillouin light scattering
BZ	: Brillouin zone
BG	: Bandgap
BBO	: Barium beta-borate
(B)MC	: (Bi-component) Magnonic crystal
cm	: Centimeter
CW	: Continuous wave
CPW	: Coplanar waveguide
CVD	: Chemical vapor deposition
DC (dc)	: Direct current
DE	: Damon–Eshbach
DMI	: Dzyaloshinskii-Moriya interaction
DW	: Domain wall
DUT	: Device under test
DMD	: Digital micromirror devices
DOF	: Depth of field
DPSS	: Diode pumped solid state laser
EBL	: Electron beam lithography
EBE	: Electron beam evaporation
EM	: Electromagnetic
EFO	: Electronic flame-off
EY	: Elliott-Yafet
ECMA	: Electric field controlled magnetic anisotropy

(FE)SEM	: (Field emission) scanning electron microscopy
EDXS	: Energy dispersive x-ray spectroscopy
EPD	: End point detection
EPMA	: Electron probe micro-analyzer
fs	: Femtosecond
FDM	: Finite difference method
FEM	: Finite element method
FMR	: Ferromagnetic resonance
FEG	: Field emission gun
FSR	: Free spectral range
FWHM	: Full width at half maximum
FE	: Ferroelectric
GMR	: Giant magnetoresistance
GSG	: Ground-signal-ground
GVD	: Group velocity dispersion
GHz	: Gigahertz
Hz	: Hertz
HWP	: Half wave plate
HAMR	: Heat assisted magnetic recording
HWHM	: Half width at half maximum
IP	: In plane
IPA	: Iso-propyl alcohol
IR	: Infrared
(I)SHE	: (Inverse) spin Hall effect
LLG	: Landau-Lifshitz-Gilbert
LBO	: Lithium triborate
LED	: Light emitting diode
ms	: Millisecond
mm	: Millimeter
mW	: Milliwatt
MAMR	: Microwave assisted magnetic recording
MFM	: Magnetic force microscopy

MTJ	: Magnetic tunnel junction
MO	: Microscope objective
MRAM	: Magneto-resistive random-access memory
MBFM	: Magnetostatic forward volume wave
MBVM	: Magnetostatic backward volume wave
MSSW	: Magnetostatic surface spin wave
ME	: Magneto-elastic
MW	: Microwave
MIBK	: Methyl isobutyl ketone
MHz	: Megahertz
ns	: Nanosecond
nm	: Nanometer
NA (N. A.)	: Numerical aperture
NC	: Nanochannel
OBD	: Optical bridge detector
OOP	: Out of plane
OOMMF	: Object oriented micromagnetic framework
ps	: Picosecond
pm	: Picometer
(i)PMA	: (Interfacial) Perpendicular magnetic anisotropy
(P)BS	: (Polarized) beam splitter
PCB	: Printed circuit board
PSSW	: Perpendicular standing spin wave
PVD	: Physical vapor deposition
PWM	: Plane wave method
Py	: Permalloy
(P)MMA	: (Poly)methyl methacrylate
QHE	: Quantum Hall effect
r.i.	: Refractive index
rpm	: Revolution per minute
RF (rf)	: Radio frequency
RR	: Retro reflector

RT	: Room temperature
SOT	: Spin-orbit torque
SHG	: Second harmonic generator
SAW	: Surface acoustic wave
(SW)WG	: (Spin wave) Waveguide
SOC	: Spin-orbit coupling
SOI	: SOI: Spin-orbit interaction
SSE	: Spin Seebeck effect
SIMS	: Secondary ion mass spectroscopy
STO	: Spin-torque oscillator
STT	: Spin transfer torque
SW	: Spin wave
SHA	: Spin Hall angle
SL	: Stripline
SNA	: Scalar network analyzer
SNR	: Signal to noise ratio
SLM	: Spatial light modulators
SQUID	: Superconducting quantum interference device magnetometry
(TR)MOKE	: (Time resolved) Magneto-optical Kerr effect
TEM	: Transmission electron microscopy
THz	: Terahertz
TMR	: Tunnelling magnetoresistance
TOM	: Torsion oscillating magnetometry
(T)FPI	: (Tandem) Fabry-Pérot interferometer
UV	: Ultraviolet
VCMA	: Voltage controlled magnetic anisotropy
VSM	: Vibrating sample magnetometry
VNA	: Vector network analyzer
XRD	: X-ray diffraction
YIG	: Yttrium iron garnet
μs	: Microsecond
μm	: Micrometer or micron

Å	: Angstrom
i.e.	: That is
e.g.	: For example
viz.	: In other words
vs.	: versus

List of Figures

Table of Contents

Chapter 1

1. Introduction

"Always ameliorating"

When the earth ages more than 4.5 billion years, the human race have always found its way to survive with a better lifestyle than the other living species. This has become possible through a series of advancement in technology and communication with the aid of science. The invention of several electrical tools like transistors [1], optical fibers [2] etc. has advanced the communication world through the digitization of the knowledge and information. As a consequence, the internet [3] has spread its web over the whole world by providing with tonnes of information to everyone. The exponential growth and development of high-performance electronic devices have boosted the impact of science in everyday life.

The ever-increasing demand of semiconductor devices [4] with high data processing speed and capacity has led to the developments of electronic components of high integration density which further gets enhanced when coupled with the advances in the optical communication. However, the semiconductor industry is expected to deal with a great number of difficulties [5] in the future due to the obstacles like miniaturization of device dimension as well their operational speed limit [6]. This reduction in size becomes more complex due to a fundamental drawback which is the waste of energy in the form of heat (Joule heating) during any kind of kinetic motion of electrons. This is an inherent property in any electronic components which causes an increase in the power consumption of such devices and this problem becomes more fatal at the time of size reduction. Several alternatives such as an all-optical circuit with photonic crystals as the base and/or phononic crystals in the field of acousto-optics have been evolved during last few decades to overcome these long-standing problems with the electrical communication. Photonic (phononic) [7-12] crystals are optical (acoustic) counterparts of the conventional atomic crystals where light (acoustic wave) are used to manipulate the frequency band structures [7,13-18] in these artificial lattices by periodically tuning dielectric constant. Thus, these artificial materials offer higher spectral selectivity

leading to the application in the various promising field of nanodevices such as waveguides [19-26], integrated circuits [2,27-31] etc.

However, the magnetism has evolved and spread its web throughout the whole world due to its propitious and rapid advancement ever since the invention of giant magnetoresistance (GMR) [32-34]. As a result, a number of subways e.g., spintronics [35-37], magnonics [38-42] and the interdisciplinary combinations of the generic streams such as spin-orbitronics [43-45], magnon-spintronics [46], magneto-electronics [47,48], magneto-photonics [49,50], magneto-phononics [51-53], spin mechatronics [54] have emerged unclogging the difficulties of the semiconductor-based industry [4,6]. Spintronics at its core has the concept of the manipulation of spin degrees of freedom [55] of the electron by diverse non-identical methods e.g., spin transfer torque (STT) [56-58] leading towards current-induced switching [59,60], (inverse) spin Hall effect ((I)SHE) [61-66] revealing a new path to generate as well as probe pure spin current, spin pumping effect [67-69] to induce local or non-local spin injection [70], spin Seebeck effect (SSE) [71,72] and spin Nernst (-Ettingshausen) effect [73-77] to produce spin current by thermal flow of electrons or utilizing magnetostriction effect [78,79] to induce magnetization by applying strain. Recently, Dzyaloshinskii Moriya interaction (DMI) [80,81], electric field controlled [82-92] magnetic properties have boosted the growth of spintronics in the development of transmission, storage and processing of information [1,93-95] based on the magnetization state of a system.

Magnonics [39] has been phenomenal over the last decade where the transfer of spin angular momentum in the form of spin waves (SWs) [96] or magnons (Bosons with spin 1) [97] occurs inside the magnetic materials instead of using electrical charge current or the thermal means. The pillars of magnonics [41] are termed as the magnonic crystals (MCs) [98] formed by periodic magnetic structures which have the advantages like non-volatility and faster data processing speed with less power consumption integrated with a much higher density as opposed to the modern semiconductor technology. Classically, the SWs can be realized as a phase coherent precession of microscopic magnetization vectors of the concerned magnetic medium. Ever since the realization of the concept of SW, these spin counterparts of the electrons are considered as the potential information carriers for future computing devices analogous to quantum computation providing a passage for spin transfer over macroscopic space in a Joule heating free environment.

Thus, an analogy can be drawn between electromagnetic (EM) waves and SWs except the fact that the feasible wavelength for the SWs are few orders of magnitude smaller than that of EM waves. This, in fact, boosts the possibility of manufacturing on-chip microwave communication devices at the nanoscale with low power consumption which can contribute to the sustainable green information technology world. Thus, the ever-increasing demand of obtaining SW-based communication system, control and manipulation of functionalities of such MCs are required which can be achieved by tuning the magnon bands and bandgaps via wide variety of parameter including the physical quantities like the choice of combination of the magnetic (and/or non-magnetic) materials, the geometrical parameters such as shape, size, thickness, periodic spacing and arrangement of the magnetic systems or by playing with the strength and orientation of the magnetic field applied to the material. Recently, the invention of topologically protected magnetic skyrmion lattices [99-101] and the artificial spin ice systems [102-107], as well as three-dimensional magnetic systems[108-110], are booming with new prospects in the fundamental physics and technologies to discover the possibilities of inventing next generation SW-based logic devices, magneto-bio medics [111,112]. Nowadays, a great deal of research is going on to hybridize different aspects of the magnetic materials e.g. magnonic, photonic, phononic crystals in order to increase the range of tuning parameters to create a whole new bunch of artificial crystals such as magneto-photonic or mag-phonic crystals [53] etc. Recently, a new genre of hybrid organic-inorganic materials has demonstrated [49,113] their auspicious facets in spin-optoelectronics [24] effectuating the vision of building a spin-based transistor one step closer to reality. Unlike EM waves or acoustic or photonic waves, SWs possess distinct dispersion behaviours that depend upon either the applied magnetic field orientation or the thickness of the magnetic material e.g. in case of dipole dominated SWs in thin ferromagnetic (FM) thin films, the dispersions stoutly relies on the relative orientation between the magnetic field and SW propagation (wave) vector which gives rise to Damon Eshbach (DE) [114] or backward volume (BV) [115,116] behaviour when the magnetic field is perpendicular to the wave vector both lying in the same plane while forward volume (FV) [117] nature can be observed when magnetic field becomes out of plane to the SW propagation and mixed breed of these species can be observed depending upon the magnetic field orientation. On the other hand,

perpendicular standing SWs with different nodal planes can be found across the thickness of the FM films. As a whole, the magnonic crystals being the pillar of magnonics [41] can pave the future pathway to tailor ultrafast transmission of information under miniaturized spin devices which necessitates a comprehensive understanding of fundamental properties and also technological aspects of SWs such as frequency band dispersion [118], band structures [119], amplitude [120], phase [121], group velocity [122], non-reciprocity [123,124], anisotropy [125] etc. under various experimental [126-129] and theoretical appliances [110,130] to provide SWs with a puissant drive towards the future multifunctional efficacious communication systems.

In the succeeding paragraphs, an aphoristic overview of a few salient aspects of the research field magnon-spintronics is delineated which has instigated the present dissertation work. Eventually, the silhouette of the content of the thesis will be bestowed.

1.1. Thin Films

Since the demonstration of the principle of magnetic recording in the last century, the science community has indulged into developing high-density magnetic storage media concerted with fast, reproducible and controlled magnetization switching for magnetic reading and writing. This has sparked a substantial enthrallment in the amelioration of the magnetic switching properties, magnetic anisotropy, interlayer interactions and magnetic damping in diverse mono or multi-layered magnetic heterostructures. In the last century, researchers were tangled with the magnetic drum, tape, disk and bubble alike memory systems where the memory was used to store by the presence and withdrawal of magnetic domains. With the aid of GMR or tunnelling magnetoresistance (TMR) [131-135], the invention of longitudinal recording media such as thin single layered granular film comes under spotlight where magnetization orientation in each grain can be thought of as individual domain with in-plane magnetization refers to a single bit of information while this can be rewritten and retrieved by employing GMR or TMR based write and read heads [136,137]. However, this achievement soon received severe challenges in keeping pace with the increasing importunity of high storage density having altitudinous thermal stability primarily due to the superparamagnetic effect [138,139]. This backlash occurs during the reduction of grain size as the grains fail to retain the magnetic orientation due to random thermal vibration even at room

temperature while cross-talks between the magnetic bits also tend to become baleful. As an alternative, antiferromagnetically coupled media [34,140-142] consisting of magnetic layers antiferromagnetically coupled through a thin nonmagnetic film also receive a good amount of attention by removing the superparamagnetic bottleneck along with higher storage density. However, the magnetic materials in the form of single or multi-layered heterostructures with perpendicular magnetic anisotropy (PMA) [143-146] were introduced as imperious contenders in this field. Here, the magnetic anisotropy may originate from several different fountainheads e.g. the crystalline edifice (such as in Co, CoPt, CoCrPt) and also the shape and aspect ratio of patterned magnetic media. These PMA systems endeavour a high areal density of data storage [147] along with the bit patterned media [148-150] which are magnetostatically as well as thermally much more stable than the earlier granular media. Consequently, a meticulous investigation of such PMA materials was pulled off in Co [151], CoCr [152], CoPt [153], CoCrPt [154] films and more recently on multi-layered heterostructures such as Co/Pd [150], Co/Pt [155], Co/Ni [156] systems as a high storage density along with improved interfacial anisotropy leading towards higher and tunable PMA can be attained in these multilayers. Nevertheless, the PMA has to contend with the magnetostatic energy of the system which may eventually give rise to fascinating phenomena such as stripe domain structures depending upon the film thickness over a critical value and plenty of research work [157-164] have been carried out on the formation and evolution of such stripe domains and their SW response in various metallic heterostructures.

The most critical issue with the PMA systems is the requirement of a very high magnetic field to switch the magnetization [144] and later on, heat-assisted magnetic recording (HAMR)[165,166] has been proposed to overcome this barrier by tuning the anisotropy locally by applying local heating preferably a laser source to switch the magnetization. However, implementation of such focussed laser beam for the development of practical SW based devices is very challenging until very recently microwave assisted magnetic recording (MAMR) [167,168] technology has snatched all the eyeballs due to its astounding storage density as well as thermal stability.

Further, low power manipulation of magnetization in nanoscale systems is an ever-demanding issue and the current advances in spin transfer induced switching

mechanism have stimulated the evolution of magnetic random-access memory (MRAM) [169,170]. Nevertheless, it faces the thermalization backlash and in order to overpower this obstacle, the magnetoelectric effect [90,92,171] i.e. the electric field control of magnetic properties such as magnetic anisotropy etc. can be one of the feasible and intriguing avenues. Multitudinous efforts have been attempted e.g. modulation of magnetostriction in multi-layered systems with piezoelectric substrates, interplaying with the Curie temperature of the FM semiconductors, tailoring the interlayer properties like interlayer exchange or exchange bias, magnetoelectric effect in single phase multiferroics or composites such as ferroelectric (FE)/FM heterostructures, interfacial magnetic anisotropy at the dielectric/FM systems. Among these riveting approaches, direct electric field effects on the magnetic properties of ultrathin FM films have been proliferated in the recent time because of their tremendous potential in today's prevailing MgO-based magnetic tunnel junctions (MTJs) [132,172,173] due to the ultralow power consumption along with their dynamic control over magnetization and thermal stability.

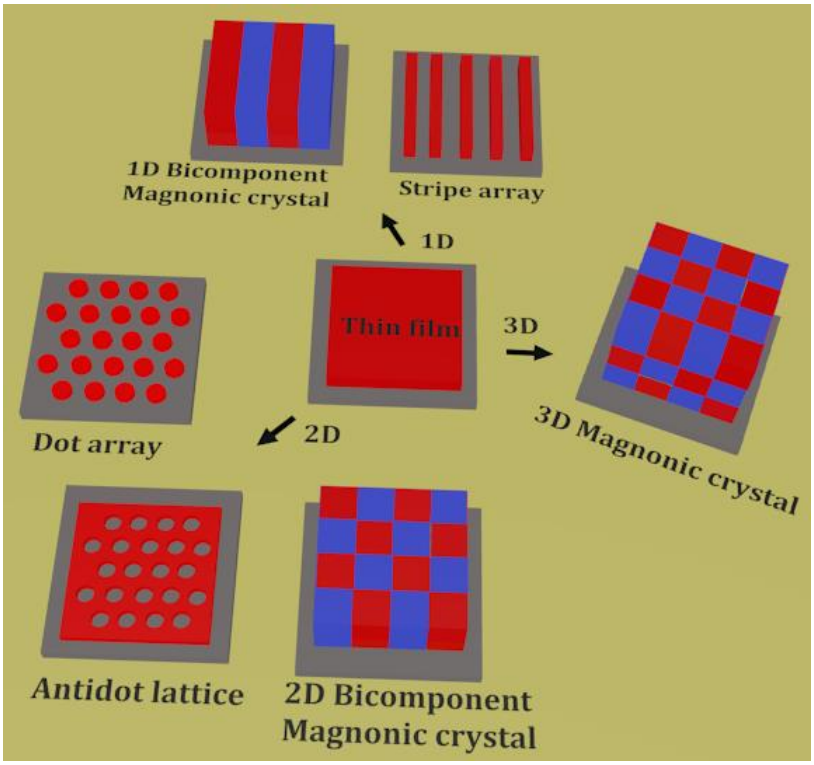

Figure 1.1. Schematics of different genres of magnonic crystals (MCs) in 1-, 2- and 3D fabricated from ferromagnetic (FM) material(s).

1.2. Magnonic Crystals (MCs)

As mentioned previously, the notion of SWs in a periodically patterned magnetic medium was introduced long back and since then these periodically modulated magnetic media namely MCs [174,175] have been anticipated to have the pioneering impact in a broad spectrum of magnetic device applications where SWs are employed to convey and process information at different length scales ranging from micro- to nano-regime. However, the billows of interest in manipulating the static and dynamic properties of MCs have started almost three decades ago [176-178]. Subsequently, a newly born and blisteringly evolving research field called magnonics [40] has been introduced, where numerous theoretical and experimental investigations have been conducted in such MCs with periodic distribution of various materials with diverse material parameters e.g. saturation magnetization, magnetic anisotropy [179,180] or other external controllers like magnetic field [181], stress [182], charge current [121,183], electric field [171,184] etc. or by machining the material periodically to provoke the modulation in the magnonic band structures as well as SW propagation. So far, the materials which have been widely exploited on the research scale are yttrium iron garnet (YIG) [42] as an excellent insulating ferrimagnet with very small damping for SW propagation, metallic FMs and their alloys such as Ni [185], Fe [186] and Ni_xFe_{1-x} (commonly known as permalloy, Py) [187] is a soft magnet possessing very negligible magnetocrystalline anisotropy making it a robust material for patterning into all sorts of geometrical configuration, Co having a reasonably high magnetic moment while $Co_xFe_yB_{1-x-y}$ (CoFeB) [122,188] for its sensational applications in the present micro- and nanostructured devices such as in MTJs with high TMR values [135] even at room temperature and many other aspects. Typically, modulation of magnetic features in these MCs leads to the revamping in coercivity and switching field, induced anisotropy as well as collective behaviour of the constituent material in one-dimension (1D, e.g. array of stripes) [189-191] or two-dimension (2D such as array of dots or antidots or the combination of both) [192-199] or even in three-dimension (3D like array of spheres and self-standing particles or patterned magnetic systems) [109,200,201]. As a consequence, SWs get localized or confined due to the periodic distribution of local or internal magnetic field or coherent coupling according to the periodic arrangement (due to exchange or anisotropic dipolar interaction) which leads towards the conformation

of dispersive energy bands similar to the electronic band structures when arranged in a suitable lattice. These waves may also experience coherent scattering as well as Bragg reflection at specific wave vectors depending upon the periodicity revealing a tailored band structure with complete (direct or indirect or a combination of both) or partial bandgaps. A plethora of research studies have been carried out in the last two decades in the quest of efficient and bridled tailoring of the band structures present in these novel MCs, where the current progress in fabrication and lithography have made possible to design and periodically pattern the FM materials into intriguing MCs in 1D [202-205] or 2D [206-215] or even in 3D [109,200,201]. In the following, we review existing research works in 1-, 2- or 3D that have been exercised on that pursuit.

1.2.1. 1D Magnonic Crystals

Modulated ferromagnetic thin films with gap solitons were proposed in the early 1990s [216]. After one decade the focus shifted towards 1D and 2D arrays including the quasiperiodic and fractal magnetic structures [217,218]. The spectrum of magnons in closely packed 1D arrays of magnetic nanoelements i.e. nanowires and nanostripes (see Figure 1.1) also reveal magnonic band structure with Brillouin zone (BZ) boundaries determined by the artificial periodicity of the arrays while, homogeneously magnetized wire can also act as a spin waveguide (WG) that can channel, split, and manipulate sub-micrometer width SW beams analogous to the optical fiber in photonics. Early studies [129,219-222] were focused on 1D arrays of different magnetic materials such as NiFe, Co etc. to investigate their (non-) collective behaviour on the SW dynamics. Several experimental and theoretical studies of the magnonic band structure, as well as SW propagation, have been demonstrated [191,203,223,224] in various types of geometrically engineered 1D magnonic WGs.

1.2.2. 2D Magnonic Crystals

2D MCs can be categorized into different genres on the basis of the physical structure and the underlying physics and they are described below:

1.2.2.1. Ferromagnetic Dot Array

The SW frequency and wavelength can both be tailored by periodic modulation of exchange and dipolar field present inside an array of magnetic elements commonly known as FM dots (see Figure 1.1). Therefore, such unique systems have been

incorporated to utilize their characteristic SW for logic devices or non-volatile elements for information storage.

So far, the intense research on confined magnetic elements unveils distinct differences between their static and dynamic magnetic properties and their bulk counterpart. Due to confinement in various dimensions, the usual magnetic domain formation gets affected and several anisotropic energies (e.g. surface anisotropy, shape anisotropy, configurational anisotropy) come into the picture for periodically patterned dot arrays. This results in multi-resonance SW spectra corresponding to nonuniform magnon modes which strongly depend on the orientation of the external magnetic field and the inter-element interaction as well as the physical and geometrical aspects such as shape, size, thickness, lattice arrangement and periodicity or material(s) of the nanomagnets [128,225-229]. The magnetization dynamics in nanodot arrays also confirms a transition from a collective behaviour (i.e. uniform precessional SW mode) to completely isolated nature (observation of edge mode) of the individual nanodots due to the reduction in inter-element interaction strength which also affects the anisotropic contribution to the SW dynamics [125,187,230-234]. In addition, the shape of the individual nanomagnets also plays a crucial role in controlling the spin dynamics [235-238] due to the interplay of the stray field and internal field distributions.

1.2.2.2. Ferromagnetic Antidot (AD) Array

The introduction of periodic antidots (Ads, i.e. holes) into a continuous FM thin film is a very effective way to tailor their magnetic properties leading to non-uniform and complex magnetization dynamics. This nonuniformity can significantly contribute to the noise in the read sensor devices and may affect the ultrafast precessional switching of magnetic data storage elements. This has a very promising future in the modern SW-based applications, e.g. in microwave-assisted magnetic recording (MAMR) technology. FM AD lattices (ADLs), i.e. periodically arranged holes on an FM thin film (see Figure 1.1) are one of the strongest candidates for reconfigurable MCs because of higher SW propagation velocity and longer propagation distance for the SWs as compared to FM dot systems as these AD systems have some unique advantages over the array of magnetic dots at the deep nanoscale regime due to the absence of any small isolated magnetic entity. Consequently, these novel AD heterostructures do not suffer from the superparamagnetic bottleneck as opposed to the magnetic dot array structures. They

can also be considered as a potential candidate of magneto-photonic crystals because of their strong influence of the magnetic field on the light (phonon) coupling to the surface plasmons. Consequently, extensive research has been carried out to investigate the SW dynamics in 1-D and 2-D arrays of magnetic AD structures at different length scales using various methods ranging from numerical and theoretical techniques to several experimental tools [130,212,239,240]. The pattern induced splitting of surface and volume modes have been observed as the magnon spectra get strongly affected by the local modulation of the demagnetizing field around the ADs as well as the interlayer coupling [209,211,241-247]. Further, the field-controlled SWs revealing their filtering behaviour have been investigated in such SW waveguides (SWWGs) [248,249] where the SWs are strongly tailored by the field strength and its orientation or lattice periodicity or symmetry as well as the hole shape, size, thickness or the constituent material [197,214,215,250-253] which strongly affects the magnonic band structure [254-256] and the anisotropic nature of SWs due to the controlled engineering of the magnetostatic field distribution [122,257-266]. The introduction of various defects in the AD shape or its arrangement in one lattice [267-269] unravels a significant tunability in spin dynamics which may lead to next-generation MC-based microwave devices [208,270-275].

Recently, artificial quasicrystals have become an emerging topic of research as the most beneficial feature of quasi-periodicity is that it can combine perfectly ordered structures with purely point-diffractive spectra of arbitrarily high rotational symmetry leading to a range of different interesting features like branching in the band structure, self-similarity and scaling properties in the transmission spectra and unusual manifold rotational symmetry in the anisotropic contribution to the SWs [194,204,276-281].

1.2.2.3. Ferromagnetic Nanorings

FM nanorings can be identified as the combination of FM dot and AD systems viz. ADs fabricated inside each element of the FM dot array. Extensive research has been carried out on micro- and nanoscale magnetic rings [282-289] revealing the immense role of the inhomogeneous internal field at various regions leading to the SW confinement [290,291].

1.2.2.4. Bicomponent Magnonic Crystals (BMCs)

Recently, bicomponent magnonic crystals (BMCs) have emerged as the future metamaterials with vast application potentials. In case of BMC, one FM element is embedded into a matrix (or the continuous film) of another FM material viz. where two different magnetic materials are in direct contact with each other (see Figure 1.1) so that the dynamic dipole coupling is maximized due to the presence of exchange coupling at their interface. As a result, SWs are subjected to scattering at the interface between the two materials and can easily transmit through the interface and SWs can propagate across its entire structure with large group velocities.

Initial studies on 1-D BMCs have revealed [118,205,292,293] well-defined frequency bandgaps strongly dependent on their structural dimensions. Such functionality can lead to the tailoring of magnonic bandgap structure and thereby controlling the transmission of information carrying SWs in the nanoscale microwave devices [51,123,294]. However, the exploration of magnetic aspects in 2-D BMCs unveil various intriguing properties such as magnonic bandgap which can be efficiently controlled by magnetic field [119,195,295-301] making these systems suitable in cellular nonlinear networks and integrated magnonics [193,302,303] as the demagnetizing field as well as the exchange interaction at the interface of the two constituent FM elements play a crucial role in manipulating the magnon dynamics.

1.2.2.5. Topological Magnetic Solitons

During the intensive research on the static magnetic properties and internal domain configuration of micron-sized ferromagnetic disks, a highly interesting spin texture has been highlighted namely magnetic vortex. In such novel systems, curling of in-plane spin configuration is energetically favored with an out-of-plane magnetization appearing at the core of the vortex system giving rise to the chirality of the spin orientation as well as the polarity of the vortex core. A plethora of research works [304-321] has proved them to be ideal candidates for different SW logic devices.

Recently a different class of magnetic textures known as skyrmions has been discovered which also has a curling spin orientation analogous to the magnetic vortex. However, the spins inside a skyrmion rotate progressively radially inward or outward with a fixed chirality forming more like a whirl shape instead of in-plane curling like vortex [101]. Two typical types of magnetic skyrmions, i.e. Neel and Bloch types have been observed

which are primarily induced by interfacial Dzyaloshinskii-Moriya interaction (DMI) between atomic spins in non-centrosymmetric magnetic compounds or in thin films with broken inversion symmetry [322]. Recently, patterning of confined nanostructures with topologically protected skyrmion is being exploited even at ambient condition [99,323,324]. Making them ideal for future applications [100,325].

1.2.2.6. Artificial Spin Ice (ASI) Systems

Over long time, the possibility of the presence of magnetic monopoles have triggered the imagination of the scientific community as their existence can be reconciled with the quantum phenomena [326] where the observation of such magnetic monopoles can support the out-of-the-box models proposed in various fields of physics, e.g. string theory [327], grand unified theory in the particle physics. Similarly, different approaches have been initiated in the condensed matter physics to find out the presence of monopoles which share similarities with that in quantum mechanics in terms of an artificial frustrated system [328] namely artificial spin ice (ASI) structure [106] in the form of lithographically fabricated single-domain FM islands. There the dipolar interactions create a 2-D analogue to the spin ice. Here, both ice-like short-range correlations and absence of long-range correlations can be observed which are strikingly similar to the low-temperature state of spin ice. Such artificial frustrated magnets can provide an uncharted arena where the direct visualization of the physics of frustration can be possible. However, one of the most exciting and modest approaches is to predict the monopoles occurring as fractional quasiparticles inside pyrochlore spin ice [107] which are characterized by ice rules. In case of the tetrahedral coordination of the pyrochlore structure, two of the four Ising-type spins on the vertices point towards the tetrahedral centre as opposed to the other two spins [102,104,329,330] and this resembles the Pauling's ice rule [331] that determines the configuration of the proton ordering in water ice. The decay of a dipolar excitation into constituent monopoles provides the phenomenon of fractionalization [107,328,332] in 2D and 3D [333-336] via fractionally charged excitations in the quantum Hall effect [337,338]. However, the magnetic monopoles accompanied by Dirac strings [107,339-341] in such pyrochlore systems which are frustrated magnetic insulators have been realized [342,343]. However, the direct and real-time observations of emergent monopoles associated with the Dirac strings have been successfully demonstrated along with the exploitation of

their static and dynamic features in 2D or 3D [103,344-360]. Thus, the chiral control of magnetic charge to the magnetic charge path selectivity can provide an interesting tool leading to a new architecture for parallel computation. In addition, the magnetization dynamics in ASI systems made of square or interconnected kagome lattice [361-364] open up opportunities for further application of such systems in reprogrammable magnonics in both 2D and 3D [105,365-370].

1.2.3. 3D Magnetic Nanostructures

The inclusion of structural freedom in the third dimension for magnetic nanostructures (see Figure 1.1) has made more complex magnetic configurations possible with various unprecedented phenomena. The most difficult part of sample fabrication and detection of high-frequency dynamics are subjected to rigorous technological advancement as the 3D patterning gives more control points than 2D nanomagnets. Such 3D magnetic nanostructures can possess several fundamental aspects such as 3D racetrack memory and many other exquisite systems [108,109,371-374] which can create complex 3D networks of fascinating nanostructures unlocking a new computational paradigm.

Investigation of fundamental SW properties in these magnetic nanostructures has unlocked the possibility of constructing a number of novel SW-based devices such as magnonic waveguides [115,375-377], filters [378], splitters [379], valves [380], phase shifters [381], grating couplers [301], emitters [382,383], amplifiers [384], multiplexers [385] and interferometers [386-388]. In an MC, SWs of different frequencies can be harnessed for various logic operations [124] where magnon phase or density can be encoded in the form of information. While, the intermediate band gaps [51,272,292,293,300,376,389] in the magnonic band diagram are significant for SW to be used as filters as well as transistors [319,390], which can be controlled by applying electric fields to construct SW logic gates [391,392]. In case of reconfigurable or dynamic MC [365,393,394], which forms an attractive class of MC, it is possible to realize universal data processing units with switchable SW properties [386,395]. While, the single micropatterned waveguides are also important, where the SW channelling along the distribution of local magnetic field can be controlled by inducing different potentials such as magnetostatic potential [396], domain wall [397,398], local Oersted field [121], interfacial interactions [242] etc. The application of the electric field further modulates the SW phase, which can be implemented in SW logic gates [171], where the

output is processed by SW interference [386,391,392]. In addition to magnon-based elements, another important requirement is converter devices which efficiently interface the magnonic circuitry with spintronic and electronic environments. So far, the techniques that have been successfully improvised for magnon excitation (SW source) are inductive microwave technique, STT and SHE based magnon injection.

1.3. Objectives of the Thesis

The skeleton of this thesis is comprised of experimental and theoretical investigation of static and dynamic magnetization in diverse classes of MCs primarily novel 2D ADs and BMCs as well as multi-layered heterostructures with the aid of frequency- (broadband ferromagnetic resonance (FMR)), time- (time-resolved magneto-optical Kerr effect microscopy (TRMOKE)) and wavevector resolved (conventional Brillouin light scattering (BLS)) methods. The precise objectives of this research are to investigate the magnetic parameters and characterization of SW properties of the 2D MCs under the influence of kaleidoscopic geometrical parameters of the MCs, the external bias magnetic field strength and its orientation and also by employing an external electric field in case of some intriguing magnetic heterostructures and nanopatterns. Broadly, the investigated complex systems can be categorized as the following:

1. Periodic MCs in the form of arrays of ADs: the role of complex internal field distribution on the SW dynamics in periodically and their efficient modulation is investigated.
2. MCs as AD arrays with the heterodox arrangement of ADs: the influence of the geometrical configuration on the demagnetization field leading towards an efficient modulation of SWs in these maverick genres of MCs as a function of magnetic field orientation.
3. BMCs in the form of periodically arranged two interconnected dissimilar FM elements: the fascinating nature of the SWs due to the dynamic coupling between the constituent FM elements at their lateral interface and their tunability with the magnetic field strength and orientation.
4. Magnetic/non-magnetic insulator multi-layered heterostructures: the bridled modulation of the nature of propagating SWs with the external direct component (dc) of an external electric field due to the stark variation in the magnetic anisotropy at the FM/insulator interface.

5. Dynamic MCs having FM/insulator multi-layered nanostructures: Interesting response of magnon properties due to the electric (voltage) field controlled magnetic anisotropy (ECMA or VCMA) giving rise to an entirely new genre of MCs in magnonics.

References

[1] J. Bardeen, W. H. Brattain, Phys. Rev. 74 (1948) 230.
[2] F. Van Laere, G. Roelkens, M. Ayre, J. Schrauwen, D. Taillaert, D. Van Thourhout, T. F. Krauss, R. Baets, J. Light. Technol. 25 (2007) 151.
[3] B. M. Leiner, V. G. Cerf, D. D. Clark, R. E. Kahn, L. Kleinrock, D. C. Lynch, J. Postel, L. G. Roberts, S. Wolff, SIGCOMM Comput. Commun. Rev. 39 (2009) 22.
[4] R. C. Levin, Prometheus 2 (1984) 141.
[5] G. E. Moore, in *Readings in computer architecture*, edited by D. H. Mark, P. J. Norman, and S. S. Gurindar (Morgan Kaufmann Publishers Inc., 2000), p. 56.
[6] W. M. Arden, Current Opinion in Solid State and Materials Science 6 (2002) 371.
[7] S. S. Oh, C.-S. Kee, J.-E. Kim, H. Y. Park, T. I. Kim, I. Park, H. Lim, Appl. Phys. Lett. 76 (2000) 2301.
[8] L. M., D. T., V. J., S. A., J. Light. Technol. 18 (2000) 1402.
[9] Y. E., J. Mod. Opt. 41 (1994) 173.
[10] M.-H. Lu, L. Feng, Y.-F. Chen, Mater. Today 12 (2009) 34.
[11] M. S. Kushwaha, P. Halevi, L. Dobrzynski, B. Djafari-Rouhani, Phys. Rev. Lett. 71 (1993) 2022.
[12] M. Jacoby, Chem. Eng. News 76 (1998) 38.
[13] M. N. Armenise, C. E. Campanella, C. Ciminelli, F. Dell'Olio, V. M. N. Passaro, Phys. Procedia 3 (2010) 357.
[14] E. Yablonovitch, J. Opt. Soc. Am. B 10 (1993) 283.
[15] M. E. Zoorob, M. D. B. Charlton, G. J. Parker, J. J. B. &, M. C. Netti, Nature 404 (2000) 740.
[16] M. Florescu, S. Torquato, P. J. Steinhardt, Phys. Rev. B 80 (2009) 155112.
[17] A. L. Chen, Y.-S. Wang, Y.-F. Guo, Z.-D. Wang, Solid State Commun. 145 (2008) 103.
[18] I. E. Psarobas, N. Stefanou, A. Modinos, Phys. Rev. B 62 (2000) 5536.
[19] J. Li, K. S. Chiang, J. Opt. Soc. Am. B 24 (2007) 1942.
[20] J. C. Knight, Nature 424 (2003) 847.
[21] P. A. Y., E. M., IEEE J. Sel. Areas Commun. 23 (2005) 1396.
[22] J. Li, T. P. White, L. O'Faolain, A. Gomez-Iglesias, T. F. Krauss, Opt. Express 16 (2008) 6227.
[23] J. Li, K. S. Chiang, Opt. Commun. 281 (2008) 5797.
[24] N. T. Otterstrom, R. O. Behunin, E. A. Kittlaus, Z. Wang, P. T. Rakich, Science 360 (2018) 1113.
[25] A. Khelif, B. Djafari-Rouhani, J. O. Vasseur, P. A. Deymier, Phys. Rev. B 68 (2003) 024302.
[26] M. Kurosu, D. Hatanaka, K. Onomitsu, H. Yamaguchi, Nat. Commun. 9 (2018) 1331.
[27] S. J. McNab, N. Moll, Y. A. Vlasov, Opt. Express 11 (2003) 2927.
[28] F. Van Laere, T. Stomeo, C. Cambournac, M. Ayre, R. Brenot, H. Benisty, G. Roelkens, T. F. Krauss, D. Van Thourhout, R. Baets, J. Light. Technol. 27 (2009) 417.

[29] A. Akjouj, H. Al-Wahsh, B. Sylla, B. Djafari-Rouhani, L. Dobrzynski, J. Phys. Condens. Matter 16 (2003) 37.
[30] Y.-F. Wang, T.-T. Wang, Y.-S. Wang, V. Laude, Phys. Rev. Appl. 8 (2017) 014006.
[31] S.-Y. Yu, C. He, Z. Wang, F.-K. Liu, X.-C. Sun, Z. Li, H.-Z. Lu, M.-H. Lu, X.-P. Liu, Y.-F. Chen, Nat. Commun. 9 (2018) 3072.
[32] M. N. Baibich, J. M. Broto, A. Fert, F. N. Van Dau, F. Petroff, P. Eitenne, G. Creuzet, A. Friederich, J. Chazelas, Phys. Rev. Lett. 61 (1988) 2472.
[33] P. Grünberg, R. Schreiber, Y. Pang, M. B. Brodsky, H. Sowers, Phys. Rev. Lett. 57 (1986) 2442.
[34] S. S. P. Parkin, Z. G. Li, D. J. Smith, Appl. Phys. Lett. 58 (1991) 2710.
[35] S. A. Wolf, D. D. Awschalom, R. A. Buhrman, J. M. Daughton, S. von Molnár, M. L. Roukes, A. Y. Chtchelkanova, D. M. Treger, Science 294 (2001) 1488.
[36] A. Fert, Rev. Mod. Phys. 80 (2008) 1517.
[37] B. Geoffrey, Nat. Mater. 9 (2010) 959.
[38] V. V. Kruglyak, R. J. Hicken, J. Magn. Magn. Mater. 306 (2006) 191.
[39] S. Neusser, D. Grundler, Adv. Mater. 21 (2009) 2927.
[40] V. V. Kruglyak, S. O. Demokritov, D. Grundler, J. Phys. D: Appl. Phys. 43 (2010) 264001.
[41] B. Lenk, H. Ulrichs, F. Garbs, M. Münzenberg, Phys. Rep. 507 (2011) 107.
[42] A. A. Serga, A. V. Chumak, B. Hillebrands, J. Phys. D: Appl. Phys. 43 (2010) 264002.
[43] A. Manchon, H. C. Koo, J. Nitta, S. M. Frolov, R. A. Duine, Nat. Mater. 14 (2015) 871.
[44] T. Kuschel, G. Reiss, Nat. Nanotechnol. 10 (2014) 22.
[45] V. Dugaev, I. Tralle, A. Wal, J. Barna, *Spin Orbitronics and Topological Properties of Nanostructures* (WORLD SCIENTIFIC, 2017).
[46] A. V. Chumak, V. I. Vasyuchka, A. A. Serga, B. Hillebrands, Nat. Phys. 11 (2015) 453.
[47] C. Chappert, A. Fert, F. N. Van Dau, Nat. Mater. 6 (2007) 813.
[48] G. A. Prinz, Science 282 (1998) 1660.
[49] J. Wang, C. Zhang, H. Liu, R. McLaughlin, Y. Zhai, S. R. Vardeny, X. Liu, S. McGill, D. Semenov, H. Guo, R. Tsuchikawa, V. V. Deshpande, D. Sun, Z. V. Vardeny, Nat. Commun. 10 (2019) 129.
[50] G. Ctistis, E. Papaioannou, P. Patoka, J. Gutek, P. Fumagalli, M. Giersig, Nano Lett. 9 (2009) 1.
[51] V. L. Zhang, F. S. Ma, H. H. Pan, C. S. Lin, H. S. Lim, S. C. Ng, M. H. Kuok, S. Jain, A. O. Adeyeye, Appl. Phys. Lett. 100 (2012) 163118.
[52] P. Graczyk, M. Krawczyk, Phys. Rev. B 96 (2017) 024407.
[53] H. H. Pan, V. L. Zhang, K. Di, M. H. Kuok, H. S. Lim, S. C. Ng, N. Singh, A. O. Adeyeye, Nanoscale Res. Lett. 8 (2013) 115.
[54] M. Matsuo, E. Saitoh, S. Maekawa, J. Phys. Soc. Jpn. 86 (2016) 011011.
[55] A. Manchon, S. Zhang, Phys. Rev. B 79 (2009) 094422.
[56] L. Berger, Phys. Rev. B 54 (1996) 9353.
[57] J. C. Slonczewski, J. Magn. Magn. Mater. 159 (1996) L1.
[58] L. Liu, O. J. Lee, T. J. Gudmundsen, D. C. Ralph, R. A. Buhrman, Phys. Rev. Lett. 109 (2012) 096602.
[59] J. Grollier, V. Cros, A. Hamzic, J. M. George, H. Jaffrès, A. Fert, G. Faini, J. Ben Youssef, H. Legall, Appl. Phys. Lett. 78 (2001) 3663.
[60] E. B. Myers, D. C. Ralph, J. A. Katine, R. N. Louie, R. A. Buhrman, Science 285 (1999) 867.
[61] J. E. Hirsch, Phys. Rev. Lett. 83 (1999) 1834.

[62] Y. K. Kato, R. C. Myers, A. C. Gossard, D. D. Awschalom, Science 306 (2004) 1910.
[63] E. Saitoh, M. Ueda, H. Miyajima, G. Tatara, Appl. Phys. Lett. 88 (2006) 182509.
[64] J. Wunderlich, B. Kaestner, J. Sinova, T. Jungwirth, Phys. Rev. Lett. 94 (2005) 047204.
[65] S. O. Valenzuela, M. Tinkham, Nature 442 (2006) 176.
[66] E. H. Hall, Am. J. Math. 2 (1879) 287.
[67] A. Brataas, Y. Tserkovnyak, G. E. W. Bauer, B. I. Halperin, Phys. Rev. B 66 (2002) 060404.
[68] Y. Tserkovnyak, A. Brataas, G. E. W. Bauer, Phys. Rev. Lett. 88 (2002) 117601.
[69] A. Brataas, A. D. Kent, H. Ohno, Nat. Mater. 11 (2012) 372.
[70] Y. Tserkovnyak, A. Brataas, G. E. W. Bauer, B. I. Halperin, Rev. Mod. Phys. 77 (2005) 1375.
[71] K. Uchida, S. Takahashi, K. Harii, J. Ieda, W. Koshibae, K. Ando, S. Maekawa, E. Saitoh, Nature 455 (2008) 778.
[72] K. Uchida, J. Xiao, H. Adachi, J. Ohe, S. Takahashi, J. Ieda, T. Ota, Y. Kajiwara, H. Umezawa, H. Kawai, G. E. W. Bauer, S. Maekawa, E. Saitoh, Nat. Mater. 9 (2010) 894.
[73] S.-G. Cheng, Y. Xing, Q.-F. Sun, X. C. Xie, Phys. Rev. B 78 (2008) 045302.
[74] X. Liu, X. C. Xie, Solid State Commun. 150 (2010) 471.
[75] S. Meyer, Y. T. Chen, S. Wimmer, M. Althammer, T. Wimmer, R. Schlitz, S. Geprägs, H. Huebl, D. Ködderitzsch, H. Ebert, G. E. W. Bauer, R. Gross, S. T. B. Goennenwein, Nat. Mater. 16 (2017) 977.
[76] P. Sheng, Y. Sakuraba, Y.-C. Lau, S. Takahashi, S. Mitani, M. Hayashi, Sci. Adv. 3 (2017) e1701503.
[77] A. v. Ettingshausen, W. Nernst, Ann. Phys. 265 (1886) 343.
[78] M. Wuttig, Philos. Mag. A 77 (1998) 1273.
[79] V. Novosad, Y. Otani, A. Ohsawa, S. G. Kim, K. Fukamichi, J. Koike, K. Maruyama, O. Kitakami, Y. Shimada, J. Appl. Phys. 87 (2000) 6400.
[80] I. Dzyaloshinsky, J. Phys. Chem. Solids 4 (1958) 241.
[81] T. Moriya, Phys. Rev. 120 (1960) 91.
[82] C.-G. Duan, S. S. Jaswal, E. Y. Tsymbal, Phys. Rev. Lett. 97 (2006) 047201.
[83] J. M. Rondinelli, M. Stengel, N. A. Spaldin, Nat. Nanotechnol. 3 (2007) 46.
[84] M. Weisheit, S. Fähler, A. Marty, Y. Souche, C. Poinsignon, D. Givord, Science 315 (2007) 349.
[85] D. Chiba, M. Sawicki, Y. Nishitani, Y. Nakatani, F. Matsukura, H. Ohno, Nature 455 (2008) 515.
[86] I. Stolichnov, S. W. E. Riester, H. J. Trodahl, N. Setter, A. W. Rushforth, K. W. Edmonds, R. P. Campion, C. T. Foxon, B. L. Gallagher, T. Jungwirth, Nat. Mater. 7 (2008) 464.
[87] P. Borisov, A. Hochstrat, X. Chen, W. Kleemann, C. Binek, Phys. Rev. Lett. 94 (2005) 117203.
[88] Y.-H. Chu *et al.*, Nat. Mater. 7 (2008) 478.
[89] W. Eerenstein, N. D. Mathur, J. F. Scott, Nature 442 (2006) 759.
[90] T. Maruyama, Y. Shiota, T. Nozaki, K. Ohta, N. Toda, M. Mizuguchi, A. A. Tulapurkar, T. Shinjo, M. Shiraishi, S. Mizukami, Y. Ando, Y. Suzuki, Nat. Nanotechnol. 4 (2009) 158.
[91] Y. Shiota, T. Nozaki, F. Bonell, S. Murakami, T. Shinjo, Y. Suzuki, Nat. Mater. 11 (2011) 39.
[92] T. Nozaki, Y. Shiota, S. Miwa, S. Murakami, F. Bonell, S. Ishibashi, H. Kubota, K. Yakushiji, T. Saruya, A. Fukushima, S. Yuasa, T. Shinjo, Y. Suzuki, Nat. Phys. 8 (2012) 491.

[93] G. E. W. Bauer, A. Brataas, Y. Tserkovnyak, B. J. van Wees, Appl. Phys. Lett. 82 (2003) 3928.
[94] J. Wunderlich, B.-G. Park, A. C. Irvine, L. P. Zârbo, E. Rozkotová, P. Nemec, V. Novák, J. Sinova, T. Jungwirth, Science 330 (2010) 1801.
[95] T. Chiba, G. E. W. Bauer, S. Takahashi, Appl. Phys. Lett. 102 (2013) 192412.
[96] A. I. Akhiezer, S. V. Peletminskii, V. G. e. Bar'iakhtar, *Spin waves* Amsterdam, North-Holland Pub. Co., 1968).
[97] F. Bloch, Z. Physik 61 (1930) 206.
[98] S. A. Nikitov, P. Tailhades, C. S. Tsai, J. Magn. Magn. Mater. 236 (2001) 320.
[99] L. Sun, R. X. Cao, B. F. Miao, Z. Feng, B. You, D. Wu, W. Zhang, A. Hu, H. F. Ding, Phys. Rev. Lett. 110 (2013) 167201.
[100] F. S. Ma, Y. Zhou, H. B. Braun, W. S. Lew, Nano Lett. 15 (2015) 4029.
[101] A. Fert, N. Reyren, V. Cros, Nat. Rev. Mater. 2 (2017) 17031.
[102] Y. Qi, T. Brintlinger, J. Cumings, Phys. Rev. B 77 (2008) 094418.
[103] W. R. Branford, S. Ladak, D. E. Read, K. Zeissler, L. F. Cohen, Science 335 (2012) 1597.
[104] A. P. Ramirez, A. Hayashi, R. J. Cava, R. Siddharthan, B. S. Shastry, Nature 399 (1999) 333.
[105] Y.-L. Wang, Z.-L. Xiao, A. Snezhko, J. Xu, L. E. Ocola, R. Divan, J. E. Pearson, G. W. Crabtree, W.-K. Kwok, Science 352 (2016) 962.
[106] R. F. Wang, C. Nisoli, R. S. Freitas, J. Li, W. McConville, B. J. Cooley, M. S. Lund, N. Samarth, C. Leighton, V. H. Crespi, P. Schiffer, Nature 439 (2006) 303.
[107] C. Castelnovo, R. Moessner, S. L. Sondhi, Nature 451 (2008) 42.
[108] A. Fernández-Pacheco, R. Streubel, O. Fruchart, R. Hertel, P. Fischer, R. P. Cowburn, Nat. Commun. 8 (2017) 15756.
[109] G. Williams, M. Hunt, B. Boehm, A. May, M. Taverne, D. Ho, S. R. Giblin, D. Read, J. Rarity, R. Allenspach, S. Ladak, Nano Res. 11 (2018) 845.
[110] M. Krawczyk, H. Puszkarski, Phys. Rev. B 77 (2008) 054437.
[111] N. Tran, T. J. Webster, J. Mater. Chem. 20 (2010) 8760.
[112] V. F. Cardoso, A. Francesko, C. Ribeiro, M. Bañobre-López, P. Martins, S. Lanceros-Mendez, Adv. Healthc. Mater. 7 (2018) 1700845.
[113] P. Odenthal, W. Talmadge, N. Gundlach, R. Wang, C. Zhang, D. Sun, Z.-G. Yu, Z. V. Vardeny, Y. S. Li, Nat. Phys. 13 (2017) 894.
[114] R. W. Damon, J. R. Eshbach, J. Phys. Chem. Solids 19 (1961) 308.
[115] A. N. Slavin, S. O. Demokritov, B. Hillebrands, in *Spin Dynamics in Confined Magnetic Structures I*, edited by B. Hillebrands, and K. Ounadjela (Springer Berlin Heidelberg, Berlin, Heidelberg, 2002), p. 35.
[116] M. Chen, M. A. Tsankov, J. M. Nash, C. E. Patton, Phys. Rev. B 49 (1994) 12773.
[117] C. R., S. C., O. J., IEEE Trans. Magn. 16 (1980) 1159.
[118] V. L. Zhang, H. S. Lim, C. S. Lin, Z. K. Wang, S. C. Ng, M. H. Kuok, S. Jain, A. O. Adeyeye, M. G. Cottam, Appl. Phys. Lett. 99 (2011) 143118.
[119] J. O. Vasseur, L. Dobrzynski, B. Djafari-Rouhani, H. Puszkarski, Phys. Rev. B 54 (1996) 1043.
[120] P. S. Keatley, P. Gangmei, M. Dvornik, R. J. Hicken, J. R. Childress, J. A. Katine, Appl. Phys. Lett. 98 (2011) 082506.
[121] V. E. Demidov, S. Urazhdin, S. O. Demokritov, Appl. Phys. Lett. 95 (2009) 262509.
[122] T. Schwarze, D. Grundler, Appl. Phys. Lett. 102 (2013) 222412.

[123] M. Mruczkiewicz, M. Krawczyk, G. Gubbiotti, S. Tacchi, A. F. Yu, D. V. Kalyabin, I. V. Lisenkov, S. A. Nikitov, New J. Phys. 15 (2013) 113023.
[124] M. Jamali, J. H. Kwon, S.-M. Seo, K.-J. Lee, H. Yang, Sci. Rep. 3 (2013).
[125] B. Rana, D. Kumar, S. Barman, S. Pal, R. Mandal, Y. Fukuma, Y. Otani, S. Sugimoto, A. Barman, J. Appl. Phys. 111 (2012) 07D503.
[126] R. Mandal, S. Saha, D. Kumar, S. Barman, S. Pal, K. Das, A. K. Raychaudhury, Y. Fukuma, Y. Otani, A. Barman, ACS Nano 6 (2012) 3397.
[127] J. Jorzick, S. O. Demokritov, C. Mathieu, B. Hillebrands, B. Bartenlian, C. Chappert, F. Rousseaux, A. N. Slavin, Phys. Rev. B 60 (1999).
[128] G. Gubbiotti, G. Carlotti, T. Okuno, T. Shinjo, F. Nizzoli, R. Zivieri, Phys. Rev. B 68 (2003) 184409.
[129] C. Schoeppner, K. Wagner, S. Stienen, R. Meckenstock, M. Farle, R. Narkowicz, D. Suter, J. Lindner, J. Appl. Phys. 116 (2014) 033913.
[130] O. N. Martyanov, V. F. Yudanov, R. N. Lee, S. A. Nepijko, H. J. Elmers, R. Hertel, C. M. Schneider, G. Schönhense, Phys. Rev. B 75 (2007) 174429.
[131] M. Julliere, Phys. Lett. A 54 (1975) 225.
[132] M. Bowen *et al.*, Appl. Phys. Lett. 79 (2001) 1655.
[133] T. Miyazaki, N. Tezuka, J. Magn. Magn. Mater. 139 (1995) L231.
[134] S. S. P. Parkin, C. Kaiser, A. Panchula, P. M. Rice, B. Hughes, M. Samant, S.-H. Yang, Nat. Mater. 3 (2004) 862.
[135] S. Ikeda, J. Hayakawa, Y. Ashizawa, Y. M. Lee, K. Miura, H. Hasegawa, M. Tsunoda, F. Matsukura, H. Ohno, Appl. Phys. Lett. 93 (2008) 082508.
[136] E. N. Abarra, A. Inomata, H. Sato, I. Okamoto, Y. Mizoshita, Appl. Phys. Lett. 77 (2000) 2581.
[137] J. R. Childress, R. E. Fontana Jr, C. R. Physique 6 (2005) 997.
[138] S. H. Charap, L. Pu-Ling, H. Yanjun, IEEE Trans. Magn. 33 (1997) 978.
[139] D. Weller, A. Moser, IEEE Trans. Magn. 35 (1999) 4423.
[140] E. E. Fullerton, D. T. Margulies, M. E. Schabes, M. Carey, B. Gurney, A. Moser, M. Best, G. Zeltzer, K. Rubin, H. Rosen, M. Doerner, Appl. Phys. Lett. 77 (2000) 3806.
[141] G. Binasch, P. Grünberg, F. Saurenbach, W. Zinn, Phys. Rev. B 39 (1989) 4828.
[142] M. E. Schabes, E. E. Fullerton, D. T. Margulies, IEEE Trans. Magn. 37 (2001) 1432.
[143] X. M. Cheng, S. Urazhdin, O. Tchernyshyov, C. L. Chien, Phys. Rev. Lett. 94 (2005) 017203.
[144] S.-i. Iwasaki, J. Magn. Magn. Mater. 235 (2001) 227.
[145] J. Moritz, S. Landis, J. C. Toussaint, R. Bayle-Guillemaud, B. Rodmacq, G. Casali, A. Lebib, Y. Chen, J. P. Nozires, B. Dieny, IEEE Trans. Magn. 38 (2002) 1731.
[146] S. N. Piramanayagam, J. Appl. Phys. 102 (2007) 011301.
[147] Y. Hsu *et al.*, IEEE Trans. Magn. 43 (2007) 605.
[148] M. Todorovic, S. Schultz, J. Wong, A. Scherer, Appl. Phys. Lett. 74 (1999) 2516.
[149] G. F. Hughes, IEEE Trans. Magn. 36 (2000) 521.
[150] O. Hellwig, T. Hauet, T. Thomson, E. Dobisz, J. D. Risner-Jamtgaard, D. Yaney, B. D. Terris, E. E. Fullerton, Appl. Phys. Lett. 95 (2009) 232505.
[151] C. Chappert, P. Bruno, J. Appl. Phys. 64 (1988) 5736.
[152] K. Kobayashi, G. Ishida, J. Appl. Phys. 52 (1981) 2453.
[153] D. Makarov, E. Bermúdez-Ureña, O. G. Schmidt, F. Liscio, M. Maret, C. Brombacher, S. Schulze, M. Hietschold, M. Albrecht, Appl. Phys. Lett. 93 (2008) 153112.
[154] Q. Leng, M. Mao, C. Hiner, L. Miloslavsky, M. Miller, S. Tran, C. Qian, H. C. Tong, IEEE Trans. Magn. 35 (1999) 2553.

[155] O. Hellwig, S. Maat, J. B. Kortright, E. E. Fullerton, Phys. Rev. B 65 (2002) 144418.
[156] F. J. A. den Broeder, E. Janssen, A. Mud, J. M. Kerkhof, J. Magn. Magn. Mater. 126 (1993) 563.
[157] N. Amos, R. Fernandez, R. Ikkawi, B. Lee, A. Lavrenov, A. Krichevsky, D. Litvinov, S. Khizroev, J. Appl. Phys. 103 (2008) 07E732.
[158] J. Yoon, S.-Y. Park, Y. Jo, M.-H. Jung, C.-Y. You, T. Kim, J. R. Rhee, Y. K. Kim, Curr. Appl. Phys. 9 (2009) 688.
[159] M. Hehn, S. Padovani, K. Ounadjela, J. P. Bucher, Phys. Rev. B 54 (1996) 3428.
[160] D. Wu, T. Jin, Y. Lou, F. Wei, Appl. Surf. Sci. 346 (2015) 567.
[161] M. Coïsson, F. Vinai, P. Tiberto, F. Celegato, J. Magn. Magn. Mater. 321 (2009) 806.
[162] F. Luo, F. Zheng, G. Yin, D. Wu, F. Wei, Appl. Phys. Express 6 (2013) 073003.
[163] N. Vukadinovic, H. L. Gall, J. B. Y. V. Gehanno, A. Marty, Y. Samson, B. Gilles, Eur. Phys. J. B 13 (2000) 445.
[164] C. Banerjee, P. Gruszecki, J. W. Klos, O. Hellwig, M. Krawczyk, A. Barman, Phys. Rev. B 96 (2017) 024421.
[165] A. Moser, K. Takano, D. T. Margulies, M. Albrecht, Y. Sonobe, Y. Ikeda, S. Sun, E. E. Fullerton, J. Phys. D: Appl. Phys. 35 (2002) R157.
[166] M. H. Kryder, E. C. Gage, T. W. McDaniel, W. A. Challener, R. E. Rottmayer, G. Ju, Y. Hsia, M. F. Erden, Proc. IEEE 96 (2008) 1810.
[167] Z. Liu, P. Huang, S. Hernandez, G. Ju, T. Rausch, IEEE Trans. Magn. 54 (2018) 1.
[168] S. Okamoto, N. Kikuchi, M. Furuta, O. Kitakami, T. Shimatsu, J. Phys. D: Appl. Phys. 48 (2015) 353001.
[169] S. Tehrani, E. Chen, M. Durlam, M. DeHerrera, J. M. Slaughter, J. Shi, G. Kerszykowski, J. Appl. Phys. 85 (1999) 5822.
[170] R. C. Sousa, I. L. Prejbeanu, C. R. Physique 6 (2005) 1013.
[171] B. Rana, Y. Otani, Phys. Rev. Appl. 9 (2018) 014033.
[172] S. Yuasa, T. Nagahama, A. Fukushima, Y. Suzuki, K. Ando, Nat. Mater. 3 (2004) 868.
[173] J. M. Teixeira, J. D. Costa, J. Ventura, M. P. Fernandez-Garcia, J. Azevedo, J. P. Araujo, J. B. Sousa, P. Wisniowski, S. Cardoso, P. P. Freitas, Appl. Phys. Lett. 102 (2013) 212413.
[174] A. V. Chumak, A. A. Serga, B. Hillebrands, J. Phys. D: Appl. Phys. 50 (2017) 244001.
[175] J. Rychły, P. Gruszecki, M. Mruczkiewicz, J. W. Kłos, S. Mamica, M. Krawczyk, Low Temp. Phys. 41 (2015) 745.
[176] B. Hillebrands *et al.*, J. Magn. Magn. Mater. 175 (1997) 10.
[177] M. Grimsditch, Y. Jaccard, I. K. Schuller, Phys. Rev. B 58 (1998) 11539.
[178] C. Mathieu, J. Jorzick, A. Frank, S. O. Demokritov, A. N. Slavin, B. Hillebrands, B. Bartenlian, C. Chappert, D. Decanini, F. Rousseaux, E. Cambril, Phys. Rev. Lett. 81 (1998) 3968.
[179] N. I. Polushkin, S. A. Michalski, L. Yue, R. D. Kirby, Phys. Rev. Lett. 97 (2006) 256401.
[180] B. Obry, P. Pirro, T. Brächer, A. V. Chumak, J. Osten, F. Ciubotaru, A. A. Serga, J. Fassbender, B. Hillebrands, Appl. Phys. Lett. 102 (2013) 202403.
[181] L. Bai, M. Kohda, J. Nitta, Appl. Phys. Lett. 98 (2011) 172508.
[182] K. Roy, S. Bandyopadhyay, J. Atulasimha, Phys. Rev. B 83 (2011) 224412.
[183] A. V. Chumak, T. Neumann, A. A. Serga, B. Hillebrands, M. P. Kostylev, J. Phys. D: Appl. Phys. 42 (2009) 205005.
[184] Q. Wang, A. V. Chumak, L. Jin, H. Zhang, B. Hillebrands, Z. Zhong, Phys. Rev. B 95 (2017) 134433.

[185] M. Rollinger, P. Thielen, E. Melander, E. Östman, V. Kapaklis, B. Obry, M. Cinchetti, A. García-Martín, M. Aeschlimann, E. T. Papaioannou, Nano Lett. 16 (2016) 2432.
[186] E. T. Papaioannou, V. Kapaklis, P. Patoka, M. Giersig, P. Fumagalli, A. Garcia-Martin, E. Ferreiro-Vila, G. Ctistis, Phys. Rev. B 81 (2010) 054424.
[187] B. Rana, D. Kumar, S. Barman, S. Pal, Y. Fukuma, Y. Otani, A. Barman, ACS Nano 5 (2011) 9559.
[188] H. Ulrichs, B. Lenk, M. Münzenberg, Appl. Phys. Lett. 97 (2010) 092506.
[189] M. P. Kostylev, G. Gubbiotti, J. G. Hu, G. Carlotti, T. Ono, R. L. Stamps, Phys. Rev. B 76 (2007) 054422.
[190] G. Gubbiotti, S. Tacchi, G. Carlotti, N. Singh, S. Goolaup, A. O. Adeyeye, M. Kostylev, Appl. Phys. Lett. 90 (2007) 092503.
[191] C. Banerjee, S. Choudhury, J. Sinha, A. Barman, Phys. Rev. Appl. 8 (2017) 014036.
[192] S. Tacchi, M. Madami, G. Gubbiotti, G. Carlotti, H. Tanigawa, T. Ono, M. P. Kostylev, Phys. Rev. B 82 (2010) 024401.
[193] G. Gubbiotti, S. Tacchi, M. Madami, G. Carlotti, S. Jain, A. O. Adeyeye, M. P. Kostylev, Appl. Phys. Lett. 100 (2012) 162407.
[194] S. Choudhury, S. Barman, Y. Otani, A. Barman, ACS Nano 11 (2017) 8814.
[195] A. O. Adeyeye, S. Jain, Y. Ren, IEEE Trans. Magn. 47 (2011) 1639.
[196] S. Choudhury, S. Saha, R. Mandal, S. Barman, Y. Otani, A. Barman, ACS Appl. Mater. Interfaces 8 (2016) 18339.
[197] R. Mandal, S. Barman, S. Saha, Y. Otani, A. Barman, J. Appl. Phys. 118 (2015) 053910.
[198] L. J. Heyderman, H. H. Solak, C. David, D. Atkinson, R. P. Cowburn, F. Nolting, Appl. Phys. Lett. 85 (2004) 4989.
[199] R. L. Stamps, R. E. Camley, Phys. Rev. B 60 (1999) 12264.
[200] M. Hänze, C. F. Adolff, B. Schulte, J. Möller, M. Weigand, G. Meier, Sci. Rep. 6 (2016) 22402.
[201] S. Mamica, J. Appl. Phys. 114 (2013) 043912.
[202] A. V. Chumak, A. A. Serga, B. Hillebrands, M. P. Kostylev, Appl. Phys. Lett. 93 (2008) 022508.
[203] M. Kostylev, P. Schrader, R. L. Stamps, G. Gubbiotti, G. Carlotti, A. O. Adeyeye, S. Goolaup, N. Singh, Appl. Phys. Lett. 92 (2008) 132504.
[204] C. H. Chen, R. Z. Qiu, C. H. Chang, W. J. Hsueh, AIP Adv. 4 (2014) 087102.
[205] Z. K. Wang, V. L. Zhang, H. S. Lim, S. C. Ng, M. H. Kuok, S. Jain, A. O. Adeyeye, Appl. Phys. Lett. 94 (2009) 083112.
[206] R. Zivieri, S. Tacchi, F. Montoncello, L. Giovannini, F. Nizzoli, M. Madami, G. Gubbiotti, G. Carlotti, S. Neusser, G. Duerr, D. Grundler, Phys. Rev. B 85 (2012) 012403.
[207] G. Gubbiotti, S. Tacchi, M. Madami, G. Carlotti, A. O. Adeyeye, M. Kostylev, J. Phys. D: Appl. Phys. 43 (2010) 264003.
[208] A. Barman, J. Phys. D: Appl. Phys. 43 (2010) 195002.
[209] C. L. Hu, R. Magaraggia, H. Y. Yuan, C. S. Chang, M. Kostylev, D. Tripathy, A. O. Adeyeye, R. L. Stamps, Appl. Phys. Lett. 98 (2011) 262508.
[210] S. Choudhury, S. Barman, Y. Otani, A. Barman, ACS Nano (2017).
[211] S. Neusser, B. Botters, D. Grundler, Phys. Rev. B 78 (2008) 054406.
[212] P. Vavassori, G. Gubbiotti, G. Zangari, C. T. Yu, H. Yin, H. Jiang, G. J. Mankey, J. Appl. Phys. 91 (2002) 7992.
[213] R. P. Cowburn, A. O. Adeyeye, J. A. C. Bland, Appl. Phys. Lett. 70 (1997) 2309.
[214] H. Ulrichs, B. Lenk, M. Münzenberg, Appl. Phys. Lett. 97 (2010) 092506.

[215] S. Neusser, H. G. Bauer, G. Duerr, R. Huber, S. Mamica, G. Woltersdorf, M. Krawczyk, C. H. Back, D. Grundler, Phys. Rev. B 84 (2011) 184411.
[216] N.-N. Chen, A. N. Slavin, M. G. Cottam, Phys. Rev. B 47 (1993) 8667.
[217] E. L. Albuquerque, M. G. Cottam, Phys. Rep. 376 (2003) 225.
[218] M. Wu, B. A. Kalinikos, L. D. Carr, C. E. Patton, Phys. Rev. Lett. 96 (2006) 187202.
[219] G. Gubbiotti, S. Tacchi, G. Carlotti, P. Vavassori, N. Singh, S. Goolaup, A. O. Adeyeye, A. Stashkevich, M. Kostylev, Phys. Rev. B 72 (2005) 224413.
[220] S. Goolaup, A. O. Adeyeye, N. Singh, G. Gubbiotti, Phys. Rev. B 75 (2007) 144430.
[221] S. Tacchi, M. Madami, G. Gubbiotti, G. Carlotti, S. Goolaup, A. O. Adeyeye, N. Singh, M. P. Kostylev, Phys. Rev. B 82 (2010) 184408.
[222] S. Saha, S. Barman, Y. Otani, A. Barman, Nanoscale 7 (2015) 18312.
[223] V. E. Demidov, J. Jersch, K. Rott, P. Krzysteczko, G. Reiss, S. O. Demokritov, Phys. Rev. Lett. 102 (2009) 177207.
[224] A. V. Chumak, P. Pirro, A. A. Serga, M. P. Kostylev, R. L. Stamps, H. Schutheiss, K. Vogt, S. J. Hermsdoerfer, B. Laegel, P. A. Beck, B. Hillebrands, Appl. Phys. Lett. 95 (2009) 262508.
[225] S. Jung, B. Watkins, L. DeLong, J. B. Ketterson, V. Chandrasekhar, Phys. Rev. B 66 (2002) 132401.
[226] G. N. Kakazei, P. E. Wigen, K. Y. Guslienko, V. Novosad, A. N. Slavin, V. O. Golub, N. A. Lesnik, Y. Otani, Appl. Phys. Lett. 85 (2004) 443.
[227] S. M. Weekes, F. Y. Ogrin, P. S. Keatley, J. Appl. Phys. 99 (2006) 08B102.
[228] V. V. Kruglyak, A. Barman, R. J. Hicken, J. R. Childress, J. A. Katine, J. Appl. Phys. 97 (2005) 10A706.
[229] V. V. Kruglyak, A. Barman, R. J. Hicken, J. R. Childress, J. A. Katine, Phys. Rev. B 71 (2005) 220409(R).
[230] B. Rana, S. Pal, S. Barman, Y. Fukuma, Y. Otani, A. Barman, Appl. Phys. Express. 4 (2011) 113003.
[231] S. Mondal, S. Choudhury, S. Barman, Y. Otani, A. Barman, RSC Adv. 6 (2016) 110393.
[232] S. Saha, R. Mandal, S. Barman, D. Kumar, B. Rana, Y. Fukuma, S. Sugimoto, Y. Otani, A. Barman, Adv. Funct. Mater. 23 (2013) 2378.
[233] S. Saha, S. Barman, S. Sugimoto, Y. Otani, A. Barman, RSC Adv. 5 (2015) 34027.
[234] S. Mondal, S. Barman, S. Choudhury, Y. Otani, A. Barman, J. Magn. Magn. Mater. 458 (2018) 95.
[235] B. K. Mahato, B. Rana, D. Kumar, S. Barman, S. Sugimoto, Y. Otani, A. Barman, Appl. Phys. Lett. 105 (2014) 012406.
[236] K. Adhikari, S. Choudhury, R. Mandal, S. Barman, Y. Otani, A. Barman, J. Appl. Phys. 121 (2017) 043909.
[237] G. Shimon, A. A. O., Adv. Electron. Mater. 1 (2015) 1500070.
[238] A. De, S. Mondal, C. Banerjee, A. K. Chaurasiya, R. Mandal, Y. Otani, R. K. Mitra, A. Barman, J. Phys. D: Appl. Phys. 50 (2017) 385002.
[239] C. T. Yu, H. Jiang, L. Shen, P. J. Flanders, G. J. Mankey, J. Appl. Phys. 87 (2000) 6322.
[240] S. McPhail, C. M. Gürtler, J. M. Shilton, N. J. Curson, J. A. C. Bland, Phys. Rev. B 72 (2005) 094414.
[241] C. C. Wang, A. O. Adeyeye, N. Singh, Y. S. Huang, Y. H. Wu, Phys. Rev. B 72 (2005) 174426.
[242] C. C. Wang, A. O. Adeyeye, N. Singh, Appl. Phys. Lett. 88 (2006) 222506.
[243] D. Tripathy, A. O. Adeyeye, J. Appl. Phys. 105 (2009) 07D703.

[244] S. Pal, J. W. Klos, K. Das, O. Hellwig, P. Gruszecki, M. Krawczyk, A. Barman, Appl. Phys. Lett. 105 (2014) 162408.
[245] M. Yu, L. Malkinski, L. Spinu, W. Zhou, S. Whittenburg, J. Appl. Phys. 101 (2007) 09F501.
[246] J. Ding, D. Tripathy, A. O. Adeyeye, J. Appl. Phys. 109 (2011) 07D304.
[247] R. Zivieri, P. Malagò, L. Giovannini, S. Tacchi, G. Gubbiotti, A. Adeyeye, J. Phys. Condens. Matter 25 (2013) 336002.
[248] M. Kostylev, G. Gubbiotti, G. Carlotti, G. Socino, S. Tacchi, C. Wang, N. Singh, A. O. Adeyeye, R. L. Stamps, J. Appl. Phys. 103 (2008) 07C507.
[249] S. Neusser, G. Duerr, H. G. Bauer, S. Tacchi, M. Madami, G. Woltersdorf, G. Gubbiotti, C. H. Back, D. Grundler, Phys. Rev. Lett. 105 (2010) 067208.
[250] S. Tacchi, M. Madami, G. Gubbiotti, G. Carlotti, A. O. Adeyeye, S. Neusser, B. Botters, D. Grundler, IEEE Trans. Magn. 46 (2010) 1440.
[251] N. G. Deshpande, M. S. Seo, X. R. Jin, S. J. Lee, Y. P. Lee, J. Y. Rhee, K. W. Kim, Appl. Phys. Lett. 96 (2010) 122503.
[252] S. Tacchi, B. Botters, M. Madami, J. W. Kłos, M. L. Sokolovskyy, M. Krawczyk, G. Gubbiotti, G. Carlotti, A. O. Adeyeye, S. Neusser, D. Grundler, Phys. Rev. B 86 (2012) 014417.
[253] S. Tacchi, M. Madami, G. Gubbiotti, G. Carlotti, A. O. Adeyeye, S. Neusser, B. Botters, D. Grundler, IEEE Trans. Magn. 46 (2010) 172.
[254] S. Neusser, G. Duerr, S. Tacchi, M. Madami, M. L. Sokolovskyy, G. Gubbiotti, M. Krawczyk, D. Grundler, Phys. Rev. B 84 (2011) 094454.
[255] R. Mandal, S. Saha, D. Kumar, S. Barman, S. Pal, K. Das, A. K. Raychaudhuri, Y. Fukuma, Y. Otani, A. Barman, ACS Nano 6 (2012) 3397.
[256] V. Bhat, J. Woods, L. E. De Long, J. T. Hastings, V. V. Metlushko, K. Rivkin, O. Heinonen, J. Sklenar, J. B. Ketterson, Physica C: Superconductivity 479 (2012) 83.
[257] R. Bali, M. Kostylev, D. Tripathy, A. O. Adeyeye, S. Samarin, Phys. Rev. B 85 (2012) 104414.
[258] N. G. Deshpande, M. S. Seo, S. J. Lee, L. Y. Chen, K. W. Kim, J. Y. Rhee, Y. H. Kim, Y. P. Lee, J. Appl. Phys. 111 (2012) 013906.
[259] N. G. Deshpande, J. S. Hwang, K. W. Kim, J. Y. Rhee, Y. H. Kim, L. Y. Chen, Y. P. Lee, Appl. Phys. Lett. 100 (2012) 222403.
[260] J. Ding, D. Tripathy, A. Adeyeye, EPL 98 (2012) 16004.
[261] M. Madami, S. Tacchi, G. Gubbiotti, G. Carlotti, J. Ding, A. O. Adeyeye, J. W. Klos, M. Krawczyk, IEEE Trans. Magn. 49 (2013) 3093.
[262] R. Mandal, P. Laha, K. Das, S. Saha, S. Barman, A. K. Raychaudhuri, A. Barman, Appl. Phys. Lett. 103 (2013) 262410.
[263] A. De, S. Mondal, S. Sahoo, S. Barman, Y. Otani, R. K. Mitra, A. Barman, Beilstein J. Nanotechnol. 9 (2018) 1123.
[264] F. Haering, U. Wiedwald, S. Nothelfer, B. Koslowski, P. Ziemann, L. Lechner, A. Wallucks, K. Lebecki, U. Nowak, J. Gräfe, E. Goering, G. Schütz, Nanotechnology 24 (2013) 465709.
[265] U. Wiedwald, J. Gräfe, K. M. Lebecki, M. Skripnik, F. Haering, G. Schütz, P. Ziemann, E. Goering, U. Nowak, Beilstein J. Nanotechnol. 7 (2016) 733.
[266] Y. H. Jang, J. H. Cho, J. Appl. Phys. 115 (2014) 063903.
[267] M. Madami, G. Gubbiotti, S. Tacchi, G. Carlotti, S. Jain, Physica B 435 (2014) 152.
[268] S. Tacchi, P. Gruszecki, M. Madami, G. Carlotti, J. W. Kłos, M. Krawczyk, A. Adeyeye, G. Gubbiotti, Sci. Rep. 5 (2015) 10367.

[269] N. Porwal, S. Mondal, S. Choudhury, A. De, J. Sinha, A. Barman, P. K. Datta, J. Phys. D: Appl. Phys. 51 (2018) 055004.
[270] J. W. Kłos, D. Kumar, J. Romero-Vivas, H. Fangohr, M. Franchin, M. Krawczyk, A. Barman, Phys. Rev. B 86 (2012) 184433.
[271] D. Kumar, P. Sabareesan, W. Wang, H. Fangohr, A. Barman, J. Appl. Phys. 114 (2013) 023910.
[272] J. W. Kłos, D. Kumar, M. Krawczyk, A. Barman, Sci. Rep. 3 (2013) 2444.
[273] J. W. Kłos, D. Kumar, M. Krawczyk, A. Barman, Phys. Rev. B 89 (2014) 014406.
[274] D. Kumar, J. W. Kłos, M. Krawczyk, A. Barman, J. Appl. Phys. 115 (2014) 043917.
[275] R. Zivieri, L. Giovannini, Photonics Nanostructures: Fundam. Appl. 11 (2013) 191.
[276] C. H. O. Costa, M. S. Vasconcelos, P. H. R. Barbosa, F. F. Barbosa Filho, J. Magn. Magn. Mater. 324 (2012) 2315.
[277] W. J. Hsueh, C. H. Chen, R. Z. Qiu, Phys. Lett. A 377 (2013) 1378.
[278] J. Rychły, S. Mieszczak, J. W. Kłos, J. Magn. Magn. Mater. 450 (2018) 18.
[279] J. Ding, M. Kostylev, A. O. Adeyeye, Phys. Rev. Lett. 107 (2011) 047205.
[280] S. V. Grishin, E. N. Beginin, M. A. Morozova, Y. P. Sharaevskii, S. A. Nikitov, J. Appl. Phys. 115 (2014) 053908.
[281] V. S. Bhat, J. Sklenar, B. Farmer, J. Woods, J. T. Hastings, S. J. Lee, J. B. Ketterson, L. E. De Long, Phys. Rev. Lett. 111 (2013) 077201.
[282] V. Metlushko *et al.*, in *Proceedings of the 2nd IEEE Conference on Nanotechnology*2002), pp. 63.
[283] L. Tripp S., E. Dunin-B. R., A. Wei, Angew. Chem. 42 (2003) 5591.
[284] P. Vavassori, M. Grimsditch, V. Novosad, V. Metlushko, B. Ilic, J. Appl. Phys. 93 (2003) 7900.
[285] J. Wang, A. O. Adeyeye, N. Singh, Appl. Phys. Lett. 87 (2005) 262508.
[286] L. J. Chang, C. Yu, T. W. Chiang, K. W. Cheng, W. T. Chiu, S. F. Lee, Y. Liou, Y. D. Yao, J. Appl. Phys. 103 (2008) 07C514.
[287] X. Zhu, M. Malac, Z. Liu, H. Qian, V. Metlushko, M. R. Freeman, Appl. Phys. Lett. 86 (2005) 262502.
[288] G. Gubbiotti, M. Madami, S. Tacchi, G. Carlotti, H. Tanigawa, T. Ono, L. Giovannini, F. Montoncello, F. Nizzoli, Phys. Rev. Lett. 97 (2006) 247203.
[289] H. Schultheiss, S. Schäfer, P. Candeloro, B. Leven, B. Hillebrands, A. N. Slavin, Phys. Rev. Lett. 100 (2008) 047204.
[290] J. Ding, M. Kostylev, A. O. Adeyeye, Appl. Phys. Lett. 100 (2012) 062401.
[291] C. Banerjee, S. Saha, S. Barman, O. Rousseau, Y. Otani, A. Barman, J. Appl. Phys. 116 (2014) 163912.
[292] Z. K. Wang, V. L. Zhang, H. S. Lim, S. C. Ng, M. H. Kuok, S. Jain, A. O. Adeyeye, ACS Nano 4 (2010) 643.
[293] C. S. Lin, H. S. Lim, Z. K. Wang, S. C. Ng, M. H. Kuok, Appl. Phys. Lett. 98 (2011) 022504.
[294] D. Giridharan, P. Sabareesan, M. Daniel, Phys. Rev. E 94 (2016) 032222.
[295] F. S. Ma, H. S. Lim, Z. K. Wang, S. N. Piramanayagam, S. C. Ng, M. H. Kuok, Appl. Phys. Lett. 98 (2011) 153107.
[296] F. S. Ma, H. S. Lim, Z. K. Wang, S. N. Piramanayagam, S. C. Ng, M. H. Kuok, IEEE Trans. Magn. 47 (2011) 2689.
[297] G. Duerr, M. Madami, S. Neusser, S. Tacchi, G. Gubbiotti, G. Carlotti, D. Grundler, Appl. Phys. Lett. 99 (2011) 202502.

[298] G. Duerr, S. Tacchi, G. Gubbiotti, D. Grundler, J. Phys. D: Appl. Phys. 47 (2014) 325001.
[299] M. Krawczyk, S. Mamica, M. Mruczkiewicz, J. W. Klos, S. Tacchi, M. Madami, G. Gubbiotti, G. Duerr, D. Grundler, J. Phys. D: Appl. Phys. 46 (2013) 495003.
[300] S. Tacchi, G. Duerr, J. W. Klos, M. Madami, S. Neusser, G. Gubbiotti, G. Carlotti, M. Krawczyk, D. Grundler, Phys. Rev. Lett. 109 (2012) 137202.
[301] H. Yu, G. Duerr, R. Huber, M. Bahr, T. Schwarze, F. Brandl, D. Grundler, Nat. Commun. 4 (2013) 2702.
[302] X. M. Liu, J. Ding, A. O. Adeyeye, Appl. Phys. Lett. 100 (2012) 242411.
[303] S. Choudhury, S. Saha, R. Mandal, S. Barman, Y. Otani, A. Barman, ACS Appl. Mater. Interfaces 8 (2016) 18339.
[304] T. Shinjo, T. Okuno, R. Hassdorf, K. Shigeto, T. Ono, Science 289 (2000) 930.
[305] K. Shigeto, T. Okuno, K. Mibu, T. Shinjo, T. Ono, Appl. Phys. Lett. 80 (2002) 4190.
[306] A. Wachowiak, J. Wiebe, M. Bode, O. Pietzsch, M. Morgenstern, R. Wiesendanger, Science 298 (2002) 577.
[307] K. Y. Guslienko, W. Scholz, R. W. Chantrell, V. Novosad, Phys. Rev. B 71 (2005) 144407.
[308] B. Van Waeyenberge, A. Puzic, H. Stoll, K. W. Chou, T. Tyliszczak, R. Hertel, M. Fahnle, H. Bruckl, K. Rott, G. Reiss, I. Neudecker, D. Weiss, C. H. Back, G. Schutz, Nature 444 (2006) 461.
[309] K. Yamada, S. Kasai, Y. Nakatani, K. Kobayashi, H. Kohno, A. Thiaville, T. Ono, Nat. Mater. 6 (2007) 270.
[310] K. Y. Guslienko, X. F. Han, D. J. Keavney, R. Divan, S. D. Bader, Phys. Rev. Lett. 96 (2006) 067205.
[311] J. P. Park, P. Eames, D. M. Engebretson, J. Berezovsky, P. A. Crowell, Phys. Rev. B 67 (2003) 020403.
[312] A. Vogel, A. Drews, T. Kamionka, M. Bolte, G. Meier, Phys. Rev. Lett. 105 (2010) 037201.
[313] K. S. Buchanan, P. E. Roy, M. Grimsditch, F. Y. Fradin, K. Y. Guslienko, S. D. Bader, V. Novosad, Nat. Phys. 1 (2005) 172.
[314] S. Sugimoto, Y. Fukuma, S. Kasai, T. Kimura, A. Barman, Y. Otani, Phys. Rev. Lett. 106 (2011) 197203.
[315] V. S. Pribiag, I. N. Krivorotov, G. D. Fuchs, P. M. Braganca, O. Ozatay, J. C. Sankey, D. C. Ralph, R. A. Buhrman, Nat. Phys. 3 (2007) 498.
[316] R. Antos, Y. Otani, J. Shibata, J. Phys. Soc. Jpn. 77 (2008) 031004.
[317] S. Barman, A. Barman, Y. Otani, IEEE Trans. Magn. 46 (2010) 1342.
[318] H. Jung, Y.-S. Choi, K.-S. Lee, D.-S. Han, Y.-S. Yu, M.-Y. Im, P. Fischer, S.-K. Kim, ACS Nano 6 (2012) 3712.
[319] D. Kumar, S. Barman, A. Barman, Sci. Rep. 4 (2014).
[320] S. Barman, S. Saha, S. Mondal, D. Kumar, A. Barman, Sci. Rep. 6 (2016) 33360.
[321] W. Jung, F. J. Castaño, C. A. Ross, Phys. Rev. Lett. 97 (2006) 247209.
[322] C. Moreau-Luchaire *et al.*, Nat. Nanotechnol. 11 (2016) 444.
[323] D. A. Gilbert, B. B. Maranville, A. L. Balk, B. J. Kirby, P. Fischer, D. T. Pierce, J. Unguris, J. A. Borchers, K. Liu, Nat. Commun. 6 (2015) 8462.
[324] K. Y. Guslienko, IEEE Magn. Lett. 6 (2015) 1.
[325] S. Woo *et al.*, Nat. Mater. 15 (2016) 501.
[326] P. A. M. Dirac, Proc. Royal Soc. Lond. 133 (1931) 60.
[327] G. t. Hooft, Nucl. Phys. B 79 (1974) 276.

[328] L. Balents, Nature 464 (2010) 199.
[329] M. J. Harris, S. T. Bramwell, D. F. McMorrow, T. Zeiske, K. W. Godfrey, Phys. Rev. Lett. 79 (1997) 2554.
[330] S. T. Bramwell, M. J. P. Gingras, Science 294 (2001) 1495.
[331] L. Pauling, J. Am. Chem. Soc. 57 (1935) 2680.
[332] O. Tchernyshyov, Nature 451 (2008) 22.
[333] A. J. Heeger, S. Kivelson, J. R. Schrieffer, W. P. Su, Rev. Mod. Phys. 60 (1988) 781.
[334] L. D. Faddeev, L. A. Takhtajan, Phys. Lett. A 85 (1981) 375.
[335] B. Lake, D. A. Tennant, C. D. Frost, S. E. Nagler, Nat. Mater. 4 (2005) 329.
[336] H.-B. Braun, J. Kulda, B. Roessli, D. Visser, K. W. Krämer, H.-U. Güdel, P. Böni, Nat. Phys. 1 (2005) 159.
[337] R. de-Picciotto, M. Reznikov, M. Heiblum, V. Umansky, G. Bunin, D. Mahalu, Physica B: Condensed Matter 249-251 (1998) 395.
[338] M. Dolev, M. Heiblum, V. Umansky, A. Stern, D. Mahalu, Nature 452 (2008) 829.
[339] L. D. C. Jaubert, P. C. W. Holdsworth, Nat. Phys. 5 (2009) 258.
[340] D. J. P. Morris, D. A. Tennant, S. A. Grigera, B. Klemke, C. Castelnovo, R. Moessner, C. Czternasty, M. Meissner, K. C. Rule, J. U. Hoffmann, K. Kiefer, S. Gerischer, D. Slobinsky, R. S. Perry, Science 326 (2009) 411.
[341] T. Fennell, P. P. Deen, A. R. Wildes, K. Schmalzl, D. Prabhakaran, A. T. Boothroyd, R. J. Aldus, D. F. McMorrow, S. T. Bramwell, Science 326 (2009) 415.
[342] A. D. Bianchi, M. Kenzelmann, L. DeBeer-Schmitt, J. S. White, E. M. Forgan, J. Mesot, M. Zolliker, J. Kohlbrecher, R. Movshovich, E. D. Bauer, J. L. Sarrao, Z. Fisk, C. Petrović, M. R. Eskildsen, Science 319 (2008) 177.
[343] M. Laver, E. M. Forgan, Nat. Commun. 1 (2010) 45.
[344] E. Mengotti, L. J. Heyderman, A. F. Rodríguez, F. Nolting, R. V. Hügli, H.-B. Braun, Nat. Phys. 7 (2010) 68.
[345] S. Ladak, D. E. Read, G. K. Perkins, L. F. Cohen, W. R. Brandford, Nat. Phys. 6 (2010) 359.
[346] C. Phatak, A. K. Petford-Long, O. Heinonen, M. Tanase, M. De Graef, Phys. Rev. B 83 (2011) 174431.
[347] J. H. Rodrigues, L. A. S. Mól, W. A. Moura-Melo, A. R. Pereira, Appl. Phys. Lett. 103 (2013) 092403.
[348] K. K. Kohli, A. L. Balk, J. Li, S. Zhang, I. Gilbert, P. E. Lammert, V. H. Crespi, P. Schiffer, N. Samarth, Phys. Rev. B 84 (2011) 180412.
[349] L. Sam, R. Dan, T. Tolek, R. B. Will, F. C. Lesley, New J. Phys. 13 (2011) 023023.
[350] S. Ladak, D. E. Read, W. R. Branford, L. F. Cohen, New J. Phys. 13 (2011) 063032.
[351] S. D. Pollard, V. Volkov, Y. Zhu, Phys. Rev. B 85 (2012) 180402.
[352] U. B. Arnalds, A. Farhan, R. V. Chopdekar, V. Kapaklis, A. Balan, E. T. Papaioannou, M. Ahlberg, F. Nolting, L. J. Heyderman, B. Hjörvarsson, Appl. Phys. Lett. 101 (2012) 112404.
[353] J. M. Porro, A. Bedoya-Pinto, A. Berger, P. Vavassori, New J. Phys. 15 (2013) 055012.
[354] A. Farhan, P. M. Derlet, A. Kleibert, A. Balan, R. V. Chopdekar, M. Wyss, J. Perron, A. Scholl, F. Nolting, L. J. Heyderman, Phys. Rev. Lett. 111 (2013) 057204.
[355] L. J. Heyderman, Nat. Nanotechnol. 8 (2013) 705.
[356] Y. Li, G. Gubbiotti, F. Casoli, S. A. Morley, F. J. T. Gonçalves, M. C. Rosamond, E. H. Linfield, C. H. Marrows, S. McVitie, R. L. Stamps, J. Appl. Phys. 121 (2017) 103903.

[357] Y. Li, G. Gubbiotti, F. Casoli, F. J. T. Gonçalves, S. A. Morley, M. C. Rosamond, E. H. Linfield, C. H. Marrows, S. McVitie, R. L. Stamps, J. Phys. D: Appl. Phys. 50 (2017) 015003.
[358] J. Sklenar, V. S. Bhat, L. E. DeLong, J. B. Ketterson, J. Appl. Phys. 113 (2013) 17B530.
[359] S. Gliga, A. Kákay, R. Hertel, O. G. Heinonen, Phys. Rev. Lett. 110 (2013) 117205.
[360] K. Zeissler, S. K. Walton, S. Ladak, D. E. Read, T. Tyliszczak, L. F. Cohen, W. R. Branford, Sci. Rep. 3 (2013) 1252.
[361] M. B. Jungfleisch, W. Zhang, E. Iacocca, J. Sklenar, J. Ding, W. Jiang, S. Zhang, J. E. Pearson, V. Novosad, J. B. Ketterson, O. Heinonen, A. Hoffmann, Phys. Rev. B 93 (2016) 100401.
[362] V. S. Bhat, F. Heimbach, I. Stasinopoulos, D. Grundler, Phys. Rev. B 93 (2016) 140401.
[363] V. S. Bhat, F. Heimbach, I. Stasinopoulos, D. Grundler, Phys. Rev. B 96 (2017) 014426.
[364] M. Pohlit, I. Stockem, F. Porrati, M. Huth, C. Schröder, J. Müller, J. Appl. Phys. 120 (2016) 142103.
[365] M. Krawczyk, D. Grundler, J. Phys. Condens. Matter 26 (2014) 123202.
[366] X. Zhou, G.-L. Chua, N. Singh, A. O. Adeyeye, Adv. Funct. Mater. 26 (2016) 1437.
[367] G.-W. Chern, M. J. Morrison, C. Nisoli, Phys. Rev. Lett. 111 (2013) 177201.
[368] G.-W. Chern, C. Reichhardt, C. Nisoli, Appl. Phys. Lett. 104 (2014) 013101.
[369] E. Östman, H. Stopfel, I.-A. Chioar, U. B. Arnalds, A. Stein, V. Kapaklis, B. Hjörvarsson, Nat. Phys. 14 (2018) 375.
[370] U. B. Arnalds, M. Ahlberg, M. S. Brewer, V. Kapaklis, E. T. Papaioannou, M. Karimipour, P. Korelis, A. Stein, S. Ólafsson, T. P. A. Hase, B. Hjörvarsson, Appl. Phys. Lett. 105 (2014) 042409.
[371] S. S. P. Parkin, M. Hayashi, L. Thomas, Science 320 (2008) 190.
[372] H. Forster, T. Schrefl, D. Suess, W. Scholz, V. Tsiantos, R. Dittrich, J. Fidler, J. Appl. Phys. 91 (2002) 6914.
[373] M. Yan, C. Andreas, A. Kákay, F. García-Sánchez, R. Hertel, Appl. Phys. Lett. 99 (2011) 122505.
[374] M. Gavagnin, H. D. Wanzenboeck, S. Wachter, M. M. Shawrav, A. Persson, K. Gunnarsson, P. Svedlindh, M. Stöger-Pollach, E. Bertagnolli, ACS Appl. Mater. Interfaces 6 (2014) 20254.
[375] V. E. Demidov, M. P. Kostylev, K. Rott, J. Münchenberger, G. Reiss, S. O. Demokritov, Appl. Phys. Lett. 99 (2011) 082507.
[376] K.-S. Lee, D.-S. Han, S.-K. Kim, Phys. Rev. Lett. 102 (2009) 127202.
[377] D. R. Birt, B. O'Gorman, M. Tsoi, X. Q. Li, V. E. Demidov, S. O. Demokritov, Appl. Phys. Lett. 95 (2009) 122510.
[378] S. K. Kim, K. S. Lee, D. S. Han, Appl. Phys. Lett. 95 (2009) 082507.
[379] F. Heussner, A. A. Serga, T. Brächer, B. Hillebrands, P. Pirro, Appl. Phys. Lett. 111 (2017) 122401.
[380] H. W. Schumacher, C. Chappert, P. Crozat, R. C. Sousa, P. P. Freitas, M. Bauer, Appl. Phys. Lett. 80 (2002) 3781.
[381] Y. Au, M. Dvornik, O. Dmytriiev, V. V. Kruglyak, Appl. Phys. Lett. 100 (2012) 172408.
[382] T. Brächer, O. Boulle, G. Gaudin, P. Pirro, Phys. Rev. B 95 (2017) 064429.
[383] M. Voto, L. Lopez-Diaz, E. Martinez, Sci. Rep. 7 (2017) 13559.

[384] Y. Acremann, X. W. Yu, A. A. Tulapurkar, A. Scherz, V. Chembrolu, J. A. Katine, M. J. Carey, H. C. Siegmann, J. Stohr, Appl. Phys. Lett. 93 (2008) 102513.
[385] K. Vogt, F. Y. Fradin, J. E. Pearson, T. Sebastian, S. D. Bader, B. Hillebrands, A. Hoffmann, H. Schultheiss, Nat. Commun. 5 (2014) 3727.
[386] K. S. Lee, S. K. Kim, J. Appl. Phys. 104 (2008) 053909.
[387] S. K. Choi, K. S. Lee, S. K. Kim, Appl. Phys. Lett. 89 (2006) 062501.
[388] J. Podbielski, F. Giesen, D. Grundler, Phys. Rev. Lett. 96 (2006) 167207.
[389] R. Zivieri, IEEE Trans. Magn. 50 (2014) 1.
[390] A. V. Chumak, A. A. Serga, B. Hillebrands, Nat. Commun. 5 (2014).
[391] T. Schneider, A. A. Serga, B. Leven, B. Hillebrands, R. L. Stamps, M. P. Kostylev, Appl. Phys. Lett. 92 (2008) 022505.
[392] M. P. Kostylev, A. A. Serga, T. Schneider, B. Leven, B. Hillebrands, Appl. Phys. Lett. 87 (2005) 153501
[393] J. Topp, D. Heitmann, M. P. Kostylev, D. Grundler, Phys. Rev. Lett. 104 (2010) 207205.
[394] J. Ding, M. Kostylev, A. O. Adeyeye, Appl. Phys. Lett. 100 (2012) 073114.
[395] J. Åkerman, Science 308 (2005) 508.
[396] V. E. Demidov, J. Jersch, S. O. Demokritov, K. Rott, P. Krzysteczko, G. Reiss, Phys. Rev. B 79 (2009) 054417.
[397] P. Pirro, T. Koyama, T. Brächer, T. Sebastian, B. Leven, B. Hillebrands, Appl. Phys. Lett. 106 (2015) 232405.
[398] K. Wagner, A. Kákay, K. Schultheiss, A. Henschke, T. Sebastian, H. Schultheiss, Nat. Nanotechnol. 11 (2016) 432.

Chapter 2

2. Theoretical Backdrop

The fundamental origin of the intrinsic magnetic properties of one material lies in its molecular structure as well as in its electronic arrangement. The spin of the electrons, together with the number of unpaired electrons, the interactions between their spin and orbital momenta and finally their ordering determine the magnetic response both in microscopic and macroscopic level. Based on that, materials can be classified as diamagnet [1-4], paramagnet [5], ferromagnet [6-10], ferrimagnet [11,12], and antiferromagnet [13,14]. Amongst them, the ferromagnetic (FM) and ferrimagnetic materials possess spontaneous magnetization [15]. This thesis will focus on the properties of ferromagnetic (FM) materials. The transition metals (to which iron, cobalt and nickel belong) are characterized by partially filled internal electron shell corresponding to the 3*d* levels. The 3*d* band is very narrow and hence the kinetic energy of 3*d* electrons is small while the density of states is very high. These facts lead to the intricate interaction between the 3*d* electrons of neighbouring atoms (known as exchange interaction) which is responsible for the magnetic ordering of the material. According to the Weiss theory [16,17], this exchange interaction has to compete with the dipolar interaction caused by the free magnetic poles on the surface (i.e. demagnetizing field), which ends up in the FM to break up into small domains for the minimization of the free energy.

The individual moments of an FM material collectively contribute to a volume magnetization *M*, which is maximum when the moments are fully aligned under a large enough external magnetic field. In presence of the magnetic field, the coupled moments precess about the field direction, which is called the ferromagnetic resonance (FMR) in case of uniform precession (the moments have same frequency and phase) [18,19]. When the precession is not uniform, each individual dipole precesses slightly out-of-phase with its nearest neighbour. This produces a propagating wave, known as spin-wave (SW) [20], with its energy and momentum related by characteristic dispersion relations. The parameter that describes the rate of energy loss of precessing magnetization, is called magnetic damping, which can be intrinsic (e.g. due to spin-orbit

coupling) or extrinsic (e.g. due to two-magnon scattering) depending upon its origin. Another exotic property observed in FM materials is magnetic anisotropy that is the dependence of magnetic energy on the direction of the spins with respect to the crystal lattice, or, in patterned structures, with respect to the geometrical axes. This chapter starts off with an overview of the energies that play a role in the dynamics of an FM system followed by the illustration of different aspects of SWs. Next, several aspects of spin currents and the underlying physics behind their generation and manipulation have been discussed. Consequently, different phenomena of probing SWs will be explained.

2.1. Magnetic Energy

The static and dynamic behaviours of magnetic material are strongly dependent on the relative contribution of different energy terms e.g. Zeeman energy, magnetostatic self-energy (demagnetizing energy), exchange energy, and magnetic anisotropy energy [8,9,21-23]. In equilibrium condition, the system always tries to stay at a local minimum of the total free energy. This section presents a brief outline of crucial energy contributions.

2.1.1. Zeeman Energy

This [3,24-26] reflects the interaction between the magnetization (M) of the specimen and an externally applied magnetic field ($\boldsymbol{H}_{\text{ext}}$) and it can be expressed as:

$$E_{\text{Zeeman}} = \mu_0 \int_0^{\text{V}} \boldsymbol{M}.\boldsymbol{H}_{\text{ext}} dV \tag{2.1}$$

where, V is the total volume occupied by the magnetic specimen, dV is the volume element and μ_0 corresponds to the permeability of free space. This reveals that in the presence of a magnetic field, the magnetization tends to align along $\boldsymbol{H}_{\text{ext}}$ to keep its energy to a minimum.

2.1.2. Exchange Energy

This is quantum-mechanical in nature consequently giving rise to the short-range magnetic ordering in magnetic materials through exchange interaction [27,28]. This interaction has a strong influence not only in ferromagnets but also in ferrimagnets and antiferromagnets, where the exchange interaction between the neighbouring magnetic ions tend to force the moments for parallel or antiparallel alignment to each other. Its origin can be explained from the Coulombic interaction energy and Pauli exclusion

principle, which can be phenomenologically described by the Heisenberg exchange Hamiltonian, given by

$$\widehat{\mathrm{H}}_{\mathrm{ex}} = -\sum_{i\neq j} J_{ij}\boldsymbol{S}_i.\boldsymbol{S}_j \tag{2.2}$$

where, $\boldsymbol{S}_i$ and $\boldsymbol{S}_j$ are the spin operators of the i-th and j-th atoms respectively and J_{ij} is the as exchange integral between them [29]. Here, depending upon the polarity (sign) of J_{ij} the material can be classified as ferromagnet or antiferromagnet. In the continuum model, the above equation can be written as:

$$E_{\mathrm{ex}} = A\int_0^{\mathrm{V}}(\nabla m)^2 dV \tag{2.3}$$

where, the magnetic moment (m) is a continuous vector quantity and A is called the exchange stiffness constant which can be expressed as:

$$A = \frac{2JS^2}{a} \tag{2.4}$$

where, a is the lattice constant while the exchange (J) is considered to be isotropic in the FM medium.

The aforementioned exchange interaction is known as direct exchange interaction where the electrons of magnetic atoms interact with its nearest neighbours. Howbeit, such exchange interaction can also take place in indirect ways [30,31], which couple magnetic moments over relatively larger distances. Some indirect exchanges are listed below.

2.1.2.1. RKKY Exchange

Here, the metallic ions are coupled through itinerant electrons [14,32,33].

2.1.2.2. Super-exchange

Here, the spins of the magnetic cations are exchange-coupled via different non-magnetic anions [34-39].

2.1.2.3. Antisymmetric (or Anisotropic) Exchange

In this three-site exchange interaction (also known as Dzyaloshinskii-Moriya interaction: DMI), the spin-orbit interaction and super-exchange play major role often leading to the canting of spins by a small angle [40-45].

2.1.3. Magnetic Dipolar Interaction

The interaction [8,9,21,22,46] between two magnetic dipoles can be observed in all material irrespective of whether it is FM material or not (but with different strength). The corresponding energy term is written as:

$$E_{\mathrm{d}} = \frac{\mu_0}{4\pi r^3}\left[\boldsymbol{m}_1.\boldsymbol{m}_2 - \frac{3}{r^2}(\boldsymbol{m}_1.\boldsymbol{r})(\boldsymbol{m}_2.\boldsymbol{r})\right] \quad (2.5)$$

where, μ_0 is the permeability in free space, m_1 and m_2 are the moments of the two magnetic dipoles and $\boldsymbol{r}$ is the vector connecting the two dipoles which experience the magnetic field generated by each other. The above Equation 2.5 explains that the energy reduces with the third order of their distance, *r*. In case of ferromagnets, although this interaction does not contribute to magnetic ordering, it plays a pivotal role in a number of phenomena such as domain formation, demagnetizing field distributions and characterization of SWs in the long wavelength regime.

2.2. Magnetic Anisotropy

This can be treated as the directional preference of magnetic properties of the material. As a result, there are preferential directions in space (known as easy axes of magnetization) along which a magnetic system is easier to magnetize than to other directions. Deviation from these directions imposes an energy loss, called the anisotropy energy [47-50]. Basically, there are two primary (microscopic) sources of magnetic anisotropy which are magnetic dipolar interaction [32,51] and the spin-orbit interaction (SOI) [52,53]. As the dipolar interaction is long-range in nature, its contribution to the anisotropy depends on the shape of the specimen [3,54]. This is crucial for thin films and is greatly responsible for the in-plane (IP) magnetization observed usually in these films. In the absence of dipolar interaction and SOI, the total energy of the electron-spin system is independent of the magnetization direction. In a localized picture, the spins are coupled to the orbits via the SOI which in turn get influenced by the crystal lattice. The SOI induces a small orbital momentum for itinerant materials which therefore couples the total magnetic moment (i.e. spin and orbital moments) to the crystal axes. As a result, the total energy becomes dependent on the magnetization orientation relative to the crystalline axes which reflect the symmetry of the crystal. This is known as the magnetocrystalline contribution to the anisotropy. Also, the lowered symmetry at an interface strongly modulates this contribution in comparison with the bulk counterpart giving rise to an interfacial anisotropy. In conjunction with the overlap in wavefunctions between the neighbouring atoms, the SOI is also responsible for the magnetostrictive or magneto-elastic (ME) anisotropy induced in a system under strain and this is frequently observed in multilayers because of the

lattice mismatch between the adjacent layers. Here, different anisotropy contributions are discussed briefly in the following.

2.2.1. Volume, Surface and Interface Anisotropy

The broken symmetry at surfaces and interfaces of magnetic thin films and multilayers often induces some anisotropy in the system. This results in the effective anisotropy (K_{eff}) constant to be divided into two parts as given below:

$$K_{\text{eff}} = K_{\text{V}} + \frac{2K_{\text{S}}}{t} \tag{2.6}$$

Here, K_{V} denotes the volume dependent magnetocrystalline anisotropy constant while K_{S} is the contribution from the surface anisotropy. The latter generally possesses an inverse dependence on the thickness (t) of the system and prefers an out of plane magnetization of the sample. The competition between volume and surface anisotropy gives rise to a dependence of the magnetization on the film thickness. The magnetization favours an out of plane orientation (i.e. perpendicular magnetic anisotropy: PMA) and vice versa below a critical thickness expressed as:

$$t_{\text{c}} = \left|\frac{2K_{\text{S}}}{K_{\text{V}}}\right| \tag{2.7}$$

In case of some multilayer systems (e.g. Co/Pd, Co/Pt, Fe/Pd, Co/MgO, CoFeB/MgO, Fe/MgO heterostructures), the interfacial anisotropy has been observed [55-66] which stems from the interfacial hybridization of the electronic band structure. These hybridizations are sensitive to the local interface structure and affect the spin-orbit coupling (SOC) strength, which in turn changes the magnetic anisotropy energy.

2.2.2. Magnetocrystalline Anisotropy

This is an inherent behaviour of the magnetic material originating from the spin-orbit interaction (SOI) of the electrons [67-74]. The spatial arrangement of the electron orbitals is strongly linked to the crystallographic structure. As a consequence, the interaction with the electron spins leads towards the alignment of spins along the well-defined crystallographic axes. Now, the foldedness of the magnetic anisotropy can be determined from the symmetry of the lattice structure. In general, the magnetocrystalline anisotropy energy (G_{crystal}) can be expressed in successive powers of components (α_i):

$$G_{\text{crystal}}(\hat{m}) = b_0(\hat{m}) + \sum_{ij} b_{ij}\alpha_i\alpha_j + \sum_{ijkl} b_{ijkl}\alpha_i\alpha_j\alpha_k\alpha_l \tag{2.8}$$

where, α_i are the direction cosines of the magnetization m ($\hat{m}$ is the unit vector along m) with respect to the Cartesian axes of the lattice such that:

$$\sum_i {\alpha_i}^2 = 1 \tag{2.9}$$

For instance, in cubic systems the energy density due to crystal anisotropy can be written as:

$$E_{\text{ani}} = K_0 + K_1\left(\alpha_x^2\alpha_y^2 + \alpha_y^2\alpha_z^2 + \alpha_z^2\alpha_x^2\right) + K_2\alpha_x^2\alpha_y^2\alpha_z^2 \tag{2.10}$$

K_i's are the magnetocrystalline anisotropy constants, e.g. K_0, K_1, and K_2 are the crystalline anisotropy constants of zero, first and second order, respectively. On the other hand, for crystals having uniaxial anisotropy, the energy density is given by

$$E_{\text{ani}} = K_U(\alpha_x^2) \tag{2.11}$$

where, K_U is the uniaxial anisotropy constant.

2.2.3. Magnetic Dipolar (Shape) Anisotropy and Demagnetizing Energy

Another root cause behind the magnetic anisotropy comes from the anisotropic shape of the magnetic element which becomes more prominent at micro- or nanoscale. It is basically the anisotropic dipolar interaction of unsaturated magnetic dipoles (stray and demagnetization fields) which arises when the geometry of magnetic elements is not symmetric [54,75-81]. A magnetic system with finite boundaries exhibits poles at its surfaces leading towards a stray field distribution (lines of force) outside the sample. This, in effect, gives rise to the demagnetizing field inside the sample. The energy corresponding to the stray field is given by:

$$E_{\text{demag}} = -\frac{1}{2}\int_0^V \mu_0 \boldsymbol{M}.\boldsymbol{H}_{\text{demag}} dV \tag{2.12}$$

For an arbitrarily shaped element, $\boldsymbol{H}_{\text{demag}}$ is strongly dependent on the shape and geometry of the element and forms a complex function of position. Finally, the preferred orientation of magnetization lies along which E_{demag} becomes minimum.

2.2.4. Strain-induced Anisotropy

A magnetic system under strain acquires some anisotropy energy due to the change in the magnetoelastic (ME) energy [82-85]. Various sources can induce strain in the films, e.g. intrinsic strain brought about by the nature of the deposition process, strain because of non-matching lattice parameters of adjacent layers and thermal strain associated with differences in thermal expansion coefficients. During the fabrication of ultrathin films/multilayers, a great amount of strain can arise due to the epitaxial growth on a substrate with different lattice parameters (i.e. lattice mismatch between

the constituent materials of two consecutive layers) [86,87]. As a result, this strain induced anisotropy plays a crucial role in case of ultrathin heterostructures. It is also evident that under strain the symmetry of the material will be lowered. Consequently, new energy terms in the total anisotropy energy can be included which is forbidden in the unstrained state. On the other hand, as the magneto-elastic energy [88,89] is linear with respect to strain so the system tries to minimize its energy by acquiring an anisotropic non-zero strain, and this phenomenon is known as magnetostriction. The strain depends on the direction of magnetization and the magnitude is given by the competition between the elastic and magnetoelastic energy terms. Strain inside one FM material can modulate the magnetocrystalline anisotropy and therefore, it may alter the direction of the magnetization. This effect can be interpreted as the inverse of magnetostriction which can be defined as the change in the sample dimensions when the direction of the magnetization (M) is altered [90,91]. For an elastically isotropic medium with isotropic magnetostriction, the energy per unit volume associated with this effect can be expressed as:

$$E_{\mathrm{ME}} = -K_{\mathrm{ME}} \cos^2 \theta \tag{2.13}$$

where,

$$K_{\mathrm{ME}} = -\frac{3}{2}\lambda\sigma = -\frac{3}{2}\lambda M_{\mathrm{E}}\epsilon \tag{2.14}$$

Here, σ is the stress tensor which is related to the strain tensor (ϵ) via the elastic modulus M_{E} by:

$$\sigma = \epsilon M_{\mathrm{E}} \tag{2.15}$$

The magnetostriction constant λ can be positive or negative depending upon the orientation. The angle θ denotes the direction of the magnetization (M) relative to the direction of uniform stress. As the strain being present throughout the sample, this strain induced anisotropy contribution can be interpreted as a volume contribution to the total magnetic anisotropy.

2.2.5. Configurational Anisotropy

When the length scale of a magnetic element is reduced, the competition between exchange energy and the magnetostatic energy becomes very critical [92]. For non-ellipsoidal element, the deviation from uniform magnetization to the non-uniform magnetized state results in a strong anisotropy with symmetry known as configurational anisotropy [93-95], which corresponds to the shape of the magnetic

elements as well as the arrangement of these elements and this can be classified as below.

2.2.5.1. Intrinsic Configurational Anisotropy

Here the anisotropy [95,96] arises due to the deviation from single domain state to different magnetization state, e.g. leaf, flower, C- or S-state in a single magnetic element in the micro- or nanoscale as a result of different shape of that single element when kept under the various orientation of bias magnetic field.

2.2.5.2. Extrinsic Configurational Anisotropy

Magnetostatically unsaturated regions situated near the edges of an element vary with the azimuthal (in-plane) orientation of the external bias magnetic field. As a result, the magnetostatic interaction between the elements also changes drastically which will in turn influence the magnetic stray field (or demagnetizing field) distributions as well as the configurational magnetic anisotropy [94,97] depending upon the geometry of arrangement of the magnetic elements.

2.2.6. Perpendicular Magnetic Anisotropy (PMA)

The physical basis behind a preferred magnetic moment orientation in ultrathin magnetic films and multilayers can differ significantly from their bulk counterparts. The prominent presence of symmetry-breaking elements such as planar interfaces and surfaces or by choosing appropriate materials or changing the thicknesses of the individual layers, the magnetic anisotropy can be tailored. The most fascinating manifestation in this regard is the change of the preferential direction of the magnetization (M) from the commonly observed in-plane orientation to the direction perpendicular to the sample plane. This phenomenon is generally known as perpendicular magnetic anisotropy (PMA) [56,98-102] and it can play a pivotal role in information storage and retrieval applications as PMA is crucial to enhance the thermal stability of nanomagnets at room temperature. Usually, PMA is observed if the electron orbitals in an FM material are deformed in the direction perpendicular to the film interface. When M of the specimen is maintained along the out-of-plane (OOP) direction, the effective magnetic field (H_{eff}) of the system is substantially increased due to SOI (orbital deformation occurs in OOP direction). However, there is no effect of SOI when M lies in-plane (as the orbital is not deformed along the in-plane direction). Consequently, there is a stark difference in the absolute value of the magnetic energy

(i.e. |-($\boldsymbol{M}.\boldsymbol{H}_{\text{eff}}$)|) between the IP and OOP orientation of $\boldsymbol{M}$ and as a result, the direction of the easy axis of magnetization lies perpendicular to the sample plane. However, the origin of PMA has become a debated issue where few possible explanations are, reduced coordination symmetry, altered electronic structure, localized epitaxial strain at the interface, electronic band structure interactions etc.

Generally, strong PMA is observed at the interfaces between 3*d* transition metal FMs (e.g. Co) and heavy nonmagnetic metals (e.g. W, Au, Pt, Pd) [103]. Since the spins of electrons from localized *d* or *f* orbitals primarily contribute to the magnetization of an FM material, the PMA is mainly determined by the deformation and symmetry of these orbitals. For instance, in case of a FM with *d*-orbitals (e.g. Co), the OOP d_z^2 and d_{xz}, d_{yz} states located near the Fermi energy (E_F) possess smaller dispersion due to less overlap of neighbouring FM atoms as compared to in-plane d_{xy} and $d_{x^2-y^2}$ states because of strong interaction between Co atoms in the film plane. When, this FM layer is in contact with a non-magnetic layer, the energies and wave-functions of OOP states get modulated due to interfacial hybridization. These hybridizations are sensitive to the local interface structure and affect the SOC perturbation, which in turn changes the anisotropy energy. Hence, the PMA increases with the strength of the hybridization.

However, PMA can also be observed at the interfaces between 3*d* transition FMs (e.g. Co, Fe and their alloys like CoFeB) and MO_x (M = Mg, Al, Ta, Ru). However, the heterostructures made from CoFeB and MgO have drawn particular attention among the aforementioned materials due to lower damping constant of CoFeB and high tunnelling magnetoresistance (TMR) ratio at room temperature [58,104]. At CoFeB/MgO interface, the OOP $3d_z^2$ orbitals of Fe strongly bond with OOP $2p_z$ orbitals of O which results in a significant charge transfer from $3d_z^2$ to $2p_z$ orbitals. Thus, the number of electrons in OOP orbitals is decreased as compared to that in in-plane orbitals which introduces a moderate PMA via SOC [105].

2.2.7. Exchange Anisotropy

Exchange bias or exchange anisotropy [106-112] is found at the interface of FM/antiferromagnetic heterostructure when it is cooled in the presence of a static magnetic field through the Néel temperature (T_N) of the antiferromagnet (the Curie temperature (T_C) of the FM should be larger than T_N). This is a unidirectional anisotropy, e.g. the hysteresis loop of the such system, when it is field cooled (i.e. in the

presence of the magnetic field, H) at temperature $T < T_N$, has an increased coercivity and the loop shifts along the applied field axis (this is generally termed as the exchange bias). Both these effects disappear at $T \approx T_N$ which confirms that the presence of the antiferromagnet is crucial to achieve the exchange anisotropy. The exchange bias properties disappear if the FM/antiferromagnetic interface is cooled at zero field from demagnetized state although, the properties are retained if it is cooled at zero field from a remanent state.

Magnetic anisotropy can be measured from either static or dynamic response of the magnetic system. The static response can be investigated by torque magnetometry, torsion oscillating magnetometry (TOM), the magneto-optical Kerr effect (MOKE: static MOKE) [113-116] and other various methods which can measure the magnetic moment e.g. vibrating sample magnetometry (VSM), fluxgate magnetometry, superconducting quantum interference device (SQUID) magnetometry, pendulum magnetometry, alternating gradient magnetometry (AGM), Faraday balance [117-134] etc. However, the magnetic anisotropy is most frequently measured from magnetization measurements (by SQUID or VSM) along the two orthogonal directions of the magnetic field relative to the sample. On the other hand, the dynamic response of the magnetic systems can be investigated by Brillouin light scattering (BLS), ferromagnetic resonance (FMR) and MOKE (e.g. time-resolved MOKE: TRMOKE) [135-147] etc.

2.3. Voltage (or Electric Field) Controlled Magnetic Anisotropy (VCMA or ECMA)

The magneto-electric effect allows us to control magnetic properties by an electric field. Generally, multiferroic materials possess strong magneto-electric effect because of the presence of magnetic and electrical ordering simultaneously [148]. The strong coupling between magnetic and electric polarization allows to manipulate magnetic properties by an electric field and vice versa. However, multiferroic materials show low saturation magnetization and spin polarization, and there are only a few single-phase multiferroic materials available at room temperature as opposed to FM materials [149]. However, FM semiconductors such as (In, Mn)As, (Ga, Mn)As etc. also show electric field tunability of magnetic anisotropy and exchange interaction through electric field controlled carrier density[150]. Alternatively, the magneto-electric effect can be observed when a magnetostrictive film (e.g. Ni) is placed on a piezoelectric substrate (such as

$Pb(Mg_{1/3}Nb_{2/3})O_3$-$PbTiO_3$, $LiNbO_3$) [151]. Here, the strain induced in the piezoelectric substrate under the application of the electric field gets transferred to the adjacent FM layer and its magnetic properties are modified via magnetostriction. However, piezoelectric thin films are required instead of a piezoelectric substrate for practical applications. Another alternative route can be the voltage (i.e. electric field) controlled magnetic anisotropy (VCMA) which is generally observed at the interface between ultrathin 3*d* transition FM materials (e.g. Co, Fe and their alloys such as CoFeB) and nonmagnetic insulators (e.g. MgO, Al_2O_3) [152]. This VCMA is believed to be observed because of the relative changes of electronic occupation state in 3*d* orbitals of FM under the application of electric field [153,154].

As discussed earlier, a strong PMA can be achieved at 3*d* FM and heavy nonmagnetic metal interface although such systems also possess relatively high Gilbert damping parameter which is not desirable for current-induced magnetization switching and other spintronics applications. Moreover, it is not possible to modulate interfacial PMA (iPMA) by the electric field in these systems because of the absence of oxide or dielectric layer at the interface which is a basic criterion for observing VCMA effect. Hence, VCMA is primarily studied at the interfaces between FM and oxide heterostructures. When an electric field is applied at FM/oxide interface, the number of electrons in OOP *d* orbitals of FM is changed with respect to in-plane orbitals as explained from first principle calculations [153,155]. This affects the bonding strength between *d* and *p* orbitals leading to a substantial change of iPMA. Since the penetration depth of the electric field in metal is only few Å, this VCMA effect is only limited to ultrathin FM films (~ few nm). Although electric field control of electronic occupation state is believed to be the main mechanism behind VCMA, several alternative theories are also found in the literature. One of the alternative approaches has been taken where the inhomogeneous electric field at the FM metal/oxide interface couples to the quadrupole of electronic orbital in FM [156]. This electric quadrupole again couples to the magnetic dipoles and controls iPMA. Also, iPMA can be generated due to the presence of Rashba SOC at FM/oxide interface while, the applied electric field at the interface modifies Rashba SOC which further modulates iPMA [157]. Also, the development of tensile and compressive strain in the MgO layer has been demonstrated due to the application of an electric field with opposite polarity at FM/oxide interface [158]. Therefore, it is possible that the iPMA is

modulated by the piezoelectric property of MgO through the magneto-elastic coupling. In reality, all the above mechanisms may be present and contribute simultaneously to the modulation of iPMA. Moreover, these mechanisms neither require atomic movement nor require any chemical reaction, which enables high-speed operation of VCMA magnonic devices with high cycling endurance.

First principle calculation reveals that the change in the number of electrons in d orbitals of FM material is linearly proportional to the applied electric field (E) at FM/oxide interface [154]. Thus, the modulation in the magnetic moment and iPMA should also be linearly proportional to the electric field, i.e.

$$\Delta K_s = \beta E \tag{2.16}$$

Here, ΔK_s denotes the change in iPMA while, β is known as magneto-electric or VCMA coefficient [153]. This linear variation of iPMA with the electric field has been confirmed by Several experimental studies although the magnitude and sign of β depend upon several factors [159-161]. For instance, the VCMA coefficient and its sign can be same or different for the opposite polarity of electric field whereas, β and iPMA strongly depend upon annealing and measurement temperature [162,163]. These behaviours can be attributed to have intrinsic origin due to the electronic band structure at the FM/oxide interface. In addition, it has been shown that β can be dependent on the substrate, underlayer material, FM layer and MgO overlayer thickness [159,164-168]. Notably, only first-order anisotropy varies with an electric field, while the second order anisotropy remains unaltered which proves that only the first order anisotropy has interfacial origin [164,169]. Interestingly, the electric field applied at the FM/oxide interface not only changes the iPMA but also modulates Gilbert damping parameter. This can be attributed to the fact that both iPMA and Gilbert damping are originated from SOC. However, no correlation between the VCMA coefficient and electric field variation of Gilbert damping has been found so far.

2.4. Magnetization Dynamics:

The magnetic moments present in a magnetic material under the influence of an external magnetic field experience a torque which induces a precessional motion about the direction of the external field. In addition, the moments try to align themselves along the external field to minimize the Zeeman energy [170,171]. Effectively, they execute a damped spiral motion about the field direction which is referred to as

precessional magnetization dynamics [172,173] (See Figure 2.1). The net behaviour of dynamic magnetization is phenomenologically illustrated by the Landau-Lifshitz and Gilbert equation of motion. The Landau-Lifshitz-Gilbert (LLG) equation is generally a torque equation derived from quantum mechanical arguments which is further modified by the addition of a damping term [174-177]. The formulation is briefly described in the following.

When a magnetic moment $\boldsymbol{\mu}_{\mathrm{m}}$ is kept under the influence of an effective magnetic field H_{eff}, it experiences a torque given by:

$$\boldsymbol{\tau} = \boldsymbol{\mu}_{\mathrm{m}} \times \boldsymbol{H}_{\mathrm{eff}} \tag{2.17}$$

In a semiclassical approach, the magnetic moment ($\boldsymbol{\mu}_{\mathrm{m}}$) can be related to the angular momentum L of electrons as follows:

$$\boldsymbol{\mu}_{\mathrm{m}} = -\gamma \boldsymbol{L} \tag{2.18}$$

where,

$$\gamma = \frac{g\mu_{\mathrm{B}}}{\hbar} \tag{2.19}$$

is the gyromagnetic ratio, g is the Landé g-factor ($g \approx 2$), μ_{B} ($= \frac{e\hbar}{2m_e}$, e and m_{e} being the charge and mass of the electron) is the Bohr magneton and $\hbar$ ($= \frac{h}{2\pi}$, h being Planck's constant) is the reduced Planck's constant[178-181]. By applying the momentum theorem one can express Equation 2.17 as the rate of change of angular momentum L:

$$\frac{d\boldsymbol{L}}{dt} = \boldsymbol{\mu}_{\mathrm{m}} \times \boldsymbol{H}_{\mathrm{eff}} \tag{2.20}$$

This can be simplified as:

$$\frac{d\boldsymbol{\mu}}{dt} = -\gamma \boldsymbol{\mu} \times \boldsymbol{H}_{\mathrm{eff}} \tag{2.21}$$

Here, the effective magnetic field $\boldsymbol{H}_{\mathrm{eff}}$ is a sum of all external and internal magnetic fields which can be expressed as:

$$\boldsymbol{H}_{\mathrm{eff}} = \boldsymbol{H}_{\mathrm{ext}} + \boldsymbol{H}_{\mathrm{ex}} + \boldsymbol{H}_{\mathrm{demag}} + \boldsymbol{H}_{\mathrm{ani}} + \boldsymbol{h}(t) \tag{2.22}$$

Here, $\boldsymbol{H}_{\mathrm{ext}}$ is the applied bias magnetic field, $\boldsymbol{H}_{\mathrm{ex}}$ is the exchange field and $\boldsymbol{H}_{\mathrm{demag}}$ represents the demagnetization field created by the dipolar interaction of magnetic surface and volume charges. The field, $\boldsymbol{H}_{\mathrm{ani}}$ includes all kinds of anisotropic fields described above while, $\boldsymbol{h}(t)$ is the dynamic component.

In the continuum limit, the atomic magnetic moment can be replaced by the macroscopic magnetization ($\boldsymbol{M}$) resulting in the equation of motion, i.e. Landau-Lifshitz (LL) equation:

$$\frac{d\boldsymbol{M}}{dt} = -\gamma \boldsymbol{M} \times \boldsymbol{H}_{\text{eff}} \tag{2.23}$$

Physically, the above Equation 2.23 features a continuum precession which means that the system is non-dissipative. To avoid this impractical situation, Landau and Lifshitz proposed the damping term [176] to be:

$$-\lambda \boldsymbol{m} \times (\boldsymbol{m} \times \boldsymbol{H}_{\text{eff}}) \tag{2.24}$$

Later, Gilbert introduced another damping term [177,182] into the LL equation resulting in the modified Landau-Lifshitz-Gilbert (LLG) equation as:

$$\frac{d\boldsymbol{M}}{dt} = -\gamma(\boldsymbol{M} \times \boldsymbol{H}_{\text{eff}}) + \frac{\alpha}{M_s}\left(\boldsymbol{M} \times \frac{d\boldsymbol{M}}{dt}\right) \tag{2.25}$$

Here α is the dimensionless Gilbert damping parameter while, M_s is the saturation magnetization of the magnetic material.

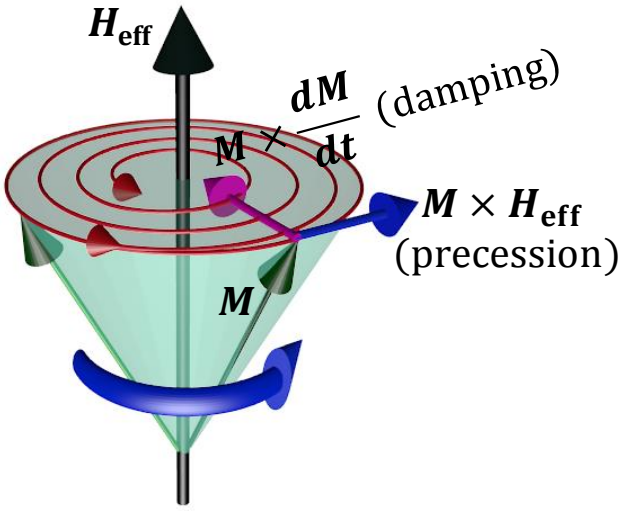

Figure 2.1. The precessional motion of the magnetization ($\boldsymbol{M}$) around the effective magnetic field ($\boldsymbol{H}_{\text{eff}}$) direction revealing the separate torque components of the LLG equation. Here, $\boldsymbol{H}_{\text{eff}}$ initiates the precessional motion of $\boldsymbol{M}$ while, the energy is dissipated through magnetic damping and $\boldsymbol{M}$ will relax along the $\boldsymbol{H}_{\text{eff}}$ direction.

Figure 2.1 schematically illustrates the interplay between different torques acting on the magnetization vector ($\boldsymbol{M}$). The precessional torque (the first term on the right-hand side of Equation 2.25) acts tangentially to the circle traced by the tip of the magnetization vector, while the damping torque (the second term) acts radially to align

the magnetization along the effective magnetic field. Magnetic damping can be described as the energy dissipation from the magnetisation to the thermal bath [183]. However, the effective damping can arise due to the intrinsic and extrinsic factors. The intrinsic mechanism [184] of damping primarily originates from the SOI by which the spin is coupled to the lattice making the damping parameter (α) a material parameter [185-187] or due to the interfacial effects such as interfacial *d*-*d* hybridisation, spin pumping etc. occurring across the interface in case of FM/nonmagnetic heterostructures [188,189]. However, apart from SOI, different external stimuli, such as magnon-electron scattering, eddy currents, spin pumping, multimagnon scattering [190-208] etc. can also contribute to the relaxation of magnetization precession amplitude. Howbeit, the intrinsic and extrinsic contributions can be separated from each other as the extrinsic contribution results in a shift in the precessional frequency. Also, extrinsic damping depends on the magnetic field (H_{eff}) value whereas the intrinsic damping is independent of such aforementioned factors [209,210].

2.4.1. Time Scales of Magnetization Dynamics

Magnetization dynamics covers a broad range of phenomena occurring at various timescales [211] starting from a few fs to μs. The fastest dynamics which typically covers the time scales in fs range includes fundamental exchange interaction (~ 10 fs), spin transfer-torque (~ 10 fs–1 ps) and laser-induced ultrafast demagnetization (~ hundreds of fs). The relatively slower phenomenon is the precession of magnetization (characteristic time scale ~ few tens to hundreds of picoseconds which causes the propagation of SWs in FM materials) before it gets damped in sub-ns to tens of ns. Afterwards, the reversal of spins (characteristic time scale few ps to few hundreds of ps, useful in magnetic recording technology), as well as vortex core switching (few tens of ps to several ns), take place. Finally, the slowest one is the domain wall dynamics which typically takes place between few nanoseconds (ns) to few μs.

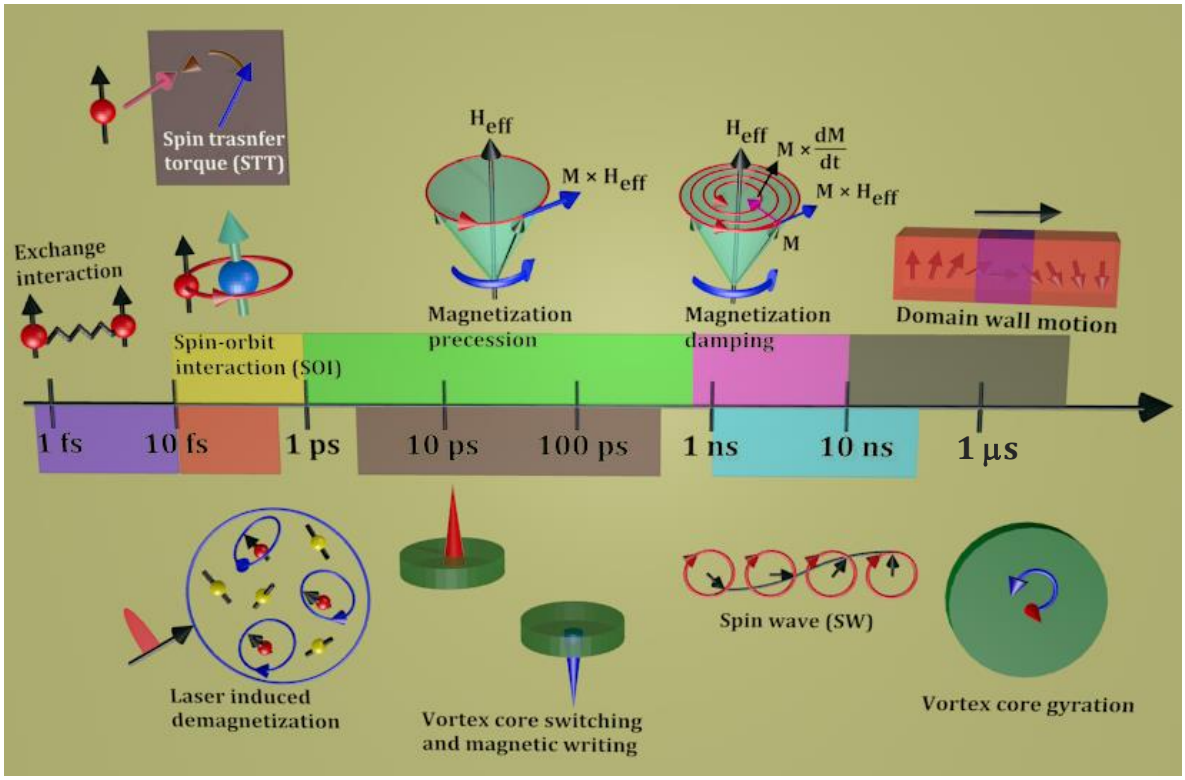

Figure 2.2. Characteristic time scales of different genres of physical phenomena in magnetization dynamics.

2.4.2. Laser-Induced Magnetization Dynamics

When a very short (in the order of fs) high energy laser pulse is made incident on a magnetized FM sample, it leads to ultrafast demagnetization within about hundreds of fs. The physical origin behind the ultrafast demagnetization is still a topic of intense debate after its successful demonstration which has been explained by considering a three-temperature model (here, the system is assumed to be comprised of three thermalized reservoirs for exchanging energy namely, electron, lattice and spin systems at different temperatures) [212]. However, there are several different approaches pursued to explain the underlying physical mechanism, such as, excitation of stoner pairs, spin-orbit coupling (SOC), coupling with the electromagnetic field via a terahertz emission, considering relativistic quantum electrodynamics (non-linear modulation of angular momentum after the coherent interaction of photon or laser with electron and spin), scattering of spins with impurity centres or phonons, e.g. Elliott-Yafet (EY) type of scattering (the transfer of angular momentum between electron, spin and lattice is considered), electron-magnon spin-flip scattering and Coulomb exchange spin-flip scattering (considers electron-electron Coulomb scattering), laser-induced spin flip

(considering many-body theory with quantum optics), superdiffusive spin transport (assuming spin-dependent transport of laser-excited electrons) [213-238] etc. As soon as the laser pulse is withdrawn, the system tries to recover its equilibrium state via remagnetization process. This initially happens through a fast relaxation precess (within few tens of ps) due to the exchange of energy from hot electrons (electrons in the system get highly energised during the altercation with laser or photons) and spins to the lattice which has been phenomenologically described by the three-temperature model [212,221] (earlier, the role of spins has been ignored in two-temperature model [239]). Subsequently, there is a slow recovery of magnetization via the diffusion of electron and lattice heat to the surrounding environment [240,241]. In the course of the slow relaxation process, the magnetization of the FM system also undergoes a precessional motion about the effective magnetic field, which eventually damps out within a few ns.

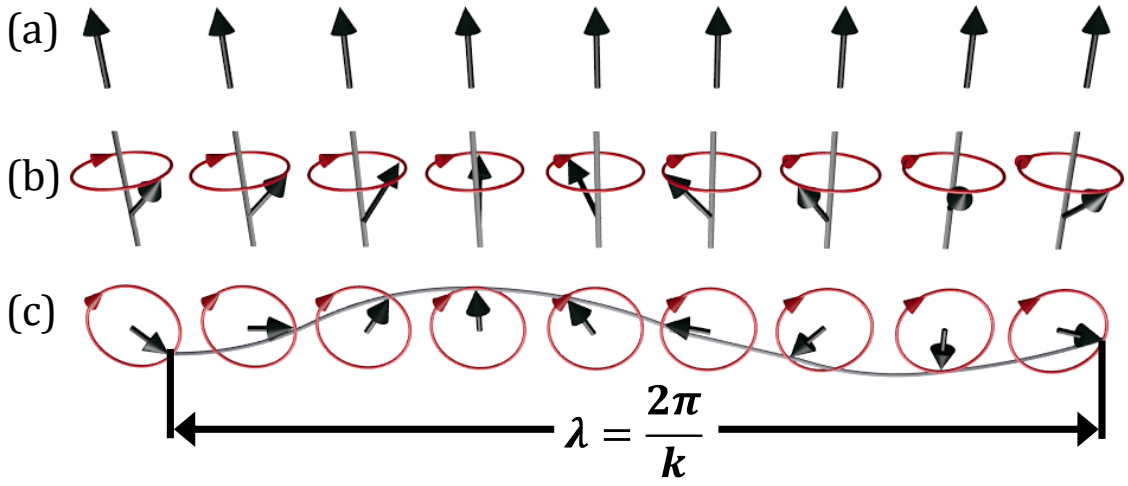

Figure 2.3. Semiclassical representation of spin wave in an FM material: (a) the ground state of the magnetic moments, (b) precessing magnetic moments with different phases and (c) the spin wave (SW) (top view) showing a complete wavelength (λ).

2.5. Spin Waves (SWs)

The concept of spin waves (SWs) has been introduced in order to explain the reduction of the spontaneous magnetization in an FM system [20,242]. Perturbations created in ordered magnetic materials can set off a wave which can travel through the magnetic material. These waves are known as SWs [243], which are basically dynamic eigenmodes of magnetic materials. The particle counterpart of SW is commonly known

as magnon [244]. It can be described by a semi-classical approach where all the atomic magnetic moments of a ferromagnet are aligned in the same direction as shown in Figure 2.3(a), at absolute zero temperature which is the ground state of the system. When the temperature is increased, the thermal agitation perturbs the spontaneous magnetization creating a deviation of the spins from their aligned direction or ground state. This phase of the disturbance is mediated through the system in the form of SW as depicted in Figure 2.3(b, c). In case of uniform precession in presence of a magnetic field, the spins of the system precess in phase about the field direction, i.e. the wavelength (wave vector) of SW is nearly infinity (zero). By solving LLG equation (Equation 2.25) the frequency of uniform precession (known as uniform ferromagnetic resonance or FMR frequency) can be calculated by considering:

$$\frac{d\boldsymbol{M}}{dt} = 0 \tag{2.26}$$

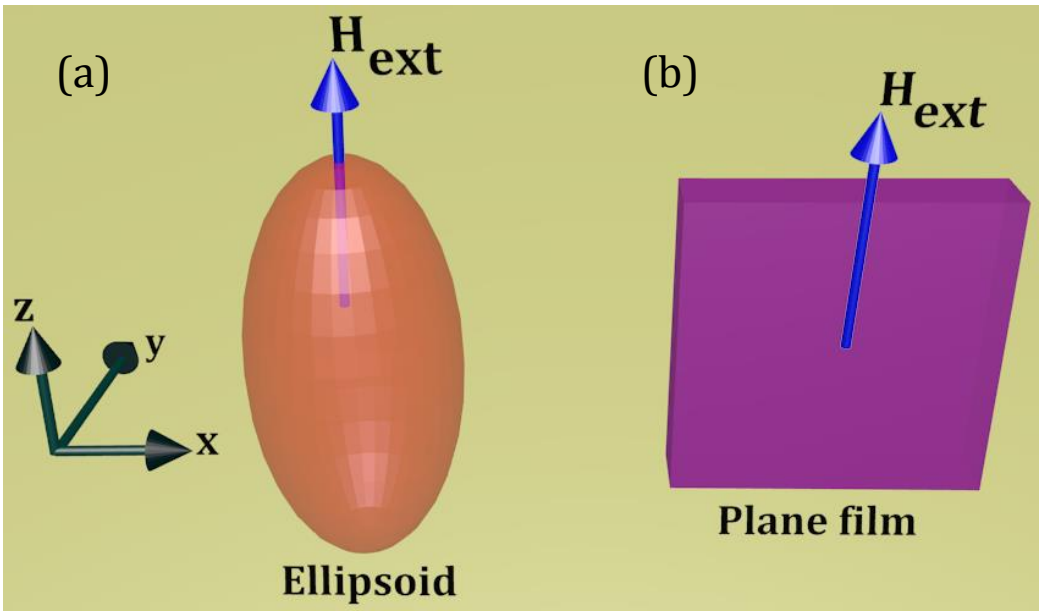

Figure 2.4. Schematic of the coordinate systems used for FM material in the forms of (a) an ellipsoid and (b) a plane.

For a general ellipsoid, the corresponding solutions have been calculated (neglecting exchange and anisotropy contributions) which is provided in the following equation (also known as Kittel equation) [19]:

$$f_{\mathrm{FMR}} = \frac{\gamma}{2\pi}\left[\{H_{\mathrm{ext}} + (N_{\mathrm{y}} - N_{\mathrm{z}})M_{\mathrm{s}}\}\{H_{\mathrm{ext}} + (N_{\mathrm{x}} - N_{\mathrm{z}})M_{\mathrm{s}}\}\right]^{\frac{1}{2}} \tag{2.27}$$

Here, N_x, N_y and N_z are the demagnetizing factors in the x, y and z-directions, respectively and the bias magnetic field (H_{ext}) is applied along the z-direction as shown in Figure 2.4.

However, in case of plane film, $N_x = N_z = 0$, $N_y = 4\pi$ and the Equation 2.27 is simplified to:

$$f_{FMR} = \frac{\gamma}{2\pi}[H_{ext}(H_{ext} + 4\pi M_s)]^{\frac{1}{2}} \quad (2.28)$$

On the other hand, the non-uniform precession can be classified as the propagation of a phase shift across the spin system and hence the mutual interactions between the moments play a pivotal role in determining the wavelength, frequency and overall dispersion behaviour of the SW [245,246]. In the long wavelength regime, the phase difference between consecutive spins is rather small, the SW energy is primarily dominated by dipolar energy and the SWs are referred to as dipolar-dominated or magnetostatic SWs. In contrast, the short wavelength SWs are governed by the exchange interaction and known as exchange SWs [247]. The characteristics of these different genres of SWs are discussed below.

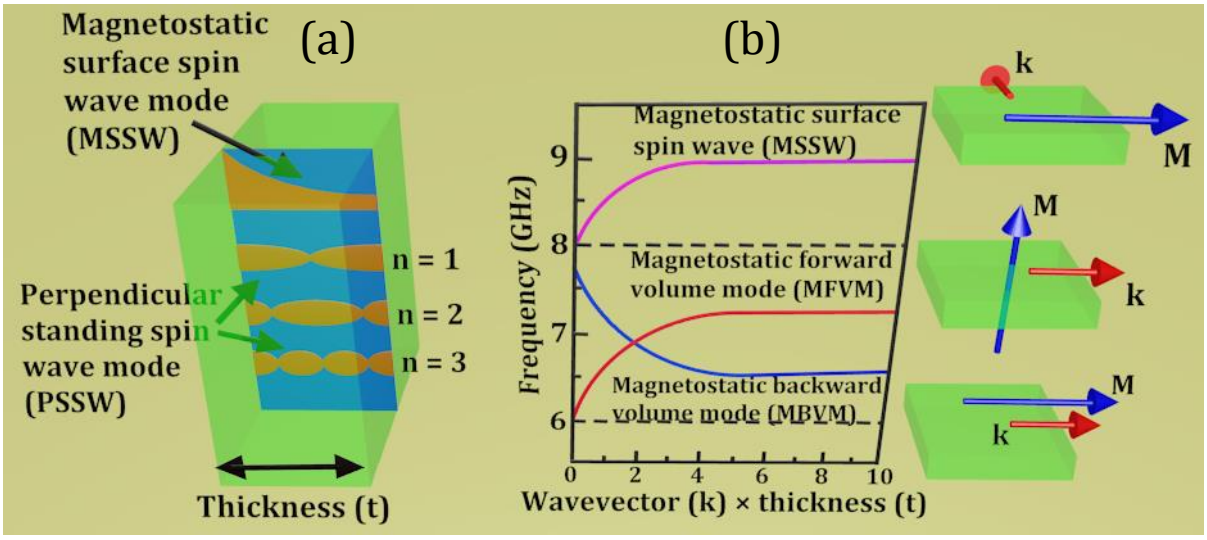

Figure 2.5. Schematic illustration of (a) perpendicular standing spin wave mode (PSSW) and magnetostatic surface spin wave mode (MSSW) are represented for an FM thin film. (b) The dispersion relations for three different types of magnetostatic SW modes are described.

2.5.1. Magnetostatic Spin Waves

Since the dipolar interaction is anisotropic in nature, the frequency, amplitude and propagation properties of magnetostatic modes strongly rely on the geometry of their propagation direction (i.e. wave vector: k) with respect to the magnetization (M: its direction depends on the strength of the applied bias magnetic field) direction of the specimen and the film plane [248]. For instance, when both the M and k lie in the film plane and are perpendicular (or parallel) to each other, a magnetostatic surface SW viz. MSSW (or magnetostatic backward volume mode: MBVM) is generated. On the contrary, if the magnetic field is applied out of the film plane and SW propagates parallel to the surface, it is known as magnetostatic forward volume mode (MFVM). The frequency versus wave vector dispersion characteristics of these modes are presented in Figure 2.5. The MSSW mode, also known as Damon-Eshbach (DE) mode [249], possesses a positive dispersion starting from the Kittel mode at k = 0. This mode is further characterized by the localization of SW amplitude in the vicinity of the top and bottom surfaces along with its nonreciprocal behaviour, i.e. the propagation is possible for either positive or negative direction of the wave vector for each surface. In absence of any exchange interaction and magnetic anisotropy, the dispersion relation [143] of the DE mode can be described as:

$$f_{\mathrm{DE(or\ MSSW)}} = \frac{\gamma}{2\pi}\left[H_{\mathrm{ext}}(H_{\mathrm{ext}} + M_{\mathrm{s}}) + (2\pi M_{\mathrm{s}})^2(1 - e^{-2kt})\right]^{\frac{1}{2}} \tag{2.29}$$

where, k is the in-plane component of the wave vector of SW while, t is the thickness of the film and H_{ext} and M_{s} denote the applied magnetic field and saturation magnetization of the FM material. In case of MBVM, the SW amplitude prevails throughout the thickness of the sample and the dispersion features a characteristic negative slope (i.e. group and phase velocities are in opposite direction to each other). The corresponding dispersion relation [250] is given by:

$$f_{\mathrm{MBVM}} = \frac{\gamma}{2\pi}\left[H_0\left(H_0 + 4\pi M_{\mathrm{s}}\frac{1-e^{-2kt}}{kt}\right)\right]^{\frac{1}{2}} \tag{2.30}$$

However, the expression [251] for MFVM can be depicted as,

$$f_{\mathrm{MFVM}} = \frac{\gamma}{2\pi}\left[(H_0 - 4\pi M_{\mathrm{s}})\left(H_0 - 4\pi M_{\mathrm{s}}\frac{1-e^{-kt}}{kt}\right)\right]^{\frac{1}{2}} \tag{2.31}$$

2.5.2. Exchange Spin Waves

When the wave vector of SW is increased (i.e. wavelength is decreased), the exchange interaction plays a crucial role. Basically, the exchange interaction becomes dominant when the SW wavelength is of the order of the exchange length (l_{ex}) which is given by:

$$l_{ex} = \sqrt{\frac{2A}{\mu_0 M_s^2}} \tag{2.32}$$

where, A is the exchange stiffness constant. The exchange dominated SW mode [252,253] does not depend on the relative orientation of the wave vector and magnetic field. The SW dispersion relation with dipolar-exchange interactions [193,254] taken into account is given as:

$$f_{dip-ex} = \frac{\gamma}{2\pi}\left[\left(H_{ext} - 2\pi M_s kt \sin^2\theta_k + \frac{2A}{M_s}k^2\right)\left(H_{ext} + 4\pi M_s - 2\pi M_s kt + \frac{2A}{M_s}k^2\right)\right]^{\frac{1}{2}} \tag{2.33}$$

where, θ_k is the angle between the applied field H_{ext} and k. However, in addition to k, it is also possible to excite SWs propagating perpendicular to the film plane forming perpendicular standing spin wave (PSSW) as described in Figure 2.5(a). For a film of thickness t, the wave vector (q) of PSSW mode can be written as:

$$q = \frac{n\pi}{t} \tag{2.34}$$

Their dynamic magnetization profile is sinusoidal and depends on their quantization number n given by:

$$m_n(z) = a_n \cos\left[q_n\left(z + \frac{t}{2}\right)\right];\ -\frac{t}{2} < z < \frac{t}{2} \tag{2.35}$$

where, z corresponds to the coordinate along the film thickness. The above Equation 2.35 actually describes a standing wave consisting of two counterpropagating waves with quantized wave vectors. Without considering the contribution of in-plane wave vector (k), the frequency for the PSSW mode [255] is given by:

$$f_{PSSW} = \frac{\gamma}{2\pi}\left[\left(H_{ext} + \frac{2A}{M_s}q^2\right)\left(H_{ext} + 4\pi M_{eff} + \frac{2A}{M_s}q^2\right)\right]^{\frac{1}{2}} \tag{2.36}$$

where, M_{eff} represents the effective magnetization of the FM system.

In case of magnetostatic modes, the exchange interaction is generally neglected considering the exchange stiffness constant (A) to be very small. However, the value of A is much larger in some FM materials (e.g. NiFe, CoFeB) and hence the contribution of exchange interaction cannot be neglected. Consequently, the frequency of dipole-

exchange modes, therefore, becomes larger than the dipolar modes while the contribution from exchange interaction becomes more prominent for higher k as the exchange has a quadratic contribution ($\sim k^2$) to the dispersion relation [3,256].

2.5.3. Confined Spin Waves in Magnetic Structures

In case of a confined magnetic structure [175,257,258], the spectrum of SW is substantially modulated by the boundary conditions imposed by the lateral dimensions [259]. In particular, the SW finds a propagation channel to mediate through it or it forms standing wave depending upon the distribution of potential barriers defined by the geometry of the structure [260,261]. The formation of standing wave often leads to localized or confined or quantized mode (with multiple quantization numbers) when the feature dimensions are of the order of the wavelength of the SW. Overall, the number of SW modes increases whose properties are strongly dependent on the system geometry as well as on the orientation of the magnetic field. The structural confinement also affects the dispersion relation, resulting in a number of allowed and forbidden bands (magnonic bands) [262,263] in case of periodic patterned structure (known as Magnonic crystal: MC [264]). The band structure of MC is comprised of Brillouin Zones (BZs) [265], which provides the flexibility to tailor the SW properties by manipulating external structuring. The nature of SWs in such confined system can be investigated by solving the LLG equation in the micromagnetic framework or using other numerical methods such as plane wave method (PWM) etc.

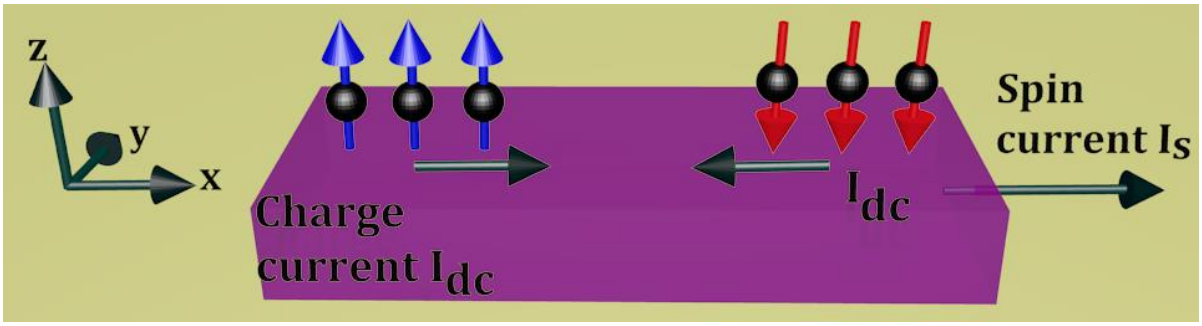

Figure 2.6. Schematic representation of pure spin current (I_s) flow. If a charge current (I_{dc}) with only spin ↑ electrons are moving while a similar charge current that contains only spin ↓ electrons, is flowing in the opposite direction then a pure spin current will be generated as there is no net charge current.

2.6. Spin Current

Generally, charge current can be treated as the flow of electrons generated by a potential (voltage) difference. However, besides its charge, the electron also carries a spin (with the spin angular momentum), whose projection along the spin axis can point up (↑) or down (↓). Unlike conventional electronic devices (the electron spin contribution is neglected), recent advances in spintronics [266,267] deal with the control and manipulation of spin degrees of freedom so that these spin-based devices possess faster switching times and lower power consumption than conventional devices at lower energy cost than the charge carriers. These spin-based systems are operated by spin currents [268] as opposed to the conventional electronic devices which require charge currents. To understand the concept of spin current [269-271], one can consider a flow of dc electron current (I_{dc}) through one channel that contains only ↑ spin-polarized electrons as illustrated in Figure 2.6. while, a similar current (I_{dc}) is flowing in the opposite direction in which all electrons are ↓ spin polarized. This results in a flow of spin current (I_s) only as there is no net transfer of charge carriers (electrons) across any cross-section of the channel. A spin current differs from a charge current in two important ways:

1. Spin current possesses time-reversal symmetry, i.e. spin current will flow in the same direction under time reversal while, charge current will change its sign.
2. Unlike charge current, the spin current is associated with a flow of angular momentum which is a vector quantity. This unique aspect allows quantum information to be transferred across the spin-based systems similar to the quantum optics which involves the distribution of information across optical networks via polarization states of the photon.

However, it is challenging to generate and explore the spin current [272]. The spin Hall effect (SHE) [273,274] plays a crucial role in this scenario where an unpolarized charge current gives rise to a pure spin current in the transverse direction [275,276]. So far, different routes have been developed for exploring pure spin current (using indirect or direct methods [277-286]) such as nonlocal spin injection [287-289], spin transfer torque (STT) [290-292], spin pumping [293-296], spin Seebeck effect [277,297-299], mechanical method [300-302] etc.

2.7. Ordinary Hall Effect

If a nonmagnetic conductor carries charge current, in presence of a transverse magnetic field, an electric field is developed within the conductor in a direction perpendicular to both current and magnetic field. The phenomenon is known as the Hall effect or ordinary Hall effect [303,304].

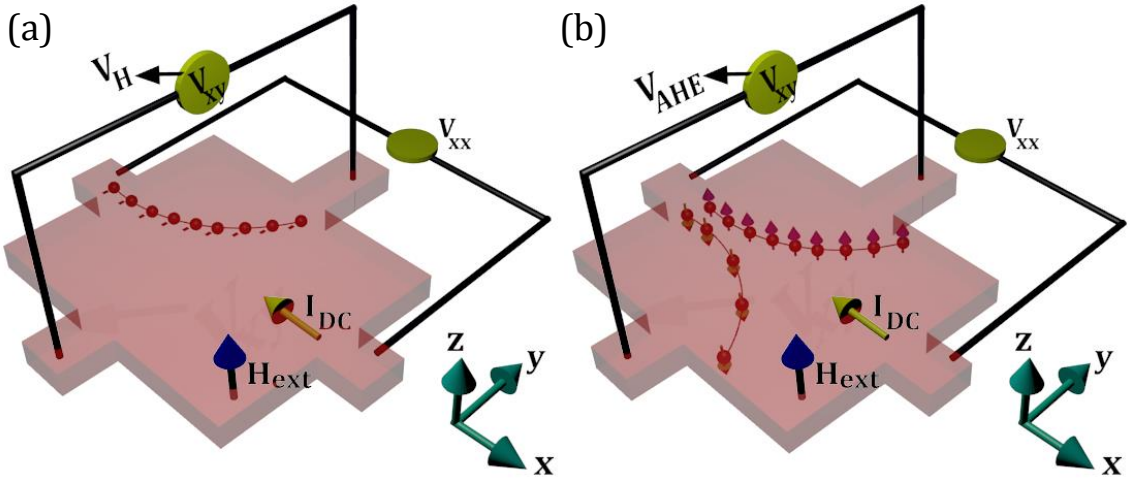

Figure 2.7. Schematic demonstration of (a) ordinary Hall effect and (b) anomalous Hall effect (AHE).

If a rectangular-sized conductor carries dc current I_{dc} along x-direction under the influence of an external magnetic field (H_{ext}) applied along z-direction as shown in Figure 2.7(a), the charge carriers (i.e. electrons or holes) will be deflected by the Lorentz force [305,306], given by:

$$\boldsymbol{F} = q(\boldsymbol{v} \times \boldsymbol{B}) \tag{2.37}$$

Here, q and $\boldsymbol{v}$ are the charge and average velocity of the carrier respectively. Here, the direction of $\boldsymbol{F}$ will be along y-direction leading towards an accumulation of charge on the top surface. If the charge carrier is electron (for metal or n-type semiconductor) the top surface will be negatively charged with respect to the bottom surface or vice versa in case of hole (for p-type semiconductor). The accumulation of charge gives rise to an electric field (known as Hall field, E_H) that exerts a force on the charge carriers opposite to the Lorentz force. Hence, in steady state (i.e. when these two opposing forces are equal) the force equation for the charge carrier can be expressed by as:

$$q\boldsymbol{E}_H = q(\boldsymbol{v} \times \boldsymbol{B}) \tag{2.38}$$

Now, the expression for current can be written as:

$$I = nyzvq \tag{2.39}$$

where, n, y and z indicate number density of electron, width and thickness of the conductor. Thus, the expression for Hall voltage can be described as:

$$V_{\mathrm{H}} = E_{\mathrm{H}}z = vBz = \frac{IB}{nyq} \tag{2.40}$$

In this case, the total electric field in the system is given by:

$$E_{\mathrm{T}} = \sqrt{{E_{\mathrm{x}}}^2 + {E_{\mathrm{H}}}^2} \tag{2.41}$$

where, E_{x} is the applied electric field along x-direction due to the charge current (I). The angle

between E_{x} and E_{H} is denoted as Hall angle (θ_{H}) which can be expressed as the following:

$$\theta_{\mathrm{H}} = \tan^{-1}\frac{E_{\mathrm{H}}}{E_{\mathrm{x}}} = \frac{Bv}{E_{\mathrm{x}}} = B\mu_{\mathrm{m}} \tag{2.42}$$

Here, the mobility of the charge carrier is defined by:

$$\mu_{\mathrm{m}} = \frac{v}{E_{\mathrm{x}}} \tag{2.43}$$

2.8. Anomalous Hall Effect (AHE)

This corresponds to the generation of a large Hall voltage in a magnetic system in response to an applied electric current [307-310] as described in Figure 2.7(b). The total Hall resistance (R_{H}) in an FM material can be divided into two phenomenologically different contributions. First one is proportional to applied B corresponding to the ordinary Hall effect, while the other section arises from the anomalous behaviour which is often proportional to the magnetization (M) of the system so that the expression of R_{H} is given by:

$$R_{\mathrm{H}} = R_{\mathrm{O}}B + R_{\mathrm{A}}M \tag{2.44}$$

where, R_{O} and R_{A} are the ordinary and anomalous Hall coefficients, respectively. Usually, at normal temperature, R_{O} is larger than R_{A} although they become comparable as the temperature decreases [307]. The microscopic origin of AHE is still a matter of debate although, three mechanisms have been identified as contributing factors to AHE namely,

1. intrinsic effect
2. skew scattering
3. side jump mechanism.

The intrinsic effect can be observed in a pure system with no impurity scattering involved. Rather, it can be described in terms of momentum-space (or *K*-space) in the form of Berry phase [311,312] which is inherent to the band structure of the pure crystal. The intrinsic contribution was introduced when an anomalous transverse current component is produced due to the perturbation of a system of spin-orbit (SO) coupled Bloch states in the presence of an electric field. The origin of the transverse velocity is intrinsic to the band structure and does not require scattering i.e. it originates directly from the non-equilibrium spin dynamics. A quantum approach towards the intrinsic AHE has been considered in terms of quantum Hall effect (QHE) [313-317] in 2D electron gas (2DEG) which can be realised in terms of either Landau quantization or depending upon the collective behaviour of 2DEG.

On the other hand, the last two effects (i.e. skew scattering and side jump) are extrinsic in nature originating from asymmetric spin-dependent scattering from un-polarised impurities with strong SO coupling. Skew scattering (Mott effect) [318-320] can be explained through a semiclassical Boltzmann transport treatment. It stems from the inclusion of SOC within the disorder scattering potential resulting in different scattering cross-sections for spin ↑ and spin ↓ electrons. The electrons are therefore skew scattered depending upon the projection of their spins on the *z*-component of angular momentum. As represented pictorially in Figure 2.8(a), the electron spins experience an effective magnetic field ($\boldsymbol{B}$) induced by the impurity of potential $V(x, y, z)$ due to the SOI which is given by,

$$\boldsymbol{B} \propto \boldsymbol{v} \times \boldsymbol{E} \tag{2.45}$$

where, $\boldsymbol{v}$ (= $\boldsymbol{v}(x, y, z)$) is the relative velocity of electron and $\boldsymbol{E}$ (= $\boldsymbol{E}(x, y, z)$) is electric field induced by the impurity. Here, $\boldsymbol{B}$ is inhomogeneous over space due to the non-uniformity of $\boldsymbol{E}$ whereas $\boldsymbol{v}$ is also space dependent in the electron trajectory. Consequently, a spin ↑ electron passing to the left of the impurity will experience the effective magnetic field antiparallel to its spin and hence, it will get repelled from the impurity (as the field is strongest there) due to the force originating from the Zeeman (Oersted) field given by,

$$\boldsymbol{F} \propto \nabla(\boldsymbol{\sigma}.\boldsymbol{B}) \tag{2.46}$$

Here, σ denotes the spin polarization vector of the electron. However, a spin ↑ electron passing to the right of the impurity experience a magnetic field parallel to its spin and is

therefore attracted towards the impurity. Consequently, the spin ↑ electron is always deflected left regardless of which side of the impurity it approaches. Similarly, spin ↓ electrons would be scattered to the right as shown in the schematically in Figure 2.8(b).

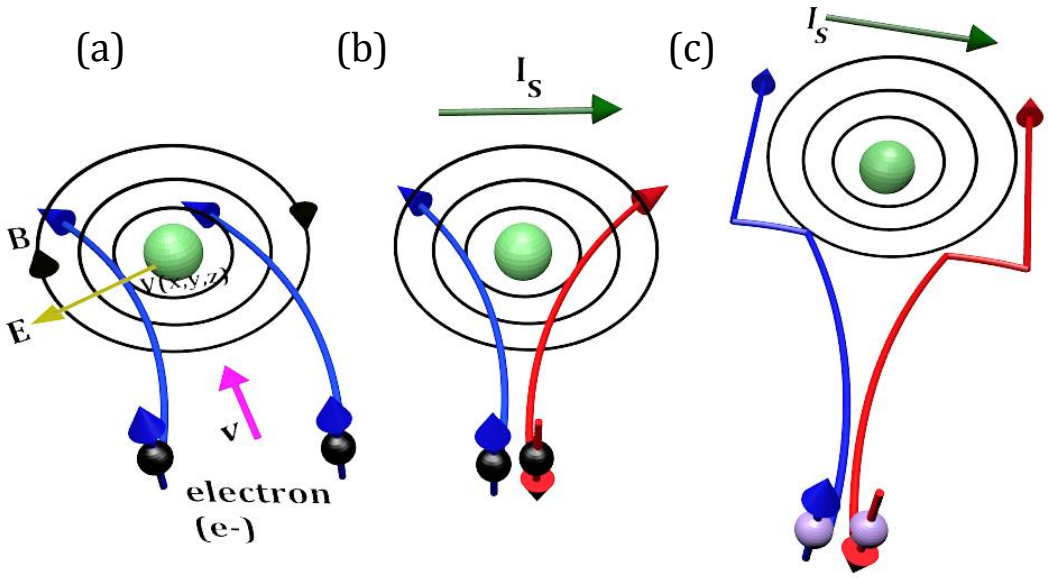

Figure 2.8. (a) Schematic of the skew scattering mechanism where the spin ↑ electrons get scattered in the same direction irrespective of the side of their approach with a relative velocity (***v***) towards the impurity of scattering potential V(x, y, z) which induces an effective magnetic field (***B***) due to SOI. (b) Overall, the spin ↑ electrons are collectively scattered to the left while, the spin ↑ electrons are scattered to the right giving rise to a spin current (I_S). (c) Pictorial demonstration of side-jump mechanism.

The side jump mechanism [321] also stems from impurity scattering in the presence of the SOI as illustrated schematically Figure 2.8(c). However, the effect occurs due to the difference between the response of spin ↑ and spin ↓ electrons to the gradient of the electric field on their approach towards the impurity centre. There is no classical analogy to this effect as it originates as a consequence of the Gaussian probability distribution for the position of the electron. The SO perturbation due to the impurity distorts the probability distribution in such a way that there is a high probability of a spin ↑ electron being spontaneously displaced to the left while, for a spin ↓ electron the reverse i.e. displacement towards right becomes more probable.

Although these mechanisms have been developed for detailed interpretation AHE, it was quickly realised that the same mechanisms are valid even for a non-magnetic material with strong SOI, leading towards the prediction of the SHE [276,322].

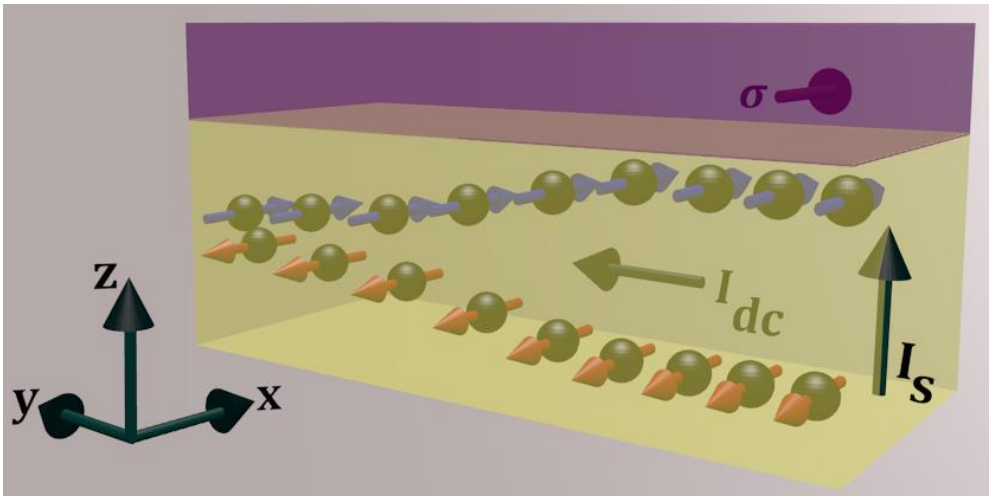

Figure 2.9. Schematic illustration of spin Hall effect (SHE): spin-dependent scattering mechanisms occurring due to the strong SOI within a heavy metal separate spatially the electrons by their spin under the application of a charge current (I_{dc}). This gives rise to spin accumulation at the interfaces generating spin current (I_s). Here, $\boldsymbol{\sigma}$ represents the spin polarization vector of the spin current.

2.9. Spin Hall Effect (SHE)

The SOI can give rise to spin-dependent scattering mechanisms, whereby spin ↑ and spin ↓ electrons obtain opposite transverse velocity components after scattering. This results in a spin accumulation transverse to the current flow and is shown schematically in Figure 2.9. Analogous to the ordinary Hall effect, where opposite charges accumulate on opposite sides of the material (usually a nonmagnetic material with large SOC), this effect results in accumulation of electrons with opposite spins on either side which is called the spin Hall effect (SHE) [274,323-325]. The mechanisms by which the spin accumulation occurs is the same as that which gives rise to the anomalous Hall effect in FM materials where the mechanisms can be split into two varieties: extrinsic contributions (skew-scattering and side jump) which originate from spin-dependent scattering from impurities and intrinsic contributions [307] which are inherent to the band structure of the pure crystal. Although the extrinsic factors contributing to the SHE phenomenon has been proposed earlier, the prediction of the intrinsic SHE [326,327] has been made later by focusing on semiconductors [328,329]. Furthermore, the reciprocal effect, i.e. the inverse spin Hall effect (ISHE) [288,289,293,330,331] by which a spin current is converted into a charge current has been intensively investigated [332-

335]. A key parameter in the SHE is the spin Hall angle (SHA: θ_H) which characterizes the conversion efficiency between the charge and the spin currents. Most of the approaches to generate spin current require a bilayer heterostructure where the spin current is generated in a magnetic material, while the converted charge current is detected in the other layer with large SOC [292,336,337]. However, one inevitably encounters complications in such bilayers due to interfaces of different materials and the shunting effect (if both materials are metallic in nature). These complications are the major concerns for the large variance of SHA value, i.e. spin to charge conversion [338] factor even for the same combination of materials [268] which leads to the efforts of exploring the alternative ways to generate and detect the spin current in a single material [339].

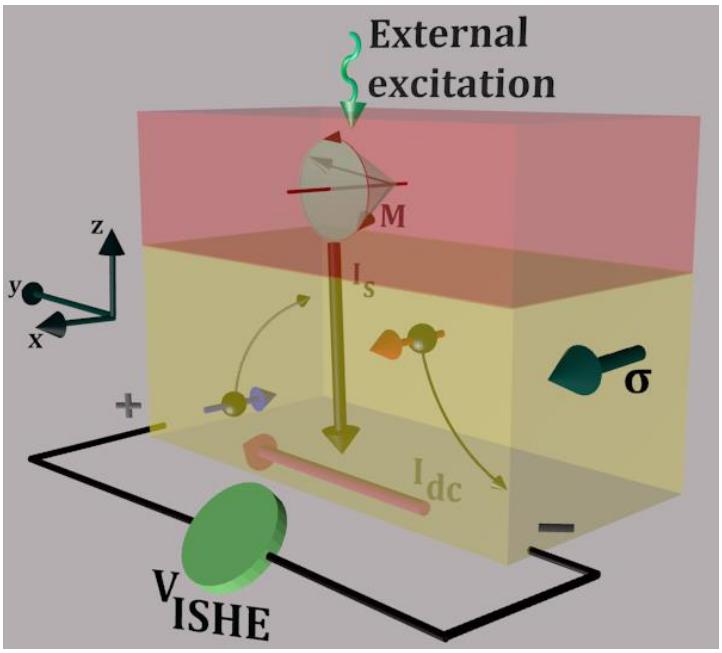

Figure 2.10. Schematic illustration of spin pumping and inverse spin Hall effect (ISHE) mechanisms in an FM/NM heterostructures. The microwave excitation induces magnetization (***M***) in FM layer generating a pure spin current (I_S) due to the transfer of spin angular momentum into the NM layer with large SOC where $\boldsymbol{\sigma}$ is the spin polarization vector of the spin current. I_{dc} denotes charge current generated by ISHE while, V_{ISHE} represents the corresponding voltage.

2.10. Spin Pumping

Spin current can exert spin transfer torque (STT) on magnetization (M) which cause the switching or modification of magnetization dynamics in FM heterostructures. However,

the reverse process is also possible where precessing magnetization ($\boldsymbol{M}$) gives rise to the spin current that gets transferred to an adjacent normal metal at the cost of its own angular momentum. Consequently, the amplitude of precession suffers a faster decay leading to an enhancement of damping. In the magnetization precession as described in the LLG equation as shown in Equation 2.25, the first term on the right-hand side represents the torque responsible for the magnetization precession which can be physically related to the volume (bulk) injection of spin current. When the spin current is allowed to leak through an adjacent nonmagnetic (NM) material, the Gilbert damping (α) gets enhanced. In other words, an external excitation (optical, electrical or microwave) [340-345] can induce magnetization precession and if there is a difference in the spin chemical potential between the FM and NM layers, then the spin angular momentum is transferred from FM to the nonmagnetic layer in form of spin current. This is similar to a physical pumping mechanism and hence, this is defined as the spin pumping effect [346] as shown in Figure 2.10. Spin pumping and a consequent enhancement of damping can be described analytically in terms of scattering matrix at the Fermi energy level of the FM layer which is in contact with a normal metal [188,347]. This effect is analogous to the parametric pumping of charge current in mesoscopic systems [348] which is governed by periodically varying two independent parameters of the system. The enhancement of damping depends strongly on the type of normal metal adjacent to the FM layer which gives rise to the concept of spin sink materials (enhancement of α will be larger for better spin sink systems) [188,349-352]. The spin absorption efficiency can be estimated by the inverse of spin-flip relaxation time (τ_{SF}) which is proportional to Z^4 (Z being the atomic number) [208,353,354]. Hence, a stronger spin pumping is expected in the presence of a heavy metal layer adjacent to the FM layer [290-292,355]. Also, ISHE can be observed in such metal layer due to the conversion of this spin current into charge current (voltage) [294,356-358]. The spin pumping phenomenon has been investigated using theoretical as well as experimental approaches [273,294,295,358,359] in order to explain the underlying mechanism.

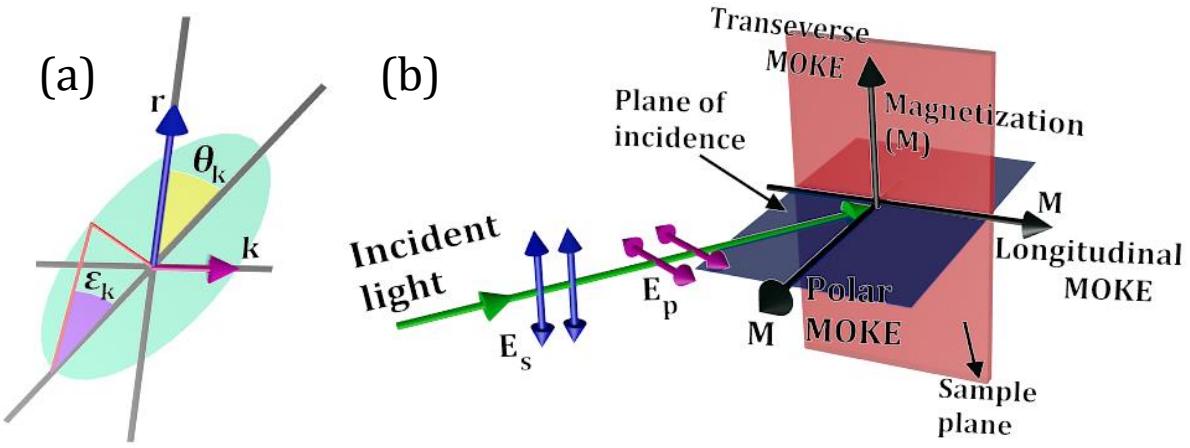

Figure 2.11. (a) The geometry of the Kerr rotation (θ_k) and Kerr ellipticity (ε_k) in magneto-optical Kerr effect (MOKE). (b) Schematics of polar, longitudinal and transverse MOKE geometries of a sample with magnetization (M).

2.11. Magneto-optical Kerr Effect (MOKE)

The discovery of the magneto-optic effect [360-363] has unveiled that the magnetic moment of a material has a strong influence on the polarization of the light wave. It was observed that the plane of polarization of a linearly polarized light gets rotated when the light is transmitted through a magnetized material. Later, a similar rotation of polarization is demonstrated in reflected light as well. After reflection from a magnetized sample, a plane polarized light is converted to an elliptically polarized light, which is defined as Kerr effect [364-366] and the corresponding rotation of the plane of polarization (i.e. the major axis of the ellipse) is called the Kerr rotation. Since its discovery, the Kerr effect has been widely embraced to study the quasi-static and dynamic responses of magnetic systems. Figure 2.11(a) schematically illustrates the Kerr rotation (θ_k) and ellipticity (ε_k), which are proportional to the magnetization of the sample. If r and k denote the parallel and perpendicular components of the electric field vector of the reflected light with respect to that of the incident light, then the following relation [367] is satisfied:

$$\theta_k + i\varepsilon_k = \frac{k}{r} \tag{2.47}$$

where, $k << r$.

2.11.1 Origin of MOKE

The origin of MOKE can be explained either from a macroscopic or microscopic point of view [360,368-374]. Macroscopically, magneto-optic effects originate from the antisymmetric, off-diagonal elements in the dielectric tensor which plays a crucial role in determining the optical properties of a medium that are associated with the motion of its itinerant electrons. When light propagates through a medium, the movement of its electrons follows the electrical field of the light. Thus, for a linearly polarized light, the response of the electrons can be considered as a combination of left and right circular motions where the radii of the circles of both chiralities are the same. Since the electric dipole moment is proportional to the radius of the circular orbit, it will be same for the left and right circularly polarized (LCP or RCP) light and as a consequence, no Faraday rotation will be present. Now, in presence of a magnetic field, there will be an additional Lorentz force acting on the electrons and this force acts on the electrons with left and right circular motions in the opposite directions, pointing either towards or away from the centre of the circle. Thus, the radius for LCP light will reduce while, that for RCP light gets expanded, or vice versa, depending on the direction of the magnetic field. The difference in the radii of LCP and RCP lights will result in a finite difference in dielectric constants subsequently leading towards the phenomenon called MOKE. The difference in the dielectric constants also affects the refractive indices (r.i.) for the two different circularly polarized lights, which is responsible for the phase difference between the orthogonal components of the reflected light as expressed in Equation 2.47.

However, the quantum mechanical approach stresses on the SOI that couples the electron spin to its motion to cause the Kerr effect in an FM material. The movement of electrons under the influence of the electric field vector of light affects the SOI, which can be thought of as an effective magnetic field vector potential ($\boldsymbol{A}$) given by,

$$\boldsymbol{A} \sim \boldsymbol{s} \times \nabla V \tag{2.48}$$

where, $\boldsymbol{s}$ and ∇V depict the electron spin and the electric field ($\boldsymbol{E}$ = -∇V, V being the electric field potential), respectively, acting on the motion of the electron. Despite the fact that this effect is present in all materials, it not prominent in NM materials, because of the presence of an equal amount of up and down spins cancelling out the effect. For FM materials, the effect manifests itself because of the unbalanced population of electron spins in its electronic band structure.

2.11.2. MOKE Geometry

There are three types [145,367,369,375] of MOKE geometry, namely, polar, longitudinal and transverse, which are classified depending upon the orientation of magnetization with respect to the sample surface and plane of incidence. Figure 2.11(b) shows the relative orientations of the magnetization, plane of incidence and polarization direction in different MOKE geometries. In polar MOKE, the magnetization is perpendicular to the sample surface and parallel to the plane of incidence. Since the plane of polarization of both *p*-polarized light (polarization parallel to the plane of incidence) and *s*-polarized light (polarization perpendicular to the plane of incidence) is always perpendicular to the magnetization (irrespective of the angle of incidence) a Lorentz force always exists resulting in a Kerr rotation. The polar configuration is generally used to study thin films, where light is made incident normal to the sample surface. In the longitudinal Kerr effect, the magnetization lies in the plane of the sample and parallel to the plane of incidence. However, the longitudinal Kerr effect depends upon the angle of incidence. In case of normal incidence, the Kerr effect is absent because either the Lorentz force vanishes (for *p*-polarized light) or points along the direction of the light (for *s*-polarized light). In transverse MOKE, the magnetization (M) is perpendicular to the plane of incidence and parallel to the reflection surface. Here also no Kerr effect is observed for normal incidence of light. Moreover, in case of oblique incidence, the polarization does not change, since there is either no Lorentz force present (for *s*-polarized light) or the direction of polarization of the induced component is same as the incident polarization (for *p*-polarized light). Instead, the transverse effect is associated with a change in the intensity of the reflected light when magnetization changes its orientation. The change in the intensity is dependent upon the component of magnetization perpendicular to the plane of incidence.

2.12. Ferromagnetic Resonance (FMR)

When a steady magnetic field is applied to an FM material, its magnetization starts to precess around the effective magnetic field (H_{eff}) with an angular frequency according to the Larmor condition for electron spin:

$$\omega_{\text{L}} = \gamma H_{\text{eff}} \tag{2.49}$$

where, γ is the gyromagnetic ratio. If an alternating magnetic field (H_{RF}) with an angular frequency (ω) is applied in the transverse direction to the bias field, then resonance will take place under the following condition:

$$\omega = \gamma\sqrt{BH_{eff}} \tag{2.50}$$

where, B is the magnetic induction. As a consequence, the magnetization will precess in the resonant frequency absorbing power from the alternating field. This phenomenon is called ferromagnetic resonance (FMR) [18,376]. Although the resonance frequency (ω) has been found to be quite higher than the expected Larmor frequency (ω_L) which has been explained by considering the dynamic coupling arising from the demagnetizing field around the magnetic specimen [19,377].

2.12.1. Microwave Excitation and Detection

Ferromagnetic resonance (FMR) [18,19] is a spectroscopic method to investigate the magnetization dynamics of FM materials to extract the information about SWs by probing the sample magnetization resulting from its magnetic moments. There are various methods developed for the FMR measurement in a broad frequency regime such as,

2.12.1.1. FMR Technique Based on Stripline (SL)

This [378] is closely related to the standard shortened waveguide and microwave cavity FMR measurement techniques [379-381] where one can measure FMR by sweeping the magnetic field at a fixed frequency.

2.12.1.2. FMR using a Pulsed Inductive Microwave Magnetometry (PIMM)

This technique [382-384] relies upon the inductive detection of magnetization through the use of drive electronics with fast rise time and coplanar waveguide (CPW) for simultaneous drive and detection as well as digital signal processing. The Fourier transform of the time domain response obtained from this method yields the FMR absorption profile in the frequency domain.

2.12.1.3. FMR Incorporating a Vector Network Analyzer (VNA) Instrumentation (VNA-FMR)

Here, the magnetization dynamics is acquired directly in the frequency domain by sweeping the frequency over a broad frequency window at a fixed magnetic field. Consequently, the SW absorption spectra are recorded in terms of the scattering (S) parameters [135,137,385-387].

The SL FMR approach is simple although the sensitivity is low. The VNA-FMR is advantageous because it can extract both amplitude and phase information of the signal with the aid of VNA. However, this method needs careful calibration and the proper subtraction of reference signals in order to achieve accurate results. The PIMM FMR method is beneficial due to the use of a dc field instead of a microwave excitation and time-resolved magnetization relaxation data (corresponding to a broadband FMR response in the frequency domain) is recorded without any complicated calibration procedure. However, its prime disadvantage is that the data analysis is extremely complicated with the requirement of a critical subtraction of the background pulse as opposed to that with the VNA-FMR approach.

In the following, the VNA-FMR technique has been explained elaborately which has been mainly employed during the investigation of spin dynamics of magnetic specimens presented in this thesis.

2.12.2. Network Analyzer

Network analyzers are mostly used at high frequencies although the special type of analyzers can also cover lower frequency ranges [388]. There are two types of network analyzers:

2.12.2.1. Scalar Network Analyzer (SNA)

It measures amplitude properties only. It is functionally identical to a spectrum analyzer in combination with a tracking generator [389].

2.12.2.2. Vector Network Analyzer (VNA)

It calculates both amplitude and phase properties which are the most commonly used of network analyzers [390-392]. However, there is another category of network analyzer known as the microwave transition analyzer (MTA) or large signal network analyzer (LSNA) [393-398] which measures both amplitude and phase of the fundamental and harmonics. In the works presented in this dissertation, a Vector Network Analyzer-(VNA-) based FMR spectrometer has been employed. Such network analyzer can measure complex (i.e. both amplitude and phase) ratio of reflected and/or transmitted electrical signals to the incident signals by sampling out the frequency dependent signals while, gain and phase information are kept preserved. Unlike conventional ferromagnetic resonance spectrometer where a resonant cavity of the specific

frequency with high quality factor (Q) is used [399-402], the reason behind using broadband ferromagnetic resonance spectrometer are manifold such as:

1. The non-resonant cavity used here gives a reflection/transmission band with flat Q factor over a broad frequency range making the system robust for investigating an FM system especially, patterned heterostructures that possess a number of resonant SW frequencies.
2. The sweeping frequency band can range from few MHz to tens of GHz making the spectrometer extremely useful for investigation of SWs over broad frequency response.
3. This offers the operation of magnetization dynamics from MHz to high GHz regime which is difficult in conventional systems especially in the low-frequency range (< 1 GHz) which is necessary for the investigation of different interesting magnetic structures, e.g. magnetic vortex systems [403-405] etc.
4. This is suitable for investigation of magnetic heterostructures which possess a transition from in-plane to out-of-plane magnetization (M) if there is a competition between the strength of the applied magnetic field and that of its magnetic property (such as magnetic anisotropy) contributing to the effective M.

A brief description of a VNA system is discussed in the following section.

2.12.3. Mechanism of Vector Network Analyzer (VNA)

It is a precision measuring instrument that tests the electrical performance of high-frequency components in the radio frequency (RF), microwave (MW) and millimetre-wave frequency bands [406-410]. A VNA is a stimulus-response test system, composed of an RF source and multiple measurement receivers. It is specifically designed to measure the forward and reverse reflection and transmission responses in terms of scattering (S) parameters [411,412]. S-parameters have both a magnitude and a phase component and they characterize the linear performance of the device under test (DUT), i.e. the magnetic sample measured in this dissertation. However, it can also be utilized for characterizing some non-linear behaviour like amplifier gain compression or inter-modulation distortion, through calibration. VNAs provide the highest level of accuracy for measuring RF components. One of the most fundamental concepts of the high-frequency network analysis involves incident, reflected and transmitted waves travelling along transmission lines. It is helpful to think of travelling waves along the transmission line in terms of an optical (light wave) analogy. Some of the light is

reflected off the surface of a lens when light is incident on the lens but most of the light is transmitted through it while, the remaining part will be absorbed by the material of the lens. If the lens is mirrored then most of the light wave will be reflected. The similar concept holds good for RF signals except that the electromagnetic (EM) energy is in the RF range instead of the optical range and the experimental contents involve electrical devices. Usually, network analysis is concerned with the accurate measurement of the ratios of the reflected signal to the incident signal, and the transmitted signal to the incident signal. In VNA, measurements with both magnitude and phase are required for the best measurement accuracy and best calibration. Also, the complete characterization of devices and networks involves measurement of magnitude and phase.

2.12.3.1. Architecture

The basic components of a network analyzer involve signal generator(s), test set(s), receiver(s) and display(s). In some set-ups, these units are distinct instruments. Most VNAs have two test ports permitting measurement of *S*-parameters in transmission geometry for 2 × 2 *S*-matrix (i.e. S_{11}, S_{12}, S_{21} and S_{22}) but instruments more than two ports are also available commercially.

2.12.3.1.A. Signal Generator

The network analyzer is comprised of one signal generator (source) which will produce the oscillating signal in terms of RF current.

2.12.3.1.B. Test Set

The test set takes the signal generator output and routes it to the DUT, and it routes the signal to be measured to the receivers. It often splits off a reference channel for the incident wave. In a VNA, the reference channel goes to the receivers, which is needed to serve as a phase reference.

2.12.3.1.C. Receiver

The receivers perform the measurements. A network analyzer will have one or more receivers connected to its test ports. Some analyzers will dedicate a separate receiver to each test port, but others share one or two receivers among the ports. For the VNA, the receiver measures both the magnitude and the phase of the signal. It needs a reference channel (R) to determine the phase, and hence a VNA needs at least two receivers. However, some systems are equipped with three or four receivers to

permit simultaneous measurement of different parameters.

2.12.3.1.D. Processor and Display

With the processed RF signal available from the receiver and detector section it is necessary to display the signal in a format that can be interpreted. With the levels of processing that are available today, some very sophisticated solutions are available in RF network analyzers. Here, the reflection and transmission data are formatted to enable the information to be interpreted as easily as possible.

2.12.3.2. Transmission Line

The requirement for efficient transfer of RF signal (power) is one of the main reasons behind the use of transmission lines [413-416]. Generally, at low frequencies (~ DC behaviour) where the wavelengths of the signals are much larger than the length of the circuit conductors so that a simple wire is very useful for carrying power where the current travels down the wire easily, and voltage and current are the same no matter where we measure along the wire. However, at high frequencies, the wavelength of signals of interest is comparable to or much smaller than the length of conductors. Here, power transmission can be best thought of in terms of travelling waves. RF transmission lines can be made in a variety of transmission media such as coaxial, waveguide, twisted pair, coplanar, microstrip, stripline etc. The fundamental parameter of this line is its characteristic impedance (Z_0) as it describes the relationship between the voltage and current travelling waves [417]. For most systems, Z_0 varies from 50 Ω to 75 Ω. Now if the transmission line is terminated with Z_0, there will be no reflected signal due to the maximum transfer of power to the load. However, when the termination is not matched with Z_0, the portion of the signal which is not absorbed by the load is reflected back towards the source. For instance, if the line is terminated in a short circuit, as purely reactive elements cannot dissipate power and there will be nowhere else for the energy to transfer. Consequently, a reflected wave will be launched back down the line toward the source and the reflected wave must be equal in voltage magnitude to the incident wave. On the other hand, if the line is open the current at the open will be zero. Thus, for both the short and open cases, a standing wave pattern will be formed on the transmission line.

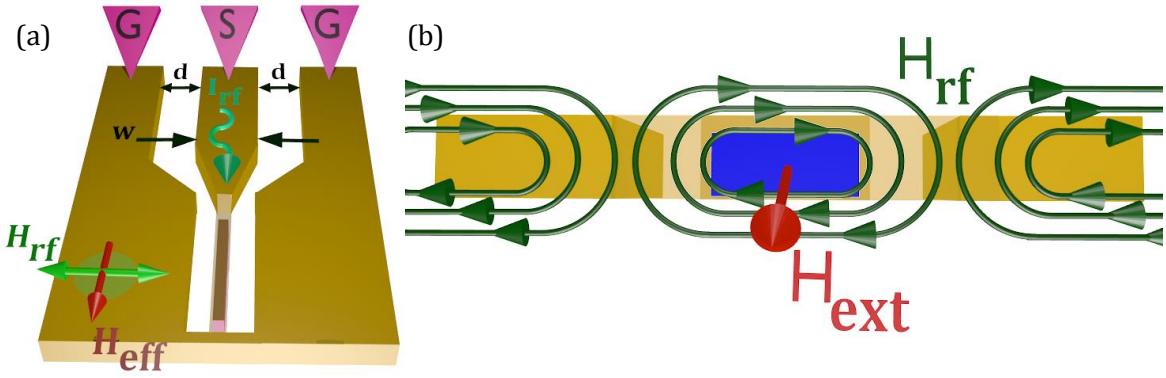

Figure 2.12. (a) Schematic of coplanar waveguide (CPW) with a width of the signal line (w) separated from two ground lines by (d) shown in reflection geometry while, the magnetic sample is beneath the central conducting (signal) line. (b) Cross section of the CPW revealing the distribution of the magnetic field lines (solid) generated by the RF field (H_{rf}) produced from the RF current (I_{rf}).

2.12.3.2.A. Coplanar Waveguide (CPW)

It belongs to a genre of electrical transmission lines which can be fabricated using lithography (optical) technique and various other means (e.g. printed circuit board: PCB etc.) and it is used to convey RF/MW frequency signals [418-420]. Generally, CPW consists of a single conducting line (called signal line) together with a single or pair of return conductor(s) (usually the signal line lies in between them) which are termed as ground lines. All these three lines are fabricated on the same side (plane) of the dielectric substrate (and hence is the name coplanar). The ground lines are separated from the signal line by a small gap (d) width which plays a crucial role in determining the impedance of the whole system along with the contribution from the width (w) of the signal line. Depending upon the measurement geometry these three lines can be either shorted at one end (reflection geometry) or they can be always separated by maintaining a gap (transmission geometry). In the works presented in this thesis, only reflection geometry has been used where the CPW is schematically shown in the Figure 2.12(a) where the FM samples lie above or below the central (signal) line separated by a moderately thick insulating layer in order to avoid any damage to the sample due to the RF current. The distribution of the oscillating magnetic field generated by the RF current (I_{RF}) reveals that the magnetic field lines get flattened near the surface of the signal line because of its rectangular shape. Hence, it produces an in-plane RF magnetic field (H_{RF}) to perturb the FM specimen from its equilibrium state under the application of an external bias magnetic field (H_{ext}) as depicted in the Figure 2.12(b).

2.12.3.3. High-frequency Device Characterization

In general, a network analyzer measures the incident wave measured with the reference receiver signal. The reflected wave is measured with one receiver while, the transmitted wave is measured with another receiver. With amplitude and phase information of these three waves, one can quantify the reflection and transmission characteristics of our DUT. Now in VNA, return loss is a scalar measurement of reflection while, impedance results from a vector reflection measurement (e.g. group delay is purely phase related measurements).

2.12.3.3.A. Reflection Parameters

Reflection coefficient (R) is the ratio of the reflected signal to the incident signal. Now, if the transmission line is terminated in Z_0 then reflected signal will be zero so that $R = 0$, but when Z_L is not equal to Z_0 then some value of R will be obtained. If Z_L is a short or open circuit then R will be unity, so the value of R ranges from $0 \leq R \leq 1$. Return loss is expressed in terms of decibel (-milliwatts) (dB(m)) and is a scalar quantity which is an electrical power unit in decibels (dB), referenced to 1 milliwatt (mW). It can be thought of as the number of dB(m) that the reflected signal is below the incident signal and it varies between infinity and 0 for an open or short circuit. Generally, dB is a relative measurement (e.g. positive dB means gain while, negative dB denotes loss) unlike dBm (here, 'm' stands for mW) which is an absolute unit making it very critical to convert from dBm to dB. However, the relationship between powers expressed in dBm (P_{dBm}) and mW (P_{mW}) is given by,

$$P_{\mathrm{dBm}} = 10 \log_{10} \left(\frac{P_{\mathrm{mW}}}{1\mathrm{mW}} \right) \tag{2.51}$$

2.12.3.3.B. Transmission Parameters

Transmission coefficient (T) is defined as the ratio of the transmitted signal to the incident signal and it is expressed in terms of dBm. The phase portion of the transmission coefficient is called the insertion phase. Notably, the S-parameters are generally expressed in dBm unit.

2.12.3.3.C. Group Delay

It is a measure of the transit time of a signal through the DUT versus frequency. It is calculated by differentiating the insertion phase response of DUT versus frequency, i.e. it is a measure of the transmission line response.

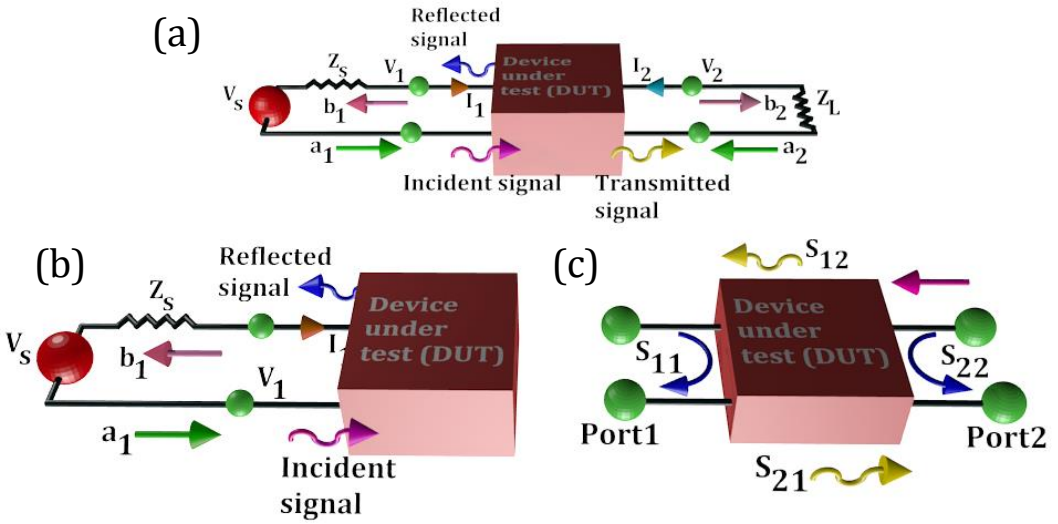

Figure 2.13. Schematic of (a) two- and (b) one-port microwave excitation and detection systems. (c) Graphical representation of scattering (*S*) parameters.

2.12.3.4. Scattering (*S*-) Parameters

These are generally the elements of scattering (*S*-) matrix. It is mostly used for electrical circuits which are operated at RF or microwave (MW) frequency [421]. These parameters get modified with the measurement frequency and system impedance. The electrical circuit usually behaves like a black box which can interact with other circuits through ports. The network is characterized by *S*-matrix. An *S*-matrix can describe *N*-port network which has *N*-dimensions and N^2 ($N \times N$) elements and each of these elements is a complex number, i.e. they possess both magnitude and phase. At high RF or MW regime, direct measurement of admittance (*Y*) or impedance (*Z*) or hybrid (*h*) parameters become difficult due to the following reasons:

1. Unavailability of equipment to measure total current and voltage in RF/ MW regime.
2. It is difficult to obtain a perfect open/short condition.
3. Active devices may be unstable under open/short conditions or such high-frequency domain.

However, in order to avoid such difficulties, *S*-parameters have the following benefits:

1. Relatively easy to measure at the high-frequency regime.
2. These parameters can be related to familiar measurements, e.g. gain, loss, reflection or transmission coefficients,

3. Y, Z or h-parameters can be calculated from *S*-parameters if necessary.

2.12.3.4.A. Calculation for Scattering (*S*-) Parameters

As schematically illustrated in Figure 2.13(a, b), the necessary measurement conditions have been depicted for two- and one-port measurement systems respectively, where Z_S and Z_L represent the source and load impedances which are matched (terminated) with the characteristic impedance, Z_0. V_S, V_1 and V_2 denote the signals at the generator (source), potential differences across the two leads on both sides (1 and 2) and I_1 and I_2 are the corresponding currents. If a_1 and a_2 represent the incident signals from the two ports while, b_1 and b_2 are the acquired signals respectively at the two corresponding ends then b_1 and b_2 can be expressed as,

$$b_1 = S_{11}a_1 + S_{12}a_2 \tag{2.52}$$

$$b_2 = S_{21}a_1 + S_{22}a_2 \tag{2.53}$$

This can be expressed in the matrix form given by,

$$\begin{bmatrix} b_1 \\ b_2 \end{bmatrix} = \begin{bmatrix} S_{11} & S_{12} \\ S_{21} & S_{22} \end{bmatrix} \begin{bmatrix} b_1 \\ b_2 \end{bmatrix} \tag{2.54}$$

Here, *S*-parameters can be defined as the following:

1. Input reflection coefficient,

$$S_{11} = \left.\frac{b_1}{a_1}\right|_{a_2=0} \tag{2.55}$$

2. Forward transmission (insertion) gain,

$$S_{12} = \left.\frac{b_1}{a_2}\right|_{a_1=0} \tag{2.56}$$

3. Reverse transmission (insertion) gain,

$$S_{21} = \left.\frac{b_2}{a_1}\right|_{a_2=0} \tag{2.57}$$

4. Output reflection coefficient,

$$S_{22} = \left.\frac{b_2}{a_2}\right|_{a_1=0} \tag{2.58}$$

These parameters can be visualized as Figure 2.13(c). Generally, *S*-parameters are expressed in terms of dB as $20 \log_{10}|S_{ij}|$ where, i, j = 1, 2 respectively.

During the work presented in this thesis, one-port measurement has been carried out where only S_{11} parameter is extracted to investigate the SW spectra in magnetic samples.

2.13. Brillouin Light Scattering (BLS)

For many decades, the light scattering technique has been employed to investigate coherent dynamic properties in gases, liquids, and solids. Here, the properties of the scattered light from the specimen are measured and compared to that of the incident light. This yields information about the mechanisms that have a contribution to the scattering procedure. In Raman Scattering [422], light interacts with vibrational or rotational degree of freedom. However, the Brillouin light scattering (BLS) [423], named after its inventor deals with the inelastic scattering of photons [424-426] from a comparatively smaller frequency (~ GHz) quasiparticle excitations, e.g. magnons, phonons, plasmons [427,428] etc. Here, the physics underlying such a phenomenon is explained briefly in the following.

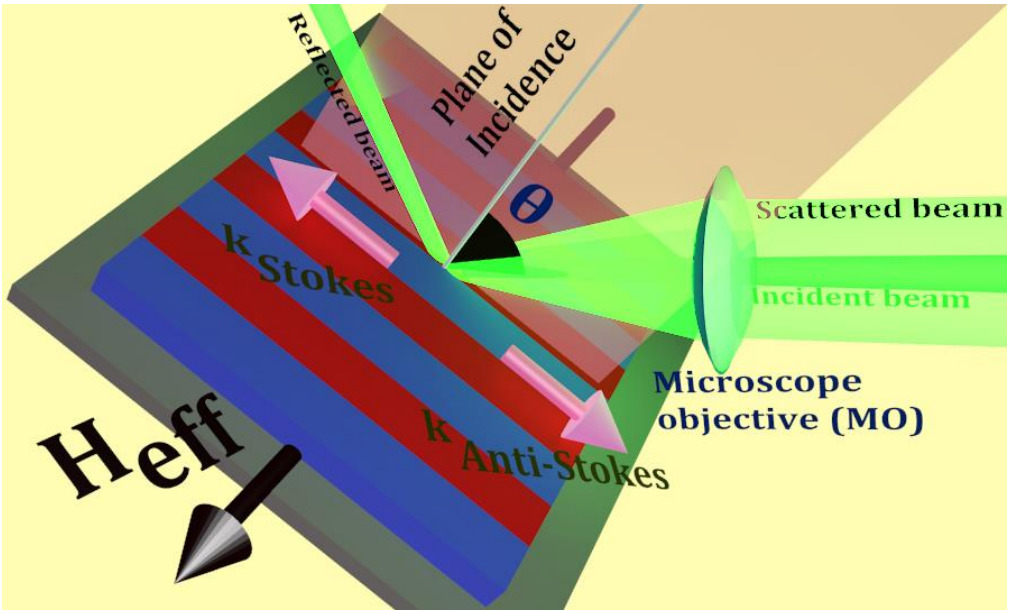

Figure 2.14. The scattering geometry demonstrating the incident, reflected and scattered beams as well as the direction of magnon wavevectors for Stokes and anti-Stokes processes in BLS in Damon-Eshbach (DE) geometry.

2.13.1. Principles

Figure 2.14 demonstrates the scattering geometry describing the incident and scattered beams, the angle of incidence (θ) and the wave vector (k) direction. The inelastic scattering mechanism can be defined as a photon-magnon collision from a quantum mechanical viewpoint, i.e. in terms of the creation (Stokes process) and annihilation (anti-Stokes process) of a magnon of angular frequency (ω) and wavevector (k) which is illustrated in Figure 2.15. If the conservation of energy (frequency) and momentum

(wave vector) between the magnon and the incident and scattered photons are considered, then:

$$\hbar\omega_s = \hbar\omega_i \pm \hbar\omega \tag{2.59}$$

$$\hbar k_s = \hbar k_i \pm \hbar k \tag{2.60}$$

where, + (−) sign stands for the anti-Stokes (Stokes) shift and k_i, k_s, ω_i, ω_s denote the wavevectors and angular frequencies of the incident and scattered lights, respectively. However, because of the translational symmetry breaking, the perpendicular component of the wave is not conserved in case of light scattered from a thin film. Therefore, the above Equations 2.59 and 2.60 only hold good for k which corresponds the wavevector component parallel to the film plane.

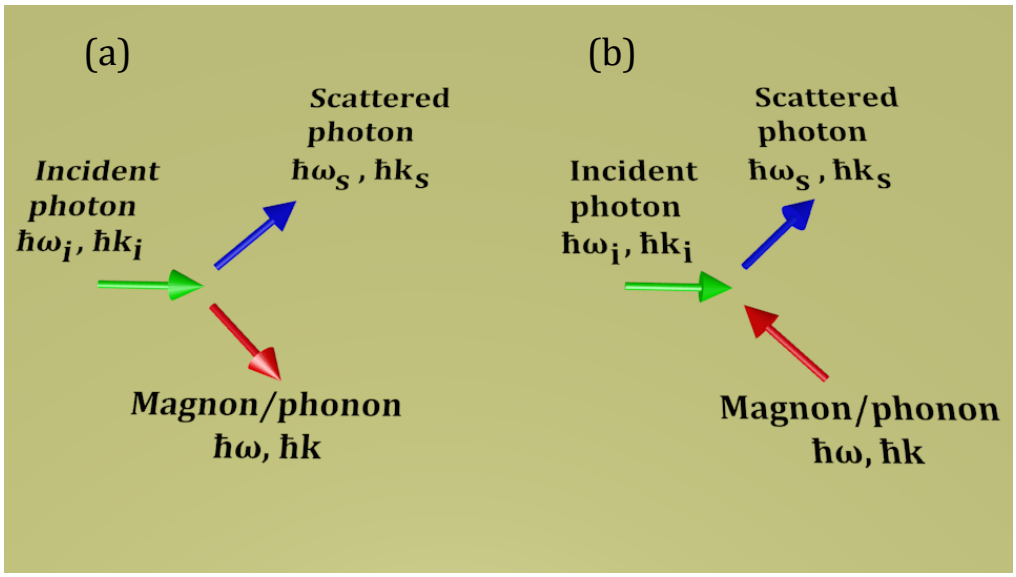

Figure 2.15. Pictorial representation of the (a) Stokes and (b) anti-Stokes scattering processes in BLS.

From the conservation of momentum described above, wavevector of SW involved in the scattering process can be determined. Usually, during the scattering, the amount of energy of incident light exchanged with the system (i.e., the energy of the magnon itself) is very small in comparison with that of the incident photon. The energy of magnon observed in BLS is ~ 10^{-4} eV whereas that of a visible photon is few eV. As a result, the magnitude of the scattered photon wavevector(k_s) should be very close to that of the incident photon wavevector (k_i). The schematic illustration of the scattering profile of a photon by a bulk magnon is depicted in Figure 2.16(a), which denotes that the SW

participating in the scattering possesses a component perpendicular to the surface. Here the scattered photon wavevector (k_s) must lie on the blue circular path which has a radius equal to the magnitude of incident photon wavevector (k_i). Here the cone describes the collection angle of the scattered beam in the BLS experiment where its central axis is aligned with the incident photon wavevector. Hence, by assuming that k_i and k_s are collinear ($k_s = -k_i$), i.e. the backscattered geometry, the magnitude of the wavevector ($|k|$) of the emitted or absorbed bulk magnon is always $2|k_i|$.

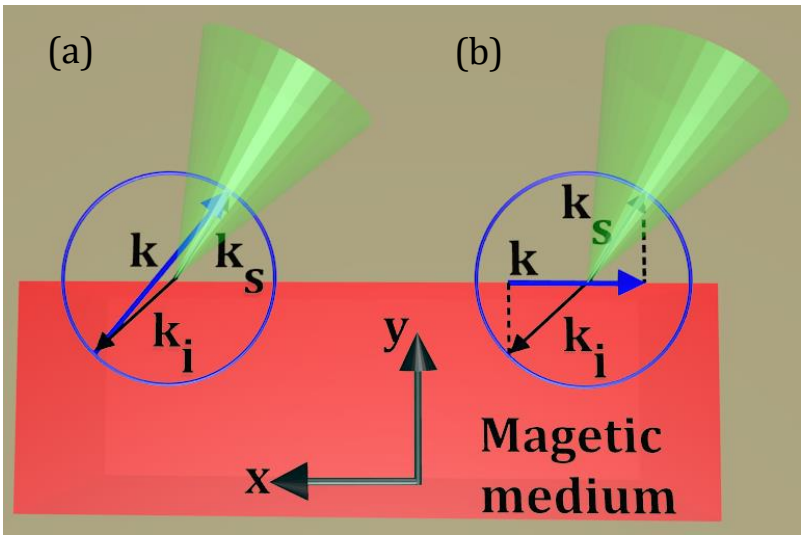

Figure 2.16. Scattering of the laser beam by (a) bulk and (b) surface magnons. Here, the direction of k corresponds to the anti-Stokes process.

Again, in case of scattering of a photon by a surface magnon as represented in Figure 2.16(b), k lies in the horizontal plane. Hence, conservation of momentum will be only in the plane along the surface of the sample. So, the conserved component of the incident beam is equal to $|k_i|\sin\theta$ where, θ is the angle between k_i and sample surface normal as shown in Figure 2.14. Therefore, the wavevector (k) of the magnon probed during the experiment can be written as:

$$|k| = |k_i \sin\theta - k_s \sin\theta| = 2|k_i| \sin\theta = 2\left(\frac{2\pi}{\lambda}\right)\sin\theta \qquad (2.61)$$

This suggests that no new information can be extracted about the bulk magnons by varying the incident angle whereas the surface magnon reveals the crucial frequency vs. wavevector dispersion relation. Equation 2.61 is known as the Bragg's condition which provides an approximation for most of the light scattering experiments. One can vary the magnitude of k according to Equation 2.61 by changing either θ or λ.

2.13.2. Uncertainty in the Selected Wavevector of Spin Wave

In BLS technique, an uncertainty is always induced in the selected SW wave vector because of the finite aperture angle of the objective lens used for focusing and collecting light from the sample. As illustrated in Figure 2.14, for the finite angle of incidence θ, the corresponding broadening in wavevector, k is given by:

$$\Delta k = 2k_{\mathrm{i}} \cos\theta \sin\left(\frac{\beta}{2}\right) = 2\left(\frac{2\pi}{\lambda}\right)(\cos\theta)(\mathrm{N.A.}) \tag{2.62}$$

where, β is the collecting angle of the lens while, its numerical aperture is defined by the following expression:

$$\mathrm{N.A.} = \sin\left(\frac{\beta}{2}\right) \tag{2.63}$$

So, for normal incidence (i.e. θ = 0°), this uncertainty becomes maximum. Also, because of the focusing of the incident beam, a possible uncertainty can be present in θ. However, a very narrow beam (width $\sim$ 500 μm) is used to reduce this during the practical experiment which in turn enhances the focused spot size.

2.13.3. Polarization of Scattered Beam

The scattering of light from the SWs can be interpreted as a magneto-optic mechanism. Generally, the oscillating electric dipoles experience a Lorentz force in the presence of the precessing magnetization or SW. This effectively results in a spatially periodic fluctuation in the polarizability of the medium leading to a scattered electromagnetic (EM) wave whose electric field vector is perpendicular to that of the incident wave. This procedure is schematically described in Figure 2.17 for a p-polarized (i.e. polarization parallel to the plane of incidence) incident light in Damon-Eshbach (DE) configuration where the magnetization direction is perpendicular to the propagation of SW. As the magnetic specimen is hit by the laser beam, it provokes the electric dipoles to oscillate due to its oscillatory electric field, given by:

$$\boldsymbol{E} = E_{\mathrm{x}}\boldsymbol{e}_{\mathrm{x}} + E_{\mathrm{y}}\boldsymbol{e}_{\mathrm{y}} \tag{2.64}$$

Now, if the magnetization (M) also has a dynamic component, then M can be expressed as:

$$\boldsymbol{M} = \boldsymbol{M}_0 + \boldsymbol{m} \tag{2.65}$$

where,

$$\boldsymbol{m} = m_{\mathrm{x}}\boldsymbol{e}_{\mathrm{x}} + m_{\mathrm{y}}\boldsymbol{e}_{\mathrm{y}} \tag{2.66}$$

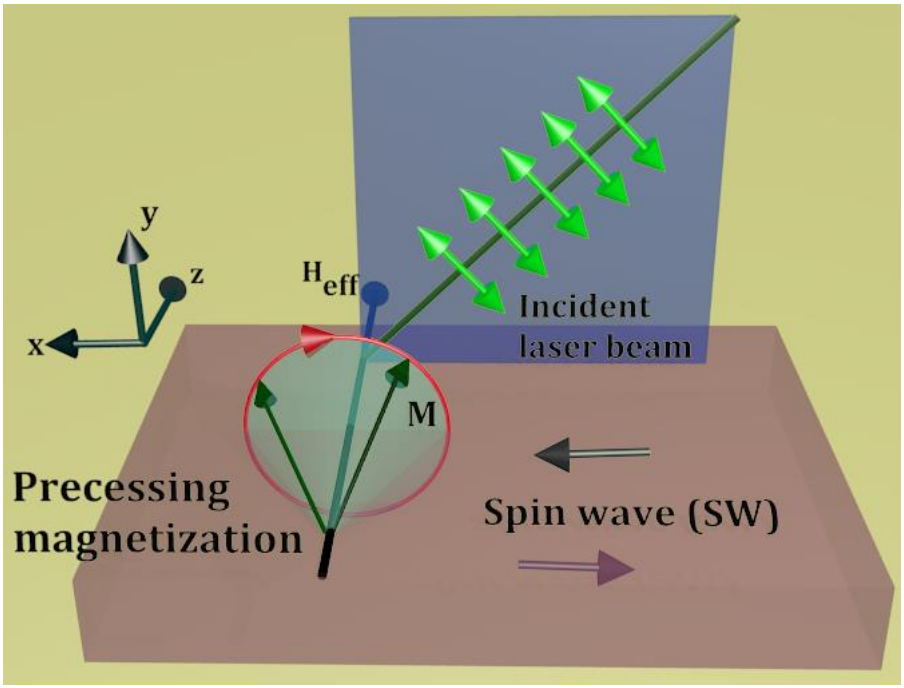

Figure 2.17. Schematic of the interaction between the *p*-polarized incident beam and the precessing magnetization (***M***).

The oscillating component of ***M*** exerts a Lorentz force (proportional to $\boldsymbol{E} \times \boldsymbol{m}$) on the electric dipoles which in this case causes polarization pointing along the *z*-direction. Consequently, the electric field of the radiated light wave is pointed along the *z*-direction (i.e. *s*-polarized). A similar argument for the incident light with *s*-polarization can be drawn when the scattered light is *p*-polarized. Hence, it can be concluded that the polarization of the incident light is perpendicular to that of light scattered by a magnon. This is different from the situation when light is scattered by acoustic phonons as here the polarizations of the incident and scattered lights lie along the same direction. This helps to isolate the scattered light by magnons from that scattered by phonons by choosing the suitable orientation of the analyzing polarizer in the experiment.

References

[1] L. Landau, Z. Phys. 64 (1930) 629.
[2] E. H. Sondheimer, A. H. Wilson, Philos. Trans. Royal Soc. A 210 (1951) 173.
[3] C. Kittel, *Introduction to Solid State Physics* 2005).
[4] P. Langevin, J. Phys. Theor. Appl. 4 (1905).
[5] A. Abragam, B. Bleaney, *Electron Paramagnetic Resonance of Transition Ions* (OUP Oxford, 2012).
[6] R. M. Bozorth, *Ferromagnetism* 1978.

[7] B. D. Cullity, C. D. Graham, in *Introduction to Magnetic Materials* (IEEE, 2009), p. 1.
[8] A. Aharoni, *Introduction to the Theory of Ferromagnetism* 2000).
[9] S. Chikazumi, *Physics of Ferromagnetism* (OUP Oxford, 2009).
[10] R. P. Feynman, R. B. Leighton, M. Sands, *The Feynman Lectures on Physics, Vol. I: The New Millennium Edition: Mainly Mechanics, Radiation, and Heat* (Basic Books, 2011).
[11] M. L. Néel, Ann. Phys. 12 (1948) 137.
[12] N. A. Spaldin, *Magnetic Materials: Fundamentals and Applications* (Cambridge University Press, 2010).
[13] P. W. Anderson, Phys. Rev. 79 (1950) 350.
[14] T. Kasuya, Prog. Theor. Exp. Phys. 16 (1956) 45.
[15] C. N. Yang, Phys. Rev. 85 (1952) 808.
[16] P. Weiss, J. Phys. Theor. Appl. 6 (1907) 661.
[17] N. W. Ashcroft, N. D. Mermin, *Solid State Physics* (Holt, Rinehart and Winston, 1976).
[18] J. H. E. Griffiths, Nature 158 (1946) 670.
[19] C. Kittel, Phys. Rev. 73 (1948) 155.
[20] F. Bloch, Z. Physik 61 (1930) 206.
[21] A. H. Morrish, *The Physical Principles of Magnetism* (R. E. Krieger Publishing Company, 1980).
[22] K. H. J. Buschow, *Handbook of Magnetic Materials* (Elsevier, North Holland: Amsterdam, The Netherlands, 2009), Vol. 18, p. 168.
[23] J. M. D. Coey, *Magnetism and Magnetic Materials* (Cambridge University Press, 2010).
[24] D. J. Griffiths, *Introduction to Quantum Mechanics* (Pearson Prentice Hall, 2005).
[25] M. Pioro-Ladrière, T. Obata, Y. Tokura, Y. S. Shin, T. Kubo, K. Yoshida, T. Taniyama, S. Tarucha, Nat. Phys. 4 (2008) 776.
[26] R. Hanson, B. Witkamp, L. M. K. Vandersypen, L. H. W. van Beveren, J. M. Elzerman, L. P. Kouwenhoven, Phys. Rev. Lett. 91 (2003) 196802.
[27] W. Heisenberg, Z. Physik 38 (1926) 411.
[28] P. A. M. Dirac, Philos. Trans. Royal Soc. A 112 (1926) 661.
[29] R. Boča, in *A Handbook of Magnetochemical Formulae*, edited by R. Boča (Elsevier, Oxford, 2012), p. 291.
[30] C. Kittel, in *Solid State Physics*, edited by F. Seitz, D. Turnbull, and H. Ehrenreich (Academic Press, 1969), p. 1.
[31] G. M. Genkin, M. V. Sapozhnikov, J. Magn. Magn. Mater. 139 (1995) 179.
[32] M. A. Ruderman, C. Kittel, Phys. Rev. 96 (1954) 99.
[33] J. H. Van Vleck, Rev. Mod. Phys. 34 (1962) 681.
[34] K.-I. Gondaira, Y. Tanabe, J. Phys. Soc. Jpn. 21 (1966) 1527.
[35] J. Kanamori, J. Phys. Chem. Solids 10 (1959) 87.
[36] M. A. Gilleo, J. Phys. Chem. Solids 13 (1960) 33.
[37] P. W. Anderson, Phys. Rev. 115 (1959) 2.
[38] J. B. Goodenough, Phys. Rev. 100 (1955) 564.
[39] H. A. Kramers, Physica 1 (1934) 182.
[40] T. Moriya, Phys. Rev. 120 (1960) 91.
[41] I. Dzyaloshinsky, J. Phys. Chem. Solids 4 (1958) 241.
[42] T. Moriya, Phys. Rev. Lett. 4 (1960) 228.
[43] F. Keffer, Phys. Rev. 126 (1962) 896.
[44] S.-W. Cheong, M. Mostovoy, Nat. Mater. 6 (2007) 13.

[45] I. A. Sergienko, E. Dagotto, Phys. Rev. B 73 (2006) 094434.
[46] P. A. Abragam, A. Abragam, *The Principles of Nuclear Magnetism* (Clarendon Press, 1961).
[47] P. Bruno, J. P. Renard, Appl. Phys. A 49 (1989) 499.
[48] M. McCaig, *Permanent magnets in theory and practice* (Pentech Press, 1977).
[49] T. Thomson, in *Metallic Films for Electronic, Optical and Magnetic Applications*, edited by K. Barmak, and K. Coffey (Woodhead Publishing, 2014), p. 454.
[50] P. Bruno, J. Seiden, J. Phys. Colloques 49 (1988) C8.
[51] J. H. Van Vleck, Phys. Rev. 74 (1948) 1168.
[52] R. Winkler, *Spin-orbit Coupling Effects in Two-Dimensional Electron and Hole Systems* (Springer Berlin Heidelberg, 2003).
[53] R. J. Elliott, Phys. Rev. 96 (1954) 266.
[54] O. Kohmoto, J. Magn. Magn. Mater. 262 (2003) 280.
[55] L. Néel, J. Phys. Radium 15 (1954) 225.
[56] N. Nakajima, T. Koide, T. Shidara, H. Miyauchi, H. Fukutani, A. Fujimori, K. Iio, T. Katayama, M. Nývlt, Y. Suzuki, Phys. Rev. Lett. 81 (1998) 5229.
[57] S. Baumann *et al.*, Phys. Rev. Lett. 115 (2015) 237202.
[58] S. Ikeda, K. Miura, H. Yamamoto, K. Mizunuma, H. D. Gan, M. Endo, S. Kanai, J. Hayakawa, F. Matsukura, H. Ohno, Nat. Mater. 9 (2010) 721.
[59] J. W. Koo, S. Mitani, T. T. Sasaki, H. Sukegawa, Z. C. Wen, T. Ohkubo, T. Niizeki, K. Inomata, K. Hono, Appl. Phys. Lett. 103 (2013) 192401.
[60] J. Torrejon, J. Kim, J. Sinha, S. Mitani, M. Hayashi, M. Yamanouchi, H. Ohno, Nat. Commun. 5 (2014) 4655.
[61] P. F. Carcia, J. Appl. Phys. 63 (1988) 5066.
[62] H. X. Yang, M. Chshiev, B. Dieny, J. H. Lee, A. Manchon, K. H. Shin, Phys. Rev. B 84 (2011) 054401.
[63] H. J. G. Draaisma, F. J. A. den Broeder, W. J. M. de Jonge, J. Appl. Phys. 63 (1988) 3479.
[64] F. J. A. den Broeder, W. Hoving, P. J. H. Bloemen, J. Magn. Magn. Mater. 93 (1991) 562.
[65] F. J. A. den Broeder, H. C. Donkersloot, H. J. G. Draaisma, W. J. M. de Jonge, J. Appl. Phys. 61 (1987) 4317.
[66] M. T. Johnson, P. J. H. Bloemen, F. J. A. d. Broeder, J. J. d. Vries, Rep. Prog. Phys. 59 (1996) 1409.
[67] P. Bruno, Phys. Rev. B 39 (1989) 865.
[68] H. B. Callen, E. Callen, J. Phys. Chem. Solids 27 (1966) 1271.
[69] G. H. O. Daalderop, P. J. Kelly, M. F. H. Schuurmans, Phys. Rev. B 41 (1990) 11919.
[70] G. H. O. Daalderop, P. J. Kelly, M. F. H. Schuurmans, Phys. Rev. B 44 (1991) 12054.
[71] G. v. d. Laan, J. Phys. Condens. Matter 10 (1998) 3239.
[72] W. Palmer, Phys. Rev. 131 (1963) 1057.
[73] J. Ye, A. J. Newell, R. T. Merrill, Geophys. Res. Lett. 21 (1994) 25.
[74] B. D. Cullity, C. D. Graham, in *Introduction to Magnetic Materials* (IEEE, 2009), p. 1.
[75] J. A. Osborn, Phys. Rev. 67 (1945) 351.
[76] D.-X. Chen, J. A. Brug, R. B. Goldfarb, IEEE Trans. Magn. 27 (1991) 3601.
[77] B. Krüger, G. Selke, A. Drews, D. Pfannkuche, IEEE Trans. Magn. 49 (2013) 4749.
[78] J. Kaczér, L. Murtinová, Phys. Status Solidi A 23 (1974) 79.
[79] D.-X. Chen, E. Pardo, A. Sanchez, IEEE Trans. Magn. 37 (2001) 3877.
[80] K. Ozaki, M. Kobayashi, IEEE Trans. Magn. 36 (2000) 210.

[81] Y. Zhai, J. Shi, X. Y. Zhang, L. Shi, Y. X. Xu, H. B. Huang, Z. H. Lu, H. R. Zhai, J. Phys. Condens. Matter 14 (2002) 7865.
[82] R. C. O'Handley, S. W. Sun, J. Magn. Magn. Mater. 104-107 (1992) 1717.
[83] L. Ranno, A. Llobet, R. Tiron, E. Favre-Nicolin, Appl. Surf. Sci. 188 (2002) 170.
[84] E. R. Callen, H. B. Callen, Phys. Rev. 129 (1963) 578.
[85] W. F. Brown, C. Truesdell, *Magnetoelastic Interactions, Springer Tracts in Natural Philosophy* 1966), Vol. 9.
[86] D. Sander, Rep. Prog. Phys. 62 (1999) 809.
[87] W. F. Brown, J. Appl. Phys. 36 (1965) 994.
[88] S. W. Sun, R. C. O'Handley, Phys. Rev. Lett. 66 (1991) 2798.
[89] W. F. Brown, *Magnetoelastic interactions* (Springer, 1966).
[90] V. Novosad, Y. Otani, A. Ohsawa, S. G. Kim, K. Fukamichi, J. Koike, K. Maruyama, O. Kitakami, Y. Shimada, J. Appl. Phys. 87 (2000) 6400.
[91] R. D. James, M. Wuttig, Philos. Mag. A 77 (1998) 1273.
[92] D. Sander, J. Phys. Condens. Matter 16 (2004) R603.
[93] M. E. Schabes, H. N. Bertram, J. Appl. Phys. 64 (1988) 1347.
[94] V. V. Kruglyak, P. S. Keatley, R. J. Hicken, J. R. Childress, J. A. Katine, Phys. Rev. B 75 (2007) 024407.
[95] R. P. Cowburn, A. O. Adeyeye, M. E. Welland, Phys. Rev. Lett. 81 (1998) 5414.
[96] B. K. Mahato, S. Choudhury, R. Mandal, S. Barman, Y. Otani, A. Barman, J. Appl. Phys. 117 (2015) 213909.
[97] S. Jain, Y. Ren, A. O. Adeyeye, N. Singh, Phys. Rev. B 80 (2009) 132401.
[98] S. Iwasaki, K. Ouchi, IEEE Trans. Magn. 14 (1978) 849.
[99] P. F. Carcia, A. D. Meinhaldt, A. Suna, Appl. Phys. Lett. 47 (1985) 178.
[100] D.-s. Wang, R. Wu, A. J. Freeman, Phys. Rev. B 48 (1993) 15886.
[101] B. N. Engel, M. H. Wiedmann, R. A. Van Leeuwen, C. M. Falco, Phys. Rev. B 48 (1993) 9894.
[102] L. Zhong, M. Kim, X. Wang, A. J. Freeman, Phys. Rev. B 53 (1996) 9770.
[103] S. Pal, B. Rana, O. Hellwig, T. Thomson, A. Barman, Appl. Phys. Lett. 98 (2011) 082501.
[104] S. Ikeda, J. Hayakawa, Y. Ashizawa, Y. M. Lee, K. Miura, H. Hasegawa, M. Tsunoda, F. Matsukura, H. Ohno, Appl. Phys. Lett. 93 (2008) 082508.
[105] C. Duan, J. P. Velev, R. F. Sabirianov, Z. Zhu, J. Chu, S. S. Jaswal, E. Y. Tsymbal, Phys. Rev. Lett. 101 (2008) 137201.
[106] W. H. Meiklejohn, C. P. Bean, Phys. Rev. 105 (1957) 904.
[107] W. H. Meiklejohn, J. Appl. Phys. 33 (1962) 1328.
[108] A. P. Malozemoff, J. Appl. Phys. 63 (1988) 3874.
[109] A. E. Berkowitz, K. Takano, J. Magn. Magn. Mater. 200 (1999) 552.
[110] J. Nogués, I. K. Schuller, J. Magn. Magn. Mater. 192 (1999) 203.
[111] M. Kiwi, J. Magn. Magn. Mater. 234 (2001) 584.
[112] J. Nogués, J. Sort, V. Langlais, V. Skumryev, S. Suriñach, J. S. Muñoz, M. D. Baró, Phys. Rep. 422 (2005) 65.
[113] E. Ohmichi, T. Osada, Rev. Sci. Instrum. 73 (2002) 3022.
[114] J. P. Eisenstein, Appl. Phys. Lett. 46 (1985) 695.
[115] D. A. Allwood, G. Xiong, M. D. Cooke, R. P. Cowburn, J. Phys. D: Appl. Phys. 36 (2003) 2175.
[116] C. Y. You, S. C. Shin, Appl. Phys. Lett. 69 (1996) 1315.
[117] S. Foner, Rev. Sci. Instrum. 30 (1959) 548.

[118] S. Foner, Rev. Sci. Instrum. 27 (1956) 548.
[119] D. O. Smith, Rev. Sci. Instrum. 27 (1956) 261.
[120] S. Foner, J. Appl. Phys. 79 (1996) 4740.
[121] R. C. Jaklevic, J. Lambe, A. H. Silver, J. E. Mercereau, Phys. Rev. Lett. 12 (1964) 159.
[122] P. W. Anderson, J. M. Rowell, Phys. Rev. Lett. 10 (1963) 230.
[123] D. Drung, C. Abmann, J. Beyer, A. Kirste, M. Peters, F. Ruede, T. Schurig, IEEE Trans. Appl. Supercond. 17 (2007) 699.
[124] G. Musmann, *Fluxgate Magnetometers for Space Research* (Books on Demand, 2010).
[125] D. Gordon, R. Brown, IEEE Trans. Magn. 8 (1972) 76.
[126] F. Primdahl, J. Phys. E: Sci. Instrum. 12 (1979) 241.
[127] P. J. Flanders, J. Appl. Phys. 63 (1988) 3940.
[128] P. J. Flanders, Rev. Sci. Instrum. 61 (1990) 839.
[129] L. W. McKeehan, Rev. Sci. Instrum. 5 (1934) 265.
[130] C. A. Domenicali, Rev. Sci. Instrum. 21 (1950) 327.
[131] E. C. Bullard, Math. Proc. Camb. Philos. Soc. 29 (2008) 288.
[132] L. F. Lindoy, V. Katovic, D. H. Busch, J. Chem. Educ. 49 (1972) 117.
[133] T. Sakakibara, H. Mitamura, T. Tayama, H. Amitsuka, Jpn. J. Appl. Phys. 33 (1994) 5067.
[134] B. L. Morris, A. Wold, Rev. Sci. Instrum. 39 (1968) 1937.
[135] V. P. Denysenkov, A. M. Grishin, Rev. Sci. Instrum. 74 (2003) 3400.
[136] S. S. Kalarickal, P. Krivosik, M. Wu, C. E. Patton, M. L. Schneider, P. Kabos, T. J. Silva, J. P. Nibarger, J. Appl. Phys. 99 (2006) 093909.
[137] I. Harward, T. O'Keevan, A. Hutchison, V. Zagorodnii, Z. Celinski, Rev. Sci. Instrum. 82 (2011) 095115.
[138] C. Bilzer, T. Devolder, P. Crozat, C. Chappert, S. Cardoso, P. P. Freitas, J. Appl. Phys. 101 (2007) 074505.
[139] E. Montoya, T. McKinnon, A. Zamani, E. Girt, B. Heinrich, J. Magn. Magn. Mater. 356 (2014) 12.
[140] Y. Takagi, K. Kurihara, Rev. Sci. Instrum. 63 (1992) 5552.
[141] M. H. Grimsditch, A. K. Ramdas, Phys. Rev. B 11 (1975) 3139.
[142] W. F. Oliver, C. A. Herbst, S. M. Lindsay, G. H. Wolf, Rev. Sci. Instrum. 63 (1992) 1884.
[143] S. O. Demokritov, B. Hillebrands, A. N. Slavin, Phys. Rep. 348 (2001) 441.
[144] Y. Okawachi, M. S. Bigelow, J. E. Sharping, Z. Zhu, A. Schweinsberg, D. J. Gauthier, R. W. Boyd, A. L. Gaeta, Phys. Rev. Lett. 94 (2005) 153902.
[145] A. Barman, T. Kimura, Y. Otani, Y. Fukuma, K. Akahane, S. Meguro, Rev. Sci. Instrum. 79 (2008) 123905.
[146] J. Fassbender, in *Spin Dynamics in Confined Magnetic Structures II*, edited by B. Hillebrands, and K. Ounadjela (Springer Berlin Heidelberg, Berlin, Heidelberg, 2003), p. 59.
[147] M. Cormier, J. Ferré, A. Mougin, J. P. Cromières, V. Klein, Rev. Sci. Instrum. 79 (2008) 033706.
[148] M. Zhu, Z. Zhou, B. Peng, S. Zhao, Y. Zhang, G. Niu, W. Ren, Z. G. Ye, Y. Liu, M. Liu, Adv. Funct. Mater. 27 (2017) 1605598.
[149] W.-Y. Tong, Y.-W. Fang, J. Cai, S.-J. Gong, C.-G. Duan, Comput. Mater. Sci. 112 (2016) 467.

[150] H. Ohno, D. Chiba, F. Matsukura, T. Omiya, E. Abe, T. Dietl, Y. Ohno, K. Ohtani, Nature 408 (2000) 944.
[151] M. Xu, J. Puebla, F. Auvray, B. Rana, K. Kondou, Y. Otani, Phys. Rev. B 97 (2018) 180301(R).
[152] B. Dieny, M. Chshiev, Rev. Mod. Phys. 89 (2017) 025008.
[153] C.-G. Duan, J. P. Velev, R. F. Sabirianov, Z. Zhu, J. Chu, S. S. Jaswal, E. Y. Tsymbal, Phys. Rev. Lett. 101 (2008) 137201.
[154] M. Tsujikawa, T. Oda, Phys. Rev. Lett. 102 (2009) 247203.
[155] T. Kawabe, K. Yoshikawa, M. Tsujikawa, T. Tsukahara, K. Nawaoka, Y. Kotani, K. Toyoki, M. Goto, M. Suzuki, T. Nakamura, M. Shirai, Y. Suzuki, S. Miwa, Phys. Rev. B 96 (2017) 220412(R).
[156] S. Miwa *et al.*, Nat. Commun. 8 (2017) 15848.
[157] S. E. Barnes, J. i. Ieda, S. Maekawa, Sci. Rep. 4 (2014) 4105.
[158] V. B. Naik, H. Meng, J. X. Xiao, R. S. Liu, A. Kumar, K. Y. Zeng, P. Luo, S. Yap, Appl. Phys. Lett. 105 (2014) 052403.
[159] Y. Shiota, F. Bonell, S. Miwa, N. Mizuochi, T. Shinjo, Y. Suzuki, Appl. Phys. Lett. 103 (2013) 082410.
[160] K. Miura, S. Yabuuchi, M. Yamada, M. Ichimura, B. Rana, S. Ogawa, H. Takahashi, Y. Fukuma, Y. Otani, Sci. Rep. 7 (2017) 42511.
[161] B. Rana, Y. Fukuma, K. Miura, H. Takahashi, Y. Otani, Sci. Rep. 7 (2017) 2318.
[162] T. Nozaki, K. Yakushiji, S. Tamaru, M. Sekine, R. Matsumoto, M. Konoto, H. Kubota, A. Fukushima, S. Yuasa, Appl. Phys. Lett. 6 (2013) 073005.
[163] A. Kozioł-Rachwał, T. Nozaki, K. Freindl, J. Korecki, S. Yuasa, Y. Suzuki, Sci. Rep. 7 (2017) 5993.
[164] A. Okada, S. Kanai, M. Yamanouchi, S. Ikeda, F. Matsukura, H. Ohno, Appl. Phys. Lett. 105 (2014) 052415.
[165] W. Skowroński, T. Nozaki, D. D. Lam, Y. Shiota, K. Yakushiji, H. Kubota, A. Fukushima, S. Yuasa, Y. Suzuki, Phys. Rev. B 91 (2015) 184410.
[166] Y. Hayashi, Y. Hibino, F. Matsukura, K. Miwa, S. Ono, T. Hirai, T. Koyama, H. Ohno, D. Chiba, Appl. Phys. Express 11 (2017) 013003.
[167] Y. Hibino, T. Koyama, A. Obinata, T. Hirai, S. Ota, K. Miwa, S. Ono, F. Matsukura, H. Ohno, D. Chiba, Appl. Phys. Lett. 109 (2016) 082403.
[168] D. D. Lam, F. Bonell, S. Miwa, Y. Shiota, K. Yakushiji, H. Kubota, T. Nozaki, A. Fukushima, S. Yuasa, Y. Suzuki, J. Korean Phys. Soc. 62 (2013) 1461.
[169] S. Kanai, M. Gajek, D. C. Worledge, F. Matsukura, H. Ohno, Appl. Phys. Lett. 105 (2014) 242409.
[170] J. Miltat, G. Albuquerque, A. Thiaville, in *Spin Dynamics in Confined Magnetic Structures I*, edited by B. Hillebrands, and K. Ounadjela (Springer Berlin Heidelberg, Berlin, Heidelberg, 2002), p. 1.
[171] M. Getzlaff, *Fundamentals of Magnetism* (Springer Berlin Heidelberg, 2007).
[172] J. Stöhr, H. C. Siegmann, *Magnetism: From Fundamentals to Nanoscale Dynamics* (Springer Berlin Heidelberg, 2007).
[173] B. Koopmans, J. J. M. Ruigrok, F. D. Longa, W. J. M. de Jonge, Phys. Rev. Lett. 95 (2005) 267207.
[174] R. M. White, *Quantum Theory of Magnetism: Magnetic Properties of Materials* (Springer Berlin Heidelberg, 2013).
[175] B. Hillebrands, K. Ounadjela, *Spin Dynamics in Confined Magnetic Structures I* 2002), Vol. 83.

[176] L. D. Landau, E. M. Lifshitz, Phys. Z. Sowietunion 8 (1935) 153.
[177] T. L. Gilbert, IEEE Trans. Magn. 40 (2004) 3443.
[178] J. A. Weil, J. R. Bolton, *Electron Paramagnetic Resonance: Elementary Theory and Practical Applications* (Wiley, 2007).
[179] B. Odom, D. Hanneke, B. D'Urso, G. Gabrielse, Phys. Rev. Lett. 97 (2006) 030801.
[180] J. L. Heilbron, T. S. Kuhn, Hist. Stud. Phys. Sci. 1 (1969) vi.
[181] R. Shankar, *Principles of Quantum Mechanics* (Springer US, 1995).
[182] T. L. Gilbert, Phys. Rev. 100 (1955) 1243.
[183] J. O. Rantschler, R. D. McMichael, A. Castillo, A. J. Shapiro, W. F. Egelhoff, B. B. Maranville, D. Pulugurtha, A. P. Chen, L. M. Connors, J. Appl. Phys. 101 (2007) 033911.
[184] M. C. Hickey, J. S. Moodera, Phys. Rev. Lett. 102 (2009) 137601.
[185] H. Suhl, IEEE Trans. Magn. 34 (1998) 1834.
[186] V. Kamberský, Phys. Rev. B 76 (2007) 134416.
[187] J. Pelzl, R. Meckenstock, D. Spoddig, F. Schreiber, J. Pflaum, Z. Frait, J. Phys. Condens. Matter 15 (2003) S451.
[188] Y. Tserkovnyak, A. Brataas, G. E. W. Bauer, Phys. Rev. Lett. 88 (2002) 117601.
[189] E. Barati, M. Cinal, D. M. Edwards, A. Umerski, Phys. Rev. B 90 (2014) 014420.
[190] V. Kambersky, C. E. Patton, Phys. Rev. B 11 (1975) 2668.
[191] B. Heinrich, R. Urban, G. Woltersdorf, J. Appl. Phys. 91 (2002) 7523.
[192] J. Z. Sun, B. Özyilmaz, W. Chen, M. Tsoi, A. D. Kent, J. Appl. Phys. 97 (2005) 10C714.
[193] R. Arias, D. L. Mills, Phys. Rev. B 60 (1999) 7395.
[194] R. Arias, D. L. Mills, J. Appl. Phys. 87 (2000) 5455.
[195] H. Schultheiss, K. Vogt, B. Hillebrands, Phys. Rev. B 86 (2012) 054414.
[196] H. A. Sodano, J. S. Bae, *Eddy Current Damping in Structures* (Sage Publ., 2004).
[197] B. Heinrich, J. F. Cochran, R. Hasegawa, J. Appl. Phys. 57 (1985) 3690.
[198] P. Dai, H. Y. Hwang, J. Zhang, J. A. Fernandez-Baca, S. W. Cheong, C. Kloc, Y. Tomioka, Y. Tokura, Phys. Rev. B 61 (2000) 9553.
[199] B. Raquet, M. Viret, E. Sondergard, O. Cespedes, R. Mamy, Phys. Rev. B 66 (2002) 024433.
[200] K. Gilmore, Y. U. Idzerda, M. D. Stiles, J. Appl. Phys. 103 (2008) 07D303.
[201] A. Hamadeh *et al.*, Phys. Rev. Lett. 113 (2014) 197203.
[202] M. Oogane, T. Wakitani, S. Yakata, R. Yilgin, Y. Ando, A. Sakuma, T. Miyazaki, Jpn. J. Appl. Phys. 45 (2006) 3889.
[203] J. Lindner, K. Lenz, E. Kosubek, K. Baberschke, D. Spoddig, R. Meckenstock, J. Pelzl, Z. Frait, D. L. Mills, Phys. Rev. B 68 (2003) 060102.
[204] A. V. Chubukov, D. M. Frenkel, Phys. Rev. Lett. 74 (1995) 3057.
[205] M. A. W. Schoen, D. Thonig, M. L. Schneider, T. J. Silva, H. T. Nembach, O. Eriksson, O. Karis, J. M. Shaw, Nat. Phys. 12 (2016) 839.
[206] A. Azevedo, L. H. Vilela-Leão, R. L. Rodríguez-Suárez, A. F. Lacerda Santos, S. M. Rezende, Phys. Rev. B 83 (2011) 144402.
[207] O. Mosendz, V. Vlaminck, J. E. Pearson, F. Y. Fradin, G. E. W. Bauer, S. D. Bader, A. Hoffmann, Phys. Rev. B 82 (2010) 214403.
[208] Y. Tserkovnyak, A. Brataas, G. E. W. Bauer, Phys. Rev. B 66 (2002) 224403.
[209] A. Ganguly, S. Azzawi, S. Saha, J. A. King, R. M. Rowan-Robinson, A. T. Hindmarch, J. Sinha, D. Atkinson, A. Barman, Sci. Rep. 5 (2015) 17596.
[210] S. Azzawi, A. Ganguly, M. Tokaç, R. M. Rowan-Robinson, J. Sinha, A. T. Hindmarch, A. Barman, D. Atkinson, Phys. Rev. B 93 (2016) 054402.
[211] S.-K. Kim, J. Phys. D: Appl. Phys. 43 (2010) 264004.

[212] E. Beaurepaire, J. C. Merle, A. Daunois, J. Y. Bigot, Phys. Rev. Lett. 76 (1996) 4250.
[213] A. Scholl, L. Baumgarten, R. Jacquemin, W. Eberhardt, Phys. Rev. Lett. 79 (1997) 5146.
[214] R. Knorren, K. H. Bennemann, R. Burgermeister, M. Aeschlimann, Phys. Rev. B 61 (2000) 9427.
[215] C. Boeglin, E. Beaurepaire, V. Halté, V. López-Flores, C. Stamm, N. Pontius, H. A. Dürr, J. Y. Bigot, Nature 465 (2010) 458.
[216] E. Beaurepaire, G. M. Turner, S. M. Harrel, M. C. Beard, J.-Y. Bigot, C. A. Schmuttenmaer, Appl. Phys. Lett. 84 (2004) 3465.
[217] G. P. Zhang, W. Hübner, Phys. Rev. Lett. 85 (2000) 3025.
[218] B. Koopmans, J. J. M. Ruigrok, F. D. Longa, W. J. M. d. Jonge, Phys. Rev. Lett. 95 (2005) 267207.
[219] C. Stamm, T. Kachel, N. Pontius, R. Mitzner, T. Quast, K. Holldack, S. Khan, C. Lupulescu, E. F. Aziz, M. Wietstruk, H. A. Dürr, W. Eberhardt, Nat. Mater. 6 (2007) 740.
[220] E. Carpene, E. Mancini, C. Dallera, M. Brenna, E. Puppin, S. De Silvestri, Phys. Rev. B 78 (2008) 174422.
[221] B. Koopmans, G. Malinowski, F. Dalla Longa, D. Steiauf, M. Fähnle, T. Roth, M. Cinchetti, M. Aeschlimann, Nat. Mater. 9 (2009) 259.
[222] T. Roth, A. J. Schellekens, S. Alebrand, O. Schmitt, D. Steil, B. Koopmans, M. Cinchetti, M. Aeschlimann, Phys. Rev. X 2 (2012) 021006.
[223] E. Turgut, C. La-o-vorakiat, J. M. Shaw, P. Grychtol, H. T. Nembach, D. Rudolf, R. Adam, M. Aeschlimann, C. M. Schneider, T. J. Silva, M. M. Murnane, H. C. Kapteyn, S. Mathias, Phys. Rev. Lett. 110 (2013) 197201.
[224] M. Cinchetti, M. Sánchez Albaneda, D. Hoffmann, T. Roth, J. P. Wüstenberg, M. Krauß, O. Andreyev, H. C. Schneider, M. Bauer, M. Aeschlimann, Phys. Rev. Lett. 97 (2006) 177201.
[225] G.-M. Choi, B.-C. Min, K.-J. Lee, D. G. Cahill, Nat. Commun. 5 (2014) 4334.
[226] M. Krauß, T. Roth, S. Alebrand, D. Steil, M. Cinchetti, M. Aeschlimann, H. C. Schneider, Phys. Rev. B 80 (2009) 180407.
[227] A. Eschenlohr, M. Battiato, P. Maldonado, N. Pontius, T. Kachel, K. Holldack, R. Mitzner, A. Föhlisch, P. M. Oppeneer, C. Stamm, Nat. Mater. 12 (2013) 332.
[228] G. P. Zhang, W. Hübner, Phys. Rev. Lett. 85 (2000) 3025.
[229] D. Steiauf, M. Fähnle, Phys. Rev. B 79 (2009) 140401.
[230] K. Carva, M. Battiato, P. M. Oppeneer, Phys. Rev. Lett. 107 (2011) 207201.
[231] J.-Y. Bigot, M. Vomir, E. Beaurepaire, Nat. Phys. 5 (2009) 515.
[232] W. Töws, G. M. Pastor, Phys. Rev. Lett. 115 (2015) 217204.
[233] G. Lefkidis, G. P. Zhang, W. Hübner, Phys. Rev. Lett. 103 (2009) 217401.
[234] G. P. Zhang, W. Hübner, G. Lefkidis, Y. Bai, T. F. George, Nat. Phys. 5 (2009) 499.
[235] G. Malinowski, F. Dalla Longa, J. H. H. Rietjens, P. V. Paluskar, R. Huijink, H. J. M. Swagten, B. Koopmans, Nat. Phys. 4 (2008) 855.
[236] M. Battiato, K. Carva, P. M. Oppeneer, Phys. Rev. Lett. 105 (2010) 027203.
[237] M. Battiato, K. Carva, P. M. Oppeneer, Phys. Rev. B 86 (2012) 024404.
[238] D. Rudolf *et al.*, Nat. Commun. 3 (2012) 1037.
[239] S. I. Anisimov, B. L. Kapeliovich, T. L. Perel'man, Zh. Eksp. Teor. Fiz. 66 (1974).
[240] A. Laraoui, V. Halté, M. Vomir, J. Vénuat, M. Albrecht, E. Beaurepaire, J. Y. Bigot, Eur. Phys. J. D 43 (2007) 251.
[241] A. Laraoui, J. Vénuat, V. Halté, M. Albrecht, E. Beaurepaire, J.-Y. Bigot, J. Appl. Phys. 101 (2007) 09C105.

[242] F. Bloch, Phys. Rev. 70 (1946) 460.
[243] D. D. Stancil, A. Prabhakar, *Spin Waves: Theory and Applications* (Springer US, 2009).
[244] A. V. Chumak, V. I. Vasyuchka, A. A. Serga, B. Hillebrands, Nat. Phys. 11 (2015) 453.
[245] D. D. Stancil, *Theory of Magnetostatic Waves* (Springer New York, 2012).
[246] B. A. Kalinikos, Russ. Phys. J. 24 (1981) 718.
[247] B. A. Kalinikos, M. P. Kostylev, N. V. Kozhus, A. N. Slavin, J. Phys. Condens. Matter 2 (1990) 9861.
[248] G. Carlotti, G. Gubbiotti, Riv. Nuovo Cimento 22 (1999) 1.
[249] R. W. Damon, J. R. Eshbach, J. Phys. Chem. Solids 19 (1961) 308.
[250] B. A. Kalinikos, A. N. Slavin, J. Phys. C: Solid State Phys. 19 (1986) 7013.
[251] B. A. Kalinikos, in *IEE Proceedings H (Microwaves, Optics and Antennas)*1980), pp. 4.
[252] T. Holstein, H. Primakoff, Phys. Rev. 58 (1940) 1098.
[253] C. Herring, C. Kittel, Phys. Rev. 81 (1951) 869.
[254] B. Lenk, H. Ulrichs, F. Garbs, M. Münzenberg, Phys. Rep. 507 (2011) 107.
[255] M. G. Cottam, D. J. Lockwood, *Light scattering in magnetic solids* (Wiley, 1986).
[256] A. G. Gurevich, G. A. Melkov, *Magnetization Oscillations and Waves* 1996).
[257] B. Hillebrands, K. Ounadjela, *Spin Dynamics in Confined Magnetic Structures II* (Springer Berlin Heidelberg, 2003).
[258] B. Hillebrands, A. Thiaville, *Spin Dynamics in Confined Magnetic Structures III* (Springer, 2006).
[259] K. Y. Guslienko, S. O. Demokritov, B. Hillebrands, A. N. Slavin, Phys. Rev. B 66 (2002) 132402.
[260] C. Yu, M. J. Pechan, W. A. Burgei, G. J. Mankey, J. Appl. Phys. 95 (2004) 6648.
[261] M. P. Kostylev, G. Gubbiotti, J. G. Hu, G. Carlotti, T. Ono, R. L. Stamps, Phys. Rev. B 76 (2007) 054422.
[262] Z. K. Wang, V. L. Zhang, H. S. Lim, S. C. Ng, M. H. Kuok, S. Jain, A. O. Adeyeye, ACS Nano 4 (2010) 643.
[263] S. Tacchi, G. Duerr, J. W. Klos, M. Madami, S. Neusser, G. Gubbiotti, G. Carlotti, M. Krawczyk, D. Grundler, Phys. Rev. Lett. 109 (2012) 137202.
[264] S. Neusser, D. Grundler, Adv. Mater. 21 (2009) 2927.
[265] M. Krawczyk, S. Mamica, M. Mruczkiewicz, J. W. Klos, S. Tacchi, M. Madami, G. Gubbiotti, G. Duerr, D. Grundler, J. Phys. D: Appl. Phys. 46 (2013) 495003.
[266] S. A. Wolf, D. D. Awschalom, R. A. Buhrman, J. M. Daughton, S. von Molnár, M. L. Roukes, A. Y. Chtchelkanova, D. M. Treger, Science 294 (2001) 1488.
[267] I. Žutić, J. Fabian, S. Das Sarma, Rev. Mod. Phys. 76 (2004) 323.
[268] S. Maekawa, S. O. Valenzuela, E. Saitoh, T. Kimura, *Spin Current* (Oxford University Press, 2017).
[269] J. Shi, P. Zhang, D. Xiao, Q. Niu, Phys. Rev. Lett. 96 (2006) 076604.
[270] Q.-f. Sun, X. C. Xie, Phys. Rev. B 72 (2005) 245305.
[271] Z. An, F. Q. Liu, Y. Lin, C. Liu, Sci. Rep. 2 (2012) 388.
[272] P. Sharma, Science 307 (2005) 531.
[273] J. Sinova, S. O. Valenzuela, J. Wunderlich, C. H. Back, T. Jungwirth, Rev. Mod. Phys. 87 (2015) 1213.
[274] J. E. Hirsch, Phys. Rev. Lett. 83 (1999) 1834.
[275] C. G. Shull, C. T. Chase, F. E. Myers, Phys. Rev. 63 (1943) 29.
[276] M. I. Dyakonov, V. I. Perel, ZhETF Pis. Red. 13 (1971).

[277] T. Kikkawa, K. Uchida, Y. Shiomi, Z. Qiu, D. Hou, D. Tian, H. Nakayama, X. F. Jin, E. Saitoh, Phys. Rev. Lett. 110 (2013) 067207.
[278] Y. M. Lu, Y. Choi, C. M. Ortega, X. M. Cheng, J. W. Cai, S. Y. Huang, L. Sun, C. L. Chien, Phys. Rev. Lett. 110 (2013) 147207.
[279] J. Li, L. R. Shelford, P. Shafer, A. Tan, J. X. Deng, P. S. Keatley, C. Hwang, E. Arenholz, G. van der Laan, R. J. Hicken, Z. Q. Qiu, Phys. Rev. Lett. 117 (2016) 076602.
[280] R. Kukreja, S. Bonetti, Z. Chen, D. Backes, Y. Acremann, J. A. Katine, A. D. Kent, H. A. Dürr, H. Ohldag, J. Stöhr, Phys. Rev. Lett. 115 (2015) 096601.
[281] H. Nakayama, M. Althammer, Y. T. Chen, K. Uchida, Y. Kajiwara, D. Kikuchi, T. Ohtani, S. Geprägs, M. Opel, S. Takahashi, R. Gross, G. E. W. Bauer, S. T. B. Goennenwein, E. Saitoh, Phys. Rev. Lett. 110 (2013) 206601.
[282] D. Qu, S. Y. Huang, J. Hu, R. Wu, C. L. Chien, Phys. Rev. Lett. 110 (2013) 067206.
[283] B. F. Miao, S. Y. Huang, D. Qu, C. L. Chien, Phys. Rev. Lett. 112 (2014) 236601.
[284] B. Heinrich, Y. Tserkovnyak, G. Woltersdorf, A. Brataas, R. Urban, G. E. W. Bauer, Phys. Rev. Lett. 90 (2003) 187601.
[285] S. I. Kiselev, J. C. Sankey, I. N. Krivorotov, N. C. Emley, R. J. Schoelkopf, R. A. Buhrman, D. C. Ralph, Nature 425 (2003) 380.
[286] L. K. Werake, H. Zhao, Nat. Phys. 6 (2010) 875.
[287] T. Seki, Y. Hasegawa, S. Mitani, S. Takahashi, H. Imamura, S. Maekawa, J. Nitta, K. Takanashi, Nat. Mater. 7 (2008) 125.
[288] T. Kimura, Y. Otani, T. Sato, S. Takahashi, S. Maekawa, Phys. Rev. Lett. 98 (2007) 156601.
[289] S. O. Valenzuela, M. Tinkham, Nature 442 (2006) 176.
[290] L. Liu, C.-F. Pai, Y. Li, H. W. Tseng, D. C. Ralph, R. A. Buhrman, Science 336 (2012) 555.
[291] C.-F. Pai, L. Liu, Y. Li, H. W. Tseng, D. C. Ralph, R. A. Buhrman, Appl. Phys. Lett. 101 (2012) 122404.
[292] L. Liu, T. Moriyama, D. C. Ralph, R. A. Buhrman, Phys. Rev. Lett. 106 (2011) 036601.
[293] E. Saitoh, M. Ueda, H. Miyajima, G. Tatara, Appl. Phys. Lett. 88 (2006) 182509.
[294] K. Ando, S. Takahashi, J. Ieda, Y. Kajiwara, H. Nakayama, T. Yoshino, K. Harii, Y. Fujikawa, M. Matsuo, S. Maekawa, E. Saitoh, J. Appl. Phys. 109 (2011) 103913.
[295] O. Mosendz, J. E. Pearson, F. Y. Fradin, G. E. W. Bauer, S. D. Bader, A. Hoffmann, Phys. Rev. Lett. 104 (2010) 046601.
[296] L. Bocklage, Phys. Rev. Lett. 118 (2017) 257202.
[297] K. Uchida, S. Takahashi, K. Harii, J. Ieda, W. Koshibae, K. Ando, S. Maekawa, E. Saitoh, Nature 455 (2008) 778.
[298] S. Y. Huang, W. G. Wang, S. F. Lee, J. Kwo, C. L. Chien, Phys. Rev. Lett. 107 (2011) 216604.
[299] K. Uchida, H. Adachi, T. An, T. Ota, M. Toda, B. Hillebrands, S. Maekawa, E. Saitoh, Nat. Mater. 10 (2011) 737.
[300] M. Matsuo, E. Saitoh, S. Maekawa, J. Phys. Soc. Jpn. 86 (2016) 011011.
[301] M. Matsuo, J. i. Ieda, E. Saitoh, S. Maekawa, Phys. Rev. Lett. 106 (2011) 076601.
[302] M. Matsuo, J. i. Ieda, K. Harii, E. Saitoh, S. Maekawa, Phys. Rev. B 87 (2013) 180402.
[303] E. H. Hall, Am. J. Math. 2 (1879) 287.
[304] T. Ohgaki, N. Ohashi, S. Sugimura, H. Ryoken, I. Sakaguchi, Y. Adachi, H. Haneda, J. Mater. Res. 23 (2011) 2293.

[305] D. J. Griffiths, *Introduction to Electrodynamics* (Prentice Hall, 1999).
[306] P. G. Huray, *Maxwell's Equations* (Wiley, 2010).
[307] R. Karplus, J. M. Luttinger, Phys. Rev. 95 (1954) 1154.
[308] N. A. Sinitsyn, J. Phys. Condens. Matter 20 (2007) 023201.
[309] T. Jungwirth, Q. Niu, A. H. MacDonald, Phys. Rev. Lett. 88 (2002) 207208.
[310] N. Nagaosa, J. Sinova, S. Onoda, A. H. MacDonald, N. P. Ong, Rev. Mod. Phys. 82 (2010) 1539.
[311] Y. Taguchi, Y. Oohara, H. Yoshizawa, N. Nagaosa, Y. Tokura, Science 291 (2001) 2573.
[312] D. Xiao, M.-C. Chang, Q. Niu, Rev. Mod. Phys. 82 (2010) 1959.
[313] Y. Yao, L. Kleinman, A. H. MacDonald, J. Sinova, T. Jungwirth, D.-s. Wang, E. Wang, Q. Niu, Phys. Rev. Lett. 92 (2004) 037204.
[314] R. B. Laughlin, Phys. Rev. Lett. 50 (1983) 1395.
[315] R. Yu, W. Zhang, H.-J. Zhang, S.-C. Zhang, X. Dai, Z. Fang, Science 329 (2010) 61.
[316] C.-Z. Chang *et al.*, Science 340 (2013) 167.
[317] Z. Fang, N. Nagaosa, K. S. Takahashi, A. Asamitsu, R. Mathieu, T. Ogasawara, H. Yamada, M. Kawasaki, Y. Tokura, K. Terakura, Science 302 (2003) 92.
[318] N. F. Mott, H. S. W. Massey., *The theory of atomic collisions* (Oxford : Clarendon Press, 1933).
[319] N. F. Mott, N. H. D. Bohr, Proc. Royal Soc. Lond. A 124 (1929) 425.
[320] J. Smit, Physica 24 (1958) 39.
[321] L. Berger, Physica 30 (1964) 1141.
[322] M. I. Dyakonov, V. I. Perel, Phys. Lett. A 35 (1971) 459.
[323] Y. Bychkov, É. Rashba, Pis'ma Zh. Eksp. Teor. Fiz. 39 (1984).
[324] T. Jungwirth, J. Wunderlich, K. Olejník, Nat. Mater. 11 (2012) 382.
[325] C. L. Kane, E. J. Mele, Phys. Rev. Lett. 95 (2005) 226801.
[326] S. Murakami, N. Nagaosa, S.-C. Zhang, Science 301 (2003) 1348.
[327] J. Sinova, D. Culcer, Q. Niu, N. A. Sinitsyn, T. Jungwirth, A. H. MacDonald, Phys. Rev. Lett. 92 (2004) 126603.
[328] Y. K. Kato, R. C. Myers, A. C. Gossard, D. D. Awschalom, Science 306 (2004) 1910.
[329] J. Wunderlich, B. Kaestner, J. Sinova, T. Jungwirth, Phys. Rev. Lett. 94 (2005) 047204.
[330] N. S. Averkiev, M. I. Dyakonov, Sov. Phys. JETP Lett. 35 (1983).
[331] A. A. Bakun, B. P. Zakharchenya, A. A. Rogachev, M. N. Tkachuk, V. G. Fleĭsher, J. Exp. Theor. Phys. Lett. 40 (1984).
[332] B. F. Miao, S. Y. Huang, D. Qu, C. L. Chien, Phys. Rev. Lett. 111 (2013) 066602.
[333] M. Kimata, H. Chen, K. Kondou, S. Sugimoto, P. K. Muduli, M. Ikhlas, Y. Omori, T. Tomita, A. H. MacDonald, S. Nakatsuji, Y. Otani, Nature 565 (2019) 627.
[334] M. Arana, M. Gamino, E. F. Silva, V. M. T. S. Barthem, D. Givord, A. Azevedo, S. M. Rezende, Phys. Rev. B 98 (2018) 144431.
[335] D. Sun, K. J. van Schooten, M. Kavand, H. Malissa, C. Zhang, M. Groesbeck, C. Boehme, Z. Valy Vardeny, Nat. Mater. 15 (2016) 863.
[336] A. R. Mellnik, J. S. Lee, A. Richardella, J. L. Grab, P. J. Mintun, M. H. Fischer, A. Vaezi, A. Manchon, E. A. Kim, N. Samarth, D. C. Ralph, Nature 511 (2014) 449.
[337] Y. Zhang, Y.-W. Tan, H. L. Stormer, P. Kim, Nature 438 (2005) 201.
[338] Y. Otani, M. Shiraishi, A. Oiwa, E. Saitoh, S. Murakami, Nat. Phys. 13 (2017) 829.
[339] C. Chen, D. Tian, H. Zhou, D. Hou, X. Jin, Phys. Rev. Lett. 122 (2019) 016804.

[340] C. W. Sandweg, Y. Kajiwara, A. V. Chumak, A. A. Serga, V. I. Vasyuchka, M. B. Jungfleisch, E. Saitoh, B. Hillebrands, Phys. Rev. Lett. 106 (2011) 216601.
[341] H. Hayashi, K. Ando, Phys. Rev. Lett. 121 (2018) 237202.
[342] Y. Shiomi, J. Lustikova, S. Watanabe, D. Hirobe, S. Takahashi, E. Saitoh, Nat. Phys. 15 (2019) 22.
[343] M. V. Costache, M. Sladkov, S. M. Watts, C. H. van der Wal, B. J. van Wees, Phys. Rev. Lett. 97 (2006) 216603.
[344] L. Bai, P. Hyde, Y. S. Gui, C. M. Hu, V. Vlaminck, J. E. Pearson, S. D. Bader, A. Hoffmann, Phys. Rev. Lett. 111 (2013) 217602.
[345] M. Weiler, H. Huebl, F. S. Goerg, F. D. Czeschka, R. Gross, S. T. B. Goennenwein, Phys. Rev. Lett. 108 (2012) 176601.
[346] J. Korringa, D. O. Seevers, H. C. Torrey, Phys. Rev. 127 (1962) 1143.
[347] L. Berger, Phys. Rev. B 54 (1996) 9353.
[348] P. W. Brouwer, Phys. Rev. B 58 (1998) R10135.
[349] J. C. Rojas-Sánchez, N. Reyren, P. Laczkowski, W. Savero, J. P. Attané, C. Deranlot, M. Jamet, J. M. George, L. Vila, H. Jaffrès, Physical Review Letters 112 (2014) 106602.
[350] Y. Kajiwara, K. Harii, S. Takahashi, J. Ohe, K. Uchida, M. Mizuguchi, H. Umezawa, H. Kawai, K. Ando, K. Takanashi, S. Maekawa, E. Saitoh, Nature 464 (2010) 262.
[351] C. Hahn, G. de Loubens, O. Klein, M. Viret, V. V. Naletov, J. Ben Youssef, Phys. Rev. B 87 (2013) 174417.
[352] M. Caminale, A. Ghosh, S. Auffret, U. Ebels, K. Ollefs, F. Wilhelm, A. Rogalev, W. E. Bailey, Phys. Rev. B 94 (2016) 014414.
[353] R. Meservey, P. M. Tedrow, Phys. Rev. Lett. 41 (1978) 805.
[354] A. Brataas, Y. Tserkovnyak, G. E. W. Bauer, B. I. Halperin, Phys. Rev. B 66 (2002) 060404.
[355] W. Zhang, W. Han, X. Jiang, S.-H. Yang, S. S. P. Parkin, Nat. Phys. 11 (2015) 496.
[356] H. Jiao, G. E. W. Bauer, Phys. Rev. Lett. 110 (2013) 217602.
[357] H. Nakayama, K. Ando, K. Harii, T. Yoshino, R. Takahashi, Y. Kajiwara, K. Uchida, Y. Fujikawa, E. Saitoh, Phys. Rev. B 85 (2012) 144408.
[358] W. Zhang, M. B. Jungfleisch, W. Jiang, J. Sklenar, F. Y. Fradin, J. E. Pearson, J. B. Ketterson, A. Hoffmann, J. Appl. Phys. 117 (2015) 172610.
[359] S. Mizukami, Y. Ando, T. Miyazaki, J. Magn. Magn. Mater. 226-230 (2001) 1640.
[360] P. N. Argyres, Phys. Rev. 97 (1955) 334.
[361] M. Faraday, T. Martin, R. I. o. G. Britain, *Faraday's diary* (Bell, 1932).
[362] M. Faraday, T. Martin, R. I. o. G. Britain, *Faraday's Diary: Nov. 24, 1855-Mar. 12, 1862* (G. Bell and sons, ltd., 1936).
[363] M. Faraday, F. A. J. L. James, *The Correspondence of Michael Faraday: 1841-1848* (Institution of Engineering and Technology, 1991).
[364] J. Kerr, Philos. Mag. Series 5 3 (1877) 321.
[365] A. Kundt, Philos. Mag. 18 (1884) 308.
[366] H. S. Bennett, E. A. Stern, Phys. Rev. 137 (1965) A448.
[367] Z. Q. Qiu, S. D. Bader, Rev. Sci. Instrum. 71 (2000) 1243.
[368] R. P. Hunt, J. Appl. Phys. 38 (1967) 1652.
[369] C.-Y. You, S.-C. Shin, J. Appl. Phys. 84 (1998) 541.
[370] M. Freiser, IEEE Trans. Magn. 4 (1968) 152.
[371] Z. Q. Qiu, S. D. Bader, J. Magn. Magn. Mater. 200 (1999) 664.
[372] T. W. McDaniel, R. Victora, *Handbook of Magento-Optical Data Recording: Materials, Subsystems, Techniques* (Elsevier Science, 1995).

[373] P. Bruno, Y. Suzuki, C. Chappert, Phys. Rev. B 53 (1996) 9214.
[374] R. Kubo, Can. J. Phys. 34 (1956) 1274.
[375] A. Barman, A. Haldar, in *Solid State Physics*, edited by R. E. Camley, and R. L. Stamps (Academic Press, 2014), p. 1.
[376] C. Kittel, Phys. Rev. 70 (1946) 281.
[377] C. Kittel, Phys. Rev. 71 (1947) 270.
[378] C. E. Patton, J. Appl. Phys. 39 (1968) 3060.
[379] I. Bady, IEEE Trans. Magn. 3 (1967) 521.
[380] J. J. Green, T. Kohane, Semicond. Prod. Solid State Technol. 7 (1964).
[381] F. J. Cadieu, R. Rani, W. Mendoza, B. Peng, S. A. Shaheen, M. J. Hurben, C. E. Patton, J. Appl. Phys. 81 (1997) 4801.
[382] P. Wolf, J. Appl. Phys. 32 (1961) S95.
[383] T. J. Silva, C. S. Lee, T. M. Crawford, C. T. Rogers, J. Appl. Phys. 85 (1999) 7849.
[384] A. B. Kos, T. J. Silva, P. Kabos, Rev. Sci. Instrum. 73 (2002) 3563.
[385] W. Barry, IEEE Trans. Microw. Theory Tech. 34 (1986) 80.
[386] J. Ding, M. Kostylev, A. O. Adeyeye, Appl. Phys. Lett. 100 (2012) 062401.
[387] J. Sklenar, V. S. Bhat, L. E. DeLong, J. B. Ketterson, J. Appl. Phys. 113 (2013) 17B530.
[388] R. A. Witte, *Spectrum and Network Measurements* (Institution of Engineering and Technology, 2014).
[389] B. Neumeyer, in *1986 16th European Microwave Conference*1986), pp. 779.
[390] C. J. Clark, A. A. Moulthrop, M. S. Muha, C. P. Silva, IEEE Trans. Microw. Theory Tech. 44 (1996) 2724.
[391] K. Hoffmann, Z. Skvor, IEEE Trans. Microw. Theory Tech. 46 (1998) 2520.
[392] D. K. Gifford, B. J. Soller, M. S. Wolfe, M. E. Froggatt, Appl. Opt. 44 (2005) 7282.
[393] J. Verspecht, IEEE Microw. Mag. 6 (2005) 82.
[394] M. E. Yaagoubi, G. Neveux, D. Barataud, T. Reveyrand, J. Nebus, F. Verbeyst, F. Gizard, J. Puech, IEEE Trans. Microw. Theory Tech. 56 (2008) 1180.
[395] G. Kompa, F. v. Raay, IEEE Trans. Microw. Theory Tech. 38 (1990) 358.
[396] W. V. Moer, Y. Rolain, IEEE Microw. Mag. 7 (2006) 46.
[397] V. David, Microw. J. 53 (2010).
[398] V. Teppati, A. Ferrero, M. Sayed, *Modern RF and Microwave Measurement Techniques* (Cambridge University Press, 2013).
[399] R. S. Kwok, L. Ji-Fuh, IEEE Trans. Microw. Theory Tech. 47 (1999) 111.
[400] W. B. Kuhn, A. P. Boutz, IEEE Trans. Microw. Theory Tech. 58 (2010) 1046.
[401] A. A. Savin, in *2013 European Microwave Conference*2013), pp. 60.
[402] P. J. Petersan, S. M. Anlage, J. Appl. Phys. 84 (1998) 3392.
[403] X. Zhu, Z. Liu, V. Metlushko, P. Grütter, M. R. Freeman, Phys. Rev. B 71 (2005) 180408.
[404] A. A. Awad, G. R. Aranda, D. Dieleman, K. Y. Guslienko, G. N. Kakazei, B. A. Ivanov, F. G. Aliev, Appl. Phys. Lett. 97 (2010) 132501.
[405] A. Vogel, A. Drews, T. Kamionka, M. Bolte, G. Meier, Phys. Rev. Lett. 105 (2010) 037201.
[406] R. Y. Yu, J. Pusl, Y. Konishi, M. Case, M. Kamegawa, M. Rodwell, IEEE Microw. Wirel. Compon. Lett. 2 (1992) 319.
[407] M. Beruete, M. Sorolla, I. Campillo, J. S. Dolado, L. Martín-Moreno, J. Bravo-Abad, F. J. García-Vidal, Opt. Lett. 29 (2004) 2500.
[408] R. A. Dudley, N. M. Ridler, IEEE Trans. Instrum. Meas. 52 (2003) 130.

[409] D. Barataud, C. Arnaud, B. Thibaud, M. Campovecchio, J. Nebus, J. P. Villotte, IEEE Trans. Instrum. Meas. 47 (1998) 1259.
[410] R. L. Olmon, M. Rang, P. M. Krenz, B. A. Lail, L. V. Saraf, G. D. Boreman, M. B. Raschke, Phys. Rev. Lett. 105 (2010) 167403.
[411] M. Rafie, *Network Scattering Parameters* (World Scientific Publishing Company, 1996).
[412] D. E. Bockelman, W. R. Eisenstadt, IEEE Trans. Microw. Theory Tech. 43 (1995) 1530.
[413] C. Caloz, T. Itoh, *Electromagnetic Metamaterials: Transmission Line Theory and Microwave Applications* (Wiley, 2005).
[414] R. Redheffer, J. Math. Phys. 41 (1962) 1.
[415] W. J. R. Hoefer, IEEE Trans. Microw. Theory Tech. 33 (1985) 882.
[416] R. W. Klopfenstein, Proc. IEEE 44 (1956) 31.
[417] R. B. Marks, D. F. Williams, IEEE Microw. Wirel. Compon. Lett. 1 (1991) 141.
[418] R. N. Simons, *Coplanar Waveguide Circuits, Components, and Systems* (Wiley, 2004).
[419] C. P. Wen, IEEE Trans. Microw. Theory Tech. 17 (1969) 1087.
[420] M. Riaziat, R. Majidi-Ahy, I. Feng, IEEE Trans. Microw. Theory Tech. 38 (1990) 245.
[421] W. R. Eisenstadt, Y. Eo, IEEE Trans. Adv. Packag. 15 (1992) 483.
[422] C. V. Raman, Nature 121 (1928) 619.
[423] L. Brillouin, Ann. Phys. 9 (1922) 88.
[424] L. I. Mandelstam, Zh. Russ. Fiz-Khim. Ova. 58 (1926) 381.
[425] E. Gross, Nature 126 (1930) 201.
[426] G. Gubbiotti, S. Tacchi, M. Madami, G. Carlotti, A. O. Adeyeye, M. Kostylev, J. Phys. D: Appl. Phys. 43 (2010) 264003.
[427] B. Heinrich, J. A. C. Bland, *Ultrathin Magnetic Structures II: Measurement Techniques and Novel Magnetic Properties* (Springer Berlin Heidelberg, 2006).
[428] S. O. Demokritov, V. E. Demidov, IEEE Trans. Magn. 44 (2008) 6.

Chapter 3

3. Fabrication and Characterization Techniques

Here, a brief discussion of the fabrication [1] and characterization tools which have been employed to investigate the properties of the magnetic heterostructures and nanopatterns in the course of the thesis work will be furnished. Nanofabrication [2,3] being the core of nanoscience and nanotechnology [4,5] demands continuous improvement and upgradation in order to procure high quality thin films and confined structures with minimum and undesirable structural defects or without any repugnant elemental composition. Eventually, the intrinsic features of a magnetic material at nanoscale stoutly rely upon the crystalline and chemical ordering as well as the quality of the surface of the patterned structure. Consequently, an elaborate characterization is imperative to catechize and optimize the magnetic parameters of the nanostructures. Numerous techniques have been developed to fabricate nanocomposites with such superior qualities. Howbeit, the increasing demand of preparing nanoscale patterns with fine and desirable abilities with a cost-effective fabrication method has always been a challenging hurdle. As per requirement, a chromatic range of lithography and deposition systems have been delved into preparing the heterostructures which demand a thorough investigation of their physical aspects prior to be utilized for any industrial application. Over the course of advancement in the fabrication procedures, lithography techniques remain an essential accessory for developing superfine patterned structures despite of being complex chemical procedures which is time consuming as well as expensive. For the research works presented in this dissertation, the magnetic heterostructures in the form of thin films have been grown by electron beam evaporation (EBE) and magnetron sputtering techniques whereas the patterning of such films has been carried out by optical (photo) or ultraviolet (UV) lithography[1], electron beam lithography (EBL) [6,7] while ion milling method [8] has been also deployed. The characterization to determine the crystal structure, surface imaging and morphology and the chemical compositions of these heterostructures and structured magnetic materials has been performed by X-ray diffraction (XRD) [9,10], scanning electron microscopy (SEM) [11,12], surface profiler [13], atomic force microscopy

(AFM) [14] and energy dispersive X-ray spectroscopy (EDXS) [15]. The static and quasi-static magnetic characterizations have been probed by magnetic force microscopy (MFM) [16-19], magneto-optical Kerr effect (MOKE) [20-22], vibrating sample magnetometry (VSM) [23,24]. In addition, a scriber is also employed in order to cut the substrate into precise sized chips which have been used as the base to fabricate the magnetic materials. In the following, we briefly discuss the working principles and advantages of the aforementioned tools.

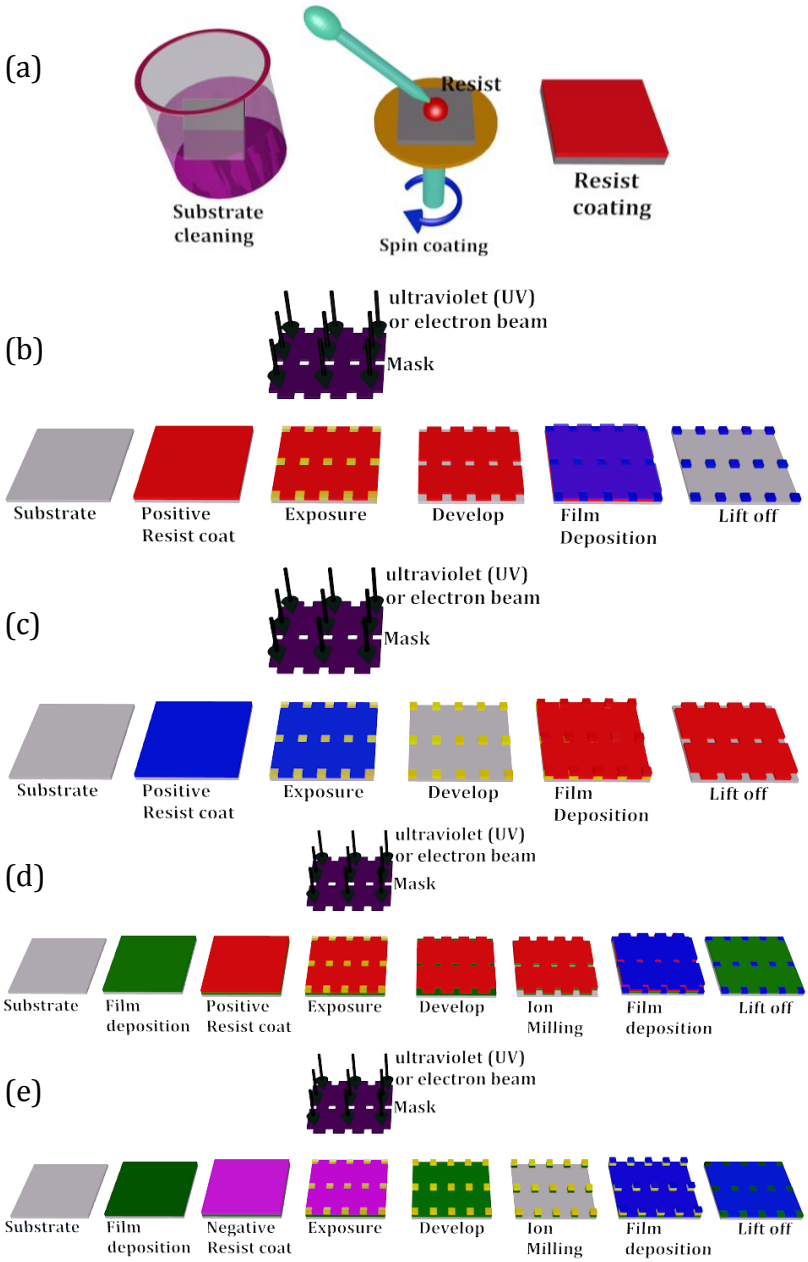

Figure 3.1. Schematic illustration of photo- (UV-) and electron beam lithography processes describing (a) resist coating of a substrate, (b) bottom-up and (c) top-down

approaches. Combination of top-down and bottom-up approaches using (d) positive and (e) negative resists.

3.1. Lithography Techniques

Lithography [25] is an essential procedure in patterning precise and fine-scale structures on a substrate. Here, different kinds [26] of radiation such as optical [27], electron beam [28], X-ray [29] and ion beam [30] are exposed to a chemically active medium known as resist [27] where the pattern of ordered arrays of nanostructures is efficiently and precisely drawn. Afterwards, the desired material is deposited which follows the footprint of the patterned resist to render the final structure.

3.1.1. Top-down and Bottom-up Approaches

In current lithography technology, two completely opposite paths are pursued depending upon the requirements. First is top-down strategy of miniaturization while, the second one is bottom-up (or self-assembly) approach of fabricating complex systems [31-34] (see Figure 3.1). Top-down fabrication [35] is a subtractive process in which material is removed to produce patterns with controlled physical features (i.e. shape and size). This is different than the bottom-up fabrication approach [36] which is an additive process where atoms and molecules are used to build up the desired patterns. Top-down strategy is better for creating long-range ordered patterns and making macroscopic connections. On the other hand, bottom-up technique is suitable for producing structures with short range order especially at nanoscale and making assemblies. Hence, the best combination of tools for nanofabrication can be achieved by integrating top-down and bottom-up techniques. The most common top-down approach to fabrication involves lithographic patterning techniques using optical sources with short wavelength. In top-down approach, the main advantage is that the structures are both patterned and built in the same area and hence no assembly step is required. However, even though top-down methods work fine at the microscale, it becomes increasingly difficult to apply them at nanoscale regime when heat dissipation can become a serious issue. A second disadvantage is that they involve planar techniques, which means that structures are created by the addition and subtraction of patterned layers (deposition and etching) and as a result, arbitrary 3D objects are difficult to construct. On the contrary, bottom-up approaches to nanofabrication use chemical or physical forces operating at the nanoscale to assemble basic units into

larger structures. As component size decreases in nanofabrication, bottom-up approaches provide an increasingly important complement to top-down techniques. In this dissertation, the fabrication of nanostructures has been carried out using a combination of both top-down and bottom-up approaches.

3.1.2. Optical (Photo-) Lithography

Photolithography is broadly used to produce microstructures with micron and submicron range feature sizes. It relies on photosensitive resists, which are coated on substrates, e.g. silicon wafers. Generally, an intensity pattern is projected on the resist to create the microstructure to be fabricated. Subsequently, in the development step depending on the specific type of resist employed, either the illuminated or the nonilluminated part of the resist is removed. Optical lithography is composed of four fundamental elements such as:

1. Illumination system with energy source
2. A photo mask containing the desired pattern
3. exposure system to generate a virtual image of the mask pattern
4. a medium known as photoresist (in case of photolithography) for recording the image generated by the exposure system.

Here, a parallel growth of all the nanostructure using photo-mask is possible which reduces the fabrication time significantly. Howbeit, optical lithography has a drawback that it is difficult to fabricate sub-micrometer ($< 1\ \mu m$) patterns using this method due to the resolution limitation by the diffraction of light.

3.1.2.1. Substrate Cleaning

At first a silicon (Si) wafer is taken on which the sample will be grown. Then, the wafer is sliced into desirable sizes of piece using a scriber which has either a diamond or carbide tip as the slicing tool. It has to undergo a proper cleaning procedure by ultrasonicating it in acetone (propanone) for some time which is then washed by iso-propyl alcohol (IPA: 2-propanol). This will help to remove inorganic and organic impurity materials from the top of the substrate. The substrate is dried by a dry nitrogen flow.

3.1.2.2. Resist Coating

In bottom-up approach, a uniform layer of photo resist dissolved in an organic solvent is coated on the substrate. In our case, a thin layer of primer HMDS [37] (1,1,1,3,3,3-

Hexamethyldisilazane: [dimethyl-(trimethylsilylamino)silyl]methane: $C_6H_{10}NSi_2$) or Omnicoat [38] (contains cyclopentanone and propylene glycol monomethyl ether) is coated using a spin coater system [39,40] which is an efficient mechanical tool that can rotate a substrate under a pre-set revolution per minute (rpm) for a particular amount time depending upon the required thickness of the primer. First the substrate is fixed on top of the spindle of a spin coater using a vacuum pump. A few drops of primer solution are put on the substrate which can be rotated at different rotational speed for a certain time as per requirement. The centrifugal force makes the liquid uniformly distributed on the substrate although there can be some non-uniformity at the edges. The substrate is then baked in an oven at a pre-set temperature for a fixed time. Thereafter, either a positive photoresist (AZ-1500 [41]: composed of Novolac, a cresol resin that is synthesized from phenol and formaldehyde where the photo active compound of this photoresist belongs to the group of diazonaphtho-quinones (DNQ) and the solvent is PGMEA (propylene-glycol-mono-methylether-acetate) with different concentration depending on the formulation) or a negative photoresist SU8 [42,43] (composed of Novolac epoxy that is dissolved in an organic solvent (gamma-butyrolactone: GBL or cyclopentanone, depending on the formulation and up to 10 wt% of mixed Triarylsulfonium/hexafluoroantimonate salt as the photoacid generator) is coated on top of the primer coated substrate in a similar way and baked at fixed temperature and time. Baking essentially removes solvent from the photoresist and increase the adhesion. With the recipe described one can achieve a coating of resist having few μm (~ 0.5 – 2 μm) thickness as the thicknesses of both primer and resist layers depend heavily on their densities and viscosities and also upon speed and time of rotation. In this context it is worth mentioning that photoresist can be of two types either positive or negative. For positive photoresist (AZ-1500) chemical changes occur at UV light exposure. Hence, the exposed part becomes more soluble in the developer solution. Conversely in case of negative photoresist (SU8) the exposed part becomes more polymerized and less soluble.

3.1.2.3. UV light Exposure and Developing

The resist coated substrate is exposed to UV light with typical energy (70-90 mJ/mm^2) through a mask containing the pattern. In this step the desired structure is drawn using commercially available design software (Auto CAD: computer aided design [44]) or a

photo mask (chrome on glass) containing the desired patterns to be fabricated was placed on top of the substrate while a convex lens was used in between the source and the mask for uniform illumination of the source on the mask. Thereby, the resist reacts at the exposed part which becomes soluble/insoluble in the developer depending upon positive/negative resist. Then the substrate is dipped into a developer solution (AZ/SU8 developer for AZ-1500/SU8 resist) for few seconds (~ 40 – 80 s) followed by a rinsing in de-ionized water (AZ-1500) or IPA (SU8) for about few minutes (~ 1 – 2 min). Then it is dried by dry nitrogen (N_2) flow. The process makes the resist pattern visible at the exposed/unexposed part depending upon positive/negative resist.

3.1.2.4. Lift-off and Etch-back Processes

Single or multilayer thin films are deposited on the whole substrate followed by a treatment with acetone (for AZ-1500) or remover PG [45,46] (for SU8 resist: remover PG is comprised of N-methyl-2-pyrrolidinone and surfactant) for few minutes (~ 1 – 5 min) to remove the residual resist and then they are finally cleaned with IPA for few minutes (~ 5 – 10 min) and finally blown by dry N_2 gas. Ergo, we achieve a fine patterned microscale single or multilayer thin film heterostructures. Sometimes thin films are deposited on the substrate first on top of which resist is patterned using photolithography method as mentioned above and this procedure is called top-down approach. In this case, the films are etched back in the weaker part of the resist using reactive ions in the physical/chemical ion milling instrument and the harder part remains unaffected. Finally, the residual resists are removed and we get the desired fine structure on the thin film.

In this thesis, all the thin film heterostructures and coplanar waveguides (CPWs) are fabricated using the maskless UV photolithography system which is described briefly in the following.

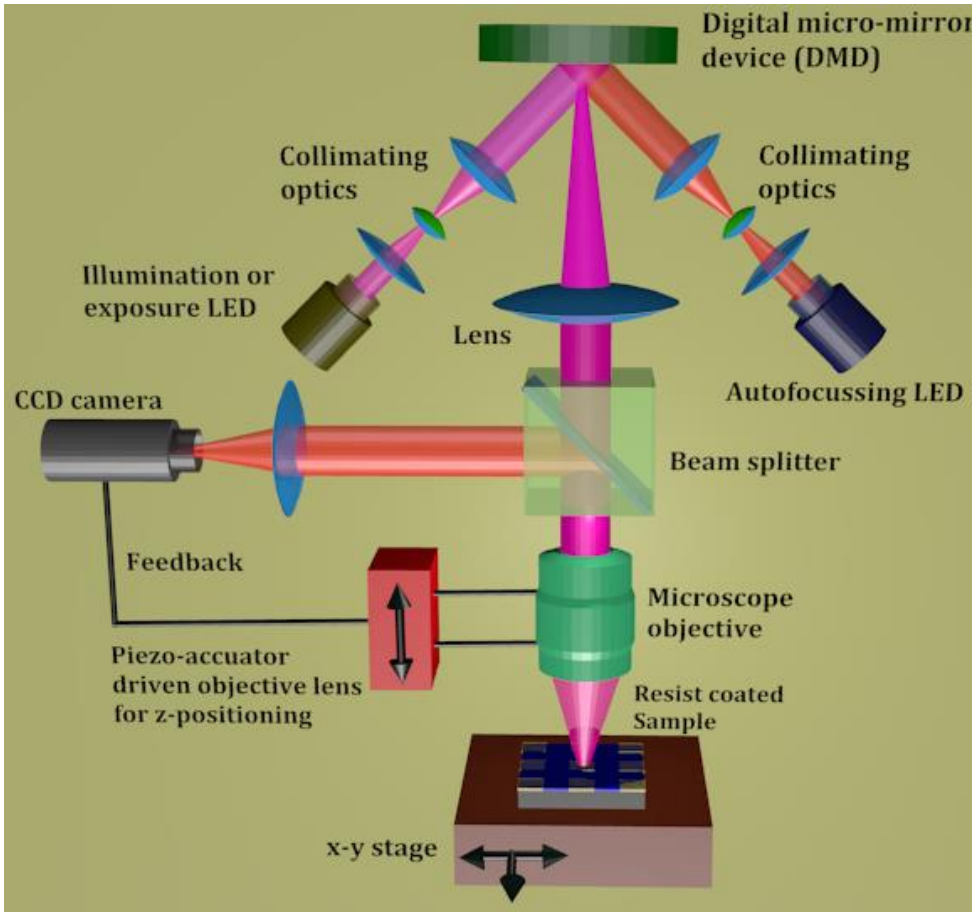

Figure 3.2. Schematic of maskless optical lithography system.

3.1.3. Maskless Optical Photolithography

In conventional photolithography, microstructures are transferred from a physical lithography mask (made of chrome (oxide: opaque) and glass (or quartz: transparent)) into a photosensitive resist. Recently, maskless lithography [47-50] set-ups have become very popular in order to avoid cost- and time-consuming mask generation. On the other hand, current advances in microelectronic mechanical systems (MEMS) has unlocked new pathways for light manipulation. This leads to new lithographic tools which depends on spatial light modulators (SLMs) such as digital micromirror devices (DMDs) [51] or liquid crystal (LC) light modulators for transferring microstructures to the photoresist. Since DMD is employed to project the intensity pattern, this also can be employed to create a test illumination pattern required during contrast measurements and schematic illustration of a maskless lithography is represented in Figure 3.2. Here, SLM-based techniques in contrary to mask-based proximity lithography tools, require projection systems particularly when the structures lying in the submicron range need

to be transferred. Hence, these small feature sizes demand on optical lithography tools which employ projection lenses having large numerical aperture (NA) resulting in having a depth of field (DOF: distance between the nearest and the furthest objects that are in acceptably sharp focus) ~ few hundreds of nm. Although, precise projection of the SLM onto the wafer coated with resist strongly controls the quality of the fabricated microstructures. Manual focusing most often does not meet the demands in terms of accuracy when utilizing high NA projection systems. On the other hand, the time required for focusing leads to high production costs which is rectified by using the autofocusing systems to create submicron structures. Usually, autofocus systems can be classified in active and passive systems.

3.1.3.1. Active Autofocus System

Here, focusing is achieved by measuring the distance between the substrate surface and the lens and controlling that distance accordingly. In general, ultrasonic or infrared light-based triangulation sensors are employed for distance measurement. However, because of insufficient measurement accuracy, the applicability of ultrasonic sensors in lithography is limited. Also, such system becomes difficult to use because of the temperature dependence of sound propagation implying a continuous requirement of temperature control. In addition, it is challenging to trail the focus when the photoresist becomes transparent during the illumination process.

3.1.3.2. Passive Autofocus System

It depends on either contrast measurement or phase comparison (or a combination of both). However, the main disadvantage of active method and passive phase comparison approach is that they are expensive due to the need for additional sensors as well as more complex optical systems. On the other hand, the projection lens is gradually moved along its optical axis while an image is taken at each position step for contrast evaluation. In this technique, the image exhibiting the highest contrast is assumed to correlate with the optimal focal position of the imaging system. From the recorded images, the contrast (or focus) value is calculated. The position of the projection lens required for an optimal focusing is indicated by the highest contrast value. The primary advantages of contrast measurement techniques are the robustness and the cost-effectiveness because of the absence of additional measurement technology. However, realization of an optimal algorithm adapted to the scope of a specific application is the

main challenge for developing a passive autofocus system using contrast measurement. Also, a homogeneous illumination and a sufficient object contrast are required for focusing in addition to the contrast evaluation algorithm.

In this thesis, the maskless photolithography systems D-light-DL1000RS and DL1000SG/RWC from NanoSystem Solutions, Inc. with some salient features which are as follows:

1. It uses long life light sources (such as LED and/or semiconductor laser)
2. This system employs DMD and a telecentric optics illumination system to perform immediate exposure of desired pattern onto the photo resist where the pattern is designed on a PC screen using a designing software (e.g. AutoCAD) without using a physical mask. This allows easy and accurate overlay of alignment markers on the sample as compared to an individual optical path observation system.
3. It possesses a high-speed patterning speed using the laser light source and DMD system as high-resolution pattern generator with ultrafast mirror switching speed.
4. The patterning can be performed on a wide range of substrate size ranging few mm to few tens of cm with a resolution ~ 1μm.
5. It is comprised of a smart real-time auto focus which is capable of patterning even on thin transparent substrate or warped substrate.
6. It is possible to simultaneously observe the surface pattern as well as exposure pattern by utilizing coaxial observation system.
7. Grayscale image can be exposed for 3D structuring here.
8. The system is equipped CCD camera which enables to observe the substrate coaxially to the optical path of exposure which ensures easy and accurate alignment.

This maskless lithography system has been heavily utilized to pattern the microscale magnetic heterostructures as well as the electrodes (electrical measurements) and the CPWs (required for FMR measurements).

3.1.4. Electron Beam Lithography (EBL)

This unique technique is widely used for the precise and controlled fabrication of 2D arrays with submicron (< 1 μm) features. Here, an electron beam is employed to expose an electron-sensitive resist to write patterns on the substrate or on the thin film heterostructures. The resolution of EBL is much higher than that for optical lithography due to the thinner resist thickness (~ few tens to hundreds of nm: depends upon the

resist and the rpm and time of rotation in the spin coater) and shorter wavelength (~ 0.01 nm) of the high energy (~ keV) electron beam used in this method. This makes the formation of nanoscale patterns on the EBL resist possible, where the resist is sensitive to e-beam similar to that used during optical lithography. The basic principle of EBL is very similar with that of optical lithography. Here, firstly the pre-cleaned substrate is coated with a single layer or bilayer of EBL resist(s). First a bottom layer of positive resist 950K PMMA A4 [52-54] (950K: denotes the molecular weight of the resist; PMMA: polymethyl methacrylate; A4: 4% resist in Anisole solution) is spun onto the substrate at a certain rpm (~ 4000 - 6000) for a fixed time (~ 30 – 50 s) and baked at particular temperature (~ 170 – 180 °C) for certain time (~ 80 – 90 s) as per the requirement of the resist thickness. Then, the second layer of copolymer resist MMA EL9 [55] (MMA: methyl methacrylate; EL9: 9% copolymer resist in Ethyl Lactate solution) is rotated at fixed rate (~ 1500 – 2000 rpm) for a certain time (~ 80 – 90 s) followed by baking process at fixed temperature (170 - 180 °C) for a particular time (~ 80 – 90 s). The reason behind using a bilayer resist onto the substrate is to get an undercut edge profile [56] of the resist after development of the pattern onto it. This is because the PMMA layer is developed faster than the MMA layer forming an overhung structure. Sometimes, bilayer resists consisting of 495K PMMA and 950K PMMA or only a single layer resist 950K PMMA can also be used using similar procedure. However, in case of single layer negative resist ma-N 2405 [57] (solution of 1-Methyl-2pyrrolidone, n-Butyl acetate & cyclohexanone), EBL can also be employed to prepare the resist pattern on top of a thin film (in case of fabrication of BMCs presented in this thesis). In this dissertation, the electron beam writing process is carried out in an efficient EBL system (Elionix Inc.: ELS-7700H) consisting of a scanning electron microscope (SEM) which is capable of exposing the resist with focused electrons. Auto CAD system is employed to create the pattern according to which the writing process of the EBL system is controlled. The system subsequently scans the drawing regions or patterns with the accelerated electron beam with pre-defined parameters such as electron beam current (~ hundreds of pA), dose (energy per unit area), energy (keV), resolution (scan points per dose). After electron beam writing, the resist is then developed in MIBK [58,59] (Methyl isobutyl ketone) diluted in IPA (MIBK:IPA = 1:3) solvent for a fixed time (~ 30 - 40 s). In case of ma-N 2405 resist, ma-D developer [60,61] (contains either

Tetramethylammonium hydroxide: TMAH or Sodium Hydroxide: NaOH) has been used. The substrate is finally rinsed in IPA to remove the remaining developer for some time (~ 50 – 60 s). The high resolution of the EBL technique with its mask-less feature gives better degree of freedom to control the fabrication. However, the main disadvantage of this technique is the long writing or processing time as compared to the time of exposure in other lithographic techniques.

In this thesis, Elionix, ELS-7700H EBL system has been expansively applied to prepare array of ADLs and BMCs and also patterned nanoscale electrodes.

3.1.5. Ion Milling

This belongs to the class of physical etching techniques [62,63] where the ions of an inert gas (typically Ar) in vacuum are accelerated from a wide beam ion source (can be either DC or RF) onto a substrate surface (substrate can be resist-coated) in order to remove a specific material to some desired depth or underlayer. Figure 3.3 illustrates the schematic of such milling system in which vacuum levels are typically maintained ~ 10^{-4} – 10^{-5} Torr range where the mean free path (i.e. the average distance an atom, ion or molecule can travel before it collides with another particle to perturb its direction) is longer than the distance between ion source and the substrate. This pressure range is also very crucial for the operation of typical wide beam ion sources as it is difficult to sustain plasma below this range. The continuous bombardment of ions on the substrate causes the conversion of kinetic to heat energy resulting in substrate heating and hence, substrate cooling is often necessary to prevent damage. On the other hand, a fraction of kinetic energy from the incident ions drive away the atoms or atom clusters or molecules or secondary ions from top layer of the surface. Interestingly, it is possible to accelerate the etch rate by heating the substrate as it enhances energy to the surface particles allowing them to be ejected with less kinetic energy. However, this can be undesirable as it is a runaway condition with increased current flow and power dissipation to further uncontrolled increase of the temperature due to the strong exothermic nature. Generally, the sample is tilted to keep the incident beam angle between 30° to 60° (preferably 45°) which significantly increases the etch rate as compared that for normal incidence. Also, this tilting helps in selective detection of the material being etched as well as to calculate its etching rate with the aid of end point detection technique which is described briefly below:

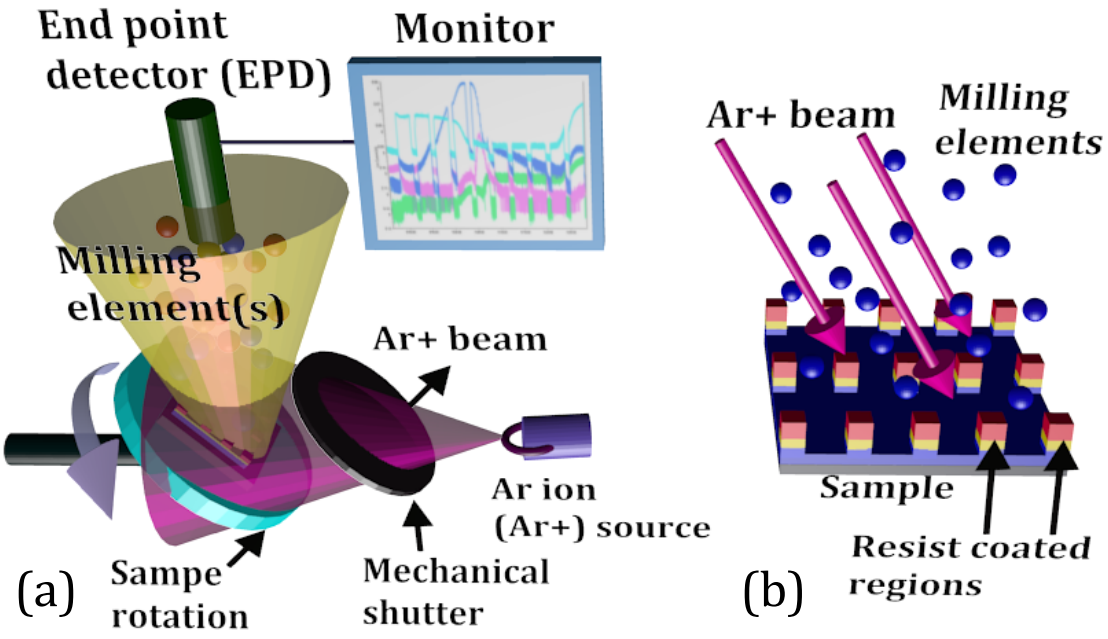

Figure 3.3. (a) Schematic of the ion milling system with end point detection (EPD) tool. (b) The diagram for the milling procedure.

3.1.6. End Point Detection

This is also known as secondary ion mass spectroscopy (SIMS) [64,65]. During the etching procedure, the arrival at a specific underlayer can be determined from the in-situ analysis of the secondary ions coming from the material layers on the substrate surface. Here, a detector is placed near the substrate surface (generally the sample is placed at 45° to both ion source and the detector which are situated orthogonal to each other) to collect the etched charged particles from the surface and to determine their relative intensities. When the ion milling begins, secondary ions are detected by the SIMS detector as having a significant intensity. As soon as the top layer gets almost removed, the intensity of the top layer element starts to diminish and the presence of the bottom layer material starts getting detected which starts to increase substantially. Eventually, the intensity of the top layer element becomes minimal while that for the bottom layer gets significant.

During the lithography of the patterned structure shown in this thesis, Ar ion milling system equipped with the end point detector (Model: EPD 700, PFEIFFER Vacuum) has been utilized.

3.2. Thin film Deposition Technique

Lithography techniques help to fabricate arrays of nanoscale elements on the resist/thin film, while in this section the deposition techniques [66] that have been employed to grow thin film heterostructures on top of a substrate or resist patterns used during works described in this dissertation will be discussed. Here, sputtering [67,68] and electron beam evaporation (EBE) [69] systems have been used for this purpose which will be briefly reviewed in the following.

3.2.1. Sputtering

This method [70] belongs to an idiomatic genre of physical vapor deposition (PVD) [71] techniques which is used for controlled deposition of thin films and multilayers with very high quality in terms of chemical composition as well as surface morphology [72]. Its theory is based upon multiple collision process where the positive ions of a gaseous plasma (e.g. inert gases like Argon: Ar, Krypton: Kr, or reactive gases like Nitrogen: N_2, Oxygen: O_2 depending upon the requirement) are accelerated which then dislodge and eject atoms from the source (target) material. These eroded atoms (or cluster of atoms) then condense over the substrate to form a thin film of desired parameters.

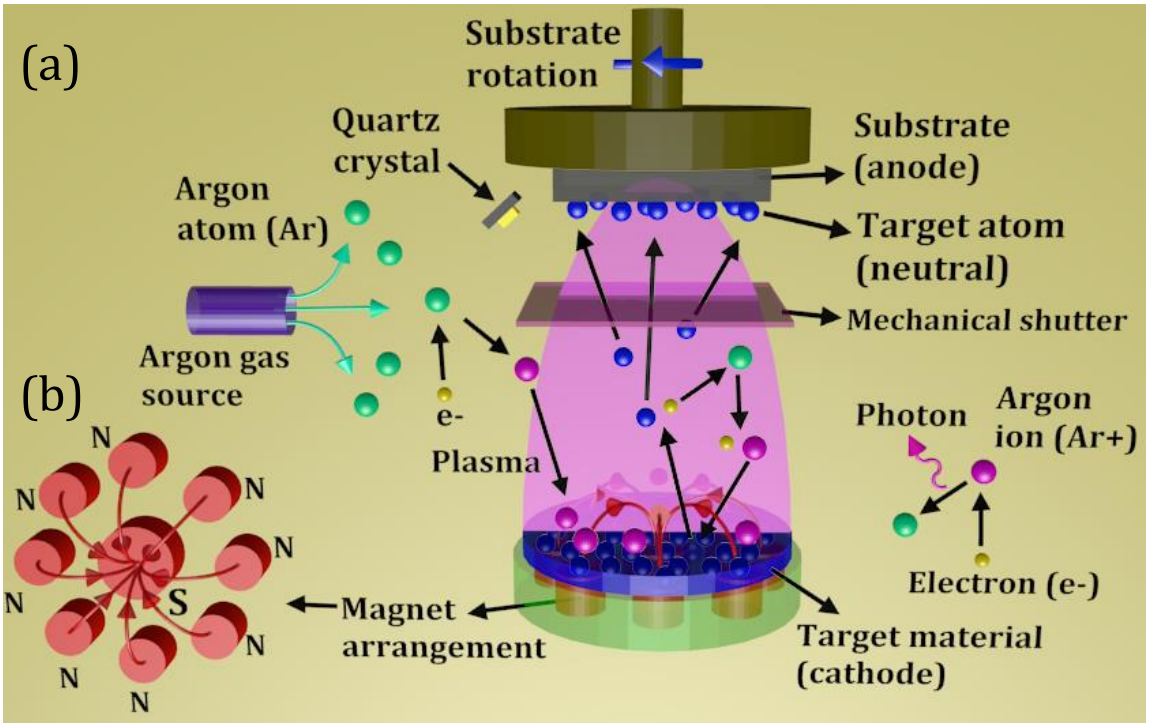

Figure 3.4. (a) Schematic illustration of magnetron sputtering tool. (b) The profile of the magnetic lines of forces has been depicted.

At the beginning, an inert gas (generally Ar [73,74]) is introduced into a pre-pumped vacuum chamber as illustrated in Figure 3.4(a). In the next step, a gaseous plasma is created and sustained inside the chamber using a high energy source (ranging from a few hundred to a few thousand electron volts). Here, the cathode or target is composed of the material or alloy to be deposited and the substrate serves as the anode. Depending on whether the target material is conductive (e.g. metals such as Ni, Co, Au, W, Ta, Cu, NiFe, CoFe, CoFeB etc.) or non-conductive (oxides or insulators, such as Al_2O_3, SiO_2 etc.), a direct current (DC) or radio frequency (RF) power supply can be used although RF source is capable of igniting plasma for both conducting and non-conducting targets [75,76]. The plasma is described as the fourth state of matter where neutral gas atoms, ions, electrons and photons exist simultaneously in a nearly balanced state. As soon as the power supply is on, the free electrons present in the plasma immediately accelerate away from the negatively charged cathode. The accelerated electrons then collide with the neutral gas atoms in their path, driving them off their electrons, therefore leaving the positively charged ions (i.e. Ar^+). At this point the positively charged ions are accelerated into the target to strike its surface and eject neutral atoms and electrons (which further feed the formation of ions and the continuation of the plasma) out of it. These ejected atoms then travel in a typical line-of-sight cosine path and gets subsequently deposited on the substrate which is kept in proximity with the target [77]. The substrate is rotated at a suitable speed for uniform deposition of the films.

This conventional sputtering technique experiences two major challenges which are slow deposition rate and overheating of the target (due to extensive electron bombardment). One possibility to address these issues is to use magnetron sputtering. In this case, magnets are used behind the cathode to trap the free electrons in a cyclic path just above the cathode as shown in Figure 3.4(b). In this method, not only the probability of ionizing neutral gas molecules increases (this in turn enhances the deposition rate) but also the velocity of electrons near the target decreases. As a result, it is possible to deposit layered structures in lesser time and with lower substrate temperature.

It is important to note that, DC Sputtering is a cost-effective method for depositing conducting material like metals. Howbeit, this is not suitable for non-conducting/dielectric target materials such as oxides or insulators that can generate a polarized charge which can cause serious problems, e.g. arcing (where an intensely focused and localized discharge coming from the target material into the plasma which can generate material droplets causing non-uniform film deposition) or the poisoning of the target material with a charge that can stop sputtering procedure completely. Also, positive ions are generated over time which accumulate on the surface of target material leading towards a complete ceasing of sputtering atoms. In order to avoid building up polarized charge, RF sputtering is employed where the electrical potential of the current is alternatively changed at radio frequencies in the vacuum environment.
Also, the surface of the target material can also be cleaned in each cycle using the alternating electrical potential which reduces the chance of a charge build up. On the positive cycle, electrons are attracted to the target material (cathode) giving it a negative bias which is opposite for the negative cycle. Consequently, sputtering can take place smoothly without any disturbance.
There are several other advantages of RF sputtering, e.g. RF plasmas tend to defuse throughout the entire chamber instead of getting concentrated around the cathode or target material as with DC sputtering. Also, RF sputtering can sustain a plasma throughout the chamber at a lower gas pressure which results in fewer ionized gas collisions, i.e. more efficient line-of-site deposition of the coating material. Sputtering using RF also reduces the creation of race track erosion [78,79] on the surface of the target material which can be observed during magnetron sputtering especially in DC sputtering where the surface of the target material gets etched into a circular pattern. This is because of the circular magnetic field of the magnets beneath the target material which focuses the charged plasma particles near the surface of target and the diameter of the circular pattern depends on the magnetic field. However, with RF sputtering the width and depth of the race track is much less due to the alternating nature of the RF discharge with electrons causing less confinement by the magnetic field and hence, the plasma gets spread out more resulting in a wider, larger and shallower racetrack. This makes more uniform and efficient utilization of the target.

Although, deposition rates are considerably slower with RF sputtering and require significantly higher power as compared to DC sputtering so that overheating becomes a critical issue. Also, high voltage power supplies and cabling/connectors required for applying RF power are expensive and critical as the RF currents travel on the surface of target materials only. Another critical issue associated with RF sputtering rates is the decrease in deposition rates due to the lack of secondary electrons being trapped above the target as opposed to conventional magnetron sputtering for gas ionization. In all sputtering types, the plasma is sustained by the breakdown and ionization of an inert gas like Ar which is commonly used because of its large mass as well as cost effectiveness compared to the other inert gasses such as Helium (He) and Neon (Ne).
During the works presented in this thesis, Shinko Seiki, STV4321 sputtering system [80] has been used to deposit transparent electrodes (Indium tin oxide: ITO) and insulating layers (SiO_2, Al_2O_3).

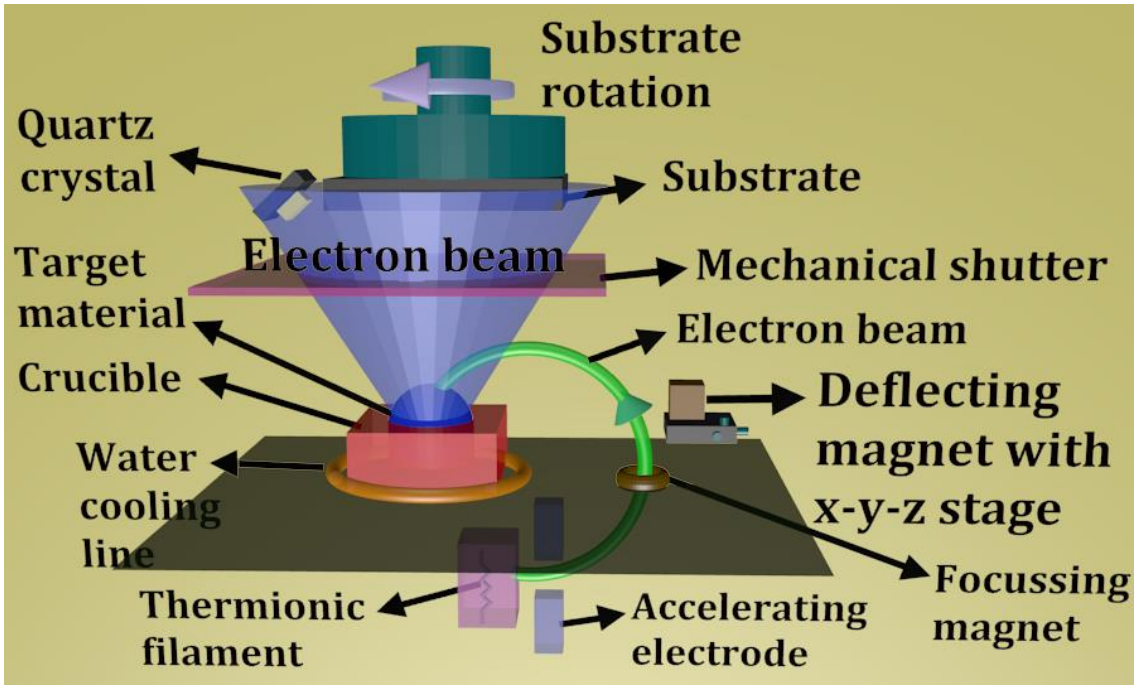

Figure 3.5. Schematic illustration of electron beam evaporation (EBE) system.

3.2.2. Electron Beam Evaporation (EBE)

This technique [81] falls under a special species of PVD methods [71]. Here the material to be deposited is placed in a water-cooled graphite crucible which is kept inside an evacuated chamber as schematically demonstrated in Figure 3.5. A beam of electrons

generated by a hot tungsten filament by thermionic emission [82] is guided and focused onto the target material with the aid of deflecting and focusing magnets. The focused beam heats the sample to its boiling point. Thus, the target material evaporates which moves towards the substrate which is loaded on a sample holder and gets condensed all over its surface. The sample holder is mounted on a rotation motor, which rotates during the deposition, in order to obtain a uniform deposition.

A load-locked chamber is integrated with the system to transfer samples into the chamber without disturbing the vacuum of the main/growth chamber. The EBE can be employed to melt both nonmagnetic materials (such as Au, Ti, Al_2O_3, SiO_2 etc.) and FM elements (such as Ni, Fe, Co, NiFe, CoFe etc.). Various materials to be evaporated are kept in separate crucibles which are then placed on a linear/circular train and its position can be adjusted from outside without breaking the vacuum in the chamber. Due to the long distance (~ 15 – 20 cm) between the substrate and the source, the evaporated material can be considered as deposited on the substrate perpendicularly and the substrate is rotated to maintain uniformity. This is very essential while depositing the film on the arrays of patterned micro- or nanostructures as it reduces the undesired side-wall coating during the deposition. This causes the lift-off process relatively easier because the solvent can seep into the resist layer without much resistance.

During the works presented in this thesis, Katagiri Eng. EB-evaporator system has been used to deposit Au electrodes and CPWs.

3.3. Sample Characterization

Sample characterization is a vital procedure after any kind of fabrication of patterns or deposition of heterostructures. Nonetheless, the lithography method is employed in fabricating magnetic nanostructures, these delicate systems deviate from their nominal dimensions, physical shape and chemical composition to an extent due to various factors such as fabrication conditions like quality of the vacuum/growth chamber, chemical process during multi-step lithography process and also ambient condition of the surroundings. Any distortion like sharp edges becoming rounded corners can be almost always observed due to the finite spot size of the optical and electron beams used for patterning. However, defects may also arise during the lift-off process of the resist due to the over- or under-treatment. The deformities such as inhomogeneity in

physical dimensions of patterned elements may appear while using un-optimized dose current and dose time. The edge roughness is another inherent issue which comes from the roughness of the side walls of resist and causes during lift-off process of the resist. The imperfection in the chemical composition of the thin film made of alloys (e.g. $Ni_{80}Fe_{20}$, $Co_{50}Fe_{50}$, $Co_{20}Fe_{60}B_{20}$) and impurity arises during the deposition of the film. Beyond all these defects, sometimes different kinds of mechanical or human blemishes may also turn out due to the mishandling of the samples. The top surface of the sample can also get contaminated if they are not preserved properly in the vacuum desiccator. The fabrication imperfections are minimized by optimizing the dose current, dose time and lift-off procedure. The right choice of developer solution and time are very essential for such delicate lithography methods. The optimization of deposition parameters is necessary to achieve a thin film heterostructures with high quality in terms of chemical purity. The contamination of the sample is prevented by coating the sample with a transparent nonmagnetic material usually oxides, which generally remain unaffected by the ambient environment. Finally, proper handling of sample is always necessary to preserve the samples in a good ambient condition. The characterization techniques along with their working principles utilized for the samples studied in this dissertation are delineated below.

3.3.1. Optical and Laser Microscopes

Light microscopy is the one of the genres of microscopy which is used to observe systems having dimensions of the order of μm or hundreds of nm. It is comprised of all types of microscopic methods that utilize electromagnetic radiation to achieve magnification. The light is produced by a visible lamp (e.g. halogen) as source and light rays are focused on the sample. The sample is placed on the *x*-*y*-*z* scanning stage while the light reflected from the sample surface is acquired by the objective lens (objective lens varies from 5X – 100X magnification) and additional magnification is achieved by the eyepiece (usually has an additional 10X magnification). During the works performed in the thesis, Olympus MX51 [83] has been used which has bright field, dark-field, and differential interference contrast (DIC) imaging modes that generates 2D images of the sample with high resolution even with ultralow contrast.

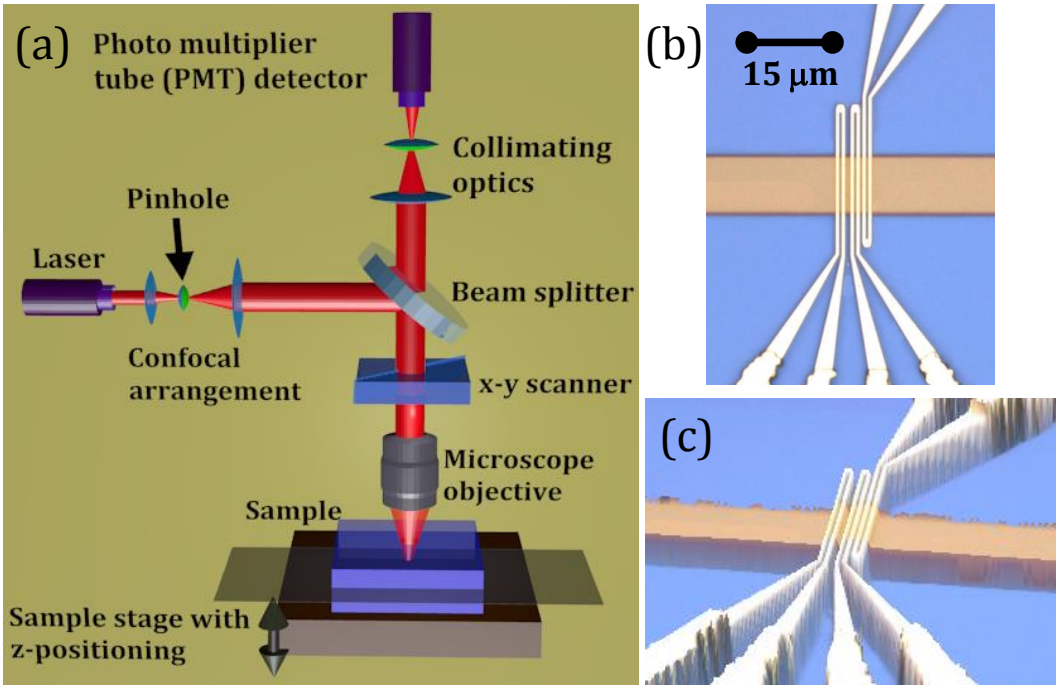

Figure 3.6. (a) Schematic of the laser microscope. Microscopic image of a microscale waveguide acquired by the laser microscope in (b) 2D and (c) 3D.

Laser microscopes [84] are designed to produce optical images with high resolution as well as characterization of surface profile accurately. Laser microscopes conjugate the advantages of magnified observation and measurement devices in order to procure both fully focussed images and reliable profile analysis in 3D. Its working operation is very straight forward to perform in a manner similar to optical microscopes and the capturing of sample morphology can be done at room temperature without the need for a vacuum unlike SEM or TEM. In addition, no pre-processing of the samples is necessary while, it is also possible to acquire color observation. All of these advantageous factors enable quick and accurate analysis of samples. This novel microscope can also be employed to view the 3D profile of the surface layer specifically for a rough calculation of the corresponding layer thickness. During the works presented in this dissertation, Olympus LEXT OLS4000 is employed. This microscope consists of a confocal optical system which only captures the in-focus image while simultaneously eliminating undesirable flare. Also, this confocal technology can be employed as a height sensor as it can capture image planes of same height. As described schematically in Figure 3.6(a) that the focusing as well the magnification of the sample are carried out by digital motorized focusing mechanism fed by the computer. Here, the contrast of the image is

enhanced by using the laser light with dichromatic mirror concentrated at one pinhole while the higher resolution is generated by reducing the wavelength of the laser light source accordingly. Here, the planar profile is procured with the laser source scanning at high speeds in the *x*-*y* co-ordinates while the 3D morphology is achieved when the objective lens is moved in the *z*-direction where a precise *z*-drive coordinated with a linear scale provides accurate information about the location along *z*-direction as demonstrated in Figure 3.6(b, c). Here, the color information is acquired by brightfield observation which can also create 3D image with a real color by combining the 3D image and color information.

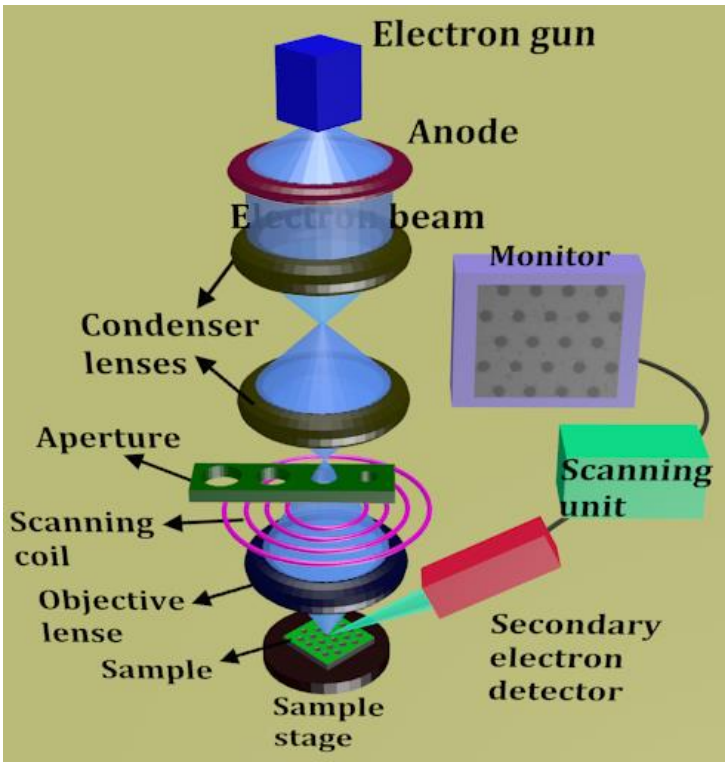

Figure 3.7. Schematic illustration of scanning electron microscope (SEM).

3.3.2. Scanning Electron Microscope (SEM)

This is one of the most well-known and commonly used characterization tools for imaging structures ranging from millimeter (mm) to nanometer (nm) length scale. This is employed to characterize the surface topography and morphology of specimens by scanning them with a focused beam of electrons [15,85]. The beam of electrons interacts with the sample which generates various signals to provide the information about the surface texture and composition. The advantage of this technique over the

conventional optical microscopy lies in its high resolution (~ 1 nm) due to the much shorter de Broglie wavelength of electrons.

In a typical SEM instrument as schematically described in Figure 3.7, a stream of accelerated electrons is generated from a cathode either by using thermionic emission (environmental SEM: ESEM [86,87]) or an electric field (field emission SEM: FESEM [88,89]) based upon the difference in the emitter type. Single or multiple electromagnetic (EM) condenser lenses are placed to focus the emitted beam. Subsequently, the beam passes through a pair of scanning coils or deflector plates which can deflect the beam path inside a 2D rectangular region of the sample surface in order to scan it in a raster manner. As the sample surface is hit by the electron beam, the electrons lose their energy due to scattering and absorption within the interaction volume. This leads to the generation of a variety of signals which can be detected by specific detectors. These signals include secondary electrons (this generate SEM images), backscattered electrons (arise due to elastic scattering), auger electrons, transmitted electrons, photons (characteristic X-rays that are used for elemental analysis and continuum X-rays), visible light (cathodoluminescence: CL), and heat energy. Finally, a 2D image is generated for the selected area of the sample surface which displays the spatial variations of the intensity of secondary electrons with respect to that of the incident electrons. Due to the very narrow electron beam, SEM micrographs have a large depth of field rendering the capability of producing 3D images which are crucial in order to understand the surface structure of a sample. However, to prevent any scanning errors and other image artefacts, the samples should be electrically conductive at the surface and electrically grounded, because a non-conductive surface accumulates electric charge when scanned by the electron beam leading towards a distortion in the acquired images. In case of non-conductive/insulating specimens, this can be avoided by coating them first by a thin layer of highly conducting material (preferably gold (Au)) before acquiring the desired surface morphology.

In case of thermionic emitters, electrical current is applied to heat up the filament where either Tungsten (W) or Lanthanum Hexaboride (LaB_6) is mainly used as the material of the filament. The electrons can escape from the material itself when the heat energy is enough to overcome the work function of the filament material. However,

thermionic sources face challenges such as low brightness, thermal drift or evaporation of cathode material during operation. Nowadays, Cerium Hexaboride (CeB_6) is being employed as filament material recently due to its higher brightness and longer lifetime**.** On the other hand, field emission is one route to produce electron beam to elude these critical issues. Here, the field emission gun (FEG), also known as cold cathode field emitter does not heat the filament to produce electron beam, whereas emission is achieved by keeping the filament at a large gradient of an electric potential. The FEG generally consists of W in the form of a wire which is sharpened to have a pointed end in order to proliferate the electric potential. Thus, the increase of the beam density enhances the brightness of the images significantly which is convenient when it is necessary to decrease the spot size in order to increase the resolution or to decrease the accelerating voltage to get detailed features of the sample surface. In addition, the beam energy should be coherent as it has to overcome the magnetic fields of the condenser lens(es) and all the electrons are supposed to follow the similar track to achieve the same initial conditions. Incoherent beam can cause increase in the aberration as well as decrease in the resolution specially at low accelerating voltage. These make FESEM a reliable and efficient instrument for acquiring sample morphology and its image with a high resolution even at low electric field (voltage). FEI QUANTA 200 [90] and Hitachi S-4800 [91] systems have been used for characterization of samples in this thesis.

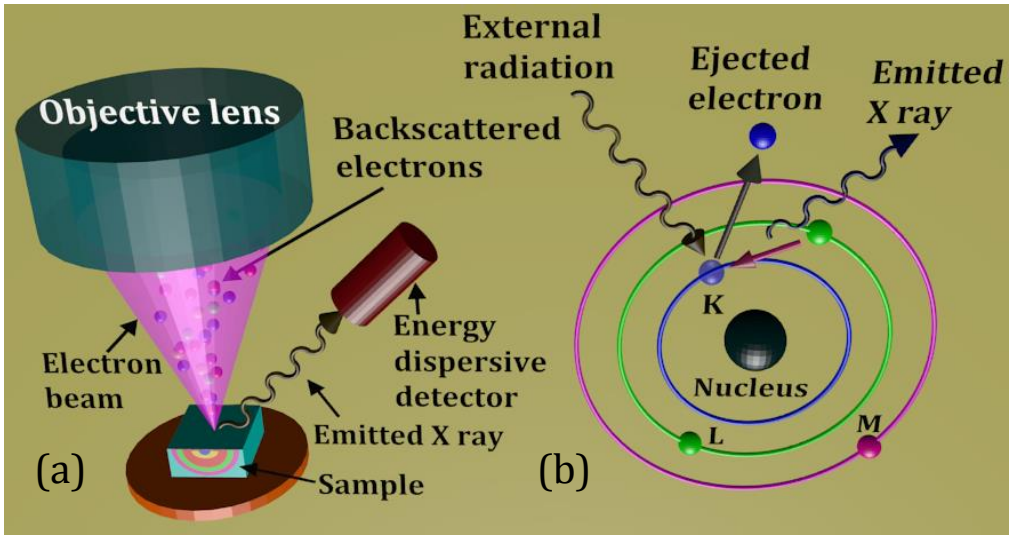

Figure 3.8. (a) Schematic of energy dispersive X-ray spectroscopy (EDXS) system. (b) Demonstration of the interaction of accelerated electrons with sample and emission of X ray.

3.3.3. Energy Dispersive X-ray Spectroscopy (EDXS)

This is a powerful technique [92,93] for the elemental analysis and chemical characterization of the materials present in a sample. Generally, it is used in conjunction with SEM or electron probe micro-analyzer (EPMA). The working principle is based upon on the phenomenon that each element possesses a unique atomic structure which corresponds to a particular emission spectrum and this can be employed to detect the elements present in the specimen as pictorially described in Figure 3.8(a). Basically, at ground state, an atom contains a number of electrons revolving around the nucleus while arranged in discrete characteristic shells. As a high energy beam of charged particles such as electrons, protons or X-ray falls on the sample, it excites and ejects out the electrons from an inner shell and creates electron-hole pairs. The outer shell electrons having high energy then jump to the inner shell to fill the holes where the difference in the two energy levels is emitted in the form of an X-ray as described in Figure 3.8(b). A detector consisting of a Silicon (Si) or Lithium (Li) crystal is employed in the EDXS to measure the energy and number of the emitted X-rays and it operates at low voltages to improve sensitivity. The crystal absorbs the energy of incoming X-rays by ionization generating free electrons in the crystal and they create an electrical charge bias due to their conductive property. Thus, the X-ray absorption converts the energy of individual X-rays into electrical voltages of proportional amount and the electrical pulses correspond to the characteristic X-rays of the element present in the specimen. The detector is mounted in the sample chamber which is cooled by liquid nitrogen but recently the silicon drift detector is capable of operating at higher count rates without liquid nitrogen cooling. The elements are identified from the peak energy values of the X-rays and the relative amplitudes of the peaks give the atomic percentage of the elements present in the specimen. In this dissertation, an EDXS system from EDAX attached with FEI QUANTA 200 SEM system has been employed.

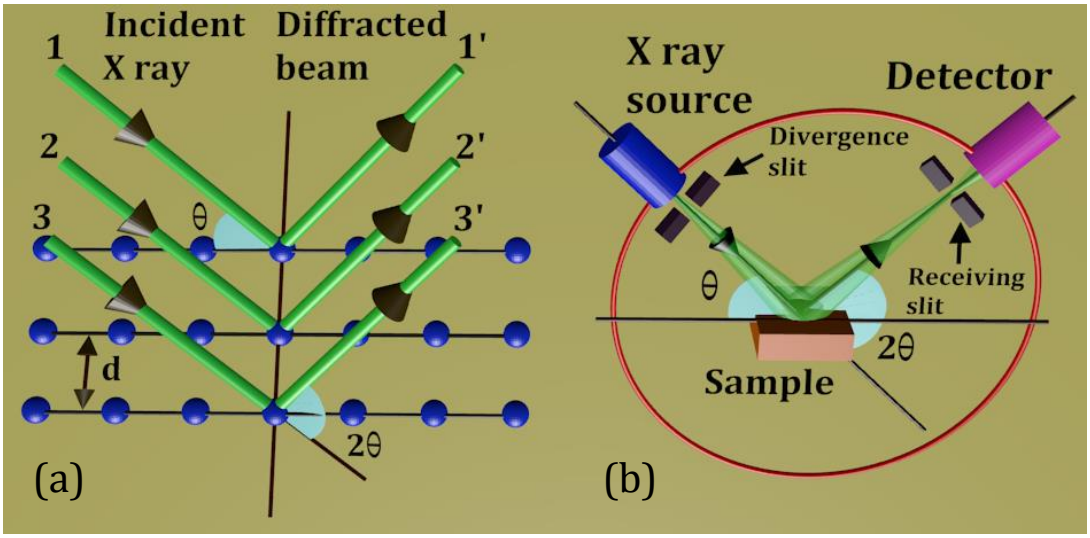

Figure 3.9. (a) Mechanism of X ray diffraction (XRD). (b) Schematic illustration of XRD system.

3.3.4. X-ray Diffraction (XRD)

This technique [94-96] investigates the crystallinity of the material structure, including atomic arrangement, crystallite size and imperfections. Here, an X-ray beam (typical average wavelength ~ 1.5418 angstrom (Å): the K_α radiation (X-ray) from a copper target) is made incident on the specimen and gets diffracted by the crystalline atoms as shown schematically in Figure 3.9(a). By calculating the angles and intensities of these diffracted beams, one can extract the atomic arrangement, atomic disorder and various other information. A crystal can be treated as a regular array of atoms which can elastically scatter EM waves like X-rays. The scattered beams form secondary waves which can interfere constructively at certain directions according to the Bragg's condition:

$$2d \sin\theta = n\lambda \tag{3.1}$$

Here, d is the spacing between the atomic planes, θ is the angle of incidence, n is an integer and λ is the wavelength of the X-ray beam. Hence, for a certain lattice structure corresponding to a specific d, the diffraction spots appear only at certain θ. During the measurement, θ is varied between a range of angles at small and regular intervals as shown in Figure 3.9(b) and the corresponding reflected intensities are measured as a function of the angle of the reflected beam with respect to the direction of the incident beam, i.e. 2θ. Subsequently, the diffraction peaks are converted to d-spacings to identify the elements present in the sample. Typically, this is accomplished by comparing the

experimental data with standard reference patterns (can be obtained from inorganic crystal structure database: ICSD [97,98]). For the characterization of samples used in this thesis, Panalytical X'PERT PRO X-ray diffractometer [99] have been employed.

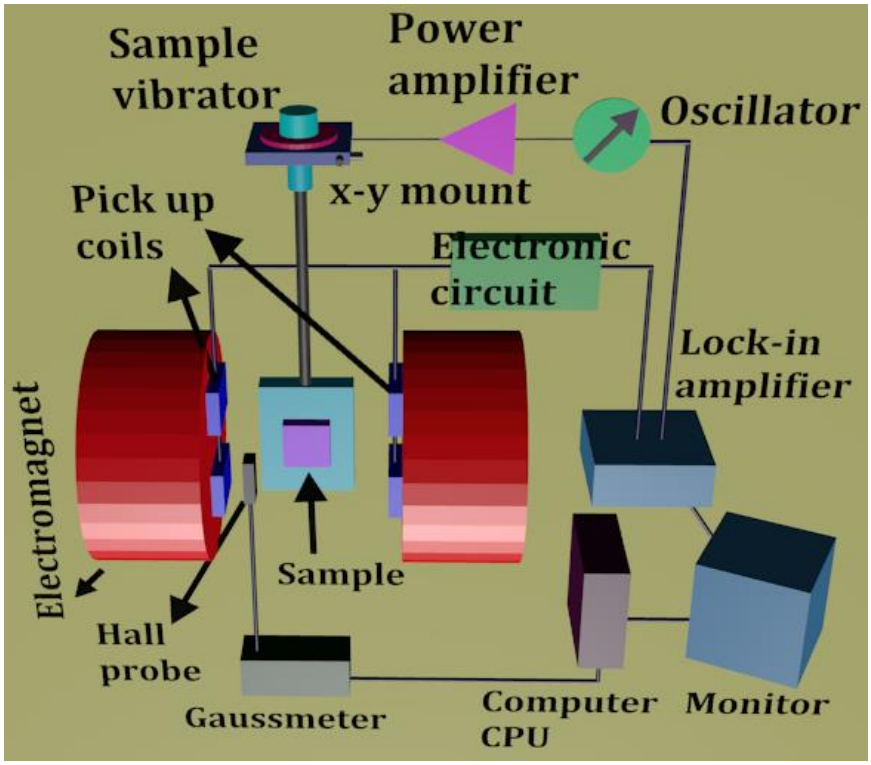

Figure 3.10. Schematic of vibrating sample magnetometer (VSM).

3.3.5. Vibrating Sample Magnetometry (VSM)

This popular technique [23,24,100] is utilized to investigate the static magnetic properties of a specimen including the magnetic moment, its behavior as a function of applied magnetic field (H) and temperature (T) which is demonstrated in Figure 3.10. Its operation is based on the Faraday's law of induction which states that a changing magnetic flux through a coil gives rise to an electromotive force (EMF) induced in terms of voltage (V_{in}) in the coil. Mathematically,

$$V_{in} = -n_w A \frac{dB}{dt} \tag{3.2}$$

Here, E_{in} is the induced electric field, A is the area of the coil with number of windings (turns) n_w and B is the magnetic flux per unit area. Using the relation between B and H, i.e. $B = \mu_0(H+M)$ (M is the magnetization of the sample), the expression for V_{in} under constant H takes the following form,

$$V_{\text{in}} = -n_{\text{w}} A \frac{dM}{dt} \tag{3.3}$$

Also, If the initial magnetization is negligible compared to the induced magnetization then,

$$V_{\text{in}} dt = -n_{\text{w}} A(4\pi M) \tag{3.4}$$

Here, V_{in} is linearly proportional to M of the sample. For the measurement, the magnetic specimen is first kept under a constant magnetic field. The magnetic dipole moment (m) of the sample then produces a stray magnetic field around the sample. Usually, the sample is attached to a piezoelectric transducer assembly which transforms sinusoidal electric signal (generated by an oscillator/amplifier) into a sinusoidal vertical vibration of the sample rod resulting in a sinusoidal oscillation of the sample. The resulting oscillation in m induces a voltage in the pickup coil located close to the sample and this voltage is independent of the applied field. Thus, the VSM technique converts the dipole field of the sample into an ac electrical signal, which can be amplified and measured using a lock in amplifier where the output of the piezoelectric signal serves as the reference signal. Any change in the applied magnetic field or temperature introduces modulation in m of the sample, which can be traced to investigate the dependence of M on H (hysteresis) or temperature (T: to determine the Curie temperature of the magnetic material). For the characterization of samples used in this thesis, Lake Shore (model: 7407) VSM system [101] has been employed.

3.3.6. Atomic Force Microscope (AFM) and Magnetic Force Microscope (MFM)

These methods [102-104] belong to a specific genre of scanning probe microscope [16] which has been designed to investigate superficial properties of the specimen such as morphology, roughness and also magnetic fingerprints [105] in the absence or presence of an external parameter such as magnetic field, electric current etc. The information is acquired by measuring the force between a probe and the sample. Piezoelectric actuators enabling small and accurate movements of the sample at nanoscale facilitates very precise scanning with a resolution thousand times better than that of the optical diffraction limit. In general, the AFM probe is comprised of one cantilever (coated with Co-Cr, Pt-Ir etc.) having a sharp tip (coated with Co-Cr, Pt-Ir or doped diamond etc.) at its end. When the tip is brought into the proximity of the sample surface, it experiences vertical and lateral deflections due to forces such as van der Waals force, force due to chemical bonding, capillary force, electrostatic force as well as magnetic force. Thereby,

this deflection is mapped by employing a laser spot reflected from the top surface of the cantilever. The reflected laser beam strikes a position sensitive photo detector consisting of four segments. The differences between the signals of different segments of photo detector provides an estimation of the angular deflections of the cantilever. A 2D profile of the local parameters can then be acquired by performing a raster-scan over a small area (~ few tens of μm^2) of the specimen as demonstrated schematically in Figure 3.11.

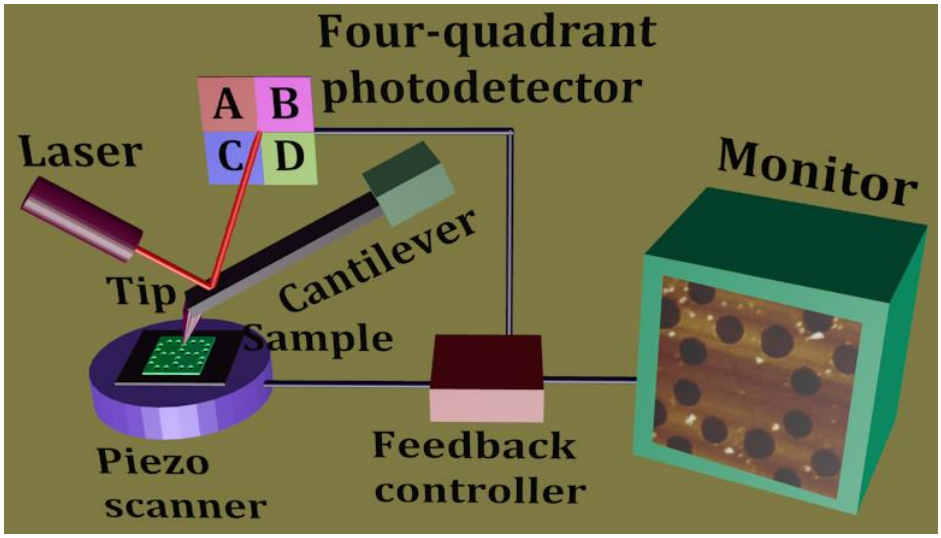

Figure 3.11. Schematic demonstration of atomic force microscope (AFM) module.

Depending on the sample surface and the acting force between the probe and the sample, AFM [106,107] can be operated in three disparate manners which have been discussed briefly in the following:

3.3.6.1. Contact Mode

This is also comprehended as static mode AFM, where the tip scans the sample in close contact with its surface while a constant repulsive force between the tip and the surface is applied during the scan [108]. A feedback amplifier is employed to apply feedback voltage to the piezoelectric actuator to maintain this criterion during scanning which determines the height of features on the sample surface. As such measurement of static signal can affect the cantilever as well sample surface, generally cantilevers with low stiffness are incorporated to achieve a large enough deflection signal (the amplitude ranges from few tens of nm to few hundreds of nm) while keeping the interaction force feasible.

3.3.6.2. Non-Contact Mode

This efficient method [109,110] is used in situations when a sample is prone to degradation caused by the cantilever tip. Here, the tip hovers few tens of Å above the specimen and attractive force like Van der Waals force is probed to construct the topographical image of its surface. Such force is substantially weaker than the forces in contact mode so that a small oscillation is applied (the amplitude of oscillation typically ranges from few nm (< 10 nm to the tip) and the small forces between the tip and the sample is measured by calculating the modulation in amplitude, phase or frequency of the oscillating cantilever in response to the force gradients from the sample.

3.3.6.3. Tapping Mode

It is the most commonly used technique [111] in ambient conditions. It is implemented by oscillating the cantilever at or near its resonant frequency using a piezoelectric crystal. The tip is then brought close to the sample until it begins to lightly touch or tap the surface. The intermittent contact of the tip with the surface affects the cantilever oscillation causing an energy loss. The resulting change in the oscillation amplitude is employed to identify and interpret surface features. This method is capable of measuring a number of forces other than the atomic forces. Amongst them, one crucial variant is magnetic force microscopy (MFM) [18,112-115], where the interaction between the tip and the magnetic specimen are perceived to determine the magnetic topology of the sample surface. The cantilever tip is coated with a thin magnetic layer of high coercivity (like Co or Co-Cr) so that magnetization state of the tip does not change during imaging. As this tip is brought close to the sample, it senses the magnetic forces as well as the atomic and electrostatic forces. Howbeit, the AFM image is first captured in order to enhance the magnetic contrast. Followed by this, the tip is lifted further away and scanned over the sample again at that particular height to extract the magnetic signal. Depending on the strength of the stray field originating from the magnetic sample, MFM can operate in both static and dynamic modes. In course of characterizing the surface morphology as well as magnetic topology of the samples discussed in this thesis, Veeco (diInnova) system [116] have been employed.

3.3.7. Wire Bonder

This is an electrical inter-connection technique [117] using thin microscale wire (usually Au, Al or sometimes Cu [118]) and a combination of heat, pressure and/or

ultrasonic energy. It is a solid phase welding process in which the two metallic materials (i.e. the wire and pad surface of the sample) are brought into close contact. When the surfaces come very close to each other, formation of wire bond occurs due to the electron sharing or interdiffusion of atoms. Here, bonding force can lead to deformation of material, breaking the contamination layer thereby smoothing out surface asperity and this can be controlled by applying the ultrasonic energy. However, heat can accelerate interatomic diffusion leading to the bond formation. At the beginning of wire bonding process, the backside of the sample is attached to a sample carrier using either an organic or inorganic adhesive (e.g. resist or sticky tape) or a solder. Subsequently, the wires are welded by a special bonding tool (capillary or wedge). Depending on bonding parameters (i.e. heat and ultrasonic energy), the bonding process can be categorized into three different classes:

3.3.7.1. Thermosonic Bonding

This [119] uses ultrasonic energy and force to slightly heat the material of the connecting pad and the wire while pressing them together. To solidify the connection, both are held in place and vibrated for a suitable amount of time.

3.3.7.2. Thermocompression Bonding

Here [120,121], the contact surface is heated (and sometimes the wire is heated as well). Afterwards, both are pressed together to make the bond. Here, ultrasonic energy and friction are not required and suitable for bonding with gold wire on a gold surface.

3.3.7.3. Ultrasonic Bonding

In this case, force and ultrasonic are employed although heat is not required as the wire and the material are kept at room temperature during the entire procedure. This can be utilized with any kind of bonding wire and similar metal with satisfactory results.

There are also specific bonding techniques [122,123] within each of the general bonding types. These methods vary depending upon the application, the metal and the type of wire used in the system. These are described below:

3.3.7.4. Wedge Bond

In this method [124-126], a clamped wire (preferably Al) is made in contact with Al bond pad. Then, ultrasonic energy [127] is applied to the wire for a suitable time while being held down by a specific amount of force forming the first wedge bond between the wire and bonding pad. The wire is then run to another desirable position where it is

again pressed. The second bond is again formed by applying ultrasonic energy to the wire and finally, the wire is broken off by clamping and movement of the wire.

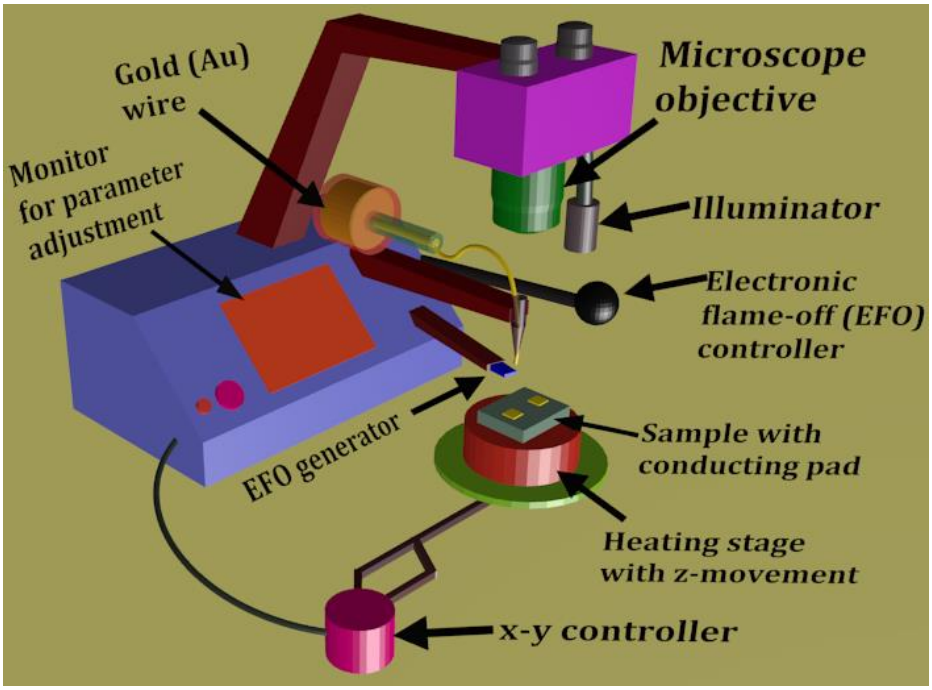

Figure 3.12. Schematic of wire bonding tool.

3.3.7.5. Ball Bond

Thermosonic ball bonding [128,129] is the most widely used bonding technique primarily because it is faster than ultrasonic bonding. Once the ball bond is made on the device, the wire (preferably Au) can be moved in any direction without stress on the wire, which greatly facilitates automatic wire bonding, as the movement needs only be along *x*- or *y*-direction. During gold ball wire bonding, one Au ball is first formed by melting the end of the wire through electronic flame-off (EFO). Here, the wire with melted end is held by a bonding tool known as the capillary). This Au ball (usually has a diameter ranging from 1.5 to 2.5 times the diameter of Au wire) is brought into contact with the bonding pad. Suitable amounts of heat, pressure and ultrasonic forces are then applied to the ball for a certain time, forming the initial metallurgical weld between the ball and the bond pad as well as deforming the ball bond itself into its final shape. The wire is then run to another suitable position of the bonding pad creating a shape of an arc or loop of Au wire between the first and second positions of the bonding pad. Consequently, to form the second bond, adequate pressure and ultrasonic forces are applied to the wire. The wire bonding machine (wire bonder) breaks the wire in

preparation for the next wire bonding cycle by clamping the wire and raising the capillary.

During the works in this thesis, TPT HB05 wire bonder [130,131] (this system can be configured for both Au and Al wire bonding) has been employed to use ball bond procedure for Au wire bonding as illustrated in Figure 3.12. It comprises of one stereo microscope which has an adjustable focus and magnification, while the adjacent optical illuminator system adjusts its illumination level. The heating stage is also installed which allows substrate temperatures up to 250° C. A substrate temperature of ~ 100°C is usually recommended for quick Au wire bonding although it is also possible even at room temperature (the Au wire bonding done during the works in this thesis are done in ambient temperature).

3.3.8. Static Magneto-Optical Kerr Effect (SMOKE) Magnetometer

This optical technique [132-135] is a non-invasive route to investigate static magnetization properties (magnetic hysteresis) of various FM systems ranging from single- or multilayer thin films, patterned nanostructures or even cluster of nanoparticles. The basic difference of this method from VSM is that static MOKE is a surface sensitive technique which allows to perform localized measurement of magnetization characteristics in case of non-uniform distribution. The physics behind this system relies on MOKE [20] which is basically the rotation of plane of polarization of a plane polarized light in presence of magnetization. MOKE can be measured in three different geometries [136,137] which are longitudinal, polar, and transverse MOKE depending upon the relative orientation among magnetization vector $\boldsymbol{M}$, sample surface plane and plane of incidence of light. In longitudinal geometry [138,139], $\boldsymbol{M}$ lies in the sample plane parallel to the plane of reflection whereas in polar MOKE [140], $\boldsymbol{M}$ is parallel to the plane of reflection but perpendicular to the sample surface. However, in case of transverse MOKE [141], $\boldsymbol{M}$ lies in the plane of the sample transverse to the plane of reflection.

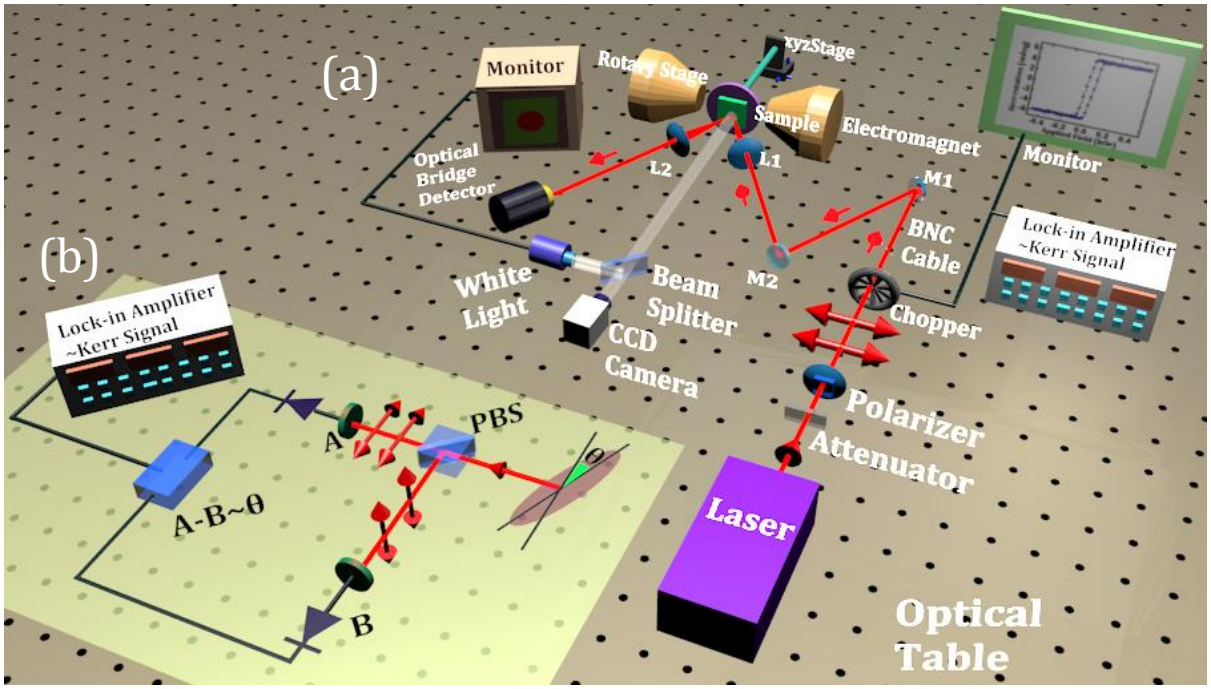

Figure 3.13. (a) Schematic of the static MOKE system present at S. N. Bose National Centre for Basic Sciences, Kolkata, India. (b) Working diagram of optical bridge detector (OBD).

The static MOKE system [142] present in the laboratory at S. N. Bose National Centre for Basic Sciences is based upon longitudinal geometry [143] to investigate Kerr rotation (or ellipticity) as a function of applied magnetic field as explained schematically in Figure 3.13(a). In the experimental set-up, a He-Ne laser [144-146] (output power ~ 30 mW) of wavelength (λ) = 632 nm is used as light source which traverses through a variable attenuator (to control the intensity of the laser) and a Glan-Thompson polarizer consecutively. The linearly polarized (s-polarization) output beam is then chopped at 2 kHz frequency by a mechanical chopper [147-149] controlled by a controller unit while this frequency fed to the chopper serves as a reference signal to one lock-in amplifier [150-152]. Therefore, the combination of lock-in amplifier and the chopper [153] is used for phase sensitive detection [154,155] to achieve better signal to noise ratio. The chopped beam is then guided by mirrors (M1 and M2) to a lens (L1) (in case of thin films) or long working distance microscope objective or MO (in case of patterned structures) which focuses the beam onto the sample. The sample is mounted in between the pole pieces of a magnet. Here, the bias magnetic field is applied along the sample plane by an electromagnet, while the field is varied by changing the current in its coil. The magnetic moment present in the sample causes the polarization of the

reflected beam to rotate from its initial direction due to Kerr effect. Thereby, the reflected beam is collected by another lens (L2) followed by which the beam is fed to the detector, known as optical bridge detector (OBD) [156]. Also, some high reflecting mirrors are used to guide the laser beam from the source to the detector.

As schematically depicted in Figure 3.13(b), the OBD is comprised of one polarizing beam splitter (PBS), which divides the beam in two perpendicularly polarized components (A and B) which then fall on two Si photodiode detectors to convert the incident photon to electrical signal (voltage) and a complex electronic circuitry to obtain the electrical signal through the lock-in amplifier (Model: SR830 DSP, Stanford Research Systems). In absence of any magnetic field, the OBD is brought to its balanced condition (i.e. A = B) by rotating the axis of the PBS. As the magnetic field is applied, the OBD no longer remains balanced (as the polarization of the beam is now changed) and the difference in the signals, i.e. (A – B) which is proportional to the magnetization of the sample, is measured as a function of the bias magnetic field to obtain the hysteresis loop. The OBD signal can further be converted to Kerr rotation. To achieve this, the polarizing beam splitter is rotated 1° away from its balanced condition and the equivalent voltage is recorded, which can be subsequently used as the calibration factor. The hysteresis loop obtained from static-MOKE technique helps to get information like switching field, coercivity, remanence, domain property and magnetic anisotropy, which are useful for the sample characterization.

References

[1] R. C. Jaeger, *Introduction to Microelectronic Fabrication* (Prentice Hall, 2002).
[2] B. Ziaie, A. Baldi, M. Z. Atashbar, in *Springer Handbook of Nanotechnology*, edited by B. Bhushan (Springer Berlin Heidelberg, Berlin, Heidelberg, 2004), p. 147.
[3] A. Sarangan, in *Fundamentals and Applications of Nanophotonics*, edited by J. W. Haus (Woodhead Publishing, 2016), p. 149.
[4] K. E. Drexler, Science 255 (1992) 268.
[5] K. E. Drexler, *Engines of Creation: The Coming Era of Nanotechnology* 1986).
[6] T. R. Groves, in *Nanolithography*, edited by M. Feldman (Woodhead Publishing, 2014), p. 80.
[7] A. A. Tseng, C. Kuan, C. D. Chen, K. J. Ma, IEEE Trans. Adv. Packag. 26 (2003) 141.
[8] Science 180 (1973) 1303.
[9] A. K. Chatterjee, in *Handbook of Analytical Techniques in Concrete Science and Technology*, edited by V. S. Ramachandran, and J. J. Beaudoin (William Andrew Publishing, Norwich, NY, 2001), p. 275.

[10] P. P. Ewald, *Fifty Years of X-ray Diffraction: Dedicated to the International Union of Crystallography on the Occasion of the Commemoration Meeting in Munich, July 1962* (International Union of Crystallography, 1962).
[11] D. McMullan, Scanning 17 (1995) 175.
[12] K. C. A. Smith, C. W. Oatley, Br. J. Appl. Phys. 6 (1955) 391.
[13] J. M. Bennett, L. Mattsson, *Introduction to Surface Roughness and Scattering* (Optical Society of America, 1999).
[14] G. Binnig, C. F. Quate, C. Gerber, Phys. Rev. Lett. 56 (1986) 930.
[15] J. Goldstein, J. I. Goldstein, Y. Goldshtain, D. E, D. E. Newbury, O. R. N. L. D. S. D. E. M. F. D. C. Joy, D. C. Joy, C. E, P. Echlin, C. E. Lyman, *Scanning Electron Microscopy and X-Ray Microanalysis: Third Edition* (Springer US, 2003).
[16] H. Hopster, H. P. Oepen, *Magnetic Microscopy of Nanostructures* (Springer, 2005).
[17] L. Abelmann *et al.*, J. Magn. Magn. Mater. 190 (1998) 135.
[18] U. Hartmann, Annu. Rev. Mater. Sci. 29 (1999) 53.
[19] Y. Martin, H. K. Wickramasinghe, Appl. Phys. Lett. 50 (1987) 1455.
[20] J. Kerr, Philos. Mag. 3 (1877) 321.
[21] P. Weinberger, Philos. Mag. Lett. 88 (2008) 897.
[22] Z. Q. Qiu, S. D. Bader, Rev. Sci. Instrum. 71 (2000) 1243.
[23] S. Foner, Rev. Sci. Instrum. 27 (1956) 548.
[24] S. Foner, Rev. Sci. Instrum. 30 (1959) 548.
[25] P. Weaver, *The Technique of Lithography* (Batsford, 1964).
[26] M. Kaestner, Y. Krivoshapkina, I. W. Rangelow, in *Frontiers of Nanoscience*, edited by A. Robinson, and R. Lawson (Elsevier, 2016), p. 479.
[27] C. G. Willson, R. R. Dammel, A. Reiser, *Photoresist materials: a historical perspective* (SPIE, 1997), Vol. 3049, Microlithography '97, p. AL.
[28] N. W. Parker, A. D. Brodie, J. H. McCoy, *High-throughput NGL electron-beam direct-write lithography system* (SPIE, 2000), Vol. 3997, Microlithography 2000, p. AL.
[29] F. Cerrina, G. Grenci, in *Reference Module in Materials Science and Materials Engineering* (Elsevier, 2016).
[30] H. Morimoto, Y. Sasaki, K. Saitoh, Y. Watakabe, T. Kato, Microelectron. Eng. 4 (1986) 163.
[31] P. Du, M. Q. Li, K. Douki, X. F. Li, C. R. W. Garcia, A. Jain, D. M. Smilgies, L. J. Fetters, S. M. Gruner, U. Wiesner, C. K. Ober, Adv. Mater. 16 (2004) 953.
[32] J. U. Kim, S. Lee, T. I. Kim, J. Nanomater. (2016) 17 7602395.
[33] D. Mijatovic, J. C. T. Eijkel, A. van den Berg, Lab Chip 5 (2005) 492.
[34] M. Heule, S. Vuillemin, L. J. Gauckler, Adv. Mater. 15 (2003) 1237.
[35] R. G. Hobbs, N. Petkov, J. D. Holmes, Chem. Mater. 24 (2012) 1975.
[36] W. Lu, C. M. Lieber, Nat. Mater. 6 (2007) 841.
[37] A. Kawai, J. Kawakami, J. Photopolym. Sci. Technol. 20 (2007) 815.
[38] R. Engelke, G. Engelmann, G. Gruetzner, M. Heinrich, M. Kubenz, H. Mischke, Microelectron. Eng. 73-4 (2004) 456.
[39] S. K. Wilson, R. Hunt, B. R. Duffy, J. Fluid Mech. 413 (2000) 65.
[40] L. E. Scriven, Mater. Res. Soc. Symp. Proc. 121 (2011) 717 717.
[41] A. Fauthan, M. N. Hamidon, B. Y. Majlis, Ieee, *Lithography Method for Selective Area of CNTs Growth* (Ieee, New York, 2013), 2013 Ieee Regional Symposium on Micro and Nanoelectronics.
[42] S. M. P. Kalaiselvi, T. L. Tan, A. Talebitaher, P. Lee, S. P. Heussler, M. B. H. Breese, R. S. Rawat, Phys. Lett. A 379 (2015) 560.

[43] C. A. E. Hamlett, G. McHale, M. I. Newton, Surf. Coat. Technol. 240 (2014) 179.
[44] M. K. Lubow, Adv. Mater. Process. 132 (1987) 18.
[45] C. H. Lu, X. F. Yin, M. Wang, Sens. Actuators A Phys. 136 (2007) 412.
[46] S. Petroni, C. La Tegola, G. Caretto, A. Campa, A. Passaseo, M. De Vittorio, R. Cingolani, Microelectron. Eng. 88 (2011) 2372.
[47] M. J. Yin, Q. Zhao, J. S. Wu, K. Seefeldt, J. Y. Yuan, Acs Nano 12 (2018) 12551.
[48] K. E. Paul, T. L. Breen, J. Aizenberg, G. M. Whitesides, Appl. Phys. Lett. 73 (1998) 2893.
[49] R. Menon, A. Patel, D. Gil, H. I. Smith, Mater. Today 8 (2005) 26.
[50] S. Schlangen, M. Ihme, M. Rahlves, B. Roth, Appl. Opt. 55 (2016) 1863.
[51] M. Rahlves, C. Kelb, M. Rezem, S. Schlangen, K. Boroz, D. Gödeke, M. Ihme, B. Roth, *Digital mirror devices and liquid crystal displays in maskless lithography for fabrication of polymer-based holographic structures* (SPIE, 2015), Vol. 14, 4.
[52] V. A. Kudryashov, P. D. Prewett, A. G. Michette, Microelectron. Eng. 53 (2000) 333.
[53] A. Uhl, J. Bendig, U. Jagdhold, J. Bauer, in *Microlithography 1999: Advances in Resist Technology and Processing Xvi, Pts 1 and 2*, edited by W. Conley (Spie-Int Soc Optical Engineering, Bellingham, 1999), p. 1381.
[54] M. A. Z. Hupcey, C. K. Ober, *Positive-tone conducting E-beam resists* (Spie - Int Soc Optical Engineering, Bellingham, 1997), Vol. 3048, Emerging Lithographic Technologies.
[55] P. Mansky, Y. Liu, E. Huang, T. P. Russell, C. Hawker, Science 275 (1997) 1458.
[56] P. Pal, S. Haldar, S. S. Singh, A. Ashok, X. Yan, K. Sato, J. Micromech. Microeng. 24 (2014) 095026.
[57] L. H. D. Skjolding, G. T. Teixidor, J. Emneus, L. Montelius, Microelectron. Eng. 86 (2009) 654.
[58] S. Yasin, D. G. Hasko, H. Ahmed, Microelectron. Eng. 61-2 (2002) 745 Pii s0167-9317(02)00468-9.
[59] P. R. Deshmukh, W. S. Khokle, Microelectron. Reliab. 31 (1991) 1091.
[60] M. De Silva, in *Encyclopedia of Microfluidics and Nanofluidics*, edited by D. Li (Springer US, Boston, MA, 2008), p. 1635.
[61] C. L. Henderson, in *Encyclopedia of Microfluidics and Nanofluidics*, edited by D. Li (Springer US, Boston, MA, 2008), p. 2073.
[62] Y. Kitade, H. Komoriya, T. Maruyama, IEEE Trans. Magn. 40 (2004) 2516.
[63] Y. Kamata, A. Kikitsu, H. Hieda, M. Sakurai, K. Naito, J. Appl. Phys. 95 (2004) 6705.
[64] V. Patel, B. Singh, J. H. Thomas, Appl. Phys. Lett. 61 (1992) 1912.
[65] R. Levisetti, J. M. Chabala, J. Li, K. L. Gavrilov, R. Mogilevsky, K. K. Soni, Scanning Microsc. 7 (1993) 1161.
[66] C. J. Petti, M. M. Hilali, G. Prabhu, in *Handbook of Thin Film Deposition (Third Edition)*, edited by K. Seshan (William Andrew Publishing, Oxford, 2012), p. 313.
[67] R. Behrisch, *Sputtering by particle bombardment* (Springer-Verlag, 1981), v. 1.
[68] T. Schenkel, M. A. Briere, H. Schmidt-Böcking, K. Bethge, D. H. Schneider, Phys. Rev. Lett. 78 (1997) 2481.
[69] K. Wasa, M. Kitabatake, H. Adachi, in *Thin Film Materials Technology*, edited by K. Wasa, M. Kitabatake, and H. Adachi (William Andrew Publishing, Norwich, NY, 2004), p. 191.
[70] S. Swann, Phys. Technol. 19 (1988) 67.
[71] J. E. Mahan, *Physical Vapor Deposition of Thin Films* (Wiley, 2000).
[72] S. Swann, Vacuum 38 (1988) 791.

[73] J. Yang, W. Cui, Y. Li, G. Xie, N. Zhang, R. Wang, T. Hu, H. Zhang, Appl. Surf. Sci. 382 (2016) 88.
[74] E. Marenkov, K. Nordlund, I. Sorokin, A. Eksaeva, K. Gutorov, J. Jussila, F. Granberg, D. Borodin, J. Nucl. Mater. 496 (2017) 18.
[75] K. Wasa, M. Kitabatake, H. Adachi, in *Thin Film Materials Technology*, edited by K. Wasa, M. Kitabatake, and H. Adachi (William Andrew Publishing, Norwich, NY, 2004), p. 465.
[76] G. Bräuer, in *Comprehensive Materials Processing*, edited by S. Hashmi *et al.* (Elsevier, Oxford, 2014), p. 57.
[77] S. Swann, J. Vac. Sci. Technol. A 5 (1987) 1750.
[78] Y. Ohtsu, S. Tsuruta, T. Tabaru, M. Akiyama, Surf. Coat. Technol. 307 (2016) 1134.
[79] K. Strijckmans, D. Depla, Appl. Surf. Sci. (2015) 185.
[80] S. Aikawa, P. Darmawan, K. Yanagisawa, T. Nabatame, Y. Abe, K. Tsukagoshi, Appl. Phys. Lett. 102 (2013) 102101.
[81] M. W. Pyun, E. J. Kim, D. H. Yoo, S. H. Hahn, Appl. Surf. Sci. 257 (2010) 1149.
[82] K. Masood, M. Iqbal, M. Zakaullah, Nucl. Instrum. Methods Phys. Res. A 584 (2008) 9.
[83] J. Shang, Y. Zhang, L. Yu, B. Shen, F. Lv, P. K. Chu, Mater. Chem. Phys. 134 (2012) 867.
[84] K. Carlsson, P. E. Danielsson, R. Lenz, A. Liljeborg, L. Majlöf, N. Åslund, Opt. Lett. 10 (1985) 53.
[85] H. Seiler, J. Appl. Phys. 54 (1983) R1.
[86] G. D. Danilatos, Microsc. Res. Tech. 25 (1993) 354.
[87] D. J. Stokes, A. M. Donald, J. Mater. Sci. 35 (2000) 599.
[88] S. Fan, M. G. Chapline, N. R. Franklin, T. W. Tombler, A. M. Cassell, H. Dai, Science 283 (1999) 512.
[89] A. A. Talin, K. A. Dean, J. E. Jaskie, Solid State Electron. 45 (2001) 963.
[90] H. Fitzek, H. Schroettner, J. Wagner, F. Hofer, J. Rattenberger, J. Microsc. 262 (2016) 85.
[91] A. Endo, M. Yamada, S. Kataoka, T. Sano, Y. Inagi, A. Miyaki, Colloids Surf. A 357 (2010) 11.
[92] R. Van Grieken, A. Markowicz, *Handbook of X-Ray Spectrometry, Second Edition* (Taylor & Francis, 2001).
[93] K. T. Moore, Micron 41 (2010) 336.
[94] H. P. Klug, L. E. Alexander, *X-Ray Diffraction Procedures: For Polycrystalline and Amorphous Materials* (Wiley, 1974).
[95] C. Suryanarayana, M. G. Norton, *X-Ray Diffraction: A Practical Approach* (Springer US, 2013).
[96] B. E. Warren, Phys. Rev. 59 (1941) 693.
[97] I. A. Baburin, V. A. Blatov, L. Carlucci, G. Ciani, D. M. Proserpio, J. Solid State Chem. 178 (2005) 2452.
[98] A. G. Orpen, Acta Cryst. B 58 (2002) 398.
[99] M. S. Rafique, M. Khaleeq-Ur-Rahman, T. Firdos, K. Aslam, M. S. Anwar, M. Imran, H. Latif, Laser Phys. 17 (2007) 1138.
[100] R. P. Guertin, S. Foner, Rev. Sci. Instrum. 45 (1974) 863.
[101] P. Masina, T. Moyo, H. M. I. Abdallah, J. Magn. Magn. Mater. 381 (2015) 41.
[102] E. Meyer, Prog. Surf. Sci. 41 (1992) 3.
[103] A. Schwarz, R. Wiesendanger, Nano Today 3 (2008) 28.

[104] K. C. Neuman, A. Nagy, Nat. Methods 5 (2008) 491.
[105] V. F. Puntes, P. Gorostiza, D. M. Aruguete, N. G. Bastus, A. P. Alivisatos, Nat. Mater. 3 (2004) 263.
[106] J. L. Hutter, J. Bechhoefer, Rev. Sci. Instrum. 64 (1993) 1868.
[107] M. Tello, R. García, Appl. Phys. Lett. 79 (2001) 424.
[108] C. Le Grimellec, E. Lesniewska, M.-C. Giocondi, E. Finot, V. Vié, J.-P. Goudonnet, Biophys. J. 75 (1998) 695.
[109] T. Uchihashi, Y. Sugawara, T. Tsukamoto, M. Ohta, S. Morita, M. Suzuki, Phys. Rev. B 56 (1997) 9834.
[110] Y. Sugawara, M. Ohta, H. Ueyama, S. Morita, Science 270 (1995) 1646.
[111] J. P. Cleveland, B. Anczykowski, A. E. Schmid, V. B. Elings, Appl. Phys. Lett. 72 (1998) 2613.
[112] S. Hong, J. Woo, H. Shin, J. U. Jeon, Y. E. Pak, E. L. Colla, N. Setter, E. Kim, K. No, J. Appl. Phys. 89 (2000) 1377.
[113] D. Rugar, H. J. Mamin, P. Guethner, S. E. Lambert, J. E. Stern, I. McFadyen, T. Yogi, J. Appl. Phys. 68 (1990) 1169.
[114] D. Rugar, R. Budakian, H. J. Mamin, B. W. Chui, Nature 430 (2004) 329.
[115] J. A. Sidles, J. L. Garbini, K. J. Bruland, D. Rugar, O. Züger, S. Hoen, C. S. Yannoni, Rev. Mod. Phys. 67 (1995) 249.
[116] H. K. Webb, V. K. Truong, J. Hasan, C. Fluke, R. J. Crawford, E. P. Ivanova, Scanning 34 (2012) 257.
[117] T. Krems, W. Haydl, H. Massler, J. Rudiger, in *1996 IEEE MTT-S International Microwave Symposium Digest*1996), pp. 247.
[118] K. Toyozawa, K. Fujita, S. Minamide, T. Maeda, IEEE Trans. Adv. Packag. 13 (1990) 667.
[119] G. Harman, J. Albers, IEEE Trans. Compon. Packag. Technol. 13 (1977) 406.
[120] C. H. Tsau, S. M. Spearing, M. A. Schmidt, J. Microelectromech. Syst. 11 (2002) 641.
[121] C. H. Tsau, S. M. Spearing, M. A. Schmidt, J. Microelectromech. Syst. 13 (2004) 963.
[122] I. Lum, J. P. Jung, Y. Zhou, Metall. Mater. Trans. A 36 (2005) 1279.
[123] U. Geißler, M. Schneider-Ramelow, K.-D. Lang, H. Reichl, J. Electron. Mater. 35 (2006) 173.
[124] I. Lum, M. Mayer, Y. Zhou, J. Electron. Mater. 35 (2006) 433.
[125] J. E. Krzanowski, N. Murdeshwar, J. Electron. Mater. 19 (1990) 919.
[126] J. V. Mantese, W. V. Alcini, J. Electron. Mater. 17 (1988) 285.
[127] A. Shah, H. Gaul, M. Schneider-Ramelow, H. Reichl, M. Mayer, Y. Zhou, J. Appl. Phys. 106 (2009) 013503.
[128] C. D. Breach, F. W. Wulff, Microelectron. Reliab. 50 (2010) 1.
[129] S. Murali, N. Srikanth, C. J. Vath, Mater. Res. Bull. 38 (2003) 637.
[130] K. Mistewicz, M. Nowak, D. Stróż, R. Paszkiewicz, Mater. Lett. 180 (2016) 15.
[131] K. Mistewicz, M. Nowak, R. Paszkiewicz, A. Guiseppi-Elie, Nanoscale Res. Lett. 12 (2017) 97.
[132] R. Lavrijsen, J.-H. Lee, A. Fernández-Pacheco, D. C. M. C. Petit, R. Mansell, R. P. Cowburn, Nature 493 (2013) 647.
[133] R. P. Cowburn, A. Ercole, S. J. Gray, J. A. C. Bland, J. Appl. Phys. 81 (1997) 6879.
[134] W. Zhou, T. Seki, K. Takanashi, J. Appl. Phys. 122 (2017) 5 093902.
[135] G. Garreau, M. Farle, E. Beaurepaire, K. Baberschke, Phys. Rev. B 55 (1997) 330.
[136] H. Corte-Leon, A. Beguivin, P. Krzysteczko, H. W. Schumacher, A. Manzin, R. P. Cowburn, V. Antonov, O. Kazakova, IEEE Trans. Magn. 51 (2015) 4 4001304.

[137] M. E. Stebliy, A. G. Kolesnikov, A. V. Ognev, A. S. Samardak, L. A. Chebotkevich, Beilstein J. Nanotechnol. 6 (2015) 697.
[138] R. Mattheis, G. Quednau, J. Magn. Magn. Mater. 205 (1999) 143.
[139] E. Beaurepaire, J. C. Merle, A. Daunois, J. Y. Bigot, Phys. Rev. Lett. 76 (1996) 4250.
[140] D. Weller, G. R. Harp, R. F. C. Farrow, A. Cebollada, J. Sticht, Phys. Rev. Lett. 72 (1994) 2097.
[141] V. I. Belotelov, D. A. Bykov, L. L. Doskolovich, A. N. Kalish, A. K. Zvezdin, J. Opt. Soc. Am. B 26 (2009) 1594.
[142] A. Haldar, C. Banerjee, P. Laha, A. Barman, J. Appl. Phys. 115 (2014) 133901.
[143] A. Stupakiewicz, A. Chizhik, M. Tekielak, A. Zhukov, J. Gonzalez, A. Maziewski, Rev. Sci. Instrum. 85 (2014) 103702.
[144] Y. Yeh, H. Z. Cummins, Appl. Phys. Lett. 4 (1964) 176.
[145] L. E. Hargrove, R. L. Fork, M. A. Pollack, Appl. Phys. Lett. 5 (1964) 4.
[146] A. Javan, W. R. Bennett, D. R. Herriott, Phys. Rev. Lett. 6 (1961) 106.
[147] M. E. Motamedi, *Micro-opto-electro-mechanical systems* (SPIE, 1994), Vol. 33, 11.
[148] I. Mendaš, P. V. Cvijin, Appl. Phys. B 32 (1983) 119.
[149] D. Vincent, Appl. Opt. 25 (1986) 1035.
[150] P. A. Probst, B. Collet, Rev. Sci. Instrum. 56 (1985) 466.
[151] R. Wolfson, Am. J. Phys. 59 (1991) 569.
[152] J. H. Scofield, Am. J. Phys. 62 (1994) 129.
[153] P. Dean, Y. Leng Lim, A. Valavanis, R. Kliese, M. Nikolić, S. P. Khanna, M. Lachab, D. Indjin, Z. Ikonić, P. Harrison, A. D. Rakić, E. H. Linfield, A. G. Davies, Opt. Lett. 36 (2011) 2587.
[154] P. A. Temple, Am. J. Phys. 43 (1975) 801.
[155] X. Wang, Rev. Sci. Instrum. 61 (1990) 1999.
[156] A. Barman, J. Sinha, *Spin Dynamics and Damping in Ferromagnetic Thin Films and Nanostructures* (Springer International Publishing, 2018), 1 edn.

Chapter 4

4. Experimental Tools for Magnetization Dynamics

As discussed in chapter 2, the magnetization dynamics spans over a broad timescale [1] (few fs to hundreds of μs) depending upon the mechanism involved. Diverse experimental techniques in the frequency, time and wavevector domains have been developed in the last few decades [2] in order to understand the magnetization dynamics at various time scales from a fundamental perspective. Historically, the frequency domain technique has been invented earlier, namely, conventional ferromagnetic resonance (FMR) [3,4] method where the sample is excited at a particular frequency and probed subsequently. Here, the magnetization dynamics is explored through the FMR induced in the sample while sweeping the external bias field. Later, another frequency domain technique, i.e. broadband FMR based on a vector network analyzer (VNA-FMR) [5] has been invented which facilitates very high resolution as well as sensitivity over a wide frequency window. The bias field is kept fixed in VNA-FMR while sweeping the excitation frequency from few tens of MHz to tens of GHz range. On the other hand, an extremely high resolution in temporal window (few tens of fs) along with a spatial resolution in the sub-μm regime can be achieved using the time-resolved magneto-optical Kerr effect (TR-MOKE) magnetometry [6,7]. Since the time resolution of the TR-MOKE method is limited only by the pulse width of the laser employed, it is considered to be the most efficient technique to probe ultrafast magnetization dynamics [8]. Furthermore, one can map the time evolution of the spatial distribution of magnetization in magnetic samples by associating a scanning microscope with the TR-MOKE system [9]. Likewise, Brillouin light scattering (BLS) technique [10,11] has been utilized as a puissant optical technique to investigate the spin wave (SW) dynamics where it can be employed in frequency window to calculate the magnon band structure (i.e. dispersion relation as frequency versus wavevector). Recent developments have enabled to investigate the spin dynamics with spatial, temporal or phase resolution using the advanced BLS techniques [12-17].

Here, mainly FMR, TR-MOKE and BLS techniques will be described which have been utilized over the course of experimental works on investigation of spin dynamics in FM

materials with particular emphasis on thin films and nanostructures presented in this dissertation. These experimental tools have been used for the fundamental understanding of magnetization dynamics by providing minute information on various substantial magnetic parameters, e.g. magnetic damping, magnetic anisotropy, saturation magnetization etc. These powerful techniques along with their constituent elements have been discussed in the following.

4.1. Broadband Ferromagnetic Resonance (FMR) Spectrometer

It has been employed to probe the magnetization dynamics of FM systems to extract information about their dynamic magnetic properties. Here, the SW properties are acquired originating from the magnetic moments possessing dipolar (and/or exchange) coupling. Generally, the SW response of the FM materials lies between sub-GHz to tens of GHz and hence an oscillating microwave signal with variable frequency is used to excite the SW response in the FM systems. The experimental set-up utilized during the work presented in this dissertation has been discussed in the following.

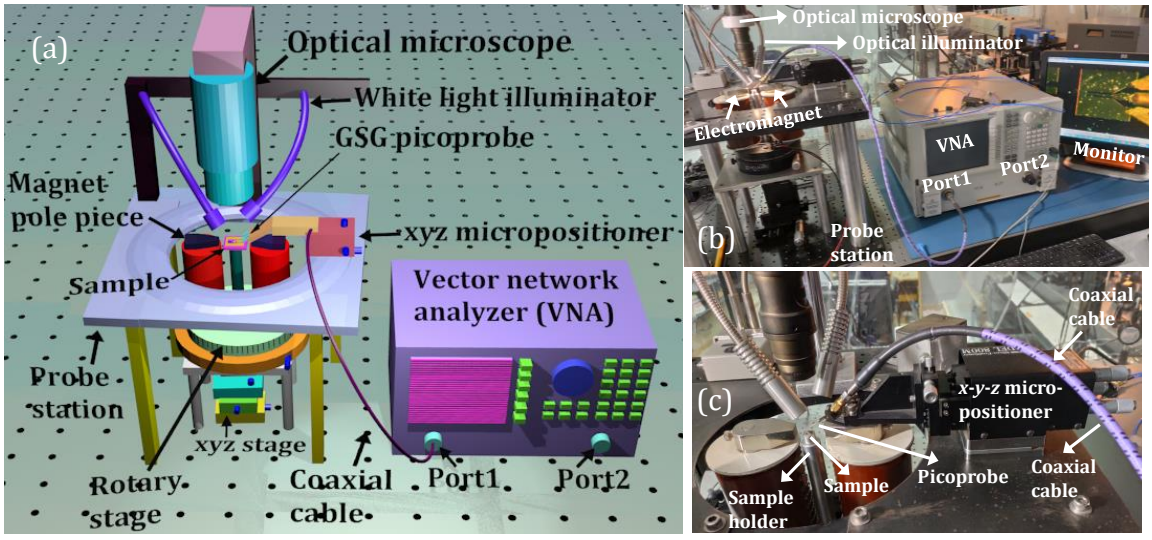

Figure 4.1. (a) Schematic of the broadband ferromagnetic resonance (FMR) spectrometer system along with the vector network analyzer (VNA). (b) Photograph of the broadband ferromagnetic resonance (FMR) spectrometer equipped with a vector network analyzer (VNA) and probe station, present in the laboratory of Prof. Anjan Barman in the S. N. Bose National Centre for Basic Sciences, Kolkata, India. (c) A pictorial description of the sample and the picoprobe mounted on the probe station.

4.1.1. Experimental Set-up

Here, the frequency domain SW dynamics of the samples are measured by using a broadband ferromagnetic resonance (FMR) spectrometer based on a vector network

analyzer (VNA, Agilent (currently Keysight) Technologies, PNA-L with model N5230C) along with a customized probe station as schematically illustrated in Figure 4.1(a). This probe station is comprised of one electromagnet (the electromagnet is fed by a bipolar power supply, KEPCO, INC. model BOP 36-6D and it can apply DC voltage from 0 to ± 36V with DC current from 0 to ± 6A) which applies the bias magnetic field which tries to align the magnetization of the FM sample in its plane. Meanwhile, the azimuthal orientation of the magnetic field can be varied over 360° within the sample plane. For that purpose, the pole pieces of the electromagnet are mounted on a high-precision rotation stage with an angular resolution of 1°. The sample can be viewed with the aid of a microscope (Shodensha Inc.) assisted by an illumination set-up (Shodensha Inc.) to put the microscale picoprobe on to the sample. Here, a microwave current (I_{rf}) of variable frequency (ranging from 10 MHz to 50 GHz) is launched in the CPW through a non-magnetic ground-signal-ground (G-S-G) picoprobe (40 GHz bandwidth, model 40A-GSG-150-EDP, GGB Industries) via a coaxial cable (model N1501A-203) using a precise micro-positioner (NPS, model 800MRF-L) for the adjustment of picoprobe to make a proper connection with the sample. This oscillating current I_{rf} generates a microwave field, H_{rf} perpendicular to I_{rf}. The works presented in this thesis has been performed in reflection geometry. For that purpose, the CPW is shorted at its one end and consequently, the forward scattering parameter (S_{11}) in reflection mode can be investigated by the VNA after being collected by the same picoprobe. The power is absorbed by the magnetic specimen at various sweeping frequencies over the onward and return journey of the microwave signal flowing through the CPW. This produces the characteristic FMR spectrum for that magnetic system. Generally, there exist some non-linear backgrounds in the directly acquired signals coming from different sources. To avoid this, a reference spectrum, i.e. spectrum at the highest value of bias field is subtracted from the signal to record the desired FMR spectrum with the minimized background. However, some background noises still sustain in the spectrum which is non-trivial to remove. Finally, the S_{11} amplitudes in terms of power (dBm) are extracted at either various magnetic field strength or azimuthal orientation to investigate the SW modes present in the magnetic structures.

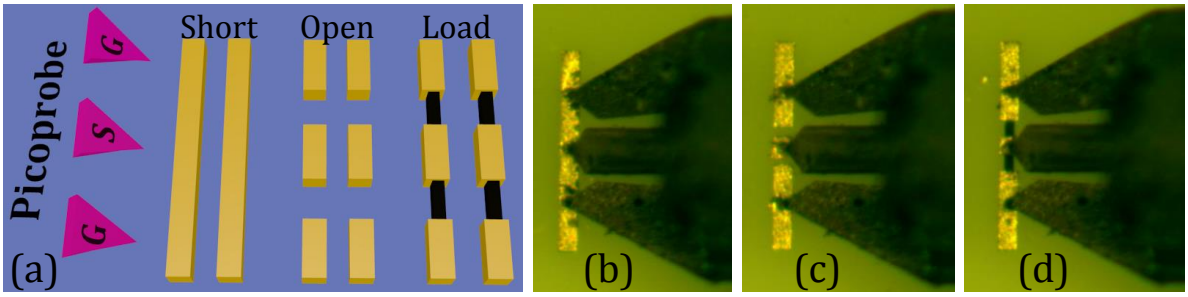

Figure 4.2. (a) Schematic of short-open-load (SOL) method used during the calibration procedure in VNA. Optical microscope images of the (b) short, (c) open and (d) load (50 Ω) lines along with the ground-signal-ground (G-S-G) type picoprobe.

4.1.2. Calibration Procedure

The basic motivation behind the utilization of the calibration process before or during the measurement is to provide more refined and accurate results free from undesirable and erroneous signals originating from any internal or external spurious noises [18-20]. Thus, when the experimental system, i.e. the combination of VNA, co-axial cable and picoprobe possesses a suspicious signal different from a standard sample, calibration is performed to reproduce a satisfactory result in agreement with the standard one. However, the accuracy of the calibration is merely limited by the standard kit and also the careful handling of the calibration routine. In the thesis, the CS-5 calibration kit from GGB Industries Inc. has been used as a standard to carry out the calibration during the electrical measurement. As illustrated in Figure 4.2, contact is made between the picoprobe and a set of patterned pads one by one which has similar dimensions to the pitch (~ 150 μm) of the G-S-G type probes to perform the short-open-load-though (SOLT) calibration method in transmission geometry (however, in reflection geometry using only one picoprobe used during the works presented in this thesis, short-open-load (SOL) method has been employed) [21-25]. Here, the 'open' pad structures used for the 'open' step helps to avoid the error caused by the fringing electric fields at the probe tip which are very different from the fields when the probe is made contact with either the 'short' or 'load' structures. The 'short' is implemented by contacting the probe to the shorting bar or offset 'short'. The electrical characteristics of the 'short' include a small inductance which depends on the probe contact spacing (i.e. pitch). This inductance is specified as an equivalent electrical length in series with a perfect 'short'. The 'load' structure consists of a pair of 100 Ω thin film resistors to provide a precise 50 Ω termination, accurate to ~ 0.25% at low frequencies. However, at high frequencies, the

'load' can exhibit either a small shunt capacitance or a small series inductance, depending upon the contact spacing (pitch) of the probe tips. The resistor pads are nearly identical to the 'open' pads so the 'load' capacitance is nearly identical with those used in 'open'. Also, the current path through the 'load' is almost identical with the current path through the 'short'. The inductance causes the current to lag the voltage whereas the capacitance causes the current to lead the voltage. These two opposing effects tend to compensate for one another so that the 'load' appears nearly perfectly resistive for some intermediate probe pitch.

4.1.3. Requirement of Calibration

Usually, calibration of a network analyzer remains valid as long as the deviations from the standard results or any other spurious errors are insignificant, viz. modifications due to the uncorrected leakage (i.e. directivity and isolation), mismatches (e.g. source match and 'load' match), and frequency response of the system are small (< 10%) relative to the required specifications. In addition, the difference of environmental condition (especially temperature as sometimes more than 1°C change in temperature may need recalibration) between calibration and measurement process may lead to a degradation in the calibration accuracy due to the possibility of a slight variation in the physical length of external and internal cables. Other important causes are dirty and damaged test port connectors and calibration standards as well as human errors (i.e. mishandling) which can greatly influence the measurement repeatability and accuracy. Here, some of the crucial factors behind the urge to calibrate the system properly are discussed below.

4.1.4. Crosstalk

Corrections from crosstalk include any signals that couple from one probe to another (i.e. transmission geometry where two picoprobes are employed). For instance, if one probe is calibrated using an 'open' pad while another probe is touching a nearby 'open' pad, a small fraction of the signal on the calibrating probe reaches the other one. This small crosstalk or leakage signal is included in the calibration of the first probe. Similarly, if the second probe is made in contact with either a 'load' or 'short' pad, the calibration of the first probe will differ slightly. Also, if the spacings between the probes are dissimilar, the calibration standards can be slightly different. Hence, if the probes are placed to measure a real device after calibration, the contributions from these

crosstalk signals will lead to further errors [26-29]. For the structures included in the calibration substrate, crosstalk is very small and can be neglected. However, if the devices to be measured require placement between the picoprobe less than the pitch (150 μm), crosstalk can limit the accuracy of the measurement.

4.1.5. Spurious Modes

The elements employed during calibration can couple signals to adjacent structures, where one 'open' or 'short' or 'load' calibration pad can absorb a noticeable fraction of the calibrating signal from another pad to produce an anomaly in the calibration [30]. The through-lines are designed to propagate the balanced coplanar mode where the electric and magnetic fields are confined near the gap between the centre line and the ground planes. If the substrate is placed on a metallic holder, a small fraction of the signal can be dissipated as the metallic holder can act as the ground plane. This can be avoided by placing the substrate on an electrically insulated holder (such as glass or coated with an insulating layer or using insulating adhesion tape).

4.1.6. Device Measurement

Generally, spurious signals originate mainly due to the difference between the probing environment of the sample (or device) and that of the standard substrate rather than the noises incurred during the calibration result. The materials of the sample and calibration substrates are often different while, the deviation from ideal line width and spacing (pitch) in the actual devices can cause a large difference in the obtained signal.

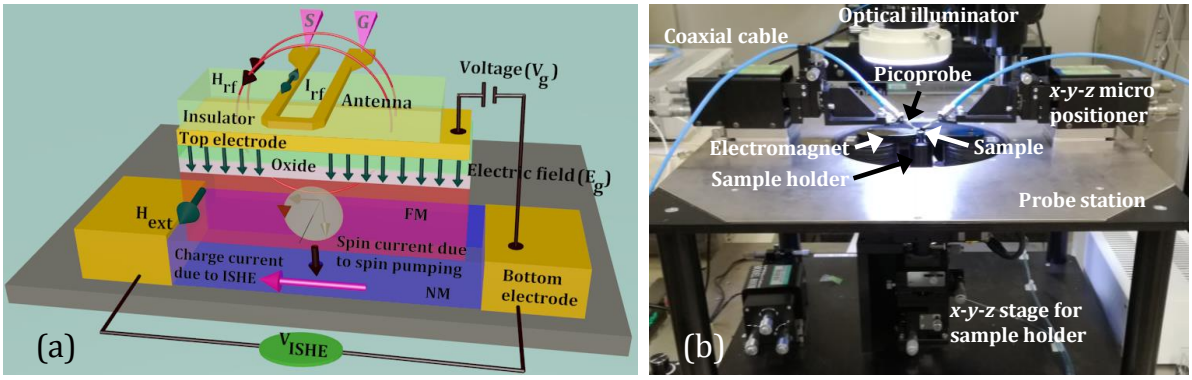

Figure 4.3. (a) Schematic demonstration of set-up for electrical measurement of spin pumping and inverse spin Hall effect (ISHE) in FM/ nonmagnetic (NM)/oxide heterostructures using microwave antenna. (b) Pictorial demonstration of the experimental set-up on the probe station present at RIKEN, Japan.

4.2. Electrical Measurement of Spin Pumping and Inverse Spin Hall Effect (ISHE)

Figure 4.3(a) describes a schematic diagram of electrical excitation and detection of SWs. Here, a signal generator (model: E8257D, Agilent Technologies) is used to send RF current (I_{rf}) through the microscale antenna (or CPW) where, this I_{rf} generates a microwave magnetic field (H_{rf}) perpendicular to the sample plane. The magnetization (M) of the FM layer is maintained along the short axis of the rectangular device structure (i.e. along y-axis) by applying external bias magnetic field (H_{ext}) using an electromagnet (the electromagnet is fed by a bipolar power supply with model: R6243, ADVANTEST) as shown in Figure 4.3(a). For uniform FMR (UFMR) measurement, the bias magnetic field is swept while, keeping the frequency of RF signal fixed. When the magnetic field satisfies the resonance condition, UFMR of the FM (e.g. CoFeB) layer is excited which pumps pure spin current (I_s) into the adjacent heavy metal (e.g. Ta) layer. This pure spin current is then transformed into transverse charge current (I_c) inside the heavy metal layer due to the ISHE. Hence, the corresponding response is acquired by measuring potential drop (V_{ISHE}) across the heavy metal layer at the bottom with the aid of a nanovoltmeter (model: 2182A, KEITHLEY). However, for investigating propagating SWs, I_{RF} is applied through a nanoscale microwave antenna as demonstrated in Figure 4.3(a), while the magnetization is set along the short axis (y-axis) of SW waveguide (SWWG) by applying a bias magnetic field H to excite the SWs in the Damon-Eshbach (DE) geometry. In contrary to the UFMR measurement, here H is kept constant, while the frequency of microwave signal is swept from 1 GHz to 10 GHz at a step of 20 MHz. The SW signals have been acquired by measuring ISHE voltage (i.e. V_{ISHE}) across the WG as depicted in Figure 4.3(a). Here, the electric field has been applied across the FM/oxide interface of the magnetic heterostructures with the aid of a DC voltage source (model: R6161, ADVANTEST). The experiments during the work presented in this thesis have been performed in the ambient condition.

4.3. Time-resolved Magneto-Optical Kerr Effect (TRMOKE) Microscopy

The rotation in polarization of light due to MOKE [31] is directly proportional to the magnetization of the system and as mentioned earlier, this phenomenon can be employed to evaluate the local magnetization states of continuous or patterned FM thin films and heterostructures. Consequently, the time-resolved magneto-optical Kerr effect

(TR-MOKE) [32] technique has become a very powerful tool to investigate the magnetization dynamics at a broad range time scale (from μs to few tens of fs). Amongst a number of variants of TRMOKE, the all-optical TRMOKE relies upon both the excitation and detection of the magnetization dynamics in optical manner. This unique system has several advantages such as,

1. This has a very high temporal resolution down to sub-100 fs (even ~ 40 fs in some advanced systems) [33,34].
2. Sample fabrication procedure is straight forward, e.g. no additional waveguide structures are required as that in case of FMR.
3. This is a local measurement technique where the spatial resolution can go down to sub-μm regime [35].
4. This is a non–invasive measurement technique.

The working principle of the TRMOKE set-up used during the works demonstrated in this thesis is based upon the two-color collinear (can be non-collinear) pump-probe geometry where the magnetic response is recorded in a stroboscopic fashion. A strong part of a femtosecond pulsed laser (also known as pump beam) is made incident on the magnetic specimen to disturb its equilibrium magnetization state towards complete or incomplete loss of its magnetization (known as ultrafast demagnetization). As the probe beam (a weak part of the fundamental laser) is reflected from the sample, it undergoes a magneto-optical Kerr rotation induced by the current magnetization state of the sample (which undergoes various stages of magnetization dynamics) and consequently, the Kerr rotation signal contains the information of the varying magnetization state with respect to the time delay between pump and probe pulses. This way the temporal resolution is solely limited by the cross-correlation width of the pump and probe laser pulses, which leads to the investigation of ultrafast demagnetization, different relaxation processes, coherent precession of magnetization and damping in a single measurement. In the following, the description of primary optical components and the optical set-up for TRMOKE magnetometry will be discussed.

4.3.1. Principal Components of TRMOKE Set-up

4.3.1.1. Laser

The optical set-up is comprised of three laser systems [36-40]. A diode-pumped solid-state laser (DPSS) with maximum power 10 W (variable) and wavelength λ = 532 nm is

used to pump a Ti: sapphire oscillator. Regenerative acousto-optic mode locking mechanism [41] is used inside the Ti:sapphire oscillator (known as Tsunami) to produce the output laser pulses of ~ 80 fs pulse width at 80 MHz repetition rate. The fundamental beam is divided into two parts: the intense part goes through a second harmonic generator to produce the second harmonic laser (λ = 400 nm), which is used to pump or excite the magnetic specimen, while the time-delayed fundamental laser (λ = 800 nm) is used to probe the magnetization dynamics. A brief discussion about the three different laser systems is described below.

4.3.1.1.A. Diode Laser

The generation of ultrashort laser pulses of the required wavelength involves a composite laser system consisting of three lasers. First, an array of twenty diode lasers [42] is used to pump a solid-state laser. The CW output of the diode laser bars, after collimated with a cylindrical micro-lens of high numerical aperture (NA), is coupled by the so-called FCbar technology [43], which is a highly efficient method of coupling the output of diode laser in fiber. Typically, 85–90% light of diode laser is coupled into the fiber bundle and this output is directly fed [36] to the DPSS laser through the fiber.

4.3.1.1.B. Diode Pumped Solid State Laser (DPSS)

This (also known as Millennia) uses Nd^{3+} ions doped in a Yttrium Vanadate crystalline matrix ($Nd:YVO_4$) to serve as the gain medium [44-48]. The output of the diode laser overlaps with the absorption spectra of the Nd^{3+} ion. The efficiency of the Millennia is further improved by focusing the diode laser output on a volume in the active medium of the Millennia in such a way that it matches with the radius of the TEM_{00} mode [49] of Millennia (known as mode matching). Here, Nd^{3+} is a four-level system which primarily emits photons of wavelength λ = 1064 nm due to the transition of electrons from $^4F_{3/2}$ to $^4I_{11/2}$ level [50-52]. However, there are also transitions at other wavelengths [53-57], although at room temperature they have lower gain along with a higher threshold value than the 1064 nm transition and the wavelength selection optics limit the oscillation to 1064 nm [36]. Subsequently, a lithium triborate (LBO: $LiBi_3O_5$) nonlinear crystal [58-62] is used to double its frequency [63-65] in order to convert the output wavelength to λ = 532 nm. As the efficiency of the LBO crystal is sensitive to temperature and humidity of the surrounding environment, it is important to maintain the crystal at the appropriate phase-matching temperature and a prescribed humidity value to optimize

its efficiency and to keep the output fixed at λ = 532 nm. This is achieved by using a temperature regulating oven while it is constantly purged by dry N_2. As the crystal itself keeps the fundamental and the second harmonic beams collinear (noncritically phase-matched) [58,66-68], a rigorous alignment of the Millennia cavity is not required. Again, a large acceptance angle makes it insensitive to any slight misalignment within the Millennia. Though the LBO crystal has a lower nonlinear coefficient [69] than other materials, these advantages make it very useful for frequency doubling in the Millennia. A mechanical shutter is also attached to the cavity to block the output beam when required.

4.3.1.1.C. Titanium (Ti):sapphire (Al_2O_3) Laser

The output of DPSS finally pumps a Ti:sapphire (Ti:Al_2O_3) oscillator (Tsunami) [38]. Here, the lasing medium is Titanium ions (Ti^{3+}) doped sapphire (Al_2O_3) crystal [70-72]. Tsunami employs regenerative acousto-optic mode locking mechanism [41,73-75] to produce the output laser pulses of ~ 80 fs pulse width at 80 MHz repetition rate, with output wavelength tunable between 700 nm to 1080 nm. To achieve that, a longer cavity is required, which is obtained by a ten-mirror folded arrangement. However, the generation of a shorter pulse comes with a greater frequency distribution within a pulse, due to the Heisenberg uncertainty principle (time-bandwidth product of a Gaussian pulse is 0.441). As the refractive index (r.i.) depends on frequency, there is a distribution of r.i. in a pulse resulting in a variation of velocity over wavelength. The variation is called the group velocity dispersion (GVD) [76-78]. In Tsunami, the intracavity GVD, the working frequency and corresponding bandwidth of the output laser can be controllably tuned using a four prism and slit arrangement. Although the wavelength of the oscillator is tunable, the wavelength is kept fixed at $\lambda \approx$ 800 nm in our experiment as the Si-based detectors used during the experiment are most sensitive near that wavelength.

4.3.1.2. Second Harmonic Generator (SHG)

One part of the output beam from Tsunami is fed to one SHG to produce the second harmonic beam of wavelength λ = 400 nm, which is used to pump the sample. The pulses of the other part of the beam are time delayed and used to probe the dynamics. Inside the SHG cavity, a nonlinear crystal [79] of barium beta-borate (BBO) [80-84] is utilized for the frequency doubling. A BBO crystal [85,86] has higher conversion

efficiency than an LBO crystal as well as this crystal does not require any heater, unlike the LBO system. A prism separates the second harmonic from the residual fundamental beam. The fundamental beam, however, cannot pass through because of the highly reflective coating on the prism at near-infrared wavelength. The second harmonic is then guided to the output end by a pair of prisms which make the beam roughly parallel to the fundamental beam and compensate the beam ellipticity. These prisms also have antireflection (AR) coating at second harmonic wavelength to minimize any reflection loss from prism surfaces.

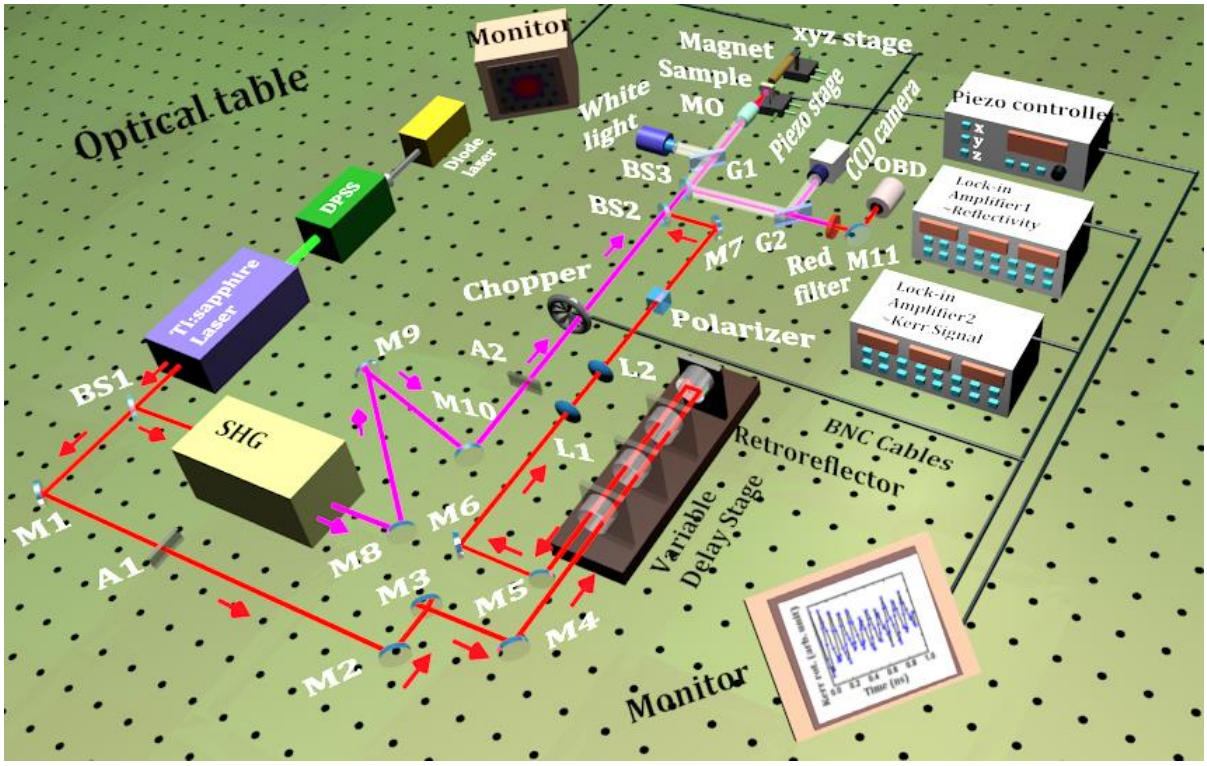

Figure 4.4. Schematic illustration of the time-resolved magneto-optical Kerr effect (TRMOKE) microscope.

4.3.2. Experimental Set-up of TRMOKE Microscopy

The customised TR-MOKE microscope present in the laboratory (Figure 4.4) of Prof. Anjan Barman at the S. N. Bose National Centre for Basic Sciences relies upon a two-color collinear pump-probe geometry [2,87,88], where the axes of both pump beam (the second harmonic output with wavelength λ_{pump} = 400 nm) and probe beam (the fundamental beam with wavelength λ_{probe} = 800 nm) are superposed before they are made incident on the sample. The fundamental beam from the Titanium (Ti): sapphire

pulsed laser source is divided into two parts by a 70:30 beam splitter. The intense part goes through the SHG to produce the pump beam, which is then guided towards the sample with the help of steering mirrors. The other part (the fundamental probe beam) goes through a retro-reflector fixed on an automated variable delay stage on the path of the probe beam. By moving the retro-reflector back and forth it is possible to introduce the desired optical path difference between pump and probe beams, which actually corresponds to the time delay in this experiment. Subsequently, both the beams are spatially overlapped using a beam combiner and are collinearly focused onto the sample using a single microscope objective (MO: M-40X with numerical aperture, N. A. = 0.65). The MO focuses the probe beam to a diffraction limited spot size (~ 800 nm) on the sample surface while the pump beam becomes slightly defocused with a spot size of ~ 1 μm because of chromatic aberration. The higher intensity of the pump beam perturbs the equilibrium magnetization of the sample, thereby inducing the dynamics. The dynamics affect the Kerr rotation of the reflected probe beam, which is in turn dependent on the time delay between pump and probe pulses. By changing the retro-reflector position on the delay stage by small steps, the time evolution of the magnetization dynamics (along with the total reflectivity signal) is measured by an optical bridge detector (OBD) and two lock-in amplifiers (to record Kerr signal and reflectivity data; Model: SR830 DSP, Stanford Research Systems) in a phase-sensitive manner (the operation of OBD is described in the static-MOKE section of chapter 3). The direction of the applied bias magnetic field is slightly tilted with respect to the magnetic anisotropy direction, so as to get a finite demagnetizing field along the direction of the pump pulse.

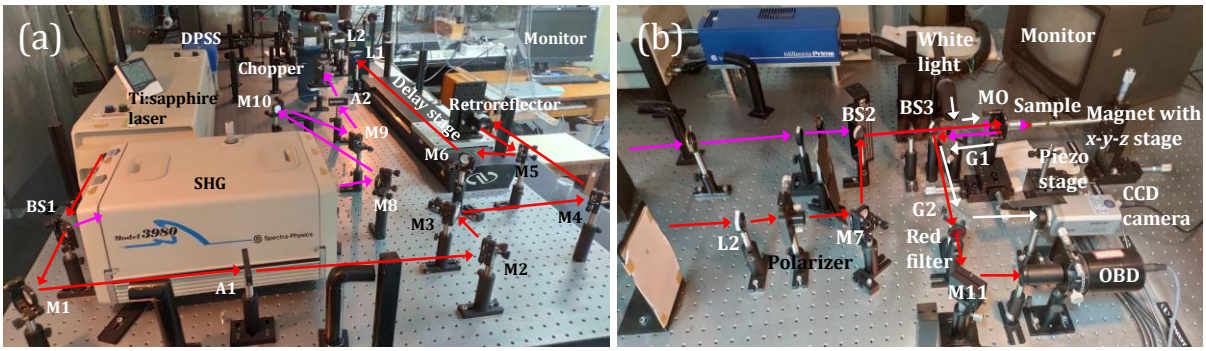

Figure 4.5. A photograph of the all-optical time-resolved magneto-optical Kerr effect (TR-MOKE) microscope present in the laboratory of Prof. Anjan Barman at the S. N. Bose

National Centre for Basic Sciences, Kolkata, India. The red and violet arrows represent the directions of the probe (fundamental) and pump beams, respectively, while the white arrows describe the path of the white light used for viewing the sample.

A typical time-resolved Kerr rotation data obtained from a 20-nm-thick NiFe film has been demonstrated in Figure 4.6(a) where the different temporal regions are indicated. The region I (t < 0) is also known as negative delay region where the sample is probed before the arrival of pump pulse and the equilibrium magnetization under external bias field is obtained. Region II contains a sharp demagnetization (within hundreds of fs) followed by a fast relaxation (Region III). In Region IV, a slower relaxation is observed together with a precession of magnetization around its new equilibrium position. Figure 4.6(b) illustrates the precessional oscillation data extracted by subtracting the bi-exponential background. The corresponding fast Fourier transform (FFT) spectrum is presented in Figure 4.6(c) which gives the precession frequency.

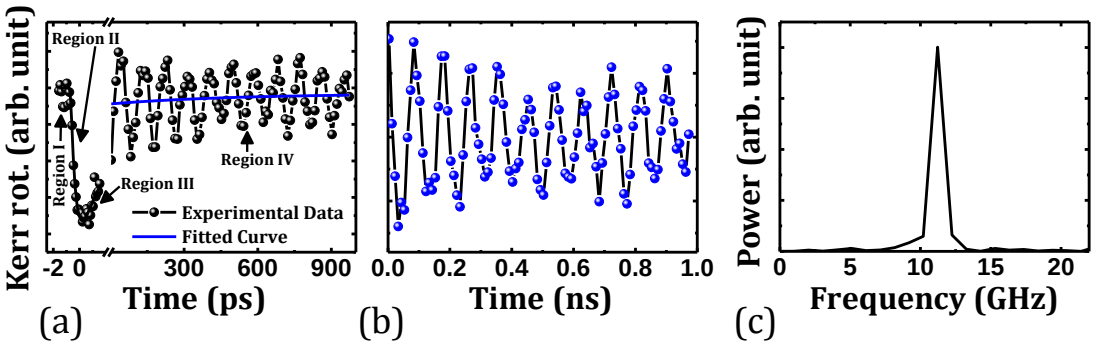

Figure 4.6. (a) Typical time-resolved Kerr rotation data taken from a $Ni_{80}Fe_{20}$ sample of 20 nm thickness with an in-plane bias field of 1.3 kOe. (b) Precessional oscillation part of the time-resolved data and (c) the corresponding precessional frequency after performing fast Fourier transformation.

4.3.3. Routine Alignments during Experiment

The collinear alignment of the pump and probe beam is very vital in our TRMOKE microscope. Therefore, some routine alignment steps are performed on a regular basis:

1. Firstly, using external micrometer controllers of Tsunami, the power of the Tsunami output is maximized while, the spectrum is optimized for desired central wavelength (λ_{probe} = 800 ± 2 nm) and FWHM (~ 12 nm or more).

2. The retro-reflector (RR) alignment is checked by observing the position of the beam after RR. If the beam moves by moving the RR position, mirrors before RR are adjusted to stop the shift.

3. The overlap between the pump and probe beams is checked after the beam combiner. If the alignment is correct, both the beams will follow the same path (i.e. collinear geometry).

4. Next, we check whether the beams are co-axial with the microscope objective (MO). For that, we check the beam positions at the back aperture of MO. Any misalignment of the beams is adjusted by changing the tilts of the respective mirrors. The adjustment is fine-tuned by monitoring the pump and probe beam spots falling on to a substrate by a CCD camera. The MO is moved back and forth about the position of its focal point and any consequent movement of the centre(s) of the pump and/or probe spot(s) on the screen implies that the beam(s) is (are) not co-axial with the MO.

5. Finally, the alignment of the OBD is adjusted by superposing the back-reflected beam from OBD with the incident beam.

6. After adjusting the optical components, the time-resolved reflectivity data from a standard Si substrate is recorded and its relaxation rate is compared with the standard data to verify the alignment condition of the delay stage and followed by this, the acquisition of the data from the magnetic specimen is being started.

4.4. Brillouin Light Scattering (BLS)

This is a spectroscopic tool where a monochromatic laser is made incident on the sample surface. Despite a great fraction of the incident beam getting absorbed or reflected, a small fraction of the light gets scattered from thermally excited SWs [89]. This can be split into two main sections where one is elastic scattering while, the other one is inelastic scattering [90]. Photon's energy or frequency remains unaltered inelastic scattering (e.g. Rayleigh scattering [91]). However, a shift in the angular frequency occurs in the inelastic scattering [92] which forms the basis of the SW detection in this method. During the work presented in this dissertation, 180°-backscattering geometry [93-96] has been used where the scattered light is collected by the same lens that has been used for incident beam within a solid angle in a direction 180° from the incident beam. Such an arrangement is advantageous because the magnitude of the SW wavevector involved in the scattering procedure gets maximized.

Afterwards, this backscattered beam is analyzed in frequency domain with the aid of a multi-pass tandem Fabry- Pérot interferometer (TFPI) [97-101] to excerpt the information about the bulk and surface magnons [102-105]. Here, the works presented in this thesis will focus on the use of BLS system to measure SW excitations in thin film heterostructures as well as nanopatterned systems. Over the last few decades, BLS has been developed to become a puissant and versatile technique in magnetic research due to the following advantages:

1. This novel method has wide flexibility in terms of measuring samples with frequency-, phase-, time- and spatial resolutions [16,17,106-110].
2. It is primarily designed to investigate the dispersive nature the SWs arising from the thermal excitations [111-113] (i.e. in the absence of any external stimulation) and the works present in this thesis have been carried out in ambient (room) temperature.
3. This can investigate the SW response over a broad frequency range up to 500 GHz with 50 MHz resolution.
4. It can be employed to investigate SW dispersions with various absolute values and orientations of the corresponding wavevectors.
5. The information about the properties of magnetic layers, e.g. magnetic damping, magnetic anisotropy, saturation magnetization as well as coupling parameter between different magnetic layers can be extracted.

4.4.1. Instrumentation

4.4.1.1. Laser

For a precise and accurate measurement of SW frequencies, laser light of single frequency mode with narrow bandwidth is indispensable. To meet this requirement, a 300 mW Excelsior solid state continuous wave (CW) laser [114-116] is used in the experiment. The laser system consists of a laser head, together with a separate controller unit, which routes the electrical power and monitors the signal between the laser head and the master system. Here a diode laser is used to pump the Nd^{3+} ions doped in the crystal of yttrium vanadate (Nd: YVO4), which emits photons at 1064 nm. This infrared (IR) output is further transformed to visible light by sending it through a non-linear crystal, lithium triborate (LBO) for frequency doubling (i.e. wavelength λ = 532 nm). The emitted laser beam has a diameter of ~ 670 µm with a beam divergence of about 1.03 mrad. Overall, the laser system is extremely reliable and stable in terms of

output power and beam divergence and requires no external adjustments during normal operation.

4.4.1.2. Tandem Fabry-Pérot Interferometer (TFPI)

The frequency analysis of SWs can be a critical challenge of BLS spectroscopy as it demands a very high spectral resolution. Generally, the observed magnon frequency lies within 300 GHz (~ 10 cm^{-1}) which is approximately 10^5 times smaller than that of a typical excitation frequency of laser beam. Also, the cross section of the inelastic scattering of photons is very small in comparison with that of elastic scattering. Hence, high contrast is necessary for efficacious detection of the fractional part of incident laser power with a large signal to noise ratio (SNR). The above criteria are achieved by implementing a Tandem Fabry-Pérot Interferometer (TPFI) in the BLS tool. TFPI is comprised of two single FPIs placed in series while the laser beam passes each FPI thrice in which is depicted in Figure 4.7. In the following, transmission characteristics of a single FPI followed by the tandem operation will be briefly discussed below.

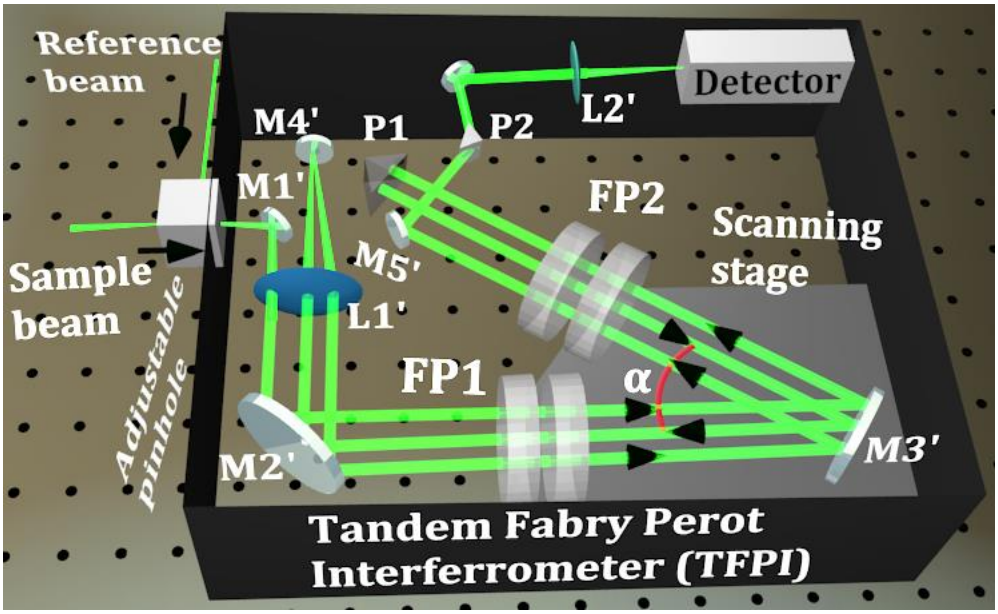

Figure 4.7. Schematic of the optical arrangement of a tandem Fabry-Pérot interferometer (TFPI).

4.4.1.2.A. Fabry-Pérot Interferometer (FPI)

One typical FPI (or etalon) [117-120] has two planar, partially reflecting mirrors mounted accurately parallel to each other at a distance (L). The light passing the FPI suffers multiple back and forth reflections and transmissions. Meanwhile, interference

between these beams forms the criterion for constructive interference for normal incidence as expressed by:

$$L = \frac{n\lambda}{2} \tag{4.1}$$

where, n is an integer (transmission order) and λ denotes the wavelength of the light. The frequency gap Δf between consecutive orders of interference is given by:

$$\Delta f = \frac{c}{2L} \tag{4.2}$$

Here, c denotes the velocity of light (3×10^8 m/s). The free spectral range (FSR) of the interferometer is defined by this inter-order spacing. Finesse (F) of the interferometer is related to FSR as the following:

$$F = \frac{\Delta f_{\mathrm{FSR}}}{\Delta f_{\mathrm{FWHM}}} \tag{4.3}$$

where, Δf_{FWHM} is the full width at half maximum (FWHM) of the transmission spectrum. The transmitted intensity (I_t) of the FPI is related with the finesse through the following expression:

$$\Delta I_t = \frac{I_0}{1+\left(\frac{4F^2}{\pi^2}\right)\sin^2\left(\frac{2\pi L}{\lambda}\right)} \tag{4.4}$$

where, I_0 represents the incident light intensity. Equation 4.4 is also known as the Airy function which describes the periodicity of transmitted intensity with frequency and mirror spacing. Here, F can be considered as a measure for the quality of the instrument which is related to the reflectivity (R) of the FP etalons through the following expression:

$$F = \frac{\pi\sqrt{R}}{1-R} \tag{4.5}$$

Therefore, a higher reflectivity not only increases F but also enhances the frequency resolution as Δf_{FWHM} decreases. Meanwhile, if R is kept fixed, enhancement in L decreases F which improves the frequency resolution as F is maintained to be constant. The contrast (C) of an FPI is defined as the following:

$$C = 1 + \frac{4R}{(1-R)^2} \tag{4.6}$$

The contrast for an n-pass interferometer is the n^{th} power of that of a single-pass one, e.g. a six-pass interferometer can attain a contrast of at least six or more orders of magnitude better than that of a single-pass interferometer.

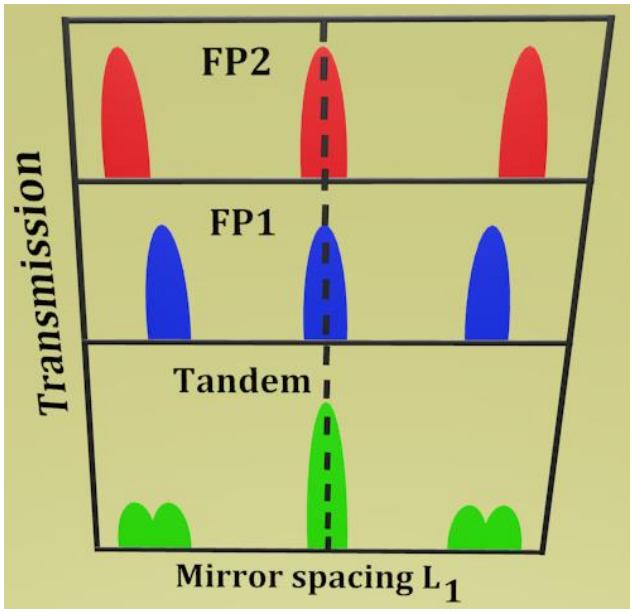

Figure 4.8. Transmission Spectra of FP1 and FP2 and in tandem operation.

4.4.1.2.B. Tandem Configuration of Fabry-Pérot Interferometer

The periodicity of transmitted intensity as a function of the mirror spacing can become a major concern which is inherent to FPI. The fact that the transmission characteristic repeats every FSR creates certain problems in the identification of the frequencies present in the scattered light. For instance, for a fixed mirror spacing L there are two wavelengths (λ_1 and λ_2) present in the measured light which can be expressed as:

$$2L = m_1\lambda_1 = m_2\lambda_2 \tag{4.7}$$

Thus, the transmission condition is satisfied for both the wavelengths of different orders. As the reference beam determines the order of transmission spectrum, the order of the second wavelength (which does not match with that of the reference beam) and consequently, the wavelength itself remains inaccessible. Also, it is challenging to identify unambiguously whether a peak signal belongs to the Stokes side of a specific transmission order or it belongs to the anti-Stokes side of the previous order. Hence, the interferometer is employed in a tandem configuration [118,121] in order to address these shortcomings. In this case, the light passes consecutively through two interferometers (FP1 and FP2) which are mounted at an angle (α) to each other as illustrated in Figure 4.7. The right mirror of each FPI is placed on the translation stage and the other one on a separate angular orientation device. The scanning stage can

move the right mirror of each pair along the optical axis of FP1. A displacement (d) of the translation stage can change the mirror distance in FP1 by:

$$\Delta L_1 = d \tag{4.8}$$

while, that change in FP2 is:

$$\Delta L_2 = \Delta L_1 \cos \alpha \tag{4.9}$$

This also satisfies the synchronization condition as the following relation:

$$\frac{\delta L_1}{\delta L_2} = \frac{L_1}{L_2} \tag{4.10}$$

This can be used for suppression of the intermixing of different orders. For that, each FPI is adjusted to transmission separately before the scanning of the linear stage. Although their transmission orders are different, they together provide a central transmission order which can be adjusted by varying the mirror spacing of FP2 as described in Figure 4.8. The other orders are suppressed at the same time because the FSR of the two FPIs become different. Also, this arrangement enhances the FSR of the final spectrum without affecting the resolution. Now, when the stage is moved, the change in the mirror spacing is given by the following:

$$l_1 = L_{10} + d \tag{4.11}$$

$$l_2 = (L_{10} + d) \cos \alpha \tag{4.12}$$

where, l_1 and l_2 correspond to the changes in mirror spacing for FP1 and FP2, respectively while, L_{10} is the initial mirror spacings of FP1 (i.e. at d = 0). The aforementioned ambiguities can be removed by this technique as the transmission order is now fixed. In addition, the light passes through each FPI thrice to improve the contrast. After the six passes through the FPIs, the light is eventually directed to a photomultiplier which counts the number of transmitted photons as a function of the mirror spacing (subsequently, as a function of the frequency shift). To achieve this, the scanning stage constantly sweeps the distance corresponding to the required frequency window and the data is acquired for a long time to attain sufficient statistics. In this way, the acquired BLS intensity is proportional to the SW intensity at a given frequency.

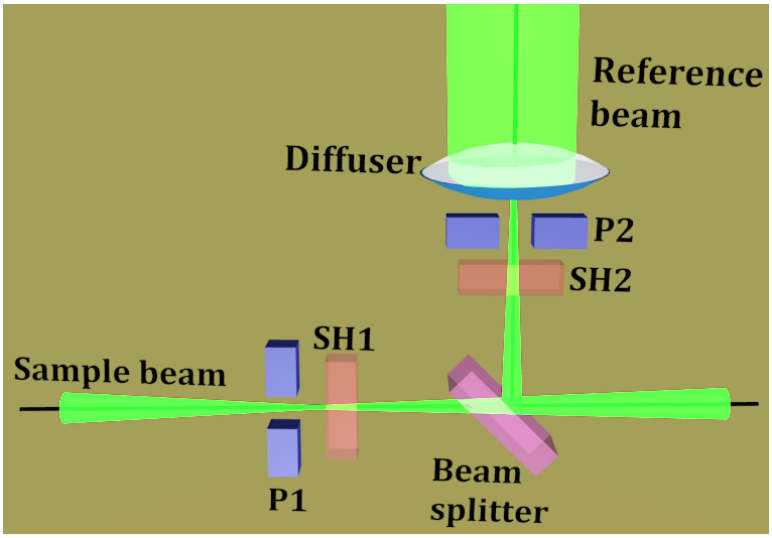

Figure 4.9. Pictorial representation of the pinhole and light modulator arrangement inside the TFPI of BLS system.

4.4.1.2.C. The Pinhole and Light Modulator

The light modulator is basically a double shutter system situated right behind the entrance pinhole of the TFPI which is shown in Figure 4.9. Together with the TFPI in operation, the shutters SH1 and SH2 are alternately opened, thereby controlling the light intensity that ultimately reaches the photon detector. Since the detector is a single photon counter, strong elastic light can cause damage to the detector. Thus, to protect it, this device operates in synchronization with the scanning stage as illustrated in Figure 4.10.

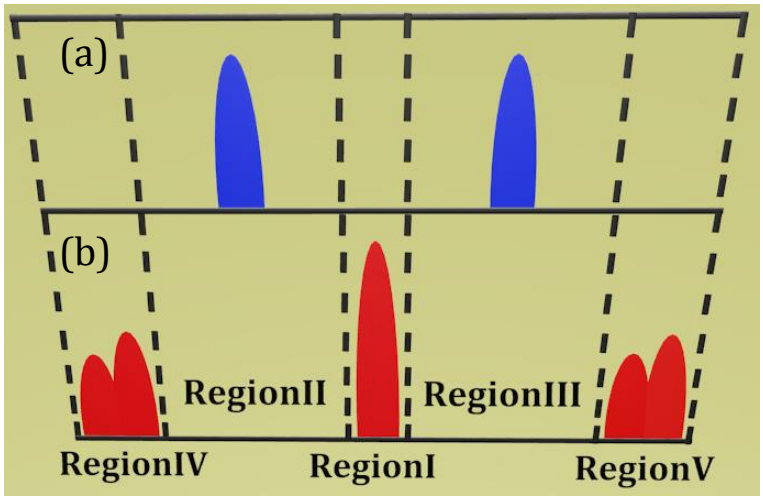

Figure 4.10. The part of the BLS spectrum that corresponds to when one of the shutters (SHs), i.e. either (a) SH1 or (b) SH2 is open. A superposition of the spectra in (a) and (b) is acquired when SH1 and SH2 operate in synchronization.

Here, Figure 4.10(a) presents the spectrum of the scattered signal captured by the first pinhole (P1), while, Figure 4.10(b) depicts that of the reference beam entering through the second pinhole (P2). During the scanning of the elastic peak (i.e. region I, IV and V), P1 is blocked and P2 is opened, allowing the reference beam to enter through it. This small intensity reference beam is further used to maintain the stabilization of the angular orientation of the FPIs. On the contrary, during the scanning for the Brillouin shifts (i.e. in regions II and III), P2 is closed but P1 is opened.

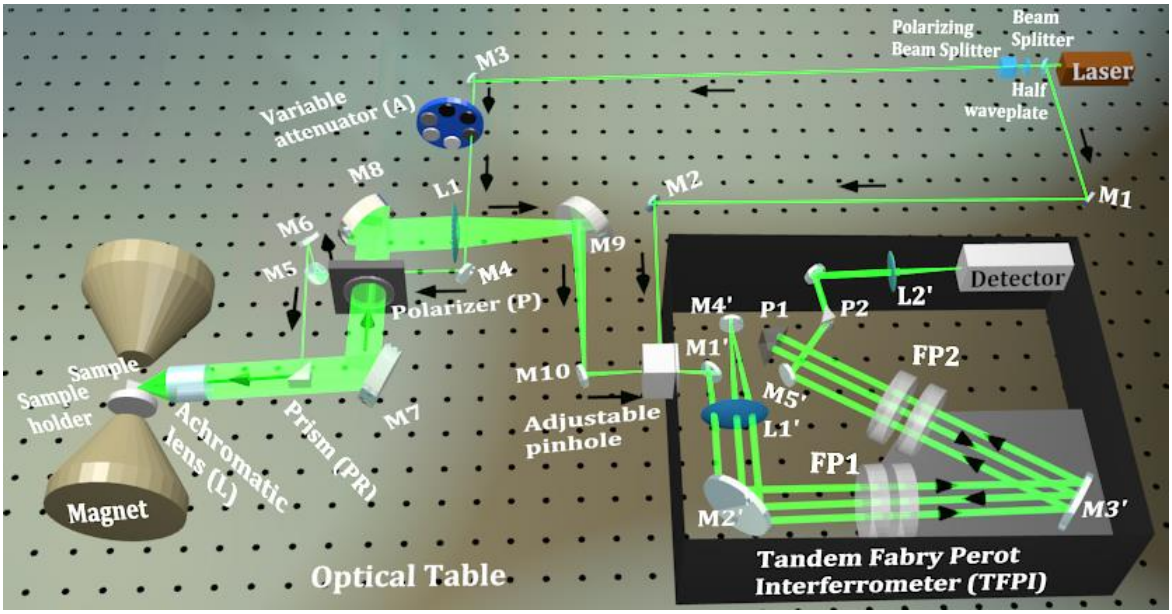

Figure 4.11. Schematic demonstration of conventional Brillouin light scattering (BLS) spectrometer.

4.4.2. Experimental Set-up

The inelastically scattered beam from a magnetic specimen carries information about the frequency and wavevector of the involved SW or magnon mode where the intensity of the scattered light is proportional to the intensity of SW. Generally, the BLS technique can work in two different measurement geometries:

4.4.2.1. Forward-scattering Geometry

Here, the scattered beam is recorded after transmission of the probing beam through a transparent sample.

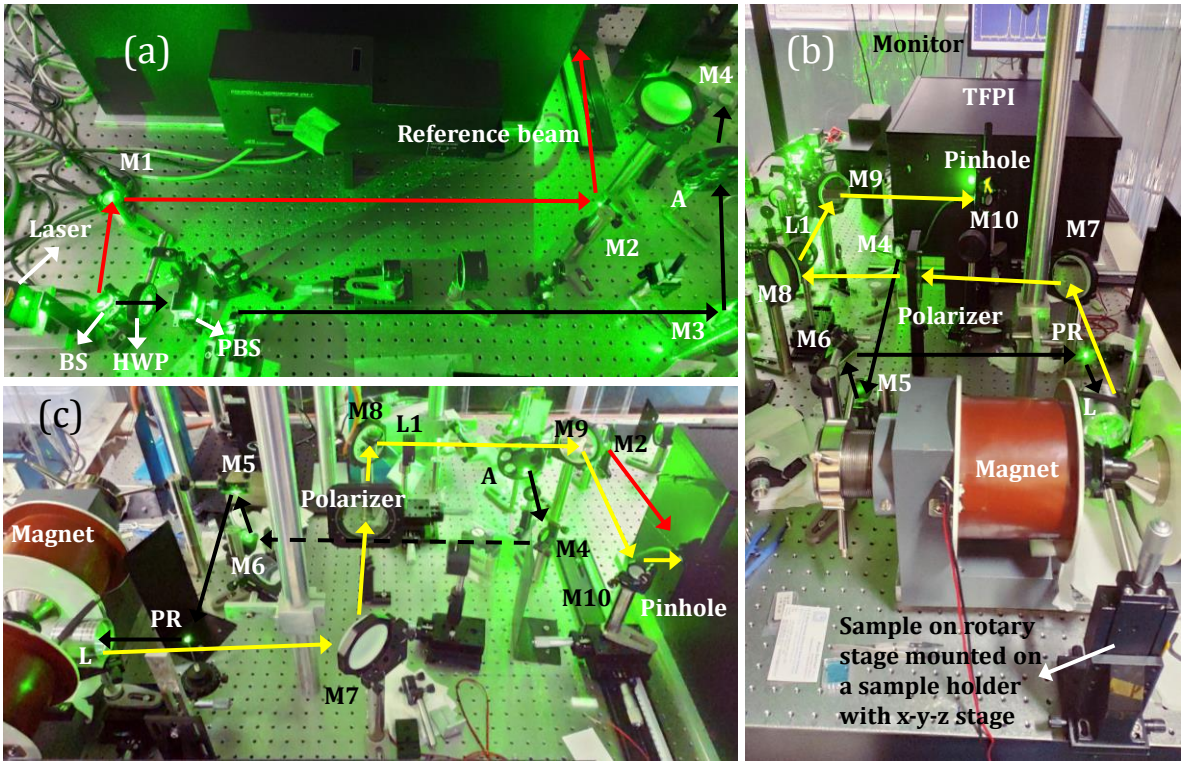

Figure 4.12. Pictorial demonstration of conventional Brillouin light scattering (BLS) spectrometer present in the lab of Prof. Anjan Barman at the S. N. Bose National Centre for Basic Sciences, Kolkata, India. The red arrows describe the direction of the reference beam while the black arrows denote the beam direction to be incident onto the sample. The yellow arrows in (b, c) describe the path of the back-scattered beam from the sample to the TFPI via the pinhole.

4.4.2.2. Backscattered Geometry

In this case, the beams which are backscattered from the surface of the opaque sample are measured. This geometry can be further incorporated to develop BLS microscopy (i.e. micro-BLS) where the SW profiles can be mapped in space-, time- or phase-resolved manner. Here, the conventional backscattered geometry has been explained that has been used during the work presented in this dissertation. Figure 4.11 demonstrates the schematic of the conventional BLS arrangement.

The laser light (λ = 532 nm) is split into two beams right after the solid-state laser using a 10:90 beam splitter (BS). The smaller part of the laser is directed straight to the TFPI using mirrors M1 and M2, where it serves as the reference beam. There are several purposes of this reference beam which are:

1. This is employed for the stabilization of the mirror spacing of the FP etalons.

2. This beam generates the central elastic peak in a BLS spectrum which helps in determining the frequency shift of the scattered beam with respect to the incident beam.

3. The reference beam is used to estimate the transmission order of the FP etalon which in turn helps to deduce the frequencies present in the scattered light.

Meanwhile, the intense beam is first sent through one half wave plate (HWP) and a polarized beam splitter (PBS) to eliminate the small in-plane polarized component from the partially polarized beam of the laser. The beam (which is perpendicularly polarized with respect to the optical table) is then guided by the mirrors M3, M4, M5, M6 and PR towards the specimen which is kept between the pole pieces of an electromagnet (sometimes a permanent magnet is used depending upon the requirement of the experiment) which produces the bias magnetic field to the sample. Interestingly, the mirror PR is chosen in the form of a very small prism mirror in order to minimize the blocking of the backscattered beam by it. Eventually, the scattered beam is focused on the sample by an achromatic doublet lens (L with numerical aperture, N. A. = 0.26). The sample is mounted on a high precision rotation stage (angular resolution 1°). The change in the rotation angle modifies the angle of incidence accordingly which addresses different transferred SW wavevector (k) according to the following relation:

$$|k| = |k_{\mathrm{i}} \sin\theta - k_{\mathrm{s}} \sin\theta| = 2|k_{\mathrm{i}}| \sin\theta \qquad (4.13)$$

Here, k_{i} and k_{s} are the wavevectors of the incident and scattered photons while, θ is the angle of between k_{i} and normal to the sample surface. A variable attenuator (A) is placed between M3 and M4 in order to control the power of the incident laser beam on to the sample.

The measurements are performed for various magnetic field values at different wavevectors of transferred SW in various geometry depending upon the relative orientation among wavevector, bias magnetic field (sets the magnetization direction of the sample) and sample plane. Subsequently, the scattered beam is collected by the same lens and continues its way towards the entrance pinhole of a (3+3)-pass TFPI (JRS Scientific Instrument) for frequency analysis using a focusing lens L1 and guiding mirrors M8, M9 and M10 respectively. To isolate the light scattered by SWs from that by phonons, a polarizer (P) set at a crossed position is placed in the path of the scattered

light which helps to suppress the elastically scattered beam as well as the beam containing the signal from phonons.

Inside the TFPI, the beam hits mirror M1' and then reaches FP1 through lens L1' and mirror M2'. After passing through FP1, the beam undergoes its first pass until it is reflected from M3' and passes through FP2. Then the beam is reflected from one prism (PR1') and traces back its path via FP2 and FP1 and reaches M4'. The beam is once again reflected at M4', and thus it gets redirected, passes through FP1 and FP2 for the third time to finally reach the single-photon counter (D) after passing through a prism (PR2'), two mirrors (M5' and M6') and one lens (L2'). Here, the resulting light has a very low intensity which is detected by the single photon counter and the signals are sent to a computer for storage and analysis.

4.5. Pros and Cons of the Magnetization Dynamics Measurement Tools

Here, the advantages and disadvantages associated with investigating magnetization dynamics using various experimental techniques have been briefly discussed. A great deal of important insights into the spin dynamics has been obtained in this thesis from magnetic measurements using FMR, TRMOKE and BLS techniques. However, the correct experimental technique to be applied for a specific study is determined by the type of information to be extracted from the spin dynamics of a magnetic system.

The broadband FMR tool can explore the magnetization dynamics which is acquired directly in the frequency domain by sweeping the frequency over a broad window at a fixed magnetic field (or vice versa) with a high frequency (or magnetic field) resolution. Since this is a global measurement technique (i.e. the whole magnetic sample is excited) to probe the magnetization dynamics, a rich information about the spin dynamics can be achieved without any undesirable or spurious modes arising due the artefacts (e.g. effect of boundary or the local defects present the sample) which are usually present in a local measurement method. Due to relatively quick and simple calibration procedures, this robust tool becomes ideal for the investigation of spin dynamics in magnetic thin films especially patterned FM structures (MCs) where multimodal magnon spectra is present [122,123], while the damping parameter can be easily extracted by calculating the linewidths of the acquired spectra [124,125]. However, its primary drawback is that complicated and expensive lithography is required to investigate the magnetization dynamics in patterned structures unlike local detection methods and it is also difficult

to probe the dynamics in a single element using FMR method. Here, the selective wavevector information can be obtained by involved microfabrication of waveguide structure to investigate the magnon dispersion although this becomes critical in case of ultrathin films.

The TRMOKE technique offers an extremely high temporal resolution while probing magnetization dynamics at various time scales including ultrafast demagnetization, mechanisms of magnetization relaxation and other nonlinear phenomena and also the carrier and phonon dynamics. It is extremely advantageous while measuring the damping parameter of a magnetic material directly in the time domain from the decaying precessional profile. Also, TRMOKE method is highly localized because of the focused laser spot which reduces the problems of variations and inhomogeneities from larger area averaging. Here, the probed area can be much smaller (sub-μm) which is significantly smaller than the probe area in frequency domain-based method [126]. Such localized measurements can thus give a better representation of the local precession, damping as well as the local physical environment which influences the magnetization dynamics. TRMOKE can also be employed to map the modulation in precession and damping behaviour across the sample. A key advantage is that the modal composition of the magnetization oscillations can be obtained in the time domain and the damping for each mode can be measured. Also, it has been extensively utilized to investigate the local precessional dynamics in nanomagnet arrays or even in a single nanomagnet [88,127]. An all-optical TRMOKE tool can probe a magnetic specimen in any form of a thin film or bulk material with the optically polished surface without the requirement of fabrication of complicated device structure for excitation of spin waves. Recently, it has also been used to efficiently detect various interface and spin-orbit effects [128,129]. Howbeit, the primary disadvantages of this method are that the optical alignment is very sensitive and non-trivial, measurement is rather time-consuming and it involves expensive equipment.

On the other hand, the primary advantage of BLS is its wavevector sensitivity which allows the investigation of SW frequency versus wavevector dispersion in various geometry in FM thin films, multilayers and patterned nanostructures. Particularly for patterned FM nanostructures (i.e. MCs), it can provide valuable information about magnon bandgap and group velocity [130]. One of the main advantages of BLS over all

competing techniques is its remarkable sensitivity down to monolayer of magnetic material thickness which enables to investigate different interfacial effects present in the magnetic heterostructures [131]. It allows the detection of thermally activated SWs in systems even without any external excitation in a non-invasive manner. Hence, this enables the flexible realization of different measurement geometries to probe magnon dynamics over a wide wavevector and spectral range. Micro-focused BLS can be employed for imaging the propagating SW which provides important insights to the operation of novel SW-based devices. This novel method also offers measurement of SWs with phase and temporal resolutions. The primary disadvantage of this method is its high cost and sensitive optical alignment procedure. Measurement of thermal magnon is also very slow due to the absence of any external stimuli (e.g. current etc.).

References

[1] S.-K. Kim, J. Phys. D: Appl. Phys. 43 (2010) 264004.
[2] A. Barman, A. Haldar, in *Solid State Physics*, edited by R. E. Camley, and R. L. Stamps (Academic Press, 2014), p. 1.
[3] C. Kittel, Phys. Rev. 73 (1948) 155.
[4] J. H. E. Griffiths, Nature 158 (1946) 670.
[5] V. P. Denysenkov, A. M. Grishin, Rev. Sci. Instrum. 74 (2003) 3400.
[6] M. R. Freeman, M. J. Brady, J. Smyth, Appl. Phys. Lett. 60 (1992) 2555.
[7] M. van Kampen, C. Jozsa, J. T. Kohlhepp, P. LeClair, L. Lagae, W. J. M. de Jonge, B. Koopmans, Phys. Rev. Lett. 88 (2002) 227201.
[8] A. Kirilyuk, A. V. Kimel, T. Rasing, Rev. Mod. Phys. 82 (2010) 2731.
[9] W. K. Hiebert, A. Stankiewicz, M. R. Freeman, Phys. Rev. Lett. 79 (1997) 1134.
[10] L. Brillouin, Ann. Phys. 9 (1922) 88.
[11] S. O. Demokritov, B. Hillebrands, A. N. Slavin, Phys. Rep. 348 (2001) 441.
[12] T. Sebastian, K. Schultheiss, B. Obry, B. Hillebrands, H. Schultheiss, Front. Phys. 3 (2015).
[13] H. J. J. Liu, G. A. Riley, C. L. Ordóñez-Romero, B. A. Kalinikos, K. S. Buchanan, Phys. Rev. B 99 (2019) 024429.
[14] M. Bauer, O. Büttner, S. O. Demokritov, B. Hillebrands, V. Grimalsky, Y. Rapoport, A. N. Slavin, Phys. Rev. Lett. 81 (1998) 3769.
[15] K. Vogt, H. Schultheiss, S. J. Hermsdoerfer, P. Pirro, A. A. Serga, B. Hillebrands, Appl. Phys. Lett. 95 (2009) 182508.
[16] T. Schneider, A. A. Serga, T. Neumann, B. Hillebrands, M. P. Kostylev, Phys. Rev. B 77 (2008) 214411.
[17] O. Büttner, M. Bauer, S. O. Demokritov, B. Hillebrands, Y. S. Kivshar, V. Grimalsky, Y. Rapoport, A. N. Slavin, Phys. Rev. B 61 (2000) 11576.
[18] D. F. Williams, J. C. M. Wang, U. Arz, IEEE Trans. Microw. Theory Tech. 51 (2003) 2391.

[19] T. V. d. Broeck, J. Verspecht, in *1994 IEEE MTT-S International Microwave Symposium Digest (Cat. No.94CH3389-4)*1994), pp. 1069.
[20] A. Ferrero, F. Sampietro, U. Pisani, IEEE Trans. Microw. Theory Tech. 42 (1994) 2455.
[21] R. B. Marks, J. A. Jargon, J. R. Juroshek, in *48th ARFTG Conference Digest*1996), pp. 38.
[22] L. A. Hayden, V. K. Tripathi, IEEE Trans. Microw. Theory Tech. 41 (1993) 415.
[23] J. T. Barr, M. J. Pervere, in *34th ARFTG Conference Digest*1989), pp. 51.
[24] J. A. Jargon, R. B. Marks, D. K. Rytting, IEEE Trans. Microw. Theory Tech. 47 (1999) 2008.
[25] L. F. Tiemeijer, R. J. Havens, A. B. M. Jansman, Y. Bouttement, IEEE Trans. Microw. Theory Tech. 53 (2005) 723.
[26] I. Novak, B. Eged, L. Hatvani, in *1993 IEEE Instrumentation and Measurement Technology Conference*1993), pp. 269.
[27] R. B. Marks, in *50th ARFTG Conference Digest*1997), pp. 115.
[28] D. E. Bockelman, W. R. Eisenstadt, IEEE Trans. Microw. Theory Tech. 46 (1998) 1009.
[29] A. Ferrero, F. Sanpietro, IEEE Microw. Wirel. Compon. Lett. 5 (1995) 119.
[30] A. Ferrero, V. Teppati, in *2006 IEEE MTT-S International Microwave Symposium Digest*2006), pp. 1456.
[31] J. Kerr, Philos. Mag. 3 (1877) 321.
[32] M. R. Freeman, R. R. Ruf, R. J. Gambino, IEEE Trans. Magn. 27 (1991) 4840.
[33] A. Barman, V. V. Kruglyak, R. J. Hicken, J. Scott, A. Kundrotaite, M. Rahman, J. Appl. Phys. 95 (2004) 6998.
[34] A. Barman, S. Wang, O. Hellwig, A. Berger, E. E. Fullerton, H. Schmidt, J. Appl. Phys. 101 (2007) 09D102.
[35] A. Barman, S. Wang, J. Maas, A. R. Hawkins, S. Kwon, J. Bokor, A. Liddle, H. Schmidt, Appl. Phys. Lett. 90 (2007) 202504.
[36] U. S. Manual, (Spectra-Physics, California, USA, 2007).
[37] U. S. Manual, (Spectra-Physics, California, USA, 2002).
[38] U. S. Manual, (Spectra-Physics, California, USA, 2002).
[39] P. D. Dragic, M. Cavillon, J. Ballato, Appl. Phys. Rev. 5 (2018) 041301.
[40] U. Keller, Nature 424 (2003) 831.
[41] J. Squier, F. Salin, S. Coe, P. Bado, G. Mourou, Opt. Lett. 16 (1991) 85.
[42] P. Zhang, Á. Valfells, L. K. Ang, J. W. Luginsland, Y. Y. Lau, Appl. Phys. Rev. 4 (2017) 011304.
[43] R. Szweda, *Diode Laser Materials and Devices - A Worldwide Market and Technology Overview to 2005* (Elsevier Science, 2001).
[44] J. Liu, W. Han, H. Zhang, X. Mateos, V. Petrov, IEEE J. Quantum Electron. 45 (2009) 807.
[45] J. L. Blows, T. Omatsu, J. Dawes, H. Pask, M. Tateda, IEEE Photon. Technol. Lett. 10 (1998) 1727.
[46] A. W. Tucker, M. Birnbaum, C. L. Fincher, J. W. Erler, J. Appl. Phys. 48 (1977) 4907.
[47] L. Yin, G. Q. Li, S. Z. Zhao, X. Li, K. Cheng, G. Zhang, Laser Phys. 21 (2011) 1151.
[48] C. Lu, M. Gong, Q. Liu, L. Huang, F. He, Laser Phys. Lett. 5 (2008) 21.
[49] N. Hodgson, K. D. Griswold, W. A. Jordan, S. L. Knapp, A. A. Peirce, C. C. Pohalski, E. A. P. Cheng, J. Cole, D. R. Dudley, A. B. Petersen, W. L. Nighan, *High-power TEM00-mode*

operation of diode-pumped solid state lasers (SPIE, 1999), Vol. 3611, Optoelectronics '99 - Integrated Optoelectronic Devices, p. PW.
[50] Y. F. Chen, T. M. Huang, C. F. Kao, C. L. Wang, S. C. Wang, IEEE J. Quantum Electron. 33 (1997) 1424.
[51] G. Turri, H. P. Jenssen, F. Cornacchia, M. Tonelli, M. Bass, J. Opt. Soc. Am. B 26 (2009) 2084.
[52] X. Délen, F. Balembois, P. Georges, J. Opt. Soc. Am. B 28 (2011) 972.
[53] Y. Yan, H. Zhang, Y. Liu, X. Yu, H. Zhang, J. He, J. Xin, Opt. Lett. 34 (2009) 2105.
[54] R. Zhou, B. Zhang, X. Ding, Z. Cai, W. Wen, P. Wang, J. Yao, Opt. Express 13 (2005) 5818.
[55] A. Sennaroglu, Opt. Commun. 164 (1999) 191.
[56] A.-Y. Yao, W. Hou, Y.-P. Kong, L. Guo, L.-A. Wu, R.-N. Li, D.-F. Cui, Z.-Y. Xu, Y. Bi, Y. Zhou, J. Opt. Soc. Am. B 22 (2005) 2129.
[57] A. Minassian, M. J. Damzen, Opt. Commun. 230 (2004) 191.
[58] S. P. Velsko, M. Webb, L. Davis, C. Huang, IEEE J. Quantum Electron. 27 (1991) 2182.
[59] D. N. Nikogosyan, Appl. Phys. A 58 (1994) 181.
[60] Z. Shuqing, H. Chaoen, Z. Hongwu, J. Cryst. Growth. 99 (1990) 805.
[61] J. Y. Zhang, J. Y. Huang, Y. R. Shen, C. Chen, J. Opt. Soc. Am. B 10 (1993) 1758.
[62] C. Chen, Y. Wu, A. Jiang, B. Wu, G. You, R. Li, S. Lin, J. Opt. Soc. Am. B 6 (1989) 616.
[63] E. Schiehlen, M. Golling, P. Unger, IEEE Photon. Technol. Lett. 14 (2002) 777.
[64] F. Seifert, J. Ringling, F. Noack, V. Petrov, O. Kittelmann, Opt. Lett. 19 (1994) 1538.
[65] J. Y. Zhang, J. Y. Huang, Y. R. Shen, C. Chen, B. Wu, Appl. Phys. Lett. 58 (1991) 213.
[66] J. Y. Huang, Y. R. Shen, C. Chen, B. Wu, Appl. Phys. Lett. 58 (1991) 1579.
[67] M. Jurna, J. P. Korterik, H. L. Offerhaus, C. Otto, Appl. Phys. Lett. 89 (2006) 251116.
[68] A. Nebel, C. Fallnich, R. Beigang, R. Wallenstein, J. Opt. Soc. Am. B 10 (1993) 2195.
[69] A. Yariv, P. Yeh, *Optical Waves in Crystals: Propagation and Control of Laser Radiation* (Wiley, 2002).
[70] J. Zhou, G. Taft, C.-P. Huang, M. M. Murnane, H. C. Kapteyn, I. P. Christov, Opt. Lett. 19 (1994) 1149.
[71] M. T. Asaki, C.-P. Huang, D. Garvey, J. Zhou, H. C. Kapteyn, M. M. Murnane, Opt. Lett. 18 (1993) 977.
[72] D. E. Spence, P. N. Kean, W. Sibbett, Opt. Lett. 16 (1991) 42.
[73] R. Roy, P. A. Schulz, A. Walther, Opt. Lett. 12 (1987) 672.
[74] P. A. Schulz, IEEE J. Quantum Electron. 24 (1988) 1039.
[75] P. F. Curley, A. I. Ferguson, Opt. Lett. 16 (1991) 321.
[76] D. Mogilevtsev, T. A. Birks, P. S. J. Russell, Opt. Lett. 23 (1998) 1662.
[77] N. Sarukura, Y. Ishida, H. Nakano, Opt. Lett. 16 (1991) 153.
[78] I. Zeylikovich, H. I. Sztul, V. Kartazaev, T. Le, R. R. Alfano, Opt. Lett. 32 (2007) 2025.
[79] Y. R. Shen, *The Principles of Nonlinear Optics* (Wiley, 1984).
[80] H. Liu, J. Yao, A. Puri, Opt. Commun. 109 (1994) 139.
[81] C. Chen, Y. Wang, Y. Xia, B. Wu, D. Tang, K. Wu, Z. Wenrong, L. Yu, L. Mei, J. Appl. Phys. 77 (1995) 2268.
[82] J.-y. Zhang, J. Y. Huang, H. Wang, K. S. Wong, G. K. Wong, J. Opt. Soc. Am. B 15 (1998) 200.
[83] P. Di Trapani, D. Caironi, G. Valiulis, A. Dubietis, R. Danielius, A. Piskarskas, Phys. Rev. Lett. 81 (1998) 570.
[84] A. Dubietis, G. Jonušauskas, A. Piskarskas, Opt. Commun. 88 (1992) 437.
[85] C. Chen, Z. Lin, Z. Wang, Appl. Phys. B 80 (2005) 1.

[86] C. Chen, T. Sasaki, R. Li, Y. Wu, Z. Lin, Y. Mori, Z. Hu, J. Wang, S. Uda, M. Yoshimura, Y. Kaneda, *Nonlinear Optical Borate Crystals: Principles and Applications* (Wiley-VCH, 2012).
[87] A. Barman, J. Sinha, *Spin Dynamics and Damping in Ferromagnetic Thin Films and Nanostructures* (Springer International Publishing, 2018).
[88] B. Rana, A. Barman, SPIN 03 (2013) 1330001.
[89] A. G. Gurevich, G. A. Melkov, *Magnetization Oscillations and Waves* 1996).
[90] B. J. Berne, R. Pecora, *Dynamic Light Scattering: With Applications to Chemistry, Biology, and Physics* (Dover Publications, 2000).
[91] A. T. Young, Appl. Opt. 20 (1981) 533.
[92] D. A. Long, *Raman Spectroscopy* (McGraw-Hill, 1977).
[93] J. R. Dutcher, S. Lee, J. Kim, G. I. Stegeman, C. M. Falco, Phys. Rev. Lett. 65 (1990) 1231.
[94] J. R. Dutcher, S. Lee, B. Hillebrands, G. J. McLaughlin, B. G. Nickel, G. I. Stegeman, Phys. Rev. Lett. 68 (1992).
[95] J. Jorzick, S. O. Demokritov, C. Mathieu, B. Hillebrands, B. Bartenlian, C. Chappert, F. Rousseaux, A. N. Slavin, Phys. Rev. B 60 (1999).
[96] Z. Wang, M. Kuok, S. Ng, D. Lockwood, M. Cottam, K. Nielsch, R. Wehrspohn, U. Gösele, Phys. Rev. Lett. 89 (2002) 027201.
[97] M. Vaughan, *The Fabry-Pérot Interferometer: History, Theory, Practice and Applications* (Taylor & Francis, 1989).
[98] S. M. Lindsay, A. J. Hartley, I. W. Shepherd, Polymer 17 (1976) 501.
[99] M. Čopič, M. Zgonik, Opt. Commun. 41 (1982) 310.
[100] S. M. Lindsay, M. W. Anderson, J. R. Sandercock, Rev. Sci. Instrum. 52 (1981) 1478.
[101] J. G. Dil, N. C. J. A. van Hijningen, F. van Dorst, R. M. Aarts, Appl. Opt. 20 (1981) 1374.
[102] J. R. Sandercock, W. Wettling, J. Appl. Phys. 50 (1979) 7784.
[103] L. Dobrzynski, B. Djafari-Rouhani, H. Puszkarski, Phys. Rev. B 33 (1986) 3251.
[104] P. Grünberg, F. Metawe, Phys. Rev. Lett. 39 (1977) 1561.
[105] J. Sandercock, W. Wettling, IEEE Trans. Magn. 14 (1978) 442.
[106] V. E. Demidov, S. O. Demokritov, K. Rott, P. Krzysteczko, G. Reiss, Appl. Phys. Lett. 92 (2008) 232503.
[107] P. Benassi, M. Krisch, C. Masciovecchio, V. Mazzacurati, G. Monaco, G. Ruocco, F. Sette, R. Verbeni, Phys. Rev. Lett. 77 (1996) 3835.
[108] F. Fohr, A. A. Serga, T. Schneider, J. Hamrle, B. Hillebrands, Rev. Sci. Instrum. 80 (2009) 043903.
[109] M. Covington, T. M. Crawford, G. J. Parker, Phys. Rev. Lett. 89 (2002) 237202.
[110] O. Büttner, M. Bauer, S. O. Demokritov, B. Hillebrands, Y. S. Kivshar, V. Grimalsky, Y. Rapoport, M. P. Kostylev, B. A. Kalinikos, A. N. Slavin, J. Appl. Phys. 87 (2000) 5088.
[111] V. E. Demidov, S. Urazhdin, R. Liu, B. Divinskiy, A. Telegin, S. O. Demokritov, Nat. Commun. 7 (2016) 10446.
[112] C. Bayer, S. O. Demokritov, B. Hillebrands, A. N. Slavin, Appl. Phys. Lett. 82 (2003) 607.
[113] V. E. Demidov, S. O. Demokritov, K. Rott, P. Krzysteczko, G. Reiss, Appl. Phys. Lett. 91 (2007) 252504.
[114] M. Cui, C. Yang, Opt. Express 18 (2010) 3444.
[115] E. A. Simpson, P. Campuzano-Jost, S. J. Hanna, D. B. Robb, J. H. Hepburn, M. W. Blades, A. K. Bertram, Int. J. Mass Spectrom. 281 (2009) 140.

[116] M. Thiel, J. Fischer, G. von Freymann, M. Wegener, Appl. Phys. Lett. 97 (2010) 221102.
[117] G. Hernandez, *Fabry-Pérot Interferometers* (Cambridge University Press, 1986).
[118] J. R. Sandercock, Operator Manual for the Tandem Fabry-Pérot Interferometer (1999).
[119] C. Fabry, A. Pérot, Ann. Chim. Phys. 16 (1899) 115.
[120] A. Pérot, C. Fabry, Astrophys. J. 9 (1899) 87.
[121] J. R. Sandercock, Operator Manual for the Tandem Fabry-Pérot Interferometer TFP-1 (2010).
[122] B. K. Mahato, S. Choudhury, R. Mandal, S. Barman, Y. Otani, A. Barman, J. Appl. Phys. 117 (2015) 213909.
[123] K. Adhikari, S. Choudhury, R. Mandal, S. Barman, Y. Otani, A. Barman, J. Appl. Phys. 121 (2017) 043909.
[124] C. Hauser, T. Richter, N. Homonnay, C. Eisenschmidt, M. Qaid, H. Deniz, D. Hesse, M. Sawicki, S. G. Ebbinghaus, G. Schmidt, Sci. Rep. 6 (2016) 20827.
[125] H. Chang, P. Li, W. Zhang, T. Liu, A. Hoffmann, L. Deng, M. Wu, IEEE Magn. Lett. 5 (2014) 1.
[126] I. Neudecker, G. Woltersdorf, B. Heinrich, T. Okuno, G. Gubbiotti, C. H. Back, J. Magn. Magn. Mater. 307 (2006) 148.
[127] B. Rana, D. Kumar, S. Barman, S. Pal, Y. Fukuma, Y. Otani, A. Barman, ACS Nano 5 (2011) 9559.
[128] A. Ganguly, R. M. Rowan-Robinson, A. Haldar, S. Jaiswal, J. Sinha, A. T. Hindmarch, D. A. Atkinson, A. Barman, Appl. Phys. Lett. 105 (2014) 112409.
[129] S. N. Panda, S. Mondal, J. Sinha, S. Choudhury, A. Barman, Sci. Adv. 5 (2019) eaav7200.
[130] C. Banerjee, S. Choudhury, J. Sinha, A. Barman, Phys. Rev. Appl. 8 (2017) 014036.
[131] A. K. Chaurasiya, S. Choudhury, J. Sinha, A. Barman, Phys. Rev. Appl. 9 (2018) 014008.

Chapter 5

5. Numerical Method

The magnetization dynamics in FM thin films with uniform magnetization can be realised under the macrospin formalism as described in chapter 2. Here, the non-linear ordinary differential LLG equation is linearized under small angle approximation to calculate the SW frequency and other material parameters. Howbeit, the materials having finite boundaries, e.g. in case of multi-layered and/or patterned heterostructures, the calculations become quite critical. Basically, the finite magnetic boundaries are associated with the presence of uncompensated magnetic dipoles at their surfaces, which creates a demagnetizing field in a direction opposite to the external bias magnetic field. The information about the distribution of the demagnetizing field (which heavily depends on the geometry) is extremely crucial for a proper understanding of the magnetization dynamics. To find out the local demagnetizing field profile in order to investigate the behaviour of the consequent SW in such non-uniformly magnetized heterostructures, various numerical techniques have been developed. One of the most popular methods is the micromagnetic approach, where the magnetization is considered to be a continuous function of position. Here, the sample is divided into a large number of cells where the dynamic motion of each cell is considered as a macrospin interacting with the neighbouring cells by short-range exchange and long-range dipolar interactions under the influence of anisotropy field and external magnetic field. Also, there exist different theoretical models, which, under certain assumptions, calculate the magnetic parameters. In this thesis work, micromagnetic simulations [1] (e.g. OOMMF: object-oriented micromagnetic framework [2], LLG micromagnetic simulator [3] and Mumax3 [4]) and also a combination of analytical and numerical technique (e.g. PWM: plane wave method) have been used to investigate the nature of static and dynamic magnetization of the studied systems.

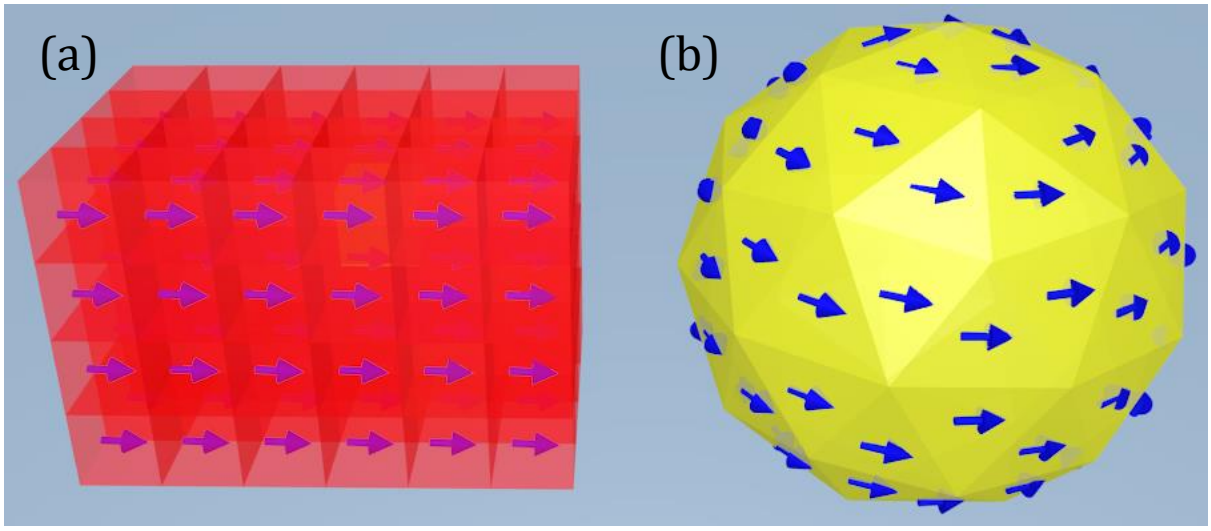

Figure 5.1. Discretization of a sample into (a) cuboidal cells following finite difference method (FDM) and (b) tetrahedral cells following finite element method (FEM) where each cell is assigned with a magnetization vector.

5.1. Micromagnetic Simulation

This is an efficient tool [1] for investigating a broad range of magnetic phenomena including static as well as dynamic properties. Based on either finite difference method (FDM) or finite element method (FEM) [5,6], this technique employs the continuum theory to estimate the magnetic features of several nanometers length scale in terms of the local arrangement of magnetic moments. In case of FDM, the system space is discretized into a number of regular parallelepiped cells as shown in Figure 5.1(a). Afterwards, the continuous solution domain is replaced by a discrete set of lattice points and the domain boundaries are substituted by their discrete counterparts. Subsequently, each cell is assigned with a magnetization vector and their relative interactions are considered through the minimization of total energy. A few examples of FDM simulators are Object Oriented Micromagnetic Frameworks (OOMMF) [2], LLG micromagnetic simulator [3], MicroMagus [7,8], MuMax3 [9], Magsimus [10,11], GoParallel [12] etc. Generally, FDM features a faster computation unlike FEM, however, it is not very accurate for complicated geometry like a curved boundary or irregular microstructures. The aforementioned issue can be resolved by using FEM. Here the system is discretized into finite elements, which can be 2D (like triangles, squares, or rectangles) or 3D (like tetrahedrons, cubes, or hexahedra) depending on the dimension and shape of the system as described in Figure 5.1(b). Despite of reproducing complex

geometries easily, this method is much slower than FDM due to the requirement of much more computational resource (or memory). Examples of various FEM simulators are NMAG [13,14], MAGPAR [15,16], MicroMagnum [17,18], TetraMag [19,20], FEELLGOOD [21], FastMag [22] etc. As mentioned earlier, OOMMF and LLG micromagnetic simulators have been used during this thesis work. Although both OOMMF and LLG simulator employ FDM based discretization, the latter offers better visualization of the system while OOMMF works faster than LLG simulator even on bigger system size. The programming language in OOMMF is written in C^{++} and Tcl script and the LLG equation is solved in space and time at temperature T = 0 K. The input parameters (like bulk saturation magnetization, exchange stiffness constant, magnetocrystalline anisotropy, Zeeman field, sample structure and dimensions and the magnetic field geometry) and the initial conditions of any problem are given using external script file. One of the advantages of using micromagnetic simulations is that one can feed the sample structure to the software by using an image file (bitmap format in OOMMF or LLG simulator). This helps to incorporate any structural artefacts of the system under consideration in the simulation. The sample space is divided into identical parallelepiped cells with dimensions equal to or less than the exchange length in order to consider the exchange interaction among the cells and each cell is assigned with a single spin. Subsequently, the LLG equation is solved assuming the magnetization to be a continuous function of position and deriving relevant expressions for different energy terms. Then the stable equilibrium state is achieved by minimizing the total Gibb's free energy with respect to the magnetization. Before starting the calculations for magnetization dynamics, the system is brought to its equilibrium state under the effect of static bias magnetic field. First, a large enough bias field (greater than the saturating field value) is applied to fully magnetize the sample where the magnetization is allowed to relax for a long time. The applied field is then reduced to the required bias field value and the magnetization is further kept to relax for a longer time while a large enough damping value (< 1) is given to stabilize the system under the applied magnetic field quickly. During each step, the magnetization configuration is updated by two types of evolvers: the first one is a time evolver which tracks the LLG dynamics and the second one is an energy minimization evolver that calculates the local minima in energy using energy minimization approach. A fourth order Runge-Kutta evolver is used as a time

evolver which solves LLG equation considering an ordinary differential equation in time. The time and minimization evolvers are controlled by corresponding drivers namely, time driver and minimization driver, respectively. The purpose of the drivers is to determine the completion of a simulation stage depending upon the stopping criteria described in the script file. The stopping criterion is determined by the convergence of the maximum torque expressed as ($m \times H$), where $m = M/M_s$. In the script file, either a stopping time or a stopping value of dm/dt is incorporated which is kept in such a manner that the value of maximum torque ($m \times H$) should be less than a certain value ($\approx 10^{-6}$ A/m). The simulation gets completed when the stopping criteria are fulfilled. After the system acquires a static equilibrium state under the influence of the bias magnetic field, the magnetization dynamics is triggered under a uniform excitation (spatially and temporally varying 'sinc' function) to simulate the FMR, TRMOKE or BLS results. In case of uniform excitation, the optical perturbation used in the experiment is mimicked in the form of a pulsed magnetic field of the suitable rise time and peak amplitude applied perpendicular to the sample plane. The time evolution of the different components of dynamic magnetization averaged over the entire sample volume are then recorded for a total timescale of several nanoseconds at intervals of few picoseconds. A small value for damping parameter (e.g. 0.008 for $Ni_{80}Fe_{20}$) is assumed during the dynamic simulation depending upon the material of the system which can be either extracted from Kittel fit of the experimental results or can be found in the literature.

5.1.1. Calculation of Power and Phase Profiles of the Resonating Modes

To unveil the nature of the resonant magnonic modes, the spatial profiles of the corresponding dynamic magnetization component are calculated [23]. The output files of the simulations actually consist of a number of open media framework (e.g. omf extension) files containing the information about the magnetization distribution ($M(r, t)$) over the entire simulation volume at a particular instance of simulation time. These files can be further utilized to inspect the time as well as the spatial distribution of the spin wave amplitude, phase and propagation. For that, first, the $M(r, t)$ is rearranged into three 4D matrices, i.e. $m_i(x, y, z, t)$, $m_j(x, y, z, t)$ and $m_k(x, y, z, t)$, respectively, where each matrix corresponds to each component of magnetization (m). Subsequently, one spatial coordinate (say z) of one of the 4D matrices (say, m_k) is fixed, which reduces the matrix dimension to three (m_k (x, y, z_m, t)). Then a discrete Fourier transform with

respect to the time dimension (t) is performed for each elemental cell. Next, the power value of the FFT spectrum corresponding to the desired frequency is extracted and plotted for each cell. This gives the in-plane space dependent power profiles at a particular resonance frequency (f_{res}). Similarly, the phase profile can be plotted by extracting the phase of complex dynamic magnetization. The frequency resolution depends on the simulation time window and the spatial resolution depends on the discretization of the sample used during the micromagnetic simulations. The expressions for the power and phase profiles for a particular resonant mode at $f = f_{\text{res}}$ can then be described as:

Power:

$$P^{z_m,f_r}(x,y) = 20\log_{10}\left|\widehat{M}^{z_m}(f_{\text{res}},x,y)\right| \tag{5.1}$$

Phase:

$$\delta^{z_m,f_r}(x,y) = \tan^{-1}\left[\frac{\text{Im}(\widehat{M}^{z_m}(f_{\text{res}},x,y))}{\text{Re}(\widehat{M}^{z_m}(f_{\text{res}},x,y))}\right] \tag{5.2}$$

5.1.2. LLG Micromagnetic Simulator

This is another genre of micromagnetic solver based upon FDM solving the LLG equation [3]. The main advantages of LLG micromagnetic simulator are the following:

1. It can provide a graphical animation of the magnetic domain or magnetostatic field profiles in the simulated FM samples during the simulation in both 2D and 3D.
2. It is possible to simulate the magnetic features as a function of temperature.
3. It also can calculate the magnetization parameters of magnetic multilayers where the material parameters for each layer can be easily manipulated for such multilayer system.
4. This simulator facilitates to calculate as well as visualize the domain wall dynamics in patterned or un-patterned magnetic heterostructures, while the spin-polarized current can also be injected in order to simulate the working condition of the magnetic spin valve or MTJ like nanostructures. There is a provision to calculate and visualize the effective magnetic field strength inside or outside of the sample considered in the simulation. Hence, it is possible to calculate the internal field and demagnetization field distributions in order to interpret the nature of the inter-element interaction or the magnetic profile inside the element itself.

5.2. Plane Wave Method (PWM)

This novel numerical approach is extensively used to calculate the excitation spectra (band structure) for an inhomogeneous or periodic geometry, e.g. in electronic [24-26], photonic [27-30], phononic [31,32] or magnonic crystals [33] (viz. this tool is useful irrespective of whether the medium is magnetic or not). This is a simple method which can give a complete spectrum of eigen excitations for any type of lattice, any shape of scattering centres and for various dimensions of the periodicity. In magnonic crystals (MCs)[34], the inhomogeneity of the internal magnetic field is taken into account in the form of the superposition of plane waves, which eventually converts the LLG equation to an eigenvalue problem. The problem is subsequently solved using standard numerical routines to find out the eigenvalues (SW frequencies) and eigen vectors (amplitude of the dynamical component of the magnetization vector).

In order to calculate the SW dispersion in magnonic crystals (MCs), the Landau–Lifshitz (LL) equation, i.e. the equation of motion of the magnetization vector $M(r,\ t)$ in space and time, neglecting the damping, is solved as given by:

$$\frac{\partial \vec{M}(r,t)}{\partial t} = \gamma \mu_0 \vec{M}(r,t) \times \vec{H}_{\text{eff}}(r,t) \tag{5.3}$$

As discussed in the previous section, the effective magnetic field (H_{eff}) is comprised of the Zeeman field ($H_0 = |H_0|\hat{k}$), anisotropy field (H_{ani}), exchange field (H_{ex}) and the magnetostatic field (H_{demag}). Both M and H_{demag} can be split into static and dynamic parts:

$$M(r,t) = M_s\hat{k} + m(r,t) \tag{5.4}$$

$$H_{\text{demag}} = H_{\text{ms}}(r) + h_{\text{ms}}(r,t) \tag{5.5}$$

In the magnetostatic approximation, using Maxwell's equations, we have:

$$\vec{\nabla} \times h_{\text{ms}}(r,t) = 0 \tag{5.6}$$

$$\vec{\nabla}.(h_{\text{ms}}(r,t) + m(r,t)) = 0 \tag{5.7}$$

The exchange contribution can be written in terms of the exchange length $\lambda_{\text{ex}}(r)$ as:

$$H_{\text{ex}}(r,t) = (\vec{\nabla}.\lambda_{\text{ex}}^2(r)\vec{\nabla})M(r,t) \tag{5.8}$$

where,

$$\lambda_{\text{ex}}(r) = \sqrt{\frac{2A(r)}{\mu_0 M_S^2(r)}} \tag{5.9}$$

Here, $A(r)$ is the exchange stiffness constant. If anisotropy contribution (H_{ani}) is neglected, the expression of H_{eff} can be written as:

$$H_{\text{eff}}(r,t) = H_0\hat{k} + \left(\vec{\nabla}.\lambda_{\text{ex}}^2(r)\vec{\nabla}\right)M(r,t) + h_{\text{ms}}(r,t) \tag{5.10}$$

The aforementioned LL equation is solved under linear approximation. In PWM tool, a solution is achieved in the form of a monochromatic SW which can be expressed as:

$$m(r,t) \sim e^{i\omega t} \tag{5.11}$$

Here, ω is the angular frequency of the SW. The dynamic component of H_{demag} can also be written [35] in the time-dependent expression as:

$$h_{\text{ms}}(r,t) = h_{\text{ms}}(r)e^{i\omega t} \tag{5.12}$$

Considering linear approximation, it can be expressed as:

$$i\Omega m_x(r) + \frac{1}{H_0}M_{\text{s}}(r)\left(\vec{\nabla}.\lambda_{\text{ex}}^2(r)\vec{\nabla}\right)m_y(r) - m_y(r) - \frac{1}{H_0}m_y(r) \times \left(\vec{\nabla}.\lambda_{\text{ex}}^2(r)\vec{\nabla}\right)M_{\text{s}}(r) + \frac{M_{\text{s}}(r)}{H_0}\frac{\partial\psi(r)}{\partial y} = 0 \tag{5.13}$$

$$i\Omega m_y(r) + \frac{1}{H_0}M_{\text{s}}(r)\left(\vec{\nabla}.\lambda_{\text{ex}}^2(r)\vec{\nabla}\right)m_x(r) + m_x(r) + \frac{1}{H_0}m_x(r) \times \left(\vec{\nabla}.\lambda_{\text{ex}}^2(r)\vec{\nabla}\right)M_{\text{s}}(r) - \frac{M_{\text{s}}(r)}{H_0}\frac{\partial\psi(r)}{\partial x} = 0 \tag{5.14}$$

$$\nabla^2\psi(r) - \left[\frac{\partial m_x(r)}{\partial x} + \frac{\partial m_y(r)}{\partial y}\right] = 0 \tag{5.15}$$

$\psi(r,t)$ is known as the magnetostatic potential while, Ω is a dimensionless parameter called the reduced frequency defined as:

$$\Omega = \frac{\omega}{|\gamma|\mu_0 H_0} \tag{5.16}$$

In case of periodic magnetic structures, i.e. MCs, M_{s} and λ_{ex} are assumed to be periodic functions of the in-plane position vector with a periodicity a, viz.:

$$M_{\text{s}}(r+a) = M_{\text{s}}(r) \tag{5.17}$$

$$\lambda_{\text{ex}}^2(r+a) = \lambda_{\text{ex}}^2(r) \tag{5.18}$$

According to Bloch's theorem, the solution of a differential equation with periodic coefficients can be expressed as a product of plane wave functions and a periodic Bloch function, i.e.:

$$m_{\text{s}}(r) = m_k(r)e^{ik.r} = \sum_G m_k(G)e^{i(k+G).r} \tag{5.19}$$

$$\psi(r) = \psi_k(r)e^{ik.r} = \sum_G \psi_k(G)e^{i(k+G).r} \tag{5.20}$$

where,

$$m_k(r + a) = m_k(r) \tag{5.21}$$

$$\psi_k(r + a) = \psi_k(r) \tag{5.22}$$

Here, k is the wavevector in the first Brillouin zone (BZ) while G (= $G(x, y)$) represents the reciprocal lattice vector. Consequently, Fourier transformation is performed in order to calculate the coefficients M_s and λ_{ex} into the reciprocal space using the following expressions:

$$M_s(r) = \sum_G M_s(G) e^{iG.r} \tag{5.23}$$

$$\lambda_{ex}^2(r) = \sum_G \lambda_{ex}^2(G) e^{iG.r} \tag{5.24}$$

If a finite number (N) of reciprocal lattice vectors is employed in the above expressions (i.e. the set of equations becomes finite), the calculation reduces to an eigenproblem having an expression in the form of a matrix:

$$\widehat{M} m_k = i\Omega m_k \tag{5.25}$$

Here, the eigenvalues are Ω which is solved numerically and $\widehat{M}$ has the following form:

$$\widehat{M} = \begin{pmatrix} \widehat{M}^{xx} & \widehat{M}^{xy} \\ \widehat{M}^{yx} & \widehat{M}^{yy} \end{pmatrix} \tag{5.26}$$

Here [34],

$$\widehat{M}^{xx} = \widehat{M}^{yy} = 0 \tag{5.27}$$

Thus, one can calculate the SW dispersion for a periodic system for different SW wave vector k by standard numerical procedures (by considering a finite number of plane waves) to extract the corresponding eigenvalues (which gives the SW frequency, ω) and the eigen vectors (m_k). Here, it is sometimes necessary to put the solutions obtained by PWM to satisfy the convergence criterion.

In addition, to compare the calculated dispersion with the experimentally obtained magnon band structure through Brillouin light scattering (BLS) spectroscopy, it is necessary to estimate the square of the modulus of the fundamental harmonics of magnetization as the BLS intensity (I_{BLS}) can be expressed as,

$$I_{BLS} \propto |m_k(G = 0)|^2 \tag{5.28}$$

Subsequently, the spatial mode profiles can also be calculated for a given wave vector and frequency, by determining the modulus of the dynamic magnetization (i.e. $m_x(r)$) for each spatial point. It is noteworthy that the PWM calculations stand upon the consideration that both the scattering centre and the matrix consist of FM materials (e.g. for bi-component MC or BMC). For instance, in case of dot or antidot (AD) array

where either the scattering centres or the matrix are constituted of a non-magnet material, a very small value is assigned to the material parameters in order to avoid any unphysical solutions.

References

[1] S.-K. Kim, J. Phys. D: Appl. Phys. 43 (2010) 264004.
[2] M. Donahue, D. G. Porter, *OOMMF User's Guide, Version 1.0, NIST Interagency Report No. 6376* 1999).
[3] LLG Micromagnetics Simulator, http://llgmicro.home.mindspring.com (2018).
[4] A. Vansteenkiste, J. Leliaert, M. Dvornik, M. Helsen, F. Garcia-Sanchez, B. Van Waeyenberge, AIP Adv. 4 (2014) 107133.
[5] B. Dieny, R. B. Goldfarb, K.-J. Lee, *Introduction to Magnetic Random-Access Memory* (Wiley-IEEE Press, New York, 2016).
[6] T. Schrefl, J. Magn. Magn. Mater. 207 (1999) 45.
[7] O. Dmytriiev, M. Dvornik, R. V. Mikhaylovskiy, M. Franchin, H. Fangohr, L. Giovannini, F. Montoncello, D. V. Berkov, E. K. Semenova, N. L. Gorn, A. Prabhakar, V. V. Kruglyak, Phys. Rev. B 86 (2012) 11 104405.
[8] MicroMagus, http://www.micromagus.de/home.html.
[9] A. Vansteenkiste, B. Van de Wiele, J. Magn. Magn. Mater. 323 (2011) 2585.
[10] J. O. Oti, IEEE Trans. Magn. 46 (2010) 2338.
[11] A. Bordianu, V. Ionita, L. Petrescu, Rev. Roum. Sci. Tech.-El. 57 (2012) 3.
[12] L. Lopez-Diaz, D. Aurelio, L. Torres, E. Martinez, M. A. Hernandez-Lopez, J. Gomez, O. Alejos, M. Carpentieri, G. Finocchio, G. Consolo, J. Phys. D: Appl. Phys. 45 (2012) 323001.
[13] H. Fangohr, M. Albert, M. Franchin, Ieee, *Nmag micromagnetic simulation tool - software engineering lessons learned* (Ieee, New York, 2016), Proceedings of 2016 Ieee/Acm International Workshop on Software Engineering for Science.
[14] T. Fischbacher, M. Franchin, G. Bordignon, H. Fangohr, IEEE Trans. Magn. 43 (2007) 2896.
[15] W. Scholz, J. Fidler, T. Schrefl, D. Suess, R. Dittrich, H. Forster, V. Tsiantos, Comput. Mater. Sci. 28 (2003) 366.
[16] T. Blachowicz, A. Ehrmann, Iop, in *4th International Conference on Competitive Materials and Technology Processes* (Iop Publishing Ltd, Bristol, 2017).
[17] B. Krüger, G. Selke, A. Drews, D. Pfannkuche, IEEE Trans. Magn. 49 (2013) 4749.
[18] C. Abert, L. Exl, G. Selke, A. Drews, T. Schrefl, J. Magn. Magn. Mater. 326 (2013) 176.
[19] A. Kakay, E. Westphal, R. Hertel, IEEE Trans. Magn. 46 (2010) 2303.
[20] R. Hertel, in *Handbook of Magnetism and Advanced Magnetic Materials*.
[21] FEELLGOOD, http://feellgood.neel.cnrs.fr./.
[22] J. K. Byun, I. Volvach, V. Lomakin, IEEE Trans. Magn. 52 (2016) 9 7100509.
[23] D. Kumar, O. Dmytriiev, S. Ponraj, A. Barman, J. Phys. D: Appl. Phys. 45 (2012) 015001.
[24] M. D. Segall, R. Shah, C. J. Pickard, M. C. Payne, Phys. Rev. B 54 (1996) 16317.
[25] V. Milman, B. Winkler, J. A. White, C. J. Pickard, M. C. Payne, E. V. Akhmatskaya, R. H. Nobes, Int. J. Quantum Chem. 77 (2000) 895.
[26] F. Herman, Phys. Rev. 88 (1952) 1210.

[27] Z.-Y. Li, L.-L. Lin, Phys. Rev. E 67 (2003) 046607.
[28] Y. A. Vlasov, M. O'Boyle, H. F. Hamann, S. J. McNab, Nature 438 (2005) 65.
[29] S. Guo, S. Albin, Opt. Express 11 (2003) 167.
[30] J. Broeng, D. Mogilevstev, S. E. Barkou, A. Bjarklev, Opt. Fiber Technol. 5 (1999) 305.
[31] V. Laude, M. Wilm, S. Benchabane, A. Khelif, Phys. Rev. E 71 (2005) 036607.
[32] J. O. Vasseur, P. A. Deymier, B. Djafari-Rouhani, Y. Pennec, A. C. Hladky-Hennion, Phys. Rev. B 77 (2008) 085415.
[33] M. Krawczyk, H. Puszkarski, Phys. Rev. B 77 (2008) 054437.
[34] M. Krawczyk, S. Mamica, M. Mruczkiewicz, J. W. Klos, S. Tacchi, M. Madami, G. Gubbiotti, G. Duerr, D. Grundler, J. Phys. D: Appl. Phys. 46 (2013) 495003.
[35] J. Kaczér, L. Murtinová, Phys. Status Solidi A 23 (1974) 79.

Chapter 6

6. Active Control of Mode Crossover and Mode Hopping of Spin Waves in a Ferromagnetic Antidot Lattice

Active control of spin wave dynamics is demonstrated using broadband ferromagnetic resonance in two-dimensional $Ni_{80}Fe_{20}$ antidot lattices arranged in hexagonal lattice with fixed lattice constant but varying antidot diameter. A strong modification in the spin-wave spectra is obtained with the variation in the antidot diameter as well as with the strength and orientation of the bias magnetic field. A broad band of modes is observed for the lattice with higher antidot diameter which decreases systematically as the antidot diameter is reduced. A crossover between the higher frequency branches is achieved in lattices with higher antidot diameter. In addition, the spin-wave modes in all lattices show a strong six-fold anisotropic behaviour due to the variation of internal field distribution as a function of the bias-field orientation. A mode hopping-like behavior is observed in the angular dispersions of spin-wave spectra for samples having intermediate hole diameters. Micromagnetic simulations qualitatively reproduce the experimentally observed spin-wave modes and the simulated mode profiles reveal the presence of extended and quantized standing spin-wave modes in these lattices. These observations are significant for large tunability and anisotropic propagation of spin waves in GHz frequency magnetic devices.

6.1. Introduction

Ferromagnetic (FM) antidot (AD or hole) lattices (ADLs) [1], i.e. periodically arranged holes embedded in a ferromagnetic thin film are artificial crystals, which are fabricated by structuring known ferromagnetic materials at different length scales. Exploitation of their dynamic responses over a broad temporal and spatial regimes can offer various exciting properties. These magnetic nanostructures form the basis of future technologies including magneto-photonic crystals [2,3] and ultrahigh density storage device. They also possess exciting prospects in the field of magnonics as magnonic crystals (MCs) [4] where spin waves (SWs) are used to carry and process the

information in the microwave band analogous to photonic and phononic crystals. They can play a key role in building nanoscale magnonic devices for GHz frequency communication [5], waveguides [6], phase shifters [7], filters [8], interferometers [9], spin-wave logic devices [10] and spin-wave nano-optics [11] with spin waves in multiple connected magnon waveguides. More recently, the filled antidot lattices also have gained a great interest as bi-component MCs [5,12] (BMCs) for the additional tunability in the magnonic band structures due to the differences between the magnetic parameters of two magnetic materials in those systems. The upsurge in the nanofabrication and detection techniques with improved spatio-temporal resolution boost in the study of high-frequency magnetization dynamics in a variety of such nanoscale antidot lattices. One important problem of magnonics research is to tune the magnonic spectra and the band structures of the MCs by varying its physical parameters such as antidot shape [13], lattice symmetry [14,15], lattice constant [16], base material [17] as well as strength and orientation of the bias magnetic field [18,19] which can greatly affect the SW dynamics.

In the past few years, the high-frequency magnetization dynamics of magnetic ADLs have been explored by various experimental and numerical methods [18-23]. Initial studies on ADLs showed attenuation of uniform ferromagnetic resonance mode due to the excitation of non-uniform in-plane SW mode [24] and also the pattern induced splitting of surface and volume modes [25] were observed. Later, field dependent localization of SW mode, SW confinement and field-controlled propagation of SWs [26,27] as well as the formation of magnonic miniband with large SW velocities [28,29] have been observed. Recently, the dispersive and entangled SWs between the antidots [30] and anisotropic propagation and damping of SWs [18] were also observed due to the magnetic field-induced SW guiding in a network of interconnected nanowires. Further works showed high-symmetric magnonic modes having a linear bias magnetic field dependence for perpendicularly magnetized ADLs [31], and conversion of quantized SWs to propagating ones by varying the bias magnetic field orientation [19]. Micromagnetic simulations reported [32] the effect of the antidot shape on the magnonic band structure in exchange-dominated one-dimensional magnonic waveguides. The effects of lattice defects [33] and broken translational symmetry [34] have also attracted great interest due to their unique properties. However, there are

very few reports exploring the effect of the size of the antidots [35], which can play a key role in determining the nature of SW propagation and confinement due to the modulation of the magnonic band gaps in such MCs.

Here, we investigate the SW dynamics of 2D arrays of circular shaped $Ni_{80}Fe_{20}$ antidots arranged in hexagonal lattice with fixed lattice constant but varying antidot diameter by manipulating the strength and orientation of the in-plane bias magnetic field. A drastic variation in the magnonic spectra is observed when the diameter of the antidot is systematically tuned. A rich band of SW modes for highest antidot diameter reduced systematically to a fewer number of modes with the reduction in antidot diameter. Further, a mode crossover with bias-field strength and mode hopping-like behaviour with bias-field orientation are observed, which are explained with the aid of micromagnetic simulations.

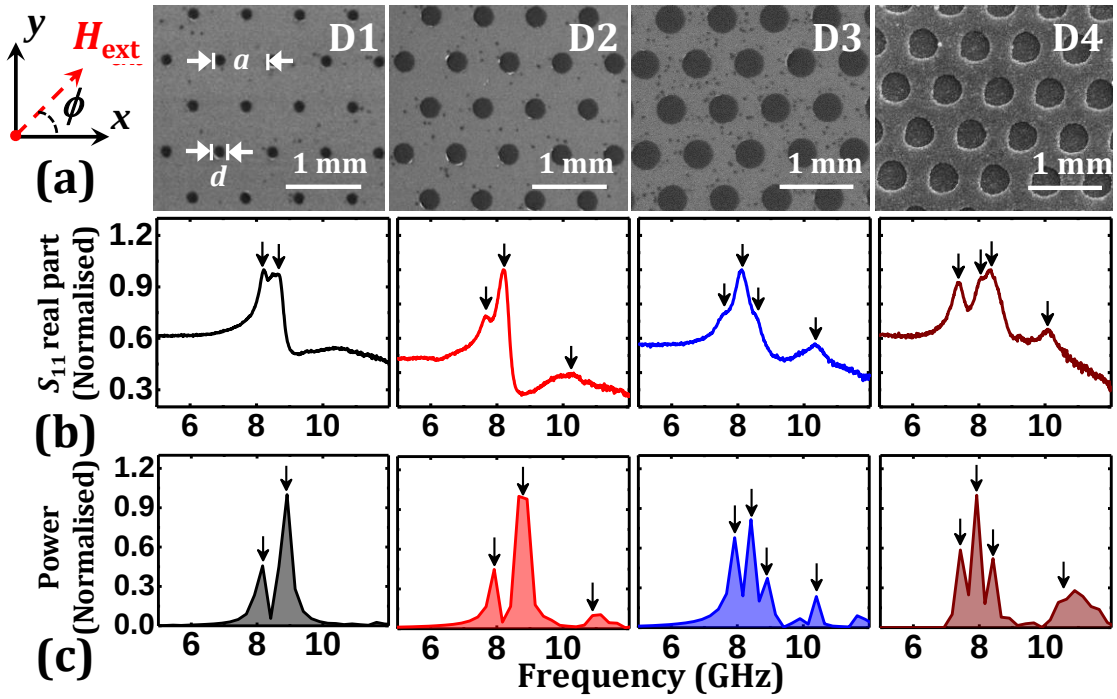

Figure 6.1. (a) Scanning electron micrographs of circular-shaped $Ni_{80}Fe_{20}$ (NiFe) antidots (ADs) arranged in hexagonal lattices of constant lattice spacing a = 700 nm with variable antidot (hole) diameter d = 140 (D1), 240 (D2), 340 (D3) and 440 (D4) nm. (b) Real parts of the forward scattering parameter (S_{11}) representing the FMR spectra for all four samples at bias magnetic field H_{ext} = 800 Oe applied at an azimuthal angle ϕ = 0° and the observed SW modes were marked by down arrows. (c) Corresponding simulated SW spectra of four different lattices at H_{ext} = 800 Oe applied at ϕ = 0° and the arrows represent different SW modes. The orientation of the bias magnetic field H_{ext} is shown at the top left of the figure.

6.2. Experimental Details

Circular shaped antidots are patterned in a 20-nm-thick $Ni_{80}Fe_{20}$ (NiFe) film by using a combination of e-beam lithography (EBL), e-beam evaporation (EBE) and ion milling [15]. The antidots with variable diameters (d) of 140 (D1), 240 (D2), 340 (D3), 440 (D4) nm and fixed lattice spacing (a) of 700 nm are arranged in hexagonal lattice symmetry with total array dimension of 25 μm × 250 μm, as shown in the scanning electron micrographs of Figure 6.1(a). A co-planar waveguide (CPW) made of Au with a thickness of 150 nm was deposited on top of the array for the broadband ferromagnetic resonance measurement. The width and length of the signal line of this CPW were 30 μm and 300 μm, respectively so that the whole array could remain under the centre of the signal line of CPW which has a nominal characteristic impedance of 50 Ω.

The measurement of SW spectra from the samples was performed using a broadband ferromagnetic resonance (FMR) spectrometer [36] consisting of a vector network analyzer (Agilent PNA-L, Model No.: N5230C, frequency range: 10 MHz to 50 GHz) and a high-frequency probe station along with a nonmagnetic ground-signal-ground (G-S-G) type pico-probe (GGB Industries, Model No. 40A-GSG-150-EDP). The system has an inbuilt electromagnet within the probe station generating a bias magnetic field (H_{ext}) of ± 1800 Oe. The electromagnet is mounted on a high-precision rotary mount which enables the electromagnet to rotate over 360° angle within the plane of the sample. The sample is viewed with the help of a microscope and illumination set-up. Microwave signal with variable frequency is launched into the CPW using the pico-probe through a high frequency and low noise coaxial cable (Model No.: N1501A-203). The CPW is shorted at one end and the back-reflected signal is collected by the same probe to the analyzer. Absorption of the ongoing and returning signals at various SW frequencies produces the characteristic SW spectrum of the sample. The real and imaginary parts of the scattering parameter in reflection geometry measured at various magnetic fields are subtracted from its value at the maximum bias magnetic field (reference spectrum), and hence, the SW spectra are obtained.

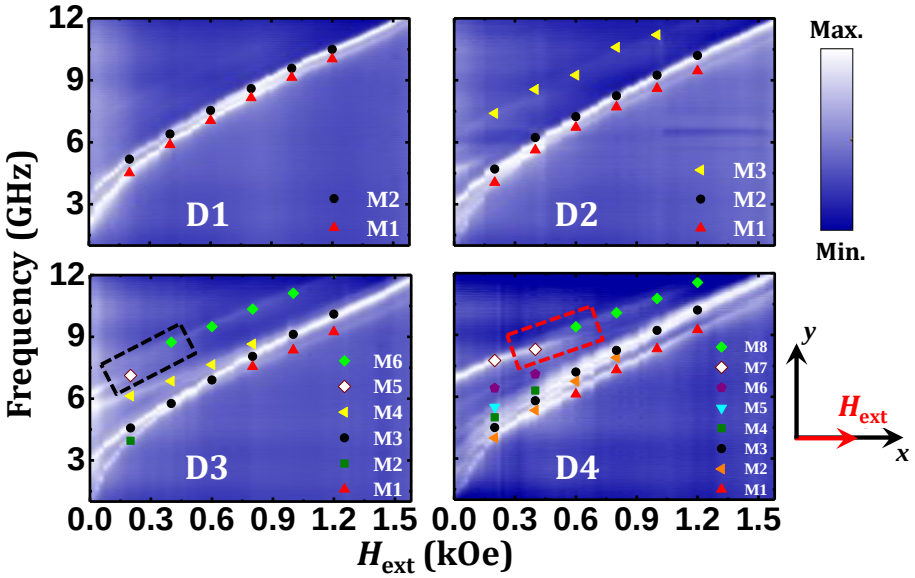

Figure 6.2. Bias field (H_{ext}) dependent SW absorption spectra of NiFe ADLs with different antidot diameters (D1-D4) are shown at ϕ = 0°. The surface plots correspond to the experimental results, while the symbols represent the simulated data. The black and red dotted boxes represent the crossover between two higher frequency branches, i.e. M5 and M6 in D3 and M7 and M8 in D4, respectively. The color map for the surface plots and the schematic of H_{ext} are given at the right side of the figure.

6.3. Results and Discussion

The real parts of the forward scattering parameter, i.e. S_{11} for the samples with varying antidot diameter (d) are shown in Figure 6.1(b) at a bias magnetic field H_{ext} = 800 Oe applied at an azimuthal angle ϕ = 0°, while their bias field dependent SW dispersion spectra measured at ϕ = 0° are represented as surface plots in Figure 6.2. The SW dynamics get drastically modified with the variation of d. For D1, two distinct SW modes are obtained, while, in case of D2, the number of modes is increased to three. On the contrary, rich multimode spectra are observed in D3 and D4 consisting of total six and eight modes. Interestingly, in D4, with the decreasing bias field, we observe a significant crossover (marked by the red dotted box in the field dispersion of D4 in Figure 6.2) between the two higher frequency branches (closed and open diamond marked modes 7 and 8, respectively) at an intermediate field value of H_{ext} ~ 525 Oe. A crossover is also observed in D3 as shown by the black dotted box in Figure 6.2 between modes 5 and 6 (closed and open diamond marked modes) at a much lower field H_{ext} ~ 170 Oe, while this phenomenon is completely absent in both D1 and D2. Also, the lowest frequency mode M1 in both D3 and D4 vanishes above a certain bias field value (~ 700 Oe for D3

and ~ 430 Oe for D4). The bias field dispersion curves of D3 and D4 also reveal that there are some SW modes e.g. M2 in D3 and M5 in D4 which are present at lower bias field. This is due to the deviation from the uniform magnetization state due to the increase in the overlapping between the demagnetizing regions around the antidots.

We have investigated the origin of the SW modes by performing micromagnetic simulations using the OOMMF software [37] for these samples consisting of 2 × 2 arrays of hexagonal unit cells for each sample where the two-dimensional (2D) periodic boundary condition has been incorporated to consider the large areas of the experimentally studied arrays. We have discretized each sample into rectangular prism-like cells with dimensions 4 × 4 × 20 nm^3. The value of exchange stiffness constant and saturation magnetization used in the simulation for NiFe are A_{NiFe} = 1.3 × 10^{-6} erg/cm [38], M_{NiFe} = 850 emu/cc, while the damping coefficient α_{NiFe} = 0.008 is used for NiFe during the dynamic simulations. The value of gyromagnetic ratio γ = 18.1 MHz/Oe and the magnetocrystalline anisotropy K = 0 are considered for NiFe. Here, the material parameters, i.e. M_s, γ and K for NiFe were extracted from the Kittel fit of the bias-field dependent SW absorption spectra of NiFe thin film in Figure 6.3. The dynamic simulations were carried out by first performing a static magnetic configuration under a bias magnetic field in the experimental geometry and then by applying a pulsed magnetic field. The details of the static and the dynamic simulations are described elsewhere [39].

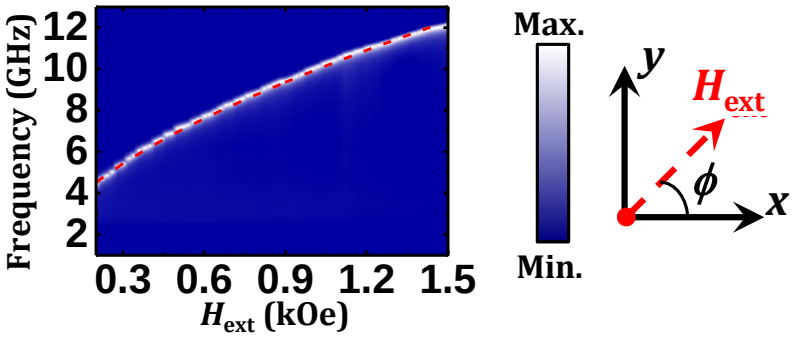

Figure 6.3. Bias field (H_{ext}) dependent spin-wave (SW) absorption spectra of $Ni_{80}Fe_{20}$ (NiFe) thin film at ϕ = 0° is shown along with the Kittel fit, which is represented by the red dotted line. The color map for the surface plot and the schematic of the orientation of H_{ext} are shown on the right side of the figure.

Figure 6.1(c) shows that the experimental data were reproduced qualitatively well using the micromagnetic simulations which were plotted at H_{ext} = 800 Oe, and also in Figure 6.2 as represented by filled symbols for all the lattices. The slight quantitative disagreements between experimental and simulated results can occur due to the deviation of the simulated samples and conditions from the experimental ones. The general deviation in the dimensions as observed in the experimental samples has already been incorporated in the simulated samples, although the precise edge deformations are not possible to include in the finite difference method based micromagnetic simulations.

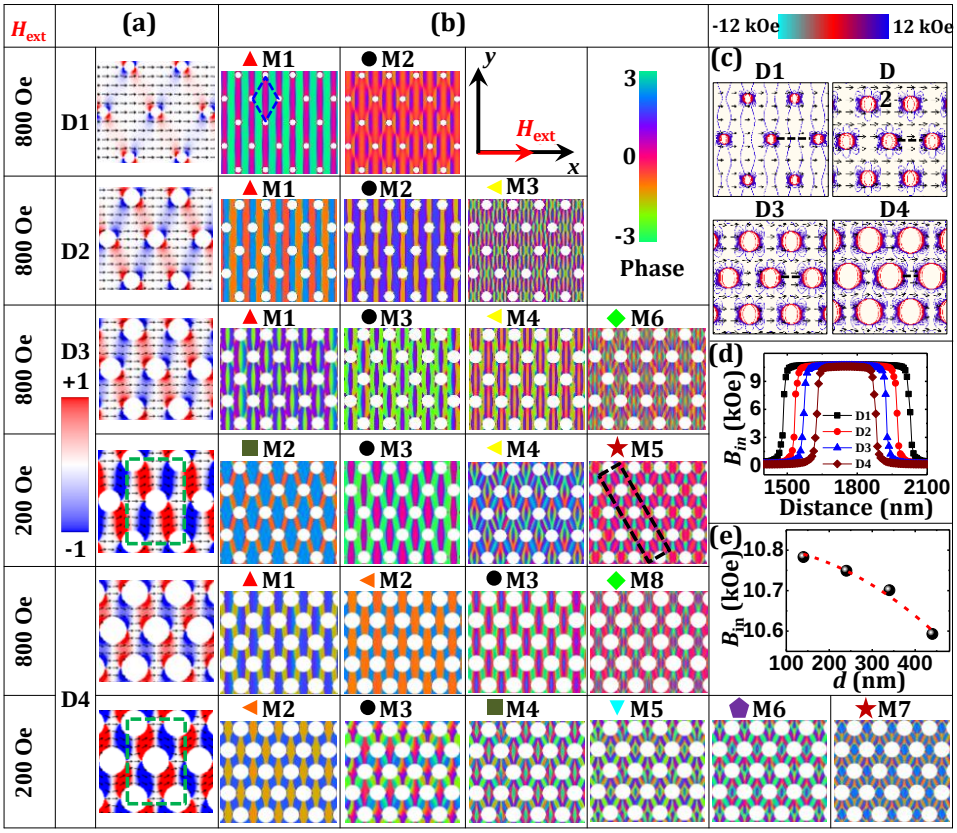

Figure 6.4. (a) Simulated static magnetic configurations of NiFe ADLs are shown for H_{ext} = 800 Oe in D1-D4 and H_{ext} = 200 Oe in D3 and D4, respectively, at ϕ = 0°. The color map is given on the left side of the figure. (b) Simulated spatial distributions of the phase profiles corresponding to different SW modes obtained at H_{ext} = 800 Oe in D1-D4 and H_{ext} = 200 Oe in D3 and D4, respectively, at ϕ = 0°. The color map for the phase distributions and the schematic of H_{ext} are shown on the right side of the figure. (c) Contour plots of the simulated magnetostatic field distributions in D1-D4 and the corresponding color map is given at the top right corner of the figure. (d) Linescans of the simulated internal field (B_{in}) taken between two consecutive antidots along the black dotted lines as shown in (c) for D1-D4. (e) The variation of B_{in} with the antidot

diameter d (black circular symbols: micromagnetic symbols; red dotted line: fitted curve).

In Figure 6.4(a), we have shown the simulated static magnetic configurations for D1 and D2 at H_{ext} = 800 Oe (ϕ = 0°), while, in order to underpin the origin of the mode crossover observed in both D3 and D4, we have presented their static magnetization states at two different bias field values, H_{ext} = 200 and 800 Oe. The static magnetization maps of D3 and D4 at H_{ext} = 200 Oe revealed a strong overlap of the demagnetized regions present between the two antidots situated diagonally (as shown by green dotted boxes) of the lattices, while this overlap reduces systematically with the increase in bias field and vanishes for H_{ext} > 300 Oe in D3 and H_{ext} > 600 Oe in D4, respectively. For a better understanding of the nature of various observed SW modes, we have calculated the spatial distributions of these SW modes by using a homebuilt code [40]. Figure 6.4(b) shows the phase profiles of the SW modes for all samples with varying d, calculated at H_{ext} = 800 Oe for ϕ = 0° while, the corresponding power profiles are shown in the Figure 6.5. We have observed different types of extended and quantized standing SW modes due to the formation of confining potentials by the demagnetizing fields around the antidots. So, in order to keep uniformity in describing the nature of the observed standing SW modes, we have assigned quantization number n for the modes forming standing waves in the rhombic-region between the two (horizontally situated) consecutive antidots along x-direction as shown by blue dotted box in the phase profile of M1 for D1. It is clear from Figure 6.4(b) that the lowest frequency mode M1 for D1 is extended through the diagonally situated antidots along y-direction. However, considering the rhombic region formed by four antidots, it also forms standing wave mode along x-direction with quantization n = 3, while the other mode M2 has quantized character along x-direction with n = 5. Similarly, in D2, both the lower frequency modes M1 and M2 represent extended nature in the y-direction. Although, M1 and M2 also possess quantized character along x-direction in the rhombic unit with n = 3 but they are in opposite phase with each other. The highest frequency mode M3 of D2 also forms standing wave pattern with n = 11. The mode profiles get substantially modified with further increase in d, as all the SWs form standing waves in x-direction for D3 and D4. However, unlike for D1 and D2, some of the SW modes show discontinuity for low or high field values in D3 and D4. To explain that, we have shown the phase maps of the

SW modes which are present at H_{ext} = 200 and 800 Oe for D3 and D4. For D3 at H_{ext} = 800 Oe, both M1 and M3 are quantized modes with n = 3 which are opposite in phase, while M4 and M6 also possess quantized character with n = 5 and 7, respectively. However, at lower bias field (H_{ext} = 200 Oe), M2 shows quantized nature with n = 1. On the other hand, due to the increase in the overlapping of demagnetized regions as evident from the static magnetization profile shown in Figure 6.4(a) for D3, a diagonal quantization between the next nearest neighbouring antidots is observed for M5 as shown by the black dotted box. We assign m as the diagonal quantization number where m = 3 for M5. In D4, at H_{ext} = 800 Oe, all the modes (M1, M2, M3 and M8) represent quantized nature with n = 1, 1, 3 and 5, respectively, where M1 and M2 are in opposite phase. However, at H_{ext} = 200 Oe, due to strong demagnetizing field, a significant modification is observed where all the SW modes M2-M7 represent quantized modes with n = 1, 3, 3, 3, 3 and 1, respectively with their diagonal quantization value m of 1, 1, 3, 3, 5 and 5 respectively. Here, M4 and M5 are in opposite phase with each other.

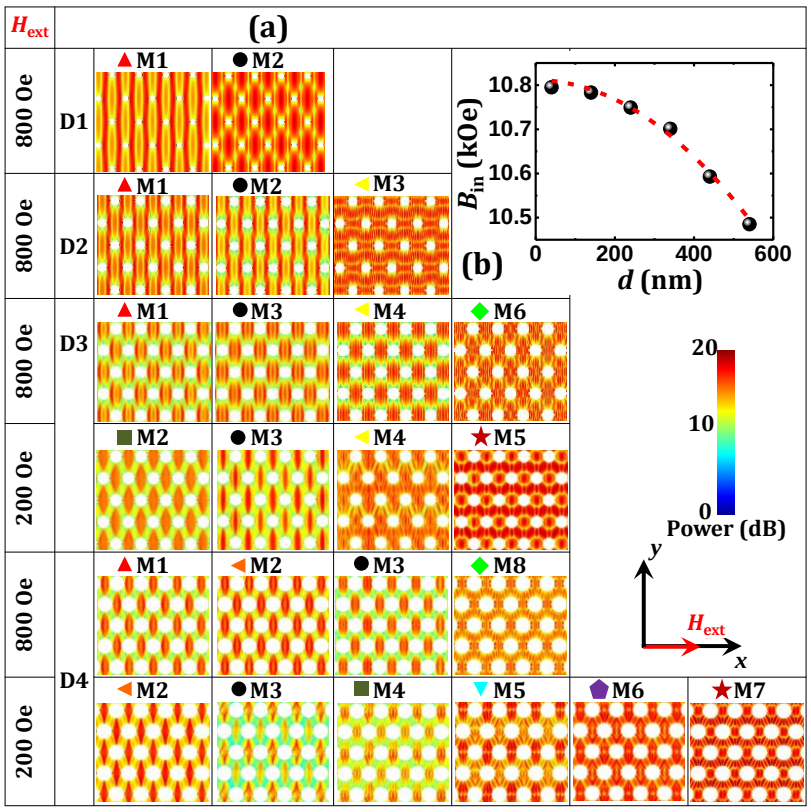

Figure 6.5. Simulated spatial distributions of the power corresponding to different SW modes obtained at H_{ext} = 800 Oe in D1-D4 and H_{ext} = 200 Oe in D3 and D4, respectively, at ϕ = 0°. The color map for the power distributions and the schematic of H_{ext} are shown

on the right side of the figure. (c) The variation of B_{in} for all the lattices with d = 40, 140, 240, 340, 440 and 540 nm (black circular symbols: micromagnetic symbols; red dotted line: fitted curve with the equation: $B_{in} = A(-d^2) + C$, where, C is the B_{in} value (~ 10.81 kOe) of thin NiFe film of 20 nm thickness).

We have further calculated the magnetostatic field distributions in the ADLs for bias field H_{ext} = 800 Oe applied at ϕ = 0° using the LLG software [41], as shown in Figure 6.4(c). It can be clearly seen that the magnetostatic field distribution is modified drastically when d is varied. We have further compared the internal field (B_{in}) values of these samples by taking a linescan between two consecutive antidots along x-direction as shown by the black dotted lines in D1-D4. It is found that B_{in} decreases significantly with the increase in d, due to the systematic increase in the overlapping between the demagnetizing fields confined around the antidots. This variation of B_{in} has been fitted using a simple parabolic equation which reflects that B_{in} varies as ($-d^2$) with the following equation:

$$B_{in} = A(-d^2) + C \tag{6.1}$$

where, C is the B_{in} value (~ 10.81 kOe) of NiFe thin film having a thickness of 20 nm. To confirm this behaviour, we have calculated the internal field values for additional simulated samples with d = 40 and 540 nm and the B_{in} values of these samples also follow the same fitting Equation 6.1 as shown in Figure 6.5(b).

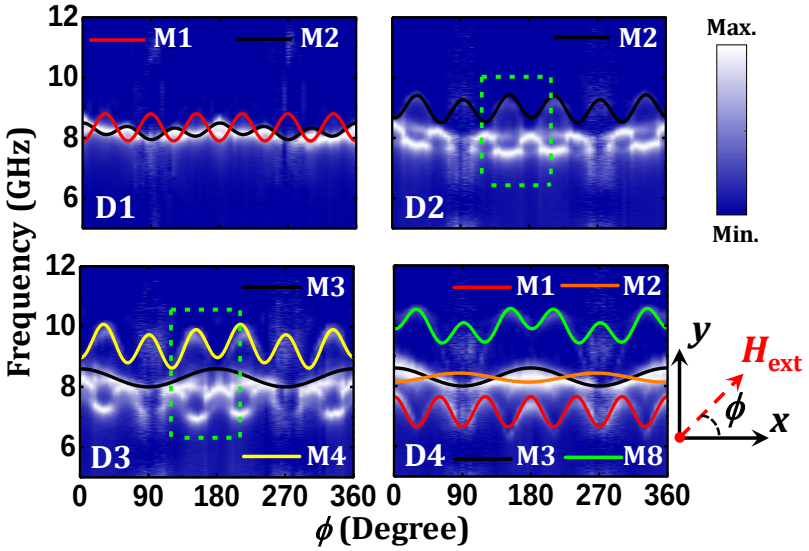

Figure 6.6. Variation of SW frequency with the azimuthal angle (ϕ) varying from 0° to 360° for NiFe ADLs with various antidot diameter (D1-D4) at H_{ext} = 800 Oe. The surface plots represent the experimental results while the solid lines describe the sinusoidal fits

to the observed anisotropic SW modes in all of the samples (D1-D4). The color map associated with the surface plots and the schematic of the orientation of H_{ext} are shown on the right side of the figure.

To investigate the configurational anisotropy in these samples, we have measured the SW spectra of these samples by varying the in-plane orientation, (ϕ) of the bias magnetic field at a fixed strength. Figure 6.6 presents surface plots of the angular dispersion of SW frequencies for all the samples (D1-D4) at H_{ext} = 800 Oe. The solid lines represent the theoretical fits using harmonic functions with different rotational symmetries. The anisotropy of the SW modes varied significantly as d is increased. The lowest frequency mode M1 for D1 shows six-fold rotational anisotropy, while M2 possesses a superposition of a strong six- and weak two-fold anisotropy. The higher frequency anisotropic modes, i.e. M2 in D2 and M4 in D3 show a combination of six- and two-fold rotational symmetry. On the other hand, M1 and M8 in D4 also possess six-fold rotational symmetry along with a weak two-fold symmetry, although M8 is in opposite phase with M1. Also, a two-fold anisotropy is observed in D4 for the two intermediate SW modes M2 and M3, while they are in opposite phase with each other.

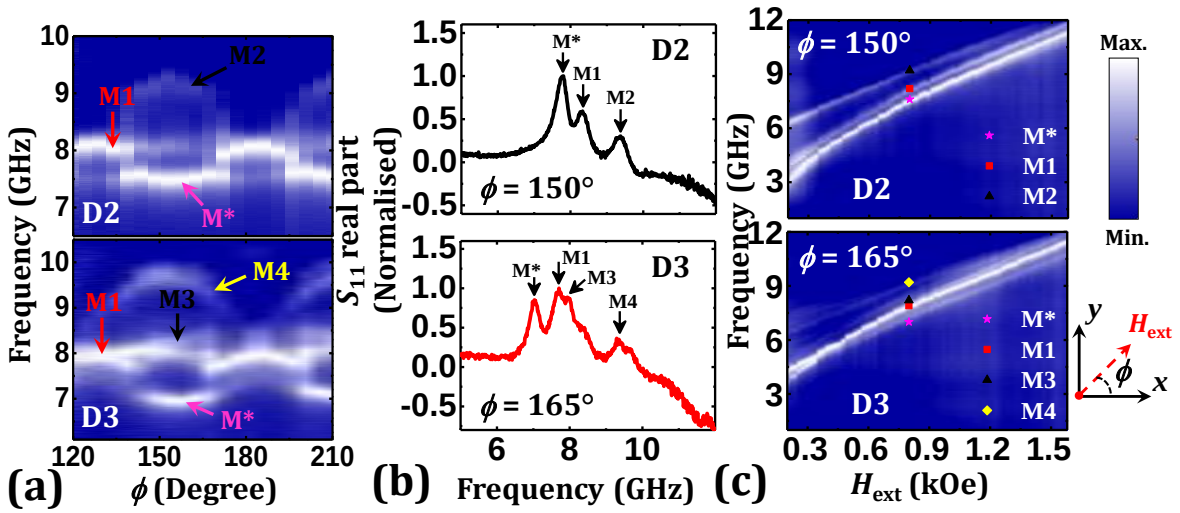

Figure 6.7. (a) Angular dispersion of FMR spectra of D2 and D3 for 120° ≤ ϕ ≤ 210° obtained from Figure 6.6 as marked by green dotted boxes in D2 and D3. (b) Real parts of the forward scattering parameter (S_{11}) representing the FMR spectra for D2 and D3 at bias magnetic field H_{ext} = 800 Oe applied at an azimuthal angle ϕ = 150° and 165°, respectively. The observed SW modes were marked by down arrows. (b) Bias field (H_{ext}) dependent SW absorption spectra of D2 at ϕ = 150° and D3 at ϕ = 165° are shown with H_{ext} = 800 Oe. The surface plots correspond to the experimental results, while the

symbols represent the simulated data. The color map for the surface plots and the schematic of H_{ext} are given on the right side of the figure.

In contrast, the angular dispersions of the SW modes for D2 and D3 reflect very interesting behaviour as there is a stark modulation in the SW intensity of M1 in both D2 and D3 when the bias field orientation is varied. This phenomenon is more prominent in Figure 6.7(a) which have been extracted from Figure 6.6, for 120° ≤ ϕ ≤ 210°, as marked by the green dotted boxes in D2 and D3, respectively. In D2, for 135° ≤ ϕ ≤ 165°, apparently a mode hopping occurs from mode M1 to a new mode M*. However, on a closer look, it appears that the mode splits into a higher power lower frequency mode M*, while M1 also remains with a very low power and M2 possesses a systematic dispersion. This multimodal oscillation for the limited angular range is similar to optical parametric generation, which appears and disappears periodically with an angular period of 60°. Similar behaviour is observed for D3, but here, in addition to the two modes (M* and M4), another mode M3 remains very close to M1. The presence of this additional mode M* has been also confirmed from bias field-dependent SW dispersion curves of D2 and D3 measured at ϕ = 150° and 165°, respectively, as demonstrated in Figure 6.7(c). This behaviour is reconfirmed by the SW spectra shown in Figure 6.1(b) and Figure 6.7(b), which shows the appearance and disappearance of the additional modes with M1 at a regular interval of 60°.

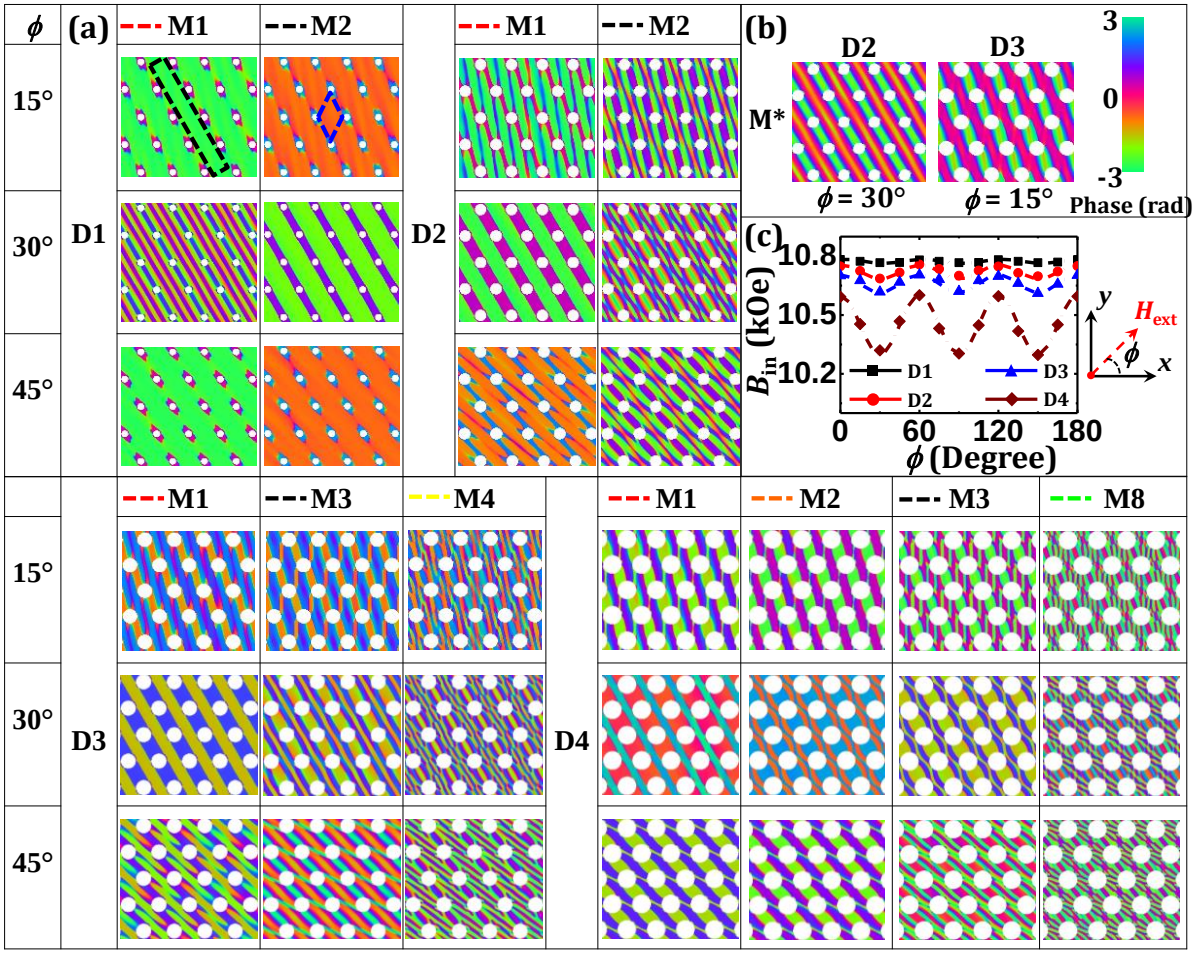

Figure 6.8. (a) Simulated spatial distributions of the phase profile corresponding to different anisotropic SW modes obtained in D1-D4 with H_{ext} = 800 Oe at ϕ = 0°, 15° and 30°, respectively. The black dotted box inside mode 1 (M1) of D1 at ϕ = 15° represents the nature of extended SW mode in a direction perpendicular to H_{ext}. (b) Simulated phase maps of the additional SW mode (M*) obtained in D2 at ϕ = 30° and D3 at ϕ = 15°, respectively with H_{ext} = 800 Oe. The color map for the phase distributions and the schematic of H_{ext} are shown on the top right corner of the figure. (c) Evolution of the simulated internal field (B_{in}) values in D1-D4 with varying ϕ at H_{ext} = 800 Oe obtained by taking linescans in the region marked by blue dotted box inside mode 2 (M2) of D1 at ϕ = 15°.

The evolution of SW phase maps with ϕ in Figure 6.8(a) (corresponding power maps are shown in Figure 6.9) shows that mode M1 in D1 remains almost invariant, i.e. extended in the direction perpendicular to the bias field along the NiFe channel between the antidots as marked by the black dotted box in M1 of D1. The quantization along the field direction is modified when ϕ is changed from 0° to 30°. However, M2 is converted into an extended mode from quantized mode when ϕ is rotated from 0° to 15° or more. On the other hand, both the SW modes (M1 and M2) in D2 experience a significant

transformation as ϕ changes to 30° and are converted to the extended modes inside the NiFe channel but with different quantization number along the field direction. Similarly, in D3 when ϕ is increased, the two lower frequency anisotropic modes M1 and M3 undergo conversion from quantized SW modes to extended modes but with different quantization number inside the NiFe channel, whereas M4 remains spatially invariant with ϕ. The asterisk marked mode M* in D2 shows extended nature at ϕ = 30°, while in D3 it represents quantized behaviour at ϕ = 15° similar to M1 although they are in opposite phase with each other as evident from Figure 6.8(a, b). Interestingly, the lowest frequency mode M1 in D4 becomes extended mode at ϕ = 30° and again becomes quantized mode when ϕ is increased to 45° but the other anisotropic modes M2, M3 and M8 remain almost unaltered with the variation of ϕ.

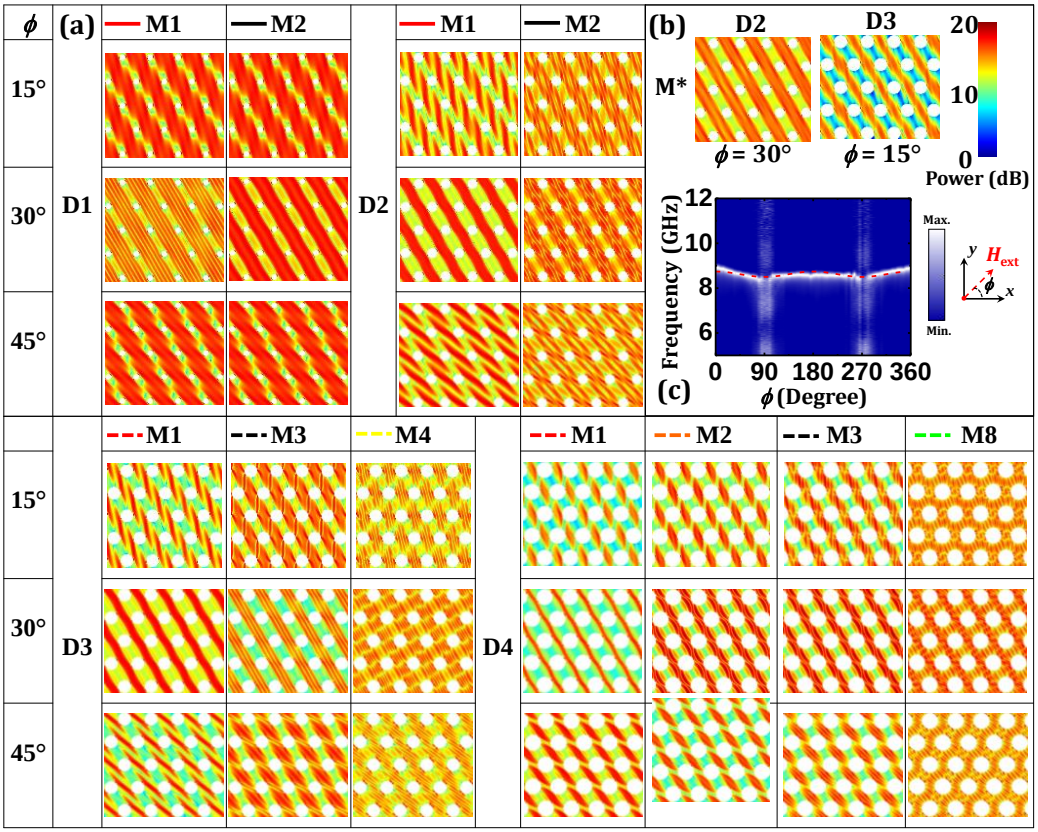

Figure 6.9. (a) Simulated spatial distributions of the power profile corresponding to different anisotropic SW modes obtained in D1-D4 with H_{ext} = 800 Oe at ϕ = 0°, 15° and 30°, respectively. The black dotted box inside mode 1 (M1) of D1 at ϕ = 15° represent the nature of extended SW mode in a direction perpendicular to H_{ext}. (b) Simulated power maps of the additional SW mode (M*) obtained in D2 at ϕ = 30° and D3 at ϕ = 15°, respectively with H_{ext} = 800 Oe. The color map for the power distributions is shown on the top right corner of the figure. (c) Variation of FMR frequency with the azimuthal

angle (ϕ) varying from 0° to 360° for NiFe thin film are shown at H_{ext} = 800 Oe. The surface plots represent the experimental results while the dotted line describe the sinusoidal fit for the observed anisotropic SW mode. The color map associated with the surface plots and the schematic of the orientation of H_{ext} are shown on the right side of the figure.

The origin of the observed two-fold rotational anisotropy can be explained by considering the boundary effect coming from the rectangular shape of the boundary of the samples which has been confirmed from the angular dispersion spectra of NiFe thin film measured at H_{ext} = 800 Oe as shown in Figure 6.9(c). To unravel the reason behind the presence of the six-fold anisotropic behaviour observed in all the lattices, the variation of the internal field (B_{in}) for D1-D4 is calculated at various orientations of the bias field by keeping its strength fixed to H_{ext} = 800 Oe in the region marked by the blue dotted box as shown in M2 of D1 at ϕ = 15° in Figure 6.8(a). It is evident from Figure 6.8(c) that the variation of B_{in} with ϕ indeed possesses a periodic six-fold rotational symmetry in case of all the samples, where this anisotropic contribution increases systematically from D1 to D4. Consequently, this is reflected as the anisotropic behaviour of the SW mode frequencies in the angular dispersion behaviour obtained for these lattices.

6.4. Conclusion

In summary, we have investigated the evolution of magnetization dynamics of hexagonally arranged NiFe circular antidot arrays with varying antidot diameter having same lattice spacing by controlling the bias magnetic field strength and its in-plane orientation using broadband ferromagnetic resonance technique. The field dispersion spectra of these systems reveal that the SW dynamics get drastically modified as the antidot diameter is varied. Rich multimodal SW spectra are obtained for the highest antidot diameter, whereas the number of SW modes reduces systematically with the decreasing antidot diameter. Moreover, a crossover between two higher frequency SW modes is observed for the lattices with higher hole diameter when the strength of the bias field is reduced. The simulated static magnetic configurations along with the power and phase profiles unravel the spatial distribution of the observed SW modes which confirms the formation of SW quantization laterally as well as diagonally inside the array having higher hole diameter at low bias field due to the strong overlapping of

demagnetization regions between the antidots. As a result, the internal field is reduced significantly with the enhancement in antidot diameter. The variation of magnonic spectra with the in-plane orientation for all the samples shows the presence of two anisotropic SW modes both in opposite phase to each other, with six-fold rotational symmetry which is strongly modulated when the hole diameter is increased. Interestingly, for intermediate antidot diameters, the lowest frequency SW mode apparently shows a mode hopping-like behaviour with 60° periodicity but a closer look reveals a parametric splitting of mode. The phase maps of these samples unveil an interesting conversion from extended nature to quantized standing wave pattern or vice-versa in most of these anisotropic SW modes with the modulation of in-plane orientation. Further, the variation of internal field with the in-plane orientation confirms the presence of six-fold anisotropy which is strongly modulated when the diameter of the antidots is modified. Thus, the variation in both the antidot size and the magnetic field orientation demonstrate active methods essentially leading to a modulation in the profile of a periodically varying SW channel which may subsequently determine the SW frequency dispersion. This property can be implemented in dynamic spin-wave filters and magnonic waveguides in the gigahertz frequency range. Also, the observed mode hopping-like behaviour can be utilized in non-linear magnonic devices or coupled waveguides analogous to opto-electronic devices in photonics. Therefore, the observed tunability of the magnetization dynamics with the antidot size as well as the strength and orientation of the in-plane bias field plays a crucial role from a fundamental scientific viewpoint as well as in terms of the nanoscale magnonic crystal-based technology.

6.5. Materials and Methods

6.5.1. Sample Preparation

The periodic arrays of $Ni_{80}Fe_{20}$ (NiFe) circular antidots arranged in hexagonal lattice were fabricated by using a combination of e-beam lithography (EBL), e-beam evaporation (EBE) and ion beam milling. The diameters (d) of the antidots were 140, 240, 340 and 440 nm with maximum ± 5% deviation, while the lattice spacing (a) was kept fixed at 700 nm in order to obtain a significant tunability in the SW spectra due to the modification of the internal field profiles. At first, 20-nm-thick NiFe film was deposited with a coating of 60 nm thickness of Al_2O_3 as a protective layer on top of a

commercially available self-oxidized silicon Si (100) substrate using e-beam evaporation in an ultra-high vacuum chamber at a base pressure of 2×10^{-8} Torr. Bi-layer (PMMA/MMA) resist was used for e-beam lithography to prepare the resist pattern on the NiFe film followed by Argon ion milling at a base pressure of 1×10^{-4} Torr to etch out the NiFe film from everywhere except the unexposed resist pattern for creating the antidots. The ion milling on the NiFe film was performed down to the base of the film for each pattern. Subsequently, a co-planer waveguide (CPW) made of Au with a thickness of 150 nm was deposited on top of the NiFe antidot lattice at a base pressure of 6×10^{-7} Torr for the broadband ferromagnetic resonance measurement. Here, the Au waveguide was patterned by using mask-less photolithography. The width and length of the central conducting line of this CPW are 30 μm and 300 μm respectively so that the array falls under the centre of the central conducting line of CPW which has a nominal characteristic impedance of 50 Ω.

6.5.2. Measurement Technique

The frequency domain SW dynamics measurements of the samples were performed using a broadband ferromagnetic resonance spectrometer based on a vector network analyzer (VNA-FMR) along with a home-built probe station, which includes an in-built electromagnet to apply the bias magnetic field of ± 1.8 kOe. The orientation of the bias field was varied by 360° within the sample plane. The microwave signal of varying frequency from 10 MHz to 50 GHz was launched in the CPW through a non-magnetic ground-signal-ground (G-S-G) probe via a coaxial cable and the CPW was shorted at one end so that the scattering parameter in the reflection mode (S_{11}) could be measured by the VNA after being collected by the same probe. The sample lying beneath the CPW absorbs the power at various SW frequencies during the onward and return journey of the microwave signal through the CPW structure. These together construct the characteristic SW spectrum for that sample. However, there were non-linear backgrounds in the directly measured signals originated from various sources. Hence during measurement at each bias field, a reference spectrum (spectrum taken at the highest value of the bias field) was subtracted from the signal to obtain a background-free spectrum. However, some background still remains in the spectrum, which is non-trivial to remove from the spectrum. For each sample, the spectra for a series of bias field from + 0.0 kOe to + 1.56 kOe at the separation of 20 Oe are plotted together as a

surface plot. In the course of measurement of the angular dispersion, the magnitude of the bias magnetic field was kept fixed at 800 Oe while its in-plane orientation was rotated from 0° to 360° at an interval of 5° by using a high-precision rotation stage mounted at the bottom of the electromagnet and plotted as the surface plot for each sample.

References

[1] S. Neusser, D. Grundler, Adv. Mater. 21 (2009) 2927.
[2] G. Ctistis, E. Papaioannou, P. Patoka, J. Gutek, P. Fumagalli, M. Giersig, Nano Lett. 9 (2009) 1.
[3] K. Kern, D. Heitmann, P. Grambow, Y. H. Zhang, K. Ploog, Phys. Rev. Lett. 66 (1991) 1618.
[4] V. V. Kruglyak, S. O. Demokritov, D. Grundler, J. Phys. D: Appl. Phys. 43 (2010) 264001.
[5] H. Yu, G. Duerr, R. Huber, M. Bahr, T. Schwarze, F. Brandl, D. Grundler, Nat. Commun. 4 (2013) 2702.
[6] V. V. Kruglyak, A. Barman, R. J. Hicken, J. R. Childress, J. A. Katine, Phys. Rev. B 71 (2005) 220409(R).
[7] Y. Au, M. Dvornik, O. Dmytriiev, V. V. Kruglyak, Appl. Phys. Lett. 100 (2012) 172408.
[8] S. K. Kim, K. S. Lee, D. S. Han, Appl. Phys. Lett. 95 (2009) 082507.
[9] J. Podbielski, F. Giesen, D. Grundler, Phys. Rev. Lett. 96 (2006) 167207.
[10] M. Jamali, J. H. Kwon, S.-M. Seo, K.-J. Lee, H. Yang, Sci. Rep. 3 (2013).
[11] V. E. Demidov, S. O. Demokritov, K. Rott, P. Krzysteczko, G. Reiss, Appl. Phys. Lett. 92 (2008) 232503.
[12] S. Choudhury, S. Saha, R. Mandal, S. Barman, Y. Otani, A. Barman, ACS Appl. Mater. Interfaces 8 (2016) 18339.
[13] R. Mandal, P. Laha, K. Das, S. Saha, S. Barman, A. K. Raychaudhuri, A. Barman, Appl. Phys. Lett. 103 (2013) 262410.
[14] S. Tacchi, M. Madami, G. Gubbiotti, G. Carlotti, A. O. Adeyeye, S. Neusser, B. Botters, D. Grundler, IEEE Trans. Magn. 46 (2010) 1440.
[15] R. Mandal, S. Barman, S. Saha, Y. Otani, A. Barman, J. Appl. Phys. 118 (2015) 053910.
[16] R. Mandal, S. Saha, D. Kumar, S. Barman, S. Pal, K. Das, A. K. Raychaudhuri, Y. Fukuma, Y. Otani, A. Barman, ACS Nano 6 (2012) 3397.
[17] S. Pal, J. W. Klos, K. Das, O. Hellwig, P. Gruszecki, M. Krawczyk, A. Barman, Appl. Phys. Lett. 105 (2014) 162408.
[18] S. Neusser, G. Duerr, H. G. Bauer, S. Tacchi, M. Madami, G. Woltersdorf, G. Gubbiotti, C. H. Back, D. Grundler, Phys. Rev. Lett. 105 (2010) 067208.
[19] S. Tacchi, B. Botters, M. Madami, J. W. Kłos, M. L. Sokolovskyy, M. Krawczyk, G. Gubbiotti, G. Carlotti, A. O. Adeyeye, S. Neusser, D. Grundler, Phys. Rev. B 86 (2012) 014417.
[20] B. Rana, D. Kumar, S. Barman, S. Pal, Y. Fukuma, Y. Otani, A. Barman, ACS Nano 5 (2011) 9559.
[21] W. J. Hsueh, C. H. Chen, R. Z. Qiu, Phys. Lett. A 377 (2013) 1378.

[22] V. N. Krivoruchko, A. I. Marchenko, J. Appl. Phys. 109 (2011) 083912.
[23] M. Krawczyk, S. Mamica, M. Mruczkiewicz, J. W. Klos, S. Tacchi, M. Madami, G. Gubbiotti, G. Duerr, D. Grundler, J. Phys. D: Appl. Phys. 46 (2013) 495003.
[24] O. N. Martyanov, V. F. Yudanov, R. N. Lee, S. A. Nepijko, H. J. Elmers, R. Hertel, C. M. Schneider, G. Schönhense, Phys. Rev. B 75 (2007) 174429.
[25] S. McPhail, C. M. Gürtler, J. M. Shilton, N. J. Curson, J. A. C. Bland, Phys. Rev. B 72 (2005) 094414.
[26] S. Neusser, B. Botters, D. Grundler, Phys. Rev. B 78 (2008) 054406.
[27] S. Neusser, B. Botters, M. Becherer, D. Schmitt-Landsiedel, D. Grundler, Appl. Phys. Lett. 93 (2008) 122501.
[28] R. Zivieri, S. Tacchi, F. Montoncello, L. Giovannini, F. Nizzoli, M. Madami, G. Gubbiotti, G. Carlotti, S. Neusser, G. Duerr, D. Grundler, Phys. Rev. B 85 (2012) 012403.
[29] S. Neusser, G. Duerr, S. Tacchi, M. Madami, M. L. Sokolovskyy, G. Gubbiotti, M. Krawczyk, D. Grundler, Phys. Rev. B 84 (2011) 094454.
[30] M. Kostylev, G. Gubbiotti, G. Carlotti, G. Socino, S. Tacchi, C. Wang, N. Singh, A. O. Adeyeye, R. L. Stamps, J. Appl. Phys. 103 (2008) 07C507.
[31] R. Bali, M. Kostylev, D. Tripathy, A. O. Adeyeye, S. Samarin, Phys. Rev. B 85 (2012) 104414.
[32] D. Kumar, P. Sabareesan, W. Wang, H. Fangohr, A. Barman, J. Appl. Phys. 114 (2013) 023910.
[33] A. Manzin, G. Barrera, F. Celegato, M. Coïsson, P. Tiberto, Sci. Rep. 6 (2016) 22004.
[34] S. Choudhury, S. Barman, Y. Otani, A. Barman, ACS Nano 11 (2017) 8814.
[35] J. Ding, D. Tripathy, A. O. Adeyeye, J. Appl. Phys. 109 (2011) 07D304.
[36] B. K. Mahato, S. Choudhury, R. Mandal, S. Barman, Y. Otani, A. Barman, J. Appl. Phys. 117 (2015) 213909.
[37] M. Donahue, D. G. Porter, *OOMMF User's guide, Version 1.0,* (NIST Interagency Report No. 6376; National Institute of Standard and Technology, Gaithersburg, MD, URL: http://math.nist.gov/oommf, 1999).
[38] K. H. J. Buschow, *Handbook of Magnetic Materials* (Elsevier, North Holland: Amsterdam, The Netherlands, 2009), Vol. 18, p. 168.
[39] A. Barman, S. Barman, Phys. Rev. B 79 (2009) 144415.
[40] D. Kumar, O. Dmytriiev, S. Ponraj, A. Barman, J. Phys. D: Appl. Phys. 45 (2012) 015001.
[41] LLG Micromagnetics Simulator, http://llgmicro.home.mindspring.com/.

Chapter 7

7. Controlled Evolution of Spin Waves in Unconventional Defective Honeycomb Antidot Lattices

Efficacious control of spin wave dynamics is demonstrated in two-dimensional magnonic crystals in the form of defective honeycomb antidot lattices. The spin wave dynamics of this system is investigated using broadband ferromagnetic resonance spectrometer. A stark modification in magnonic spectra is achieved with the modulation in the lattice spacing and with the bias magnetic field strength and its orientation. A rich band of spin wave modes are obtained for the lattice with smallest periodicity, which finally converges to two modes in case of the largest one. The spin wave modes in all lattices possess a strong anisotropic behaviour with a six- and two-fold rotational symmetries as a function of the bias field orientation originating from the strong modulation of internal field distribution at different regions of such unorthodox system. The experimentally observed spin wave modes have been qualitatively well reproduced by micromagnetic simulations and the simulated mode profiles unravel the presence of diverse genres of extended and localized standing modes in these unusual magnonic crystals. These observations are significant for tunability and anisotropic propagation of spin waves leading towards the development of efficient magnonic devices competent with the future microwave communication systems.

7.1. Introduction

Periodically milled out grooves or holes in a ferromagnetic (FM) thin film, termed as antidot (AD) lattice (ADL) [1,2] is one genre of magnonic crystals (MCs) [3], where conventional magnetic materials are efficiently engineered by patterning in one- (1-) [4], two- (2-) [5] or three- (3-) [6] dimensions at different length scales to tailor their static and dynamic responses over a broad temporal or frequency regimes offering improved functional properties [7]. These systems form the foundation of several present and future technological aspects such as magneto-electronics [8], magnon-spintronics [9], magneto-photonics [10] and even spin-optoelectronics [11] because of the influence of magnetic field on the electron spin as well as the light (photon)

coupling. These ADLs have been regarded as the potential aspirants for ultrahigh density storage devices [12], where memory bits can be trapped between the consecutive holes of the nanostructures. Due to the lack of any superparamagnetic [13] bottleneck at the deep nanoscale regime, they possess the most galvanic prospects in the field of magnonics [14] in which spin waves (SWs) or magnons [15] are manipulated to transfer and process information in microwave band. As a result, they will play a pivotal role in developing reprogrammable magnonic devices [16] for on-chip microwave communications e.g. magnon waveguides [17], SW amplifiers [18], couplers [19], valves [20], multiplexers [21], filters [22], phase shifters [20], interferometers [23], SW-based logic devices [24,25], transistors [26] as well as SW-mediated nano-optics [27]. In such periodically ordered ADLs, inhomogeneous internal magnetic fields [28] possess a significant contribution in tailoring the magnon band structure. Interestingly, magnetic ADLs are exchange-dipolar mediated systems as opposed to magnetostatically coupled FM dot arrays [29] so that they exhibit greater SW propagation speed [30] with larger SW propagation wavelength. More recently, the FM ADLs having their ADs filled with a contrasting FM material also have raised a great enthrallment as bi-component MCs (BMCs) [31,32] for the additional tunability in the SW bands because of the interplay between magnetic parameters of constituent magnetic media. The present lithography and fabrication recipes with advanced implementations have driven a tremendous acceleration to the patterning of such delicate magnetic systems. Interplaying with different geometrical parameters like shape [33], size [34], lattices symmetry [35] or lattice periodicity [36] of the ADs (holes) as well as the constituent FM material [37] and also by tailoring strength [38] and orientation [39] of the external magnetic field can greatly influence their magnon dynamics growing an immense interest due to their possible application potentials.

In the current years, a plethora of scientific investigations including theoretical approaches e.g. plane-wave method (PWM) [40], micromagnetic simulation [41] as well as analytical methods [42] and experimental techniques such as electrical [43], optical [36] or thermal [44] excitation methods has been delved into the gigahertz- (GHz-) frequency SW dynamics of FM ADLs. Since the last decade, excitation of non-uniform in-plane SW mode [41] as well as the pattern induced splitting of surface and volume modes [45] in such ADLs have been showcased which further revealed several exquisite

research outcomes e.g. the field-dependent confinement of SW mode [46,47], dispersive nature of entangled SWs along with the damped anisotropic behaviour, field-controlled propagation of SWs [46] and also the formation of magnonic miniband [48] with large SW velocities. Recently, the consequence of lattice defect [49] and broken translational symmetry [50] have also gained great attention due to their idiomatic properties. Consequently, an upsurge in the interest to exploit the rich underlying physics in such unorthodox magnonic networks has been observed. Here, we investigate the SW dynamics in two-dimensional (2D) arrays of $Ni_{80}Fe_{20}$ (NiFe) ADs with circular shape arranged in defective honeycomb basis using broadband ferromagnetic resonance (FMR) spectroscopy by manipulating the strength and orientation of in-plane bias magnetic field. A drastic modulation in the SW spectra is attained with the variation in the lattice periodicity. A strong anisotropic nature in the magnonic modes is procured when the orientation of the bias field is varied and this anisotropy is reduced with the decrease in the AD density. Further, we explore this significant modulation in the magnetization dynamics unravelling the presence of numerous confined and extended SW modes resulting from the modulation of internal field and demagnetizing field profiles around the ADs with the aid of numerical micromagnetic simulations.

7.2. Experimental Details:

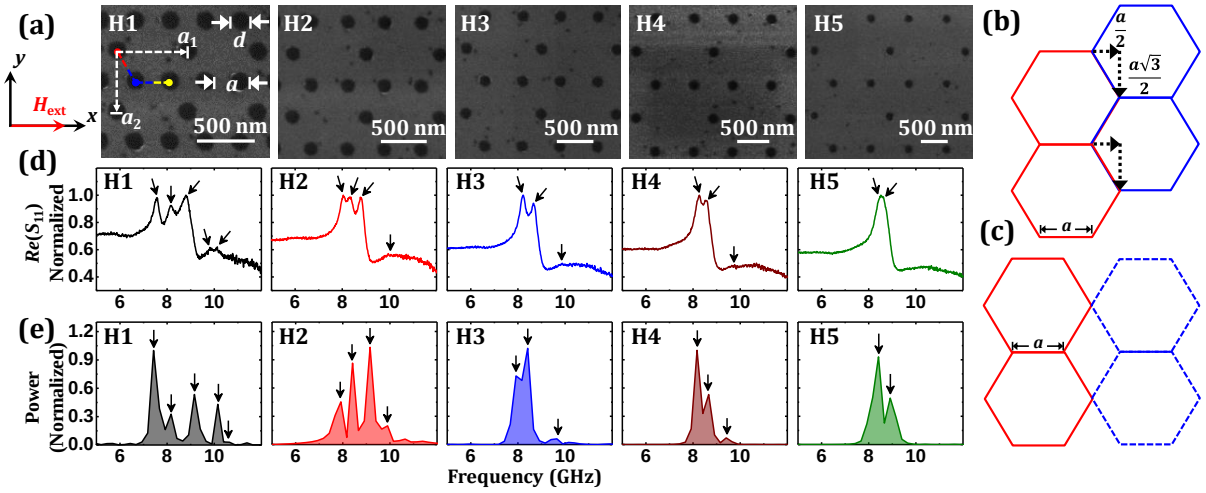

Figure 7.1. (a) Scanning electron micrographs (SEMs) of circular $Ni_{80}Fe_{20}$ (NiFe) antidots (ADs) of AD diameter (d) 140 nm, fabricated in defective honeycomb lattice with nearest AD distance, a = 300 (H1), 400 (H2), 500 (H3), 600 (H4) and 700 (H5) nm, respectively. (b) Schematic illustration of a usual honeycomb lattice. (c) Schematic of the defective honeycomb lattice obtained by shifting consecutive honeycomb cells (blue cells in Figure 7.1(b)) by $x = a/2$ and $y = (a\sqrt{3})/2$ with respect to the red honeycomb cells and the positions of the shifted cells are denoted by blue dotted honeycomb cells.

(d) Normalized real parts of the forward scattering parameter (S_{11}) denoting the SW spectra for H1-H5 at bias magnetic field, H_{ext} = 800 Oe, applied at an azimuthal angle, ϕ = 0°. The observed SW frequencies are marked by down arrows. (e) Simulated SW spectra of H1-H5 at H_{ext} = 800 Oe, applied at ϕ = 0°. The arrows denote various SW modes. The schematic of the orientation of the bias magnetic field, H_{ext} is given at the top left side.

Figure 7.1(a) exhibits in the scanning electron micrographs (SEMs) of 25 μm × 250 μm arrays of circular shaped NiFe ADs (with thickness of 20 nm) arranged in defective honeycomb lattice. As depicted in Figure 7.1(b), if the consecutive honeycomb units (blue cells) are shifted by $x = a/2$ and $y = (a\sqrt{3})/2$ with respect to the red honeycomb units, where a is the centre-to-centre distance between nearest ADs, such defective honeycomb lattice can be achieved as shown in Figure 7.1(c). Here, the lattices are attributed as H1-H5 according to ascending order of a, i.e. a = 300 (H1), 400 (H2), 500 (H3), 600 (H4) and 700 (H5) nm, respectively, which are fabricated by employing electron beam evaporation (EBE), electron beam lithography (EBL) and ion milling tools. As evident from the geometrical pattern, such unique lattice is not a familiar Bravais lattice. However, it belongs to a heretical class of tetragonal lattice under the consideration of a supercell having three-atom (three-AD in this case) basis as marked by the dotted lines connecting red, blue and yellow symbols in H1 of Figure 7.1(a). In such supercell, the primitive lattice (tetragonal) vectors are defined as $\overrightarrow{a_1}$ and $\overrightarrow{a_2}$ as depicted by two white dotted arrows in H1 of Figure 7.1(a) while, $|\overrightarrow{a_1}| = 2a$ and $|\overrightarrow{a_2}| = a\sqrt{3}$. The schematic illustration of the supercell structure and the corresponding lattice parameters for H1-H5 are tabulated in the Figure 7.2 and Table 1. This heterodox lattice structure finds similarity with the 2D stereographic projection of crystal structure (extended rhombic dodecahedron [51]) of typical Heusler alloy systems [52,53] or with the line defects in the form of grain boundaries introduced in 2D graphene-based heterostructures [54]. The diameter of each AD is d = 140 nm (± 5%). A continuous NiFe film of 20 nm thickness has also been prepared as the reference sample using the similar procedure. A 150 nm thick coplanar waveguide (CPW) made of Au is deposited on top of each AD array for the broadband FMR measurement.

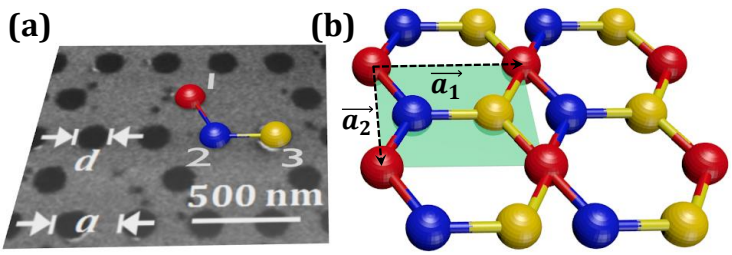

Figure 7.2. (a) Schematic illustration of the NiFe ADs arranged in an unorthodox honeycomb lattice which can form a supercell structure with three AD-basis (as represented by red (1), blue (2) and yellow (3) spheres in place of ADs) is demonstrated with a being the centre to centre distance between nearest ADs each having diameter d. (b) The primitive cell of the considered supercell structure is defined by the sides of the tetragonal lattice (as shown by the green shaded region) $\overrightarrow{a_1}$ and $\overrightarrow{a_2}$ as shown by black dotted lines where, $|\overrightarrow{a_1}| = 2a$ and $|\overrightarrow{a_2}| = a\sqrt{3}$.

Sample	AD diameter (d) in nm	Distance between nearest ADs (a) in nm	$\|\overrightarrow{a_1}\|$ in nm	$\|\overrightarrow{a_2}\|$ in nm
H1	140 (± 5%)	300 (± 2%)	600 (± 2%)	520 (± 2%)
H2	140 (± 5%)	400 (± 2%)	800 (± 2%)	693 (± 2%)
H3	140 (± 5%)	500 (± 2%)	1000 (± 2%)	867 (± 2%)
H4	140 (± 5%)	600 (± 2%)	1200 (± 2%)	1040 (± 2%)
H5	140 (± 5%)	700 (± 2%)	1400 (± 2%)	1213 (± 2%)

Table 1. The values of AD diameter (d), distance (a) nearest ADs and the magnitudes of $\overrightarrow{a_1}$ and $\overrightarrow{a_2}$ obtained for H1-H5, respectively.

The SW spectra from the arrays have been measured by employing broadband FMR spectrometer [32] associated with a vector network analyzer and a home-built probe station with nonmagnetic ground-signal-ground (G-S-G) type pico-probe. The probe station is comprised of an in-built electromagnet mounted on a high-precision rotary stage making the electromagnet capable of generating a magnetic field (H_{ext}) of ± 1.8 kOe over an in-plane (azimuthal) rotation from 0° to 360°. This is employed as an external bias magnetic field to the sample.

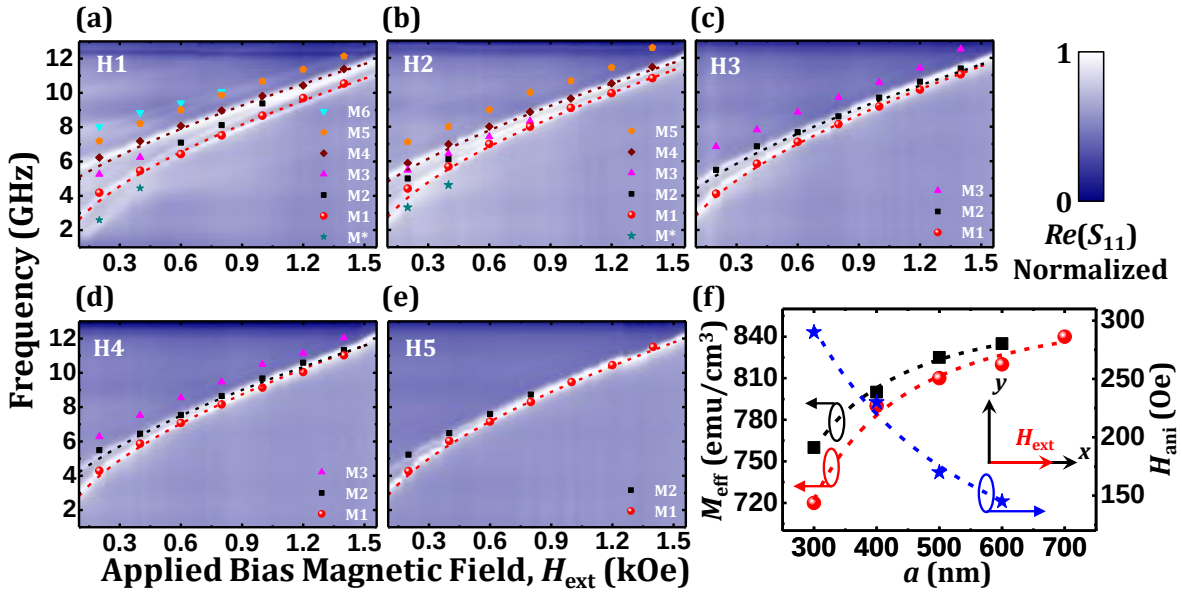

Figure 7.3. Bias field (H_{ext}) dependent SW absorption spectra of (a) H1, (b) H2, (c) H3, (d) H4 and (e) H5, respectively are shown at ϕ = 0°. The surface plots represent experimental results and symbols denote simulated results. The red dotted lines describe Kittel fit to the lower frequency SW mode M1 of H1-H5 while wine and black dotted lines denote Kittel fit to the higher frequency SW mode present in H1-H4, i.e. M4 in H1 and H2 (wine) and M2 in H3 and H4 (black), respectively. (f) The variation of effective magnetizations (M_{eff}) with the periodicity a for the two continuous SW modes (red symbols: values of M_{eff} extracted from the Kittel fit of lower frequency SW mode; red dotted line: fitted curve; black symbols: values of M_{eff} extracted from the Kittel fit of higher frequency SW mode; black dotted line: fitted curve). The variation of anisotropy field (H_{ani}: extracted from the Kittel fit of higher frequency continuous SW mode present in H1-H4) with periodicity a (blue symbols: values of H_{ani}; blue dotted line: fitted curve). The color map associated with the surface plots and schematic of H_{ext} are shown at the right side.

7.3. Results and Discussion

7.3.1. Investigation of Spin Wave (SW) Dynamics as a Function of External Magnetic Field Strength

The SW spectra in terms of real parts of the forward scattering parameter S_{11} for H1-H5, respectively are represented in Figure 7.1(d) at H_{ext} = 800 Oe applied at an in-plane (azimuthal) angle, ϕ = 0°, and the corresponding SW absorption spectra as a function of H_{ext} at ϕ = 0°, are described as SW intensity (surface) curves in Figure 7.3(a-e). The spin dynamics get drastically modified when a is varied as we have observed a transition from rich SW spectra due to the strong demagnetizing field around the ADs for H1 to a nearly uniform mode for H5 as the contribution of the demagnetizing field around the

ADs is reduced. As evident from Figure 7.3(a-e), with the variation of H_{ext}, total seven modes are observed in H1 where the number of SWs is systematically reduced to six in H2, three in both H3 and H4 and two in H5. Significantly, it is observed that, the lower frequency resonant mode M1 in H1-H5 as well as another higher frequency mode present in H1-H4, i.e. M4 in H1 and H2 (wine symbols in Figure 7.3(a, b)) and M2 in H3 and H4 (black symbols in Figure 7.3(c, d)), respectively, shows a continuous variation with H_{ext}, while the gap between these two branches gradually diminishes with increment in a where the field dispersion of H5 is very close to that of the continuous NiFe film as shown in Figure 7.4. Subsequently, both these continuous SW modes are fitted with simplified Kittel formula [55] for resonant SW frequency f, which is given by Equation 7.1:

$$f = \frac{\gamma}{2\pi}\sqrt{(H_{ext} + H_{ani})(H_{ext} + H_{ani} + 4\pi M_{eff})} \quad (7.1)$$

Here, γ is gyromagnetic ratio and H_{ani} corresponds to the total anisotropy field present in the sample, while M_{eff} represents the effective magnetization of the sample. First, the values of H_{ani} = 0 and γ = 18.1 MHz/Oe and M_{eff} = 850 emu/cm^3 are extracted for the reference NiFe thin film using the same equation as shown in Figure 7.4.

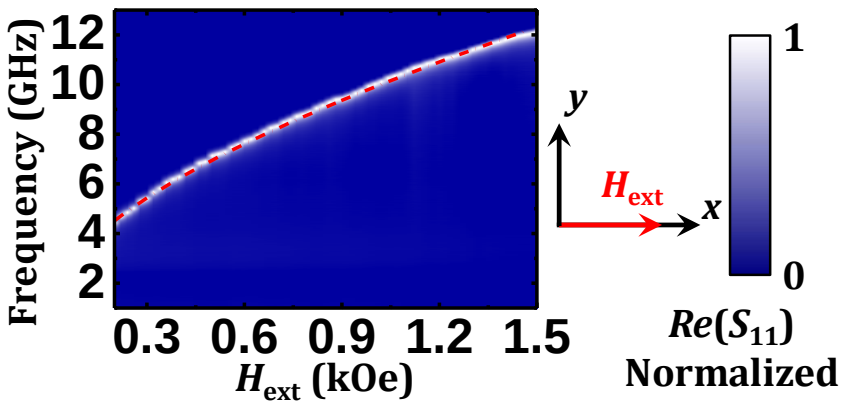

Figure 7.4. Bias field (H_{ext}) dependent spin-wave (SW) absorption spectra of continuous $Ni_{80}Fe_{20}$ (NiFe) film of 20 nm thickness at in-plane (azimuthal) angle, ϕ = 0° is shown along with the Kittel fit, which is represented by the red dotted line. The color map for the surface plot and the schematic of the orientation of H_{ext} are shown on the right side of the figure.

Interestingly, it is found that for lower frequency mode M1, M_{eff} enhances monotonically with the increase in a which is demonstrated in Figure 7.3(f) by the red symbol and this

variation of M_{eff} is fitted as shown by a red dotted line using a simple power law given by Equation 7.2:

$$M_{\text{eff}} = -\frac{A}{a^2} + C \tag{7.2}$$

This reflects that M_{eff} varies as $-1/a^2$ while, C denotes the saturation magnetization (M_S) value (≈ 860 emu/cm^3) of NiFe thin film (i.e. $a \rightarrow \infty$) which matches well with the M_{eff} value (= 850 emu/cm^3) obtained from our reference NiFe blanket film having the same thickness of 20 nm. Here, the value of H_{ani} = 0 is obtained during the fitting of M1, which is in good agreement with that obtained from the reference NiFe film. On the other hand, the M_{eff} values (black symbols) corresponding to the second continuous SW mode present in H1-H4 also follow a similar trend as represented by the black dotted line in Figure 7.3(f). However, an additional anisotropy field, H_{ani} is required for fitting the second mode and its amplitude decreases systematically with the increase in a. Figure 7.3(f) reveals that, this modulation of H_{ani} (blue symbols) can be fitted (blue dotted line) using another power law provided by Equation 7.3:

$$H_{\text{ani}} = -\frac{B}{a} + D \tag{7.3}$$

Here, D represents the H_{ani} value (≈ 0) of NiFe thin film (i.e. $a \rightarrow \infty$) which agrees very well with that obtained from our reference 20 nm-thick NiFe continuous film. Hence, the enhancement in M_{eff} for both SW modes indicates the reduction in the fraction of demagnetizing field contribution with the increase in a, eventually leading towards the behaviour of a continuous thin film.

Interestingly, a splitting is observed in H1 between the frequency branches M2 and M4 at H_{ext} ≈ 1050 Oe as well as between M5 and M6 at H_{ext} ≈ 850 Oe. However, at lower bias field, H_{ext} ≈ 450 Oe, M1 and M2 merge together while another splitting occurs between M3 and M4 at H_{ext} ≈ 530 Oe. Similar mode splitting is observed in H2 between M1 and M3 at H_{ext} ≈ 900 Oe, and M3 again split into two frequency branches (M2 and M3) at H_{ext} ≈ 500 Oe. All the SW modes in H3 and H4 are continuous although splitting between M1 and M2 is obtained at H_{ext} ≈ 830 Oe in H5. However, a very low-intensity SW mode, which is marked as M*, is observed in both H1 and H2 at lower values of H_{ext} (≤ 450 Oe).

7.3.2. Interpretation of Spin Wave (SW) Modes Using Micromagnetic Simulation

The behaviour of the SW modes has been explored by performing micromagnetic simulations employing OOMMF [56]. Here, an array of 2 × 2 honeycomb cells for each

sample has been considered incorporating the 2D periodic boundary condition (PBC) to consider the large areas of the experimentally investigated samples. Each simulated sample has been divided into rectangular parallelepiped cells having dimensions 4 × 4 × 20 nm^3. The exchange stiffness constant value of NiFe considered during the simulation is A_{NiFe} = 1.3 × 10^{-6} erg/cm [57]. The gyromagnetic ratio, γ = 18.1 MHz/Oe, anisotropy field, H_{ani} = 0 and saturation magnetization, M_{NiFe} = 850 emu/cm^3 for NiFe have been extracted from the Kittel fit of the bias field dispersion curve of NiFe film demonstrated in Figure 7.4. The micromagnetic simulation details are explained elsewhere [58].

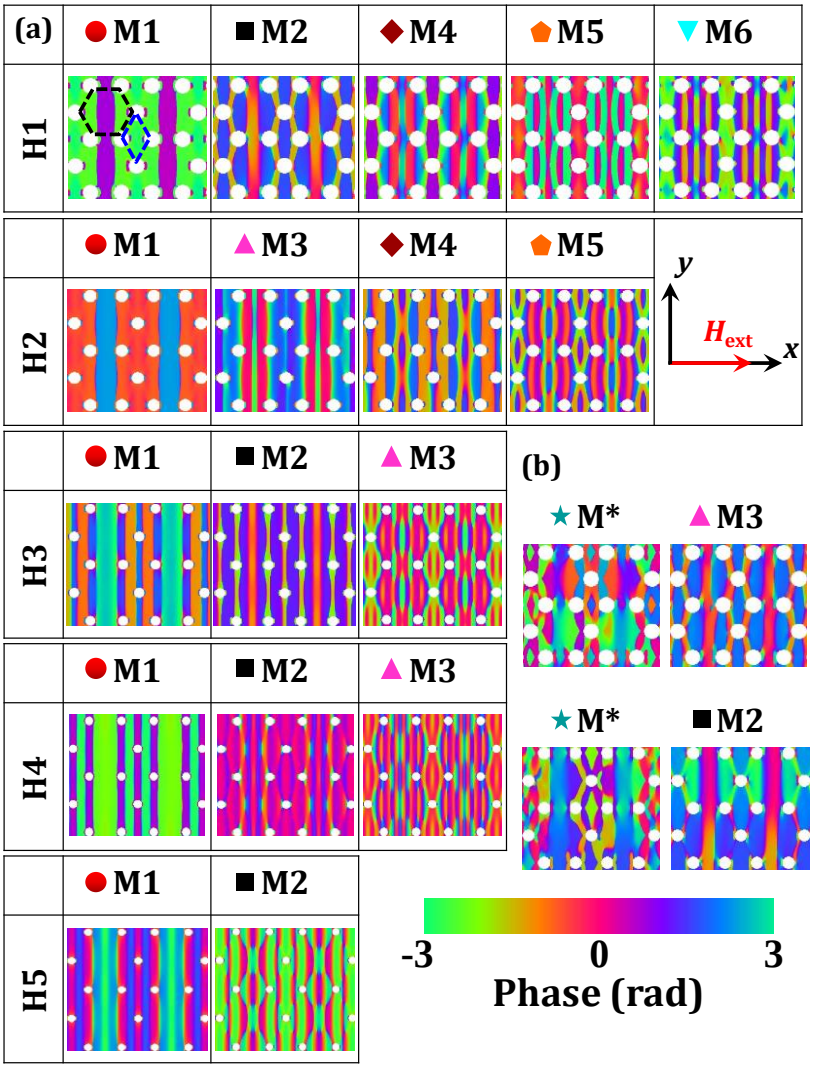

Figure 7.5. (a) Simulated spatial phase maps for different resonant SW modes observed in H1-H5 at H_{ext} = 800 Oe for ϕ = 0°. (b) Simulated phase profiles of additional SW modes observed at smaller bias field, H_{ext} = 400 Oe in H1 and H2, respectively. The color map of phase profile and the schematic of H_{ext} are given at the right side.

Figure 7.1(e) reveals that the experimental results have been qualitatively well reproduced by the micromagnetic simulations which are plotted at H_{ext} = 800 Oe, as well as in field dispersion spectra of H1-H5 in Figure 7.3(a-e) as represented by filled symbols. However, the slight quantitative disagreements between experimental and simulated outcomes may arise due to the deviation of the experimental samples and conditions from the simulated ones. The general deviation in the physical dimensions as obtained in the experimental samples has been included already in the simulations. However, it is not possible to include the precise edge deformations in the finite difference method-based micromagnetic simulations.

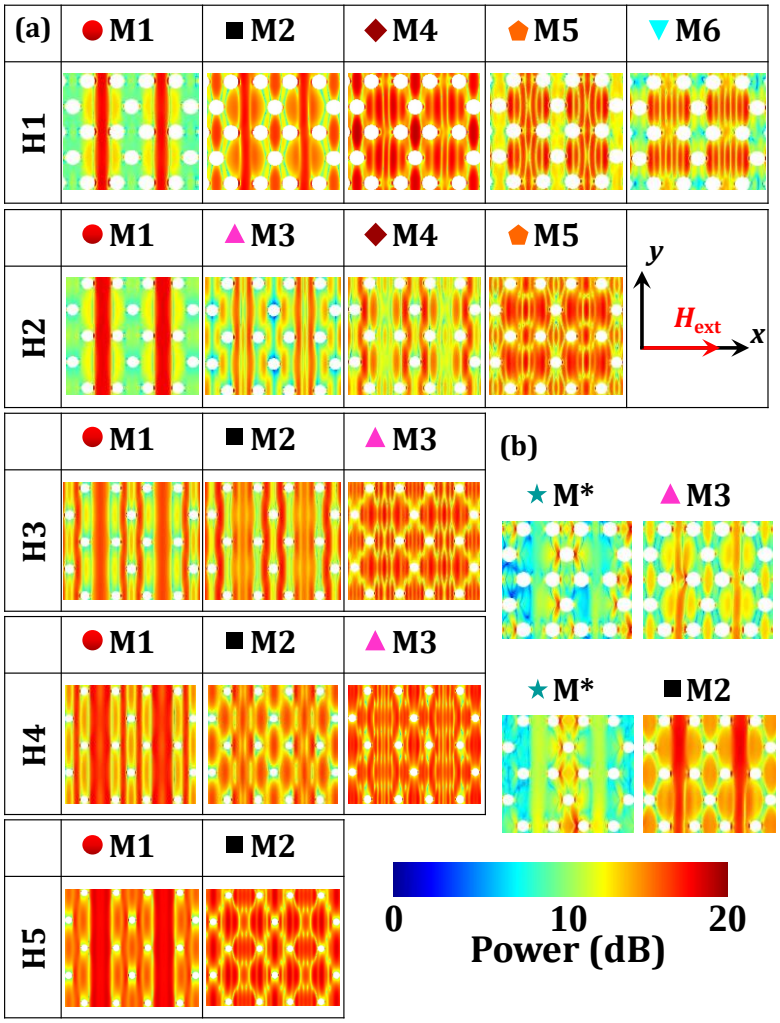

Figure 7.6. (a) Simulated spatial distributions of power profile corresponding to different resonant SW modes obtained at H_{ext} = 800 Oe applied at ϕ = 0° for H1-H5. (b) Simulated power maps of the additional SW modes obtained at a lower bias field H_{ext} = 400 Oe for H1 and H2, respectively. The color map for the power distributions and the schematic of H_{ext} are shown at the right side of the figure.

To extrapolate the understanding behind the nature of various SW modes, the spatial power and phase profiles of those SW modes have been mapped out using a homebuilt code [59]. Figure 7.5(a) demonstrates the phase profiles of the SW modes for H1-H5 at H_{ext} = 800 Oe while, Figure 7.5(b) shows the nature of the SW modes present in H1 (M* and M3) and H2 (M* and M2), respectively, at H_{ext} = 400 Oe. Different genres of extended and localized SW modes are obtained because of confining potentials originating from demagnetizing fields surrounding the ADs and different quantization numbers are assigned for the localized SW modes depending upon the number of antinodes. Also, according to the location of the SW quantization, two different quantization numbers are assigned. Here, *m* represents quantization of SWs inside the honeycomb cell in the *x*-direction as denoted by the black dotted box in M1 of H1 in Figure 7.5(a), while *n* denotes SW quantization inside the rhombic region surrounded by four such honeycomb cells in *x*-direction and this is defined by the blue dotted box in M1 of H1 in Figure 7.5(a).

The phase distributions of SW modes in H1-H5 demonstrated in Figure 7.5(a, b) (corresponding power profiles are described in Figure 7.6) unveil that, the lower frequency SW mode M1, represents an extended nature along *y*-direction (i.e. perpendicular to direction of H_{ext}) along the channel through the honeycomb cells although possessing a localized behaviour along *x*-direction with *m* = 3, 3, 5, 5 and 7, while *n* = 1, 1, 3, 3, and 3 for H1, H2, H3, H4 and H5, respectively. However, the SW modes M2 and M4 in H1, M3 in H2 and M2 in H3 also extend along *y*-direction but M2 in H4 and H5 become confined inside the honeycomb cell. In case of H1 from Figure 7.5(a), the SW modes M2, M4, M5 and M6 possess localized nature with *m* = 3, 5, 7 and 7, while *n* = 1 for all four modes (M2, M4-M6), respectively, where M5 and M6 are in opposite phase with each other. The localized SW modes M3-M5 in H2 have the quantization numbers, *m* = 5, 5 and 7 where *n* = 1, 3 and 3, respectively. However, some additional SW modes are observed at the low H_{ext} = 400 Oe in H1 (M* and M3) and H2 (M* and M2), respectively as shown in Figure 7.5(b). For both H1 and H2, M* is the edge mode where the power of M* is localized at the edges of the ADs as evident from Figure 7.6(b). On the other hand, M3 of H1 represents localized nature with *m* = 3 and *n* = 1, whereas M2 for H2 extends along *y*-direction although it shows a confined behaviour with *m* = 5

and n = 1 along the x-direction. In H3, the SW modes M2 and M3 have m = 7 and 11, while n = 3 and 5, respectively. Similarly, for M2 and M3 in H4, the quantization numbers are m = 9 and 17 and n = 5 and 7, respectively while for H5, M2 has the values of m = 11 and n = 5.

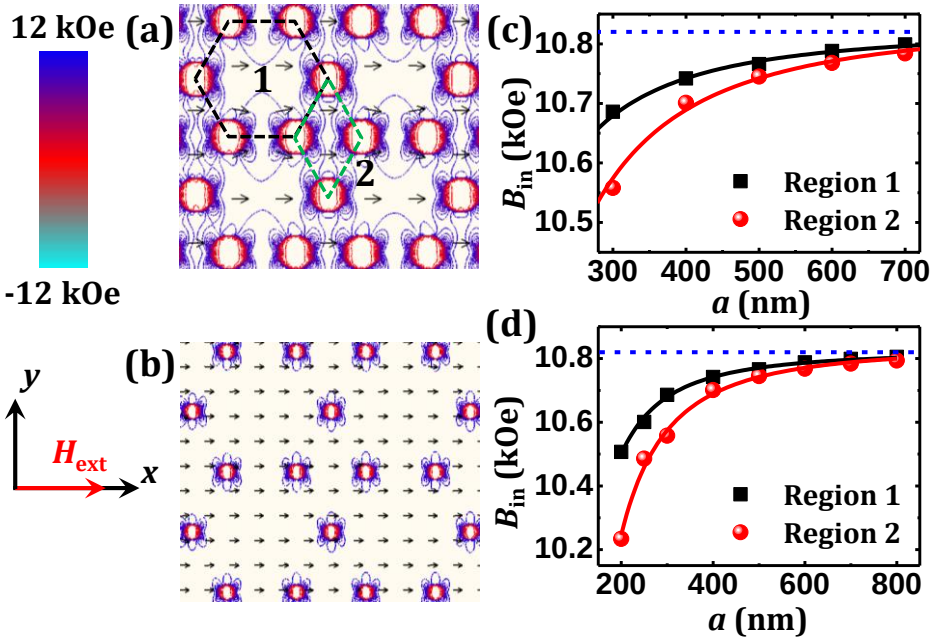

Figure 7.7. Simulated magnetostatic field distributions in (a) H1 and (b) H5 are shown at H_{ext} = 800 Oe for ϕ = 0°, while the corresponding color map is given at the left side. (c) Modulation of internal field (B_{in}) values with the periodicity a, from two different regions 1 and 2 (as shown by black and green dotted boxes in H1 of Figure 7.7(a)) from the line scan along those two different regions. (d) The variation of B_{in} with a = 200, 250, 300, 400, 500, 600, 700 and 800 nm respectively. Black and red symbols: values of B_{in} extracted from regions 1 and 2, respectively; black and red solid lines: fitted curves with the equation: $B_{in} = -\frac{A}{a^2} + C$, where, C is the B_{in} value (~ 10.82 kOe) of thin NiFe film of 20 nm thickness as described by the blue dotted line. The schematic of H_{ext} is given at the left side.

7.3.3. Investigation of Internal Field Distribution

The magnetostatic field distributions of these lattices are calculated with the aid of LLG Micromagnetic simulator [60] to interpret the large modulation of SW dynamics with the varying a in such novel honeycomb ADLs, which are described as the contour plots in Figure 7.7(a, b) for H1 and H5, respectively. It is evident from Figure 7.7(a, b) that the demagnetizing field strength surrounding the ADs is significantly decreased with the increment in a where the demagnetizing fields in H5 become very narrow and confined

around the ADs only. To unravel the strength of the total internal field (B_{in}), we have calculated the B_{in} values for H1-H5 by taking spatial line scans especially as two different regions, i.e. inside honeycomb cell (Region 1) and the rhombic region (Region 2) surrounded by four honeycomb cells as denoted by black and green dotted boxes in Figure 7.7(a) for H1. As depicted in Figure 7.7(b), B_{in} gets strongly modified with the variation of a, where a similar trend in the modulation of B_{in} with a is observed in both regions 1 and 2. Here, B_{in} enhances significantly with the increment in a because of systematic reduction in the overlapping of demagnetizing regions surrounding the ADs. Interestingly, this variation of B_{in} is well fitted using Equation 7.2, where, $C \approx 10.82$ kOe, i.e. the B_{in} value for a 20 nm-thick continuous (i.e. $a \rightarrow \infty$) NiFe thin film as shown by blue dotted line in Figure 7.7(c). To verify this behaviour, we have further calculated B_{in} values for additional simulated samples with a = 200, 250 and 800 nm, respectively where, the extracted B_{in} values from them also follow the same fitting Equation 7.2 as shown in Figure 7.7(d). This confirms that the modulation of effective magnetization, M_{eff} is in commensuration with the internal field, B_{in} which is strongly dominated by the demagnetizing field contribution present in these ADLs.

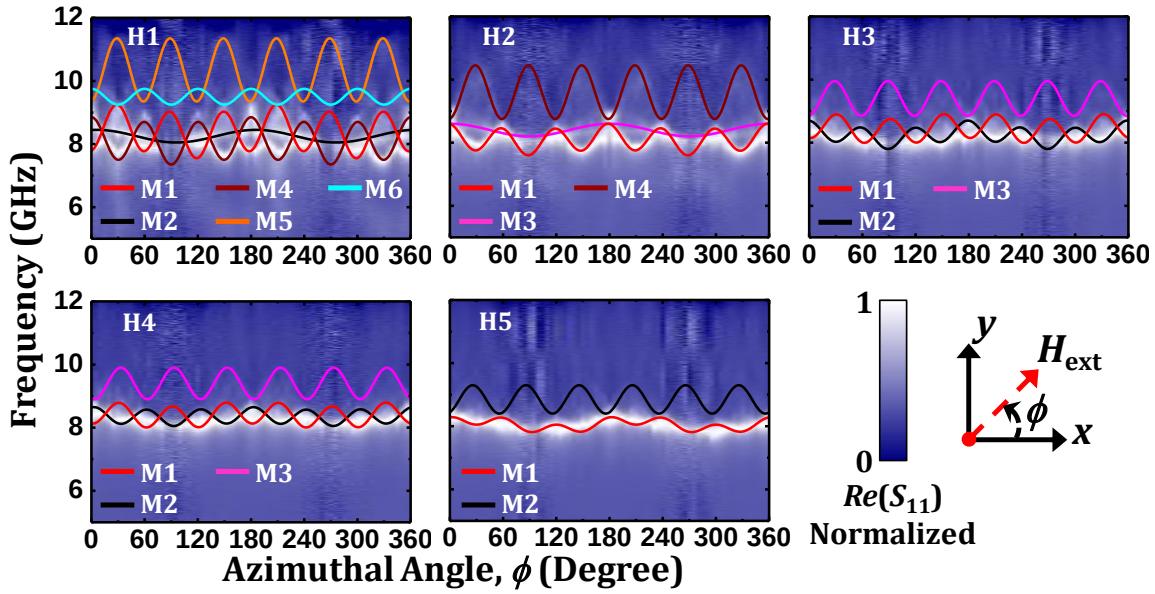

Figure 7.8. Variation of SW frequency as a function of the azimuthal angle (ϕ) varying from 0° to 360° for H1-H5 at fixed H_{ext} = 800 Oe. The surface plots denote the experimental data and the solid lines represent the sinusoidal fits to the observed anisotropic SW modes in all samples (H1-H5). The color map for the surface plots and the schematic of H_{ext} are shown on the right side.

7.3.4. Variation of Spin Wave (SW) Frequencies with the Orientation of Bias Magnetic Field

The SW spectra of H1-H5 are investigated by varying the in-plane orientation, (ϕ) of H_{ext} at a fixed strength to delve into the configurational anisotropy present in these ADLs. Figure 7.8 describes surface plots of the angular dispersion of SW frequencies in H1-H5 at H_{ext} = 800 Oe where solid lines denote theoretical fits utilizing harmonic functions with different rotational symmetries. This nature, as well as the contribution of the anisotropy of all the SW modes, get modified drastically as a is increased. In case of H1, all the SW modes show stark modulation with ϕ, e.g. both M1 and M4 possess a superposition of a strong six- and weak two-fold anisotropy although their variation is in opposite phase to each other, while M2 shows a strong two-fold anisotropy. The higher frequency modes, i.e. M5 and M6 describe six-fold rotational symmetry with a different amplitude of anisotropic contribution as well as with a phase lag of π to each other. M1 in H2 also shows six-fold rotational symmetry superposed with a weak two-fold symmetry, although M3 reveals a strong two-fold anisotropic nature while M4 possesses a six-fold anisotropy. However, a combination of two-fold and six-fold anisotropy is found for M1 and M2 in both H3 and H4 while, M3 shows a six-fold anisotropy. In H5, M1 reveals anisotropic nature with superposition of two-fold and six-fold rotational symmetry although M2 shows a six-fold anisotropy. However, the contributions of both two- and six-fold anisotropy reduce systematically from H1 to H5.

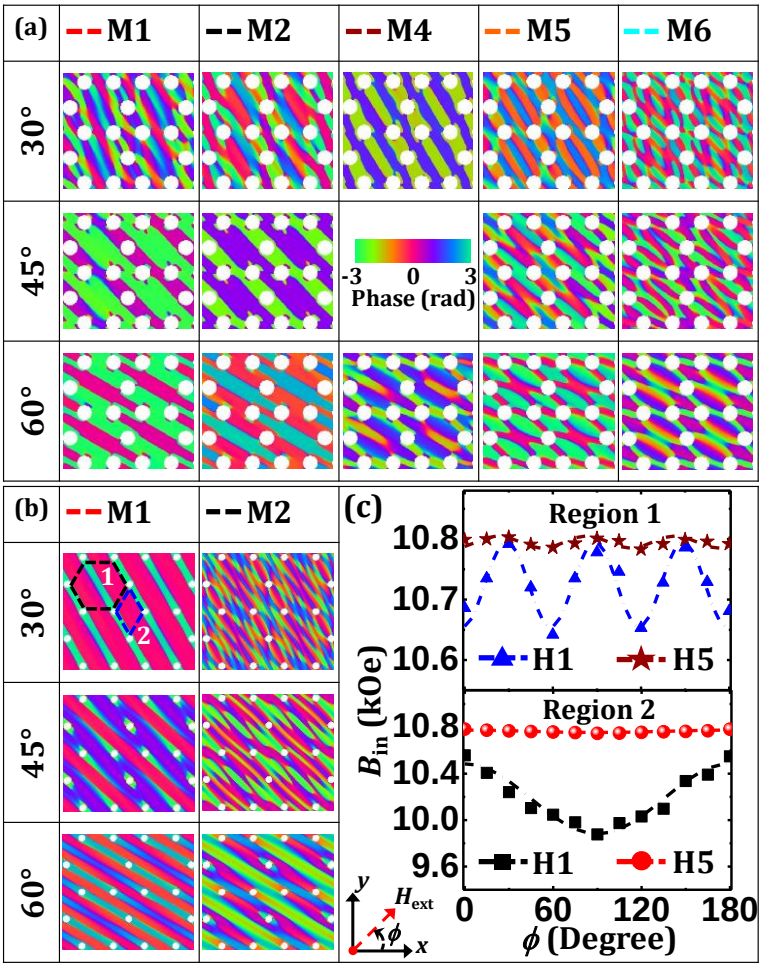

Figure 7.9. Simulated phase maps of various anisotropic SW modes obtained in (a) H1 and (b) H5 for H_{ext} = 800 Oe applied at ϕ = 30°, 45° and 60°, respectively with the corresponding color map at the centre. (c) Variation of internal field (B_{in}) in H1 and H5 as a function of ϕ for H_{ext} = 800 Oe obtained from line scans in two different regions denoted by black (region 1) and blue (region 2) dotted boxes inside M1 of H5 at ϕ = 30° in Figure 7.9(b) (symbols: simulated B_{in} values at different ϕ in regions 1 and 2 of H1 and H5, respectively; dotted lines: sinusoidal fits to the variation of B_{in} with ϕ). The schematic of H_{ext} is given at the bottom side.

The evolution of phase profiles of SWs with ϕ in Figure 7.9(a) (corresponding power distribution are described in Figure 7.10) reveals that mode M1 in H1 undergoes a drastic transformation as it converts into a localized mode from its extended nature as ϕ is increased from 0° to 30°. On the other hand, M2 and M4 possess extended behaviour till ϕ = 30° after which they become confined with further rotation of H_{ext}. However, M5 and M6 remain almost invariant with the variation of ϕ i.e. confined inside the honeycomb cell while their symmetry axes revolving continuously according to the

variation of ϕ. The behaviours of the anisotropic SW modes present in H5 i.e. M1 and M2 are found to be almost invariant with the rotation of H_{ext} as evident from Figure 7.9(b).

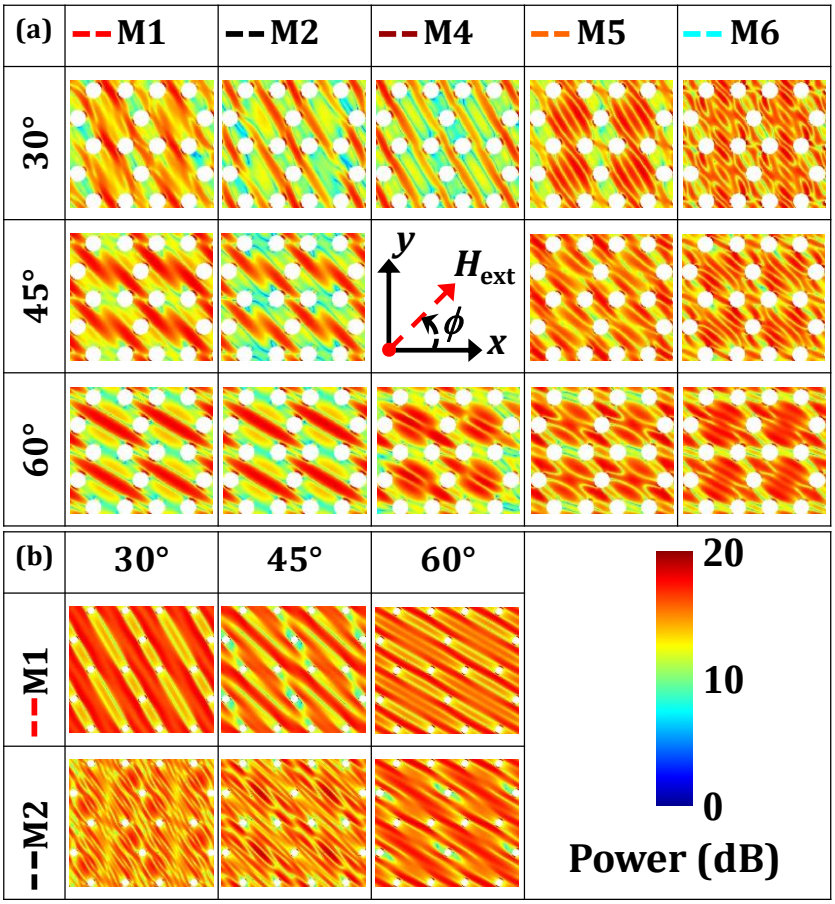

Figure 7.10. Simulated spatial distributions of power profile corresponding to different anisotropic SW modes obtained in (a) H1 and (b) H5 with bias field H_{ext} = 800 Oe applied at ϕ = 30°, 45° and 60°, respectively. The color map for the power distributions and the schematic of the orientation of H_{ext} are shown at the right side of the figure.

The power and phase maps demonstrated in Figure 7.11 describe that the anisotropic modes present in the intermediate ADLs i.e. H2, H3 and H4 also experience a significant conversion from extended to localized modes. This behaviour is periodically repeated which is commensurate with the obtained six-fold rotational anisotropy in the SW frequencies. However, the nature of the highest frequency anisotropic modes, i.e. M4 in H2 and M3 in both H3 and H4 remains almost unaffected (i.e. localized modes) with the variation of ϕ.

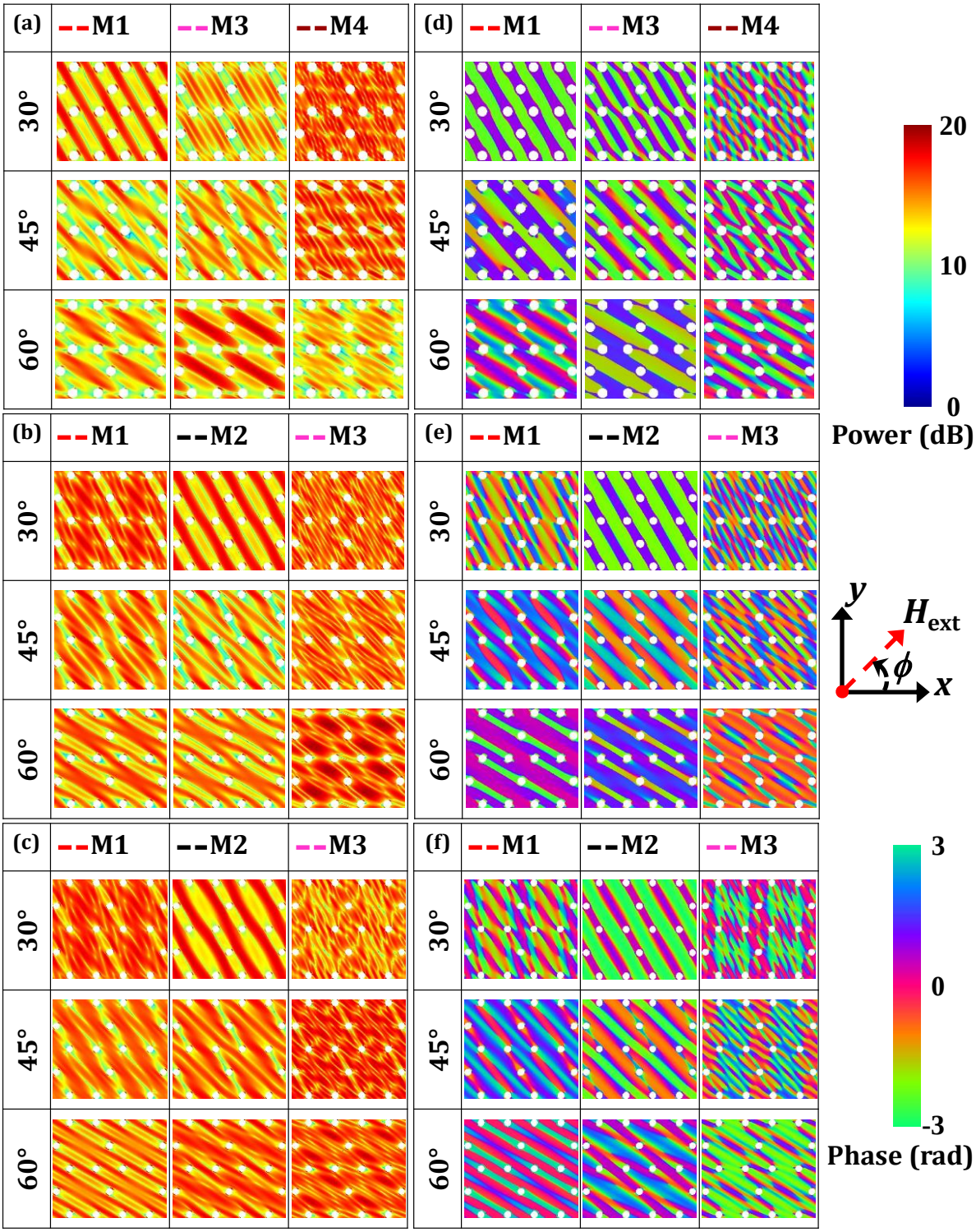

Figure 7.11. Simulated spatial distributions of power profile corresponding to different anisotropic SW modes obtained in (a) H2, (b) H3 and (c) H4 and the corresponding phase maps for (d) H2, (e) H3 and (f) H4, respectively with bias field H_{ext} = 800 Oe applied at ϕ = 30°, 45° and 60°, respectively. The color maps for power and phase distributions and the schematic of the orientation of H_{ext} are shown at the right side of the figure.

One of the reasons behind the obtained two-fold rotational anisotropy can be interpreted by considering the boundary effect originating from the sample boundary of rectangular shape which has been confirmed by measuring angular dispersion curve of NiFe thin film measured at H_{ext} = 800 Oe as shown in Figure 7.12. However, for detailed understanding about the origin of the observed six- and two-fold rotational anisotropy, the modulation of B_{in} is calculated at various ϕ for both H1 and H5 inside the honeycomb cell as well as within the rhombic region (Regions 1 and 2: marked by the black and blue dotted boxes in M1 of H5 at ϕ = 30° in Figure 7.9(b)), similarly as considered in Figure 7.7(a). The internal field profile is significantly modulated at those two different regions (1 and 2) inside the lattice as depicted in Figure 7.9(c). The modulation of B_{in} with ϕ unveils the presence of a six-fold anisotropy inside the honeycomb cell (Region 1), while a two-fold anisotropy is found in the rhombic area (Region 2). Interestingly, both the six- and two-fold anisotropy contributions in B_{in} reduce drastically for H5 as evident from Figure 7.9(c). Here, this prominent modification in B_{in} arises from the magnetic environment in different regions of these unique ADLs. Further, its systematic modulation with the orientation of the bias magnetic field is manifested as the configurational anisotropy present in the systems.

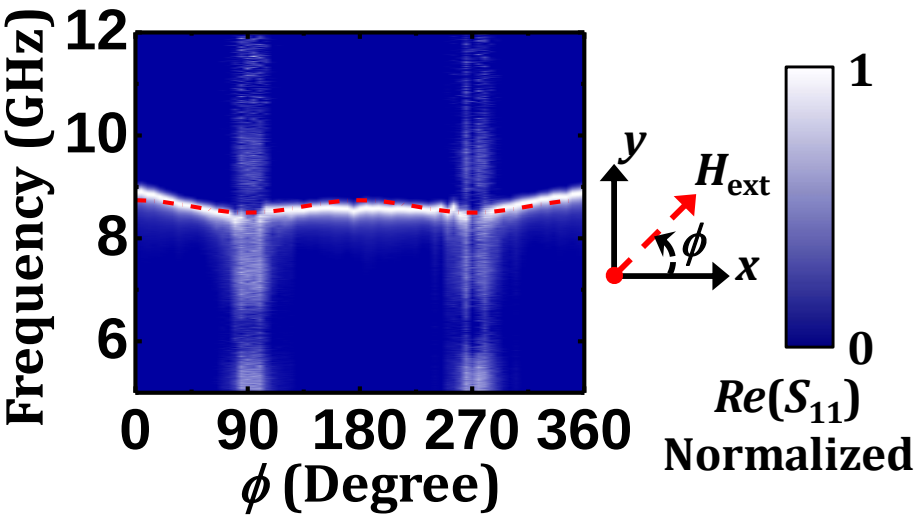

Figure 7.12. Variation of FMR frequency with the azimuthal angle (ϕ) varying from 0° to 360° for NiFe thin film are shown at constant bias magnetic field, H_{ext} = 800 Oe. The surface plots represent the experimental results while the red dotted line describe the sinusoidal fit for the observed anisotropic SW mode. The color map associated with the surface plots and the schematic of the orientation of H_{ext} are shown on the right side of the figure.

7.4. Conclusion

In summary, we have investigated the evolution of SW dynamics of NiFe circular ADs fabricated in a heterodox defective honeycomb lattice with varying periodicity by manipulating the bias magnetic field strength and its azimuthal orientation by broadband FMR method. The field dispersion curves of these samples unravel drastic modulation in the magnon modes as the periodicity is varied. Rich multimodal SW spectra are observed for the most densely packed ADL, whereas the number of SW modes reduces systematically with the decreasing periodicity approaching towards a nearly thin film-like behaviour due to the reduction of the contribution of the demagnetizing field around the ADs. The experimental observations have been reproduced by micromagnetic simulation while the spatial distribution of the SW frequencies have been numerically calculated to get an insight about the spatial nature of the dynamics. The power and phase maps have unveiled different genres of extended and localized standing SW modes. To understand the origin of the observed SW modes, internal fields including the demagnetization field contributions have been calculated. Interestingly, the modulation of the internal field follows a monotonic power-law relation with the lattice periodicity which is similar to the effective magnetization. This corroborates that the modification of effective magnetization is in commensuration with the internal field which is strongly controlled by the demagnetizing field contribution present in these ADLs. The modulation of SW spectra with in-plane orientation for all samples unveils the presence of anisotropic SW modes with six- or two-fold or a superposition of both rotational symmetries. The internal field profile inside the honeycomb cells is primarily responsible for the origin of the six-fold anisotropy whereas that within the rhombic region surrounded by four honeycomb cells gives rise to the two-fold anisotropy. The amplitudes of both six-and two-fold rotational anisotropies reduce monotonically with the enhancement in the periodicity. With the modulation of in-plane orientation, the phase profiles of the samples unravel a significant transformation from extended behaviour to quantized standing wave pattern or vice-versa for most of these anisotropic SW modes. Hence, the tuning the lattice parameter as well as the magnetic field demonstrates active methods essentially giving rise to a modification in periodically varying SW channel properties which subsequently may determine its SW frequency dispersion. Therefore, the observed tunability of the

magnetization dynamics in such novel MCs with varying periodicity and also the in-plane bias field strength and orientation can play a key role from a fundamental scientific viewpoint as along with their possible applications in magnonic crystal-based technology.

7.5. Materials and Methods

7.5.1. Sample Preparation

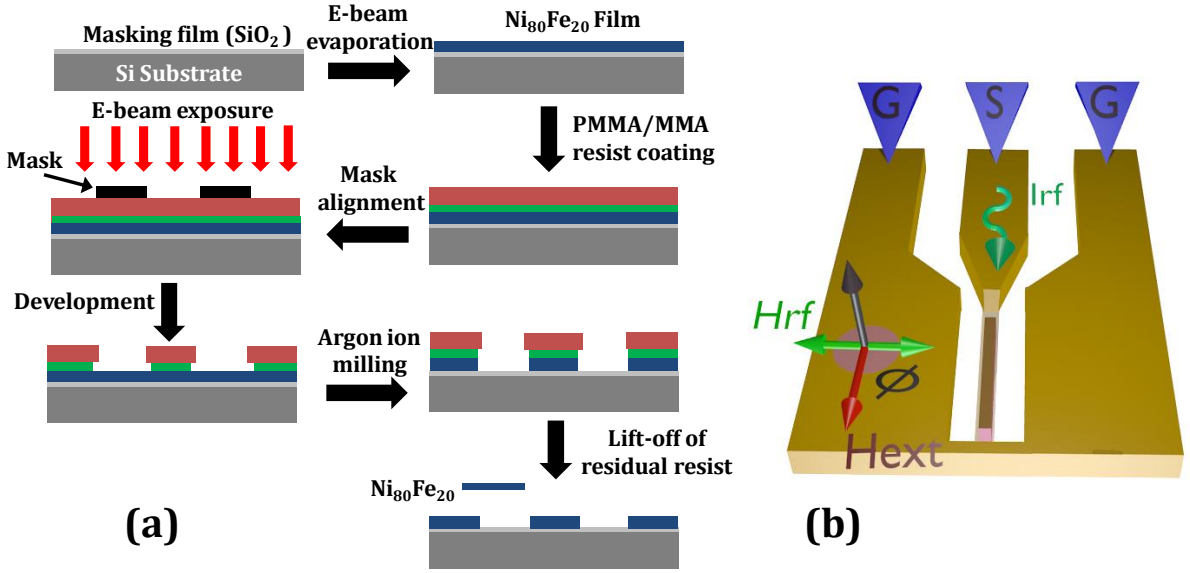

Figure 7.13. (a) Schematic of the fabrication technique used for two-dimensional (2D) array of $Ni_{80}Fe_{20}$ (NiFe) antidot lattices (ADLs). (b) Schematic of the measurement geometry employed in broadband ferromagnetic resonance (FMR) system.

The periodic arrays of $Ni_{80}Fe_{20}$ (NiFe) circular ADs arranged in defective honeycomb lattice symmetry were fabricated by using a combination of electron beam lithography (EBL), electron beam evaporation (EBE) and ion milling as described schematically in Figure 7.13(a). The diameter of each AD is about 140 nm with maximum ± 5% deviation and the centre to centre distance (a) between the nearest ADs is varied from 300 nm to 700 nm with maximum ± 2% deviation in order to obtain a significant tunability on the SW spectra due to the modification of the internal field profiles. At first, a 20 nm-thick NiFe film is deposited with a coating of 60 nm-thick Al_2O_3 as a protective layer on top of a commercially available self-oxidized Silicon (Si) (100) substrate using e-beam evaporation in an ultra-high vacuum chamber at a base pressure of 2×10^{-8} Torr. Bi-layer (PMMA/MMA) resist was used for e-beam lithography to prepare the resist pattern on the NiFe film followed by Argon ion milling at a base pressure of 1×10^{-4}

Torr to etch out the NiFe film from everywhere except the unexposed resist pattern for creating the ADs. The ion-milling on the NiFe film was performed down to the base of the film for each pattern. Subsequently, a co-planar waveguide (CPW) made of Au with a thickness of 150 nm was deposited on top of the NiFe ADL at a base pressure of 6×10^{-7} Torr for the broadband ferromagnetic resonance (FMR) measurement. The waveguide was patterned by using mask-less photolithography which is followed by the deposition Au of thickness 150 nm on top of a 5 nm-thick Ti layer at the same base pressure. The width and length of the central conducting line of this CPW are 30 μm and 300 μm, respectively, so that the array (width 25 μm and length 250 μm) lies under the centre of the central conducting (signal) line of CPW with a nominal characteristic impedance of 50 Ω. A continuous 20 nm-thick NiFe film has also been prepared as the reference sample using the similar fabrication procedure.

7.5.2. Measurement Technique

The frequency domain SW dynamics of the samples were measured by using a broadband ferromagnetic resonance (FMR) spectrometer (demonstrated schematically in Figure 7.13(b)) based on a vector network analyzer (VNA) along with a home-built probe station, which includes an in-built electromagnet to apply the bias magnetic field (H_{ext}) of ± 1.8 kOe while, its orientation can be varied by 360° within the sample plane. The sample is viewed with the aid of a microscope assisted by an illumination set-up. The microwave current (I_{rf}) of varying frequency from 1 GHz to 20 GHz is launched in the CPW (this generates a radio frequency (rf) field, H_{rf} perpendicular to I_{rf}) through a non-magnetic ground-signal-ground (G-S-G) probe via a co-axial cable and the CPW is shorted at one end so that the scattering parameter in the reflection mode (S_{11}) can be measured by the VNA after being collected by the same probe. The sample absorbs the power at various SW frequencies during the onward and return journey of the microwave signal through the CPW structure, which forms the characteristic SW spectrum for that sample. However, there are non-linear backgrounds in the directly measured signals originated from various sources. Hence, during measurement at each H_{ext}, a reference spectrum (spectrum at the highest value of the bias field) is subtracted from the signal to obtain a background free spectrum. However, some background still remains in the spectrum, which is non-trivial to remove. For each sample, the spectra for a series of H_{ext} from + 0.1 kOe to + 1.56 kOe at an interval of 20 Oe are plotted

together as a 2D surface (intensity) plot. During the investigation of angular dispersion of the SW modes in all the samples, the magnitude of H_{ext} has been kept fixed at 800 Oe while, its in-plane orientation is rotated from 0° to 360° at an interval of 5° by using a high-precision rotation stage mounted at the bottom of the electromagnet and plotted as the surface plot for each sample.

7.5.3. Theoretical Calculation

An array of 2 × 2 defective honeycomb cells, mimicking the experimental sample, has been considered for the simulation where the 2D periodic boundary condition has been applied to incorporate the large areas of the experimentally investigated samples. Each simulated sample has been discretized into rectangular prism-like cells with lateral dimensions less than the exchange length (≈ 5.3 nm for NiFe) of the material of the samples. Initially, the static magnetic configurations of the samples were acquired at the applied bias field. This was achieved by first applying a large magnetic field to saturate each sample along the field direction and then by reducing the large magnetic field to bias field magnitude and allowing the system to reach the equilibrium. Further, the SW dynamics were achieved by applying a pulsed magnetic field and by calculating the spatial distribution of magnetization at time steps of 10 ps for a total duration of 4 ns. The convergence criterion for the dynamical calculation is applied on the time steps. The spatial profile of the power and phase information for various resonant modes are extracted by keeping one of the spatial coordinates fixed in the space and then by performing a discrete Fourier transform on the magnetization dynamics with respect to the time domain.

References

[1] K. Kern, D. Heitmann, P. Grambow, Y. H. Zhang, K. Ploog, Phys. Rev. Lett. 66 (1991) 1618.
[2] P. Vavassori, G. Gubbiotti, G. Zangari, C. T. Yu, H. Yin, H. Jiang, G. J. Mankey, J. Appl. Phys. 91 (2002) 7992.
[3] S. A. Nikitov, P. Tailhades, C. S. Tsai, J. Magn. Magn. Mater. 236 (2001) 320.
[4] A. V. Chumak, A. A. Serga, B. Hillebrands, M. P. Kostylev, Appl. Phys. Lett. 93 (2008) 022508.
[5] D. Kumar, J. W. Kłos, M. Krawczyk, A. Barman, J. Appl. Phys. 115 (2014) 043917.
[6] A. Fernández-Pacheco, R. Streubel, O. Fruchart, R. Hertel, P. Fischer, R. P. Cowburn, Nat. Commun. 8 (2017) 15756.

[7] R. L. Stamps, S. Breitkreutz, J. Åkerman, A. V. Chumak, Y. Otani, G. E. W. Bauer, J. U. Thiele, M. Bowen, S. A. Majetich, M. Kläui, J. L. Prejbeanu, B. Dieny, N. M. Dempsey, B. Hillebrands, J. Phys. D: Appl. Phys. 47 (2014) 333001.
[8] G. A. Prinz, Science 282 (1998) 1660.
[9] A. V. Chumak, V. I. Vasyuchka, A. A. Serga, B. Hillebrands, Nat. Phys. 11 (2015) 453.
[10] G. Ctistis, E. Papaioannou, P. Patoka, J. Gutek, P. Fumagalli, M. Giersig, Nano Lett. 9 (2009) 1.
[11] J. Wang, C. Zhang, H. Liu, R. McLaughlin, Y. Zhai, S. R. Vardeny, X. Liu, S. McGill, D. Semenov, H. Guo, R. Tsuchikawa, V. V. Deshpande, D. Sun, Z. V. Vardeny, Nat. Commun. 10 (2019) 129.
[12] L. Torres, L. Lopez-Diaz, O. Alejos, J. Appl. Phys. 87 (2000) 5645.
[13] S. H. Charap, L. Pu-Ling, H. Yanjun, IEEE Trans. Magn. 33 (1997) 978.
[14] V. V. Kruglyak, S. O. Demokritov, D. Grundler, J. Phys. D: Appl. Phys. 43 (2010) 264001.
[15] S. Neusser, D. Grundler, Adv. Mater. 21 (2009) 2927.
[16] M. Krawczyk, D. Grundler, J. Phys. Condens. Matter 26 (2014) 123202.
[17] V. E. Demidov, M. P. Kostylev, K. Rott, J. Münchenberger, G. Reiss, S. O. Demokritov, Appl. Phys. Lett. 99 (2011) 082507.
[18] Y. Acremann, X. W. Yu, A. A. Tulapurkar, A. Scherz, V. Chembrolu, J. A. Katine, M. J. Carey, H. C. Siegmann, J. Stohr, Appl. Phys. Lett. 93 (2008) 102513.
[19] H. Yu, G. Duerr, R. Huber, M. Bahr, T. Schwarze, F. Brandl, D. Grundler, Nat. Commun. 4 (2013) 2702.
[20] Y. Au, M. Dvornik, O. Dmytriiev, V. V. Kruglyak, Appl. Phys. Lett. 100 (2012) 172408.
[21] K. Vogt, F. Y. Fradin, J. E. Pearson, T. Sebastian, S. D. Bader, B. Hillebrands, A. Hoffmann, H. Schultheiss, Nat. Commun. 5 (2014) 3727.
[22] S. K. Kim, K. S. Lee, D. S. Han, Appl. Phys. Lett. 95 (2009) 082507.
[23] K. S. Lee, S. K. Kim, J. Appl. Phys. 104 (2008) 053909.
[24] M. P. Kostylev, A. A. Serga, T. Schneider, B. Leven, B. Hillebrands, Appl. Phys. Lett. 87 (2005) 153501
[25] M. Gavagnin, H. D. Wanzenboeck, S. Wachter, M. M. Shawrav, A. Persson, K. Gunnarsson, P. Svedlindh, M. Stöger-Pollach, E. Bertagnolli, ACS Appl. Mater. Interfaces 6 (2014) 20254.
[26] A. V. Chumak, A. A. Serga, B. Hillebrands, Nat. Commun. 5 (2014).
[27] V. E. Demidov, S. O. Demokritov, K. Rott, P. Krzysteczko, G. Reiss, Appl. Phys. Lett. 92 (2008) 232503.
[28] A. Barman, J. Phys. D: Appl. Phys. 43 (2010) 195002.
[29] B. K. Mahato, S. Choudhury, R. Mandal, S. Barman, Y. Otani, A. Barman, J. Appl. Phys. 117 (2015) 213909.
[30] T. Schwarze, D. Grundler, Appl. Phys. Lett. 102 (2013) 222412.
[31] S. Tacchi, G. Duerr, J. W. Klos, M. Madami, S. Neusser, G. Gubbiotti, G. Carlotti, M. Krawczyk, D. Grundler, Phys. Rev. Lett. 109 (2012) 137202.
[32] S. Choudhury, S. Saha, R. Mandal, S. Barman, Y. Otani, A. Barman, ACS Appl. Mater. Interfaces 8 (2016) 18339.
[33] R. Mandal, P. Laha, K. Das, S. Saha, S. Barman, A. K. Raychaudhuri, A. Barman, Appl. Phys. Lett. 103 (2013) 262410.
[34] S. Choudhury, S. Majumder, S. Barman, Y. Otani, A. Barman, Phys. Rev. Appl. 10 (2018) 064044.
[35] C. C. Wang, A. O. Adeyeye, N. Singh, Nanotechnology 17 (2006) 1629.

[36] R. Mandal, S. Saha, D. Kumar, S. Barman, S. Pal, K. Das, A. K. Raychaudhuri, Y. Fukuma, Y. Otani, A. Barman, ACS Nano 6 (2012) 3397.
[37] R. Bali, M. Kostylev, D. Tripathy, A. O. Adeyeye, S. Samarin, Phys. Rev. B 85 (2012) 104414.
[38] R. Zivieri, P. Malagò, L. Giovannini, S. Tacchi, G. Gubbiotti, A. Adeyeye, J. Phys. Condens. Matter 25 (2013) 336002.
[39] S. Tacchi, B. Botters, M. Madami, J. W. Kłos, M. L. Sokolovskyy, M. Krawczyk, G. Gubbiotti, G. Carlotti, A. O. Adeyeye, S. Neusser, D. Grundler, Phys. Rev. B 86 (2012) 014417.
[40] M. Krawczyk, H. Puszkarski, Phys. Rev. B 77 (2008) 054437.
[41] O. N. Martyanov, V. F. Yudanov, R. N. Lee, S. A. Nepijko, H. J. Elmers, R. Hertel, C. M. Schneider, G. Schönhense, Phys. Rev. B 75 (2007) 174429.
[42] R. Zivieri, L. Giovannini, Photonics Nanostructures: Fundam. Appl. 11 (2013) 191.
[43] R. Mandal, S. Barman, S. Saha, Y. Otani, A. Barman, J. Appl. Phys. 118 (2015) 053910.
[44] S. Tacchi, M. Madami, G. Gubbiotti, G. Carlotti, A. O. Adeyeye, S. Neusser, B. Botters, D. Grundler, IEEE Trans. Magn. 46 (2010) 172.
[45] S. McPhail, C. M. Gürtler, J. M. Shilton, N. J. Curson, J. A. C. Bland, Phys. Rev. B 72 (2005) 094414.
[46] S. Neusser, B. Botters, D. Grundler, Phys. Rev. B 78 (2008) 054406.
[47] S. Neusser, B. Botters, M. Becherer, D. Schmitt-Landsiedel, D. Grundler, Appl. Phys. Lett. 93 (2008) 122501.
[48] S. Neusser, G. Duerr, S. Tacchi, M. Madami, M. L. Sokolovskyy, G. Gubbiotti, M. Krawczyk, D. Grundler, Phys. Rev. B 84 (2011) 094454.
[49] A. Manzin, G. Barrera, F. Celegato, M. Coïsson, P. Tiberto, Sci. Rep. 6 (2016) 22004.
[50] S. Choudhury, S. Barman, Y. Otani, A. Barman, ACS Nano 11 (2017) 8814.
[51] T. William, Acta Math. 11 (1887) 121.
[52] W. Shi, L. Muechler, K. Manna, Y. Zhang, K. Koepernik, R. Car, J. van den Brink, C. Felser, Y. Sun, Phys. Rev. B 97 (2018) 060406.
[53] W. Rotjanapittayakul, W. Pijitrojana, T. Archer, S. Sanvito, J. Prasongkit, Sci. Rep. 8 (2018) 4779.
[54] X. Li, X. Wu, X. C. Zeng, J. Yang, ACS Nano 6 (2012) 4104.
[55] C. Kittel, Phys. Rev. 73 (1948) 155.
[56] M. Donahue, D. G. Porter, *OOMMF User's guide, version1.0, Interagency Report NISTIR 6376* (National Institute of Standard and Technology, Gaithersburg, MD, U.S.A., 1999).
[57] K. H. J. Buschow, *Handbook of Magnetic Materials* (Elsevier, North Holland: Amsterdam, The Netherlands, 2009), Vol. 18, p. 168.
[58] A. Barman, S. Barman, Phys. Rev. B 79 (2009) 144415.
[59] D. Kumar, O. Dmytriiev, S. Ponraj, A. Barman, J. Phys. D: Appl. Phys. 45 (2012) 015001.
[60] LLG Micromagnetics Simulator, http://llgmicro.home.mindspring.com/ (2018).

Chapter 8

8. Efficient Modulation of Spin Waves in Two-Dimensional Octagonal Magnonic Crystal

Efficient tunability of magnonic spectra is demonstrated in two-dimensional ferromagnetic antidot lattices with different lattice constants arranged in the octagonal lattice which can be considered as quasi-periodic magnonic crystals due to the presence of broken translational symmetry. The precessional dynamics of these samples are investigated in the frequency domain with the help of broadband ferromagnetic resonance spectrometer. A rich variation in the spin wave spectra is observed with the variation of lattice constant as well as the strength and orientation of the bias magnetic field. A broad band of spin wave modes are observed for the denser array which finally converges to two spin wave modes for the sparsest one. In addition to this, the most intense spin wave frequency shows an eight-fold anisotropy with a superposition of weak four- and two-fold anisotropy which arises due to the angular variation of the magnetostatic field distribution at different regions of the octagonal lattice. Micromagnetic simulations qualitatively reproduce the experimentally observed modes and the simulated mode profiles reveal the presence of different types of extended and quantized standing spin wave modes in these samples. The observations are important for the tunable and anisotropic propagation of spin waves in magnonic crystal-based devices.

8.1. Introduction

In recent years, artificially patterned periodically modulated ferromagnetic media, popularly known as magnonic crystals (MCs) [1], have attracted a great attention of scientific community due to their unique features in nano-scale magnetism [2] and also for their huge potential applications in microwave resonators, waveguides [3], filters [4], phase shifters [5], interferometers [6], nanograting coupler [7], multiplexer [8] and switching operations [9] in the GHz-frequency regime. Similar to photonic [10] or phononic [11] crystals which are the building blocks of optoelectronics or acousto-optics, MCs can also be considered as the key components in magnonics [12], an

emerging research field which mainly deals with spin wave (SW)-based low power signal transmission and data processing for nanoscale on-chip microwave communication technology [13]. In addition to this, MCs also form magnonic miniband structure which consists of allowed bands separated by forbidden bandgaps. Interestingly, due to the anisotropic propagation of the SWs, these band gaps can be manipulated not only by changing the periodicity of the MCs but also by changing various material and structural parameters of the MCs [14] and also by tuning the strength and orientation of the bias magnetic field [15]. These unique features led us to the concept of reconfigurable magnonic devices which exhibits reprogrammable band structures [16].

Ferromagnetic antidot (hole) lattices (ADLs) i.e. periodically arranged holes on a ferromagnetic thin film are one of the strongest candidates for reconfigurable MCs due to higher SW propagation velocity and longer propagation wavelength for the SWs. They can also be considered as a potential candidate of magneto-photonic crystals [17,18] due to their strong influence of the magnetic field on the light (phonon) coupling to the surface plasmons [17]. In these ADLs, the inhomogeneous internal magnetic field due to the effective pinning centres for SWs created by the demagnetized regions between the neighbouring antidots is mainly responsible for the manipulation of the SW dynamics. Consequently, extensive research have been carried out to investigate the SW dynamics in one- (1-) or two-dimensional (2D) arrays of magnetic antidot structures of different shape [15], lattice arrangement [19] and compositions which were studied using various methods ranging from theoretical techniques such as plane wave method (PWM) [20] and micromagnetic simulations[21] to various experimental techniques using ferromagnetic resonance (FMR) [22], Brillouin light scattering (BLS) [23] or time-resolved magneto-optical Kerr effect (TR-MOKE) microscopy [24]. Initial studies on ADLs showed the attenuation of uniform ferromagnetic resonance mode due to the excitation of non-uniform in-plane SW mode [25] and the pattern induced splitting of surface and volume modes [26] were also observed. Later, the field dependent localization of SW mode, SW confinement and field-controlled propagation of SWs [27,28] and the formation of magnonic miniband [29] with large SW velocities have also been reported. The dispersive and entangled SWs between the antidots [30] and the anisotropic propagation and damping of SWs in a network of interconnected nanowires

[31] were also observed. In addition to these, high-symmetric magnonic modes for perpendicularly magnetized ADLs [32] having a linear bias magnetic field dependence and the transformation of quantized SWs to propagating ones by varying the in-plane orientation of the bias magnetic field [23] were also reported.

Artificial quasicrystals have become a hot topic of research in the field of photonics [33] and phononics [34] because the most beneficial feature of quasi-periodicity is that it can combine perfectly ordered structures with purely point-diffractive spectra of arbitrarily high rotational symmetry. Recently quasiperiodic structures has also started to be explored in magnonics due to their various interesting properties like branching features in the band structure, self-similarity and scaling properties in the transmission spectra [35]. Analytical calculation [36] revealed the perfect transmission of the SWs in one-dimensional quasi-magnonic crystals as well as the increase in the sharpness of perfect transmission peaks for higher order systems, which is useful for developing ultrahigh quality, multichannel, filters or resonators. The experimental and theoretical concepts of self-generation of dissipative solitons in magnonic quasi-crystals active ring resonator [37] were also reported, while another study [38] showed controlled magnetization reversal of ferromagnetic quasi-periodic magnonic crystal with long-range order but no periodic translational symmetry. However, the understanding of the SW dynamics in order to manipulate the magnonic bandgaps of these quasi-magnonic crystals [39,40] in the deep nanoscale regime has not yet been studied in detail. The recent advances in the nano-fabrication techniques enabled the fabrication of a variety of magnetic systems in the deep nanoscale regime and our state-of-the art measurement techniques allowed us to study the complex SW dynamics of these nanoscale quasiperiodic MCs.

Here, we report the investigation of the high-frequency magnetization dynamics of two-dimensional (2D) arrays of $Ni_{80}Fe_{20}$ (NiFe) antidots with circular shape arranged in octagonal lattices which may be considered as magnonic quasi-periodic crystal with varying lattice spacing. We used broadband ferromagnetic resonance (FMR) spectroscopy for the above study by controlling the strength and the orientation of the in-plane bias magnetic field. We observed a significant tunability in the SW spectra with the increase in lattice spacing. A strong anisotropic behaviour in the magnonic modes are obtained and we have observed a significant eight-fold rotational symmetry in these

octagonal crystals with the orientation of the bias magnetic field, while the value of this anisotropy is reduced with the increase in the lattice spacing. The micromagnetic simulations showed the presence of various localized and extended SW modes for these quasi-periodic magnonic crystals with the variation of strength and orientation of the in-plane bias magnetic field. Further, we demonstrate with the aid of micromagnetic simulations, that this significant variation in the SW dynamics is due to the modification of the internal field as well as the demagnetizing field profiles surrounding the antidots.

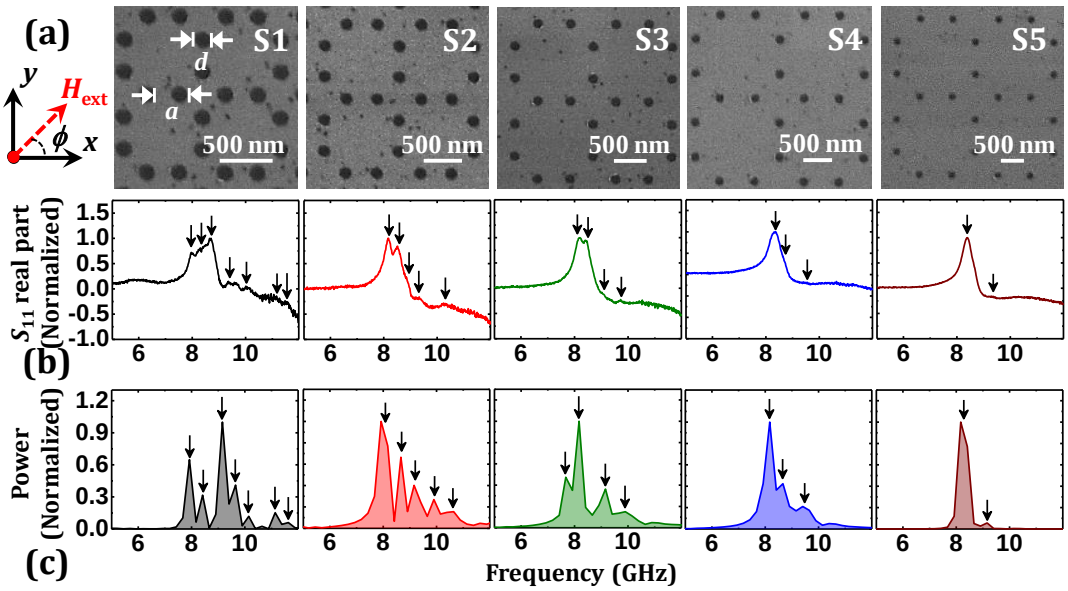

Figure 8.1. (a) Scanning electron micrographs of circular-shaped $Ni_{80}Fe_{20}$ (NiFe) antidots of antidot diameter (d) 140 nm arranged in quasiperiodic octagonal lattices with variable lattice spacing a = 300 (S1), 400 (S2), 500 (S3), 600 (S4) and 700 (S5) nm, respectively. (b) Real parts of the S_{11} parameter showing the FMR spectra for all five samples at bias magnetic field H_{ext} = 800 Oe applied at an azimuthal angle, ϕ = 0°, and the observed modes were marked by the down arrows. (c) Corresponding simulated spin wave (SW) spectra of the five different lattices at H_{ext} = 800 Oe applied at ϕ = 0° and the arrows represent different SW modes. The orientation of the bias magnetic field H_{ext} is shown at the top left of the figure.

8.2. Experimental Details

25 μm × 250 μm arrays of 20 nm thick $Ni_{80}Fe_{20}$ (NiFe) antidots of circular shapes arranged in octagonal lattice symmetry with variable lattice spacing (a) of 300 (S1), 400 (S2), 500 (S3), 600 (S4) and 700 (S5) nm, respectively, as shown in the scanning electron micrographs of Figure 8.1(a), were fabricated by using a combination of electron beam lithography (EBL), electron beam evaporation (EBE) and ion milling[22].

The diameter of the each antidot is about 140 nm (± 5%). The chemical compositions of the ADLs measured by the energy dispersive X-ray spectroscopy (EDX) agree well with the nominal composition of the target material. A co-planar waveguide (CPW) made of Au with a thickness of 150 nm was deposited on top of the array structures for the broadband ferromagnetic resonance measurement. The width and length of the central conducting line of this CPW are 30 μm and 300 μm, respectively, with a nominal characteristic impedance of 50 Ω.

The SW spectra from the arrays were measured by using broadband ferromagnetic resonance (FMR) spectrometer [41] which is based upon a vector network analyzer (Agilent PNA-L, Model No.: N5230C, frequency range: 10 MHz to 50 GHz) and a home-built high-frequency probe station with nonmagnetic G-S-G type pico-probe (GGB Industries, Model No. 40A-GSG-150-EDP). The system has an inbuilt electromagnet inside the probe station generating a variable bias field (H_{ext}) of up to ± 1.8 kOe which is used to apply an external bias magnetic field parallel to the CPW. The sample is viewed with the help of a microscope and illumination set-up. Microwave signals with varying frequency are launched into the CPW structure using the G-S-G probe through a high frequency and low noise coaxial cable (Model No.: N1501A-203). The CPW is shorted at one end and the back-reflected signal is collected by the same probe to the analyzer *via* the same coaxial cable. Absorption of the ongoing and returning signals at various SW frequencies produces the characteristic SW spectrum of the sample. The real and imaginary parts of the scattering parameter in reflection geometry (S_{11}) measured at various magnetic fields are subtracted from its value at maximum bias magnetic field which is used as the reference spectrum and the SW spectra are obtained.

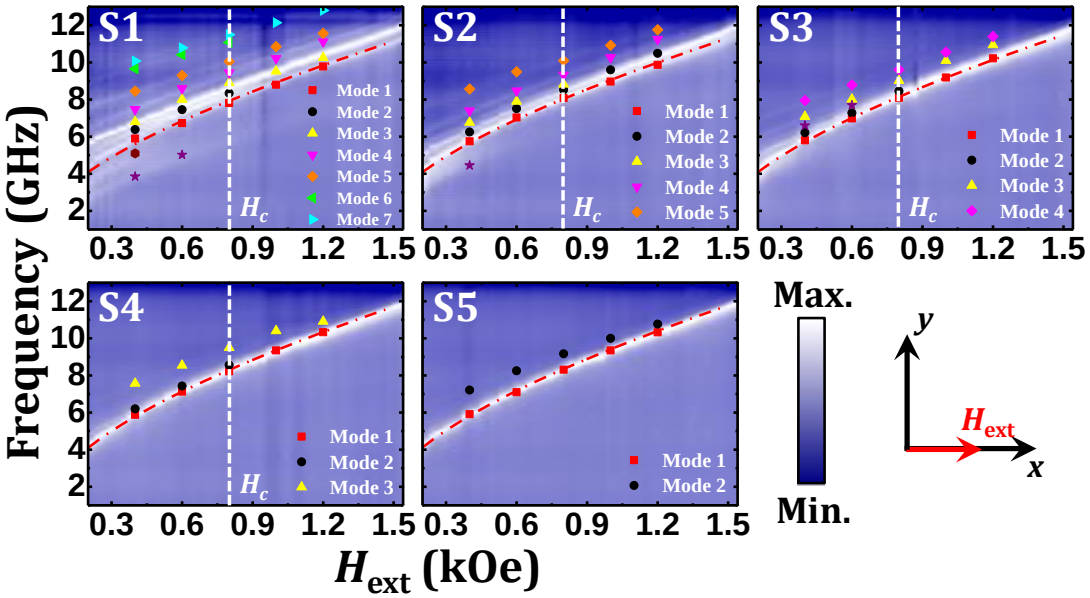

Figure 8.2. Bias field (H_{ext}) dependent spin wave (SW) absorption spectra of NiFe ADLs for different lattice spacings (S1–S5) are shown at ϕ = 0°. The critical field (H_c) is shown by white dotted lines in S1–S4, and the red dotted lines represent Kittel fit to the lower frequency mode 1 of S1–S5. The surface plots correspond to the experimental results, while the symbols represent the simulated data. The color map for the surface plots and the schematic of the external applied field (H_{ext}) are given at the bottom right corner of the figure.

8.3. Results and Discussion

The real parts of the experimental forward scattering parameter i.e. S_{11} parameter and the simulated SW spectra for $Ni_{80}Fe_{20}$ (NiFe) antidots arranged in an octagonal lattice with varying lattice spacing (a) from 300 nm to 700 nm are shown in Figure 8.1(b, c) respectively at a bias magnetic field H_{ext} = 800 Oe applied at an azimuthal angle ϕ = 0°, while their bias field dependent SW absorption spectra at ϕ = 0° are presented as surface plots in Figure 8.2. A clear variation in the SW dynamics is observed with the variation of a as well as with the strength of the external bias magnetic field. From Figure 8.2, it is clearly observed that at H_{ext} = 800 Oe for S1, seven SW modes are present but the number of SW modes is gradually reduced to six, five, three and two for S2, S3, S4, and S5 respectively. The number of SW modes also changes significantly with the variation of the strength of the external bias field for all the samples as shown in Figure 8.2. It is clear from Figure 8.2 that at or below a critical field value, $H_c \approx$ 800 Oe as shown by the white dotted lines, nine, five, five and three modes are present for S1, S2,

S3 and S4, respectively which systematically reduce to five, four, three and two modes for S1, S2, S3 and S4, respectively for bias fields above H_c. In contrast, two modes are present for all field values for S5. The bias field dependence of the lower frequency resonant mode i.e. mode 1 marked by red square is fitted with the Kittel formula [42] as given by Equation 8.1:

$$f = \frac{\gamma}{2\pi}\sqrt{(H_{\text{ext}} + H_{\text{k}})(H_{\text{ext}} + H_{\text{k}} + 4\pi M_{\text{s}})} \quad (8.1)$$

The magnetic parameters obtained from the best fit are gyromagnetic ratio γ = 18.1 MHz/Oe, and the magneto-crystalline anisotropy field $H_K \approx 0$, while the value of effective saturation magnetization (M_s) increases systematically from 720 emu/cc (S1) to 800 emu/cc (S5) with the increase of the lattice spacing a. This increase in effective M_s confirms that the fraction of demagnetization volume decreases with the increase of lattice constants and as a result, the effective magnetization of the sparsest lattice (S5, a = 700 nm) is closest to a continuous thin film value (850 emu/cc).

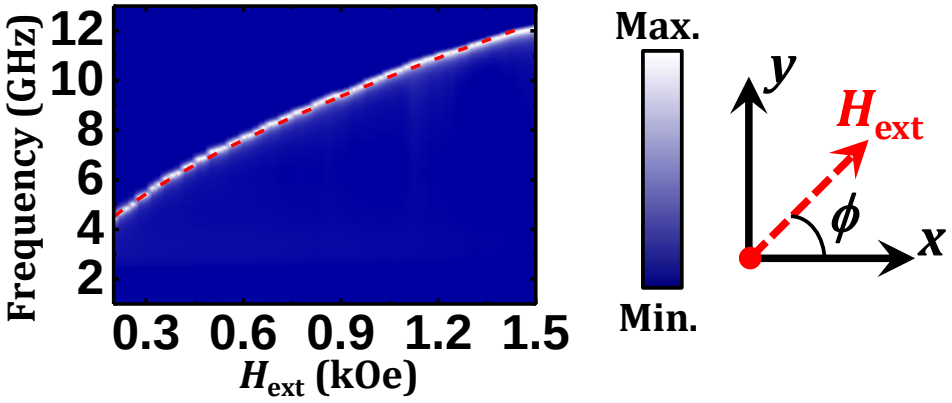

Figure 8.3. Bias field (H_{ext}) dependent spin wave (SW) absorption spectra of $Ni_{80}Fe_{20}$ thin film at ϕ = 0° is shown along with the Kittel fit which is represented by the red dotted line. The color map for the surface plot and the schematic of the orientation of H_{ext} which are shown at the right side of the figure.

We have performed micromagnetic simulations to understand the origin of the SW modes using the OOMMF software [43] considering 2 × 2 arrays of octagonal unit cells for each sample incorporating the two-dimensional periodic boundary condition in order to consider large areas of the experimentally studied arrays. The samples are discretized into rectangular prism-like cells with dimensions 4 × 4 × 20 nm^3. The value of exchange stiffness constant and saturation magnetization used in the simulation for

NiFe are A = 1.3 × 10^{-6} erg/cm [44] and M_s = 850 emu/cc, respectively. The damping coefficient for NiFe α = 0.008 is used during the dynamic simulations. The value of gyromagnetic ratio γ = 18.1 MHz/Oe and the magnetocrystalline anisotropy constant of K = 0 are considered for NiFe. Here, the material parameters of NiFe used for the simulation i.e. M_s, γ and K were extracted from the Kittel fit of the bias field dependent SW absorption spectra of NiFe thin film as shown in Figure 8.3. The dynamic simulations were performed by first obtaining a static magnetic configuration under a bias field in the experimental geometry and then by applying a pulsed magnetic field. The details of the static and dynamic simulations are described in details elsewhere [45].

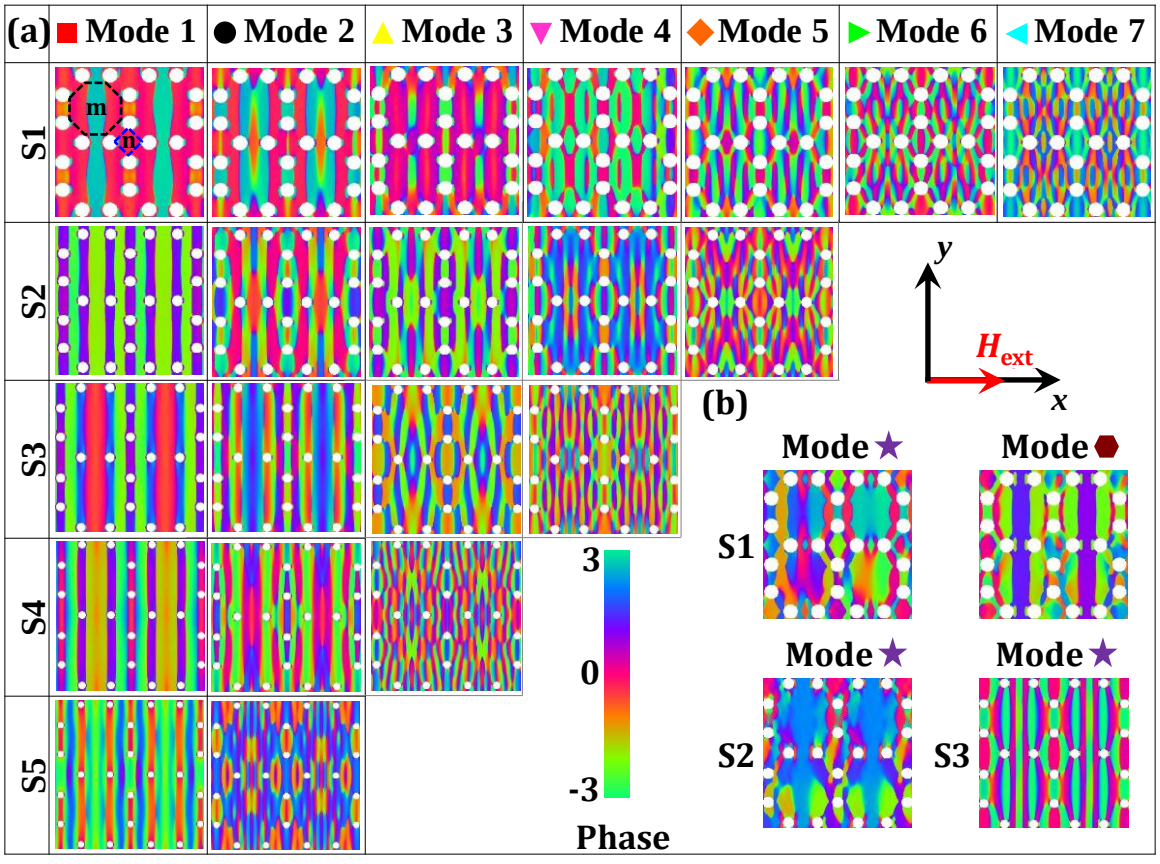

Figure 8.4. (a) Simulated spatial distributions of the phase profile corresponding to different SW modes obtained at H_{ext} = 800 Oe applied at ϕ = 0° for all the lattices (S1–S5). (b) Simulated phase maps of the additional SW modes obtained at a lower bias field H_{ext} = 400 Oe for S1, S2, and S3, respectively. The color map for the phase distributions and the schematic of the external applied field (H_{ext}) are shown at the right side of the figure.

Micromagnetic simulations reproduced the experimental data qualitatively as shown by the simulated spectra (Figure 8.1(c)) and the SW frequency values (filled symbols in Figure 8.2) for all the lattices, although the exact values of the SW frequencies are not reproduced in some cases. The latter can be attributed to the deviation of the simulated samples and simulation conditions from the experimental samples and conditions. The general deviation in the dimensions as observed in the experimental samples are incorporated in the simulated samples, but the precise edge deformations are not possible to include in the finite difference method based micromagnetic simulations.

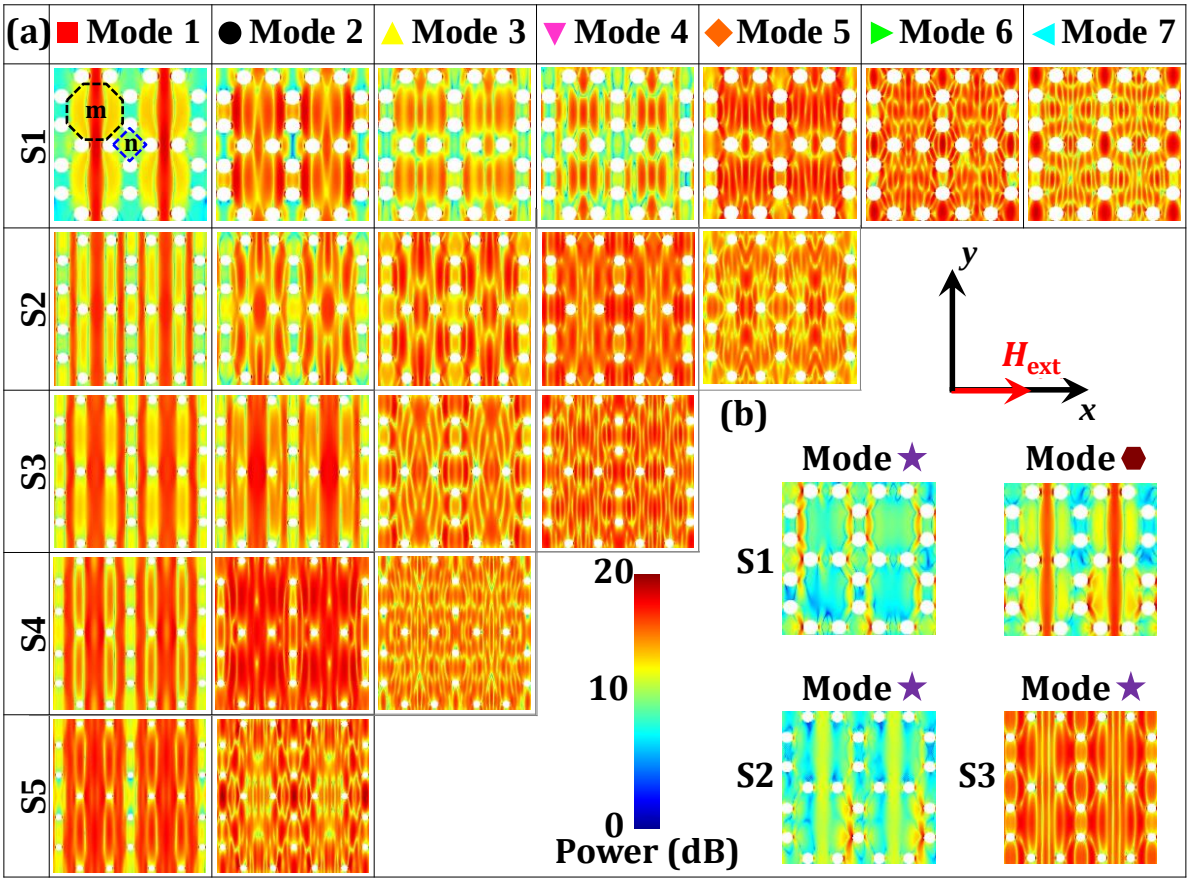

Figure 8.5. (a) Simulated spatial distributions of power profile corresponding to different resonant SW modes obtained at H_{ext} = 800 Oe applied at ϕ = 0° for all the lattices (S1-S5). (b) Simulated power maps of the additional SW modes obtained at a lower bias field H_{ext} = 400 Oe for S1, S2 and S3, respectively. The color map for the power distributions and the schematic of the external applied field (H_{ext}) are shown at the right bottom of the figure.

In order to understand the origin of various SW modes as observed both experimentally and in the simulation, we have further simulated the spatial power and phase maps of

those SW modes as observed both experimentally and in the simulation by using a homebuilt code [46]. Figure 8.4(a) shows the phase profiles of the SW modes for samples with varying values of a at H_{ext} = 800 Oe while the corresponding power maps are represented in Figure 8.5. Different types of extended and quantized SW modes due to the confining potentials created by the demagnetizing fields around the antidots are observed for different lattices and depending upon the number of antinodes, different quantization numbers for the SW modes either in backward volume (BV) geometry or in Damon-Eshbach (DE) geometry are assigned. In addition to this, depending upon the location of the quantization of the SWs, two different quantization numbers, m and n are assigned. m is assigned for the quantization of SWs along the x-direction inside the unit cell of the octagonal lattice defined by the black dotted box in Figure 8.4(a) while n represents the quantization of the SWs along the x-direction inside the rhombus present between two such consecutive octagonal unit cells defined by the blue dotted box in Figure 8.4(a). The phase profiles in Figure 8.4(a) show that for all the samples, the lowest frequency SW mode i.e. mode 1, is extended in DE geometry along the channel through the octagonal unit cells in the y-direction and quantized along x-direction in BV geometry with m = 3, 5, 5, 7 and 11 and n = 3, 3, 3, 5, and 5 for S1, S2, S3, S4 and S5, respectively. Interestingly, for mode 1, both m and n increase with the increase of a. Other SW modes for all the samples are the quantized SW mode in BV geometry with different quantization numbers. For S1, the m values of SW modes 2, 3, 4, 5, 6 and 7 are 5, 7, 7, 9, 11 and 13 while and n values of the corresponding SW modes are 3, 3, 3, 5, 5 and 5, respectively, while modes 3 and 4 are in opposite phase with each other. For S2, modes 2, 3, 4 and 5 have the quantization numbers m = 7, 7, 9 and 13 and n = 3, 5, 5 and 5, respectively. In case of S3, the quantization numbers for SW modes 2, 3 and 4 are m = 7, 9 and 15 while n = 5, 5 and 7, respectively. However, we have also obtained additional SW modes at the low bias magnetic field in case of S1 (marked by asterisk and hexagonal dots), S2 (marked by asterisk) and S3 (marked by asterisk), respectively as shown in Figure 8.4(b). As observed from Figure 8.5(b), for S1, asterisk marked mode is the edge mode where the power of the SW mode is localized at the edges of the antidots while mode denoted by filled hexagonal symbol is the extended mode in DE geometry along y-direction, but along x-direction it possesses BV-like character with m = 5 and n = 3 and it is in opposite phase with mode 1. The asterisk marked modes for S2 is the edge

mode of the antidots whereas the same for S3 is a BV-like mode with m = 7 and n = 3 along x-direction while it has an extended character along the y-direction. For S4, the quantization numbers for modes 2 and 3 are m = 9 and 17 and n = 9 and 11, respectively and in case of S5, the quantization numbers of mode 2 are m = 19 and n = 7. Interestingly, it is also observed that the intensities of the SW modes decrease systematically with increasing m and n values for all the lattices which is also evident from Figure 8.1(b, c) and Figure 8.2, respectively.

In order to investigate the origin of this large tunability of SW modes with the varying lattice constant in these octagonal ADLs, we have calculated the magnetostatic field distributions of these lattices with the help of LLG Micromagnetics software [47], which are shown in Figure 8.6. It is evident from Figure 8.6(a) that the strength of the demagnetizing fields around the holes is reduced with the increase of the lattice spacing and at the highest lattice spacing i.e. a = 700 nm, the demagnetizing fields become very narrow, concentrating mainly around the antidots. We have also calculated the total internal field (B_{in}) for these lattices by taking linescans along the both denser and sparser rows of the octagonal unit as shown by horizontal dashed lines in Figure 8.6(a) for S5. The internal field strength and its distribution are clearly modified with the variation of a. For better understanding, the whole lattice is divided into three regions named by regions 1, 2 and 3 as shown by the red, blue and green dotted boxes shown in Figure 8.6(a) and interestingly the internal field profile shows an unusual behaviour in region 1 where it reduces significantly with the enhancement of a whereas it increases gradually with the increase of a for other two regions (regions 2 and 3) as depicted in Figure 8.6(b). In addition to this, another interesting feature is that for S1, the total internal field is higher (10.92 kOe) in region 1 and lower (10.55 kOe and 10.65 kOe) in regions 2 and 3, respectively. But for S5, B_{in} is almost same (~10.83 kOe) in three different regions.

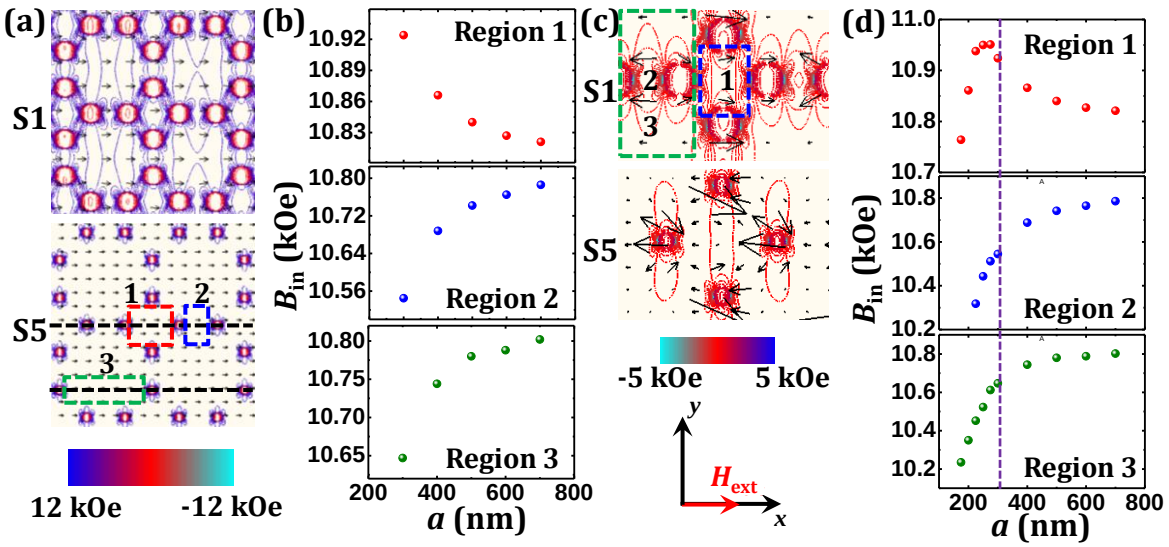

Figure 8.6. (a) Contour plots of the simulated magnetostatic field distributions in S1 and S5 are shown with bias field H_{ext} = 800 Oe applied at ϕ = 0° along with the color map for the magnetostatic field distributions shown at the bottom left corner. (b) Variation of the simulated internal field (B_{in}) values with the lattice spacing, a at three different regions (shown by red, blue and green dotted boxes in S5) of the ADLs by taking the line scan (horizontal dotted lines) along these three different regions. (c) Contour plots of the simulated demagnetization field distributions in S1 and S5 obtained at bias field H_{ext} = 800 Oe for ϕ = 0° and the corresponding color map for demagnetization field distribution at the bottom. (d) Variation of the simulated internal field (B_{in}) values with the lattice spacing, a = 175, 200, 225, 250, 275, 300, 400, 500, 600 and 700 nm respectively, at three different regions (represented by red, blue and green dotted boxes in S5) of the lattices by taking the line scan (horizontal dotted lines) along these three different regions. The schematic of the external applied field (H_{ext}) is shown at the bottom right corner of the figure.

The demagnetization field profile at different regions of the octagonal lattice provides us with the possible explanation for this unusual behaviour of the total internal field distribution. From Figure 8.6(c), it is clear that the demagnetizing field directions in both regions 2 and 3 marked by the green dotted box in Figure 8.6(c) is opposite to the direction of the applied magnetic field which is the main reason of lowering the B_{in} value at this region. On the contrary, the demagnetizing field direction in the region 1 marked by a blue dotted box in Figure 8.6(c) is along the same direction to the applied bias field which is mainly responsible for the enhancement of the internal field in this region. However, with the increase of the lattice constant, the direction of the demagnetization field in the opposite direction to the applied magnetic field again start to appear in region 1, which compensates the previous value and increase of uniformity

of magnetization as shown in Figure 8.6(c). As a result, the total internal field starts to decrease with the increase of a as shown in Figure 8.6(b) in region 1 whereas for regions 2 and 3, due to the reduction of the effective demagnetization region, the B_{in} increases with the increase of a. Interestingly for the sparsest lattice i.e. S5, the magnetization becomes spatially uniform in almost all the regions of the lattice. Consequently, the simulated internal field B_{in} converges to a single value (~ 10.83 kOe), when calculated in the three different regions of S5. We have further simulated the magnetostatic field distributions by reducing the lattice spacing down to 175 nm as shown in Figure 8.6(d) and we have found that the internal field in region 1 becomes maximum at a = 275 nm and it decreases drastically when a is reduced further. However, in regions 2 and 3 respectively, we have obtained a monotonic behaviour of B_{in} with the variation in the lattice spacing.

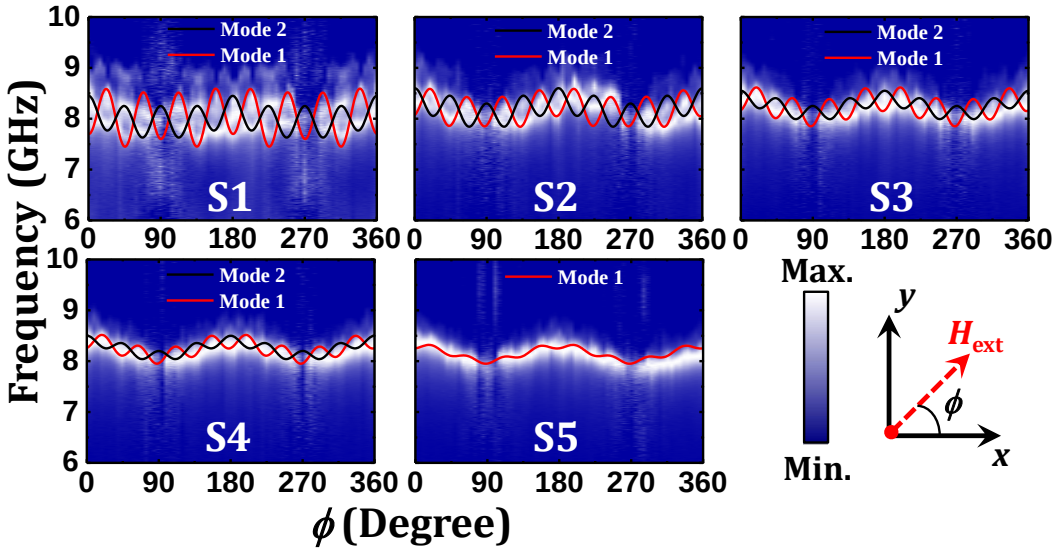

Figure 8.7. Variation of spin wave (SW) frequency with the azimuthal angle (ϕ) varying from 0° to 360° for NiFe ADLs with various lattice spacing (S1–S5) are presented at bias magnetic field, H_{ext} = 800 Oe. The surface plots represent the experimental results, while the solid lines describe the sinusoidal fits for the observed anisotropic SW modes in all of the samples (S1–S5). The color map associated with the surface plots and the schematic of the orientation of the external applied field (H_{ext}) are given at the bottom right corner of the figure.

We further investigate the variation of the SW spectra with the variation of in-plane azimuthal angle (ϕ) of the bias magnetic field H_{ext} for a fixed strength of 800 Oe in the octagonal lattice with different lattice spacing, a. The surface plots of the angular

dispersions of magnonic spectra as a function of azimuthal angle ϕ varying from 0° to 360° for different samples are shown in Figure 8.7 while the solid curves correspond to theoretical fits using harmonic functions with different symmetries. The lower frequency SW modes show the anisotropic behaviour for all samples and interestingly an eight-fold anisotropy superposed with a weak two-fold and four-fold anisotropies are observed. Significantly, the contribution of eight-fold anisotropy gradually reduces with the increase in *a* as shown in Figure 8.7.

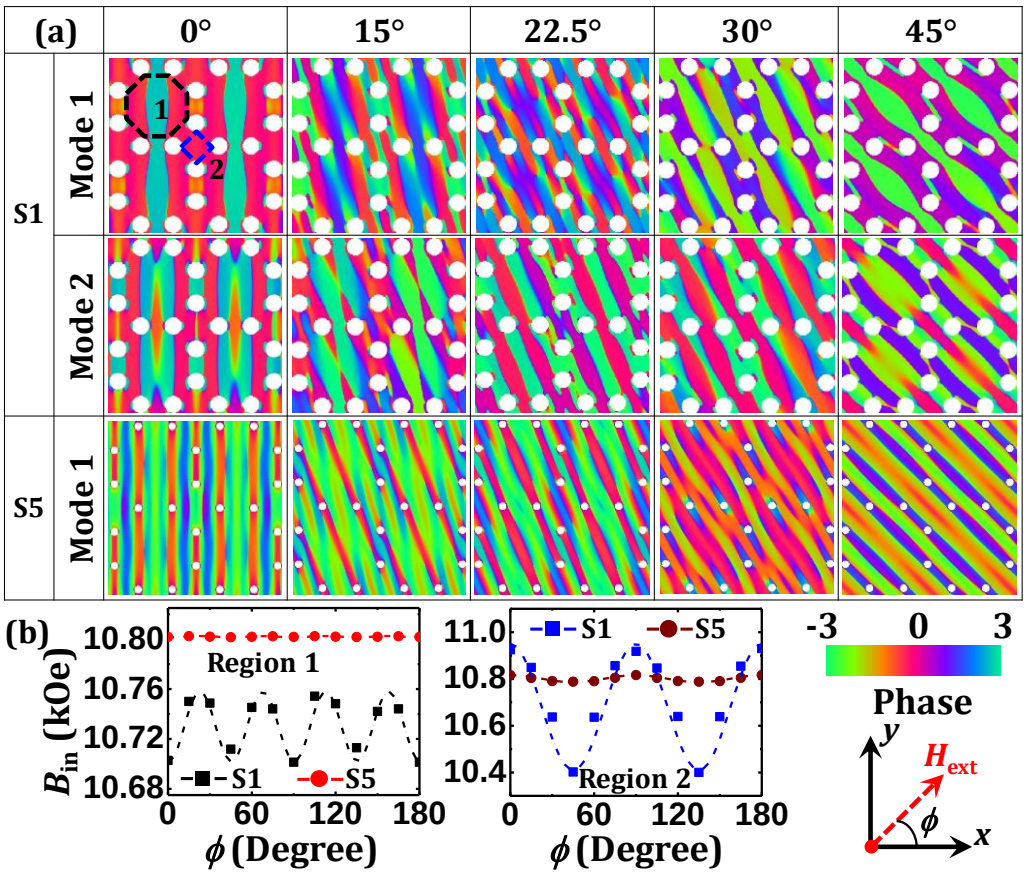

Figure 8.8. (a) Simulated spatial distributions of phase profile corresponding to different anisotropic SW modes obtained in S1 and S5 with bias field, H_{ext} = 800 Oe applied at ϕ = 0°, 15°, 22.5°, 30°, and 45°, respectively, along with the color map for the phase distributions and the schematic of the orientation of the external applied field (H_{ext}) which are shown at the bottom right corner of the figure. (b) Evolution of the simulated internal field (B_{in}) values in S1 and S5 with varying ϕ at bias field H_{ext} = 800 Oe obtained by taking line scans in two different regions marked by black and blue dotted boxes inside mode 1 of S1 at ϕ = 0°.

The phase profiles of the SW modes for S1 in Figure 8.8(a) (the corresponding power profiles are shown in Figure 8.9) shows that the higher frequency anisotropic mode i.e.

mode 2 remains as a quantized mode confined within the octagonal unit cell with the same quantization but with its symmetry axis rotating continuously with the variation of azimuthal angle. However, the extended mode (mode 1) goes through a significant modification with the variation of azimuthal angle. At ϕ = 0°, mode 1 is an extended mode which is converted into a quantized mode at ϕ = 22.5°and at ϕ = 45° it again becomes an extended mode and this behaviour is repeated periodically. This periodicity is commensurate with the observed eight-fold rotational anisotropy in the frequency of this mode. However, the behaviour of the anisotropic mode (mode 1) for S5 remains almost invariant with ϕ.

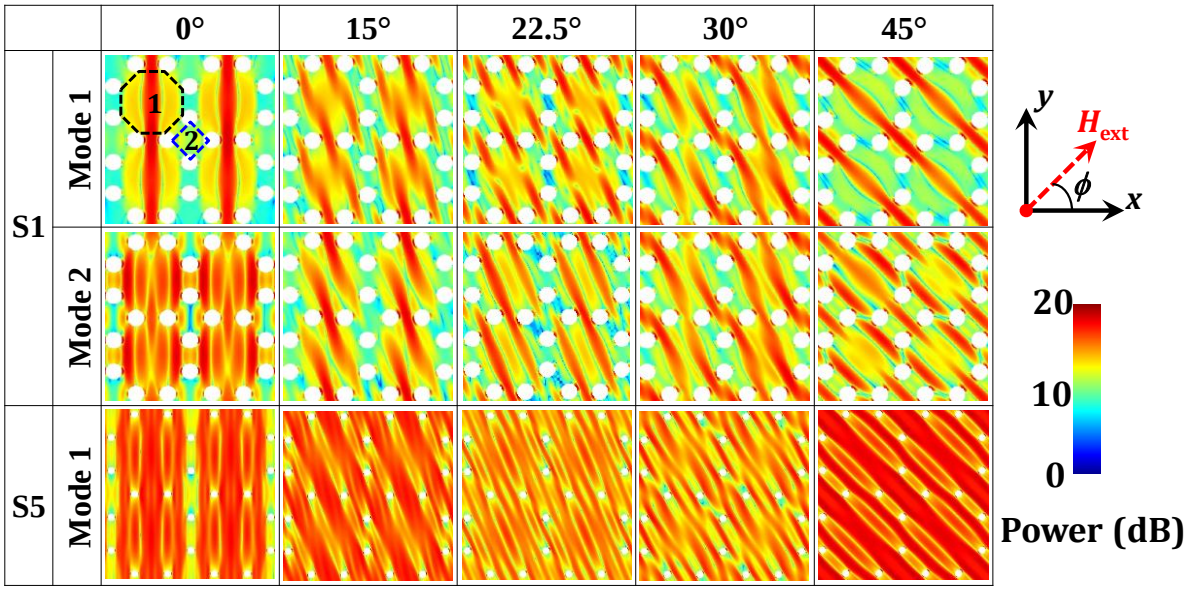

Figure 8.9. Simulated spatial distributions of power profile corresponding to different anisotropic SW modes obtained in S1 and S5 with bias field H_{ext} = 800 Oe applied at ϕ = 0°, 15°, 22.5°, 30° and 45° respectively along with the color map for the power distributions and the schematic of the orientation of the external applied field (H_{ext}) which are shown at the right side of the figure.

The origin of the weak two-fold configurational anisotropy can be explained by considering the rectangular shape of the boundary of the array. However, to understand the presence of eight- and four-fold anisotropy, the variation of the internal field for both S1 and S5 is calculated at various orientations of the bias field inside the octagonal unit cell (marked by the black dotted box) as well as within the rhombus (marked by the blue dotted box). The internal field profile is modified significantly at these two different regions (1 and 2) of the lattice as shown in Figure 8.8(b). The variation of B_{in}

shows that an eight-fold anisotropy is present inside the octagonal unit cell, whereas a four-fold anisotropy is obtained within the rhombus. Interestingly, both the eight- and four-fold anisotropy contributions decrease drastically in S5 as shown in Figure 8.8(b). This variation is a result of the magnetic environment in different regions of the ADLs and its ensuing variation with the angle of the bias field and is manifested as the configurational anisotropy in the samples.

8.4. Conclusion

In summary, we have fabricated high-quality arrays of circular shaped NiFe antidots arranged in an octagonal lattice with diameter 140 nm and the lattice constant is varied from 300 nm to 700 nm using a combination of electron beam lithography and electron beam evaporation and ion milling technique. The magnetization dynamics of these samples are investigated with the help of broadband FMR spectroscopy by varying the strength and orientation of the applied magnetic field. The experimental results showed a remarkable variation in the SW spectra with the variation of lattice constants. For the lowest value of lattice spacing, seven SW modes are observed which converge into two modes for the highest value of lattice spacing. The experimental results have been well reproduced by micromagnetic simulation and the power and phase profiles of the resonant modes have been numerically calculated to get an insight about the spatial nature of the dynamics. Different types of extended and localized standing SW modes with varying quantization numbers are observed. The magnetostatic fields including the demagnetization field distributions are calculated to interpret the origin of the observed SW modes. The configurational anisotropy of the samples is investigated by varying the azimuthal angle of the bias field and an eight-fold anisotropy superposed with four-fold and two-fold anisotropies is observed for these samples. The value of the eight-fold anisotropy is found to decrease strongly with the increase in the lattice spacing. The magnetostatic field distribution within the octagonal unit cell is mainly responsible for the origin of the eight-fold anisotropy, whereas the rhombus-like cell present between two octagonal unit cell is mainly responsible for the four-fold anisotropy. In addition to this, the phase profile shows a mode conversion from extended standing SW mode to quantized standing SW mode for these samples with the rotation of the bias field direction. These observations open more opportunities in the engineering of quasiperiodic arrays for magnonic and spintronic devices.

8.5. Materials and Methods

8.5.1. Sample Preparation

Circular shaped $Ni_{80}Fe_{20}$ (NiFe) antidot arrays (25 μm × 250 μm) arranged in two-dimensional octagonal lattice symmetry were fabricated by using a combination of e-beam lithography (EBL), e-beam evaporation (EBE) and ion milling. The diameter of the antidots was chosen to be about 140 nm with maximum ± 5% deviation, while the separation between their nearest edges was varied from 160 nm to 560 nm with maximum ± 5% deviation. At first, 20 nm thick NiFe film was deposited on commercially available self-oxidized silicon (Si) [100] substrate using e-beam evaporation in an ultra-high vacuum chamber at a base pressure of 2×10^{-8} Torr followed by depositing a 60-nm thick protective layer of Al_2O_3. Bi-layer (PMMA/MMA) resist was used to prepare the resist pattern on the NiFe film for e-beam lithography followed by Argon ion milling at a base pressure of 1×10^{-4} Torr to etch out the NiFe film from everywhere except the unexposed resist pattern for creating the antidots. The ion milling on the NiFe film was performed down to the base of the film for each pattern. Subsequently, a co-planer waveguide (CPW) made of Au with a thickness of 150 nm was deposited on top of the NiFe antidot lattice at a base pressure of 6×10^{-7} Torr for the broadband ferromagnetic resonance measurement. Here, the Au waveguide was patterned by using maskless photolithography. The width and length of the central conducting line of this CPW were 30 μm and 300 μm, respectively so that the array falls under the centre of the central conducting line of the CPW which has a nominal characteristic impedance of 50 Ω.

8.5.2. Measurement Technique

The frequency domain SW dynamics of the samples were measured by using a broadband ferromagnetic resonance spectrometer based on a vector network analyzer (VNA-FMR) along with a home-built probe station, which includes an in-built electromagnet to apply the bias magnetic field up to ± 1.8 kOe. The orientation of the bias field was varied by 360° within the sample plane. The microwave signal of varying frequency from 10 MHz to 50 GHz was launched in the CPW through a non-magnetic ground-signal-ground (G-S-G) probe *via* a co-axial cable and the CPW was shorted at one end so that the scattering parameter in the reflection mode (S_{11}) can be measured by the VNA after being collected by the same probe. The sample absorbed the power at

various SW frequencies during the onward and return journey of the microwave signal through the CPW structure. This formed the characteristic SW spectrum for that sample. However, there are non-linear backgrounds in the directly measured signals originated from various sources. Hence, during measurement at each bias field, a reference spectrum (spectrum at the highest value of the bias field) was subtracted from the signal to obtain a background free spectrum. However, some background still remained in the spectrum, which is non-trivial to remove from the spectrum. For each sample, the spectra for a series of bias fields from +0.2 kOe to +1.54 kOe at the separation of 20 Oe are plotted together as a surface plot.

References

[1] B. Lenk, H. Ulrichs, F. Garbs, M. Münzenberg, Phys. Rep. 507 (2011) 107.
[2] L. S. Robert, B. Stephan, Å. Johan, V. C. Andrii, O. YoshiChika, E. W. B. Gerrit, T. Jan-Ulrich, B. Martin, A. M. Sara, K. Mathias, P. Ioan Lucian, D. Bernard, M. D. Nora, H. Burkard, J. Phys. D: Appl. Phys. 47 (2014) 333001.
[3] V. V. Kruglyak, A. Barman, R. J. Hicken, J. R. Childress, J. A. Katine, Phys. Rev. B 71 (2005) 220409(R).
[4] S. K. Kim, K. S. Lee, D. S. Han, Appl. Phys. Lett. 95 (2009) 082507.
[5] Y. Au, M. Dvornik, O. Dmytriiev, V. V. Kruglyak, Appl. Phys. Lett. 100 (2012) 172408.
[6] J. Podbielski, F. Giesen, D. Grundler, Phys. Rev. Lett. 96 (2006) 167207.
[7] H. Yu, G. Duerr, R. Huber, M. Bahr, T. Schwarze, F. Brandl, D. Grundler, Nat. Commun. 4 (2013) 2702.
[8] K. Vogt, F. Y. Fradin, J. E. Pearson, T. Sebastian, S. D. Bader, B. Hillebrands, A. Hoffmann, H. Schultheiss, Nat. Commun. 5 (2014) 3727.
[9] J. Topp, D. Heitmann, D. Grundler, Phys. Rev. B 80 (2009) 174421.
[10] M. Jacoby, Chem. Eng. News 76 (1998) 38.
[11] I. E. Psarobas, N. Stefanou, A. Modinos, Phys. Rev. B 62 (2000) 5536.
[12] V. V. Kruglyak, S. O. Demokritov, D. Grundler, J. Phys. D: Appl. Phys. 43 (2010) 264001.
[13] H. Yu, O. d' Allivy Kelly, V. Cros, R. Bernard, P. Bortolotti, A. Anane, F. Brandl, F. Heimbach, D. Grundler, Nat. Commun. 7 (2016) 11255.
[14] H. Ulrichs, B. Lenk, M. Münzenberg, Appl. Phys. Lett. 97 (2010) 092506.
[15] R. Mandal, P. Laha, K. Das, S. Saha, S. Barman, A. K. Raychaudhuri, A. Barman, Appl. Phys. Lett. 103 (2013) 262410.
[16] M. Krawczyk, D. Grundler, J. Phys. Condens. Matter 26 (2014) 123202.
[17] G. Ctistis, E. Papaioannou, P. Patoka, J. Gutek, P. Fumagalli, M. Giersig, Nano Lett. 9 (2009) 1.
[18] K. Kern, D. Heitmann, P. Grambow, Y. H. Zhang, K. Ploog, Phys. Rev. Lett. 66 (1991) 1618.
[19] S. Tacchi, M. Madami, G. Gubbiotti, G. Carlotti, A. O. Adeyeye, S. Neusser, B. Botters, D. Grundler, IEEE Trans. Magn. 46 (2010) 1440.

[20] M. Krawczyk, S. Mamica, M. Mruczkiewicz, J. W. Klos, S. Tacchi, M. Madami, G. Gubbiotti, G. Duerr, D. Grundler, J. Phys. D: Appl. Phys. 46 (2013) 495003.
[21] V. N. Krivoruchko, A. I. Marchenko, J. Appl. Phys. 109 (2011) 083912.
[22] R. Mandal, S. Barman, S. Saha, Y. Otani, A. Barman, J. Appl. Phys. 118 (2015) 053910.
[23] S. Tacchi, B. Botters, M. Madami, J. W. Kłos, M. L. Sokolovskyy, M. Krawczyk, G. Gubbiotti, G. Carlotti, A. O. Adeyeye, S. Neusser, D. Grundler, Phys. Rev. B 86 (2012) 014417.
[24] R. Mandal, S. Saha, D. Kumar, S. Barman, S. Pal, K. Das, A. K. Raychaudhuri, Y. Fukuma, Y. Otani, A. Barman, ACS Nano 6 (2012) 3397.
[25] O. N. Martyanov, V. F. Yudanov, R. N. Lee, S. A. Nepijko, H. J. Elmers, R. Hertel, C. M. Schneider, G. Schönhense, Phys. Rev. B 75 (2007) 174429.
[26] S. McPhail, C. M. Gürtler, J. M. Shilton, N. J. Curson, J. A. C. Bland, Phys. Rev. B 72 (2005) 094414.
[27] S. Neusser, B. Botters, D. Grundler, Phys. Rev. B 78 (2008) 054406.
[28] S. Neusser, B. Botters, M. Becherer, D. Schmitt-Landsiedel, D. Grundler, Appl. Phys. Lett. 93 (2008) 122501.
[29] R. Zivieri, S. Tacchi, F. Montoncello, L. Giovannini, F. Nizzoli, M. Madami, G. Gubbiotti, G. Carlotti, S. Neusser, G. Duerr, D. Grundler, Phys. Rev. B 85 (2012) 012403.
[30] M. Kostylev, G. Gubbiotti, G. Carlotti, G. Socino, S. Tacchi, C. Wang, N. Singh, A. O. Adeyeye, R. L. Stamps, J. Appl. Phys. 103 (2008) 07C507.
[31] S. Neusser, G. Duerr, H. G. Bauer, S. Tacchi, M. Madami, G. Woltersdorf, G. Gubbiotti, C. H. Back, D. Grundler, Phys. Rev. Lett. 105 (2010) 067208.
[32] R. Bali, M. Kostylev, D. Tripathy, A. O. Adeyeye, S. Samarin, Phys. Rev. B 85 (2012) 104414.
[33] M. C. Rechtsman, H.-C. Jeong, P. M. Chaikin, S. Torquato, P. J. Steinhardt, Phys. Rev. Lett. 101 (2008) 073902.
[34] A. L. Chen, Y.-S. Wang, Y.-F. Guo, Z.-D. Wang, Solid State Commun. 145 (2008) 103.
[35] C. H. Chen, R. Z. Qiu, C. H. Chang, W. J. Hsueh, AIP Adv. 4 (2014) 087102.
[36] W. J. Hsueh, C. H. Chen, R. Z. Qiu, Phys. Lett. A 377 (2013) 1378.
[37] S. V. Grishin, E. N. Beginin, M. A. Morozova, Y. P. Sharaevskii, S. A. Nikitov, J. Appl. Phys. 115 (2014) 053908.
[38] V. S. Bhat, J. Sklenar, B. Farmer, J. Woods, J. T. Hastings, S. J. Lee, J. B. Ketterson, L. E. De Long, Phys. Rev. Lett. 111 (2013) 077201.
[39] S. Saha, R. Mandal, S. Barman, D. Kumar, B. Rana, Y. Fukuma, S. Sugimoto, Y. Otani, A. Barman, Adv. Funct. Mater. 23 (2013) 2378.
[40] S. Saha, S. Barman, S. Sugimoto, Y. Otani, A. Barman, RSC Adv. 5 (2015) 34027.
[41] S. Choudhury, S. Saha, R. Mandal, S. Barman, Y. Otani, A. Barman, ACS Appl. Mater. Interfaces 8 (2016) 18339.
[42] C. Kittel, Phys. Rev. 73 (1948) 155.
[43] M. Donahue, D. G. Porter, *OOMMF User's guide, Version 1.0,* (NIST Interagency Report No. 6376; National Institute of Standard and Technology, Gaithersburg, MD, URL: http://math.nist.gov/oommf, 1999).
[44] K. H. J. Buschow, in *Handbook of Magnetic Materials*, edited by K. H. J. Buschow (Elsevier, North Holland, Amsterdam, The Netherlands, 2009), p. 168.
[45] A. Barman, S. Barman, Phys. Rev. B 79 (2009) 144415.
[46] D. Kumar, O. Dmytriiev, S. Ponraj, A. Barman, J. Phys. D: Appl. Phys. 45 (2012) 015001.

[47] LLG Micromagnetics Simulator, http://llgmicro.home.mindspring.com/ (2016).

Chapter 9

9. Shape- and Interface-Induced Control of Spin Dynamics of Two-Dimensional Bi-component Magnonic Crystals

Controlled fabrication of periodically arranged embedded nanostructures with strong inter-element interaction through the interface between the two different materials have great potential applications in spintronics, spin logic and other spin base communication devices. Here, we report the fabrication of two-dimensional bi-component magnonic crystals (BMCs) in form of embedded $Ni_{80}Fe_{20}$ nanostructures in $Co_{50}Fe_{50}$ thin films by nanolithography. The spin wave spectra studied by a broadband ferromagnetic resonance spectroscopy showed a significant variation as the shape of the embedded nanostructure changes from circular to square. Significantly, in both shapes, a minimum in frequency is obtained at a negative value of bias field during the field hysteresis confirming the presence of a strong exchange coupling at the interface between the two materials, which can potentially increase the spin wave propagation velocity in such structures leading to faster GHz frequency magnetic communication and logic devices. The spin wave frequencies and bandgaps show bias field tunability, which is important for above device applications. Numerical simulations qualitatively reproduced the experimental results, and simulated mode profiles revealed the spatial distribution of the SW modes and internal magnetic fields responsible for this observation. Development of such controlled arrays of embedded nanostructures with improved interface can be easily applied to other forms of artificial crystals.

9.1. Introduction

Metamaterials are the smart artificial materials which are engineered to have the properties not found commonly in nature. Such new material properties may not always be possible to achieve in a single material in the bulk or thin film form. Instead, structuring of known materials in one-, two- or three-dimensions at various length scales and exploiting dynamical magnetic properties over a broad frequency range may potentially offer the desirable material properties. Magnonic crystals (MCs) [1],

photonic crystals [2] and phononic crystals [3] are popular metamaterials where spin waves (SWs) or magnons, electromagnetic waves (photons) and acoustic waves (phonons) are the transmission waves, respectively. However, due to the low speed of propagation with compared to the electromagnetic wave, SWs with frequencies in the range of tens of GHz have wavelengths in the nanometer regime, making MCs ideal candidate for cellular nonlinear network and nanoscale on-chip data communications, including magnonic waveguides [4], filters [5], splitters, phase shifters [6], spin-wave emitters [7], as well as for magnonic logic devices [8]. As a result, a new research field named magnonics has emerged which has the capability to replace current semiconductor technology. One important problem is to tune the magnonic band structure of the MCs by varying different geometrical parameters like shape [9], size [10], lattice spacing [11] and lattice symmetry [12] and also by changing the constituent ferromagnetic materials [13].

Two dimensional (2D) periodic ferromagnetic antidot lattices (ADLs) have emerged as potential candidates for magneto-photonic crystals [14,15], ultrahigh density magnetic storage media [16] and magnonic crystals. Magnonic band structures of these ADLs can be more efficiently tuned in bi-component magnonic crystals (BMCs) [17] where one magnetic material is embedded within the continuous film of another magnetic material. In such embedded structures, where two different magnetic materials are in direct contact with each other, the dynamic dipole coupling is maximized due to the presence of exchange coupling at their interface. As a result, SWs are subjected to scattering at the interface between the two materials and can easily transmit through the interface. Therefore, SWs can propagate across its entire structure with large group velocities. Thus, 2D embedded nanostructures have attracted huge attention of the scientific community due to their intriguing physical properties like broad spectrum of scattering and mode-coupling processes as well as potential applications in controlling the SW propagation in magnonic and other kinds of integrated spin-based communication devices.

In the last few years, one-dimensional (1D) [18,19] and two-dimensional (2D) [20-23] BMCs are started to be explored. The high frequency magnetization dynamics of 1D and 2D BMCs have been investigated experimentally by time domain [24], frequency domain [25] and wavevector domain [26] techniques and also by using analytical

methods [27] and micromagnetic simulations [28]. Further, the complex magnonic band structures of these 2D BMCs were investigated by using plane wave method (PWM). Recently, a circular shaped BMC has been demonstrated as an omnidirectional grating coupler [29] which shows a giant enhancement of the amplitude of the short wavelength SWs with compared to a bare microwave antenna. However, the above structures suffer from lower propagation velocity, which can be potentially overcome by an increased interface exchange interaction between the two different elements of the BMC but there are very few reports [21,29] on the fabrication of embedded magnetic structures in nanoscale regime in that pursuit. Additionally, the exchange coupling and the demagnetizing fields at the interface of the two constituent materials can be potentially modified by varying the interface area by changing the shape of the filling region, which has not been studied yet. Here, we took the challenge to fabricate such embedded nanostructures by using state-of-the art nanofabrication techniques. We have investigated the SW dynamics of 2D arrays of $Ni_{80}Fe_{20}$ (NiFe) filled antidots embedded in continuous $Co_{50}Fe_{50}$ (CoFe) film with two different antidot shapes, namely circular and square, arranged in a square lattice by using broadband ferromagnetic resonance (FMR) spectroscopy. A significant variation in the SW spectra is observed as the embedded element shape varies from circle to square. Significantly, the frequency gap between the two lowest SW modes gradually decreases with the reduction in bias field strength, shows a minimum at around 0.75 kOe for circular and 0.9 kOe for square shaped embedded magnetic structures, followed by an increase as the bias field is reduced further. Further, a minimum in the frequency value was observed for both element shapes at a negative value of bias magnetic field during the field hysteresis, which is a confirmation of the presence of an exchange coupling at the interface between the NiFe and CoFe regions. Using numerical micromagnetic simulations, we reproduced the observed behaviours and unravelled the SW mode profiles which show the presence of various extended and localized SW modes due to the modification of the interface of the embedded structures.

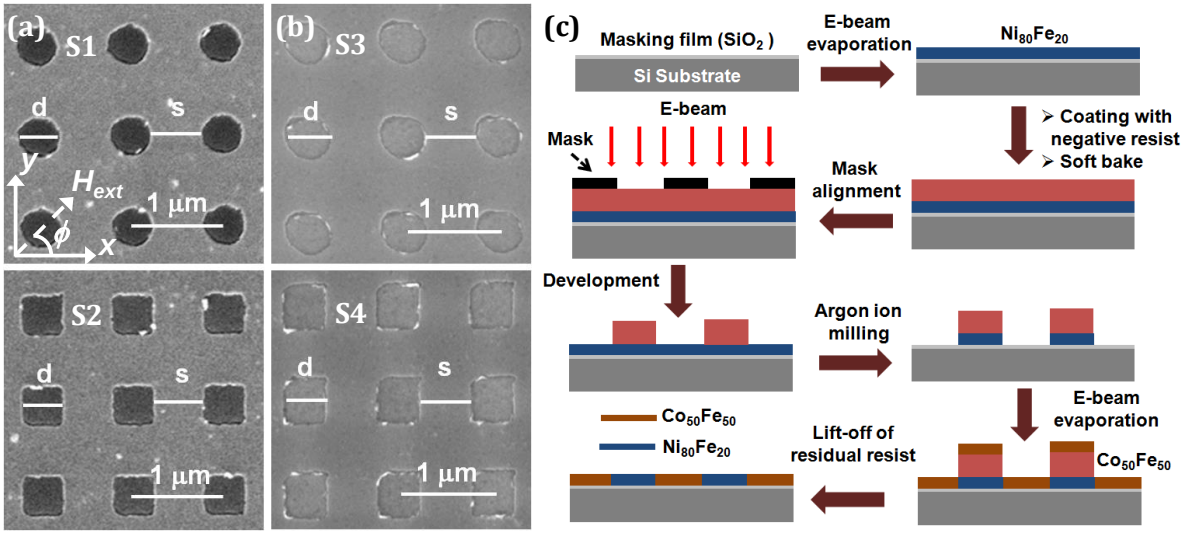

Figure 9.1. Scanning electron micrographs of circular and square shaped (a) $Co_{50}Fe_{50}$ (CoFe) antidot lattices (ADLs) named by S1 and S2 and (b) $Ni_{80}Fe_{20}$ (NiFe)-filled CoFe ADLs named by S3 and S4 arranged in square lattice symmetry are shown. The geometry of the applied magnetic field (H_{ext}) for all lattices is shown in the micrograph of S1. (c) Schematic of the techniques used for fabrication of 2D array of embedded magnetic structures.

9.2. Experimental Details

25 μm × 250 μm arrays of 20 nm thick NiFe nanostructures embedded in CoFe films named by S3 and S4 (filled ADLs) and corresponding unfilled CoFe ADLs named S1 and S2 of circular and square shapes arranged in square lattice symmetry as shown in the scanning electron micrographs of Figure 9.1(a, b) were fabricated by using a combination of e-beam lithography (EBL), e-beam evaporation (EBE) and ion milling. The schematic of the sample fabrication technique is shown in Figure 9.1(c). The width of the each NiFe filled region is about 400 nm (± 5%) and the edge to edge separation between them is about 600 nm (± 5%). The chemical compositions of the filled ADLs measured by the energy dispersive X-ray spectroscopy agree well with the nominal composition of the target materials. A co-planar waveguide (CPW) made of Au with thickness of 150 nm was deposited on top of the array structures for the broadband ferromagnetic resonance measurement. The width and length of the central conducting line of this CPW are 30 μm and 300 μm, respectively, so that the array falls under the centre of the central conducting line of CPW which has a nominal characteristic impedance of 50 Ω.

The SW spectra from the arrays were measured by using broadband ferromagnetic resonance (FMR) spectrometer which is based upon a vector network analyzer (Agilent PNA-L, Model: N5230C, frequency range: 10 MHz to 50 GHz) and a home-built high frequency probe station with nonmagnetic G-S-G type pico-probe (GGB Industries, Model: 40A-GSG-150-EDP). The system has an in-built electromagnet inside the probe-station generating a bias field (H_{ext}) of ± 1.8 kOe which is used to apply an external bias magnetic field parallel to the CPW. The sample is viewed with the help of a microscope and illumination set-up. Microwave signals with varying frequency are launched into the CPW structure using a G-S-G type probe through a high frequency and low noise co-axial cable (Model: N1501A-203). The CPW is shorted at one end and the back-reflected signal is collected by the same probe to the analyzer via the same co-axial cable. Absorption of the ongoing and returning signals at various SW frequencies produces the characteristic SW spectrum of the sample. The real and imaginary parts of the scattering parameter in reflection geometry (S_{11}) measured at various magnetic fields are subtracted from its value at maximum bias magnetic field which is used as the reference spectrum and the SW spectra are obtained.

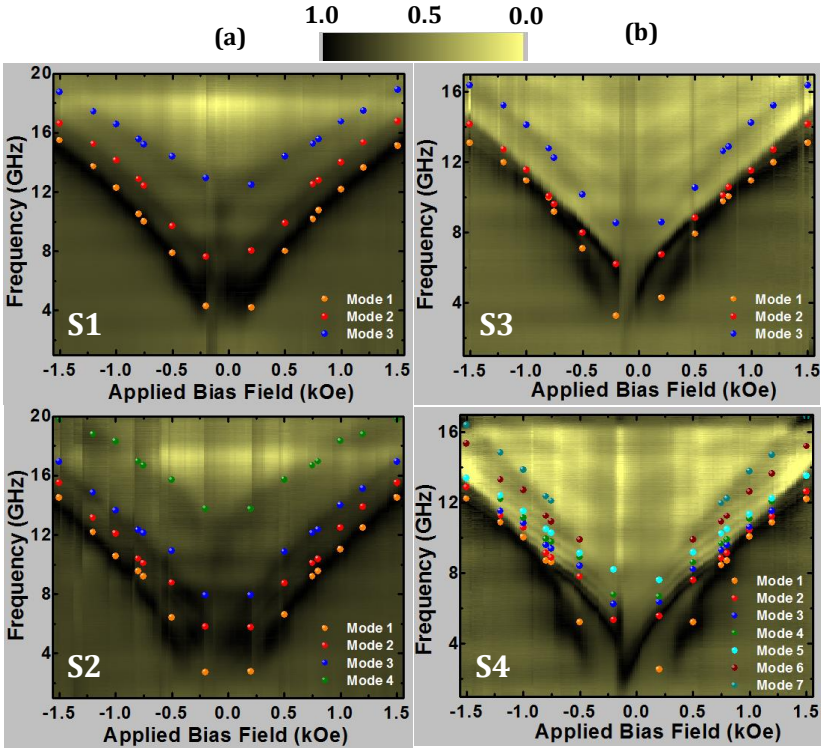

Figure 9.2. Bias field-dependent SW absorption spectra of circular and square shaped (a) CoFe ADLs (S1 and S2) and (b) NiFe-filled CoFe ADLs (S3 and S4) at ϕ = 0°. The

surface plots correspond to the experimental data, while the symbols correspond to the simulated data. The color scale for the surface plots is given at top of the figure.

9.3. Results and Discussion

The bias field dependence of the SW absorption spectra for the unfilled ADLs (S1 and S2) as well as the filled ADLs (S3 and S4) are presented as surface plots as shown in Figure 9.2(a, b). The measurement was done in the range of H_{ext} between ± 1.56 kOe at steps of 20 Oe for a fixed azimuthal angle ϕ = 0° as shown in Figure 9.1(a). The SW spectra change significantly for filled ADLs (S3 and S4) as opposed to the unfilled ADLs (S1 and S2) and the spectra is further modified when the shape of the element (antidot) is changed from circular to square. From Figure 9.2(a, b), three modes are observed for both S1 and S3. However, for S3 as shown in Figure 9.2(b), the frequencies of all the modes decrease significantly and the frequency gap (Δf) between the two lowest SW modes (modes 1 and 2) also decreases with decrease in positive field showing a minimum in Δf at H_{ext} = 0.75 kOe and below that field Δf again increases. In addition, the dispersion of frequency vs. bias field for the S3 shows an asymmetry during field hysteresis with a minimum in the frequency at a negative bias field value of H_{ext} = -150 Oe as opposed to the S1, which shows a symmetric dispersion with respect to the bias field. Since NiFe has negligible anisotropy and CoFe ADL also shows no anisotropy in the frequency vs. field dispersion, the observation of an anisotropy i.e. a minimum in frequency at a negative bias field confirms the presence of an exchange coupling at the interface between NiFe and CoFe. In case of square shaped elements (antidots), the SW spectra change drastically as compared to the circular shaped elements (antidots) for filled (unfilled) ADLs. The square shaped unfilled ADL i.e. S2 shows four distinct modes (Figure 9.2(a)) for all field values while a broad band of modes are observed for the filled ADL i.e. S4. Figure 9.2(b) reveals five modes for higher field values (H_{ext} > 1.2 kOe), which split into seven modes for an intermediate field range (0.5 kOe < H_{ext} < 1.2 kOe), and again converge to five modes for lower field values (H_{ext} < 0.5 kOe). Similar to S3, in case of S4 the frequency gap (Δf) between the two lowest modes (modes 1 and 2) becomes minimum at a relatively large bias field value of 0.9 kOe, and for H_{ext} > 0.9 kOe it increases and this trend repeats when the field value is reversed. Here also, due to the exchange coupling between two constituent materials at the interface, an asymmetry in the frequency vs. bias field dispersion is observed with a minimum of frequency at a

negative bias magnetic field value H_{ext} = -190 Oe during the field hysteresis. The presence of the exchange interaction at the boundary between CoFe and NiFe in the filled ADLs (S3 and S4) are further confirmed by simulated magnetic hysteresis loops (not shown), which are markedly different from the unfilled CoFe ADLs as well as the NiFe dots. The filled ADLs (S3 and S4) show much larger propagation velocity for spin waves as opposed to their unfilled counterparts (S1 and S2) as discussed later.

We have performed micromagnetic simulations to understand the origin of the SW modes using the OOMMF software [30] by considering unfilled and filled ADLs consisting of 5 × 5 antidots (elements) with two different shapes arranged in square lattice. The samples are discretized into rectangular prism like cells with dimensions 4 × 4 × 20 nm^3. The value of exchange stiffness constants and saturation magnetizations used in the simulation are A_{NiFe} = 1.3 × 10^{-6} erg/cm, M_{NiFe} = 800 emu/cc for NiFe, and A_{CoFe} = 3 × 10^{-6} erg/cm, M_{CoFe} = 1800 emu/cc for CoFe. The damping coefficients α_{NiFe} = 0.008 for NiFe and α_{CoFe} = 0.01 for CoFe are used during the dynamic simulations .The value of gyromagnetic ratio γ = 18.5 MHz/Oe and the magnetocrystalline anisotropy K = 0 are considered for both the materials while the exchange stiffness constant at the interface between NiFe and CoFe is found to be A_{Exch} = 2.1 × 10^{-6} erg/cm after a number of test simulation and comparison between the simulated and experimental data. This ensures a strong interface exchange interaction between CoFe and NiFe, which may enhance the dipolar coupling. The dynamic simulations were performed by first obtaining a static magnetic configuration under a bias field in the experimental geometry and then by applying a pulsed magnetic field. The details of the static and dynamic simulations are described in details elsewhere [31].

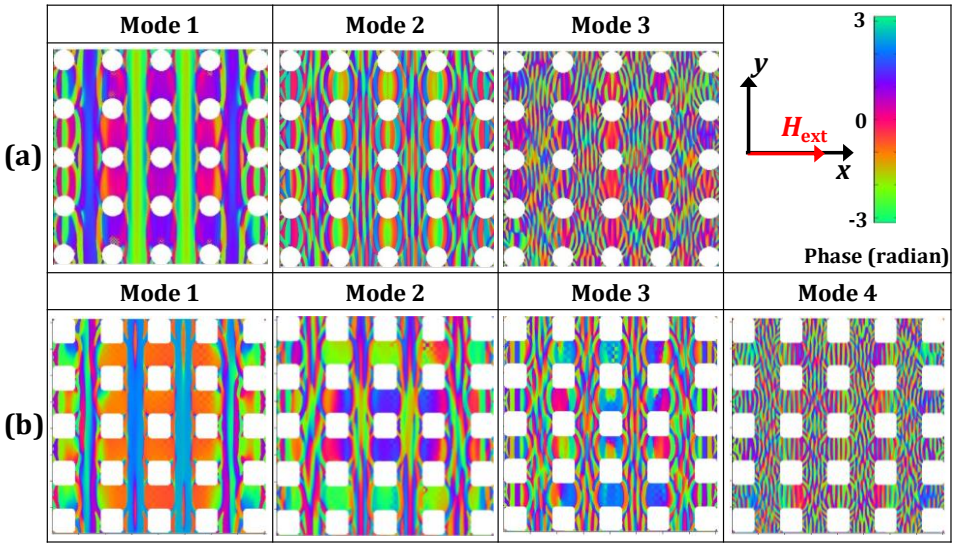

Figure 9.3. Simulated SW mode profiles (phase maps) of (a) S1 and (b) S2 with bias field H_{ext} = 1 kOe applied at ϕ = 0° along with the color scale for the phase maps and the schematic of the external applied field (H_{ext}) at the right corner of the figure.

Micromagnetic simulations reproduced the experimental data qualitatively as shown by the filled symbols in Figure 9.2(a, b), although the precise values of the SW frequencies are not always reproduced. This is expected due to the deviation of the simulated samples and conditions from the experimental samples and conditions. In general, the deviation in the dimensions as observed in the experimental samples are incorporated in the simulated samples, but the precise edge roughness profiles are not possible to include in the finite difference method based micromagnetic simulations used here, where the samples are divided into rectangular prism-like cells. Also, the simulated arrays are much smaller (5 × 5 antidots or filled antidots) than the experimental samples (up to 250 × 50 antidots or filled antidots) due to the limitations in the computational resources. In order to understand the origin of various SW modes as observed both experimentally and in the simulation, we have further simulated the power and phase maps of those SW modes by using a homebuilt code [32]. Figure 9.3(a, b) show the phase profiles of the SW modes of S1 and S2, respectively at H_{ext} = 1 kOe, while the power profiles for all these modes are shown in Figure 9.4.

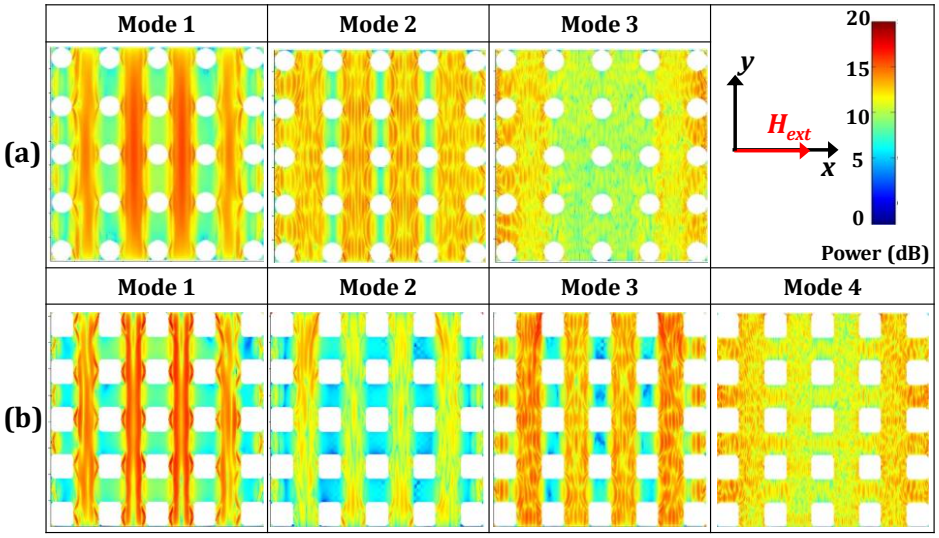

Figure 9.4. Simulated SW mode profiles (power maps) of (a) S1 and (b) S2 CoFe ADLs with bias field H_{ext} = 1 kOe applied at ϕ = 0° along with the color scales for the phase maps and the schematic of the external applied field (H_{ext}) at the right corner of the figure.

It is clear from the power and phase maps that for both S1 and S2, the lowest frequency mode i.e. mode 1, is extended along y-direction with quantization number m = 0 which corresponds to Damon Eshbach (DE) mode at the centre of the first Brillouin zone (BZ) i.e. wavevector k = 0. On the other hand, along x-direction this mode corresponds to the standing SW mode in the backward volume (BV) geometry [33] with quantization number n = 3. However, for both the shapes the higher frequency modes are more complicated and quantized modes with different quantization numbers due to the formation of standing waves in the backward volume (BV) geometry between two neighboring antidots are observed. In case of S1, modes 2 and 3 correspond to the BV-like standing SW modes with quantization numbers n = 9 and 13, respectively, whereas for S2, modes 2, 3 and 4 also correspond to the BV-like standing SW modes with quantization numbers n = 7, 9 and 13, respectively. The BV like standing wave modes with n = 1 and edge localized modes near the antidot edges observed in some antidots with different dimensions in some previous literature are not observed with detectable powers in the experimental spectra, while their power in the simulated spectra are also extremely low and hence are not discussed here. It was also reported the observation of only BV like modes with n = 3 and above and absence of n = 1 mode and edge localized mode in antidot lattices of similar dimensions studied in that report [33], supporting our present results.

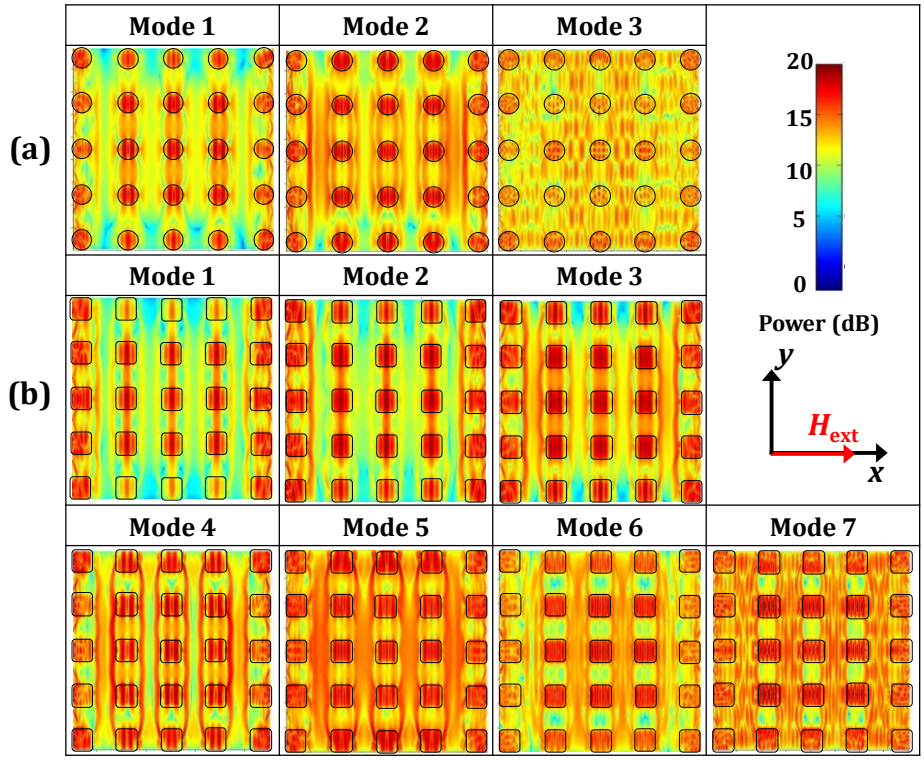

Figure 9.5. Simulated spatial distributions of power corresponding to different resonant modes for (a) S3 and (b) S4 with bias field H_{ext} = 1 kOe applied at ϕ = 0°. The color map for the power distributions and the schematic of the external applied field (H_{ext}) are shown at the right corner of the figure.

The power profile of all the SW modes for filled ADLs with both the shapes at H_{ext} = 1 kOe are shown in Figure 9.5(a, b). It is observed that the lower frequency modes for S3 and S4 (mode 1 for S3 and modes 1 and 2 for S4) are mainly confined along the NiFe filled CoFe channel and as the mode number increases the power of the SW modes gradually gets transferred into the CoFe channels between the NiFe filled regions for both the shapes. Figure 9.6(a, b) show the phase profiles of filled ADLs (S3 and S4) at bias field H_{ext} = 1 kOe applied at ϕ = 0°. The mode profiles of all the modes change significantly in filled ADLs for both the shapes with comparison to unfilled ADLs. The phase maps of the SW modes for S3 in Figure 9.6(a) reveals that the lower frequency modes i.e. modes 1 and 2 are extended modes in DE geometry in the CoFe channels, whereas within the NiFe filled regions they form BV-like standing SW modes with quantization numbers, n' = 3 and 5, respectively. The higher frequency mode i.e. mode 3 is again a quantized mode in the BV geometry in both CoFe and NiFe filled regions with quantization numbers n (CoFe) = 5 and n' (NiFe) = 7. The SW mode profiles change

drastically in S4 as opposed to S3 as shown in Figure 9.6(b). Here, for S4, modes 1 and 2 are extended modes in DE geometry in the CoFe channels while they form quantized BV-like modes in NiFe filled regions with same quantization number $n' = 3$ but the modes are out-of-phase with each other. Similarly, modes 3 and 4 are also out-of-phase with each other and form BV-like modes with $n = 3$ and $n' = 5$ in the CoFe and NiFe filled regions, respectively. Significantly, mode 5 is an extended mode in the DE geometry in the CoFe channel, while it is quantized in BV geometry in the NiFe filled region with $n' = 5$. Modes 6 and 7 are quantized modes in BV geometry in both CoFe and NiFe filled regions with quantization numbers $n = 5, 7$ and $n' = 7, 9$, respectively.

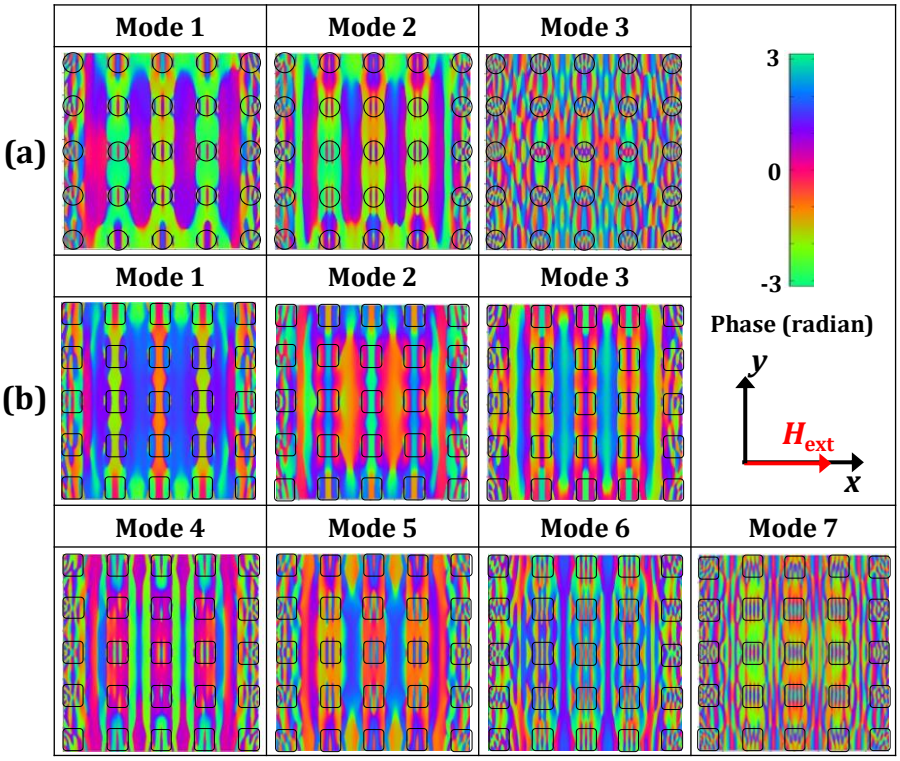

Figure 9.6. Simulated spatial distributions of phase corresponding to different resonant modes for (a) S3 and (b) S4 with bias field H_{ext} = 1 kOe applied at $\phi = 0°$. The color map for the phase distributions and the schematic of the external applied field (H_{ext}) are shown at the right corner of the figure.

To understand the origin of the differences in the SW spectra between the filled and unfilled ADLs of both circular and square shapes we have calculated the magnetostatic field distributions for these arrays, as shown in Figure 9.7(a, b). It is clearly observed from Figure 9.7(a) that the demagnetized regions as well as magnetostatic field distributions around S1 and S2 are symmetrical but in case of S2 the magnetostatic

interaction is stronger due to the presence of the corners. It is evident from Figure 9.7(b) that the volumes of the demagnetization regions in the S3 and S4 are reduced as opposed to the S1 and S2 and this behaviour is more prominent in the circular shape as opposed to the square shape. Linescans of the simulated magnetostatic fields for circular and square shaped unfilled ADLs and filled ADLs along the horizontal dashed lines drawn in Figure 9.7(a, b) are shown in the Figure 9.7(c). The magnified views (green dotted box) of the internal field in CoFe channel for all four samples are shown in Figure 9.7(d).

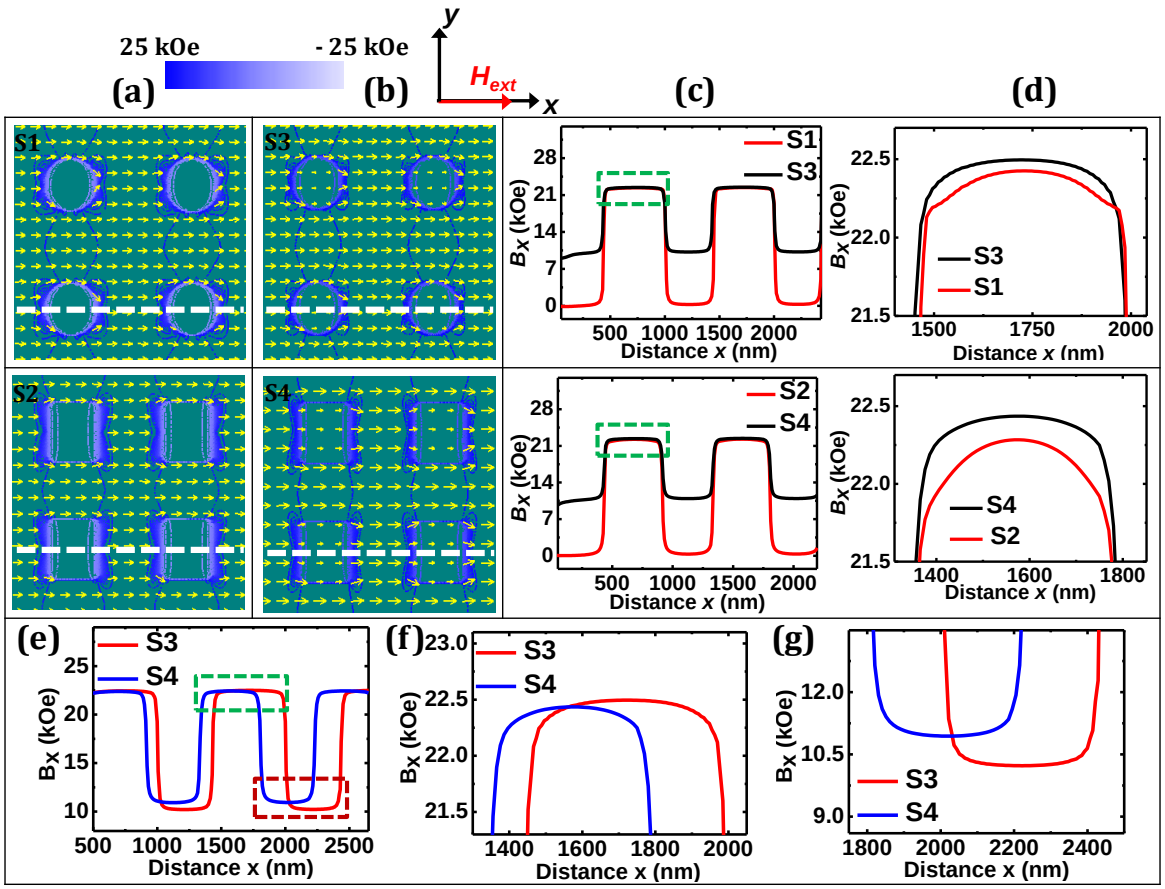

Figure 9.7. Contour plots of the simulated magnetostatic field distributions from the 2 × 2 elements at the center of the array (5 × 5 elements) in (a) S1 and S2 and (b) S3 and S4 with bias field H_{ext} = 1 kOe applied at ϕ = 0°. The color map for the magnetostatic field distributions and the schematic of the external applied field (H_{ext}) are shown at the top of the figure. (c) Linescans of the simulated magnetostatic field distributions in unfilled ADLs (S1 and S2) and filled ADLs (S3 and S4) taken along the dotted lines from (a, b) are shown for (c) whole lattices and (d) CoFe channels around the marked region in (c). Comparison of the simulated magnetostatic field distributions in S3 and S4 is shown in (e) taken along the dotted lines from (b) in the two marked regions, i.e. in the (f) CoFe channel and (g) the NiFe-filled regions.

The internal field strength and its distribution in the CoFe channel have clearly improved in S3 and S4 as opposed to its unfilled counterparts (S1 and S2) due to the strong interaction between the two constituent materials of the filled ADLs at the interface. The internal field at the centre of the CoFe channel has increased by ~ 70 Oe for the circular shape and ~ 140 Oe for the square shape. In addition, the variation in the shape (circular and square) of the filled regions further modifies the demagnetizing regions and the ensuing internal field as well as the magnetostatic interaction between the neighboring NiFe filled regions as shown in Figure 9.7(e). Figure 9.7(f) shows that the internal field in the CoFe channel (green dotted box) in S3 is greater by ~ 60 Oe in comparison with that for S4. However, in the NiFe filled region (red dotted box) the internal field in S4 is greater by a whopping 760 Oe as opposed to S3 due to the shape effect as shown in Figure 9.7(g). The above variations in the total internal magnetic fields in the CoFe channels and NiFe filled regions are responsible for the observed variations in the SW spectra and also in the mode frequencies and mode profiles.

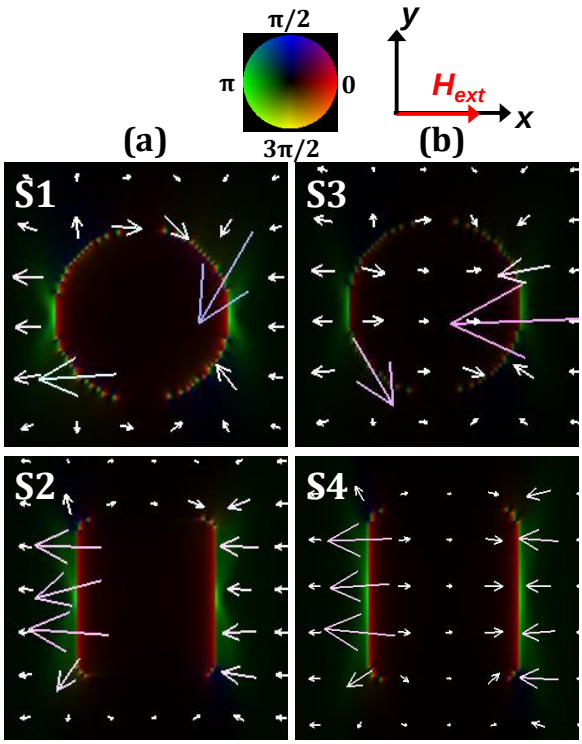

Figure 9.8. Simulated demagnetization field distributions in (a) unfilled ADLs (S1 and S2) and (b) filled ADLs (S3 and S4) with bias field H_{ext} = 1 kOe applied at ϕ = 0°. The

color map and the schematic of the external applied field (H_{ext}) are shown at the top of the figure.

We have further calculated demagnetizing field distributions for the unfilled and filled ADLs and the phase plots of the above fields are shown in Figure 9.8(a, b). Figure 9.8(b) shows that for both shapes, the demagnetizing field in the NiFe filled region is opposite to that in the CoFe region. While in the NiFe filled regions demagnetizing field is parallel to the applied bias field but in the CoFe regions, it is antiparallel. Even then, due to the much smaller value of saturation magnetization in NiFe as opposed to CoFe, the total internal field in the NiFe filled region is less than that in the CoFe regions as shown in Figure 9.7(c). As a result, the lowest frequency mode is confined within the NiFe filled regions and the higher frequency modes are quantized in both NiFe filled as well as CoFe regions for both the shapes.

Our claim of possible increase of spin wave propagation velocity due to the achievement exchange coupling between CoFe and NiFe in the BMCs could not be demonstrated experimentally here. The spin wave propagation velocity can be found by measuring the frequency versus wavevector dispersion using Brillouin light scattering. It may also be measured by ferromagnetic resonance in the transmission geometry using an excitation antenna and detection using inductive coupling. All these require either new technique and/or a more involved and time-taking sample fabrication method, which is beyond the scope of this paper. In this manuscript, we have used broadband ferromagnetic resonance technique to study the uniform precessional mode (k = 0) and standing spin wave spectra. However, using micromagnetic simulations, we have shown (see supplementary movies M1-M4) that the velocity of the spin wave increases significantly in case of the BMCs (S3 and S4) as opposed to the CoFe ADLs (S1 and S2). A local line excitation at the centre of the stripe like simulated samples propagate nearly 3 times faster in S3 and S4 as opposed to S1 and S2.

9.4. Conclusion

We have fabricated arrays of circular and square shaped NiFe filled CoFe antidot lattices (ADLs) and unfilled CoFe ADLs with nominal width of 400 nm and nominal edge-to-edge separation of 600 nm, arranged in square lattice symmetry by using a combination of electron beam lithography, electron beam evaporation and ion milling technique. We have investigated the spin wave (SW) spectra of these samples by varying the bias

magnetic field and element shape using broadband ferromagnetic resonance spectroscopy. A remarkable difference in the SW spectra between the filled and unfilled ADLs is observed for both the shapes. An asymmetry in the dispersion of spin wave frequency with bias field is observed in the filled ADLs with both circular and square shapes as opposed to their unfilled counterparts, with a minimum in the frequency occurring at a negative bias field, confirming the presence of inter-element exchange interaction at the NiFe and CoFe interface. For the circular shaped filled ADL, the SW spectra show three distinct modes similar to the corresponding unfilled ADL. However, unlike in the unfilled ADL, here we observe a decrease in the frequency gap between the two lowest modes (modes 1 and 2) down to a bias field of 0.75 kOe, below which the gap increases. A further change occurs with the element shape. While the unfilled square shaped ADL shows four modes, the corresponding filled ADL shows seven modes in the SW spectra. The inter-element exchange field value at the interface is greater in the square shaped filled ADL (-190 Oe) as opposed to that in the circular shaped filled ADLs (-150 Oe) probably due to a better-quality interface between NiFe and CoFe in the former. In addition, for square shaped filled ADL a gradual increase in the frequency gap between the two lowest modes (modes 1 and 2) is also observed below a bias field of 0.9 kOe. Micromagnetic simulations qualitatively reproduced the observed SW dynamics and the simulated SW mode profiles show a significant variation between the filled and unfilled ADLs as well as with the shape of the antidots (NiFe filled regions). For filled ADLs with both the shapes, the lowest lying SW modes are extended DE-like modes in CoFe channel and BV-like standing waves in the NiFe filled region. The higher frequency modes are the quantized BV-like modes in both CoFe and NiFe filled regions with different mode quantization numbers. Simulations show a significant difference in the magnetostatic field distributions for both circular and square shaped filled ADLs as opposed to their unfilled counterparts. The demagnetization region in filled ADL is modified due to change in the element shape, and as a result, the total internal field in the square shaped filled NiFe regions is larger as compared to the circular shaped filled NiFe regions. Finally, the demagnetizing fields in the CoFe and NiFe channels are opposite to each other, which give rise to a significant modification of the SWs in these samples. The observed tunability of SW spectra by filling the ferromagnetic antidots with another ferromagnetic material and the

modification of the exchange coupling between the two materials at the interface opens up the possibility of development of rich class of magnonic and magnetoelectronic devices. Finally, the fabrication method developed for the preparing the arrays of embedded magnetic nanostructures can easily be applied to develop other types of artificial crystals such as photonic, phononic and plasmonic crystals.

9.5. Materials and Methods

9.5.1. Sample Preparation

The periodic arrays of embedded nanostructures in the form of NiFe filled CoFe antidot lattices arranged in square lattice symmetry were fabricated by a combination of e-beam lithography (EBL), e-beam evaporation (EBE) and ion milling as shown in Figure 9.1(c). The width of the each NiFe filled region (antidot) is about 400 nm with maximum ± 5% deviation and the edge to edge separation between them is 600 nm with maximum ± 5% deviation, so that both the magnetostatic interaction and the exchange interaction play significant roles on the SW spectra. At first, 20 nm thick NiFe film is deposited on top of a self-oxidized silicon (Si) [100] substrate using e-beam evaporation in an ultra-high vacuum chamber at a base pressure of 2×10^{-8} Torr. Single layer negative resist (ma-N 2405) was used for e-beam lithography with a beam current of 100 pA to prepare the resist pattern on top of the NiFe film followed by Argon ion milling at a base pressure of 1.8×10^{-4} Torr to etch out the NiFe film from everywhere except the exposed resist pattern. The ion-milling on the NiFe film was performed down to the base of the film for each pattern. Subsequently, CoFe was deposited on top of this substrate in the e-beam evaporation chamber at the same base pressure used during NiFe deposition. The thickness of CoFe is kept as 20 nm so that after lift-off process the height of the NiFe filled regions and the surrounding CoFe regions remain the same. A co-planer waveguide (CPW) made of Au with thickness of 150 nm was deposited on top of the NiFe filled CoFe ADLs at a base pressure of 6×10^{-7} Torr for the broadband ferromagnetic resonance measurement. The Au waveguide was patterned by using mask-less photolithography. The width and length of the central conducting line of this CPW are 30 μm and 300 μm respectively so that the array falls under the centre of the central conducting line of CPW which has a nominal characteristic impedance of 50 Ω. Unfilled CoFe ADLs and Au co-planar waveguides on top of them with same dimensions

are also prepared separately under the same conditions for measurement of the ferromagnetic resonance spectra of those samples.

9.5.2. Measurement Technique

The frequency domain SW dynamics of the samples were measured by using a broadband ferromagnetic resonance spectrometer based on a vector network analyzer (VNA-FMR) along with a home-built probe station, which includes an in-built electromagnet to apply the bias magnetic field of 1.8 kOe. The bias field can be rotated by 360° within the sample plane. The microwave signal of varying frequency from 10 MHz to 50 GHz is launched in the CPW through a non-magnetic ground-signal-ground (G-S-G) probe via a co-axial cable and the CPW is shorted at one end so that the scattering parameter in the reflection mode (S_{11}) can be measured by the VNA after being collected by the same probe. The sample absorbs the power at various SW frequencies during the onward and return journey of the microwave signal through the CPW structure. This forms the characteristic SW spectrum for that sample. However, there are non-linear backgrounds in the directly measured signals originated from various sources. Hence during measurement at each bias field, a reference spectrum (spectrum at the highest value of the bias field) is subtracted from the signal to obtain a background free spectrum. However, some background still remains in the spectrum, which is non-trivial to remove from the spectrum. For each sample the spectra for a series of bias field from -1.56 kOe to +1.56 kOe at separation of 20 Oe are plotted together as a surface plot.

References

[1] S. Neusser, D. Grundler, Adv. Mater. 21 (2009) 2927.
[2] M. Jacoby, Chem. Eng. News 76 (1998) 38.
[3] I. E. Psarobas, N. Stefanou, A. Modinos, Phys. Rev. B 62 (2000) 5536.
[4] V. V. Kruglyak, A. Barman, R. J. Hicken, J. R. Childress, J. A. Katine, Phys. Rev. B 71 (2005) 220409(R).
[5] S. K. Kim, K. S. Lee, D. S. Han, Appl. Phys. Lett. 95 (2009) 082507.
[6] Y. Au, M. Dvornik, O. Dmytriiev, V. V. Kruglyak, Appl. Phys. Lett. 100 (2012) 172408.
[7] S. Kaka, M. R. Pufall, W. H. Rippard, T. J. Silva, S. E. Russek, J. A. Katine, Nature 437 (2005) 389.
[8] J. Ding, M. Kostylev, A. O. Adeyeye, Appl. Phys. Lett. 100 (2012) 073114.
[9] B. K. Mahato, S. Choudhury, R. Mandal, S. Barman, Y. Otani, A. Barman, J. Appl. Phys. 117 (2015) 213909.

[10] B. Rana, D. Kumar, S. Barman, S. Pal, Y. Fukuma, Y. Otani, A. Barman, ACS Nano 5 (2011) 9559.
[11] R. Mandal, S. Saha, D. Kumar, S. Barman, S. Pal, K. Das, A. K. Raychaudhuri, Y. Fukuma, Y. Otani, A. Barman, ACS Nano 6 (2012) 3397.
[12] S. Saha, R. Mandal, S. Barman, D. Kumar, B. Rana, Y. Fukuma, S. Sugimoto, Y. Otani, A. Barman, Adv. Funct. Mater. 23 (2013) 2378.
[13] J. Ding, A. O. Adeyeye, Adv. Funct. Mater. 23 (2013) 1684.
[14] K. Kern, D. Heitmann, P. Grambow, Y. H. Zhang, K. Ploog, Phys. Rev. Lett. 66 (1991) 1618.
[15] G. Ctistis, E. Papaioannou, P. Patoka, J. Gutek, P. Fumagalli, M. Giersig, Nano Lett. 9 (2009) 1.
[16] L. Torres, L. Lopez-Diaz, O. Alejos, J. Appl. Phys. 87 (2000) 5645.
[17] J. O. Vasseur, L. Dobrzynski, B. Djafari-Rouhani, H. Puszkarski, Phys. Rev. B 54 (1996) 1043.
[18] Z. K. Wang, V. L. Zhang, H. S. Lim, S. C. Ng, M. H. Kuok, S. Jain, A. O. Adeyeye, ACS Nano 4 (2010) 643.
[19] K. L. Livesey, J. Ding, N. R. Anderson, R. E. Camley, A. O. Adeyeye, M. P. Kostylev, S. Samarin, Phys. Rev. B 87 (2013) 064424.
[20] A. O. Adeyeye, S. Jain, Y. Ren, IEEE Trans. Magn. 47 (2011) 1639.
[21] G. Duerr, M. Madami, S. Neusser, S. Tacchi, G. Gubbiotti, G. Carlotti, D. Grundler, Appl. Phys. Lett. 99 (2011) 202502.
[22] G. Gubbiotti, S. Tacchi, M. Madami, G. Carlotti, S. Jain, A. O. Adeyeye, M. P. Kostylev, Appl. Phys. Lett. 100 (2012) 162407.
[23] S. Tacchi, G. Duerr, J. W. Klos, M. Madami, S. Neusser, G. Gubbiotti, G. Carlotti, M. Krawczyk, D. Grundler, Phys. Rev. Lett. 109 (2012) 137202.
[24] S. Saha, S. Barman, J. Ding, A. O. Adeyeye, A. Barman, Appl. Phys. Lett. 102 (2013) 242409.
[25] X. M. Liu, J. Ding, A. O. Adeyeye, Appl. Phys. Lett. 100 (2012) 242411.
[26] G. Duerr, S. Tacchi, G. Gubbiotti, D. Grundler, J. Phys. D: Appl. Phys. 47 (2014) 325001.
[27] M. Krawczyk, S. Mamica, M. Mruczkiewicz, J. W. Klos, S. Tacchi, M. Madami, G. Gubbiotti, G. Duerr, D. Grundler, J. Phys. D: Appl. Phys. 46 (2013) 495003.
[28] F. S. Ma, H. S. Lim, Z. K. Wang, S. N. Piramanayagam, S. C. Ng, M. H. Kuok, Appl. Phys. Lett. 98 (2011) 153107.
[29] H. Yu, G. Duerr, R. Huber, M. Bahr, T. Schwarze, F. Brandl, D. Grundler, Nat. Commun. 4 (2013) 2702.
[30] M. Donahue, D. G. Porter, *OOMMF User's guide, Version 1.0,* (NIST Interagency Report No. 6376; National Institute of Standard and Technology, Gaithersburg, MD, URL: http://math.nist.gov/oommf, 1999).
[31] A. Barman, S. Barman, Phys. Rev. B 79 (2009) 144415.
[32] D. Kumar, O. Dmytriiev, S. Ponraj, A. Barman, J. Phys. D: Appl. Phys. 45 (2012) 015001.
[33] R. Mandal, S. Barman, S. Saha, Y. Otani, A. Barman, J. Appl. Phys. 118 (2015) 053910.

Chapter 10

10. Anisotropic Spin Waves in Two-Dimensional Triangular Shaped Bi-Component Magnonic Crystal

Bi-component magnonic crystals with a strong dipole-exchange interaction across the interface of the constituent magnetic elements have shown promising potentials in magnonics and magnon-spintronics. Here, we have reported an all-optical investigation of spin wave dynamics in an array of periodically arranged bi-component magnonic crystal in the form of triangular-shaped $Ni_{80}Fe_{20}$ nanoelements embedded in $Co_{50}Fe_{50}$ matrix using time-resolved magneto-optical Kerr effect magnetometry. The spin wave spectra obtained from the sample reveal a broad band of spin wave modes where they possess a strong and systematic bias magnetic field tunability which is crucial for active control over such system in device applications. Further, the spin wave modes show a six-fold and four-fold rotational anisotropy with the bias field orientation due to combined effects of element shape and lattice symmetry. Micromagnetic simulations reproduce the experimental results qualitatively where the simulated mode profiles unravel the spatial distribution of spin wave frequencies inside both constituent elements while the internal magnetic fields play a crucial role for the observed tunability of spin wave dynamics. Development of such magnetically coupled embedded magnetic nanostructures can pave a new pathway in designing the future magnonic devices and faster microwave communication systems.

10.1. Introduction

Magnonic crystals (MCs) [1,2] are smart artificial materials which have emerged during last one decade as a powerful sub-field of spintronics and nanotechnology, where spin waves (SWs) are being utilized and manipulated to transfer and process information. By structuring a known magnetic material into one-, two- or three-dimensions (1, 2 or 3D) at different length scales [1,3,4], one can introduce and tailor magnonic band structure, band gap and SW propagation velocity. This makes them useful for SW-based communication devices e.g. magnonic waveguides [5], SW filters [6], phase shifters [7], SW emitters [8], SW-based logic devices [9], transistor [10] as well as for cellular non-

linear networking. Subsequently, the rapidly emerging field of magnonics [11-13] has shown the potential to compete with the charge-based semiconductor technology. Further development of magnon-spintronics [14] where spin current can be carried by magnons and inter-conversion between magnon current and electric charge-based spin and charge current is possible. Consequently, spin-orbitronics [15,16] (interconversion between spin and charge current due to spin-orbit effects) has given a strong impetus to this highly interdisciplinary research areas. In addition, both these new fields promise energy-efficient computing as opposed to its existing counterparts. Magnonic crystals can act as building blocks for the development of the above devices and a plethora of work have been done in this field during the last one decade. Ferromagnetic (FM) dot arrays [17-20], antidot (AD) arrays [21-24] and nanowires [25-27] have emerged as promising candidates as MCs. Here, the magnonic band structures can be significantly tailored by tuning different physical or geometrical features such as constituent material [28], shape [29], size [30], lattice spacing [31] and also by changing or breaking the translational [32] and rotational symmetry [33] of these nanostructure arrays.

The magnetization dynamics can be efficaciously modulated in bi-component magnonic crystals (BMCs) [34-36]. Here, one FM element is embedded into a matrix of another FM material in a periodic manner so that the difference between their magnetic parameters and magnetic coupling between them give more control over their magnonic bands. Further, the coupling can be maximized at their physical boundaries because of the exchange interaction between the two constituent FM materials. Therefore, these embedded nanostructures have become a subject of extreme importance due to their salient physical aspects like mode-coupling process and large SW group velocity through the lateral interface which may find potential applications in magnonics as well as in spintronics as a tool to bridge between them.

In recent years, SW dynamics of different kinds of 1D [37,38] and 2D BMCs [35,36,39-41] have been studied experimentally by electrical [42] and thermal [43] excitation methods and theoretically by analytical and numerical methods [44,45]. A more recent study [46] on circular shaped BMC shows that they can be used as an omnidirectional nanograting coupler. However, the rotational anisotropy in BMC, particularly in various non-ellipsoidal shaped elements have not been studied in details. This will have an important influence on the anisotropic SW propagation and its possible applications

such as SW splitter, directional couples and other reconfigurable devices. Furthermore, time-domain investigation of the magnetization dynamics in complex BMC structures have not been performed so far. Here, we present an all-optical investigation of time-resolved magnetization dynamics of a new BMC structure made of triangular shaped $Ni_{80}Fe_{20}$ (NiFe) elements embedded in $Co_{50}Fe_{50}$ (CoFe) thin film matrix where CoFe and NiFe are physically connected at their boundaries. We have obtained rich SW spectra consisting of four dominant SW modes along with an additional weak SW mode which follow a systematic variation with the strength of the bias magnetic field. A strong anisotropic behaviour of the SW is observed by varying the in-plane orientation of the bias magnetic field, where we obtain strong six-fold and four-fold rotational symmetries in the SW modes. The micromagnetic simulations unravel the presence of different localized and extended SW modes and also help to interpret the effect of demagnetizing field due to the modulation at the interface of the embedded BMC system.

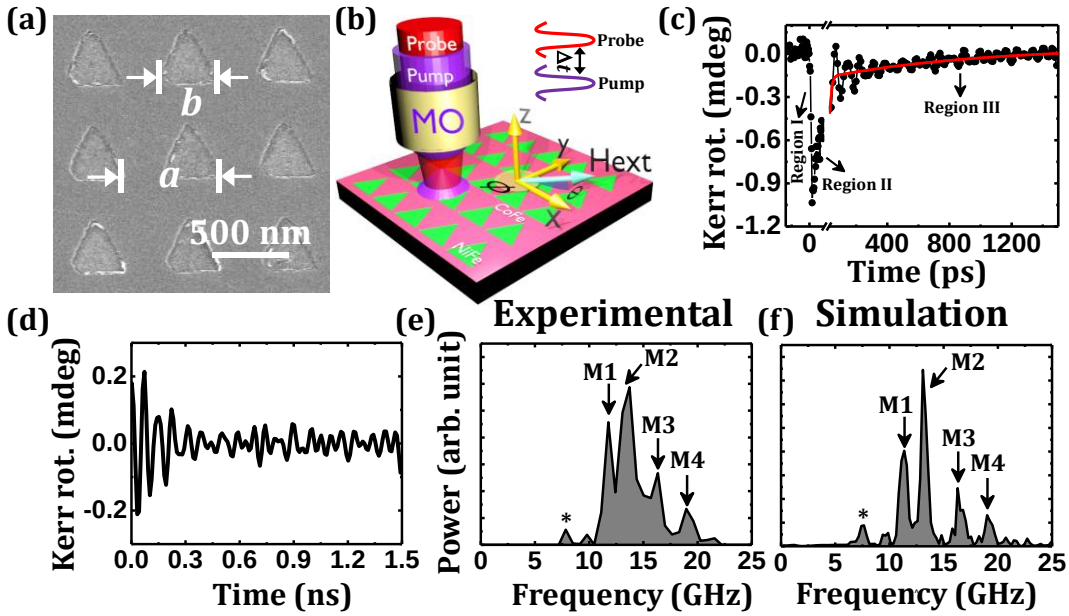

Figure 10.1. (a) Scanning electron micrograph (SEM) of triangular-shaped $Ni_{80}Fe_{20}$ (NiFe) elements of base length, b = 330 nm arranged in a square lattice of periodicity, a = 600 nm embedded in $Co_{50}Fe_{50}$ (CoFe) matrix. (b) Schematic of the experimental arrangement used for TRMOKE measurement technique and the geometry of the applied magnetic field (H_{ext}). (c) Unprocessed time-resolved Kerr rotation data obtained from the BMC sample at H_{ext} = 1.3 kOe applied at an azimuthal angle, ϕ = 0°. (d) Time-domain precessional data obtained after background subtraction using a bi-exponential fit as shown by the red solid line in Figure 10.1(c). Corresponding FFT power spectra of

(e) experimental and (f) simulated time-domain precession with H_{ext} = 1.3 kOe for ϕ = 0°.

10.2. Experimental Details

A 2D array of 20-nm thick (t) triangular-shaped NiFe nanostructures embedded in square lattice on the CoFe thin film matrix of the same thickness, as shown in the scanning electron micrograph (SEM) in Figure 10.1(a), has been fabricated by electron beam evaporation (EBE), electron beam lithography (EBL) and ion milling tools. The side (b) of each triangle is 330 nm (± 5%) while the periodicity (a) of the square lattice has been kept at 600 nm (± 2%). The NiFe and CoFe regions are physically connected at their boundaries and hence, both exchange and the magnetostatic interactions will play significant roles in their SW dynamics.

The ultrafast magnetization dynamics have been measured by employing the time-resolved magneto-optical Kerr effect microscope [30] as demonstrated schematically in Figure 10.1(b). The second harmonic (wavelength λ_{pump}: 400 nm) of a mode-locked Ti-Sapphire oscillator has been employed as the pump beam to excite the magnetization dynamics in the BMC, while the fundamental laser beam (wavelength λ_{probe}: 800 nm) has been employed to probe the polar Kerr rotation from the BMC as a function of the time delay (Δt) between the pump and probe laser beams. A time window of 1.5 ns has been used in our experiment. A magnetic field is applied at a small tilt angle (θ) ~ 15° from the sample plane, the in-plane component of which (H_{ext}) is considered as the bias magnetic field. Here, the slight tilt of the magnetization from the plane of the sample introduces a finite demagnetizing field along the pump beam direction and this is modulated by the pump laser to induce a precessional dynamics in the sample. The pump and the probe beams, which are aligned in a colinear geometry, are focused on the sample through a single microscope objective (MO). Here, the measurement is done by keeping the sample at the focal plane of the probe laser (diameter ~800 nm), while the pump laser (diameter ~1 μm) is slightly defocused on the sample plane. The probe is carefully placed at the centre of the pump beam so that we can probe the local magnetization dynamics from a uniformly excited region of the sample. The Kerr rotation present in the back-reflected probe beam and the total reflectivity signals have been unambiguously recorded with the aid of a balanced photodiode detector and two

lock-in amplifiers using a phase-sensitive manner, where the breakthrough of reflectivity and Kerr signals into one another has been eliminated. In the experimental set-up, the in-plane (azimuthal) angle (ϕ) of H_{ext} was precisely varied at an interval of 15° which is achieved by rotating the sample mounted on a high precision rotation stage while the MO and H_{ext} have been kept fixed. Both pump and the probe beams have been made incident on the same region of the BMC sample for each value of ϕ.

The micromagnetic simulations have been performed to interpret the origin of the observed SW frequencies using the OOMMF software [47] where a finite array consisting of 7 × 7 triangular-shaped NiFe elements has been considered in square lattice arrangement on CoFe matrix. The sample has been divided into parallelepiped cells having dimensions 3 × 3 × 20 nm^3. The saturation magnetization and exchange stiffness parameters used during the simulation [41] are M_{NiFe} = 800 emu/cc, A_{NiFe} = 1.3 × 10^{-6} erg/cm, for NiFe, and M_{CoFe} = 1800 emu/cc, A_{CoFe} = 3 × 10^{-6} erg/cm, for CoFe. The magnetocrystalline anisotropy, K = 0 and the gyromagnetic ratio, γ = 18.5 MHz/Oe have been considered for both the materials. After performing numerous test simulations and comparing those results with the experimental results, the exchange stiffness constant is found to be A_{Exch} = 2.1 × 10^{-6} erg/cm at the NiFe/CoFe interface ensuring a strong inter-component interaction between NiFe and CoFe [48,49]. The micromagnetic simulations are described in details elsewhere [50].

10.3. Results and Discussion

10.3.1. Evolution of Spin Wave (SW) Frequencies with Strength and Orientation of the External Bias Magnetic Field

Figure 10.1(c) represents a typical time-resolved Kerr rotation trace obtained from the triangular- shaped BMC at a bias magnetic field, H_{ext} = 1.3 kOe applied at ϕ = 0°. Here, the ultrafast demagnetization [51] (region I, demagnetization time τ_{demag} = 171 ± 3 fs) takes place during the thermalization of the electron and spin system which was disturbed by the pump pulse at the zero delay [52]. This phenomenon is followed by a fast (region II, time τ_{fast} = 0.363 ± 0.009 ps) and a slow (region III, time τ_{slow} = 0.56 ± 0.01 ns) relaxation processes [53] with two different relaxation time scales because of the transfer of electron and spin energies to lattice and further to the substrate and the surrounding environment. The precessional magnetization dynamics is observed as an oscillatory signal over the slowly decaying magnetization. After subtracting a bi-

exponential background as shown by the red solid line in Figure 10.1(c), the time-resolved precessional dynamics is illustrated in Figure 10.1(d) which shows a damped non-uniform oscillation consisting of multiple precessional modes. Fast Fourier transform (FFT) is performed over this precessional data to obtain the power versus frequency spectrum as shown in Figure 10.1(e), which clearly indicates the presence of four distinct SW modes in this sample, which have been named as M1-M4 according to the ascending order of their frequency values. Interestingly, we have also obtained another low power SW mode in the lower frequency regime, which is denoted by an asterisk mark (M*) in Figure 10.1(e, f). Notably, the spatial uniformity of the sample has been checked by measuring the dynamics at different positions of the sample which ensures that the time-resolved dynamics and the corresponding SW spectra obtained by FFT of the time-resolved Kerr rotation from different positions of the same sample are very similar indicating spatial uniformity of the sample.

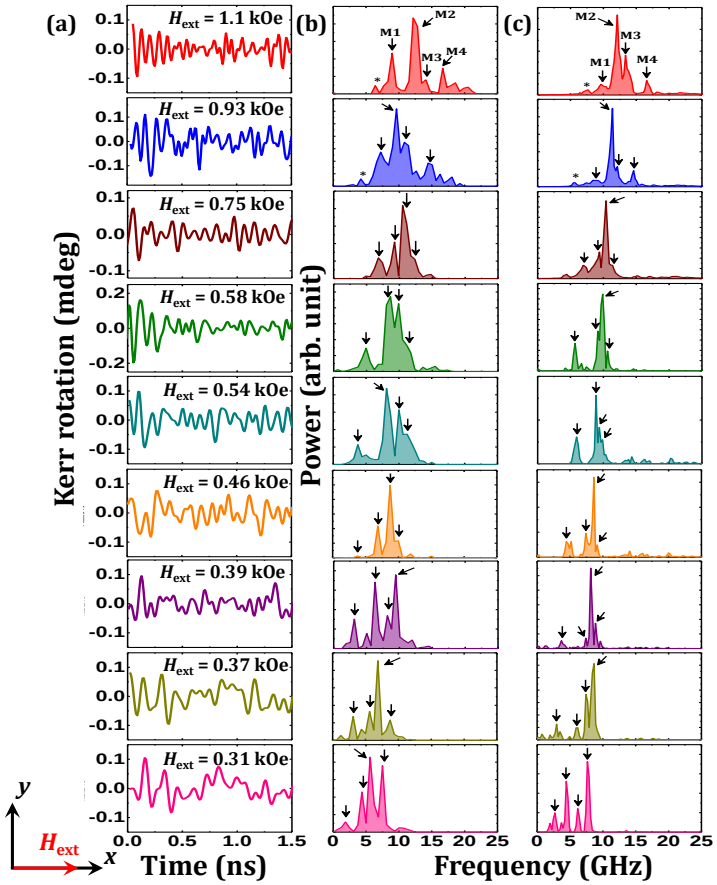

Figure 10.2. (a) Experimental time-domain Kerr rotation showing precessional dynamics for the triangular BMC at various bias magnetic field (H_{ext}) between 1.1 kOe ≤

H_{ext} ≤ 0.31 kOe applied at azimuthal angle ϕ = 0°. FFT power spectra of (b) experimental and (c) simulated time-domain Kerr rotation. The schematic of the orientation of H_{ext} are shown at the bottom left side of the figure.

Subsequently, we measured the time-resolved magnetization dynamics from the central region of the array systematically for consistency. The time-domain precessional dynamics along with the experimental and simulated FFT power spectra at different strength of H_{ext} applied at ϕ = 0° are shown in Figure 10.2. Figure 10.3(a) describes the variation of the SW frequencies present in the BMC with the variation of external bias field (H_{ext}). This reveals that all the SW frequencies decrease systematically with the reduction in H_{ext} while, M* disappears for H_{ext} < 0.93 kOe.

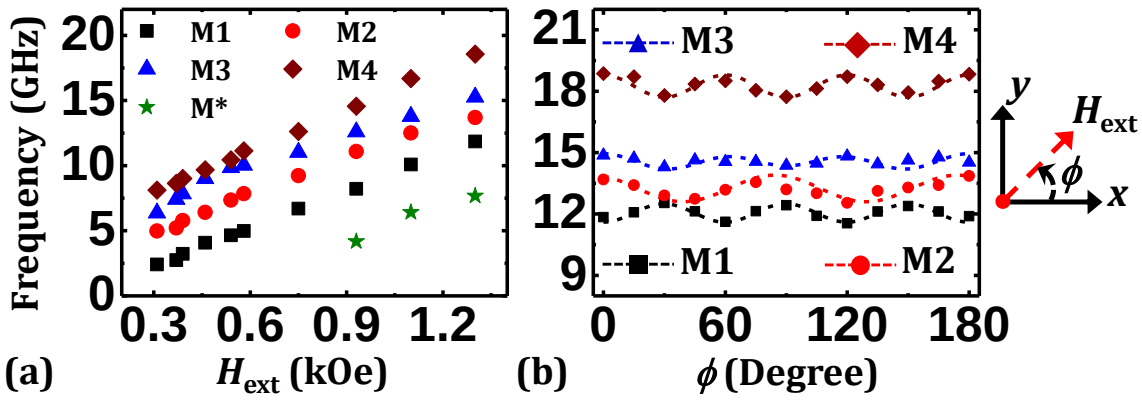

Figure 10.3. (a) Variation of precessional frequencies of the SW modes as a function of the strength of the external magnetic field (H_{ext}) applied at an azimuthal angle ϕ = 0°. (b) Modulation of SW frequencies (M1-M4) with ϕ is presented for H_{ext} = 1.3 kOe. The symbols denote the experimental results, while the dotted lines represent sinusoidal fits for the anisotropic SW modes obtained in the BMC. The schematic of the orientation of H_{ext} is given at the right side of the figure.

The time-domain magnetization dynamics with the experimental and simulated FFT power spectra obtained at ϕ = 15°, 30°, 45°, 60°, 75° and 90° respectively at constant H_{ext} = 1.3 kOe are shown in Figure 10.4. Figure 10.3(b) demonstrates the modulation of the precessional dynamics for the triangular-shaped BMC with ϕ at H_{ext} = 1.3 kOe. A distinct modulation in the SW frequencies is observed with the variation of ϕ. The dotted curves in Figure 10.3(b) describe the theoretical fits employing harmonic functions having different rotational symmetries which clearly show that both the lowest and highest frequency modes (M1 and M4) show anisotropic behaviour with six-

fold rotational symmetry although their anisotropic nature is in opposite phase with each other. Interestingly, M2 shows an anisotropic nature with a four-fold symmetry but the other mode, i.e. M3 shows negligible anisotropy with a superposition of weak four- and six-fold rotational symmetries.

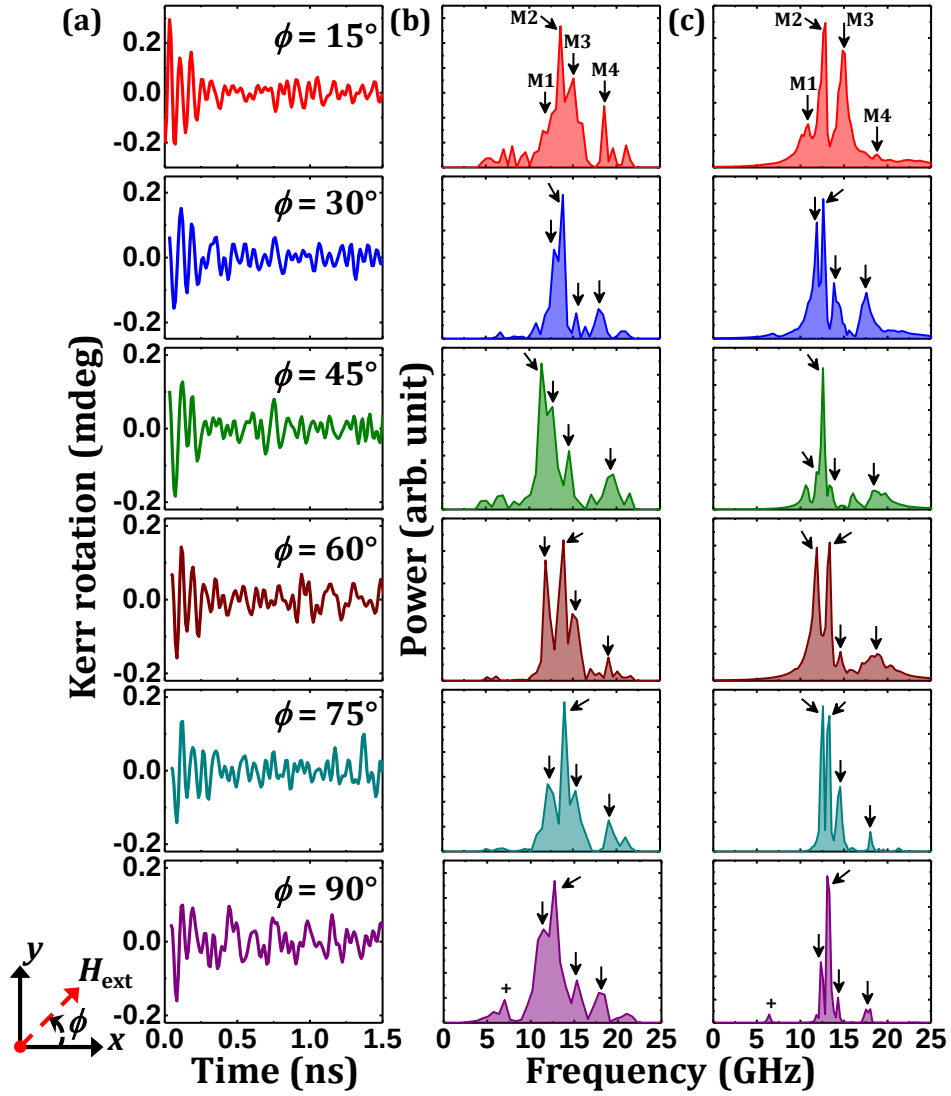

Figure 10.4. (a) Experimental time-resolved Kerr rotation data obtained for the triangular BMC for H_{ext} = 1.3 kOe applied at ϕ = 15°, 30°, 45°, 60°, 75° and 90°. FFT power spectra of (b) experimental and (c) simulated time-resolved magnetization. Here, the '+' marked mode in both experimental and simulated power spectra at ϕ = 90° represent the edge mode. The schematic of the orientation of H_{ext} is shown at the bottom left side of the figure.

10.3.2. Micromagnetic Analysis of Spin Wave (SW) Mode Profiles

Micromagnetic simulations have qualitatively reproduced the experimental results as shown in Figure 10.1(f) where FFT power spectra obtained for H_{ext} = 1.3 kOe at ϕ = 0° is presented. However, the precise values of the SW modes have not been reproduced always because of the deviation of the experimental conditions from the simulated ones. Generally, the deviation in the physical entities (e.g. roundedness at edges of the triangular elements) as observed in the experimental sample have been included during the simulation. However, the precise edge roughness profiles are difficult to incorporate in the micromagnetic simulations used here which relies on a finite difference method. Also, to avoid the boundary effects, as the boundaries of the arrays experience non-uniform magnetostatic environment due to the finite array size, we extracted magnetization response from a much smaller area (3 × 3 elements from the centre of 7 × 7 elements) from the simulated array. For this the magnetostatic environment is almost identical due to the absence of the edge effect of the boundary of the array.

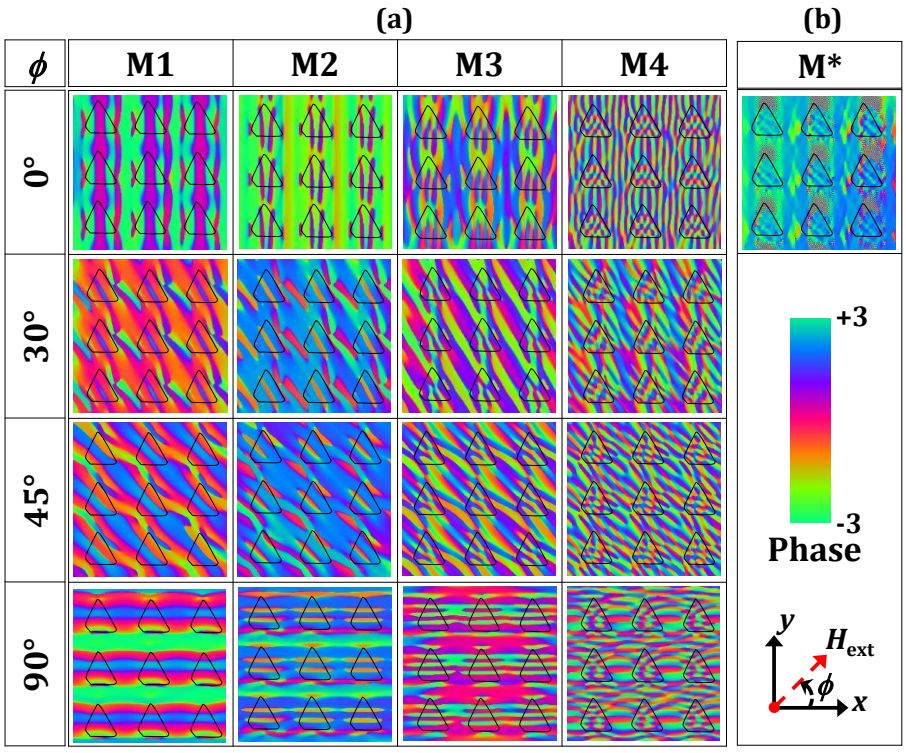

Figure 10.5. (a) Simulated spatial distributions of the phase of the SW modes obtained for the triangular BMC with bias field H_{ext} = 1.3 kOe applied at ϕ = 0°, 30°, 45° and 90°, respectively. (b) Simulated power map corresponding to the edge mode (M*) obtained

at H_{ext} = 1.3 kOe at ϕ = 0°. The color map for the power distribution and the orientation of H_{ext} are shown at the bottom right side of the figure.

The power and phase maps of the SW modes by using a homebuilt code [54] have been simulated to understand their origins. Figure 10.5 and Figure 10.6 illustrate the phase and power maps of the SW frequencies obtained in the triangular-shaped BMC at H_{ext} = 1.3 kOe applied at different ϕ values. As evident from Figure 10.5, various extended and quantized SW modes are observed for the lattice because of the confining potentials created by the demagnetizing field around the triangular-shaped NiFe elements causing the formation of standing SW between two neighbouring NiFe elements. Different quantization numbers for the SW modes in the backward volume (BV) geometry (viz. localization along the direction of H_{ext}) are assigned which is denoted by m and n for NiFe and CoFe regions, respectively based on the number of antinodes. Interestingly, it is observed from Figure 10.6 that at ϕ = 0°, the power of the lowest frequency mode M1 is primarily confined along the NiFe filled CoFe channel as shown by the black dotted lines in M1 of Figure 10.6(a). As the frequency of SW modes increases the power gets transferred to the CoFe channels as shown by the blue dotted lines in M2 of Figure 10.6(a). The phase profiles of the SW frequencies at ϕ = 0° in Figure 10.5(a) show that M1 represents edge-mode in CoFe channel although it forms standing SW in BV-geometry with m = 3 inside the triangular NiFe element. On the other hand, M2 shows extended Damon-Eshbach (DE)-like nature in the CoFe channel while it shows BV-like standing SW within the NiFe elements having m = 5. M3 represents localized BV-like mode in both NiFe and CoFe with m = 7 and n = 3, respectively. However, the highest frequency mode M4 shows a mixed quantized nature along both x- and y-directions inside the NiFe element, while it represents a BV-like mode in the CoFe region with n = 5.

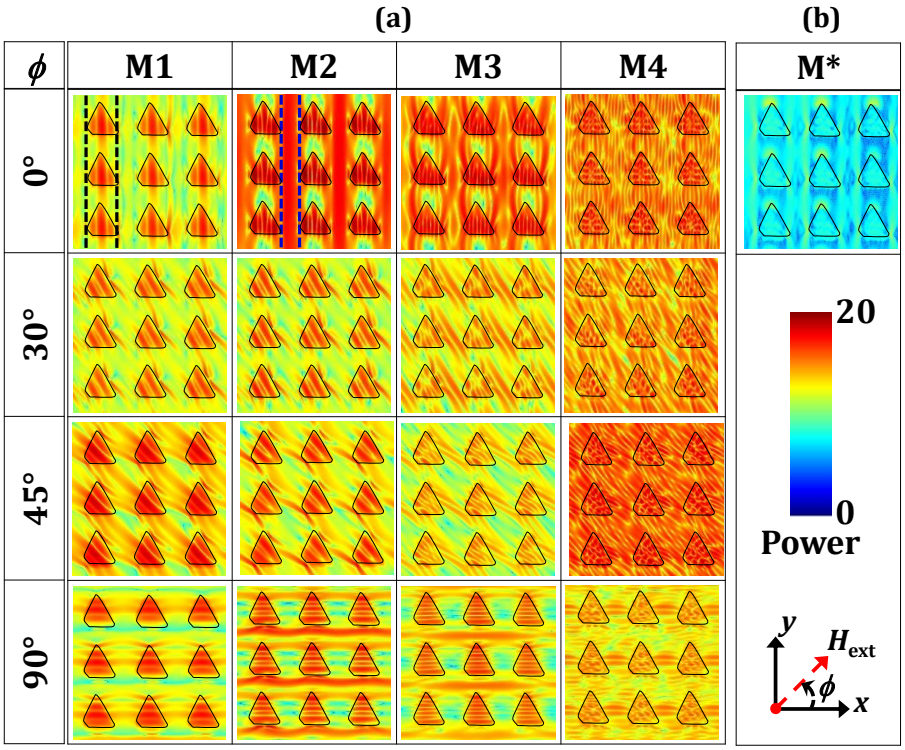

Figure 10.6. (a) Simulated spatial distributions of power of the SW modes obtained for the triangular BMC with bias field H_{ext} = 1.3 kOe applied at ϕ = 0°, 30°, 45° and 90°, respectively. (b) Simulated power map corresponding to the edge mode (M*) obtained at H_{ext} = 1.3 kOe at ϕ = 0°. The color map for the power distribution and the orientation of H_{ext} are given at the bottom right side of the figure.

Interestingly, the spatial evolution of the SW frequencies with the in-plane orientation of the bias field as demonstrated in Figure 10.5(a) and Figure 10.6(a) revealed that the nature of M1 remains unaltered when ϕ is varied from 0° to 90°, while its quantization axis rotates in commensuration with the direction of H_{ext}. However, M2 gets drastically modified with the variation of ϕ as it undergoes a mode conversion from DE-like to BV-like mode when ϕ is increased from 0° and it regains its extended DE-like nature at ϕ = 90°. In M3, the spatial quantization of the modes remains unaffected with the variation of ϕ, but the power of the mode reduces drastically as ϕ is increased above 0°, while the power is regained at ϕ = 90°. However, the behaviour of highest frequency mode M4 remains almost invariant with ϕ. In addition, the asterisk (M*) marked mode as shown in Figure 10.1(e, f) represents the edge mode of the array where the power of the SW frequency is localized only at the edges of the triangular-shaped NiFe regions which is demonstrated in Figure 10.5(b) and Figure 10.6(b). This reflects that the power of this edge mode M* is very small compared to other prominent SW modes.

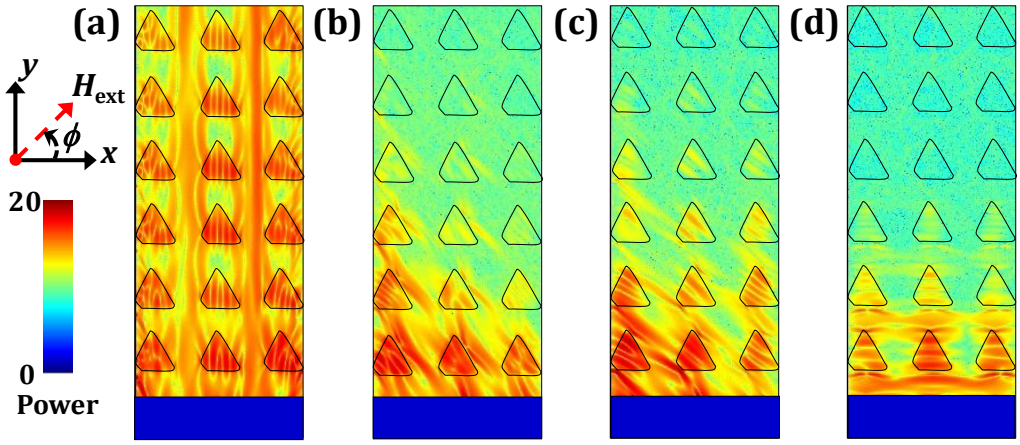

Figure 10.7. Power profiles of SW mode M2 excited locally at the blue shaded region at H_{ext} = 1.3 kOe applied at ϕ = (a) 0° (b) 30° (c) 45° and (d) 90° respectively. The color map associated with the power distributions and the orientation of H_{ext} are given at the bottom right side of the figure.

Figure 10.7 demonstrates an exemplary simulation of the manipulation of the propagating nature of the extended SW mode M2. For that, microwave line excitation has been employed to stimulate the SW response with the aid of OOMMF micromagnetic simulation. Here, SWs are launched at one end of the considered BMC as shown by blue shaded rectangular regions in Figure 10.7(a-d) with an area, 1750 (x) × 350 (y) nm^2, where a time-varying field with "sinc" functional form with a 30 GHz frequency cut-off is applied for the SW excitation. In the simulation, the bias magnetic field, H_{ext} = 1.3 kOe is applied at different in-plane orientation of ϕ = 0°, 30°, 45° and 90°. The results reveal an exciting feature that the excited SW mode M2 propagates uniformly through the waveguide to its other end at ϕ = 0° as shown in Figure 10.7(a). However, it decays very fast and disappears within about 1000 nm from the excitation region with the increase in ϕ, as evident from Figure 10.7(b, c), while it almost ceases to propagate when ϕ becomes 90° as shown in Figure 10.7(d). Thus, this waveguide may act as an angular filter for the extended mode M2 depending mainly upon the orientation of the magnetic field suggesting this triangular BMC suitable for magnonic circuits for faster microwave communication.

10.3.3. Calculation of Magnetostatic Field Profile

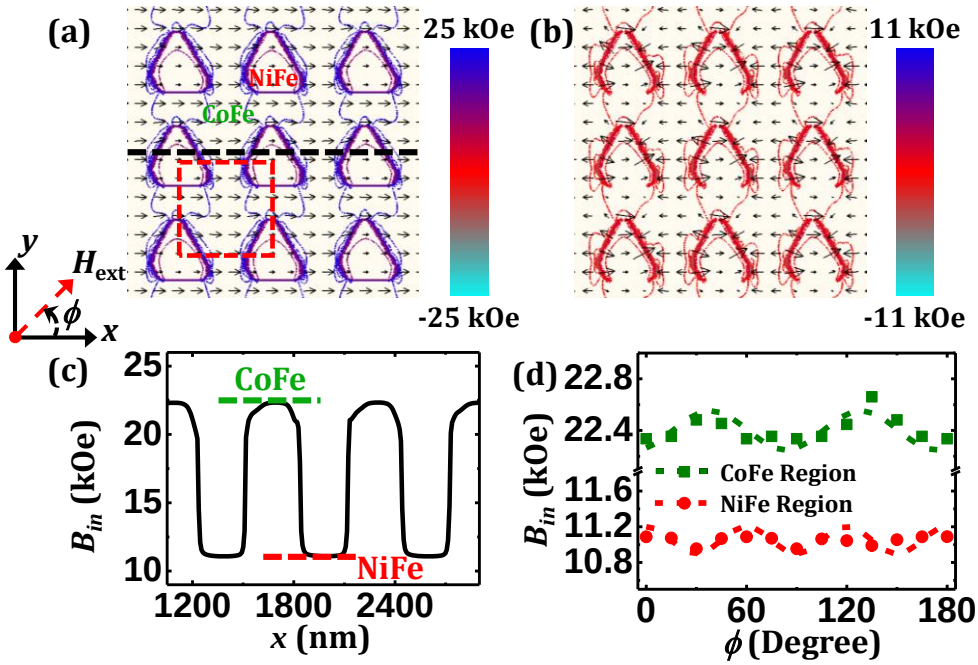

Figure 10.8. (a) Contour plot of the simulated magnetostatic field profile inside the triangular-shaped BMC at magnetic field H_{ext} = 1.3 kOe for ϕ = 0° and the corresponding color map shown at the right side. (b) Contour plot of the simulated demagnetization field profile in the BMC at bias field H_{ext} = 1.3 kOe for ϕ = 0° and the corresponding color map is given at the right side. (c) Linescan of the simulated internal field (B_{in}) inside the BMC taken along the black dotted line from Figure 10.8(a). (d) Evolution of B_{in} values with varying ϕ at H_{ext} = 1.3 kOe obtained from the NiFe and CoFe regions of the array. The symbols denote the simulated results whereas the dotted lines represent the sinusoidal fits for anisotropic behaviour in B_{in}. The H_{ext} is given schematically at the left side of the figure.

Further, the tunability of the SW dynamics present in the BMC has been investigated by calculating the magnetostatic field distributions using LLG Micromagnetics simulator [55] as shown in Figure 10.8(a), which clearly indicates the non-uniform magnetostatic field distribution around the edges of the NiFe elements and this is asymmetric in nature due to the triangular shape of the NiFe element. Interestingly, when we calculate the demagnetizing field distributions as demonstrated in Figure 10.8(b), we observe a stark difference in demagnetizing field inside the CoFe region as opposed to that in the NiFe region. This means the demagnetizing field in NiFe element is parallel to the H_{ext} while it is antiparallel to H_{ext} in the CoFe region which helps to increase or decrease the internal field (B_{in}) in the NiFe or CoFe region. However, when a line scan is performed

across the black dotted line as represented in Figure 10.8(c) to determine the B_{in} values in the NiFe and the CoFe regions, we find that the total B_{in} inside the NiFe element is much smaller than that in CoFe region due to a comparatively smaller value of saturation magnetization of NiFe than CoFe. Consequently, the lowest frequency mode, i.e. M1 is confined mainly inside the NiFe regions, whereas the power of SW mode gets gradually shifted to CoFe channels for the higher frequency mode M2. In order to understand the anisotropic behaviour of the SW mode, we have also calculated the variation of B_{in} for the triangular shaped BMC at different ϕ inside both NiFe and CoFe regions as shown in Figure 10.8(a). Interestingly, B_{in} varies significantly with the variation of ϕ as evident from Figure 10.8(d). The variation of B_{in} also confirms that a six-fold anisotropy is present inside NiFe element, whereas a four-fold anisotropic behaviour is obtained in the CoFe region. This is due to a combined effect of the triangular shape of the NiFe element and the square lattice symmetry (as shown by red dotted box in Figure 10.8(a)), which play a crucial role for the variation of B_{in} in NiFe and CoFe regions as a function of ϕ. This is manifested as the configurational anisotropy present in the SW frequencies of the BMC.

10.4. Conclusion

In summary, the ultrafast magnetization dynamics of triangular-shaped NiFe filled CoFe BMC has been investigated by controlling the strength and the azimuthal orientation of the bias magnetic field by employing time-resolved MOKE magnetometry. The magnetization dynamics of the BMC reveals rich SW spectra where four distinct SW modes along with an additional weak low-frequency SW mode are observed which vary systematically with the strength of the applied magnetic field. The experimentally observed SW dynamics has been qualitatively reproduced by micromagnetic simulations while the simulated profiles of the SW modes unravel some interesting features. The SW modes possess either extended DE- or BV-like behaviour depending upon their frequency with different mode quantization numbers in NiFe and CoFe regions. Also, the power of the SW mode is transferred from NiFe channel (M1) to CoFe channel (M2) when the frequency is increased. The configurational anisotropy present in the BMC is investigated by varying the azimuthal orientation of the applied magnetic field where two SW modes (M1 and M4) possess six-fold anisotropy having an opposite phase to each other. However, one of the intermediate SW modes (M2) shows four-fold

anisotropy, while the other one (M3) has a weak anisotropic behaviour with a superposition of six- and four-fold symmetry. The magnetostatic fields including the demagnetizing field distributions reveal that the demagnetizing fields in NiFe and CoFe regions are opposite to each other although there is a large difference of saturation magnetization values between the constituent FM materials which gives rise to a significant modification in the SW spectra. Also, the in-plane variation of the internal field reveals that the triangular shape of NiFe element is mainly responsible for the observed six-fold anisotropy, whereas the four-fold anisotropy arises due to the lattice arrangement of these NiFe elements on the CoFe matrix. In addition to this, the power profiles of the SW mode (M2) show an interesting mode conversion from extended to quantized standing SW mode with the azimuthal rotation of bias magnetic field direction. Further, this fascinating property of M2 is improvised to numerically demonstrate a potential application of such BMC as a dynamic filter integrated with the magnonic waveguide. This efficient modulation of SW dynamics due to the coupling between the constituent FM materials at their interface unlocks a new possibility of developing magnonic as well as spintronic devices.

10.5. Materials and Methods

10.5.1. Sample Preparation

The periodic arrays of embedded nanostructures in the form of NiFe filled CoFe antidot lattices arranged in square lattice symmetry were fabricated on 15 × 15 μm^2 area by a combination of e-beam lithography (EBL), e-beam evaporation (EBE) and ion milling as shown in Figure 10.9. The width of the each NiFe filled region (antidot) is about 330 nm with maximum ± 5% deviation and the lattice periodicity is about 600 nm with maximum ± 2% deviation, so that both the magnetostatic interaction and the exchange interaction play significant roles on the spin wave (SW) spectra. At first, 20-nm-thick NiFe film is deposited on top of a self-oxidized silicon (Si) [100] substrate using e-beam evaporation in an ultra-high vacuum chamber at a base pressure of 2×10^{-8} Torr. Single layer negative resist (ma-N 2405) was used for the e-beam lithography with a beam current of 100 pA to prepare the resist pattern on top of the NiFe film followed by Argon ion milling at a base pressure of 1.8×10^{-4} Torr to etch out the NiFe film from everywhere except the exposed resist pattern. The ion-milling on the NiFe film was performed down to the base of the film for each pattern. Subsequently, CoFe was

deposited on top of this substrate in the e-beam evaporation chamber at the same base pressure used during NiFe deposition. The thickness of CoFe is kept as 20 nm so that after lift-off process the height of the NiFe filled regions and the surrounding CoFe regions remain the same.

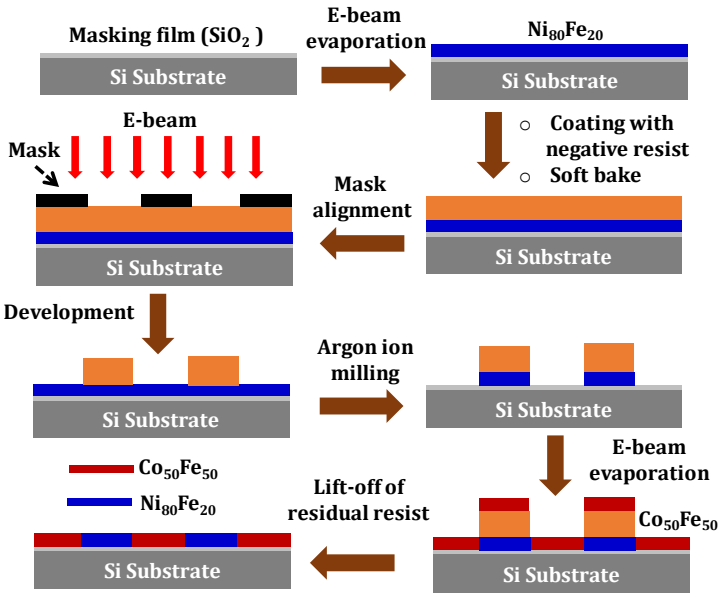

Figure 10.9. Schematic of the nano-fabrication technique used for the development of the two-dimensional triangular shaped bi-component magnonic crystal.

10.5.2. Measurement Technique

The ultrafast magnetization dynamics have been investigated using time-resolved magneto-optical Kerr effect magnetometry. Here, the second harmonic (wavelength λ_{pump}: 400 nm; pulse width: 100 fs) of a mode-locked Ti-Sapphire oscillator (Tsunami, Spectra Physics) was used as the pump beam to excite the spin dynamics in the BMC, while the fundamental laser beam (wavelength λ_{probe}: 800 nm; pulse width: 80 fs; repetition rate: 80 MHz) was employed to probe the polar Kerr rotation from the BMC as a function of the time delay (Δt) between the pump and the probe laser beams where the temporal resolution of the measurement is limited by the cross-correlation between these two beams and a time window of 1.5 ns has been used in our experiment. At first, a large magnetic field is applied at a small tilt angle (θ) ~ 15° from the sample plane in order to saturate its magnetization, which is followed by the decrease in the magnetic field to the bias field value (H_{ext}: in-plane component of the bias magnetic field) and this ensures that the magnetization remains oriented along the bias field direction. Here, the

slight tilt of the magnetization from the sample plane introduces a finite demagnetizing field along the direction of the pump beam and this is further modified by the pump pulse itself to induce a precessional dynamics within the sample. The pump and the probe beams, which are aligned in a colinear geometry, are focused on the sample through a microscope objective (MO) having numerical aperture NA: 0.65, where the SW dynamics is investigated by keeping the sample at the focal plane of probe pulse (diameter ~ 800 nm) while the pump pulse (diameter: 1 μm) is slightly defocused to measure the local magnetization dynamics of the sample. The probe beam is centered on the pump beam so that the Kerr signal can be collected from the uniformly excited region of the BMC. Here, the pump beam is modulated at 2 kHz frequency which is used as the reference frequency of the lock-in amplifier. Therefore, the Kerr rotation signal present in the back-reflected probe beam can be efficiently detected by a balanced photodiode detector and lock-in amplifier in a phase-sensitive manner. The reflectivity is simultaneous measured using the same detector and a separate lock-in amplifier. The pump and probe fluences were kept at around and 10 and 2 mJ/cm^2, respectively to avoid any damage due to laser heating. All the experiments were performed under ambient condition. In the experimental set-up the azimuthal angle (ϕ) of H_{ext} was effectively varied at an interval of 15° which is done by rotating the sample mounted on a high precision rotary stage while keeping the microscope objective and H_{ext} fixed. Both pump and the probe beams were made to incident on the same region of the BMC array for each value of ϕ.

References

[1] S. Neusser, D. Grundler, Adv. Mater. 21 (2009) 2927.
[2] S. A. Nikitov, P. Tailhades, C. S. Tsai, J. Magn. Magn. Mater. 236 (2001) 320.
[3] C. Banerjee, S. Choudhury, J. Sinha, A. Barman, Phys. Rev. Appl. 8 (2017) 014036.
[4] A. Fernández-Pacheco, R. Streubel, O. Fruchart, R. Hertel, P. Fischer, R. P. Cowburn, Nat. Commun. 8 (2017) 15756.
[5] V. V. Kruglyak, A. Barman, R. J. Hicken, J. R. Childress, J. A. Katine, Phys. Rev. B 71 (2005) 220409(R).
[6] S. K. Kim, K. S. Lee, D. S. Han, Appl. Phys. Lett. 95 (2009) 082507.
[7] Y. Au, M. Dvornik, O. Dmytriiev, V. V. Kruglyak, Appl. Phys. Lett. 100 (2012) 172408.
[8] S. Kaka, M. R. Pufall, W. H. Rippard, T. J. Silva, S. E. Russek, J. A. Katine, Nature 437 (2005) 389.
[9] J. Ding, M. Kostylev, A. O. Adeyeye, Appl. Phys. Lett. 100 (2012) 073114.

[10] A. V. Chumak, A. A. Serga, B. Hillebrands, Nat. Commun. 5 (2014).
[11] V. V. Kruglyak, S. O. Demokritov, D. Grundler, J. Phys. D: Appl. Phys. 43 (2010) 260301.
[12] B. Lenk, H. Ulrichs, F. Garbs, M. Münzenberg, Phys. Rep. 507 (2011) 107.
[13] M. Krawczyk, D. Grundler, J. Phys. Condens. Matter 26 (2014) 123202.
[14] A. V. Chumak, V. I. Vasyuchka, A. A. Serga, B. Hillebrands, Nat. Phys. 11 (2015) 453.
[15] A. Manchon, H. C. Koo, J. Nitta, S. M. Frolov, R. A. Duine, Nat. Mater. 14 (2015) 871.
[16] A. Soumyanarayanan, N. Reyren, A. Fert, C. Panagopoulos, Nature 539 (2016) 509.
[17] R. P. Cowburn, J. Magn. Magn. Mater. 242–245 (2002) 505.
[18] G. Gubbiotti, G. Carlotti, T. Okuno, T. Shinjo, F. Nizzoli, R. Zivieri, Phys. Rev. B 68 (2003) 184409.
[19] L. J. Heyderman, H. H. Solak, C. David, D. Atkinson, R. P. Cowburn, F. Nolting, Appl. Phys. Lett. 85 (2004) 4989.
[20] V. Novosad, F. Y. Fradin, P. E. Roy, K. S. Buchanan, K. Y. Guslienko, S. D. Bader, Phys. Rev. B 72 (2005) 024455.
[21] S. Neusser, G. Duerr, H. G. Bauer, S. Tacchi, M. Madami, G. Woltersdorf, G. Gubbiotti, C. H. Back, D. Grundler, Phys. Rev. Lett. 105 (2010) 067208.
[22] S. Neusser, B. Botters, D. Grundler, Phys. Rev. B 78 (2008) 054406.
[23] S. Pal, J. W. Klos, K. Das, O. Hellwig, P. Gruszecki, M. Krawczyk, A. Barman, Appl. Phys. Lett. 105 (2014) 162408.
[24] S. Tacchi, B. Botters, M. Madami, J. W. Kłos, M. L. Sokolovskyy, M. Krawczyk, G. Gubbiotti, G. Carlotti, A. O. Adeyeye, S. Neusser, D. Grundler, Phys. Rev. B 86 (2012) 014417.
[25] G. Gubbiotti, S. Tacchi, G. Carlotti, N. Singh, S. Goolaup, A. O. Adeyeye, M. Kostylev, Appl. Phys. Lett. 90 (2007) 092503.
[26] S. Pal, S. Saha, M. V. Kamalakar, A. Barman, Nano Res. 9 (2016) 1426.
[27] J. Topp, D. Heitmann, D. Grundler, Phys. Rev. B 80 (2009) 174421.
[28] J. Ding, A. O. Adeyeye, Adv. Funct. Mater. 23 (2013) 1684.
[29] R. Mandal, P. Laha, K. Das, S. Saha, S. Barman, A. K. Raychaudhuri, A. Barman, Appl. Phys. Lett. 103 (2013) 262410.
[30] B. Rana, D. Kumar, S. Barman, S. Pal, Y. Fukuma, Y. Otani, A. Barman, ACS Nano 5 (2011) 9559.
[31] R. Mandal, S. Saha, D. Kumar, S. Barman, S. Pal, K. Das, A. K. Raychaudhuri, Y. Fukuma, Y. Otani, A. Barman, ACS Nano 6 (2012) 3397.
[32] S. Choudhury, S. Barman, Y. Otani, A. Barman, ACS Nano 11 (2017) 8814.
[33] V. S. Bhat, J. Sklenar, B. Farmer, J. Woods, J. T. Hastings, S. J. Lee, J. B. Ketterson, L. E. De Long, Phys. Rev. Lett. 111 (2013) 077201.
[34] J. O. Vasseur, L. Dobrzynski, B. Djafari-Rouhani, H. Puszkarski, Phys. Rev. B 54 (1996) 1043.
[35] S. Tacchi, G. Duerr, J. W. Klos, M. Madami, S. Neusser, G. Gubbiotti, G. Carlotti, M. Krawczyk, D. Grundler, Phys. Rev. Lett. 109 (2012) 137202.
[36] G. Gubbiotti, S. Tacchi, M. Madami, G. Carlotti, S. Jain, A. O. Adeyeye, M. P. Kostylev, Appl. Phys. Lett. 100 (2012) 162407.
[37] Z. K. Wang, V. L. Zhang, H. S. Lim, S. C. Ng, M. H. Kuok, S. Jain, A. O. Adeyeye, ACS Nano 4 (2010) 643.
[38] K. L. Livesey, J. Ding, N. R. Anderson, R. E. Camley, A. O. Adeyeye, M. P. Kostylev, S. Samarin, Phys. Rev. B 87 (2013) 064424.
[39] A. O. Adeyeye, S. Jain, Y. Ren, IEEE Trans. Magn. 47 (2011) 1639.

[40] G. Duerr, M. Madami, S. Neusser, S. Tacchi, G. Gubbiotti, G. Carlotti, D. Grundler, Appl. Phys. Lett. 99 (2011) 202502.
[41] S. Choudhury, S. Saha, R. Mandal, S. Barman, Y. Otani, A. Barman, ACS Appl. Mater. Interfaces 8 (2016) 18339.
[42] X. M. Liu, J. Ding, A. O. Adeyeye, Appl. Phys. Lett. 100 (2012) 242411.
[43] G. Duerr, S. Tacchi, G. Gubbiotti, D. Grundler, J. Phys. D: Appl. Phys. 47 (2014) 325001.
[44] M. Krawczyk, S. Mamica, M. Mruczkiewicz, J. W. Klos, S. Tacchi, M. Madami, G. Gubbiotti, G. Duerr, D. Grundler, J. Phys. D: Appl. Phys. 46 (2013) 495003.
[45] F. S. Ma, H. S. Lim, Z. K. Wang, S. N. Piramanayagam, S. C. Ng, M. H. Kuok, Appl. Phys. Lett. 98 (2011) 153107.
[46] H. Yu, G. Duerr, R. Huber, M. Bahr, T. Schwarze, F. Brandl, D. Grundler, Nat. Commun. 4 (2013) 2702.
[47] M. Donahue, D. G. Porter, *OOMMF User's guide, Version 1.0,* (NIST Interagency Report No. 6376; National Institute of Standard and Technology, Gaithersburg, MD, URL: http://math.nist.gov/oommf, 1999).
[48] P. Malagò, L. Giovannini, R. Zivieri, P. Gruszecki, M. Krawczyk, Phys. Rev. B 92 (2015) 064416.
[49] V. L. Zhang, H. S. Lim, C. S. Lin, Z. K. Wang, S. C. Ng, M. H. Kuok, S. Jain, A. O. Adeyeye, M. G. Cottam, Appl. Phys. Lett. 99 (2011) 143118.
[50] A. Barman, S. Barman, Phys. Rev. B 79 (2009) 144415.
[51] G. Malinowski, F. Dalla Longa, J. H. H. Rietjens, P. V. Paluskar, R. Huijink, H. J. M. Swagten, B. Koopmans, Nat. Phys. 4 (2008) 855.
[52] E. Beaurepaire, J. C. Merle, A. Daunois, J. Y. Bigot, Phys. Rev. Lett. 76 (1996) 4250.
[53] A. Laraoui, J. Vénuat, V. Halté, M. Albrecht, E. Beaurepaire, J.-Y. Bigot, J. Appl. Phys. 101 (2007) 09C105.
[54] D. Kumar, O. Dmytriiev, S. Ponraj, A. Barman, J. Phys. D: Appl. Phys. 45 (2012) 015001.
[55] LLG Micromagnetics Simulator, http://llgmicro.home.mindspring.com/ (2018).

Chapter 11

11. Electric Field Control of Spin Waves in Ultrathin CoFeB Films

Recently, investigation and control of propagating spin wave (SW) properties in ultrathin ferromagnetic films are achieving particular attention due to possible technological impact in future nanoscale magnonic devices. Control of SWs properties through voltage-controlled magnetic anisotropy (VCMA) may significantly reduce the power consumption of future magnonic devices. Here, we report an experimental study on manipulation of uniform ferromagnetic resonance (UFMR) and dipole-exchange spin waves by VCMA in ultrathin $Co_{20}Fe_{60}B_{20}$ (CoFeB) films with thicknesses 1.6, 1.8 and 2.0 nm. UFMR and SWs are excited by microwave antenna and detected by spin pumping and inverse spin Hall effect (ISHE) technique. UFMR study shows that interfacial perpendicular magnetic anisotropy (iPMA) and damping constant increases monotonically with the decrease of CoFeB thickness. A significant change in SW frequency by VCMA is observed, especially for 1.6-nm-thick CoFeB film, where the effective demagnetizing field is quite small due to the presence of strong iPMA. Moreover, we perform micromagnetic simulations to demonstrate that SWs in 1.6-nm-thick CoFeB film, with the in-plane easy axis of magnetization, can be guided through virtual nanochannels (NCs) formed by VCMA.

11.1. Introduction

Perturbations created in ordered magnetic materials can set off a wave which can travel through the magnetic material. These waves are known as spin waves (SWs), which are basically dynamic eigenmodes of magnetic materials [1-4]. The SWs, i.e. magnons (particle counterpart of SWs) have been the center of attention in research fields, known as magnonics [5,6] and magnon spintronics [7], magnetic analogue to photonics, at least for last two decades [5,8-12]. Microwave communications and digital operations can be performed by encoding data into the amplitude, phase and polarization of propagating SWs [13,14]. Various types of magnonic devices such as oscillators, filters, attenuators, switch, multiplexer, logic gates, transistors, converters have been proposed

in the literature by utilizing SWs. Although, SWs have much lower group velocity and propagation length as compared to light wave in optical fibers, the wide variety of SW frequency ranging from few gigahertz (GHz) to few terahertz (THz) and corresponding wavelength ranging from few tens of micrometer (μm) down to sub-nanometer makes them suitable for on-chip microwave applications and compatible with modern nanotechnology [15,16]. Moreover, SWs are almost free from Joule heating as they are not associated with any translation motion of charged particles such as electrons. However, SWs, i.e. magnons often interact with the free electrons of metallic ferromagnets (FMs), and lose their angular momentum shortly after excitation [4]. Alternatively, insulating ferrimagnets, such as yttrium iron garnet (YIG) [17,18] and ferromagnetic Heusler alloys [19,20] can be used to reduce energy losses due to magnon and free electron interaction.

Generally, a magnonic device consists of four basic components: SW waveguide (SWWG), microwave source for SW excitation, component for detection and components for SW manipulation, i.e. modulation, amplification, channelling in between excitation and detection points [6,13]. In spite of many methods available in the literature for the operation of magnonic devices, all-electrical methods are preferable due to the ease of integration with modern nanotechnology. A significant number of reports are found in the literature about charge current induced electrical methods for excitation [21-23], manipulation [24,25] and amplification [26-28] of SWs. It turns out that even though SWs are capable of carrying and processing information at the cost of low power consumptions, the charge current induced methods do not allow us to develop magnonic devices which can be operated at ultralow power. Therefore, a significant research is dedicated to find out materials with very high spin Hall angle, which can, in principle, provide an efficient way of current-induced operation of magnonic devices [29,30]. Some recent reports demonstrate that electric field modulation of interfacial perpendicular magnetic anisotropy (iPMA) can be an excellent alternative method for the development of ultralow power nanoscale magnonic devices [31-34]. Perpendicular magnetic anisotropy (PMA) is observed at the interfaces of 3*d* transition metal ferromagnets (e.g. Fe, CoFeB) and nonmagnetic insulators (e.g. MgO, Al_2O_3) due to the hybridization of out-of-plane 3*d* orbitals of ferromagnets (FM) and out-of-plane 2*p* orbital of Oxygen [35-38]. When an electric field is applied at the

FM/oxide interface, the number of electrons in out-of-plane 3*d*-orbitals of Fe is changed with respect to in-plane orbitals as shown from first principles calculations [39,40]. The relative change in electronic occupation state modifies the bonding strength of 3*d*-2*p* orbitals, which in fact modulates iPMA through spin-orbit coupling (SOC) of FM [38,39,41]. The VCMA has been used for changing FM phase [42], controlling the coercive field [43,44], magnetization switching [45,46] and controlling domain wall motion [47,48]. Nozaki *et al.* [31] and Zhu *et al.* [49] have shown that VCMA can efficiently excite uniform ferromagnetic resonance (UFMR) with ultralow power consumption. A number of reports have been published after these revealing that VCMA can be an excellent tool for excitation of linear [32] and nonlinear [50-52] SWs and nonlinear ferromagnetic resonance [52]. These reports discuss several advantages of VCMA excitation of SWs as compared to Oersted field excitation. After excitation, SWs need to be guided through a channel so the that they can reach to a target position on the SWWG. Rana *et al.* have proposed that SWs can be guided through reconfigurable nanochannels formed by VCMA [34]. Recently, the directional channelling of SWs has been proposed by controlling SW phase by VCMA [53]. It is also important to modulate SW frequency, wavevector, propagation length, group velocity, and dispersion character, i.e. magnonic band structures for the development of various magnonic devices, such as interferometer, logic gates, filters and attenuators. Development of various logic gates, switches, multiplexers by utilizing VCMA has already been proposed [34]. Wang *et al.* proposed reconfigurable magnonic crystals formed by VCMA [33], where magnonic band structure and band gaps can be tuned by controlling applied gate voltage. Nagaoka *et al*. have shown that the resonance field of propagating magnetostatic surface spin waves (MSSWs) in relatively thick FM film possessing iPMA can be modulated by VCMA without charge current [54]. As thicker FM film was used as SWWG, the change in resonance field was quite small. In that report, SWs were excited and detected by using microwave antenna through inductive coupling. Unfortunately, this detection method becomes very inefficient for ultrathin FM films due to the reduced volume of FM material. Very recently, it has been shown that spin pumping and ensuing inverse spin Hall effect (ISHE) could be an alternative method for electrical detection of SWs in ultrathin ferromagnetic films [55]. Although it is not a local detection technique,

nevertheless, this technique can be very powerful for studying resonance field and frequency of SWs.

In the present study, we excited UFMR and dipole-exchange SWs in ultrathin FM films by using microwave antenna (i.e. charge current induced Oersted field) and detected those by spin pumping and ISHE technique. We chose ultrathin $Co_{20}Fe_{60}B_{20}$ (CoFeB) films as our SWWG with three different thicknesses. It is observed that the iPMA of CoFeB films vary linearly as a function of gate voltage with a VCMA coefficient of about ~ 70 $fJ.V^{-1}.m^{-1}$. Although VCMA coefficients are almost same for all the CoFeB films, a significant change in SW frequency with gate voltage is found for thinner CoFeB film, where the demagnetizing field is almost compensated by iPMA, i.e. the effective value of magnetization is very small. Furthermore, we performed numerical micromagnetic simulations to demonstrate that an ultrathin FM film with the lower effective demagnetizing field is suitable for the formation of virtual nanochannel by VCMA through which SWs can be guided.

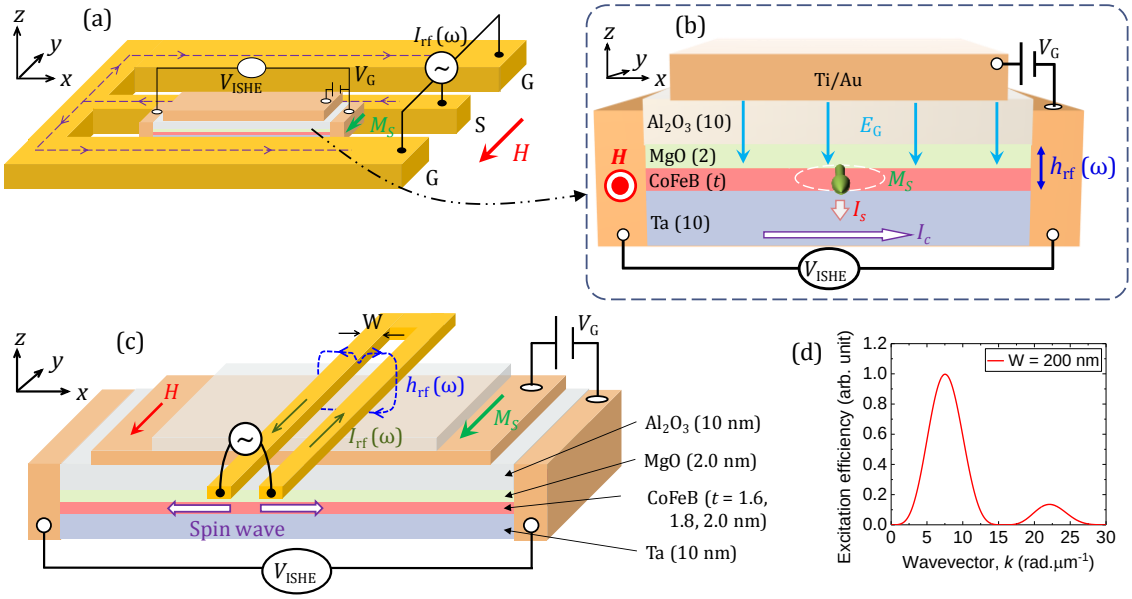

Figure 11.1. (a) Schematic illustration of a device and corresponding experimental set-up for uniform ferromagnetic resonance (UFMR) measurement. Radio frequency current (I_{rf}) is sent through a micrometer-sized antenna surrounding the rectangular shaped multilayer film. The I_{rf} induced Oersted field (h_{rf}) excites the UFMR in CoFeB layer at resonance condition given by Equation 11.2. (b) Schematic diagram shows the details of the device structure for UFMR study and the mechanism for inverse spin Hall effect (ISHE) detection of the resonance signal with the application of dc gate voltage (V_G). (c) Schematic diagram of an SWWG with a nanoscale microwave antenna on top of it. Radio frequency current (I_{rf}) is sent through a microwave antenna for excitation of

SWs in the SWWG. DC gate voltage (V_G) is applied across the top gate electrode and the CoFeB waveguide to tune SW frequency. (d) Calculated excitation efficiency of SWs as a function of SW wavevector (k) is shown.

11.2. Experimental Details

The samples for our study were fabricated by multistep fabrication method. The multilayer stacks consist of following layers: Si/SiO_2/Ta(10)/$Co_{20}Fe_{60}B_{20}$(t = 1.6, 1.8, 2.0)/MgO(2)/Al_2O_3(10), where the numbers in parentheses are the nominal thicknesses of corresponding layers in nanometers. Microwave antennae (nanoscale) for SW excitation were designed by electron beam lithography followed by deposition of Ti(5)/Au(120) layer by electron beam evaporation. The microwave antennae were designed with two parallel arms with width (W) of 200 nm and edge-to-edge separation of 200 nm. Here, all the contacts for application of dc gate voltage, measurement of ISHE signal, microwave antennae for excitation of UFMR and wider contacts of nanoscale antennae were made by photolithography and deposition of Ti(5)/Au(200) layer by electron beam evaporation.

At first, we study UFMR to characterize the iPMA, VCMA coefficient, damping parameters of CoFeB films used in this article. Figure 11.1(a) represents a schematic diagram of such a device used for UFMR measurement. A signal generator is used to send RF current (I_{rf}) through the micrometer-sized antenna surrounding the rectangular shaped (100 μm × 10 μm) magnetic structure. This RF current through the antenna generates a microwave magnetic field (h_{rf}) perpendicular to the film plane. The magnetizations of the FM films are set along the short axis of rectangular structures (along the y-axis) by applying bias magnetic field (H) from an electromagnet. For UFMR study, the H is swept from −175 mT to +175 mT at a step of 0.5 mT while keeping the frequency of RF signal as constant. When H hits resonance value, UFMR of CoFeB layer is excited, which pumps pure spin current (I_s) into the adjacent Ta layer (Figure 11.1(b)). The pure spin current is then converted into a transverse charge current (I_c) by ISHE of Ta and the corresponding signal is obtained by measuring potential drop (V_{ISHE}) across the Ta layer with the help of a nanovoltmeter. For studying propagating SWs, I_{rf} is sent through microwave antenna (Figure 11.1(c)), while the magnetization is set along the short axis (y-axis) of SWWG by applying a bias magnetic field H from an electromagnet. In this measurement, H is kept constant while, the frequency of

microwave signal is swept from 1 GHz to 10 GHz at a step of 20 MHz. The SW signals are obtained by measuring ISHE voltage (V_{ISHE}) across the SWWG as shown in Figure 11.1(c). To study electric field control of UFMR and SWs, dc gate voltage (V_G) is applied across the top metal gate electrode and CoFeB layer by using a dc power source.

11.3. Results and Discussion

11.3.1. Investigation of Uniform Ferromagnetic Resonance from CoFeB Films

Figure 11.2(a) shows an example of measured ISHE signal corresponding to the UFMR of a 1.6-nm-thick CoFeB film at an applied microwave frequency f = 4.0 GHz. The opposite sign of ISHE signal for opposite polarities of H confirms that the origin of the signal is spin pumping and ISHE [56]. To extract resonance field (H_0) and resonance line-width, the ISHE signals (V_{ISHE}) are fitted with a mathematical expression, where V_{ISHE} is written as a linear combination of symmetric and anti-symmetric Lorentzian functions given by [57,58]:

$$V_{ISHE} = C + \frac{V_s}{1+(H-H_0)^2/\sigma^2} + \frac{V_a(H-H_0)/\sigma}{1+(H-H_0)^2/\sigma^2} \quad (11.1)$$

Here, C is the dc background of ISHE signal, V_s & V_a are the weightages of symmetric and anti-symmetric Lorentzian functions, respectively and σ is the half width at half maximum (HWHM) of the resonance spectrum. The fitted curve is represented by a solid line in Figure 11.2(a). In Figure 11.2(b), the UFMR frequencies (f_{UFMR}) are plotted as a function of H for CoFeB films with three different thicknesses. The values of iPMA are extracted by fitting f_{UFMR} versus H data points with analytical Kittel formula given by [15,32]:

$$f_{UFMR} = \left(\frac{\mu_0\gamma}{2\pi}\right)\left[H\left(H + M_s - H_p(V_G)\right)\right]^{1/2} \quad (11.2)$$

where γ is the gyromagnetic ratio, H_p is the iPMA field, M_s is the saturation magnetization. We adapted γ = 29.4 GHz.T^{-1} and $\mu_0 M_s$ = 1.5 T from Refs. [32,34], while setting $\mu_0 H_p$ as a free parameter for fitting. The extracted values of $\mu_0 H_p$ are 1.463 T, 1.358 T and 1.144 T for CoFeB thickness t_{CoFeB} = 1.6, 1.8 and 2.0 nm, respectively, as plotted in Figure 11.2(c). The reduction of $\mu_0 H_p$ with an increment of t_{CoFeB} confirms the interfacial origin of PMA. As $\mu_0 M_s > \mu_0 H_p$ for all the CoFeB films, the easy axis of magnetization lies in the plane of the films. This is further confirmed from the anomalous Hall effect (AHE) measurement as shown in Figure 11.6.

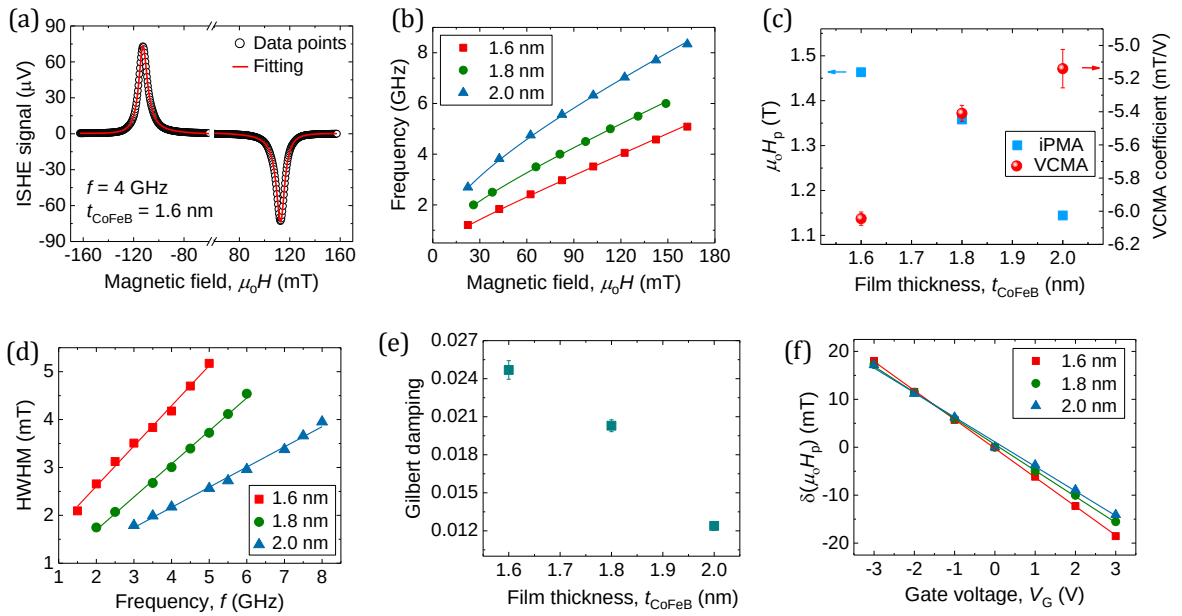

Figure 11.2. Measured ISHE signal corresponding to UFMR of a 1.6-nm-thick CoFeB film at 4.0 GHz microwave frequency is plotted as a function of bias magnetic field. (b) UFMR frequencies of three different CoFeB films are plotted as a function of bias magnetic field. Solid curves are the fits with Kittel formula described in Equation 11.2. (c) Extracted values of iPMA fields and VCMA coefficients are plotted as a function of inverse CoFeB film thickness. (d) Extracted values of HWHM are plotted as a function of frequency. Solid lines represent linear fits. (e) Extracted values of Gilbert damping parameters are plotted as a function of CoFeB thickness (t_{CoFeB}). (f) Change in the iPMA fields as a function of gate voltage is plotted for three different CoFeB thicknesses. Solid lines are the linear fits.

To evaluate Gilbert damping parameter (α), the HWHM of resonance curves are plotted as a function of f (Figure 11.2(d)) and fitted with a linear function. Values of α are extracted from the slopes (Δ) of the linear fits by using the following expression [58,59]:

$$\alpha = \frac{\gamma}{2\pi}\Delta \tag{11.3}$$

Figure 11.2(e) shows the plot of α as a function of t_{CoFeB}, which reflects that Gilbert damping parameter monotonically increases from 0.0124 to 0.0247 with the decrease of CoFeB thickness from 2.0 nm to 1.6 nm. The enhancement of damping for thinner films is due to increment of iPMA which has been reported previously [60-62].

To evaluate VCMA coefficients, i.e. change of iPMA per unit gate voltage (V_{G}), we measured UFMR signals of CoFeB films for different values of V_{G}. Here, positive gate voltage means the top gate electrode has positive potential with respect to CoFeB film. We fit resonance spectra with Equation 11.1 to find out resonance field for each value of V_{G} and then calculate the anisotropy field ($\mu_0 H_{\mathrm{p}}$) by using Equation 11.2. In Figure

11.2(f), the changes in $\mu_0 H_p$ as a function of V_G are plotted for different values of t_{CoFeB}. It is observed that the iPMA varies linearly with V_G and the slope of linear variation gives the value of the VCMA coefficient. The extracted values of VCMA coefficients are −6.04, −5.41 and −5.14 mT.V^{-1} for t_{CoFeB} = 1.6, 1.8 and 2.0 nm, respectively, as plotted in Figure 11.2(c). In another unit, the value of the VCMA coefficient becomes about −70 fJ.V^{-1}.m^{-1} for these three CoFeB films.

11.3.2. ISHE Detection of Spin Waves without Gate Voltage

Next, we study nanoscale microwave antennae induced propagating SW signals. We designed microwave antennae having two parallel arms with width (W) of 200 nm and edge-to-edge separation of 200 nm as schematically shown in Figure 11.1(c). The center-to-center separation (d) between the arms of the antennae is 400 nm. The Fourier transform of current distribution through the antenna gives the SW excitation efficiency for various values of SW wavevector k [22]. In Figure 11.1(d), the excitation efficiency of SWs by our antenna is plotted as a function of k, which shows that the antenna excites SWs with maximum efficiency at wavevector $k = 7.55$ rad.µm^{-1}, i.e. wavelength $\lambda = 832$ nm. Here, we neglect the second peak which appears at $k = 22$ rad.µm^{-1}, as the excitation efficiency for this wavevector is reduced to about 14% as compared to the primary wavevector. The position of the two peaks can be roughly estimated as $k = \pi/d$ and $3\pi/d$, where d is the center-to-center distance between the arms of the antenna. As the excited SWs are governed by dipole and exchange interactions in our present measurement conditions, the SWs can be called as dipole-exchange SWs. The frequency (f_{SW}) versus wavevector (k) dispersion of which can be expressed by an analytical formula given by [15,55]:

$$f_{SW} = \left(\frac{\mu_0\gamma}{2\pi}\right)\left[\begin{array}{c}\left(H + \frac{2A}{\mu_0 M_s}k^2\right)\left(H + \frac{2A}{\mu_0 M_s}k^2 + M_s - H_p(V_G)\right) \\ + \frac{1}{4}M_s\{M_s - H_p(V_G)\}(1 - e^{-2kt_{CoFeB}})\end{array}\right]^{1/2} \quad (11.4)$$

Here, A is exchange stiffness constant. In Figure 11.3(a), the calculated frequency (f_{SW}) versus wavevector (k) dispersion curves of dipole-exchange SWs at $\mu_0 H = 60$ mT are plotted for CoFeB films with three different thicknesses by adapting the parameters of γ, M_s, H_p extracted from UFMR measurement. Value of A is taken as 28 pJ.m^{-1} [34]. Dotted horizontal lines represent the frequencies of UFMR modes ($k = 0$), whereas the crossing points of the solid vertical line with the dispersion curves give the calculated

frequencies of SWs at $k = 7.55$ rad.μm^{-1}. The experimentally measured SW signals from three different SWWGs are plotted in Figure 11.3(b) (solid unfilled curves) along with the UFMR signals (filled curves). We then plot the frequencies of those UFMR modes and SWs in Figure 11.3(a). It can be seen that the measured frequency shifts of SWs from UFMR match quite well with the analytical calculation, whereas their absolute frequency values show a slight discrepancy with respect to the analytical values. The reason behind this discrepancy could be a small offset in the bias magnetic field value generated by the electromagnet and the difference between the real value of SW wavevector k excited by the antennae with the calculated value (in Figure 11.1(d). The real value of k may be different from the calculated one due to the slight deviation of antenna dimensions from its nominal value.

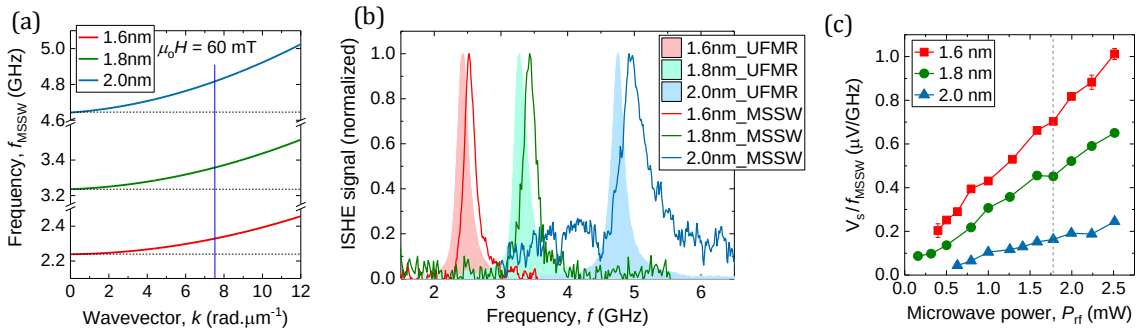

Figure 11.3. (a) Frequency versus wavevector dispersion curves of SWs are plotted at $\mu_0 H = 60$ mT for t_{CoFeB} = 1.6, 1.8 and 2.0 nm. Dotted horizontal lines represent frequencies of UFMR modes, i.e. k = 0 modes. Crossing points of the solid vertical line and dispersion curves give the numerical values of SW frequencies at $k = 7.55$ rad.μm^{-1}, excited by our microwave antenna. Measured frequencies of UFMR mode and SWs are also shown by filled and open symbols, respectively. (b) Experimentally measured ISHE signals, corresponding to SWs, are shown for three CoFeB films (solid unfilled curves). The UFMR signals are also demonstrated by filled curves. (c) Amplitudes of ISHE signals of SWs, normalized by corresponding resonance frequencies, are plotted as a function of applied microwave power (P_{rf}) to the antenna. The vertical dotted line represents the value of P_{rf} used for SW study.

In the present study, the group velocity (v_g) and decay length (L_d) of SWs cannot be directly measured from the experiment. However, they can be estimated theoretically. The SW group velocity v_g can be calculated by using the formula $v_g = 2\pi \cdot df/dk$, where df/dk is the slope of the dispersion curve. By calculating the slopes of the dispersion curves in Figure 11.3(a) at $k = 7.55$ rad.μm^{-1} the group velocities of SWs for CoFeB

films with t_{CoFeB} = 1.6, 1.8 and 2.0 nm are estimated as 142, 178, 240 m.s^{-1}, respectively. The SW decay length L_d can be expressed as: $L_d = v_g/\Gamma$, where Γ is the relaxation rate given by [55]:

$$\Gamma = 2\pi\alpha\gamma\mu_0\left[H + \frac{2A}{\mu_0 M_s}k^2 + \frac{1}{2}\left(M_s - H_p(V_G)\right)\right] \quad (11.5)$$

The calculated values of L_d for t_{CoFeB} = 1.6, 1.8 and 2.0 nm are 383, 355, 436 nm, respectively. This shows that SWs decay within a very short distance as compared to the excitation area, i.e. the lateral dimension of the antenna which is ~ 600 nm. The reasons behind this short decay length are the low value of v_g and the high value of L_d. The higher value of L_d is probably due to the presence of inhomogeneity in iPMA.

Next, we study the ISHE signal as a function of microwave power. In case of UFMR measurement, the measured ISHE signal can be written as: $V_{ISHE} \propto J_S \Theta_A R$, where J_S is the spin current density pumped into heavy metal (i.e. Ta in our case), Θ_A is the spin Hall angle of Ta and R is the resistance of rectangular stack structure, i.e. Ta/CoFeB/MgO/Al_2O_3. The spin current density can be expressed as: $J_S \propto f_{UFMR} \sin^2\theta$, where θ is the cone angle of magnetization precession [63]. We checked that the resistances (R) of rectangular stack structures, i.e. Ta/CoFeB/MgO/Al_2O_3 for devices with t_{CoFeB} = 1.6, 1.8 and 2.0 nm are almost same. The spin Hall angle Θ_A of Ta layer should also be same for all those devices as the films were deposited at the same time under same conditions. Therefore, the measured ISHE signal V_{ISHE} should be proportional to $f_{UFMR} \sin^2\theta$. In the limit of small cone angle of precession, i.e. in the linear regime of excitation, $\sin^2\theta$ can be approximated as θ^2, which is again proportional to UFMR intensity (I_{ISHE}). Ultimately, we obtain the relation $V_{ISHE} \propto f_{UFMR} I_{UFMR}$. Likewise, a similar relationship can be obtained for SWs in the linear regime of excitation given by: $V_{ISHE} \propto f_{SW} I_{SW}$. Here, I_{SW} is the average value of SW intensity. This shows that V_{ISHE}/f_{SW}, i.e. V_s/f_{SW} is directly proportional to SW intensity. Previous reports show that SW intensity I_{SW} is also proportional to microwave power P_{rf} in the linear regime of excitation [32], like UFMR [64]. Here, we measured SW signals (V_{ISHE}) as a function of P_{rf} from three CoFeB films with varying thickness. In Figure 11.3(c) we plot amplitudes of ISHE signals (V_s) corresponding to SWs, normalized by resonance frequency (f_{SW}), as a function of P_{rf}. The plot shows that the frequency normalized amplitudes of ISHE signals, i.e. V_s/f_{SW} increases linearly with the increase of P_{rf} at least up to 2.5 mW, i.e. ~ 4 dBm. This proves that the SWs are excited in the linear regime.

Vertical dotted line represents the power (1.58 mW, i.e. ~ 2 dBm) used for our SW measurements. Interestingly, the value of V_s/f_{SW} increases monotonically with the decrease of CoFeB thickness for the same magnitude of P_{rf}. It means the cone angle of magnetization precession, i.e. SW intensity for 1.6 nm-thick CoFeB film is maximum among all three CoFeB films due to very weak value of effective demagnetizing field, $\mu_0 H_d = \mu_0(M_s - H_p)$, as can be seen from the UFMR measurement.

11.3.3. Electric Field Control of Spin Wave Frequency and Spin Wave Channelling

Next, we have measured SW signals for different values of gate voltage (V_G) at a bias magnetic field value of 60 mT. Measured ISHE signals are plotted in Figure 11.4(a, c) and (d). For 1.6-nm-thick SWWG, signal to noise ratio is much better than 1.8 nm and 2.0 nm due to the higher value of SW intensity for the same value of excitation power as mentioned in the above section. Moreover, the change in the SW frequency with V_G for t_{CoFeB} = 1.6 nm SWWG is also much higher than other SWWGs. For instance, the SW frequency (f_{SW}) of t_{CoFeB} = 1.6 nm SWWG is 2.520 GHz at $V_G = 0$V, whereas, f_{SW} = 2.705 and 2.280 GHz at $V_G = \pm 3$V, respectively. So, the average change in f_{SW} is about 210 MHz at $|V_G| = 3$V, while full width at half maxima (FWHM) of resonance curve is about 200 MHz. In case of SWWGs with t_{CoFeB} = 1.8 and 2.0 nm, the changes in f_{SW} at $|V_G| = 3$V are about 120 and 75 MHz, whereas FWHM values are about 245 and 315 MHz, respectively. As the change in f_{SW} with V_G is higher than resonance linewidth for t_{CoFeB} = 1.6 nm SWWG, this SWWG can be used for the confinement of SWs inside the virtual nanochannels (NCs) formed by VCMA. We also measured f_{SW} as a function of bias magnetic field $\mu_0 H$ at $V_G = 0$V, ± 3V for SWWGs with t_{CoFeB} = 1.6, 1.8 and 2.0 nm which are shown for t_{CoFeB} = 1.6, 1.8 and 2.0 nm SWWG in Figure 11.4(d-f).

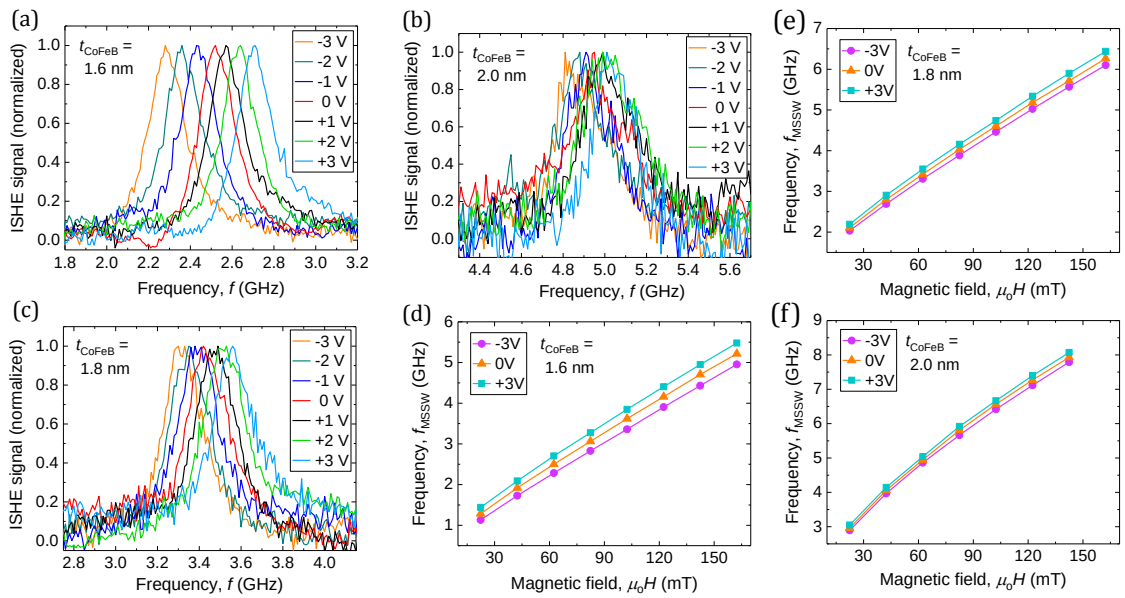

Figure 11.4. ISHE signals of SWs, measured at different values of gate voltage V_G, are plotted for SWWGs with t_{CoFeB} = (a) 1.6 nm, (c) 1.8 nm and (d) 2.0 nm. Measured SW frequencies from SWWG with t_{CoFeB} = (d) 1.6 nm, (e) 1.8 nm and (f) 2.0 nm are plotted as a function of bias magnetic field for three values of V_G.

Previously, we reported confinement of exchange-dominated magnetostatic forward volume waves (MSFVWs) in virtual NCs formed by VCMA [34]. In that report, the easy axis of magnetization was out-of-plane of CoFeB film due to strong iPMA (i.e. $\mu_0 H_p > \mu_0 M_s$). Here, we show that the dipole-exchange SWs with the in-plane orientation of static magnetization can also be guided through NCs formed by VCMA. To demonstrate this, we performed micromagnetic simulations by using Object Oriented Micromagnetic Frameworks (OOMMF) [65]. The details of the simulation procedure can be found in [34]. In this simulation, we choose an SWWG with dimension 2 μm (x) × 800 nm (y) × 1.6 nm (z). The iPMA field $\mu_0 H_p$ of the SWWG is taken as 1.463 T from UFMR measurement of t_{CoFeB} = 1.6 nm CoFeB film. We assume that an NC with dimension 2 μm (x) × 200 nm (y) is formed in the middle of the SWWG by applying $V_G = -3V$. In practice, this kind of NC can be formed by placing a metal gate electrode of dimension 2 μm (x) × 200 nm (y) on top of the oxide layer of SWWG and applying a voltage across gate electrode and CoFeB layer, as schematically shown in Figure 11.5(a). By adapting VCMA coefficient as −6.05 mT.V^{-1} from UFMR measurement, the iPMA field of the NC becomes 1.482 T, while iPMA field at the outside of NC remains as 1.463 T. All other parameters such as γ, M_s and A are adapted from UFMR measurement results. Here, we

demonstrate the confinement of dipole-exchange SWs at an in-plane bias magnetic field of $\mu_0 H = 160$ mT. The reason for choosing higher bias magnetic field is to make sure that the static magnetization becomes uniform even at the edges of SWWG so that relatively smaller components of dynamic magnetization due to the propagating SWs can be easily visualized under the background of uniform static magnetization. In Figure 11.5(b), the resonance spectra of experimentally measured SWs from 1.6 nm-CoFeB SWWG at $\mu_0 H$ = 160 mT are shown for three values of V_G. The resonance spectra show that the change in f_{SW} is about 265 MHz for $|V_G| = 3$V, whereas the average value of FWHM is about 300 MHz. This situation is almost similar to the situation at $\mu_0 H$ = 60 mT in terms of change in f_{SW} as compared to FWHM. In Figure 11.5(c), the analytical SW dispersion curves at $\mu_0 H$ = 160 mT are plotted by using Equation 11.4 for three different values of V_G. Analytical curves also show a frequency shift of about 245 MHz at $k = 7.55$ rad.μm^{-1} for $|V_G| = 3$V, which is very close to the experimentally observed frequency shift. In the simulation, SWs are excited by applying a sinusoidal magnetic field $h_z = A_0 \sin 2\pi f t$ of amplitude A_0 = 0.5 mT and frequency f = 5.04 GHz. The sinusoidal field is applied along the out-of-plane direction to the SWWG on 50 nm × 800 nm rectangular area at a distance of 50 nm from the left edge of the SWWG (Figure 11.5(d)). The frequency of the sinusoidal field is chosen from the crossing point of the vertical line at $k = 7.55$ rad.μm^{-1} and dispersion curve for $V_G = -3$V (see Figure 11.5(c)). According to the analytical curves, the SWs with f_{SW} = 5.04 GHz and $k = 7.55$ rad.μm^{-1}, i.e. $\lambda = 832$ nm can be excited only inside the NC, as SWs with this frequency is prohibited outside the NC. The spatial map of the out-of-plane component of dynamic magnetization, as plotted in Figure 11.5(d), shows that the excited SW with $\lambda = 820$ nm propagates only along the NC with width ≈ 200 nm, although sinusoidal magnetic field is applied all along the width of SWWG. The line scan of SW intensity along the width of SWWG at $x = 1$ μm is shown in the same figure. The Gaussian fit (solid curve) shows that the FWHM is about 122 nm and SW intensity is dropped by 77% (i.e. becomes 23%) at the edges of the NC with respect to the center of NC. This confirms that the SW is strictly confined inside the NC.

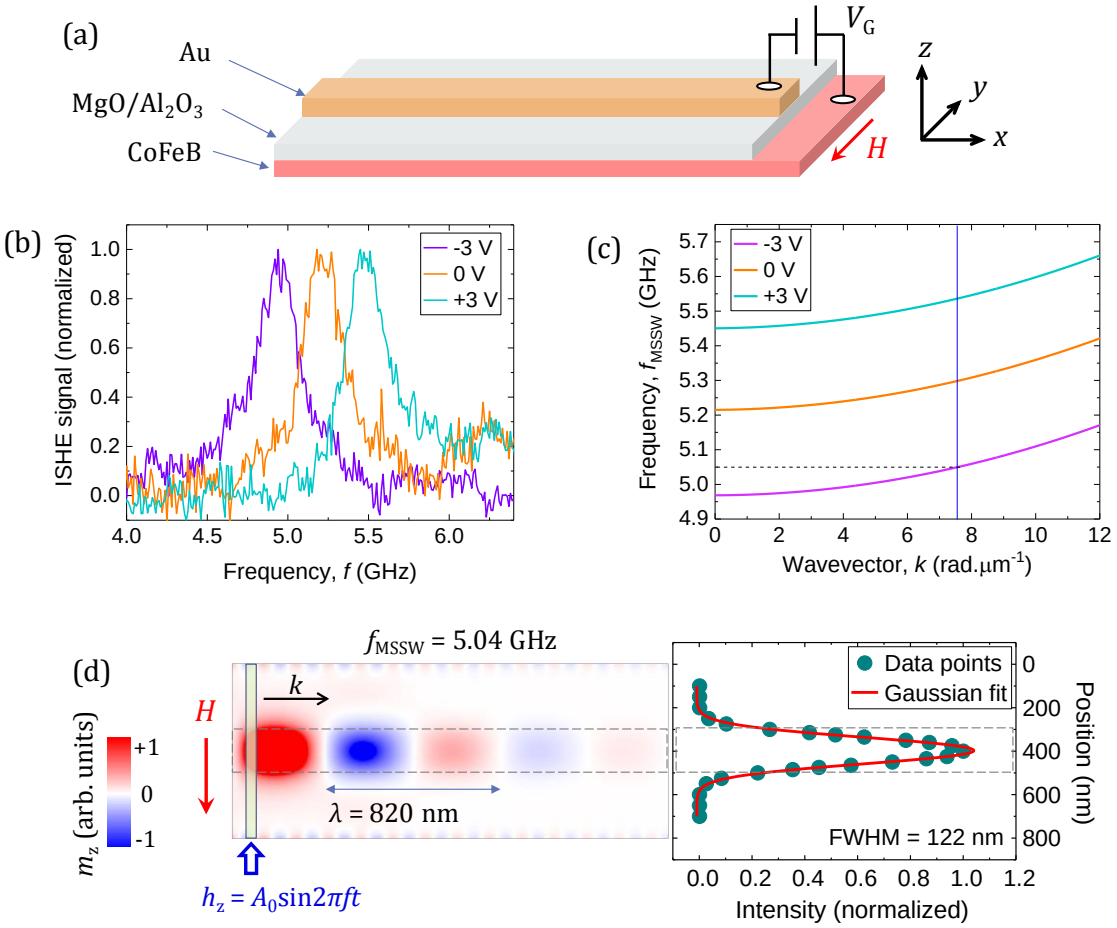

Figure 11.5. (a) Schematic illustration of a SWWG with a metal gate electrode on top of it. DC gate voltage V_G is applied across the gate electrode and SWWG to create a virtual channel for SW propagation. (b) Experimental resonance spectra of SWs, measured at bias field $\mu_0 H = 160$ mT for three values of V_G. (c) Analytical dispersion curves of dipole-exchange SWs at $\mu_0 H = 160$ mT for three values of V_G. Solid vertical line represents the wavevector of excited SWs by our nanoscale microwave antenna. Crossing points of vertical line with the analytical curves give the values of SW frequencies. (d) The left panel shows the spatial map of out-of-plane (z) component of dynamic magnetization correspond to SW with f_{SW} = 5.04 GHz and λ = 820 nm. The right panel shows the line scan (filled circles) of SW intensity along the width of SWWG at x = 1 μm. The solid curve represents the fitting with a Gaussian function.

Finally, we theoretically calculate the decay length (L_d) of SWs at $\mu_0 H = 160$ mT and compare it with the simulation result. From the slope of the theoretical dispersion curve in Figure 11.5(c), the group velocity (v_g) of SWs with $k = 7.55$ rad.μm^{-1} can be calculated as 132 m.s^{-1}. By using Equation 11.5 the SW decay length L_d, expressed by $L_d = v_g/\Gamma$, can be estimated as 168 nm. We also extracted L_d from the simulation result. The extracted values of L_d are 220 nm and 530 nm for damping constants = 0.0247 and 0.01, respectively. This clearly shows that the SWs with lower damping constant

propagates much longer distance than the SWs with higher damping constant. We have already mentioned that the reason for choosing lower damping constant is to allow SWs to propagate longer distance. Interestingly, the theoretical value of L_d is smaller than the simulation value. This is because, in theory, point-like emitters and receivers are assumed, whereas, in reality (in experiment and simulation) the emitters and receivers have a finite size [22]. Moreover, the inhomogeneous distribution of magnetization in the vicinity of the edges of SWWG may also change the SW decay length than the calculated value.

11.4. Conclusion

In summary, we have investigated electric field control of uniform ferromagnetic resonance (UFMR) and dipole-exchange SWs in three different thicknesses of CoFeB films, possessing interfacial perpendicular magnetic anisotropy (iPMA). SWs are excited electrically by using microwave antenna and detected by spin pumping and inverse spin Hall effect (ISHE) techniques. We have shown control of SW frequency by tuning iPMA of CoFeB SWWGs by applying gate voltage across the top gate electrode and SWWG. It is observed that SW frequency is significantly modified by voltage-controlled magnetic anisotropy (VCMA), especially, for 1.6 nm-thick CoFeB waveguide, where the effective demagnetizing field is significantly reduced by iPMA. By performing micromagnetic simulations we have demonstrated that an ultrathin ferromagnetic film with the lower value of effective demagnetizing field is suitable for the formation of virtual nanochannels (NCs) by VCMA through which dipole-exchange SWs can be guided, even though the VCMA coefficient is not very high. It is worth to mention here that SWs in relatively thicker films with higher value of effective demagnetizing field may also be guided through NCs by further increasing VCMA coefficient. Several reports show that it is possible to increase VCMA coefficient beyond −70 $fJ.V^{-1}.m^{-1}$ for FM/oxide heterostructures [66,67]. In this report, we have only investigated the control of SW frequency by VCMA. However, other properties of SWs such as group velocity, decay length, phase are also modulated by VCMA at the same time. Further studies are required to investigate the control of those properties of SWs.

11.5. Materials and Methods

11.5.1. Sample Preparation

The samples for our study were fabricated by multistep fabrication method. First of all, multilayer stacks were deposited on Si(001)/SiO_2(700 nm) substrates by radio frequency (RF) sputtering at room temperature at a base pressure of about 10^{-8} Torr. The multilayer stacks consist of following layers: Si/SiO_2/Ta(10)/$Co_{20}Fe_{60}B_{20}$(t = 1.6, 1.8, 2.0)/MgO(2)/Al_2O_3(10), where the numbers in parentheses are the nominal thicknesses of corresponding layers in nanometers. The sputter-deposited films were first annealed at 280°C in a vacuum under a perpendicular magnetic field of 600 mT for 1 hour. In the second step, rectangular structures (used as SWWG and for UFMR measurement) with lateral dimensions of 100 μm × 10 μm were prepared from the annealed multilayer stacks by using maskless UV photolithography followed by Ar^+ ion milling down to SiO_2. In the third step, the alignment markers for electron beam lithography and metal gate electrodes were prepared by maskless UV photolithography followed by deposition of Ti(5)/Au(100) layer by electron beam evaporation. In the fourth step, 200-nm-thick Al_2O_3 layer was deposited everywhere except on the long edges of rectangular structures (i.e. SWWG) and on the micrometer-sized rectangular areas on top of the metal gates. In the fifth step, microwave antennae (nanoscale) for SW excitation were designed by electron beam lithography followed by deposition of Ti(5)/Au(120) layer by electron beam evaporation. The microwave antennae were designed with two parallel arms with width (W) of 200 nm and edge-to-edge separation of 200 nm. In the last step, all the contacts for application of dc gate voltage, measurement of ISHE signal, microwave antennae for excitation of UFMR and wider contacts of nanoscale antennae were made by photolithography and deposition of Ti(5)/Au(200) layer by electron beam evaporation.

11.5.2. Measurement Technique

11.5.2.1. Anomalous Hall Effect (AHE) Measurement of CoFeB Films

We measured anomalous Hall effect (AHE) signals from CoFeB films with thicknesses 1.6, 1.8 and 2.0 nm. For this measurement CoFeB films were designed like Hall bar structures with dimensions 80 μm × 400 μm as shown in Figure 11.6(a). DC current (I_{dc}) of magnitude 0.5 mA is sent through the Hall bar from a current source and transverse Hall voltage (V_{AHE}) is measured by a nanovoltmeter, while sweeping out-of-plane

magnetic field (H_z) from −800 mT to +800 mT. Measured AHE signals as a function of H_z are plotted in Figure 11.6(b) for t_{CoFeB} = 1.6, 1.8 and 2.0 nm. Absence of hysteresis loop and gradual switching of magnetization confirm in-plane easy axis of magnetization.

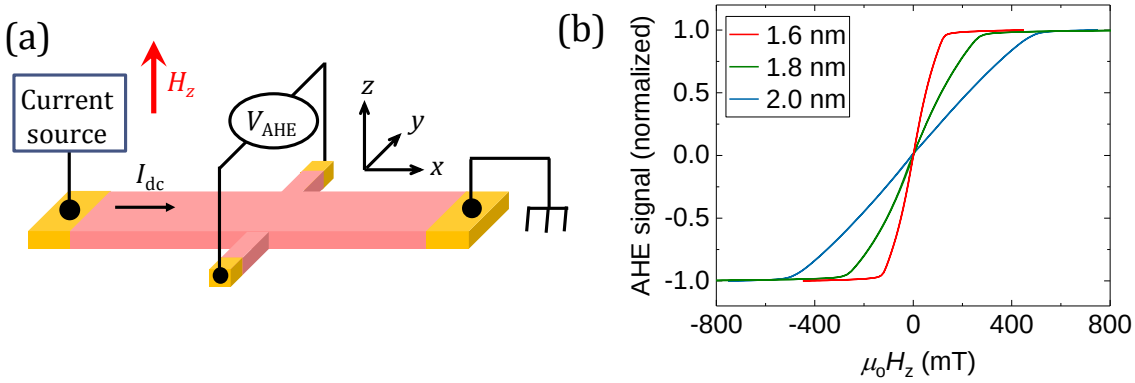

Figure 11.6. (a) Schematic diagram of device structure and experimental set-up for measuring anomalous Hall effect (AHE) of CoFeB films. (b) Measured AHE signals from CoFeB films of thickness t_{CoFeB} = 1.6, 1.8 and 2.0 nm.

11.5.3. Theoretical Calculation

For micromagnetic simulations, we choose 1.6 nm ultrathin CoFeB film with dimensions 2 μm (x) × 800 nm (y) × 1.6 nm (z). Material parameters used in the simulations are following: gyromagnetic ratio γ = 29.4 GHz.T^{-1}, exchange stiffness constant A = 28 pJ.m^{-1} [34,68,69]. Other parameters are taken from UFMR measurement of t_{CoFeB} = 1.6 nm film. To demonstrate SW confinement into NC, the Gilbert damping parameter α is chosen as 0.01 so that SWs can propagate longer distance before dying out. To prevent SW reflection from the edges of SWWG, very high value of Gilbert damping parameter (0.9) is put near the edges of the SWWG. To incorporate the role of exchange interaction, cell size is chosen as 5 × 5 × 1.6 nm^3, where the dimensions are smaller than the exchange length (~ 5.6 nm) of CoFeB as calculated by using the formula $l_{ex} = \sqrt{\frac{2A}{\mu_0 M_S^2}}$. At first, the ground states of magnetization are prepared by applying bias magnetic field (160 mT) along the short axis (y) of SWWG (Figure 11.5(a)). SWs are excited by applying a time varying sinusoidal magnetic field $h_z(t) = A_0 \, sin\, 2\pi ft$ on 50 × 800 nm^2 rectangular area (shown by shaded area in Figure 11.5(d), left panel) at 50-nm-distance from the left edge of the SWWG. Here, A_0 is the amplitude of sinusoidal field, f equals to the SW frequency, i.e. $f = f_{SW}$. We used A_0 = 0.5 mT and f_{SW} = 5.04 GHz.

References

[1] T. Moriya, *Spin fluctuations in itinerant electron magnetism* (Springer-Verlag Berlin Heidelberg, 1985).
[2] A. G. Gurevich, G. A. Melkov, *Magnetization Oscillations and Waves* (CRC Press, Boca Raton, Florida, 1996).
[3] D. D. Stancil, A. Prabhakar, *Spin waves: theory and applications* (Springer, New York, USA, 2008).
[4] A. Barman, J. Sinha, *Spin dynamics and damping in ferromagnetic thin films and nanostructures* (Springer, Cham, Switzerland, 2018).
[5] S. Neusser, D. Grundler, Adv. Mater. 21 (2009) 2927.
[6] V. V. Kruglyak, S. O. Demokritov, D. Grundler, J. Phys. D: Appl. Phys. 43 (2010) 260301.
[7] A. V. Chumak, V. I. Vasyuchka, A. A. Serga, B. Hillebrands, Nat. Phys. 11 (2015) 453.
[8] J. O. Vasseur, L. Dobrzynski, B. Djafari-Rouhani, H. Puszkarski, Phys. Rev. B 54 (1996) 1043.
[9] M. Krawczyk, H. Puszkarski, Acta Phys. Pol. Series A 93 (1998) 805.
[10] H. Al-Wahsh, A. Akjouj, B. Djafari-Rouhani, J. O. Vasseur, L. Dobrzynski, P. A. Deymier, Phys. Rev. B 59 (1999) 8709.
[11] Y. V. Gulyaev, S. A. Nikitov, L. V. Zhivotovskii, A. A. Klimov, P. Tailhades, L. Presmanes, C. Bonningue, C. S. Tsai, S. L. Vysotskii, Y. A. Filimonov, J. Exp. Theor. Phys. Lett. 77 (2003) 567.
[12] V. V. Kruglyak, R. J. Hicken, J. Magn. Magn. Mater. 306 (2006) 191.
[13] A. Khitun, M. Bao, K. L. Wang, J. Phys. D: Appl. Phys. 43 (2010) 264005.
[14] A. V. Chumak, A. A. Serga, B. Hillebrands, Nat. Commun. 5 (2014) 4700.
[15] G. Carlotti, G. Gubbiotti, Riv. Nuovo. Cimento. 22 (1999) 1.
[16] B. Lenk, H. Ulrichs, F. Garbs, M. Münzenberg, Phys. Rep. 507 (2011) 107.
[17] S. Maendl, I. Stasinopoulos, D. Grundler, Appl. Phys. Lett. 111 (2017) 012403.
[18] H. Yu, O. d'Allivy Kelly, V. Cros, R. Bernard, P. Bortolotti, A. Anane, F. Brandl, R. Huber, I. Stasinopoulos, D. Grundler, Sci. Rep. 4 (2014) 6848.
[19] T. Sebastian, Y. Ohdaira, T. Kubota, P. Pirro, T. Brächer, K. Vogt, A. A. Serga, H. Naganuma, M. Oogane, Y. Ando, B. Hillebrands, Appl. Phys. Lett. 100 (2012) 112402.
[20] C. Banerjee, L. M. Loong, S. Srivastava, S. Pal, X. Qiu, H. Yang, A. Barman, RSC Adv. 6 (2016) 77811.
[21] O. Rousseau, B. Rana, R. Anami, M. Yamada, K. Miura, S. Ogawa, Y. Otani, Sci. Rep. 5 (2015) 9873.
[22] V. Vlaminck, M. Bailleul, Phys. Rev. B 81 (2010) 014425.
[23] O. Rousseau, M. Yamada, K. Miura, S. Ogawa, Y. Otani, J. Appl. Phys. 115 (2014) 053914.
[24] V. Vlaminck, M. Bailleul, Science 322 (2008) 410.
[25] V. E. Demidov, S. Urazhdin, S. O. Demokritov, Appl. Phys. Lett. 95 (2009) 262509.
[26] O. Gladii, M. Collet, K. Garcia-Hernandez, C. Cheng, S. Xavier, P. Bortolotti, V. Cros, Y. Henry, J.-V. Kim, A. Anane, M. Bailleul, Appl. Phys. Lett. 108 (2016) 202407.
[27] R. Verba, M. Carpentieri, G. Finocchio, V. Tiberkevich, A. Slavin, Appl. Phys. Lett. 112 (2018) 042402.

[28] B. Divinskiy, V. E. Demidov, S. Urazhdin, R. Freeman, A. B. Rinkevich, S. O. Demokritov, Adv. Mater. 30 (2018) 1802837.
[29] S. Mondal, S. Choudhury, N. Jha, A. Ganguly, J. Sinha, A. Barman, Phys. Rev. B 96 (2017) 054414.
[30] D. Qu, T. Higo, T. Nishikawa, K. Matsumoto, K. Kondou, D. Nishio-Hamane, R. Ishii, P. K. Muduli, Y. Otani, S. Nakatsuji, Phys. Rev. Mater. 2 (2018) 102001.
[31] T. Nozaki, Y. Shiota, S. Miwa, S. Murakami, F. Bonell, S. Ishibashi, H. Kubota, K. Yakushiji, T. Saruya, A. Fukushima, S. Yuasa, T. Shinjo, Y. Suzuki, Nat. Phys. 8 (2012) 491.
[32] B. Rana, Y. Fukuma, K. Miura, H. Takahashi, Y. Otani, Appl. Phys. Lett. 111 (2017) 052404.
[33] Q. Wang, A. V. Chumak, L. Jin, H. Zhang, B. Hillebrands, Z. Zhong, Phys. Rev. B 95 (2017) 134433.
[34] B. Rana, Y. Otani, Phys. Rev. Applied 9 (2018) 014033.
[35] B. Dieny, M. Chshiev, Rev. Mod. Phys. 89 (2017) 025008.
[36] Z.-P. Li, S. Li, Y. Zheng, J. Fang, L. Chen, L. Hong, H. Wang, Appl. Phys. Lett. 109 (2016) 182403.
[37] S. Kanai, M. Tsujikawa, Y. Miura, M. Shirai, F. Matsukura, H. Ohno, Appl. Phys. Lett. 105 (2014) 222409.
[38] H. X. Yang, M. Chshiev, B. Dieny, J. H. Lee, A. Manchon, K. H. Shin, Phys. Rev. B 84 (2011) 054401.
[39] C. Duan, J. P. Velev, R. F. Sabirianov, Z. Zhu, J. Chu, S. S. Jaswal, E. Y. Tsymbal, Phys. Rev. Lett. 101 (2008) 137201.
[40] T. Kawabe, K. Yoshikawa, M. Tsujikawa, T. Tsukahara, K. Nawaoka, Y. Kotani, K. Toyoki, M. Goto, M. Suzuki, T. Nakamura, M. Shirai, Y. Suzuki, S. Miwa, Phys. Rev. B 96 (2017) 220412(R).
[41] M. Tsujikawa, T. Oda, Phys. Rev. Lett. 102 (2009) 247203.
[42] D. Chiba, S. Fukami, K. Shimamura, N. Ishiwata, K. Kobayashi, T. Ono, Nat. Mater. 10 (2011) 853.
[43] T. Seki, M. Kohda, J. Nitta, K. Takanashi, Appl. Phys. Lett. 98 (2011) 212505.
[44] T. Koyama, D. Chiba, Phys. Rev. B 96 (2017) 224409.
[45] W. Wang, M. Li, S. Hageman, C. L. Chien, Nat. Mater. 11 (2012) 64.
[46] S. Kanai, M. Yamanouchi, S. Ikeda, Y. Nakatani, F. Matsukura, H. Ohno, Appl. Phys. Lett. 101 (2012) 122403.
[47] U. Bauer, S. Emori, G. S. D. Beach, Appl. Phys. Lett. 101 (2012) 172403.
[48] A. J. Schellekens, A. van den Brink, J. H. Franken, H. J. M. Swagten, B. Koopmans, Nat. Commun. 3 (2012) 847.
[49] J. Zhu, J. A. Katine, G. E. Rowlands, Y. Chen, Z. Duan, J. G. Alzate, P. Upadhyaya, J. Langer, P. K. Amiri, K. L. Wang, I. N. Krivorotov, Phys. Rev. Lett. 108 (2012) 197203.
[50] R. Verba, V. Tiberkevich, I. Krivorotov, A. Slavin, Phys. Rev. Applied 1 (2014) 044006.
[51] Y.-J. Chen, H. K. Lee, R. Verba, J. A. Katine, I. Barsukov, V. Tiberkevich, J. Q. Xiao, A. N. Slavin, I. N. Krivorotov, Nano Lett. 17 (2017) 572.
[52] B. Rana, Y. Fukuma, K. Miura, H. Takahashi, Y. Otani, Sci. Rep. 7 (2017) 2318.
[53] M. Song, K.-W. Moon, C. Hwang, K.-J. Kim, Phys. Rev. Applied 11 (2019) 024027.
[54] K. Nawaoka, Y. Shiota, S. Miwa, H. Tomita, E. Tamura, N. Mizuochi, T. Shinjo, Y. Suzuki, J. Appl. Phys. 117 (2015) 17A905.
[55] T. Brächer, M. Fabre, T. Meyer, T. Fischer, S. Auffret, O. Boulle, U. Ebels, P. Pirro, G. Gaudin, Nano Lett. 17 (2017) 7234.

[56] L. Chen, M. Decker, M. Kronseder, R. Islinger, M. Gmitra, D. Schuh, D. Bougeard, J. Fabian, D. Weiss, C. H. Back, Nat. Commun. 7 (2016) 13802.
[57] L. Liu, T. Moriyama, D. C. Ralph, R. A. Buhrman, Phys. Rev. Lett. 106 (2011) 036601.
[58] K. Kondou, H. Sukegawa, S. Mitani, K. Tsukagoshi, S. Kasai, Appl. Phys. Express 5 (2012) 073002.
[59] S. Kasai, K. Kondou, H. Sukegawa, S. Mitani, K. Tsukagoshi, Y. Otani, Appl. Phys. Lett. 104 (2014) 092408.
[60] S. Pal, B. Rana, O. Hellwig, T. Thomson, A. Barman, Appl. Phys. Lett. 98 (2011) 082501.
[61] A. Okada, S. Kanai, M. Yamanouchi, S. Ikeda, F. Matsukura, H. Ohno, Appl. Phys. Lett. 105 (2014) 052415.
[62] S. Ikeda, K. Miura, H. Yamamoto, K. Mizunuma, H. D. Gan, M. Endo, S. Kanai, J. Hayakawa, F. Matsukura, H. Ohno, Nat. Mater. 9 (2010) 721.
[63] O. Mosendz, J. E. Pearson, F. Y. Fradin, G. E. W. Bauer, S. D. Bader, A. Hoffmann, Phys. Rev. Lett. 104 (2010) 046601.
[64] V. E. Demidov, M. P. Kostylev, K. Rott, P. Krzysteczko, G. Reiss, S. O. Demokritov, Phys. Rev. B 83 (2011) 054408.
[65] M. J. Donahue, D. G. Porter, *OOMMF User's Guide, Version 1.0, Interagency Report NISTIR 6376, National Institute of Standards and Technology, Gaithersburg, MD (Sept 1999), http://math.nist.gov/oommf/*, Interagency Report NISTIR 6376, National Institute of Standards and Technology, Gaithersburg, MD (Sept 1999), http://math.nist.gov/oommf/.
[66] S. Miwa, J. Fujimoto, P. Risius, K. Nawaoka, M. Goto, Y. Suzuki, Phys. Rev. X 7 (2017) 031018.
[67] A. Kozioł-Rachwał, T. Nozaki, K. Freindl, J. Korecki, S. Yuasa, Y. Suzuki, Sci. Rep. 7 (2017) 5993.
[68] C. Bilzer, T. Devolder, J.-V. Kim, G. Counil, C. Chappert, S. Cardoso, P. P. Freitas, J. Appl. Phys. 100 (2006) 053903.
[69] H. Ulrichs, B. Lenk, M. Münzenberg, Appl. Phys. Lett. 97 (2010) 092506.

Chapter 12

12. Electric Field Controlled Magnonic Crystal: Towards Reconfigurable Magnonics with Energy Efficiency

Artificially created magnetic metamaterials in the form of magnonic crystals (or MCs i.e. periodic composites with materials having contrasting magnetic parameters) have escalated a thrust to the spintronics, which aims to steer the process and flow of information by means of spin waves with minimum energy dissipation. Several external stimuli as well as physical or geometrical parameters have been employed to maneuver the magnonic band structure for the development of realistic devices integrable at nanoscale. However, electric field (voltage) control of magnetic anisotropy (ECMA or VCMA) has shown an auspicious route to design dynamic magnonic crystal by tailoring perpendicular magnetic anisotropy (PMA) at ultrathin ferromagnetic/oxide interface in a periodic manner. Here, we probe the spinwave (SW) dispersion from thermally excited magnons with the aid of Brillouin light scattering (BLS) spectroscopy in a 1D dynamic magnonic crystal by applying a periodic electric field through a 1D stripe-like array of metallic electrodes placed on top of a CoFeB/MgO heterostructure to modulate the PMA at CoFeB/MgO interface. Here, a magnonic band structure consisting of two SW frequency modes is achieved revealing a bandgap in the dispersion curve under the influence of the applied voltage. This bandgap gets disappeared with the withdrawal of the electric field indicating towards a dynamic electric field-controlled magnonic crystal (EFCMC). This unlocks a new paradigm to reconfigurable magnonics with ultralow power consumption which is prerequisite for spintronics applications.

12.1. Introduction

The massive upsurge in the communication technology in terms of device miniaturization and operational speed has forced the modern charge-based electronics towards the fundamental quantum limit [1] because of inherent Joule heating and its ensuing power dissipation. A ceaseless quest over the last few decades has made it possible to find a suitable alternative in the form of a chargeless information carrier by

using spin angular momentum instead of the charge degree of freedom of the electrons. Here, this spin degrees of freedom can be maneuvered in the form of spin current [2] or spin waves (SWs: collective precessional motion of electron spins) which can be integrated in the next generation spin-based applications with efficient energy consumption. SW possesses wavelength several orders of magnitude shorter than that of electromagnetic (EM) wave at same frequency which makes the SW ideal for signal processing or transfer devices that can be scaled down to hundreds of nanometer (nm) as they can have wide variety of wavelengths ranging from few tens of micrometer (μm) down to few tens of nm (i.e. the corresponding frequency spans over few Gigahertz (GHz) to few Terahertz (THz)). Blending the magnon (i.e. quanta of SW) and spintronics (i.e. spin-based electronics) [3] in the form of magnon-spintronics [4], one can control and manipulate SW properties by playing with the various internal and external parameters which are crucial in future communication and storage applications. Emerged as the building blocks of magnonics [5], magnonic crystal (MC) has been developed which can be treated as the magnetic analogue of photonic or phononic crystal. Numerous theoretical and experimental investigation have been conducted in these MCs with periodic distribution of various materials with diverse material parameters, e.g. saturation magnetization, magnetic anisotropy or other external controllers like magnetic field, mechanical force (stress) or charge current to provoke the modulation in the magnonic band structures as well as SW propagation. However, the properties of most of the MCs are defined by their physical parameters (i.e. dimensions), which remains invariant once the fabrication procedure is completed. The recent advances demand the necessity of dynamic MCs where the periodic modulation of magnetic properties can be dynamically switched on and off by external factors like magnetic [6] or electric field [7] etc. This opens up new possibilities for reconfigurable magnonics [8] leading towards the realization of reprogrammable logic or GHz frequency communication devices (e.g. filter, switch etc.) which can bridge between interdisciplinary fields such as photo-magnonics [9], mag-phonics [10] or spin-mechatronics [11]. Most of the recent approaches in this regard are based upon current induced methods which is critical for low-energy dissipation of magnetization in nanoscale magnetic elements because of the thermal stability issue. To overcome this obstacle, magneto-electric coupling [12] can become an efficient approach to tailor the

magnetic properties (e.g. magnetic anisotropy) using electric field that has superior benefit of ultralow energy (power) consumption [13] because of the absence of ohmic dissipation which is an inherent backlash in charge current-controlled magnonic devices [14].

Numerous theoretical and experimental investigation have demonstrated the electric field-induced control of magnetization in magnetic heterostructures including multiferroic materials [15], ferromagnetic (FM) semiconductors [16], piezoelectric materials [17] or magneto-electric interfaces [18]. Magneto-electric interfaces have gained a significant attention due to their better control over magnetic parameters (i.e. anisotropy) at ambient condition as compared to other systems. The controlled manipulation of interfacial perpendicular magnetic anisotropy (iPMA) at the FM/insulator (oxide) interfaces [19] have accelerated the possibilities of integrating reprogrammable devices with the future spin-based applications.

Consequently, the investigation of electric field (voltage)-controlled magnetic anisotropy (ECMA or VCMA) at the interfaces has received a great thrust in the recent times using both theoretical [20] and experimental approaches [21]. Numerous strategies have been adopted for excitation, manipulation, channelling and amplification of SWs as well as development of MCs and logic gates [22]. Several studies have emphasized on the operation of various functions [23] of magnonic devices [24] using electric field (voltage) in particular, through the modulation of PMA present at the interfaces of an FM metal and oxide heterostructure [25] complying with ultralow power dissipation. Notably, SWs can be confined within nanochannels (NCs) generated by ECMA in an ultrathin FM waveguide where the width of the NC is solely determined by the width of the electrode [26]. This have triggered the quest for achieving a novel genre of electric field-controlled MCs (EFCMCs) in recent times. To the best of our knowledge, experimental realization of a dynamic MC reprogrammable by electric field has not been explored so far. However, there are few attempts to demonstrate such novel system using theoretical approach [7] which revealed immense possibilities of achieving reconfigurable magnonic band structure.

Here, we have taken this challenge to fabricate an electric field controlled dynamic MC by using state-of-the art nanofabrication and deposition tools. We have performed Brillouin light scattering (BLS) measurements [27] to demonstrate the emergence of

band diagram of a 1D EFCMC consisting of an FM/oxide heterostructure. BLS has emerged as one of the most reliable tools to probe the dispersive nature of SW frequencies directly in the wavevector (k) domain. Unlike any other complementary method where external stimuli such as electrical current, temperature gradient or optical pumping (such as laser) is necessary to excite the SWs, BLS proves to be very effective as it detects thermally excited magnons under ambient condition (i.e. room temperature). Here, we have reliably probed the magnonic band structure in FM/oxide heterostructure consisting 1D array of stripe-like electrodes serving as the top electrodes under the influence of an electric field (DC voltage) applied between the top (patterned) and bottom (unpatterned) electrodes. We have achieved a tunable band structure in the presence of moderate electric field in the system which vanishes when the electric field is removed. This remarkable observation is reconfirmed by measuring a similar heterostructure but with unpatterned electrode both at its top and bottom surfaces which unveils the absence of any magnon band structure with or without the electric field but only a modulation of SW frequency with the applied voltage. This salient observation is well supported by numerical calculations using plane wave method (PWM), which reproduced the SW dispersion behaviour modified by the electric field. This confirms that a external electric field effectively tailors the iPMA present at the FM/oxide heterostructure eventually generating such dynamic MC with the emergence of magnon band structure and opening up of a magnonic band gap.

12.2. Experimental Details

We have chosen the heterostructure: substrate|Ta(10 nm)|$Co_{20}Fe_{60}B_{20}$(1.6 nm)|MgO(2 nm)|Al_2O_3(10 nm) as the basis for the fabrication of nanostructure. It is noteworthy that, the magnetization state in an ultrathin CoFeB film strongly depends on its thickness. Here the magnetization direction tends to align along the out-of-plane (OOP) axis above a critical value of the thickness (typically ranges between 0.5 – 1.3 nm) [28]. On the contrary, the magnetization tends to be aligned along the in-plane (IP) direction above the critical thickness. In our case, the $Co_{20}Fe_{60}B_{20}$ (CoFeB) has a thickness of 1.6 nm which denotes that the magnetization lies IP of the sample. This is further confirmed from anomalous Hall effect (AHE) measured from the CoFeB/MgO heterostructure following the experimental scheme described in Figure 12.1(a). For this purpose, CoFeB/MgO film was designed like Hall bar structures with dimensions 80 μm × 400

μm. DC current (I_{DC}) of magnitude 0.5 mA is sent through the Hall bar from a current source and transverse Hall voltage (V_{AHE}) is measured by a nanovoltmeter, while sweeping an OOP magnetic field (H_z) from – 500 mT to + 500 mT as plotted in Figure 12.1(b). Here, the absence of hysteresis loop and gradual switching of magnetization confirm an IP easy axis of magnetization.

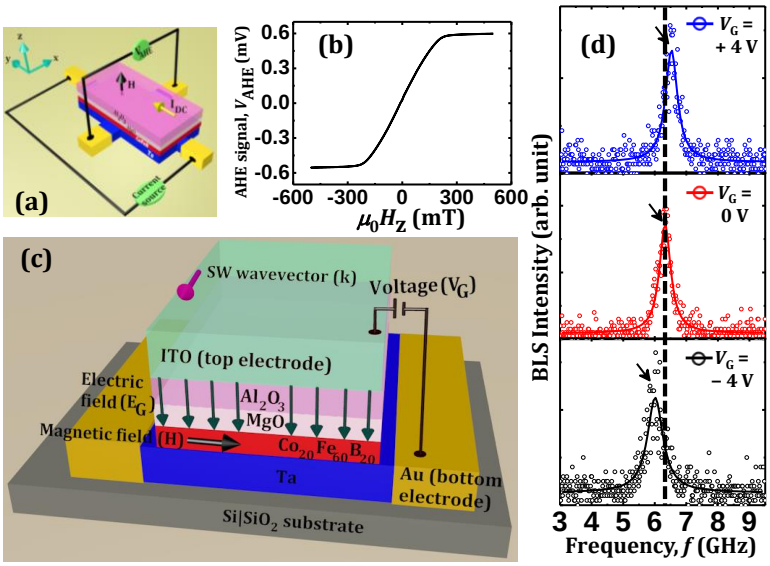

Figure 12.1. (a) Schematic diagram of device structure and experimental set-up for measuring anomalous Hall effect (AHE) and (b) the corresponding measured AHE signal from the CoFeB/MgO heterostructure with CoFeB thickness (t_{CoFeB}) of 1.6 nm. (c) Pictorial description of the CoFeB/MgO sample with a blanket ITO layer as the top electrode. (d) The Stokes side of BLS spectra taken at in-plane transferred wave vector, k = 2.05 × 10^6 rad/m for applied gate voltage, V_G = + 4 V, 0 V and – 4 V, respectively in the presence of the bias magnetic field, $\mu_0 H$ = 200 mT. The symbols represent the experimental data while, the solid curves denote fit using the Lorentzian function.

12.2.1. The Principle behind the Electric Field Modulation of Interfacial Perpendicular Magnetic Anisotropy in FM/Oxide Heterostructure

Generally, strong PMA can be observed at the interfaces between 3*d* transition metal (or their alloys) FMs and heavy nonmagnetic (NM) metals although, interfacial PMA (iPMA) cannot be modulated by electric field in such systems because of the absence of insulating or dielectric layer at the interface. However, PMA can also be obtained at the FM/oxide interfaces. Among them, the CoFeB/MgO heterostructures [28] have drawn an immense attention because of their application potentials in spintronics [29]. The reason for iPMA and VCMA at CoFeB/MgO interface can be interpreted by the following

approach. At CoFeB/MgO interface, the OOP $3d_z^2$-orbitals of Fe strongly bond with OOP $2p_z$-orbitals of O resulting in a significant charge transfer from $3d_z^2$-orbitals to $2p_z$-orbitals. Therefore, the number of electrons in OOP orbitals is reduced as compared to the number of electrons in IP orbitals, which in fact introduces a considerable PMA through the spin-orbit coupling (SOC) of FM [30]. When an electric field is applied across the FM/oxide interface, the number of electrons in the OOP $3d$-orbitals of Fe gets modified with respect to the IP orbitals as explained from first principles calculations [31]. This affects the bonding strength between $3d$- and $2p$-orbitals resulting in a substantial change of iPMA. Although, electric field control of electronic occupation state is believed to be the main mechanism behind VCMA, several alternative theories are also found in the literature. One of the interesting theories claims the control of iPMA due to the coupling between magnetic dipoles and electric quadrupole of electronic orbital in FM which is formed due to the inhomogeneous electric field at the FM/oxide interface [32]. Another theory explains that the applied electric field at FM/oxide interface modifies the Rashba SOC which in turn modulates the iPMA [33]. Recently, the piezoelectric property of oxide (MgO) layer through magneto-elastic coupling is found to be responsible for the modulation of iPMA via development of tensile and compressive strain in the oxide layer [34]. In reality, all the above mechanisms may be present and contribute simultaneously to the modulation of iPMA. Nevertheless, we can claim that the presence of an oxide layer is essential for modulation of PMA where the relative change in the electronic occupation state in the $3d$-orbitals of FM plays a crucial role for achieving VCMA. Also, since the penetration depth of electric field in a metal is only few ångström (Å), thereby the VCMA effect is only limited to ultrathin FM films. This justifies the choice of the thickness of CoFeB layer in our case.

Theoretical calculations reveal that the change in the number of electrons in $3d$-orbitals of FM is scales linearly with the applied electric field (E) at FM/oxide interface [31]. Consequently, the change in the magnetic moment and iPMA should also be linearly proportional to electric field [18], i.e.

$$\Delta K_s = \beta E \tag{12.1}$$

Here, ΔK_s is the change in iPMA while, β is defined as the magneto-electric or VCMA coefficient. The magnitude and polarity of β depends upon several factors such as

composition of FM [35] or adjacent dielectric layer [36], underlayer material (i.e. layer beneath the FM/oxide heterostructure) [37], substrate [38] as well as temperature [39].

12.3. Results and Discussion

12.3.1. Investigation of Spinwave Dispersion by Probing Thermally Excited Magnons

Figure 12.1(c) depicts the schematic illustration of the geometrical configuration adapted for the experimental investigation. Here, an unpatterned indium tin oxide (ITO) layer of thickness 120 nm has been deposited on top of the substrate|Ta(10)|$Co_{20}Fe_{60}B_{20}$(1.6)|MgO(2)|Al_2O_3(10) heterostructure. This ITO layer serves as the top gate electrode to apply the electric field (E or voltage: V_G) across the $Co_{20}Fe_{60}B_{20}$(1.6 nm)|MgO(2 nm) interface. Notably, a positive gate voltage denotes that the top gate electrode has positive potential with respect to CoFeB film. All the measurements have been carried out in Damon-Eshbach framework, i.e. the (in-plane) wavevector (k) of the SW lies perpendicular to the magnetic field (H) applied in the plane of the sample. In Figure 12.1(d), we have demonstrated the typical BLS spectra measured at wavevector, $k \approx 2.05 \times 10^6$ rad/m from a $Co_{20}Fe_{60}B_{20}$/MgO (i.e. CoFeB/MgO) heterostructure subjected to an in-plane magnetic field, $\mu_0 H$ = 200 mT for V_G = 0, ± 4 V, respectively. The BLS spectra are well fitted using the Lorentzian function to extract the frequency value (f). It is evident from Figure 12.1(d) that, the SW frequency increases or decreases monotonically as a function of V_G depending upon the polarity of the electric field. To extract the magnetic parameter especially the modulation in the iPMA field, we have performed the magnetic field ($\mu_0 H$) dependence of the SW frequency (f) which is represented in Figure 12.2(a) for V_G = 0, ± 4 V, respectively. The value of iPMA fields has been extracted by fitting f versus $\mu_0 H$ data points with the analytical formula expressed as:

$$f = \frac{\mu_0 \gamma}{2\pi}\left[\left(H + \frac{2A}{\mu_0 M_s}k^2\right)\left(H + \frac{2A}{\mu_0 M_s}k^2 + M_s - H_p(V_G)\right) + \frac{1}{4}M_s\left(M_s - H_p(V_G)\right)\left(1 - e^{-2kt_{CoFeB}}\right)\right]^{\frac{1}{2}} \quad (12.2)$$

Here, γ, $H_p(V_G)$, M_s, A represent the gyromagnetic ratio, iPMA field (which depends on the applied voltage, V_G or electric field, E), saturation magnetization and exchange

stiffness constant, respectively. Here, t_{CoFeB} denote the thickness of CoFeB layer, which is 1.6 nm in our case. Here, we have fixed the material parameters, i.e. γ = 29.4 GHz.T^{-1}, $\mu_0 M_s$ = 1.5 T and A = 28 pJ.m^{-1} [26] while, $H_p(V_G)$ has been set as a free parameter during fitting of the field dependent curves. The extracted values of $\mu_0 H_p$ are found to be 1.45, 1.43 and 1.47 T in case of V_G = 0, + 4 and – 4 V, respectively. As $\mu_0 M_s > \mu_0 H_p(V_G)$, the easy axis of magnetization always lies in the plane of the sample.

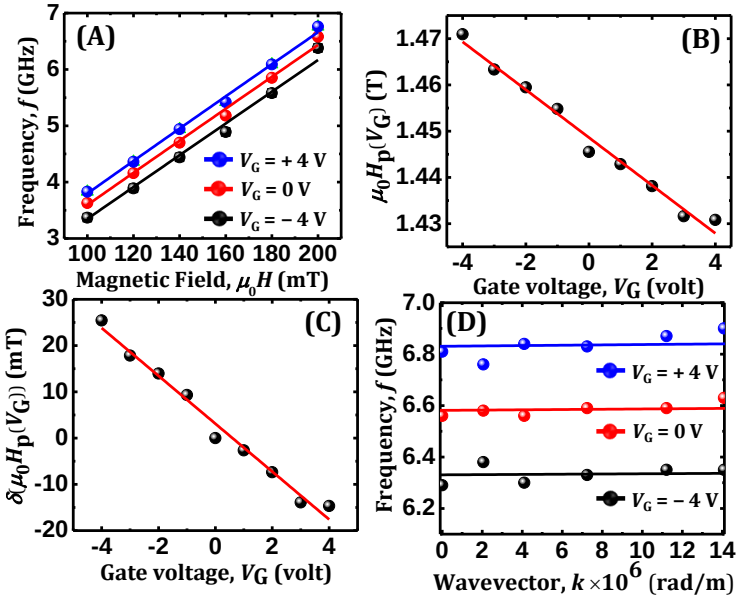

Figure 12.2. (a) Variation of SW frequency as a function of bias magnetic field ($\mu_0 H$) obtained from CoFeB/MgO heterostructure with a blanket ITO top electrode for three values of gate voltage, V_G = 0, ± 4 V, respectively. The symbols represent experimental data while, the solid lines denote fitted curves using Equation 12.2. (b) Variation of iPMA field ($\mu_0 H_p$) as a function of gate voltage (V_G) in the presence of the bias magnetic field, $\mu_0 H$ = 200 mT where the solid lines represent the linear fit. (c) Change in the iPMA field ($\mu_0 H_p$) as a function of V_G where the solid lines describe the linear fit. (d) Frequency (f) versus wavevector (k) dispersion curves for V_G = 0, ± 4 V, respectively. Symbols show the experimental data points, while the solid curves describe the fit to the data points using Equation 12.2.

In addition, we have extracted the anisotropy field ($\mu_0 H_p(V_G)$) using Equation 12.2 for each value of V_G which is shown in Figure 12.2(b). Now, to evaluate VCMA coefficient (β), i.e. the change of iPMA per unit gate voltage (V_G), the modulation of $\mu_0 H_p(V_G)$, i.e. $\delta(\mu_0 H_p(V_G))$ as a function of V_G has been plotted in Figure 12.2(c). It is observed that the iPMA varies linearly with V_G and the slope of linear variation yields the value of VCMA coefficient which is calculated to be 5.17 mT.V^{-1} in our CoFeB/MgO system. However,

the conversion of VCMA coefficient from mT/V to other unit, i.e. fJ.V^{-1}.m^{-1} for 1.6 nm-thick CoFeB (t_{CoFeB}) can be expressed using Equation 12.1 as the following:

$$\beta = \frac{d(\Delta K_S)}{dE} = \frac{1}{2}.\left(\frac{\delta(\mu_0 H_p)}{\delta V_G}\right).\frac{\mu_0 M_S}{\mu_0}.t_{CoFeB}.t_{(MgO+Al_2O_3)} \quad (12.3)$$

The electric field (E) corresponding to V_G = 1 V is given by:

$$E = \frac{1}{t_{(MgO+Al_2O_3)}} \quad (12.4)$$

while $t_{(MgO+Al_2O_3)}$ being the total thickness (12 nm) of MgO and Al_2O_3 layer on top of CoFeB. Hence, the value of VCMA coefficient (β) becomes ~ 60 fJ.V^{-1}.m^{-1}. Figure 12.2(d) describes the SW dispersion (i.e. f versus k) relation measured at an applied in-plane field, $\mu_0 H$ = 200 mT for V_G = 0 and ± 4 V, respectively, where k has been varied by changing the angle of incidence (θ) of the laser beam. It is noteworthy that, flat dispersive behaviour is observed in SW frequency as a function of k acquired at all three different electric fields (E). This is confirmed by fitting the dispersion curves with the aid of Equation 12.2 as represented in Figure 12.2(d), where the extracted values of $\mu_0 H_p(V_G)$ agree well with those calculated earlier from the magnetic field-dependent SW frequency curves in Figure 12.2(a).

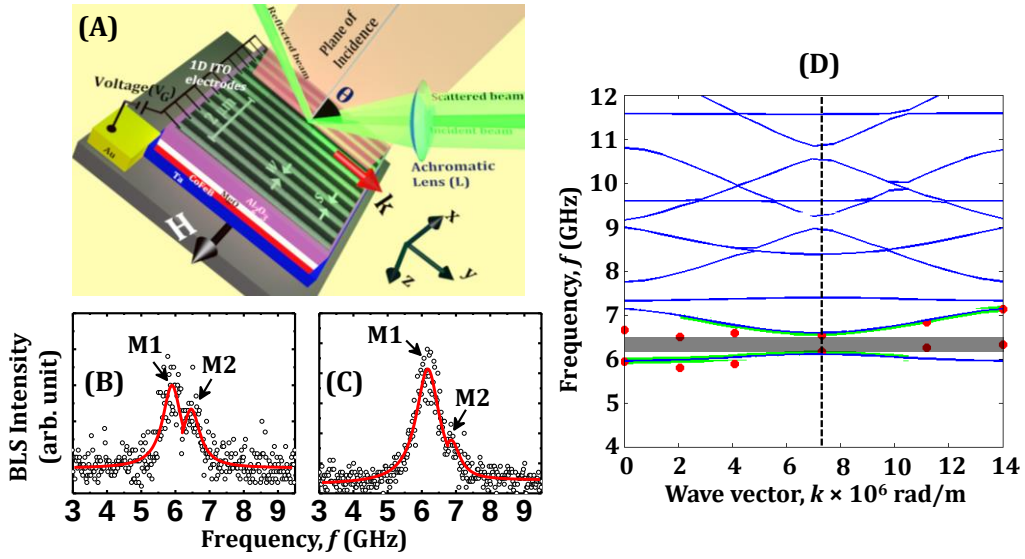

Figure 12.3. (a) Schematic of the BLS measurement geometry used for the CoFeB/MgO heterostructure with 1D patterned ITO electrodes on top showing the incident (θ denotes the angle of incidence) and scattered light beams and the direction of the magnon wave vector (k) and applied magnetic field H with both vectors lying in the sample plane. The anti-Stokes side of BLS spectra taken at k = (b) 2.05 × 10^6 rad/m and (c) 7.1 × 10^6 rad/m, respectively obtained for V_G = – 4V applied at $\mu_0 H$ = 200 mT. The

SW peaks (M1 and M2) are indicated by the arrows. (d) Magnonic band structure under the influence of V_G = − 4V applied at $\mu_0 H$ = 200 mT. Red solid circles represent peaks in the BLS spectra. Thin blue lines denote plane wave method (PWM) results, while the bold green lines emphasize intense excitations as predicted by PWM. The dashed vertical line describes the boundary of first Brillouin zone (BZ) and the bandgap is shown by the shaded region.

12.3.2. Investigation of Magnon Dispersion in 1D EFCMC

We investigated the SW dispersion in CoFeB/MgO heterostructure where the top ITO layer (120 nm) has been patterned in the form of a 1D array of stripes with width (w) 220 nm which are separated (s) by 220 nm. This is designated as 1D electric field-controlled MC (EFCMC) as schematically depicted in Figure 12.3(a) along with the experimental configuration. Here, these 1D stripes act as the top gate electrodes to apply the electric field (E or voltage, V_G) across the CoFeB/MgO interface while the bottom electrode remains unaltered. In Figure 12.3(b, c), we have demonstrated the evolution of SWs with the wavevector (k) from this novel magnetic system. These representative BLS spectra have been acquired for wavevector values, k = 2.05 × 10^6 rad/m and 7.1 × 10^6 rad/m, (i.e. near the center and edge of the first BZ) respectively, in the presence of V_G = − 4 V. Here, an in-plane magnetic field, $\mu_0 H$ = 200 mT has been set in the direction perpendicular to the stripe axis. This reveals a drastic modulation in the BLS spectra where the presence of two clear SW modes are observed which have been named as M1 and M2, respectively, according to their ascending order of frequency values. Subsequently, we have investigated their dispersive nature by varying the wavevector upto the second Brillouin zone (BZ) which is determined from the periodicity (a) of the 1D array of stripe-like top gate electrodes. Here, the periodicity is defined as, $a = w + s$, which is 440 nm in our case, so that the BZ edge (i.e. $k = \pi/a$) is ~ 7.1 × 10^6 rad/m. Figure 12.3(d) unveils the magnonic band structure for two BZs of the CoFeB/MgO heterostructure with periodically arranged electrodes while applying V_G = − 4 V. The experimental data are shown by the filled red symbols, while the calculated results from PWM method is shown by the blue solid lines. The magnonic bands with large scattering cross sections as predicted by PWM calculations have been emphasized by bold green lines. Notably, the dispersion curves have been calculated using PWM by taking the modulation of iPMA field into account while an in-plane magnetic field, $\mu_0 H$ = 200 mT, has been applied to the sample which is similar to the experimental

configuration. The experimental data points agree qualitatively well with the calculated results. In the experiment, the BLS spectra were characterized by the presence of two SW modes as depicted in Figure 12.3(b, c). As evident from Figure 12.3(d), both SW modes, i.e. M1 and M2 are dispersive modes although their natures are completely different from each other. At the edge of the first BZ (i.e. $k \sim \pi/a$), mode M1 undergoes Bragg diffraction, inducing the opening of a magnonic bandgap (BG) of width approximately 0.4 GHz.

It is noteworthy that, the iPMA has been modulated only in the regions under the periodically arranged top electrodes which have been taken into account during PWM calculations. Hence, the magnetic anisotropy will be different in two regions, i.e. (a) region 1 ($H_p(1)$) where the top electrodes are absent so that effective magnetization ($M(1)$) will remain unaltered there; (b) region 2 ($H_p(2)$) which is underneath the top electrodes where the magnetization ($M(2)$) dynamically tailored in presence of electric field/voltage (V_G) as $H_p(2)$ depends on both magnitude and polarity of V_G. In our case,

$$H_p(1) < H_p(2), \text{ for } V_G < 0 \quad (12.5)$$

$$H_p(1) > H_p(2), \text{ for } V_G > 0 \quad (12.6)$$

In order to get closer insight into the SW scattering mechanisms, we have calculated the SW mode profiles, i.e. the modulus of the amplitude of the x-component of the dynamic magnetization of the relevant experimentally observed SW modes.

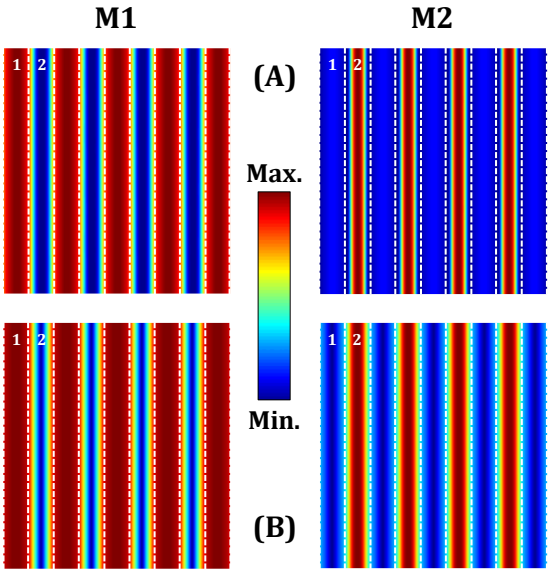

Figure 12.4. Spatial profiles of the SW modes for k = (a) 2.05 × 10^6 rad/m and (b) 7.1 × 10^6 rad/m, respectively under the application of V_G = − 4V at $\mu_0 H$ = 200 mT. The color

map is given at centre of the figure. Here, region 1 denotes the area with the absence of top electrode while, the region 2 represent the area beneath the top electrode.

The spatial maps of these SW modes are depicted in Figure 12.4 for k = 2.05 × 10^6 rad/m and 7.1 × 10^6 rad/m, (i.e. near the center and edge of the first BZ), respectively, calculated for V_G = − 4V. Here, the dotted lines represent regions (i.e. 1: regions without top electrodes and 2: regions with top electrodes, respectively) as discussed earlier. As represented in Figure 12.4, both M1 and M2 are extended modes along y-direction perpendicular to the direction of H (which is along z-direction as described in Figure 12.3(a)). However, we have observed a stark difference in the characteristics of M1 and M2 as the SW intensity of M1 is completely localized in region 1, while in case of M2, it is primarily concentrated in the region 2. Notably, as depicted in Figure 12.4(a) for k = 2.05 × 10^6 rad/m, both M1 and M2 possess quantized nature with different quantization numbers in regions 1 and 2, respectively, with the nodal planes being perpendicular to H. While M1 has quantization number of 1 in region 2, M2 has quantization number of 2 in the same region. Interestingly, both M1 and M2 have quantization number 1 in region 1. As we move to the mode profiles for $k = \pi/a$ as described in Figure 12.4(b), we observe a significant change in the quantization character of both M1 and M2. This is expected because at the BZ edge, their dispersive behaviours undergo a gradual variation from positive to negative slope. This substantially modulates the group velocity (i.e. $v = d(2\pi f)/dk$) of SW modes at the BZ edge, which is reflected in their spatial profiles. Consequently, both M1 and M2 possess quantization number of 2 in region 2, while they remain almost invariant in region 1.

The dispersion diagram is represented in Figure 12.5(a) where the polarity of the electric field is reversed i.e. for V_G = + 4V. Here, again two SW modes have been observed and both of them possess dispersive behaviour with the variation in k with a BG of ∼ 0.3 GHz. The spatial profiles of M1 and M2 have been also calculated for V_G = + 4V at k = 2.05 × 10^6 rad/m and 7.1 × 10^6 rad/m, respectively, which are shown in Figure 12.5(b, c). At k = 2.05 × 10^6 rad/m, M1 has quantization number 1 in both the regions while, M2 shows quantized character in regions 1 and 2 with quantization numbers 1 and 2, respectively. However, at $k = \pi/a$, i.e. ∼ 7.1 × 10^6 rad/m, the quantization nature of M1 changes and it shows quantization number 2 in region 1 but it has quantization

number 1 in region 2. On the contrary, spatial nature of M2 remains unaltered in both the regions.

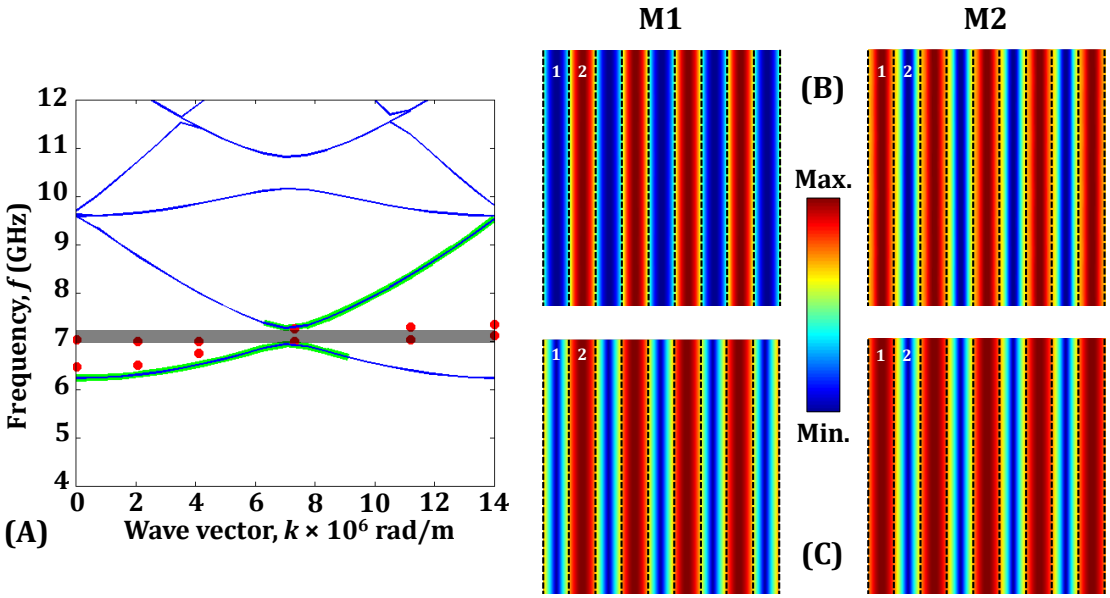

Figure 12.5. (a) Magnonic band structure under the influence of V_G = + 4V applied at $\mu_0 H$ = 200 mT. Red solid circles represent peaks in the BLS spectra. Thin blue lines denote plane wave method (PWM) results while, the bold green lines emphasize large BLS cross-section as predicted by PWM. The dashed vertical line describes the boundary of first Brillouin zone and the band gap is represented by the shaded region. Spatial profiles of the SW modes for k = (b) 2.05 × 10^6 rad/m and (c) 7.1 × 10^6 rad/m, respectively for V_G = + 4V applied at $\mu_0 H$ = 200 mT. The color map is given at centre of the figure. Here, region 1 denotes the area without the top electrode while, the region 2 represent the area beneath the top electrode.

To investigate the reconfigurability of this novel 1D system, we probed the SW dynamics by removing the electric field (voltage, V_G). The bias field-dependent result for this heterostructure with 1D patterned electrodes is presented in Figure 12.6(a) at k = 2.05 × 10^6 rad/m by setting V_G = 0 V. The results reveal the presence of SW frequency having a monotonic variation with H. Interestingly, this nature is very similar to that obtained in CoFeB/MgO film with top unpatterned electrode acquired at V_G = 0 V as shown in Figure 12.2(a). Both these field-dependent SW spectra are very similar to that recorded from a reference CoFeB/MgO film as depicted in Figure 12.6(b) while, the corresponding SW dispersion spectra obtained in both the cases are presented in Figure 12.6(c, d). This demonstrates that we have been able to develop a 1D voltage controlled dynamic MC, which can be reset to its pristine thin film-like state using by removing the

small voltage. The SW dispersion has been probed simply from thermal magnons with the aid of BLS spectroscopy. This can pave a step towards the development of a new generation of reprogrammable magnonic devices controllable by electric field with minimum Ohmic dissipation.

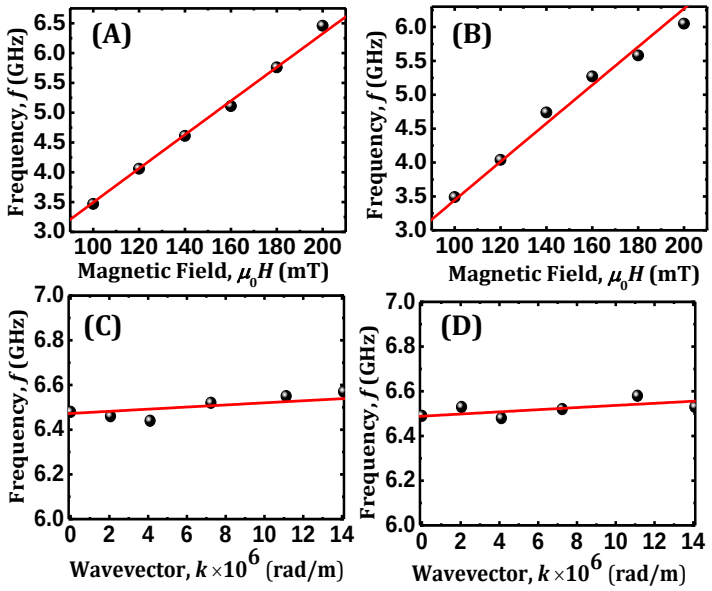

Figure 12.6. Variation of SW frequency as a function of bias magnetic field ($\mu_0 H$) at k = 2.05 × 10^6 rad/m obtained from (a) the CoFeB/MgO heterostructure with 1D patterned ITO electrodes obtained for V_G = 0V and (b) the reference CoFeB/MgO sample without any top electrode. Frequency (f) versus wavevector (k) dispersion curves in the presence of $\mu_0 H$ = 200 mT from (c) CoFeB/MgO heterostructure with 1D patterned ITO electrodes obtained for V_G = 0V and (d) reference CoFeB/MgO sample without any top electrode. The solid lines represent the fitted curves using Equation 12.2.

12.4. Conclusion

We have presented a combined experimental and theoretical investigation of a reconfigurable magnonic band structure in a dynamic 1D magnonic crystal composed of CoFeB/MgO heterostructure under the influence of electric field. The SW dispersions have been measured by probing thermal magnons using BLS spectroscopy. First, we attained a monotonic enhancement or decrement in the SW frequency depending upon the polarity of the electric field applied to CoFeB/MgO heterostructure with an unpatterned top gate electrode. Further analysis corroborates the linear dependence of interfacial PMA modulation with the applied electric field. We probed the SW dynamics in the CoFeB/MgO system with 1D array of ITO electrodes on the top of the CoFeB/MgO

heterostructure. Remarkably, a magnonic band structure consisting of two SW frequency modes along with a band gap appear in the dispersion curve under the application of a modest electric field. This band structure reverts back to its original state for the unpatterned electrode and the bandgap disappears as soon as the electric field is withdrawn. This clearly demonstrates the achievement of a reprogrammable and dynamic magnonic band structure by an electric field across CoFeB/MgO interface applied through 1D array of stripe-like electrodes. There this novel magnetic system acts as a 1D dynamic MC which can be reconfigured with the aid of electric field. This unlocks a gateway to develop a new genre of MCs invoked by an energy-efficient stimulus, i.e. electric field, which may play a key role in devicing spin-based magnonic circuits with ultralow power consuption.

12.5. Materials and Methods

12.5.1. Sample Preparation

The sample has been prepared by multistep fabrication method. First of all, multilayered heterostructure was deposited on Si(001)|SiO_2(700 nm) substrate by radio frequency (rf) sputtering at room temperature at a base pressure of about 1×10^{-8} Torr. The structure of multilayer stack is the following: Si|SiO_2|Ta(10)|$Co_{20}Fe_{60}B_{20}$(1.6)|MgO(2)|Al_2O_3(10), where the numbers in the parentheses represent the nominal thicknesses (in nm) of the corresponding layers. The sputter-deposited film was then annealed at 280°C in vacuum under a perpendicular magnetic field of 600 mT for 1 hr. Notably, since PMA present in the heterostructure is interfacial (i.e. CoFeB/MgO interface) in nature, the thickness of CoFeB is chosen to be 1.6 nm in order to enhance the magneto-electric effect while keeping the magnetization completely in-plane at the same time. In the second step, square area of lateral dimensions 60 μm × 60 μm was prepared from the annealed multilayer stacks by using maskless UV photolithography followed by Ar^+ ion milling down to SiO_2. In the third step, alignment markers for electron beam lithography and metal gate (bottom) electrodes were prepared by maskless UV photolithography followed by deposition of Ti(5)|Au(100) layer by electron beam evaporation. In the fourth step, Al_2O_3 with 100 nm thickness was deposited everywhere except on top of the sample and the metal electrodes. In the fifth step, electron beam lithography was performed to prepare the 1D grid-like pattern on the top of the sample which was followed by deposition of a 120

nm-thick indium tin oxide (ITO) layer (top gate electrode) by sputtering technique. Here, each stripe-like top gate electrode has a width of 220 nm while they are separated by a distance of 220 nm. It is noteworthy that, ITO was chosen as the top electrode as because of its transparent nature which is essential for the optical (BLS) measurement to acquire thermally excited magnons from the FM/oxide heterostructure. In the last step, all the contacts for application of dc gate voltage were made by maskless photolithography and deposition of Ti(5)|Au(200) layer by electron beam evaporation. The reference sample, i.e. FM/oxide heterostructure with a blanket (i.e. unpatterned) ITO(120) layer as the top electrode was also prepared using similar procedure.

12.5.2. Measurement Technique

BLS experiments were performed in the conventional backscattering configuration for the measurement of dispersion characteristics of thermal magnons in the sample. This technique relies on inelastic light-scattering process arising from the interaction between incident photons and magnons. Monochromatic laser beam (wavelength, λ = 532 nm, power ≈ 65 mW) from a solid-state laser was focussed on the surface of the sample. The diameter of the focused laser spot is about 40 μm which is smaller than the lateral dimensions of the sample (60 × 60 μm^2). The laser beam was carefully placed on the sample which was further confirmed by using a white illumination and CCD camera arrangement. The laser beam is inelastically scattered from the magnons and from to conservation of momentum, the magnitude of the in-plane transferred wavevector (k) depends on the incidence angle (θ) of light according to the relation:

$$k = \frac{4\pi}{\lambda} \sin\theta \tag{12.7}$$

Cross polarizations between the incident and the scattered beams are adopted during the experiment to minimize the phonon contribution to the scattered light. Subsequently, the frequencies of the scattered light were analyzed using a Sandercock-type six-pass tandem Fabry-Pérot interferometer (TFPI: JRS Scientific Instruments). There, a frequency shift is observed along with the laser frequency taking into account energy and momentum conservation. The BLS spectra were recorded after counting photons for several hours to achieve well-defined magnon spectra in all the cases. A free spectral range (FSR) of 30 GHz and a 2^{10} multichannel analyzer were used during the BLS measurement. The frequency resolution is determined by estimating FSR/2^{10} (≈ 30 MHz) for the Stokes and anti-Stokes peaks of the BLS spectra. Here, the direction of the

wavevector (k) was kept parallel to the axes of the 1D stripe-like top electrodes, i.e. along the y-direction as described in Figure 12.3(a), by making the stripe axes parallel to the light-scattering plane throughout the experiment. The BLS spectra were recorded for upto two BZs, i.e. $k \sim 14.3 \times 10^6$ rad/m by considering the periodicity (a) of the stripe array to be 440 nm. The SW dispersion was performed at an in-plane magnetic field, $\mu_0 H$ = 200 mT applied to the sample. The electric field is applied by a dc voltage source (Keithley 2450) between the top and bottom electrodes of the sample without the presence of any leakage current through the heterostructure (this was confirmed simultaneously while applying the electric field throughout the experiment).

12.5.3. Theoretical Calculation

We have numerically calculated the spectrum of magnonic excitations of the dynamic 1D MC using plane wave method (PWM) which is a robust tool because of its conceptual simplicity and its applicability to periodically patterned network with any shape of scattering centers. We solve the Landau-Lifshitz (LL) equation for the magnetization ($\boldsymbol{M} = M(\boldsymbol{r}, t)$) under the influence of an effective magnetic field, H_{eff} which can be primarily expressed as a sum of different field contributions as the following:

$$H_{\text{eff}} = H + H_{\text{ex}} + H_{\text{d}} + H_{\text{ani}} \tag{12.8}$$

Where, H, H_{ex}, H_{d} and H_{ani} represent the applied static magnetic field, exchange field, magnetostatic or demagnetizing field and anisotropy field, respectively. $M(\boldsymbol{r}, t)$ is written as:

$$M(\boldsymbol{r}, t) = M_{\text{s}}(\boldsymbol{r}) + m(\boldsymbol{r}, t) \tag{12.9}$$

Here, $M_{\text{s}}(\boldsymbol{r})$ and $m(\boldsymbol{r}, t)$ describe the components of $M(\boldsymbol{r}, t)$ parallel (constant in time) and perpendicular to H, while considering linear approximation:

$$|M_{\text{s}}(\boldsymbol{r})| \gg |m(\boldsymbol{r}, t)| \tag{12.10}$$

For a magnetically inhomogeneous medium (such as a 1D MC in our case), the spatial inhomogeneity of the material parameters, e.g. spontaneous magnetization and exchange constant as well as the magnetostatic field have been considered during the calculation so that,

$$H_{\text{d}}(\boldsymbol{r}, t) = H_{\text{d}}(\boldsymbol{r}) + h_{\text{d}}(\boldsymbol{r}, t) \tag{12.11}$$

Here, $H_{\text{d}}(\boldsymbol{r})$ and $h_{\text{d}}(\boldsymbol{r}, t)$ are static and dynamic components of $H_{\text{d}}(\boldsymbol{r}, t)$ fulfilling the Maxwell's equations, while,

$$h_{\text{d}}(\boldsymbol{r}, t) = h_{\text{d}}(\boldsymbol{r}) e^{i2\pi f t} \tag{12.12}$$

$$m(\boldsymbol{r},t) = m(\boldsymbol{r})e^{i2\pi ft} \tag{12.13}$$

In addition, H_{ex} can be expressed as,

$$H_{ex}(\boldsymbol{r},t) = \left(\vec{\nabla}.\lambda_{ex}^2(\boldsymbol{r})\vec{\nabla}\right)m(\boldsymbol{r},t) \tag{12.14}$$

where $\lambda_{ex}(\boldsymbol{r})$ denotes the exchange length which is related to exchange stiffness constant ($\boldsymbol{A} = A(\boldsymbol{r})$) as,

$$\lambda_{ex}^2(\boldsymbol{r}) = \frac{2A(\boldsymbol{r})}{\mu_0 M_s^2} \tag{12.15}$$

Subsequently, the Fourier transformation has been carried out to map all the periodic functions (in space and time) including the static and dynamic parts of the magnetic fields and magnetization components to the reciprocal space using Bloch's theorem [40]. Considering the lattice periodicity, a (in our case, $w = s = 220$ nm, so that, $a = w + s = 440$ nm), $m(\boldsymbol{r})$ can be expressed as,

$$m(\boldsymbol{r}) = \sum_G m_k(G)\, e^{i(\boldsymbol{k}+\boldsymbol{G}).\boldsymbol{r}} \tag{12.16}$$

where, $\boldsymbol{G}$ represents the reciprocal lattice vector of the considered MC such as:

$$G = (G_y, G_z) = \frac{2\pi}{a}(n_y, n_z) \tag{12.17}$$

with n_y and n_z being integers, while the Bloch wavevector, i.e. k lies along the axes of the stripe-like 1D electrodes (each having width, $w = 220$ nm) in our case. Being a periodic function of position in the MC, the saturation magnetization ($\boldsymbol{M}_s$) and $(\lambda_{ex})^2$ can be mapped onto the reciprocal space using the Fourier transformation formulas as the following:

$$M_s(\boldsymbol{r}) = \sum_G M_s(\boldsymbol{G})\, e^{i\boldsymbol{G}.\boldsymbol{r}} \tag{12.18}$$

$$\lambda_{ex}^2(\boldsymbol{r}) = \sum_G \lambda_{ex}^2(\boldsymbol{G})\, e^{i\boldsymbol{G}.\boldsymbol{r}} \tag{12.19}$$

where, the Fourier coefficients are determined analytically. It is noteworthy that, the 1D MC in our case has been dynamically created by applying electric field through the 1D patterned top electrodes to periodically modulate the PMA at CoFeB/MgO interface. Hence, the anisotropy field, i.e. H_{ani} in Equation 12.8 originates from the PMA at the CoFeB/MgO interface such that,

$$H_{ani} = H_{ani}(V_G) \tag{12.20}$$

In other words, this system behaves as a MC, which is comprised of two magnetic media having contrasting magnetic anisotropy where the anisotropy in area (region 2 in our case as shown in Figure 12.4) under top electrodes either increases or decreases periodically (i.e. H_{ani} also possesses periodic nature in the reciprocal space similar to

M_S) depending upon the polarity of the applied voltage (V_G). Hence, in our case for the dynamic 1D MC, the expressions for the static magnetization (M_S) can be calculated[41] in the reciprocal space as the following,

$$M_s(G) = \frac{w}{a} M_{s,\text{Region1}} + M_{s,\text{Region2}} \left(1 - \frac{w}{a}\right) \qquad \text{for } G = 0 \qquad (12.21)$$

$$= \frac{w}{Ga} \left(M_{s,\text{Region1}} - M_{s,\text{Region2}}\right) \sin\left(G \frac{w}{2}\right) \qquad \text{for } G \neq 0 \qquad (12.22)$$

Here, $M_{s,\text{Region1}}$ and $M_{s,\text{Region2}}$ represent the M_s values at regions 1 (remains unaltered with V_G) and 2 (controllable by V_G, i.e. by electric field) respectively. Thus, the PWM transforms the LL equation into an infinite set of algebraic equations, which leads to an eigenvalue problem. In order to find the eigenvalues (the frequencies of SWs) and eigenvectors (amplitude of the dynamic component of $\boldsymbol{M}$), the Fourier series has to be limited to the finite number of elements. The eigenvalue problem is then solved with standard numerical routines. A satisfactory convergence of the numerical solutions of the eigenvalue problem is obtained by taking 450 plane waves.

References

[1] D. D. Awschalom, L. C. Bassett, A. S. Dzurak, E. L. Hu, J. R. Petta, Science 339 (2013) 1174.
[2] J. Shi, P. Zhang, D. Xiao, Q. Niu, Phys. Rev. Lett. 96 (2006) 076604.
[3] S. A. Wolf, D. D. Awschalom, R. A. Buhrman, J. M. Daughton, S. von Molnár, M. L. Roukes, A. Y. Chtchelkanova, D. M. Treger, Science 294 (2001) 1488.
[4] A. V. Chumak, V. I. Vasyuchka, A. A. Serga, B. Hillebrands, Nat. Phys. 11 (2015) 453.
[5] V. V. Kruglyak, S. O. Demokritov, D. Grundler, J. Phys. D: Appl. Phys. 43 (2010) 260301.
[6] C. Banerjee, S. Choudhury, J. Sinha, A. Barman, Phys. Rev. Appl. 8 (2017) 014036.
[7] Q. Wang, A. V. Chumak, L. Jin, H. Zhang, B. Hillebrands, Z. Zhong, Phys. Rev. B 95 (2017) 134433.
[8] D. Grundler, Nat. Phys. 11 (2015) 438.
[9] J. W. Kłos, M. Krawczyk, Y. S. Dadoenkova, N. N. Dadoenkova, I. L. Lyubchanskii, J. Appl. Phys. 115 (2014) 174311.
[10] P. Graczyk, M. Krawczyk, Phys. Rev. B 96 (2017) 024407.
[11] M. Matsuo, E. Saitoh, S. Maekawa, J. Phys. Soc. Jpn. 86 (2016) 011011.
[12] F. Matsukura, Y. Tokura, H. Ohno, Nat. Nanotechnol. 10 (2015) 209.
[13] T. Nozaki, Y. Shiota, S. Miwa, S. Murakami, F. Bonell, S. Ishibashi, H. Kubota, K. Yakushiji, T. Saruya, A. Fukushima, S. Yuasa, T. Shinjo, Y. Suzuki, Nat. Phys. 8 (2012) 491.
[14] S. I. Kiselev, J. C. Sankey, I. N. Krivorotov, N. C. Emley, R. J. Schoelkopf, R. A. Buhrman, D. C. Ralph, Nature 425 (2003) 380.
[15] P. Rovillain, R. de Sousa, Y. Gallais, A. Sacuto, M. A. Méasson, D. Colson, A. Forget, M. Bibes, A. Barthélémy, M. Cazayous, Nat. Mater. 9 (2010) 975.

[16] H. Ohno, D. Chiba, F. Matsukura, T. Omiya, E. Abe, T. Dietl, Y. Ohno, K. Ohtani, Nature 408 (2000) 944.
[17] M. Xu, J. Puebla, F. Auvray, B. Rana, K. Kondou, Y. Otani, Phys. Rev. B 97 (2018) 180301(R).
[18] C.-G. Duan, J. P. Velev, R. F. Sabirianov, Z. Zhu, J. Chu, S. S. Jaswal, E. Y. Tsymbal, Phys. Rev. Lett. 101 (2008) 137201.
[19] T. Maruyama, Y. Shiota, T. Nozaki, K. Ohta, N. Toda, M. Mizuguchi, A. A. Tulapurkar, T. Shinjo, M. Shiraishi, S. Mizukami, Y. Ando, Y. Suzuki, Nat. Nanotechnol. 4 (2009) 158.
[20] T. Kawabe, K. Yoshikawa, M. Tsujikawa, T. Tsukahara, K. Nawaoka, Y. Kotani, K. Toyoki, M. Goto, M. Suzuki, T. Nakamura, M. Shirai, Y. Suzuki, S. Miwa, Phys. Rev. B 96 (2017) 220412(R).
[21] M. Weisheit, S. Fähler, A. Marty, Y. Souche, C. Poinsignon, D. Givord, Science 315 (2007) 349.
[22] M. Krawczyk, D. Grundler, J. Phys. Condens. Matter 26 (2014) 123202.
[23] U. Bauer, S. Emori, G. S. D. Beach, Nat. Nanotechnol. 8 (2013) 411.
[24] W.-G. Wang, M. Li, S. Hageman, C. L. Chien, Nat. Mater. 11 (2011) 64.
[25] B. Rana, Y. Fukuma, K. Miura, H. Takahashi, Y. Otani, Appl. Phys. Lett. 111 (2017) 052404.
[26] B. Rana, Y. Otani, Phys. Rev. Appl. 9 (2018) 014033.
[27] S. O. Demokritov, B. Hillebrands, A. N. Slavin, Phys. Rep. 348 (2001) 441.
[28] S. Ikeda, K. Miura, H. Yamamoto, K. Mizunuma, H. D. Gan, M. Endo, S. Kanai, J. Hayakawa, F. Matsukura, H. Ohno, Nat. Mater. 9 (2010) 721.
[29] H. Ohno, Science 291 (2001) 840.
[30] H. X. Yang, M. Chshiev, B. Dieny, J. H. Lee, A. Manchon, K. H. Shin, Phys. Rev. B 84 (2011) 054401.
[31] M. Tsujikawa, T. Oda, Phys. Rev. Lett. 102 (2009) 247203.
[32] S. Miwa *et al.*, Nat. Commun. 8 (2017) 15848.
[33] S. E. Barnes, J. i. Ieda, S. Maekawa, Sci. Rep. 4 (2014) 4105.
[34] V. B. Naik, H. Meng, J. X. Xiao, R. S. Liu, A. Kumar, K. Y. Zeng, P. Luo, S. Yap, Appl. Phys. Lett. 105 (2014) 052403.
[35] A. Okada, S. Kanai, M. Yamanouchi, S. Ikeda, F. Matsukura, H. Ohno, Appl. Phys. Lett. 105 (2014) 052415.
[36] D. D. Lam, F. Bonell, S. Miwa, Y. Shiota, K. Yakushiji, H. Kubota, T. Nozaki, A. Fukushima, S. Yuasa, Y. Suzuki, J. Korean Phys. Soc. 62 (2013) 1461.
[37] Y. Shiota, F. Bonell, S. Miwa, N. Mizuochi, T. Shinjo, Y. Suzuki, Appl. Phys. Lett. 103 (2013) 082410.
[38] Y. Hayashi, Y. Hibino, F. Matsukura, K. Miwa, S. Ono, T. Hirai, T. Koyama, H. Ohno, D. Chiba, Appl. Phys. Express 11 (2017) 013003.
[39] Y. Hibino, T. Koyama, A. Obinata, T. Hirai, S. Ota, K. Miwa, S. Ono, F. Matsukura, H. Ohno, D. Chiba, Appl. Phys. Lett. 109 (2016) 082403.
[40] M. Krawczyk, H. Puszkarski, Phys. Rev. B 77 (2008) 054437.
[41] M. L. Sokolovskyy, M. Krawczyk, J. Nanoparticle Res. 13 (2011) 6085.

Chapter 13

13. Summary and Outlook

13.1. Conclusions:

During the investigations presented in this dissertation, the quasi-static and dynamic magnetization parameters in patterned magnetic heterostructures at micro- and nanoscale the primary motivation is to promote the potential of spin-based devices for future information processing and data storage applications. Here, the patterned structures namely, MCs with improved functionalities and novel heterostructures have been explored to get an insight about the fundamental SW properties which play a pivotal role in terms of future magnonic circuits. The samples have been prepared by advanced lithography techniques, e.g. photo- and electron beam lithography and various ultrahigh vacuum deposition methods such as magnetron sputtering and electron beam evaporation. Except these, several essential tools such as ion milling with end point detection tool, laser microscope, wire bonding have been utilized. The preliminary characterizations of these samples have been carried out using scanning electron microscopy (SEM), X-ray diffraction (XRD), atomic force microscopy (AFM) and energy dispersive X-ray spectroscopy (EDXS). Here, magneto-optical Kerr effect magnetometry (MOKE), magnetic force microscopy (MFM) and vibrating sample magnetometry (VSM) have been employed to explore the static magnetic parameters. The dynamics of magnetization have been probed by several novel techniques which are, custom made broadband ferromagnetic resonance spectrometer in frequency window, home-built time-resolved magneto-optical Kerr effect (TR-MOKE) microscope (temporal regime spans from hundreds of fs to few tens of ns) and Brillouin light scattering (BLS) spectroscopy in the wavevector domain, respectively. The experimental observations have been analyzed to interpret the underlying physics for the respective systems with the aid of micromagnetic simulations and plane wave method.

The evolution of magnetization dynamics has been investigated of several 2D MCs in the form of antidots arrays either by tuning its physical structures like size or by playing with the lattice arrangement from periodic to quasi-periodic regime. Firstly, the spin

dynamics have been explored in hexagonally arranged 2D antidot systems [1] patterned on NiFe films with varying antidot diameter (size) having same lattice spacing by controlling the bias magnetic field strength and its in-plane orientation using broadband ferromagnetic resonance spectrometer. The field dispersion spectra of these systems reveal that the SW dynamics get drastically modified as the antidot diameter is varied. Rich multimodal SW spectra are obtained for the highest antidot diameter, whereas the number of SW modes reduces systematically with the decreasing antidot diameter. Moreover, a crossover between two higher frequency SW modes is observed for the lattices with higher antidot diameter when the strength of the bias field is reduced. The simulated static magnetic configurations along with the power and phase profiles unravel the spatial distribution of the observed SW modes which confirms the formation of SW quantization laterally as well as diagonally inside the array having higher antidot diameter at low bias field due to the strong overlapping of demagnetization regions between the antidots. As a result, the internal field is reduced significantly with the enhancement in antidot diameter. The variation of magnonic spectra with the in-plane orientation for all the samples shows the presence of two anisotropic SW modes both in opposite phase to each other, with six-fold rotational symmetry which is strongly modulated when the hole diameter is increased. Interestingly, for intermediate antidot diameters, the lowest frequency SW mode apparently shows a mode hopping-like behaviour with a periodicity which is commensurate with the lattice geometry but a closer look reveals a parametric splitting of mode. The phase maps of these samples unveil an interesting conversion from extended nature to quantized standing wave pattern or vice-versa in most of these anisotropic SW modes with the modulation of in-plane orientation. Further, the variation of internal field with the in-plane orientation confirms the presence of six-fold anisotropy which is strongly modulated when the diameter of the antidots is modified.

Next, the SW dynamics have been explored in circular NiFe antidots fabricated in a heterodox defective honeycomb lattice [2] with varying periodicity by broadband FMR method. The field dispersion curves of these samples unravel drastic modulation in the magnon modes as the periodicity is varied. Multimodal SW spectra have been obtained for the most densely packed ADL, whereas the number of SW modes reduces systematically with the decreasing periodicity approaching towards a nearly thin film-

like behaviour due to the reduction of the contribution of the demagnetizing field around the ADs. The experimental observations have been reproduced by micromagnetic simulation while the spatial distributions of the SW frequencies have been numerically calculated to get an insight about the spatial nature of the dynamics. The power and phase maps have unveiled different genres of extended and localized standing SW modes. To understand the origin of the observed SW modes, internal fields including the demagnetization field contributions have been calculated. Interestingly, the modulation of the internal field follows a monotonic power-law relation with the lattice periodicity which is similar to the effective magnetization. This corroborates that the modification of effective magnetization is in commensuration with the internal field which is strongly controlled by the demagnetizing field contribution present in these ADLs. The modulation of SW spectra with in-plane orientation for all samples unveils the presence of anisotropic SW modes with six- or two-fold or a superposition of both rotational symmetries. The internal field profile inside the honeycomb cells is primarily responsible for the origin of the six-fold anisotropy whereas that within the rhombic region surrounded by four honeycomb cells gives rise to the two-fold anisotropy.

The lattice symmetry of the antidot array have been further tailored in circular shaped NiFe antidots arranged in an octagonal lattice [3] where broadband FMR spectroscopy has been employed to probe the spin dynamics. The experimental results have shown a remarkable variation in the SW spectra with the variation of lattice spacing. For the lowest value of lattice spacing, seven SW modes are observed which converge into two modes for the highest value of lattice spacing. The experimental results have been well reproduced by micromagnetic simulation, and the power and phase profiles of the resonant modes have been numerically calculated to get an insight about the spatial nature of the dynamics. Different types of extended and localized standing SW modes with varying quantization numbers are observed. The magnetostatic fields including the demagnetization field distributions are calculated to interpret the origin of the observed SW modes. The configurational anisotropy of the samples is investigated by varying the azimuthal angle of the bias field where interestingly, an eight-fold rotational anisotropy superposed with four-fold and two-fold anisotropies is observed for these samples. The value of the eight-fold anisotropy is found to decrease strongly with the increase in the lattice spacing. The magnetostatic field distribution within the octagonal unit cell is

mainly responsible for the origin of the eight-fold anisotropy, whereas the rhombus-like cell present between two octagonal unit cell is mainly responsible for the four-fold anisotropy.

Next, the modulation of SW spectra has been investigated in a new genre of 2D MCs which is known as bi-component MC (BMC) and arrays of circular and square shaped NiFe filled CoFe antidot lattices [4] arranged in square lattice symmetry show a remarkable variation in the SW spectra. An asymmetry in the dispersion of SW frequency with bias field is observed in the BMCs with both shapes as opposed to their antidot counterparts, with a minimum in the frequency occurring at a negative bias field, confirming the presence of inter-element exchange interaction at the NiFe and CoFe interface. The SW spectra unveil more tunability in square shaped BMC in comparison with circular shaped one where a decrease in the frequency gap between the two SW modes has been observed upto a certain magnetic field below which the gap again increases. The inter-element exchange field value at the interface is found to be greater in the square BMC than that in the circular BMC which is probably due to improved interface between NiFe and CoFe. Simulations show a significant difference in the magnetostatic field distributions for both circular and square shaped filled ADLs as opposed to their unfilled counterparts. The demagnetization region in filled ADL is modified due to change in the element shape, and as a result, the total internal field in the square shaped filled NiFe regions is larger as compared to the circular shaped filled NiFe regions. Finally, the demagnetizing fields in the CoFe and NiFe channels are opposite to each other, which give rise to a significant modification of the SWs in these samples.

Further, the ultrafast magnetization dynamics of BMC with more complex triangular shape [5] has been investigated by controlling the strength and the in-plane or azimuthal orientation of the bias magnetic field by employing time-resolved MOKE magnetometry. The magnetization dynamics of the BMC reveal rich magnon spectra where the SW modes possess either extended or confined behaviour in NiFe and CoFe regions depending upon their frequency. Also, the power of the SW mode is transferred from NiFe channel to CoFe channel when the frequency is increased. The configurational anisotropy present in the BMC is investigated by varying the azimuthal orientation of the applied magnetic field possessing six- or four-fold anisotropy which is

incommensurate with the shape and lattice arrangement of the BMC. In addition to this, the power profiles of the SW mode show an interesting mode conversion from extended to quantized standing SW mode with the azimuthal rotation of bias magnetic field direction. Further, this fascinating property of the SW frequency is improvised to numerically demonstrate a potential application of such BMC as dynamic filter integrated with magnonic waveguide.

Next, the propagating nature of SWs have been explored where electric field modulation of uniform ferromagnetic resonance (UFMR) and exchange-dominated magnetostatic surface spin waves (MSSWs) have been investigated in different thicknesses of CoFeB films, possessing interfacial perpendicular magnetic anisotropy (iPMA). Exchange dominated MSSWs are excited electrically by using microwave antenna and detected by spin pumping and inverse spin Hall effect (ISHE) techniques. We have shown modulation of SW frequency by tuning iPMA of CoFeB SW waveguides (SWWGs) by applying gate voltage across gate electrode and SWWG. It is observed that the SW frequency is significantly modified by voltage controlled magnetic anisotropy (VCMA), especially, for thinner CoFeB waveguide where demagnetizing field is significantly reduced by iPMA. By performing micromagnetic simulations it has been demonstrated that MSSWs in thinner CoFeB waveguide can be guided through nanochannels (NCs) formed by VCMA.

We have presented a combined experimental and theoretical investigation of a reconfigurable magnonic band structure in a dynamic 1D magnonic crystal composed of CoFeB/MgO heterostructure under the influence of electric field. The SW dispersions have been measured by probing thermal magnons using BLS spectroscopy. First, we attained a monotonic enhancement or decrement in the SW frequency depending upon the polarity of the electric field applied to CoFeB/MgO heterostructure with an unpatterned top gate electrode. Further analysis corroborates the linear dependence of interfacial PMA modulation with the applied electric field. We probed the SW dynamics in the CoFeB/MgO system with 1D array of electrodes on the top. Here, a magnonic band structure consisting of two SW frequency modes shows up in the dispersion curve under the application of a moderate electric field, which also reveals the opening of a magnonic bandgap between the SW modes. This bandgap can be switched off by withdrawing the electric field. Hence, a reprogrammable magnonic band structure is

achieved under the influence of an electric field across CoFeB/MgO interface applied through 1D array of stripe-like electrodes. There this novel magnetic system acts as a 1D dynamic MC which can be reconfigured with the aid of electric field. This unlocks a gateway to develop a new genre of MCs invoked by an electric field. This observation may play a key role in devicing spin-based magnonic circuits with ultralow power consuption.

13.2. Future Perspectives:

The current advancement in nanofabrication techniques has made it possible to grow thin film heterostructures and periodically patterned structures with high quality and resolution while the experimental realization of various theoretically proposed effects in these novel systems has shown a new pathway to understand the fundamental physics and feasible applications in last few decades.

First of all, the investigation of magnetization dynamics of arrays of magnetic antidots can play a pivotal role in future spin-based communication technology due to their efficient tunability as a function of geometrical parameters such as size, lattice arrangement and periodicity. The external factors like magnetic field also can also be employed to control their spin dynamics by simply varying its strength and orientation making them immensely useful for MC-based technology. Also, the anisotropy present in the SWs may determine their dispersions in the magnon band diagram which finds applications in SW filters, attenuators and splitters. Hence, a necessary extension of the works presented in this dissertation can be a thorough investigation of magnonic band structure of these novel MCs using BLS. There the existence of single or multiple band gaps [6] in a Brillouin zone depending upon the symmetry of the lattice or its periodicity and the size and shape of the antidots can be explored. Also, 2D antidot systems with out-of-plane magnetization can become a new genre of MCs because of their improved thermal stability, which may find applications in magnetic storage devices.

Another interesting aspect can be the investigation of spin dynamics in quasiperiodic and defective patterned structures. Recently, artificial quasicrystals have become a hot topic of research in the field of phononics and photonics, as such quasi-periodic nature can combine perfectly ordered structures with purely point-diffractive spectra of arbitrarily high rotational symmetry. Similarly, quasiperiodic structures in the field of magnonics can possess salient properties like branching in the band structure, self-

similarity and scaling properties in the transmission spectra. Exploring the perfect transmission of the SWs in quasi-periodic MCs [7] can be useful for developing ultrahigh quality, multichannel, filters or resonators. Although, different studies have been carried out so far in 1D quasi-periodic MCs while understanding of the band structures in novel 2D systems has been sparse.

In addition, the defects can be present in 2D MCs which can be classified in two types, namely, natural defects and tailored defects. The former originates during the fabrication (e.g. edge roughness and deformation or ion implantation during ion beam irradiation) while the latter originates from the controlled manipulation of the extrinsic parameters (e.g. artificially created vacancies or antidots with different sizes and shapes). These can lead to pinning or a modification of the magnetic properties around the antidot edges causing localization and/or mixing of SWs in these defect potentials. A control of defect states may lead towards a variation of transmission coefficients of the magnons through these structures which can pave a new pathway in developing reprogrammable magnonics [8]. In addition, the possibility of the presence of magnetic monopoles has triggered the imagination of the scientific community as their existence can be reconciled with the quantum phenomena. The control of magnetic charge to the magnetic charge path selectivity can provide an interesting tool leading to a new architecture for parallel computation. The magnetization dynamics in artificial spin ice (ASI) systems [9] made of square or interconnected kagome lattice can open up opportunities for further application of such systems in reprogrammable magnonics in both 2D and 3D.

The spin dynamics can be tailored more efficiently in BMCs [10] where an enhanced coupling can be achieved due to the presence of exchange coupling at the boundary of two different magnetic materials which are in direct contact with each other. This results in a scattering of SWs at the interfaces between the two materials and SW can easily transmit through the lateral interface with improved group velocity. Hence, the investigation of the magnonic band structure of these BMCs by manipulating their geometrical parameters (such as shape, lattice arrangement and periodicity) can be very interesting in terms of microwave applications such as microwave assisted magnetic recording (MAMR).

Recently, antiferromagnetic systems have been considered for storage application where the information may be free from unwanted fields as the neighbouring moments do not interact among them which is crucial at nanoscale. Hence, the investigation of spin degree of freedom in antiferromagnet [11] can become an intriguing topic in terahertz (THz) spintronics as their magnetic response lies in that regime. The magneto-elastic coupling can play a key role as a bridge between magnetic and mechanical degrees of freedom of a material. Thus, such systems with strong magneto-elastic coupling will be very useful for spin-mechatronics [12].

Different interfacial spin-orbit coupling phenomena such as Dzyaloshinskii-Moriya interaction (DMI), Rashba interaction etc. have been demonstrated in playing a key role to tailor SWs while the concept of generating pure spin current has been successfully implemented using spin pumping or spin Hall effect (SHE) [13]. Thus, the control of DMI using external stimuli such as electric field, current can be very interesting to study. In addition, the 1D or 2D patterning of a magnetic heterostructure with inherent DMI or periodic modulation of DMI can play a crucial role for future magnonics. Nowadays, 2D materials especially graphene with an FM interface has gained a great attention due to the enhanced interfacial DMI possibly because of presence of Rashba effect or defects [14]. In addition, creating a new type of interface namely, spinterface [15] between an FM and organic or inorganic material can give rise to the possibility of efficiently tuning the magnetic parameters of the interface at the atomic scale which is essential for molecular spintronics.

In this thesis, an energy efficient control parameter for the spins have been exploited where the electric field has been employed instead of using charge current that exhausts more energy due to thermal heating. This has made possible to develop the next generation spintronic and spin-based logic devices with ultralow power consumption [16] making the very first concept behind the usefulness of spin current a possible reality. Further this parameter has enabled to define reprogrammable magnonics at the nanoscale with improved functionality because of the spatially localized nature of SWs induced by electric field. It is worth to mention here that MSSWs in relatively thicker films can also be guided through NCs by further increasing VCMA coefficient (β). Several reports show that it is possible to increase β by engineering the interfaces of the FM/oxide heterostructures. For instance, insertion of ultrathin heavy

metallic layer in between FM and oxide layer can enhance β significantly. Also, the enhancement in β can be achieved by inserting light materials such as Mg, Hf etc. or heavy materials such as Ta, W, Pt, Ir etc. The possible reason behind this can be interpreted as the suppression of surface oxidization of FM layer and modification of hybridization between *d* (FM) and *p* (Oxygen) orbitals. In addition, doping of heavy metals (like Ir) at the FM/oxide interface can increase both iPMA and β substantially due to the diffusion of these elements into FM layer. Apart from these, different important properties of SWs such as group velocity, decay length, phase can also be tailored by VCMA. Hence, further studies are required to investigate the electric field modulation of those properties of SWs.

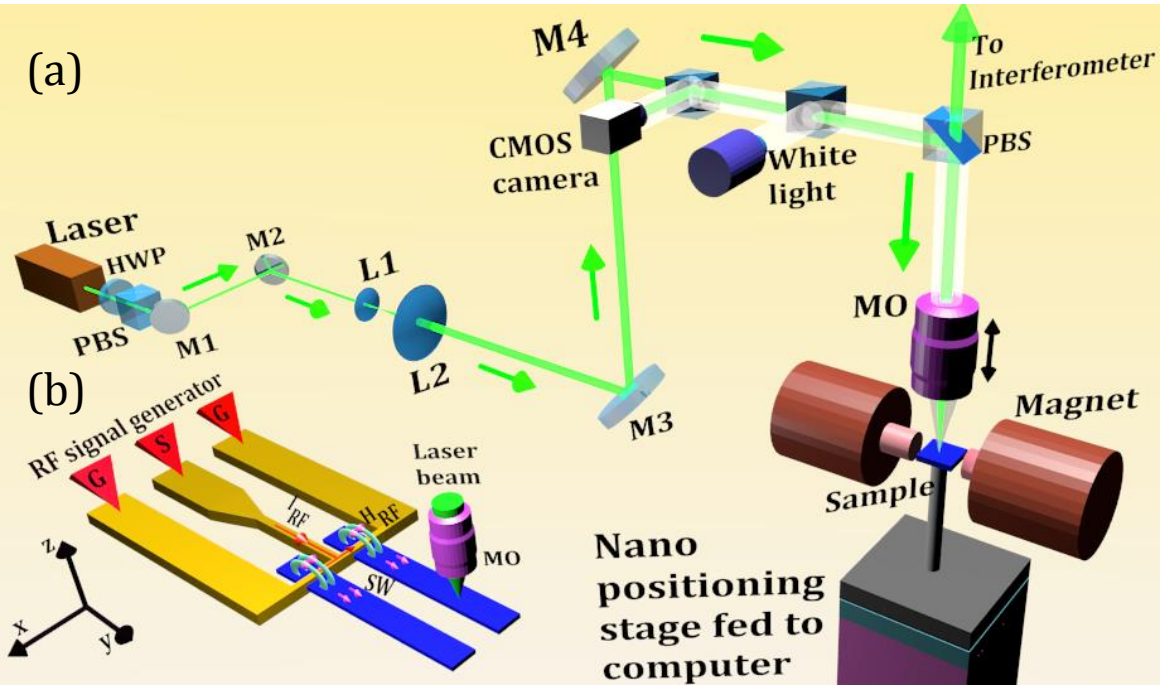

Figure 13.1. (a) Schematic of the experimental configuration of micro-BLS required for the spatial mapping the spin wave (SW) in magnetic heterostructures. Here, the laser beam is made focussed on to the sample using a microscope objective (MO) using some guiding mirrors (M's) and lenses (L's). The sample is placed on top of a nano-positioning stage and the scattered beam is collected by the same MO and directed towards an interferometer by using a polarizing beam splitter (PBS). A white light and a camera are collinearly arranged for positioning and stabilization of the sample. (b) Here, the SW of particular frequency is excited by a ground-signal-ground (GSG) type antenna which is connected to an RF signal generator. The RF current (I_{RF}) is launched on the antenna thereby creating an RF field (H_{RF}) to generate the SW into the magnetic sample which is generally prepared in the form of a stripe-like waveguide. Generally, some instruments such as the detector inside the interferometer, RF generator, the camera and the nano-

positioning stage are controlled by the computer for synchronized measurement during the spatial mapping of the SW in the sample.

The experimental tools (e.g. TRMOKE, BLS and FMR) described in this thesis possess their salient features in controlling magnetization dynamics of various patterned heterostructures. These can be employed for local or global modulation of magnetic properties which unlocks a gateway for exploring the domain wall motion, vortex and skyrmion dynamics [17] with or without of external stimuli (e.g. magnetic field, current or electric field) which can add a new edge to this booming research area. Also, several fundamental phenomena such as ultrafast demagnetization [18], damping, magneto-elastic coupling etc. can be explained using these novel techniques. Hence, the studies presented in this thesis are also useful for controlling magnetization dynamics under the influence of magnetic or electric field. This is essential for future application such as data storage or transfer and switching or logic operations.

Further, the experimental visualization of the propagating SWs under different magnetic or external parameters can be conceived for magnonic devices integrated with different genres of MCs that have been explored in this thesis. For that purpose, spatially resolved micro-BLS system [19] is necessary (schematically demonstrated in Figure 13.1) as it enables a 2D imaging of SW amplitude across a magnonic device. For instance, a SW is excited in such waveguide and it generates dynamic dipolar field (or dynamic stray field). Now, if a combination of more than one device is considered then the dynamic field in one can affect that in others. Thus, the amplitude and phase of the induced SW can be controlled by manipulating the material and physical or geometrical parameters of these waveguides which will act as input channels whereas the output (i.e. the superposition of the two induced excitations) will be extracted as the output. This can lead to the development of magnonic logic where the logic operation can be controlled by changing the parameters of these constituent waveguides.

The anisotropic propagation of SW [20] can also be very crucial for developing magnonic circuit components. When a SW of a particular frequency is launched in a magnetic medium, it follows the phase fronts of that frequency which represents the reflection of the iso-frequency contour in reciprocal space. In addition, the propagation of SW is primarily determined by the group velocity which is perpendicular to the iso-frequency contour at a certain wave vector. These contours are not isotropic viz. the

SWs do not follow a circular phase front which makes the investigation of this anisotropic propagation in MCs can be very interesting. Here, different magnonic bands possess different propagation characteristics depending upon the distribution of the scattering centres which can be tailored by material or structural parameters as well as by orientation of applied magnetic field. Hence the frequency dependent SW propagation in case of different 2D MCs demands a rigorous investigation leading to a novel approach of SW channelling controllable by SW frequency or magnetic field orientation.

References

[1] S. Choudhury, S. Majumder, S. Barman, Y. Otani, A. Barman, Phys. Rev. Appl. 10 (2018) 064044.
[2] S. Choudhury, S. Barman, Y. Otani, A. Barman, J. Magn. Magn. Mater. 489 (2019) 165408.
[3] S. Choudhury, S. Barman, Y. Otani, A. Barman, ACS Nano 11 (2017) 8814.
[4] S. Choudhury, S. Saha, R. Mandal, S. Barman, Y. Otani, A. Barman, ACS Appl. Mater. Interfaces 8 (2016) 18339.
[5] S. Choudhury, S. Pan, S. Barman, Y. Otani, A. Barman, J. Magn. Magn. Mater. 490 (2019) 165484.
[6] S. Neusser, G. Duerr, S. Tacchi, M. Madami, M. L. Sokolovskyy, G. Gubbiotti, M. Krawczyk, D. Grundler, Phys. Rev. B 84 (2011) 094454.
[7] K. Di, V. L. Zhang, M. H. Kuok, H. S. Lim, S. C. Ng, K. Narayanapillai, H. Yang, Phys. Rev. B 90 (2014) 060405.
[8] M. Krawczyk, D. Grundler, J. Phys. Condens. Matter 26 (2014) 123202.
[9] W. R. Branford, S. Ladak, D. E. Read, K. Zeissler, L. F. Cohen, Science 335 (2012) 1597.
[10] S. Tacchi, G. Duerr, J. W. Klos, M. Madami, S. Neusser, G. Gubbiotti, G. Carlotti, M. Krawczyk, D. Grundler, Phys. Rev. Lett. 109 (2012) 137202.
[11] V. Baltz, A. Manchon, M. Tsoi, T. Moriyama, T. Ono, Y. Tserkovnyak, Rev. Mod. Phys. 90 (2018) 015005.
[12] M. Matsuo, E. Saitoh, S. Maekawa, J. Phys. Soc. Jpn. 86 (2016) 011011.
[13] Y. Otani, M. Shiraishi, A. Oiwa, E. Saitoh, S. Murakami, Nat. Phys. 13 (2017) 829.
[14] H. Yang, G. Chen, A. A. C. Cotta, A. T. N'Diaye, S. A. Nikolaev, E. A. Soares, W. A. A. Macedo, K. Liu, A. K. Schmid, A. Fert, M. Chshiev, Nat. Mater. 17 (2018) 605.
[15] S. Sanvito, Nat. Phys. 6 (2010) 562.
[16] T. Nozaki, Y. Shiota, S. Miwa, S. Murakami, F. Bonell, S. Ishibashi, H. Kubota, K. Yakushiji, T. Saruya, A. Fukushima, S. Yuasa, T. Shinjo, Y. Suzuki, Nat. Phys. 8 (2012) 491.
[17] A. Fert, N. Reyren, V. Cros, Nat. Rev. Mater. 2 (2017) 17031.
[18] E. Beaurepaire, J. C. Merle, A. Daunois, J. Y. Bigot, Phys. Rev. Lett. 76 (1996) 4250.
[19] T. Sebastian, K. Schultheiss, B. Obry, B. Hillebrands, H. Schultheiss, Front. Phys. 3 (2015).
[20] S. Neusser, G. Duerr, H. G. Bauer, S. Tacchi, M. Madami, G. Woltersdorf, G. Gubbiotti, C. H. Back, D. Grundler, Phys. Rev. Lett. 105 (2010) 067208.